E. B. Podgoršak

Radiation Physics
for Medical Physicists

Springer

BIOLOGICAL AND MEDICAL PHYSICS,
BIOMEDICAL ENGINEERING

BIOLOGICAL AND MEDICAL PHYSICS, BIOMEDICAL ENGINEERING

The fields of biological and medical physics and biomedical engineering are broad, multidisciplinary and dynamic. They lie at the crossroads of frontier research in physics, biology, chemistry, and medicine. The Biological and Medical Physics, Biomedical Engineering Series is intended to be comprehensive, covering a broad range of topics important to the study of the physical, chemical and biological sciences. Its goal is to provide scientists and engineers with textbooks, monographs, and reference works to address the growing need for information.

Books in the series emphasize established and emergent areas of science including molecular, membrane, and mathematical biophysics; photosynthetic energy harvesting and conversion; information processing; physical principles of genetics; sensory communications; automata networks, neural networks, and cellular automata. Equally important will be coverage of applied aspects of biological and medical physics and biomedical engineering such as molecular electronic components and devices, biosensors, medicine, imaging, physical principles of renewable energy production, advanced prostheses, and environmental control and engineering.

E.B. Podgoršak

Radiation Physics
for Medical Physicists

With 115 Figures and 37 Tables

Springer

Professor Ervin B. Podgoršak, Ph.D., FCCPM, FAAPM, DABMP
Centre universitaire de santé McGill
McGill University Health Centre
Department of Medical Physics
1650 avenue Cedar
Montréal, Québec H3G 1A4, Canada
e-mail: epodgorsak@medphys.mcgill.ca

Mariani za razumevanje in pomoč

Preface

This book is intended as a textbook for a course in radiation physics in academic medical physics graduate programs. The book may also be of interest to the large number of professionals, not only physicists, who in their daily occupations deal with various aspects of medical physics and have a need to improve their understanding of radiation physics.

Medical physics is a rapidly growing specialty of physics, concerned with the application of physics to medicine mainly, but not exclusively, in the application of ionizing radiation to diagnosis and treatment of human disease. In contrast to other physics specialties, such as nuclear physics, solid-state physics, and high-energy physics, studies of modern medical physics attract a much broader base of professionals including graduate students in medical physics, medical residents and technology students in radiation oncology and diagnostic imaging, students in biomedical engineering, and students in radiation safety and radiation dosimetry educational programs. These professionals have diverse background knowledge of physics and mathematics, but they all have a common desire to improve their knowledge of the physics that underlies the application of ionizing radiation in diagnosis and treatment of disease.

The main target audience for this book is graduate students in medical physics and these students are assumed to possess the necessary background in physics and mathematics to be able to follow and master the complete textbook. Medical residents, technology students and biomedical engineering students, on the other hand, may find certain sections too challenging or esoteric; however, there are many sections in the book that they may find useful and interesting in their studies. Candidates preparing for professional certification exams in any of the medical physics subspecialties should find the material useful and some of the material would also help candidates preparing for certification examinations in medical dosimetry or radiation-related medical specialties.

Numerous textbooks that cover the various subspecialties of medical physics are available but they generally make a transition from elementary basic physics directly to the intricacies of the given medical physics subspecialty. The intent of this textbook is to provide the missing link between the elementary physics and the physics of the subspecialties.

The textbook is based on notes that I developed over the past 25 years of teaching radiation physics to M.Sc. and Ph.D. students in medical physics at McGill University. It contains eight chapters, each chapter covering a specific group of subjects related to radiation physics that, in my opinion, form the basic knowledge required from professionals working in contemporary medical physics. Most of the subjects covered in this textbook can be found discussed in greater detail in many other specialized physics texts, such as nuclear physics, quantum mechanics, modern physics, etc.; however, these texts are aimed at students in a specific physics specialty. They provide more in-depth knowledge of the particular specialty but provide no evident link with medical physics. Some of these important specialized texts are listed in the bibliography at the end of this book for the benefit of readers who wish to attain a better insight into the subjects discussed. To recognize the importance of relevant history for understanding of modern physics, Appendix 1 provides short biographies on scientists whose work is discussed in this book.

I am indebted to my colleagues in the Medical Physics Department of the McGill University Health Centre for their encouragement, approval and tolerance of my concentrating on the book during the past year. I am greatly indebted to my colleagues Dr. François DeBlois, Dr. Geoffrey Dean, Dr. Slobodan Devic, Michael D.C. Evans, Marina Olivares, William Parker, Horacio Patrocinio, Dr. Jan P. Seuntjens and Dr. Frank Verhaegen who helped me with discussions on specific topics as well as with advice on how to present certain ideas to make the text flow better. I also appreciate constructive comments from Dr. José M. Fernandez-Varea from the University of Barcelona.

I would also like to thank my colleague Dr. Wamied Abdel-Rahman, not only for helpful discussions of the subject matter, but also for his skillful drawing of the 100 figures presented in the textbook. Secretarial help from Margery Knewstubb and Tatjana Nišić is also very much appreciated.

Special thanks are due to my former teachers Drs. John R. Cameron and Paul R. Moran from the University of Wisconsin and Drs. Harold E. Johns and John R. Cunningham from the University of Toronto who introduced me to medical physics, a truly rewarding profession that brings together one's love of physics and compassion for patients.

Finally, I gratefully acknowledge that the completion of this book could not have been accomplished without the support and encouragement of my spouse Mariana. Especially appreciated are her enthusiasm for the project and her tolerance of the seemingly endless hours I spent on the project during the past year.

McGill University, Montréal,   *Ervin B. Podgoršak*
April 2005

Medical Physics: A Specialty and Profession

Current Status

Medical physics is a branch of physics concerned with the application of physics to medicine. It deals mainly, but not exclusively, with the use of ionizing radiation in diagnosis and treatment of human disease. In diagnostic procedures relatively low energy x rays (*diagnostic radiology*) and gamma rays (*nuclear medicine*) are used; in therapeutic procedures most commonly high energy (megavoltage) x rays and gamma rays or megavoltage electrons are used (*radiation therapy* or *radiation oncology* or *therapeutic radiology*).

Other applications of physics to medicine include the use of nuclear magnetic resonance in diagnosis of disease (*magnetic resonance imaging*), ultrasound in imaging, bioelectrical investigations of the brain (*electroencephalography*) and heart (*electrocardiography*), biomagnetic investigations of the brain (*magnetoencephalography*), medical uses of infrared radiation (*thermography*), heat for cancer therapy (*hyperthermia*), and lasers for surgery (*laser surgery*).

During the past two decades medical physics has undergone a tremendous evolution, progressing from a branch of science on the fringes of physics into an important mainstream discipline that can now be placed on equal footing with other more traditional branches of physics.

The four important sub-specialties in medical physics are related to:

1. Diagnostic imaging with x rays (*diagnostic radiology physics*)
2. Diagnostic imaging with radio-nuclides (*nuclear medicine physics*)
3. Treatment of cancer with ionizing radiation (*radiation oncology physics*)
4. Study of radiation hazards and radiation protection (*health physics*)

Brief History

The study and use of ionizing radiation in medicine started with three important discoveries: *x rays* by Wilhelm Roentgen in 1895, *natural radioactivity* by Henri Becquerel in 1896, and *radium* by Pierre and Marie Curie in 1898. Since then, ionizing radiation has played an important role in atomic and nuclear physics, and provided an impetus for development of radiology and radiotherapy as medical specialties and medical physics as a specialty of physics.

The potential benefit of x ray use in medicine for imaging and treatment of cancer was recognized within a few weeks of Roentgen's discovery of x rays. New medical specialties: radiology and radiotherapy evolved rapidly, both relying heavily on physicists for routine use of radiation as well as for development of new techniques and equipment. However, while radiology and radiotherapy have been recognized as medical professions since the early 1900s, medical physics achieved a professional status only in the second half of the last century.

Initially most technological advances in medical use of ionizing radiation were related to improvements in efficient x-ray beam delivery, development of analog imaging techniques, optimization of image quality with concurrent minimization of delivered dose, and an increase in beam energies for radiotherapy.

During the past two decades, on the other hand, most developments in radiation medicine were related to integration of computers in imaging, development of digital diagnostic imaging techniques, and incorporation of computers into therapeutic dose delivery with high-energy linear accelerators. Radiation dosimetry and treatment planning have also undergone tremendous advances in recent years: from development of new absolute and relative dosimetry techniques to improved theoretical understanding of basic radiation interactions with human tissues, and to introduction of Monte Carlo techniques in dose distribution calculations.

Educational Requirements

Pioneers and early workers in medical physics came from traditional branches of physics such as nuclear physics, high-energy physics, and solid-state physics. By chance they ended up working in nuclear medicine, radiology or radiotherapy, and developed the necessary skills and knowledge through on-the-job training. In addition to clinical work, they also promoted medical physics as a science as well as a profession, and developed graduate medical physics educational programs, first through special medical physics courses offered as electives in physics departments and later through independent, well-structured medical physics programs that lead directly to graduate degrees in medical physics.

Since medical physicists occupy a responsible position in the medical environment, they are required to have a broad background of education and experience. The requirement for basic education in physics and mathematics is obvious, but the close working relationship of medical physicists with physicians and medical scientists also requires some familiarity with basic medical sciences, such as anatomy, physiology, genetics, and biochemistry.

Today's sophistication of modern medical physics and the complexity of the technologies applied to diagnosis and treatment of human disease by radiation demand a stringent approach to becoming a member of the medical

physics profession. Currently, the most common path to a career in medical physics is academic progression, through a B.Sc. degree in one of the physical sciences but preferably in physics, to a M.Sc. degree in medical physics, and then to a Ph.D. degree in medical physics.

The minimum academic requirement for a practicing medical physicist is a M.Sc. degree in medical physics, and this level is adequate for physicists who are mainly interested in clinical and service responsibilities. However, medical physicists working in academic environments should possess a Ph.D. degree in medical physics.

Academic training alone does not make a medical physicist. In addition to academic training, practical experience with medical problems and equipment is essential, and this may be acquired through on-the-job clinical training or, preferably, through a structured two-year traineeship (also referred to as internship or residency) program in a hospital after graduation with a M.Sc. or Ph.D. degree in medical physics.

Many graduate programs are now available to an aspiring medical physicist and progression through the three educational steps (undergraduate B.Sc. degree in physics; graduate degree in medical physics; and residency in medical physics) is feasible, albeit still somewhat difficult to follow in practice because of the relatively low number of accredited academic and residency programs in medical physics. The number of these programs is growing, however. We are now in a transition period and within a decade, progression through the three steps will become mandatory for physicists entering the medical physics profession. The sooner broad-based didactic and clinical training through accredited educational programs in medical physics becomes the norm, the better it will be for the medical physics profession and for the patients the profession serves.

Accreditation of Medical Physics Educational Programs

Many universities around the world offer academic and clinical educational programs in medical physics. To achieve international recognition for its graduates a medical physics educational program should be accredited by an international accreditation body that attests to the program's meeting rigorous academic and clinical standards in medical physics. Currently, there is only one such international body, The *Commission on Accreditation of Medical Physics Educational Programs* (CAMPEP) that is sponsored by the American Association of Physicists in Medicine (AAPM), American College of Medical Physics (ACMP), American College of Radiology (ACR), and the Canadian College of Physicists in Medicine (CCPM). Eleven academic medical physics programs and 10 medical physics residency programs are currently accredited by the CAMPEP.

Certification

Several national professional medical physics organizations certify the competence of medical physicists. The certification is obtained through passing a rigorous written and oral examination that can be taken by candidates who possess a M.Sc. or Ph.D. degree in medical physics and have completed an accredited residency in medical physics. Currently the residency requirement is relaxed and a minimum of two years of work experience in medical physics after graduation with a M.Sc. or Ph.D. degree in medical physics is also accepted, because of the shortage of available residency positions.

The medical physics certification attests to the candidate's competence in the delivery of patient care in one of the subspecialties of medical physics. The requirement that its medical physics staff be certified provides a medical institution with the necessary mechanism to ensure that high standard medical physics services are given to its patients.

Appointments and Areas of Activities

Medical physicists are involved in four areas of activities: (1) *clinical service and consultation*; (2) *research and development*; (3) *teaching*; and (4) *administration*. They are usually employed in hospitals and other medical care facilities. Frequently the hospital is associated with a medical school and the physicists are members of the academic staff. In many non-teaching hospitals, physicists hold professional appointments in one of the clinical departments and are members of the professional staff of the hospital. Larger teaching hospitals usually employ a number of medical physicists who are organized into medical physics departments that provide physics services to clinical departments.

Career in Medical Physics

A career in medical physics is very rewarding and the work of medical physicists is interesting and versatile. A characteristic of modern societies is their ever-increasing preoccupation with health. Research in cancer and heart disease is growing yearly and many new methods for diagnosis and therapy are physical in nature, requiring the special skills of medical physicists not only in research but also in the direct application to patient care. Undergraduate students with a strong background in science in general and physics in particular who decide upon a career in medical physics will find their studies of medical physics interesting and enjoyable and their employment prospects after completion of studies excellent.

Contents

Appendices

First Solvay Conference on Physics

The photograph on the next page shows many of the outstanding physicists that shaped modern physics during the first decades of the 20th century. The photograph was taken during the First Solvay Conference (Conseil Solvay) on Physics held in Brussels in 1911.

The Solvay International Conferences on Physics, held every few years, are noted for their role in stimulating advances in atomic and quantum physics and were originally sponsored by Ernest Solvay (1838–1922), a Belgian industrial chemist and philanthropist who in the 1860s developed the ammonia process for the manufacture of sodium bicarbonate, widely used in the production of glass and soap.

In 1863 Solvay founded a company Solvay & Cie and during his lifetime transformed it into a global company currently headquartered in Brussels and specializing in pharmaceuticals, chemicals and plastics. Solvay was also a man of progressive social ideals and, after becoming wealthy, he founded several scientific institutes as well as philanthropic and charitable foundations. The International Solvay Institutes are now funded from an endowment fund, the Solvay Company and a number of other sources. To date 23 Solvay International Conferences on Physics were held; however, in terms of notable participants the first one that was held in 1911 seems to be of the greatest historical importance.

From left to right seated at the table:

Hermann Walther Nernst; Marcel Louis Brillouin; Ernest Solvay; Hendrik Antoon Lorentz; Emil Gabriel Warburg; Jean Baptiste Perrin; Wilhelm Wien; Marie Curie-Sklodowska; Raymond Poincaré.

From left to right standing:

Robert Goldschmidt; Max Planck; Heinrich Rubens; Arnold Sommerfeld; Frederick Lindemann; Louis de Broglie; Martin Knudsen; Fritz Hasenohrl; Georges Hostelet; Edouard Herzen; James Jeans; Ernest Rutherford; Heike Kamerlingh-Onnes; Albert Einstein; Paul Langevin.

Photograph taken by Benjamin Couprie © International Institutes for Physics and Chemistry Courtesy: Emilio Segrè Visual Archives, American Institute of Physics Reproduced with Permission.

1 Introduction to Modern Physics

This chapter provides an introduction to modern physics and covers basic elements of atomic, nuclear, relativistic and quantum physics. These elements form the background knowledge that is required for a study of medical radiation physics. The first three pages of this chapter present lists of basic physical constants, of important derived physical constants, and of milestones in modern and medical physics. These lists would normally be relegated to appendices at the end of the book; however, in this textbook they are given a prominent place at the beginning of the book to stress their importance to modern as well as to medical physics.

Medical physics is intimately related to modern physics and most milestone discoveries in modern physics were rapidly translated into medical physics, as evident from the list in Sect. 1.3. Medical physics is a perfect and long-standing example of translational research where basic experimental and theoretical discoveries are rapidly implemented into benefiting humanity through improved procedures in diagnosis and treatment of disease. A thorough understanding of the basics presented in this chapter will facilitate the readers' study of subsequent chapters and enhance their appreciation of the nature, importance and history of medical radiation physics.

1.1 Fundamental Physical Constants

Currently the best source of data on fundamental physical constants is the *Committee on Data for Science and Technology* (CODATA), an interdisciplinary scientific committee of the *International Council for Science*. The CODATA Task Group on Fundamental Constants was established in 1969 and its purpose is to periodically provide the scientific and technological communities with an internationally accepted set of values of fundamental physical constants for worldwide use. The data below (rounded off to four significant figures) were taken from the most recent CODATA set of values issued in 2002 (*www.codata.org*).

- **Avogadro's number** .... $N_A = 6.022 \times 10^{23}$ atom/g-atom

- **Avogadro's number** .... $N_A = 6.022 \times 10^{23}$ molecule/g-mole

- **Speed of light in vacuum** .... $c = 299\,800\,000$ m/s $\approx 3 \times 10^8$ m/s

- **Electron charge** .... $e = 1.602 \times 10^{-19}$ C

- **Electron rest mass** .... $m_{e^-} = 0.5110$ MeV/c^2

- **Positron rest mass** .... $m_{e^+} = 0.5110$ MeV/c^2

- **Proton rest mass** .... $m_p = 938.3$ MeV/c^2

- **Neutron rest mass** .... $m_n = 939.6$ MeV/c^2

- **Atomic mass unit** .... $u = 931.5$ MeV/c^2

- **Planck's constant** .... $h = 6.626 \times 10^{-34}$ J·s

- **Reduced Planck's constant** .... $\hbar = h/(2\pi) = 1.055 \times 10^{-34}$ J·s

- **Boltzmann's constant** ... $k = 1.381 \times 10^{-23}$ J·K^{-1} $= 0.8631 \times 10^{-4}$ eV·K^{-1}

- **Electric permittivity of vacuum** .... $\varepsilon_o = 8.854 \times 10^{-12}$ C/(V·m)

- **Magnetic permeability of vacuum** ....$\mu_o = 4\pi \times 10^{-7}$ (V·s)/(A·m)

- **Newtonian gravitation constant** ...... $G = 6.674 \times 10^{-11}$ m^3·kg^{-1}·s^{-2}

- **Proton mass / electron mass** .... $m_p/m_e = 1836.0$

- **Specific charge of electron** .... $e/m_e = 1.759 \times 10^{11}$ C·kg^{-1}

- **Planck's constant/electron charge** .... $h/e = 4.136 \times 10^{-15}$ V·s

1.2 Derived Physical Constants and Relationships

- **Speed of light** in vacuum

$$c = \frac{1}{\sqrt{\varepsilon_{\mathrm{o}}\mu_{\mathrm{o}}}} \approx 3 \times 10^8 \text{ m/s} \tag{1.1}$$

- **Reduced Planck's constant × speed of light in vacuum**

$$\hbar c = \frac{h}{2\pi}c = 197.3 \text{ MeV} \cdot \text{fm} = 197.3 \text{ eV} \cdot \text{nm} \approx 200 \text{ MeV} \cdot \text{fm} \tag{1.2}$$

- **Fine structure constant**

$$\alpha = \frac{e^2}{4\pi\varepsilon_{\mathrm{o}}}\frac{1}{\hbar c} \approx \frac{1}{137} \tag{1.3}$$

- **Bohr radius**

$$a_{\mathrm{o}} = \frac{\hbar c}{\alpha \; m_{\mathrm{e}}c^2} = \frac{4\pi\varepsilon_{\mathrm{o}}}{e^2}\frac{(\hbar c)^2}{m_{\mathrm{e}}c^2} = 0.5292 \text{ Å} \tag{1.4}$$

- **Rydberg energy**

$$E_{\mathrm{R}} = \frac{1}{2}m_{\mathrm{e}}c^2\alpha^2 = \frac{1}{2}\left[\frac{e^2}{4\pi\varepsilon_{\mathrm{o}}}\right]^2\frac{m_{\mathrm{e}}c^2}{(\hbar c)^2} = 13.61 \text{ eV} \tag{1.5}$$

- **Rydberg constant**

$$R_{\infty} = \frac{E_{\mathrm{R}}}{2\pi\hbar c} = \frac{m_{\mathrm{e}}c^2\,\alpha^2}{4\pi\,\hbar c} = \frac{1}{4\pi}\left[\frac{e^2}{4\pi\varepsilon_{\mathrm{o}}}\right]^2\frac{m_{\mathrm{e}}c^2}{(\hbar c)^3} = 109\,737 \text{ cm}^{-1} \tag{1.6}$$

- **Classical electron radius**

$$r_{\mathrm{e}} = \frac{e^2}{4\pi\varepsilon_{\mathrm{o}}m_{\mathrm{e}}c^2} = 2.818 \text{ fm} \tag{1.7}$$

- **Compton wavelength** of the electron

$$\lambda_{\mathrm{C}} = \frac{h}{m_{\mathrm{e}}c} = \frac{2\pi\hbar c}{m_{\mathrm{e}}c^2} = 0.02426 \text{ Å} \tag{1.8}$$

- **Thomson classical cross section** for free electrons

$$\sigma_{\mathrm{Th}} = \frac{8\pi}{3}r_{\mathrm{e}}^2 = 0.6653\,\text{b} = 0.6653 \times 10^{-24}\,\text{cm}^2 \tag{1.9}$$

1.3 Milestones in Modern Physics and Medical Physics

X rays	Wilhelm Konrad **Röntgen**	1895
Natural radioactivity	Antoine-Henri **Becquerel**	1896
Electron	Joseph John **Thomson**	1897
Radium-226	Pierre **Curie**, Marie **Curie**	1898
Alpha particle	Ernest **Rutherford**	1899
Energy quantization	Max **Planck**	1900
Special theory of relativity	Albert **Einstein**	1905
Photoelectric effect	Albert **Einstein**	1905
Characteristic x rays	Charles G. **Barkla**	1906
Alpha particle scattering	Hans **Geiger**, Ernest **Marsden**	1909
Atomic model	Ernest **Rutherford**	1911
Thermionic emission	Owen W. **Richardson**	1911
Electron charge	Robert **Millikan**	1911
Model of hydrogen atom	Neils **Bohr**	1913
Energy quantization	James **Franck**, Gustav **Hertz**	1914
Tungsten filament for x-ray tubes	William D. **Coolidge**	1916
Proton	Ernest **Rutherford**	1919
X-ray scattering (Compton effect)	Arthur H. **Compton**	1922
Exclusion principle	Wolfgang **Pauli**	1925
Quantum wave mechanics	Erwin **Schrödinger**	1926
Wave nature of the electron	Clinton J. **Davisson**, Lester H. **Germer**	1927
Cyclotron	Ernest O. **Lawrence**	1931
Neutron	James **Chadwick**	1932
Positron	Carl D. **Anderson**	1932
Artificial radioactivity	Irène **Joliot-Curie**, Frédéric **Joliot**	1934
Čerenkov radiation	Pavel A. **Čerenkov**, Sergei I. **Vavilov**	1934
Uranium fission	**Hahn, Strassman, Meitner, Frisch**	1939
Betatron	Donald W. **Kerst**	1940
Spontaneous fission	Gergij N. **Flerov**, Konstantin A. **Petržak**	1940
Nuclear magnetic resonance	Felix **Bloch**, Edward **Purcell**	1946
Cobalt-60 machine	Harold E. **Johns**	1951
Recoil-less nuclear transition	Rudolf L. **Mössbauer**	1957
Gamma Knife	Lars **Leksell**	1968
Computerized Tomography (CT)	Godfrey **Hounsfield**, Alan **Cormack**	1971
Magnetic resonance Imaging (MRI)	Paul C. **Lauterbur**, Peter **Mansfield**	1973

1.4 Physical Quantities and Units

Physical quantities are characterized by their numerical value (magnitude) and associated unit. The following rules apply in general:

- Customarily, symbols for *physical quantities* are set in *italic* type, while symbols for *units* are set in *roman* type (for example: $m = 21$ kg; $E = 15$ MeV; $K = 180$ cGy).
- The numerical value and the unit of a physical quantity must be separated by space (for example: 21 kg, <u>not</u> 21kg; 15 MeV, <u>not</u> 15MeV).
- The currently used metric system of units is known as the *Système International d'Unités* (International System of Units) with the international abbreviation SI. The system is founded on base units for *seven basic physical quantities*; all other quantities and units are derived from the seven base quantities and units.

  Length ℓ .... meter (m)
  Mass m .... kilogram (kg)
  Time t .... second (s)
  Electric current I .... ampere (A)
  Temperature T .... kelvin (K)
  Amount of substance .... mole (mol)
  Luminous intensity .... candela (cd)

- Examples of basic and derived quantities and their units are given in Table 1.1. The Système International obtains its international authority from the Meter Convention that was endorsed in 1875 by 17 countries; the current membership stands at 48 countries.

Table 1.1. The basic and several derived physical quantities and their units in Système International (SI) and in radiation physics

Physical quantity	Symbol	Units in SI	Units used in radiation physics	Conversion
Length	ℓ	m	nm, Å, fm	1 m = 10^9 nm = 10^{10} Å = 10^{15} fm
Mass	m	kg	MeV/c^2	1 MeV / c^2 = 1.78×10^{-30} kg
Time	t	s	ms, μs, ns	1 s = 10^3 ms = 10^6 μs = 10^9 ns
Current	I	A	mA, μA, nA	1 A = 10^3 mA = 10^6 μA = 10^9 nA
Temperature	T	K		
Velocity	υ	m/s		
Acceleration	a	m/s^2		
Frequency	ν	Hz		1 Hz = 1 s^{-1}
Charge	Q	C	e	1 e = 1.602×10^{-19} C
Force	F	N		1 N = 1 kg $\cdot$ m $\cdot$ s^{-2}
Momentum	p	N $\cdot$ s		1 N $\cdot$ s = 1 kg $\cdot$ m $\cdot$ s^{-1}
Energy	E	J	eV, keV, MeV	1 eV = 1.602×10^{-19} J = 10^{-3} keV
Power	P	W		1 W = 1 J / s = 1 V $\cdot$ A

1.5 Classification of Forces in Nature

Four distinct forces are observed in the interaction between various types of particles. These forces, in decreasing order of strength, are the *strong force*, *electromagnetic (EM) force, weak force* and *gravitational force* with relative strengths of 1, 1/137, 10^{-6}, and 10^{-39}, respectively. The four fundamental forces, their source and their transmitted particle are listed in Table 1.2.

Table 1.2. The four fundamental forces in nature

Force	Source	Transmitted particle	Relative strength
Strong	Strong charge	Gluon	1
EM	Electric charge	Photon	1/137
Weak	Weak charge	W^+, W^-, and Z^o	10^{-6}
Gravitational	Energy	Graviton	10^{-39}

- The ranges of the EM and gravitational forces are infinite ($1/r^2$ dependence where r is the separation between two interacting particles).
- The ranges of the strong and weak forces are extremely short (of the order of a few femtometers).

Each force results from a particular intrinsic property of the particles, such as strong charge, electric charge, weak charge, and energy.

- *Strong charge* enables the strong force transmitted by mass-less particles called gluons and resides in particles referred to as quarks.
- *Electric charge* enables the electromagnetic force transmitted by photons and resides in charged particles such as electrons, positrons, protons, etc.
- *Weak charge* enables the weak force transmitted by particles called W and Z^o and resides in particles called quarks and leptons.
- *Energy* enables the gravitational force transmitted by hypothetical particles called gravitons.

1.6 Classification of Fundamental Particles

Two classes of fundamental particles are known: *quarks* and *leptons.*

- *Quarks* are particles that exhibit strong interactions. They are constituents of hadrons (protons and neutrons) with a fractional electric charge (2/3 or $-$1/3) and are characterized by one of three types of strong charge called colour (red, blue, green). There are six known quarks: up, down, strange, charm, top, and bottom.
- *Leptons* are particles that do not interact strongly. Electron, muon, tau and their corresponding neutrinos fall into this category.

1.7 Classification of Radiation

Radiation is classified into two main categories, as shown in Fig. 1.1: *non-ionizing* and *ionizing*, depending on its ability to ionize matter. The ionization potential of atoms, *i.e.*, the minimum energy required for ionizing an atom, ranges from a few eV for alkali elements to 24.6 eV for helium (noble gas).

- *Non-ionizing radiation* cannot ionize matter because its energy is lower than the ionization potential of matter.
- *Ionizing radiation* can ionize matter either directly or indirectly because its energy exceeds the ionization potential of matter. It contains two major categories:
  – *Directly ionizing radiation* (charged particles)
    electrons, protons, alpha particles, heavy ions
  – *Indirectly ionizing radiation* (neutral particles)
    photons (x rays, gamma rays), neutrons

Directly ionizing radiation deposits energy in the medium through direct Coulomb interactions between the directly ionizing charged particle and orbital electrons of atoms in the medium.

Indirectly ionizing radiation (photons or neutrons) deposits energy in the medium through a two step process:

- In the first step a charged particle is released in the medium (photons release electrons or positrons, neutrons release protons or heavier ions).
- In the second step, the released charged particles deposit energy to the medium through direct Coulomb interactions with orbital electrons of the atoms in the medium.

Both directly and indirectly ionizing radiations are used in treatment of disease, mainly but not exclusively malignant disease. The branch of medicine that uses radiation in treatment of disease is called *radiotherapy*, *therapeutic radiology* or *radiation oncology*. *Diagnostic radiology* and *nuclear medicine* are branches of medicine that use ionizing radiation in diagnosis of disease.
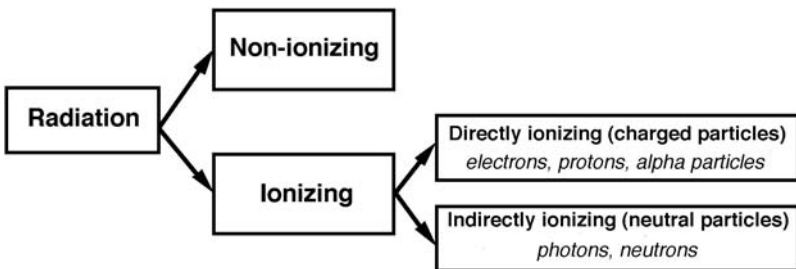
Fig. 1.1. Classification of radiation

1.8 Types and Sources of Directly Ionizing Radiation

Directly ionizing radiation consists of several groups of charged particles, such as light charged particles (electrons and positrons), heavy charged particles (protons, deuterons, and alpha particles), and heavier charged particles (e.g., carbon-12).

1.8.1 Electrons

Electrons play an important role in medical physics. They are used directly as beams for cancer therapy, they are responsible for the dose deposition in media by photon and electron beams, and they govern the experimental and theoretical aspects of radiation dosimetry.

- Electrons released in medium by photoelectric effect are referred to as *photoelectrons*.
- Electrons released in medium by Compton effect are referred to as *Compton* or *recoil electrons*.
- Electrons produced in medium by pair production interactions in the field of the nucleus or in the field of an orbital electron are referred to as *pair production electrons*.
- Electrons emitted from nuclei by β^- radioactive decay are referred to as *beta particles*.
- Electrons produced by linear accelerators (linacs), betatrons or microtrons for use in radiotherapy with kinetic energies typically in the range from 4 MeV to 30 MeV are referred to as *megavoltage electrons*.
- Electrons produced through Auger effect are referred to as *Auger electrons*, *Coster-Kronig electrons* or *super Coster-Kronig electrons*.
- Electrons produced through internal conversion are referred to as *internal conversion electrons*.
- Electrons produced by charged particle collisions are of interest in radiation dosimetry and are referred to as *delta (δ) rays*.

1.8.2 Positrons

- Positrons produced by pair production or triplet production are referred to as *pair production positrons*.
- Positrons emitted from nuclei by β^+ radioactive decay are used in positron emission tomography (PET) and referred to as *beta particles*.

1.8.3 Heavy Charged Particles

Heavy charged particles are produced for use in radiotherapy through acceleration of nuclei or ions in cyclotrons, synchrotrons or heavy particle linacs

- *Proton*: nucleus of hydrogen-1 ($_1^1$H) atom.

- *Deuteron*: Nucleus of deuterium ($^2_1$H) atom that consists of a proton and a neutron bound together with a total binding energy of 2.22 MeV.
- *Triton*: Nucleus of tritium ($^3_1$H) atom consisting of one proton and two neutrons bound together with a total binding energy of 8.48 MeV.
- *Helium*-3: Nucleus of helium-3 ($^3_2$He) atom consisting of 2 protons and 1 neutron bound together with a total binding energy of 7.72 MeV.
- *α particle*: Nucleus of helium-4 ($^4_2$He) atom consisting of 2 protons and 2 neutrons bound together with a total binding energy of 28.3 MeV.

1.8.4 Heavier Charged Particles

Heavier charged particles are nuclei or ions of heavier atoms such as carbon-12 ($^{12}_6$C), nitrogen-14 ($^{14}_7$N), or neon-20 ($^{20}_{10}$Ne).

1.8.5 Pions

Pions (negative π mesons) are produced in nuclear reactions of energetic electrons or protons striking target nuclei. In the past pions showed promise for use in radiotherapy; however, during recent years the studies of pions were abandoned in favor of heavy charged particles.

1.9 Classification of Indirectly Ionizing Photon Radiation

Indirectly ionizing photon radiation consists of four distinct groups of photons:

- *Characteristic (fluorescent) x rays* (see Sect. 3.1)
  result from electron transitions between atomic shells
- *Bremsstrahlung photons* (see Sect. 3.2)
  result from electron-nucleus Coulomb interactions
- *Gamma rays* (see Sect. 8.12)
  result from nuclear transitions
- *Annihilation quanta* (see Sect. 7.6.9)
  result from positron-electron annihilation

1.10 Radiation Quantities and Units

Accurate measurement of radiation is very important in any medical use of radiation, be it for diagnosis or treatment of disease. Several quantities and units were introduced for the purpose of quantifying radiation and the most important of these are listed in Table 1.3.

Table 1.3. Radiation quantities, units, and conversion between old and SI units

Quantity	Definition	SI unit	Old unit	Conversion
Exposure X	$X = \frac{\Delta Q}{\Delta m_{\mathrm{air}}}$	$2.58 \times \frac{10^{-4}\mathrm{C}}{\mathrm{kg air}}$	$1\ \mathrm{R} = \frac{1\ \mathrm{esu}}{\mathrm{cm}^3\ \mathrm{air_{STP}}}$	$1\ \mathrm{R} = 2.58 \times \frac{10^{-4}\mathrm{C}}{\mathrm{kg\ air}}$
Dose D	$D = \frac{\Delta E_{\mathrm{ab}}}{\Delta m}$	$1\ \mathrm{Gy} = 1\frac{\mathrm{J}}{\mathrm{kg}}$	$1\ \mathrm{rad} = 100\ \frac{\mathrm{erg}}{\mathrm{g}}$	$1\ \mathrm{Gy} = 100\ \mathrm{rad}$
Equivalent dose H	$H = D\,w_{\mathrm{R}}$	$1\ \mathrm{Sv}$	$1\ \mathrm{rem}$	$1\ \mathrm{Sv} = 100\ \mathrm{rem}$
Activity $\mathscr{A}$	$\mathscr{A} = \lambda\,N$	$1\ \mathrm{Bq} = 1\ \mathrm{s}^{-1}$	$1\ \mathrm{Ci} = 3.7 \times 10^{10}\ \mathrm{s}^{-1}$	$1\ \mathrm{Bq} = \frac{1\ \mathrm{Ci}}{3.7 \times 10^{10}}$

- *Exposure* is related to the ability of photons to ionize air. Its unit roentgen (R) is defined as charge of 2.58×10^{-4} C produced per kg of air.
- *Dose* is defined as the energy absorbed per unit mass of medium. Its unit gray (Gy) is defined as 1 J of energy absorbed per kg of medium.
- *Equivalent dose* is defined as the dose multiplied by a radiation-weighting factor. The unit of equivalent dose is sievert (Sv).
- *Activity* of a radioactive substance is defined as the number of decays per time. Its unit is Becquerel (Bq) corresponding to one decay per second.

where

ΔQ	is the charge of either sign collected,
Δm_{air}	is the mass of air,
ΔE_{ab}	is the absorbed energy,
Δm	is the mass of medium,
w_R	is the radiation weighting factor,
λ	is the the decay constant,
N	is the number of radioactive atoms,
R	stands for roentgen,
Gy	stands for gray,
Sv	stands for sievert,
Bq	stands for becquerel,
Ci	stands for curie,
STP	stands for standard temperature and standard pressure (273.2 K and 101.3 kPa, respectively).

1.11 Dose in Water for Various Radiation Beams

The dose deposition in water is one of the most important characteristics of the interaction of radiation beams with matter. This is true in general radiation physics and even more so in medical physics, where the dose deposition properties in tissue govern both the diagnosis of disease with radiation (*imaging physics*) as well as treatment of disease with radiation (*radiation oncology physics*).

Imaging with ionizing radiation is limited to the use of x-ray beams in *diagnostic radiology* and gamma rays in *nuclear medicine*, while in *radiation oncology* the use of radiation is broader and covers essentially all ionizing radiation types ranging from x rays and gamma rays through electrons to neutrons, protons and heavier charged particles. In diagnostic radiology imaging one is interested in the radiation beam that propagates through the patient, while in nuclear medicine one is interested in the radiation that emanates from the patient. In radiation oncology, on the other hand, one is interested in the energy deposited in the patient by a radiation source that is located outside the patient (external beam radiotherapy) or inside the tumor (brachytherapy).

Figure 1.2 displays depth doses in water normalized to 100 percent at depth dose maximum (percent depth doses) for various radiation types and energies; for indirectly ionizing radiation: in (a) for *photons* and in (b) for *neutrons*; and for directly ionizing radiation: in (c) for *electrons* and in (d) for *protons*. It is evident that the depth dose characteristics of radiation beams depend strongly upon beam type and energy. However, they also depend in a complex fashion on other beam parameters, such as field size, source-patient distance, etc. In general, indirectly ionizing radiation exhibits exponential-like attenuation in the absorbing media, while directly ionizing radiation exhibits a range in the absorbing media.

When considering the dose deposition in tissue by radiation beams, four beam categories are usually defined: two categories (*photons* and *neutrons*) for indirectly ionizing radiations and two categories (*electrons* and *heavy charged particles*) for directly ionizing radiations. Energy deposition in water by the four categories of radiation beams is clearly highlighted in Fig. 1.2.

1.11.1 Dose Distributions for Photon Beams

A photon beam propagating through air or vacuum is governed by the inverse-square law; a photon beam propagating through a patient, on the other hand, is not only affected by the inverse-square law but also by attenuation and scattering of the photon beam inside the patient. The three effects make the dose deposition in a patient a complicated process and its determination a complex task.

Typical dose distributions for several photon beams in the energy range from 100 kVp to 22 MV are shown in Fig. 1.2a. Several important points and regions of the absorbed dose curves may be identified. The beam enters the patient on the surface where it delivers a certain surface dose D_s. Beneath the surface the dose first rises rapidly, reaches a maximum value at a depth z_{max}, and then decreases almost exponentially until it reaches an exit dose value at the patient's exit point.

The depth of dose maximum is proportional to the beam energy and amounts to 0 for superficial (50–100 kVp) and orthovoltage (100–300 kVp)
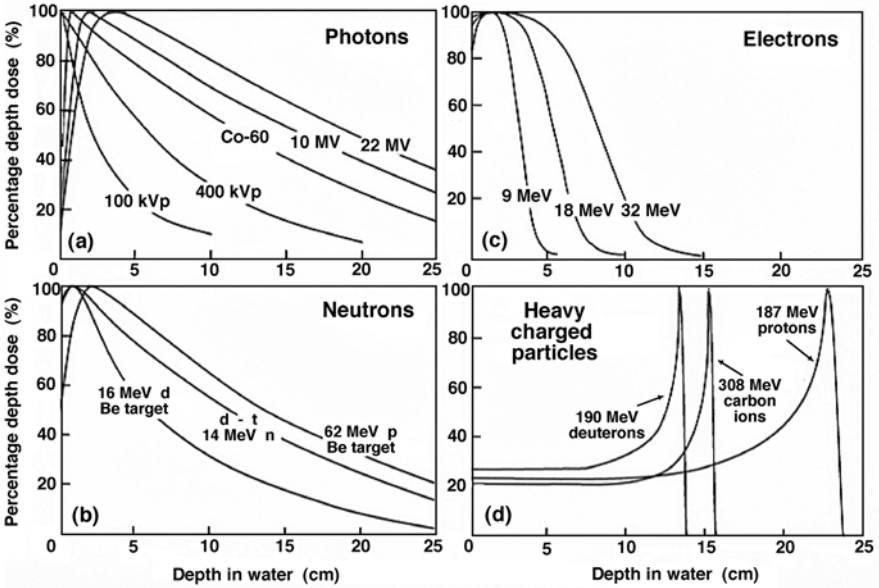
Fig. 1.2. Dose against depth in water for radiation beams of various types and energies. Parts **a** and **b** are for *indirectly ionizing radiation:* in **a** for photon beams in the range from 100 kVp to 22 MV and in **b** for neutron beams. Parts **c** and **d** are for *directly ionizing radiation*: in **c** for megavoltage electron beams in the range from 9 to 25 MeV and in **d** for heavy charged particle beams (187 MeV protons, 190 MeV deuterons and 308 MeV carbon ions)

beams; 0.5 cm for cobalt-60 gamma rays; 1.5 cm for 6 MV beams; 2.5 cm for 10 MV beams; and 4 cm for 22 MV beams.

The relatively low surface dose for high-energy photon beams (referred to as the *skin sparing effect*) is of great importance in radiotherapy for treatment of deep-seated lesions without involvement of the skin. The tumor dose can be concentrated at large depths in the patient concurrently with delivering a low dose to patient's skin that is highly sensitive to radiation and must be spared as much as possible when it is not involved in the disease.

The dose region between the surface and the depth of dose maximum z_{max} is called the dose *build-up region* and represents the region in the patient in which the dose deposition rises with depth as a result of the range of secondary electrons released in tissue by photon interactions with the atoms of tissue. It is these secondary electrons released by photons that deposit energy in tissue (indirect ionization). The larger is the photon energy, the larger is the range of secondary electrons and, consequently, the larger is the depth of dose maximum.

It is often assumed that at depths of dose maximum and beyond electronic equilibrium is achieved; however, a better term is transient electronic equilib-

rium because of the effects of photon beam attenuation as the photon beam penetrates into a patient. Electronic equilibrium or, more generally, charged particle equilibrium (CPE) exists for a volume if each charged particle of a given type and energy leaving the volume is replaced by an identical particle of the same type and energy entering the volume.

1.11.2 Dose Distributions for Neutron Beams

Neutron beams belong to the group of indirectly ionizing radiation, but, rather than releasing electrons like photons do, they release protons or heavier nuclei that then deposit their energy in absorbing medium through Coulomb interactions with the electrons and nuclei of the absorber.

As shown in Fig. 1.2b, the dose deposition characteristics in water by neutrons are similar to those of photon beams. Neutron beams exhibit a relatively low surface dose although the skin sparing effect is less pronounced than that for energetic photon beams. They also exhibit a dose maximum beneath the skin surface and an almost exponential decrease in dose beyond the depth of dose maximum. The dose build up region depends on neutron beam energy; the larger is the energy, the larger is the depth of dose maximum.

For comparison, we may state that a 14 MeV neutron beam has depth dose characteristics that are comparable to a cobalt-60 gamma ray beam; a 65 MeV neutron beam is comparable to a 10 MV x-ray beam.

1.11.3 Dose Distributions for Electron Beams

Electrons are directly ionizing radiation that deposit their energy in tissue through Coulomb interactions with orbital electrons and nuclei of the absorber atoms. Megavoltage electron beams represent an important treatment modality in modern radiotherapy, often providing a unique option for treatment of superficial tumors that are less than 5 cm deep. Electrons have been used in radiotherapy since the early 1950s, first produced by betatrons and then by linear accelerators. Modern high-energy linear accelerators used in radiotherapy typically provide, in addition to two megavoltage x-ray beams, several electron beams with energies from 4 to 25 MeV.

As shown in Fig. 1.2c, the electron beam dose distribution with depth in patient exhibits a relatively high surface dose and then builds up to a maximum dose at a certain depth referred to as the electron beam depth dose maximum z_{max}. Beyond z_{max} the dose drops off rapidly, and levels off at a small low-level dose component referred to as the *bremsstrahlung* tail. Several parameters are used to describe clinical electron beams, such as the most probable energy on the patient's skin surface, the mean electron energy on the patient's skin surface, or the depth at which the absorbed dose falls to 50 percent of the maximum dose.

The depth of dose maximum does not depend on beam energy, as is the case for photon beams; rather it is a function of machine design. On the other

hand, the beam penetration into tissue clearly depends on beam energy; the larger is the energy, the more penetrating is the electron beam, as is evident from Fig. 1.2c.

The bremsstrahlung component of the electron beam is the photon contamination of the beam that results from radiative losses experienced by the incident electrons as they penetrate the various machine components, air and the patient. The higher is the energy of the incident electrons, the higher is the bremsstrahlung contamination of the electron beam.

1.11.4 Dose Distributions for Heavy Charged Particle Beams

Heavy charged particle beams fall into the category of directly ionizing radiation and deposit their energy in tissue through Coulomb interactions with orbital electrons of the absorber. As they penetrate into tissue, heavy charged particles lose energy but, in contrast to electrons, do not diverge appreciably from their direction of motion and therefore exhibit a distinct range in tissue. This range depends on the incident particle's kinetic energy and mass.

Just before the heavy charged particle expended all of its kinetic energy, its energy loss per unit distance traveled increases drastically and this results in a high dose deposition at that point in tissue. As shown in Fig. 1.2d, this high dose region appears close to the particle's range, is very narrow, and defines the maximum dose deposited in tissue. This peak dose is referred to as the *Bragg peak* and it characterizes all heavy charged particle dose distributions.

Because of their large mass compared to the electron mass, heavy charged particles lose their kinetic energy only interacting with orbital electrons of the absorber; they do not lose any appreciable amount of energy through bremsstrahlung interactions with absorber nuclei.

1.12 Basic Definitions for Atomic Structure

The constituent particles forming an atom are *protons*, *neutrons* and *electrons*. Protons and neutrons are known as *nucleons* and form the nucleus of the atom.

- *Atomic number Z* is the number of protons and number of electrons in an atom.
- *Atomic mass number A* is the number of nucleons in an atom, i.e., number of protons Z plus number of neutrons N in an atom; i.e., $A = Z + N$.
- *Atomic mass $\mathcal{M}$* is expressed in atomic mass units u, where 1 u is equal to 1/12th of the mass of the carbon-12 atom ($A = 12$) or 931.5 MeV/c^2. The atomic mass $\mathcal{M}$ is smaller than the sum of individual masses of constituent particles because of the intrinsic energy associated with binding the particles (nucleons) within the nucleus (see Sect. 1.14).

- While for carbon-12 the atomic mass $\mathcal{M}$ is exactly 12 u, for other atoms $\mathcal{M}$ in u does not exactly match the atomic mass number A. However, for all atomic entities A (an integer) and $\mathcal{M}$ are very similar to each other and often the same symbol (A) is used for the designation of both.
- A chemical element generally contains atoms of same atomic number Z but varying atomic mass numbers A. The atomic mass A of the element is then the average atomic mass of all the chemical element's stable isotopes.
- The mass in grams equal to the average atomic mass of a chemical element contains exactly 6.022×10^{23} atoms (N_A = Avogadro's number) and is referred to as the *gram-atom* of the element. The number of atoms per gram of an element N_a/m is thus equal to the ratio N_A/A.

  For example: The atomic mass of natural cobalt is 58.9332 u. Thus a gram-atom of natural cobalt is 58.9332 g of natural cobalt and a mass of 58.9332 g of natural cobalt contains Avogadro's number of cobalt atoms.
- Number of electrons N_e per volume V of element

$$\frac{N_e}{V} = Z \frac{N_a}{V} = \rho Z \frac{N_a}{m} = \rho Z \frac{N_A}{A} \,. \tag{1.10}$$

- Number of electrons N_e per mass m of an element

$$\frac{N_e}{m} = \frac{Z N_a}{m} = \frac{Z N_A}{A} \,. \tag{1.11}$$

  Note that $(Z/A) \approx 0.5$ for all elements with one notable exception of hydrogen for which $(Z/A) = 1$. Actually, Z/A slowly decreases from 0.5 for low Z elements to 0.4 for high Z elements.
- In nuclear physics the convention is to designate a nucleus X as $^{A}_{Z}\text{X}$, where A is the atomic mass number and Z the atomic number. For example, the cobalt-60 nucleus is identified as $^{60}_{27}\text{Co}$, the radium-226 as $^{226}_{88}\text{Ra}$.
- If we assume that the mass of a molecule is equal to the sum of the masses of the atoms that make up the molecule, then for any molecular compound there are N_A molecules per g-mole of the compound where the *g-mole* (gram-mole or *mole*) in grams is defined as the sum of the atomic mass numbers of the atoms making up the molecule.

1.13 Basic Definitions for Nuclear Structure

Most of the atomic mass is concentrated in the atomic nucleus consisting of Z protons and $(A–Z)$ neutrons, where Z is the atomic number and A the atomic mass number of a given nucleus. The proton and neutron have nearly identical rest masses; the proton has positive charge, identical in magnitude to the negative electron charge and the neutron has no charge.

- There is no basic relation between the atomic mass number A and the atomic number Z in a nucleus, but the empirical relationship of (1.12)

$$Z = \frac{A}{1.98 + 0.0155A^{2/3}} \tag{1.12}$$

  provides a good approximation for stable nuclei.
- Protons and neutrons are commonly referred to as *nucleons*, have identical strong attractive interactions, and are bound in the nucleus with the *strong force*. In contrast to electrostatic and gravitational forces that are inversely proportional to the square of the distance between two particles, the strong force between two nucleons is a very short-range force, active only at distances of the order of a few fm. At these short distances the strong force is the predominant force exceeding other forces by several orders of magnitude.
- An element may be composed of atoms that all have the same number of protons, i.e., have the same atomic number Z, but have different numbers of neutrons, i.e., have different atomic mass numbers A. Such atoms of identical atomic number Z but differing atomic mass numbers A are called *isotopes* of a given element.
- The term isotope is often misused to designate nuclear species. For example, cobalt-60, cesium-137 and radium-226 are not isotopes, since they do not belong to the same element. Rather than isotopes, they should be referred to as *nuclides*. On the other hand, it is correct to state that deuterium (with nucleus called deuteron) and tritium (with nucleus called triton) are heavy isotopes of hydrogen or that cobalt-59 and cobalt-60 are isotopes of cobalt. The term *radionuclide* should be used to designate radioactive species; however, the term radioisotope is often used for this purpose.
- In addition to being classified into isotopic groups (common atomic number Z), nuclides are also classified into groups with common atomic mass number A (*isobars*) and common number of neutrons (*isotones*). For example, cobalt-60 and nickel-60 are isobars with 60 nucleons each ($A = 60$); hydrogen-3 (tritium) and helium-4 are isotones with two neutrons each ($A - Z = 2$).
- If a nucleus exists in an excited state for some time, it is said to be in an isomeric (metastable) state. *Isomers* thus are nuclear species that have common atomic number Z and common atomic mass number A. For example, technetium-99m is an isomeric state of technetium-99 and cobalt-60m is an isomeric state of cobalt-60.

1.14 Nuclear Binding Energies

The sum of masses of the individual components of a nucleus that contains Z protons and $(A - Z)$ neutrons is larger than the mass of the nucleus. This
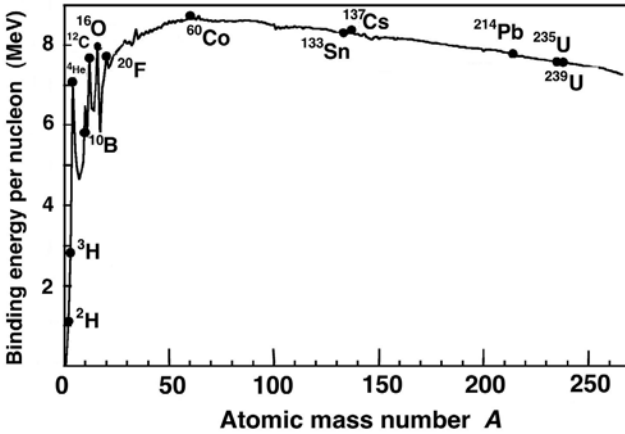
Fig. 1.3. Binding energy per nucleon in MeV/nucleon against atomic mass number A

difference in masses is called the mass defect (deficit) Δm and its energy equivalent Δmc^2 is called the total binding energy E_B of the nucleus.

- The *total binding energy* E_B of a nucleus can thus be defined as:
  1. The positive work required to disassemble a nucleus into its individual components: Z protons and $(A - Z)$ neutrons.
  2. The energy liberated when Z protons and $(A-Z)$ neutrons are brought together to form the nucleus.
- The *binding energy per nucleon* (E_B/A) in a nucleus (i.e., the total binding energy of a nucleus divided by the number of nucleons) varies with the number of nucleons A and is of the order of ~ 8 MeV/nucleon. It may be calculated from the energy equivalent of the mass deficit Δm as

$$\frac{E_B}{A} = \frac{\Delta mc^2}{A} = \frac{Zm_p c^2 + (A - Z)m_n c^2 - Mc^2}{A} \,, \qquad (1.13)$$

where

A	is the atomic mass number,
M	is the nuclear mass in atomic mass units u,
$m_p c^2$	is the proton rest energy,
$m_n c^2$	is the neutron rest energy.

As shown in Fig. 1.3, the binding energy per nucleon E_B/A against the atomic mass number A for A ranging from 1 to 270 exhibits the following characteristics:

1. For $1 \leq A \leq 4$ the binding energy per nucleon E_B/A rises rapidly from 1.1 MeV per nucleon for deuteron ($^2_1$H) through 2.8 and 2.6 MeV/nucleon for triton (^{3}H) and helium-3 ($^3_2$He), respectively, to 7.1 MeV/nucleon for helium-4 ($^4_2$He). The nucleus of the helium-4 atom is the α particle.

2. For $4 \leq A \leq 28$, E_{B}/A fluctuates and exhibits peaks for nuclides in which A is a multiple of four.
3. For $28 < A < 60$, E_{B}/A rises slowly with increasing A to reach a peak value of 8.8 MeV/nucleon for $A \approx 60$ (iron, cobalt, nickel).
4. For A exceeding 60, the E_{B}/A values fall monotonically from the peak of 8.8 MeV/nucleon to reach 7.3 MeV/nucleon for uranium-238.

The larger is the binding energy per nucleon (E_{B}/A) of an atom, the larger is the stability of the atom. Thus the most stable nuclei in nature are the ones with $A \approx 60$. Nuclei of light elements (small A) are generally less stable than the nuclei with $A \approx 60$ and the heaviest nuclei (large A) are also less stable than the nuclei with $A \approx 60$.

The peculiar shape of E_{B}/A against A curve suggests two methods for converting mass into energy: *fusion* of nuclei at low A and *fission* of nuclei at large A.

- *Fusion* of two nuclei of very small mass, e.g., $_1^2\mathrm{H} + _1^3\mathrm{H} \rightarrow {_2^4}\mathrm{He} + \mathrm{n}$, will create a more massive nucleus and release a certain amount of energy. Experiments using controlled nuclear fusion for production of energy have so far not been successful; however, steady progress is being made in various laboratories around the world.
- *Fission* of elements of large mass, e.g., $_{92}^{235}\mathrm{U}+\mathrm{n}$, will create two lower mass and more stable nuclei and lose some mass in the form of kinetic energy. Nuclear fission was observed first in 1934 by *Enrico Fermi* and described correctly by *Otto Hahn, Fritz Strassman, Lise Meitner* and *Otto Frisch* in 1939. In 1942 at the University of Chicago *Enrico Fermi* and colleagues carried out the first controlled chain reaction.

1.15 Nuclear Models

Several models of the nucleus have been proposed; all phenomenological and none of them capable of explaining completely the complex nature of the nucleus, such as its binding energy, stability, radioactive decay, etc. The two most successful models are the *liquid-drop model* that accounts for the nuclear binding energy and the *shell model* that explains nuclear stability.

1.15.1 Liquid-Drop Nuclear Model

The *liquid-drop* nuclear model, proposed by *Niels Bohr* in 1936, treats the nucleons as if they were molecules in a spherical drop of liquid. Scattering experiments with various particles such as electrons, nucleons and α particles reveal that to a first approximation nuclei can be considered spherical.

The radius R of a nucleus with atomic mass number A is estimated from the following expression

$$R = R_{\mathrm{o}} \sqrt[3]{A} \,, \tag{1.14}$$

where R_{o} is the nuclear radius constant equal to 1.2 fm (also quoted as 1.4 fm).

Using (1.14) we estimate the density of the nucleus with mass M and volume V as

$$\rho = \frac{M}{V} \approx \frac{A m_{\mathrm{p}}}{(4/3)\pi R^3} = \frac{m_{\mathrm{p}}}{(4/3)\pi R_{\mathrm{o}}^3} \approx 1.5 \times 10^{14} \ \mathrm{g \cdot cm^{-3}} \,, \tag{1.15}$$

where m_{p} is the rest mass of a proton.

Based on the liquid drop model of the nucleus the nuclear binding energy was split into various components, each with its own dependence on the atomic number Z and atomic mass number A. Four of the most important components of the nuclear binding energy are:

1. *Volume correction.* Since the binding energy per nucleon E_{B}/A is essentially constant, as shown in Fig. 1.3, the total nuclear binding energy is linearly proportional to A.
2. *Surface correction.* Nucleons on the surface of the liquid-drop have fewer neighbors than those in the interior of the drop. The surface nucleous will reduce the total binding energy by an amount proportional to R^2, where R is the nuclear radius proportional to $A^{1/3}$, as given in (1.14). Thus the surface effect correction is proportional to $A^{2/3}$.
3. *Coulomb repulsion correction* accounts for the Coulomb repulsion among protons in the nucleus. The repulsive energy reduces the total binding energy and is proportional to $Z(Z-1)$, the number of proton pairs in the nucleus, and inversely proportional to R, i.e., inversely proportional to $A^{1/3}$.
4. *Neutron excess correction* reduces the total binding energy and is proportional to $(A - 2Z)^2$ and inversely proportional to A.

The total nuclear binding energy E_{B} is then written as follows:

$$E_{\mathrm{B}} = C_1 A - C_2 A^{2/3} - C_3 \frac{Z(Z-1)}{A^{1/3}} - C_4 \frac{(A - 2Z)^2}{A} \,. \tag{1.16}$$

Equation (1.16) is referred to as the *Weizsäcker's semi-empirical binding energy formula* in which the various components are deduced theoretically but their relative magnitudes are determined empirically to match the calculated results with experimental data. The constants in (1.16) were determined empirically and are given as follows:

$$C_1 \approx 16 \ \mathrm{MeV}, C_2 \approx 18 \ \mathrm{MeV}, C_3 \approx 0.7 \ \mathrm{MeV}, \text{ and } C_4 \approx 24 \ \mathrm{MeV}.$$

1.15.2 Shell Structure Nuclear Model

Experiments have shown that the number of nucleons the nucleus contains affects the stability of nuclei. The general trend in binding energy per nucleon E_B/A, as shown in Fig. 1.3, provides the E_B/A maximum at around $A = 60$ and then drops for smaller and larger A. However, there are also considerable variations in stability of nuclei depending on the parity in the number of protons and neutrons forming a nucleus.

In nature there are approximately 275 nuclides that are considered stable with respect to radioactive decay. Some 60% of these stable nuclei have an even number of protons and an even number of neutrons (even-even nuclei); some 20% have an even-odd configuration and a further 20% have and odd even configuration. Only 5 stable nuclei are known to have an odd-odd configuration. A conclusion may thus be made that an even number of protons or even number of neutrons promotes stability of nuclear configurations.

When the number of protons is: 2, 8, 20, 28, 50, 82 or the number of neutrons is: 2, 8, 20, 28, 50, 82, 126, the nucleus is observed particularly stable and these numbers are referred to as *magic numbers*. Nuclei in which the number of protons as well as the number of neutrons is equal to a magic number belong to the most stable group of nuclei.

The existence of magic numbers stimulated a nuclear model containing a nuclear shell structure in analogy with the atomic shell structure configuration of electrons. In the nuclear shell model, often also called the independent particle model, the nucleons are assumed to move in well-defined orbits within the nucleus in a field produced by all other nucleons. The nucleons exist in quantized energy states of discrete energy that can be described by a set of quantum numbers, similarly to the situation with electronic states in atoms.

The ground state of a nucleus constitutes the lowest of the entire set of energy levels and, in contrast to atomic physics where electronic energy levels are negative, in nuclear physics the nuclear ground state is set at zero and the excitation energies of the respective higher bound states are shown positive with respect to the ground state.

To raise the nucleus to an excited state an appropriate amount of energy must be supplied. On de-excitation of a nucleus from an excited state back to the ground state a discrete amount of energy will be emitted.

1.16 Physics of Small Dimensions and Large Velocities

At the end of the 19-th century physics was considered a completed discipline within which most of the natural physical phenomena were satisfactorily explained. However, as physicists broadened their interests and refined their experimental techniques, it became apparent that classical physics suffers severe limitations in two areas:

1. *Dealing with dimensions comparable to small atomic dimensions.*
2. *Dealing with velocities comparable to the speed of light in vacuum.*

Modern physics handles these limitations in two distinct, yet related, sub-specialties: *quantum physics* and *relativistic physics*.

1. *Quantum physics* extends the range of application of physical laws to small atomic dimensions of the order of 10^{-10} m (radius of atom a), includes classical laws as special cases when dimension $\gg a$, and introduces the Planck's constant h as a universal constant of fundamental significance. *Erwin Schrödinger, Werner Heisenberg* and *Max Born* are credited with developing quantum physics in the mid 1920s.
2. *Relativistic physics* extends the range of application of physical laws to large velocities υ of the order of the speed of light c (3×10^8 m/s), includes classical laws as special cases when $\upsilon \ll c$, and introduces c as a universal physical constant of fundamental significance. The protagonist of relativistic physics was *Albert Einstein* who formulated the special theory of relativity in 1905.

1.17 Planck's Energy Quantization

Modern physics was born in 1900 when *Max Planck* presented his revolutionary idea of energy quantization of physical systems that undergo simple harmonic oscillations. Planck's energy ε quantization is expressed as

$$\varepsilon = nh\nu \ , \tag{1.17}$$

where

n is the quantum number ($n = 0,1,2,3...$),
h is a universal constant referred to as the Planck's constant,
ν is the frequency of oscillation.

The allowed energy states in a system oscillating harmonically are continuous in classical models, while in the Planck's model they consist of discrete allowed quantum states with values $nh\nu$, where n is a non-negative integer quantum number. Planck used his model to explain the spectral distribution of thermal radiation emitted by a blackbody (an entity that absorbs all radiant energy incident upon it). All bodies emit thermal radiation to their surroundings and absorb thermal radiation from their surroundings; in thermal equilibrium the rates of thermal emission and thermal absorption are equal.

- Planck assumed that sources of thermal radiation are harmonically oscillating atoms possessing discrete vibrational energy states. When an oscillator jumps from one discrete quantum energy state E_1 to another energy state E_2 where $E_1 > E_2$, the energy difference $\Delta E = E_1 - E_2$ is

emitted in the form of a photon with an energy $h\nu$, i.e.,

$$\Delta E = E_1 - E_2 = h\nu = hc/\lambda, \tag{1.18}$$

where
h is the Planck's constant,
ν is the frequency of the photon,
c is the speed of light in vacuum,
λ is the wavelength of the photon.

- Radiation, such as light, is emitted, transmitted, and absorbed in discrete energy quanta characterized by the product of frequency ν and Planck's constant h.
- Planck's postulate of energy quantization lead to the atomic model with its angular momentum quantization introduced by *Niels Bohr* in 1913 and to quantum wave mechanics developed by *Erwin Schrödinger* in 1926.
- The so-called *Schrödinger equation* (see Sect. 1.22), used extensively in atomic, nuclear and solid-state physics as well as in quantum mechanics, is a wave equation describing probability waves (wave functions) that govern the motion of small atomic particles. The equation has the same fundamental importance to quantum mechanics as Newton's laws have for large dimension phenomena of classical mechanics.

1.18 Quantization of Electromagnetic Radiation

Electromagnetic (EM) radiation incident on metallic surface may eject charged particles from the surface, as first observed by *Heinrich Hertz* in 1887. *Joseph Thomson* proved that the emitted charged particles were electrons and *Albert Einstein* in 1905 explained the effect by proposing that EM radiation was quantized similarly to the quantization of oscillator levels in matter introduced by *Max Planck* in 1900.

A quantum of electromagnetic radiation is called a *photon* and has the following properties:

- It is characterized by frequency ν and wavelength $\lambda = c/\nu$ where c is the speed of light in vacuum.
- It carries an energy $h\nu$ and momentum $p_\nu = h/\lambda$ where h is Planck's constant.
- It has zero rest mass.

In a metal the outer electrons move freely from atom to atom and behave like a gas with a continuous spectrum of energy levels. To release an electron from a metal a minimum energy characteristic of the given metal and referred to as the work function $e\phi$ must be supplied to the electron. Einstein postulated that the maximum kinetic energy $(E_K)_{max}$ of the electron ejected from

the surface of a metal by a photon with energy $h\nu$ is given by the following expression

$$(E_\text{K})_\text{max} = h\nu - e\phi \ . \tag{1.19}$$

The maximum kinetic energy of the ejected electron depends on the incident photon energy $h\nu$ and the work function $e\phi$ of the metal but does not depend on the incident radiation intensity.

- Electrons can be ejected from a metallic surface by the photoelectric effect only when the incident photon energy $h\nu$ exceeds the work function $e\phi$ of the metal, i.e., $h\nu > e\phi$.
- The photoelectric effect is a quantum phenomenon: a single electron absorbs a single photon; the photon disappears and the electron is ejected.
- The typical size of the work function $e\phi$ for metals is of the order of a few eV (e.g., aluminum: 4.3 eV; cesium: 2.1 eV; cobalt: 5.0 eV; copper: 4.7 eV; iron: 4.5 eV; lead: 4.3 eV; uranium: 3.6 eV), as given in the *Handbook of Chemistry and Physics* from the CRC Press. The work function is thus of the order of the energy $h\nu$ of visible photons ranging from 1.8 eV (700 nm) to 3 eV (400 nm) and near ultraviolet photons ranging in energy from 3 eV (400 nm) to 10 eV (80 nm).
- The effect of electron emission from metallic surfaces was called the photoelectric effect and its explanation by Einstein on the basis of quantization of EM radiation is an important contribution to modern physics.
- The surface photoelectric effect is related to the atomic photoelectric effect in which high-energy photons with energies exceeding the binding energy of orbital electrons eject electrons from atomic shells (see Sect. 7.5) rather than from metallic surfaces.

1.19 Einstein's Special Theory of Relativity

The special theory of relativity, introduced in 1905 by *Albert Einstein*, extends the range of physical laws to large velocities and deals with transformations of physical quantities from one inertial frame of reference to another. An *inertial frame of reference* implies motion with uniform velocity. The two postulates of special relativity theory are:

1. The laws of physics are identical in all inertial frames of reference.
2. The speed of light in vacuum c is a universal constant independent of the motion of the source.

Albert A. Michelson and *Edward W. Morley* in 1887 showed that the speed of light c is a universal constant independent of the state of motion of the source or observer. Einstein, with his special theory of relativity, explained the results of the Michelson-Morley experiment and introduced, in contrast to classical *Galilean transformations*, special transformations referred to as

Lorentz transformations to relate measurements in one inertial frame of reference to measurements in another inertial frame of reference.

When the velocities involved are very small, the Lorentz transformations simplify to the classical Galilean transformations, and the relativistic relationships for physical quantities transform into classical Newtonian relationships.

- Galilean and Lorentz transformations relate the spatial and time coordinates x, y, z, and t in a stationary frame of reference to the coordinates x', y', z', and t' in a reference frame moving with a uniform speed v in the x direction:

Galilean transformation   *Lorentz transformation*

$$x' = x - vt \qquad (1.20) \qquad\qquad x' = \gamma(x - vt) \qquad (1.21)$$

$$y' = y \qquad\qquad (1.22) \qquad\qquad y' = y \qquad\qquad (1.23)$$

$$z' = z \qquad\qquad (1.24) \qquad\qquad z' = z \qquad\qquad (1.25)$$

$$t' = t \qquad\qquad (1.26) \qquad\qquad t' = \gamma(t - xv/c^2) \qquad (1.27)$$

where

$$\gamma = (1 - v^2/c^2)^{-1/2}. \qquad (1.28)$$

- For $v \ll c$ the Lorentz transformation reduces to the Galilean transformation since $\gamma \approx 1$. The specific form of the Lorentz transformation is a direct consequence of $c = $ const in all frames of reference.

- Einstein also showed that atomic and subatomic particles, as they are accelerated to a significant fraction of the speed of light c, exhibit another relativistic effect, an increase in mass as a result of the mass-energy equivalence stated as $E = mc^2$, where m and E are the mass and energy, respectively, of the particle. A corollary to the second postulate of relativity is that no particle can move faster than c.

- ***Conservation of energy and momentum:***
  - In *classical mechanics* where $v \ll c$ the momentum given as $p = m_{\mathrm{o}}v$ and the kinetic energy given as $E_{\mathrm{K}} = m_{\mathrm{o}}v^2/2$ are conserved in all collisions (m_{o} is the mass of the particle at $v = 0$).
  - In *relativistic mechanics* where $v \approx c$ the relativistic momentum $p = mv = \gamma m_{\mathrm{o}}v$ and the total energy $E = m_{\mathrm{o}}c^2 + E_{\mathrm{K}}$ are conserved in all collisions.

1.20 Important Relativistic Relationships

In relativistic mechanics the mass of a particle is not a conserved quantity, since it depends on the velocity of the particle and may be converted into kinetic energy. The reverse transformation is also possible and kinetic energy may be converted into matter.

1.20.1 Relativistic Mass m

Newton's classical equation of motion is preserved in relativistic mechanics, i.e.,

$$\vec{F} = \frac{d\vec{p}}{dt} \, , \tag{1.29}$$

where $\vec{p}$ is the momentum of a particle acted upon by force $\vec{F}$. The momentum $\vec{p}$ is proportional to the velocity $\vec{v}$ of a particle through the relationship

$$\vec{p} = m\vec{v} \, , \tag{1.30}$$

where m is the mass of the particle dependent on the magnitude of the particle velocity v, i.e., $m = m(v)$.

The mass $m(v)$ is referred to as the *relativistic mass* of a particle and is given by the Einstein expression (see Fig. 1.4 and Table 1.4)

$$m(v) = \frac{m_{\mathrm{o}}}{\sqrt{1-\frac{v^2}{c^2}}} = \frac{m_{\mathrm{o}}}{\sqrt{1-\beta^2}} = \gamma m_{\mathrm{o}} \, , \tag{1.31}$$

or

$$\frac{m(v)}{m_{\mathrm{o}}} = \frac{1}{\sqrt{1 - \frac{v^2}{c^2}}} = \frac{1}{\sqrt{1 - \beta^2}} = \gamma \, , \tag{1.32}$$

where

m_{o} is the mass of a particle at $v = 0$ referred to as the particle *rest mass*,
c is the speed of light in vacuum, a universal constant,
β is v/c, i.e., particle velocity v normalized to speed of light c,
γ is $\frac{1}{\sqrt{1-\beta^2}}$ or $\frac{1}{\sqrt{1-(v^2/c^2)}}$.

Table 1.4. Mass versus velocity according to (1.32)

$(v/c) = \beta$	0.1	0.25	0.5	0.75	0.9	0.99	0.999	0.9999
$(m/m_{\mathrm{o}}) = \gamma$	1.005	1.033	1.155	1.512	2.294	7.089	22.37	70.71

1.20.2 Relativistic Force $\vec{F}$ and Relativistic Acceleration $\vec{a}$

In *classical physics* the Newton's second law of mechanics is given as follows:

$$\vec{F} = \frac{d\vec{p}}{dt} = m_{\mathrm{o}}\frac{d\vec{v}}{dt} = m_{\mathrm{o}}\vec{a} \, , \tag{1.33}$$

indicating that the acceleration $\vec{a}$ is parallel to force $\vec{F}$, and that mass m_{o} is constant.
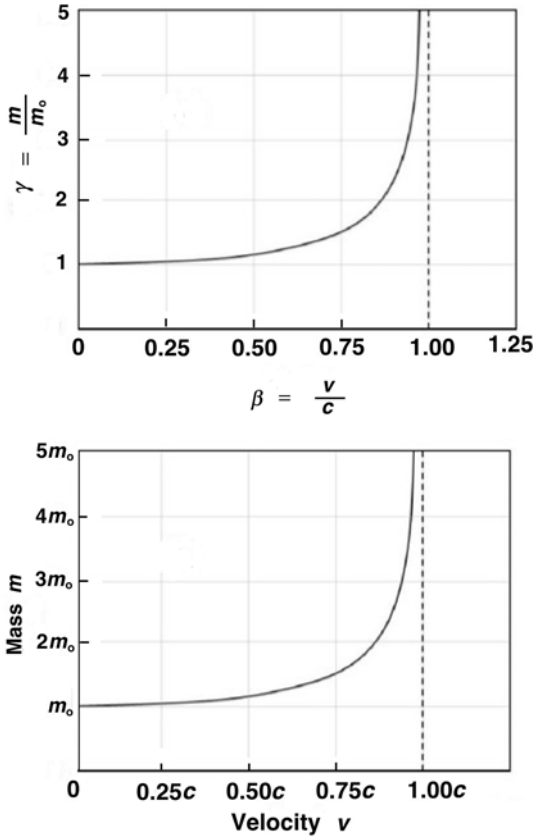
Fig. 1.4. Particle mass m as a function of its velocity v. A plot of γ against β of (1.32) in part **a**; a plot of m against v of (1.31) in part **b**

In *relativistic physics* the acceleration $\vec{a}$ is not parallel to the force $\vec{F}$ at large velocities because the speed of a particle cannot exceed c, the speed of light in vacuum. The force $\vec{F}$, with the mass m a function of particle velocity v, as given in (1.31), can be written as

$$\vec{F} = \frac{d\vec{p}}{dt} = \frac{d(m\vec{v})}{dt} = m\frac{d\vec{v}}{dt} + \vec{v}\frac{dm}{dt} \tag{1.34}$$

and

$$\vec{F} = \frac{d\vec{p}}{dt} = \frac{d(\gamma m_{\rm o}\vec{v})}{dt} = \gamma m_{\rm o}\frac{d\vec{v}}{dt} + m_{\rm o}\vec{v}\frac{d\gamma}{dt}$$

$$= \gamma m_{\rm o}\frac{d\vec{v}}{dt} + m_{\rm o}\vec{v}\frac{\gamma^3 v}{c^2}\frac{dv}{dt} , \tag{1.35}$$

where

$$\frac{d\gamma}{dt} = \frac{1}{[1 - \upsilon^2/c^2]^{3/2}} \frac{\upsilon}{c^2} \frac{d\upsilon}{dt} = \frac{\gamma^3 \upsilon}{c^2} \frac{d\upsilon}{dt} . \tag{1.36}$$

The acceleration $\vec{a} = d\vec{\upsilon}/dt$ will be determined by obtaining a dot product of the force $\vec{F}$ and velocity $\vec{\upsilon}$ as follows:

$$\vec{F} \cdot \vec{\upsilon} = \gamma m_{\mathrm{o}} \upsilon \frac{d\upsilon}{dt} + \frac{m_{\mathrm{o}} \gamma^3 \upsilon^3}{c^2} \frac{d\upsilon}{dt} = \gamma m_{\mathrm{o}} \upsilon \frac{d\upsilon}{dt} (1 + \gamma^2 \beta^2)$$

$$= \gamma^3 m_{\mathrm{o}} \upsilon \frac{d\upsilon}{dt} . \tag{1.37}$$

Inserting (1.37) into (1.35) gives the following result for the force $\vec{F}$

$$\vec{F} = \gamma m_{\mathrm{o}} \frac{d\vec{\upsilon}}{dt} + \frac{\vec{F} \cdot \vec{\upsilon}}{c^2} \vec{\upsilon} = \gamma m_{\mathrm{o}} \frac{d\vec{\upsilon}}{dt} + (\vec{F} \cdot \vec{\beta})\vec{\beta} . \tag{1.38}$$

Solving (1.38) for $\vec{a} = d\vec{\upsilon}/dt$ gives the relativistic relationship for $\vec{a}$

$$\vec{a} = \frac{d\vec{\upsilon}}{dt} = \frac{\vec{F} - (\vec{F} \cdot \vec{\beta})\vec{\beta}}{\gamma m_{\mathrm{o}}} . \tag{1.39}$$

For velocities $\upsilon \ll c$, where $\beta \to 0$ and $\gamma \to 1$, the relativistic expression for $\vec{a}$ transforms into the classical result $\vec{a} = d\vec{\upsilon}/dt = \vec{F}/m_{\mathrm{o}}$ with $\vec{a}$ parallel to $\vec{F}$.

1.20.3 Relativistic Kinetic Energy E_{K}

The expression for the relativistic kinetic energy $E_{\mathrm{K}} = E - E_{\mathrm{o}}$, where $E = mc^2$ is the total energy of the particle and $E_{\mathrm{o}} = m_{\mathrm{o}}c^2$ is its rest energy, is derived below.

The particle of rest mass m_{o} is initially at rest at the initial position x_{i} and moves under the influence of force F to its final position x_{f}. The work done by force F is the kinetic energy E_{K} of the particle calculated using the integration of (1.34) and the following five steps:

1. $$E_{\mathrm{K}} = \int\limits_{x_{\mathrm{i}}}^{x_{\mathrm{f}}} F dx = \int\limits_{x_{\mathrm{i}}}^{x_{\mathrm{f}}} \left(m \frac{d\upsilon}{dt} + \upsilon \frac{dm}{dt} \right) dx \tag{1.40}$$

2. Multiply (1.31) by c, square the result, and rearrange terms to obtain

$$m^2 c^2 - m^2 \upsilon^2 = m_{\mathrm{o}}^2 c^2 . \tag{1.41}$$

3. Differentiate (1.41) with respect to time t to obtain

$$c^2 \frac{d(m^2)}{dt} - \frac{d}{dt}(m^2 \upsilon^2) = 0 . \tag{1.42}$$

4. Equation (1.42), after completing the derivatives, gives

$$2c^2 m \frac{dm}{dt} - 2m^2 \upsilon \frac{d\upsilon}{dt} - 2\upsilon^2 m \frac{dm}{dt} = 0 . \tag{1.43}$$

5. After dividing (1.43) by $(2mv)$ we obtain the following expression

$$\frac{c^2}{v}\frac{dm}{dt} = m\frac{dv}{dt} + v\frac{dm}{dt} \ . \tag{1.44}$$

The expression for the kinetic energy E_K in (1.40) using (1.44) can be written as follows:

$$E_K = c^2 \int_{x_i}^{x_f} \frac{1}{v}\frac{dm}{dt} dx = c^2 \int_{m_o}^{m} dm = mc^2 - m_o c^2 = E - E_o \ , \tag{1.45}$$

since dx/dt is the particle velocity v by definition and the masses m and m_o correspond to particle positions x_i and x_f, respectively.

1.20.4 Total Relativistic E as a Function of Momentum p

The expression for the total relativistic energy E as a function of the relativistic momentum p is as follows:

$$E = \sqrt{E_o^2 + p^2 c^2} \ . \tag{1.46}$$

Equation (1.46) is obtained from Einstein's expression for the relativistic mass given in (1.31) as follows:

1. Square the relationship for the relativistic mass m of (1.31), multiply the result by c^4 and rearrange the terms to obtain

$$m^2 c^4 - m^2 c^2 v^2 = m_o^2 c^4 \ . \tag{1.47}$$

2. Equation (1.47) can be written as

$$E^2 - p^2 c^2 = E_o^2 \tag{1.48}$$

or

$$E = \sqrt{E_o^2 + p^2 c^2} \ , \tag{1.49}$$

using the common relativistic relationships for the total energy E, rest energy E_o and momentum p, i.e., $E = mc^2$, $E_o = m_o c^2$, and $p = mv$.

The following two relationships are also often used in relativistic mechanics:

1. The particle momentum p using (1.45) and (1.49) for the kinetic energy E_K and total energy E, respectively, can be expressed as

$$p = \frac{1}{c}\sqrt{E^2 - E_o^2} = \frac{1}{c}\sqrt{E_K^2 + 2E_K E_o} \ . \tag{1.50}$$

2. The particle speed v is, in terms of its total energy E and momentum p, given as

$$\frac{v}{c} = \frac{mvc}{mc^2} = \frac{pc}{E} \ . \tag{1.51}$$

1.20.5 Taylor Expansion for Relativistic Kinetic Energy and Momentum

The Taylor expansion of a function $f(x)$ about $x = a$ is given as follows:

$$
\begin{aligned}
f(x) = f(a) + (x - a)\left.\frac{df}{dx}\right|_{x=a} \\
+ \frac{(x - a)^2}{2!}\left.\frac{d^2 f}{dx^2}\right|_{x=a} + \ldots + \frac{(x - a)^n}{n!}\left.\frac{d^n f}{dx^n}\right|_{x=a} .
\end{aligned}
\tag{1.52}
$$

The Taylor expansion into a series given by (1.52) is particularly useful when one can neglect all but the first two terms of the series. For example, the first two terms of the Taylor expansion of the function $f(x) = (1 \pm x)^n$ about $x = 0$ for $x \ll 1$ are given as follows:

$$
f(x) = (1 \pm x)^n \approx 1 \pm nx .
\tag{1.53}
$$

- The approximation of (1.53) is used in showing that, for small velocities where $v \ll c$ or $v/c \ll 1$, the relativistic kinetic energy E_K of (1.45) transforms into the well-known classical relationship $E_K = m_o v^2 / 2$

$$
\begin{aligned}
E_K = E - E_o &= m_o c^2 \left(\frac{1}{\sqrt{1 - v^2/c^2}} - 1 \right) \\
&= m_o c^2 \left\{ (1 - v^2/c^2)^{1/2} - 1 \right\} \\
&\approx m_o c^2 \left\{ 1 - \left[-\frac{1}{2} \right] \frac{v^2}{c^2} - \ldots - 1 \right\} = \frac{m_o v^2}{2} .
\end{aligned}
\tag{1.54}
$$

- Another example for the use of the Taylor expansion of (1.53) is the classical relationship for the momentum $p = m_o v$ that, for $v \ll c$, i.e., $(v/c) \ll 1$, is obtained from the relativistic relationship for the momentum given in (1.50) as follows:

$$
\begin{aligned}
p = \frac{1}{c}\sqrt{E^2 - E_o^2} &= \frac{1}{c}\sqrt{m_o^2 c^4 \left(\frac{1}{1 - (v^2/c^2)} - 1 \right)} \\
&= \frac{m_o c^2}{c}\sqrt{\left(1 - \frac{v^2}{c^2} \right)^{-1} - 1} \\
&\approx m_o c \sqrt{1 + \frac{v^2}{c^2} + \ldots - 1} = m_o v .
\end{aligned}
\tag{1.55}
$$

1.20.6 Relativistic Doppler Shift

The speed of light emitted from a moving source is equal to c, a universal constant, irrespective of the source velocity. The energy as well as the wavelength and frequency of the emitted photons, on the other hand, depend on

the velocity of the moving source. The energy shift resulting from a moving source in comparison with the stationary source is referred to as the Doppler shift and the following conditions apply:

- When the source is moving toward the observer, the measured photon energy increases and the wavelength decreases (*blue Doppler shift*).
- When the source is moving away from the observer, the measured photon energy decreases and the wavelength increases (*red Doppler shift*).

1.21 Particle-Wave Duality: Davisson–Germer Experiment

Both the electromagnetic radiation (photons) and particles exhibit a *particle-wave duality* and both may be characterized with wavelength λ and momentum p related to one another through the following expression

$$\lambda = \frac{h}{p} , \tag{1.56}$$

where h is the Planck's constant.

In relation to particles, (1.56) is referred to as the de Broglie relationship and λ is referred to as the de Broglie wavelength of a particle in honour of *Louis de Broglie* who in 1924 postulated the existence of matter waves.

The wave nature of the electron was confirmed experimentally by *Clinton J. Davisson* and *Lester H. Germer* in 1927 who set out to measure the energy of electrons scattered from a nickel target. The target was in the form of a regular crystalline alloy that was formed through a special annealing process. The beam of electrons was produced by thermionic emission from a heated tungsten filament. The electrons were accelerated through a relatively low variable potential difference V that enabled the selection of the incident electron kinetic energy E_K.

- Davisson and Germer discovered that for certain combinations of electron kinetic energies E_K and scattering angles ϕ the intensity of scattered electrons exhibited maxima, similarly to the scattering of x rays from a crystal with a crystalline plane separation d that follows the Bragg relationship (see Fig. 1.5) with m an integer

$$2d \sin \phi = m\lambda . \tag{1.57}$$

- Similarly to Moseley's work with K_α characteristic x rays (see Sect. 2.5.2), *Davisson* and *Germer* determined the wavelength λ_e of electrons from the measured scattering angle ϕ at which the electron intensity exhibited a maximum.
- The measured λ_e agreed well with wavelengths calculated from the de Broglie relationship

$$\lambda_\mathrm{e} = \frac{h}{p} = \frac{h}{m_\mathrm{e} \upsilon} = \frac{2\pi\hbar c}{\sqrt{2m_\mathrm{e} c^2 eV}} , \tag{1.58}$$
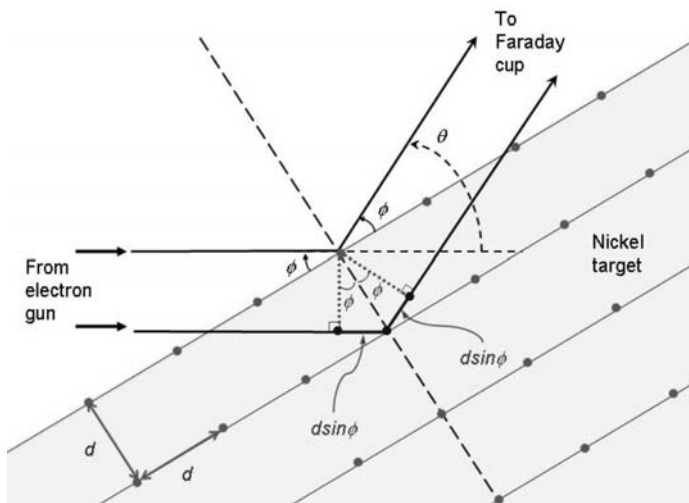
Fig. 1.5. Davisson–Germer experiment of elastic electron scattering on a nickel single crystal target. The electrons are produced in an electron gun and scattered by the nickel crystalline structure that has an atom spacing d and acts as a reflection grating. The maximum intensity of scattered electrons occurs as a result of constructive interference from electron matter waves following the Bragg relationship of (1.57)

where υ is the velocity of electrons determined from the classical kinetic energy relationship $E_{\mathrm{K}} = m_{\mathrm{e}}\upsilon^2/2 = eV$ with V the applied potential.

The experimentally determined *particle-wave duality* suggests that both the particle model and the wave model can be used for particles as well as for photon radiation. However, for a given measurement only one of the two models will apply. For example, in the case of photon radiation, the Compton effect is explained with the particle model, while the diffraction of x rays is explained with the wave model. On the other hand, the charge-to-mass ratio e/m_{e} of the electron implies a particle phenomenon, while the electron diffraction suggests wave-like behavior.

1.22 Matter Waves

Associated with any particle is a matter wave, as suggested by the de Broglie relationship of (1.56). This matter wave is referred to as the particle's wave function $\Psi(z,t)$ for one-dimensional problems or $\Psi(x,y,z,t)$ for three-dimensional problems and contains all the relevant information about the particle. Quantum mechanics or wave mechanics, developed by *Erwin Schrö-dinger* (wave mechanics) and *Werner Heisenberg* (matrix mechanics) between

1925 and 1929, is a branch of physics that deals with the properties of wave functions as they pertain to particles, nuclei, atoms, molecules and solids.

1.22.1 Introduction to Wave Mechanics

The *main characteristics* of wave mechanics are as follows:

- The theory has general application to microscopic systems and includes Newton's theory of macroscopic particle motion as a special case in the macroscopic limit.
- The theory specifies the laws of wave motion that the particles of any microscopic system follow.
- The theory provides techniques for obtaining the wave functions for a given microscopic system.
- It offers means to extract information about a particle from its wave function.

The *main attributes* of wave functions $\Psi(z,t)$ are:

- Wave functions are generally but not necessarily complex and contain the imaginary number i.
- Wave functions cannot be measured with any physical instrument.
- Wave functions serve in the context of Schrödinger's wave theory but contain physical information about the particle they describe.
- Wave functions must be single-valued and continuous functions of z and t to avoid ambiguities in predictions of the theory.

The information on a particle can be extracted from a complex wave function $\Psi(z,t)$ through a postulate proposed by *Max Born* in 1926 relating the probability density $dP(z,t)/dz$ in one dimension with the wave function $\Psi(z,t)$ as follows:

$$dP(z,t)/dz = \Psi^*(z,t) \cdot \Psi(z,t). \qquad (1.59)$$

Similarly we can relate the probability density $dP(x,y,z,t)/dV$ in three dimensions with the wave function $\Psi(x,y,z,t)$ as

$$dP(x,y,z,t)/dV = \Psi^*(x,y,z,t) \cdot \Psi(x,y,z,t), \qquad (1.60)$$

where Ψ^* is the complex conjugate of the wave function Ψ.

The probability density is real, non-negative and measurable. In one-dimensional wave mechanics, the total probability of finding the particle somewhere along the z axis in the entire range of the z axis is equal to one, if the particle exists. We can use this fact to define the following *normalization condition*

$$\int\limits_{-\infty}^{+\infty} \frac{dP(z,t)}{dz} dz = \int\limits_{-\infty}^{+\infty} \Psi^*(x,y,z,t)\Psi(x,y,z,t)dz = 1 . \qquad (1.61)$$

Similarly, in three-dimensional wave mechanics, the normalization expression is written as

$$\int\limits_{-\infty}^{+\infty} \frac{dP(z,t)}{dV} dV = \int\limits_{-\infty}^{+\infty} \int\limits_{-\infty}^{+\infty} \int\limits_{-\infty}^{+\infty} \Psi^*(x,y,z,t)\Psi(x,y,z,t)dxdydz = 1 \; , \tag{1.62}$$

where the volume integral extends over all space and represents a certainty that the particle will be found (unit probability). Any one-dimensional wave function $\Psi(z,t)$ that satisfies (1.61) is said to be normalized. Similarly, any three-dimensional wave function $\Psi(x,y,z)$ that satisfies (1.62) is also said to be normalized.

While the normalization condition expresses certainty that a particle, if it exists, will be found somewhere, the probability that the particle will be found in any interval $a \le z \le b$ is obtained by integrating the probability density $\Psi^* \cdot \Psi$ from a to b as follows:

$$P = \int\limits_{a}^{b} \Psi^* \cdot \Psi \, dV \; . \tag{1.63}$$

1.22.2 Quantum-Mechanical Wave Equation

The particulate nature of photons and the wave nature of matter are referred to as the wave-particle duality of nature. The waves associated with matter are represented by the wave function $\Psi(x,y,z,t)$ that is a solution to a quantum mechanical wave equation. This wave equation cannot be derived directly from first principles of classical mechanics; however, it must honor the following four conditions:

1. It should respect the de Broglie postulate relating the wavelength λ of the wave function with the momentum p of the associated particle: $p = h/\lambda = \hbar k$, where k is the wave number defined as $k = 2\pi/\lambda$.
2. It should respect the Planck's law relating the frequency ν of the wave function with the total energy E of the particle: $E = h\nu = \hbar\omega$.
3. It should respect the relationship expressing the total energy E of a particle of mass m as a sum of the particle's kinetic energy $E_{\mathrm{K}} = p^2/(2m)$ and potential energy V, i.e.,

$$E = \frac{p^2}{2m} + V \; . \tag{1.64}$$

4. It should be linear in $\Psi(z,t)$ which means that any arbitrary linear combination of two solutions for a given potential energy V is also a solution to the wave equation.

While the wave equation cannot be derived directly, we can determine it for a free particle in a constant potential and then generalize the result to

other systems and other potential energies. The free particle wave function $\Psi(z,t)$ can be expressed as follows:

$$\Psi(z,t) = Ce^{i(kz-\omega t)} , \tag{1.65}$$

where $(kz - \omega t)$ is the phase of the wave with $k = 2\pi/\lambda$ the wave number and $\omega = 2\pi\nu$ the angular frequency of the wave.

We now determine the partial derivatives $\partial/\partial x$ and $\partial/\partial t$ of the wave function to obtain

$$\frac{\partial \Psi(z,t)}{\partial z} = ikCe^{i(kz-\omega t)} = ik\Psi(z,t) = i\frac{p}{\hbar}\Psi(z,t) \tag{1.66}$$

and

$$\frac{\partial \Psi(z,t)}{\partial t} = -i\omega Ce^{i(kz-\omega t)} = -i\omega\Psi(z,t) = -i\frac{E}{\hbar}\Psi(z,t) . \tag{1.67}$$

Equation (1.66) can now be written as follows:

$$p\Psi(z,t) = -i\hbar\frac{\partial}{\partial z}\Psi(z,t) \tag{1.68}$$

where $(-i\hbar\partial/\partial z)$ is a differential operator for the momentum p.

Similarly we can write (1.67) as

$$E\Psi(z,t) = i\hbar\frac{\partial}{\partial t}\Psi(z,t) , \tag{1.69}$$

where $(i\hbar\partial/\partial t)$ is a differential operator for the total energy E.

Equations (1.68) and (1.69) suggest that multiplying the wave function $\Psi(z,t)$ by a given physical quantity, such as p and E in (1.68) and (1.69) has the same effect as operating on $\Psi(z,t)$ with an operator that is associated with the given physical quantity. As given in (1.64), the total energy E of the particle with mass m is the sum of its kinetic and potential energies.

If we now replace p and E in (1.64) with their respective operators, given in (1.68) and (1.69), we obtain

$$-\frac{\hbar^2}{2m}\frac{\partial^2}{\partial z^2} + V = i\hbar\frac{\partial}{\partial t} . \tag{1.70}$$

Equation (1.70) represents two new differential operators; the left hand side operator is referred to as the hamiltonian operator $[H]$, the right hand side operator is the operator for the total energy E. When the two operators of (1.70) are applied to a free particle wave function $\Psi(z,t)$ we get

$$-\frac{\hbar^2}{2m}\frac{\partial^2\Psi(z,t)}{\partial z^2} + V\Psi(z,t) = i\hbar\frac{\partial\Psi(z,t)}{\partial t} . \tag{1.71}$$

Equation (1.71) was derived for a free particle moving in a constant potential V; however, it turns out that the equation is valid in general for any potential energy $V(z,t)$ and is referred to as the time-dependent Schrödinger equation with $V(z,t)$ the potential energy describing the spatial and temporal dependence of forces acting on the particle of interest. The time-dependent

Schrödinger equation is thus in the most general three dimensional form written as follows:

$$-\frac{\hbar^2}{2m}\nabla^2\Psi(x,y,z,t) + V(x,y,z,t)\Psi(x,y,z,t) = i\hbar\frac{\partial\Psi(x,y,z,t)}{\partial t} \ .$$
(1.72)

1.22.3 Time-Independent Schrödinger Equation

In most physical situations the potential energy $V(z,t)$ only depends on z, i.e., $V(z,t) = V(z)$ and then the time-dependent Schrödinger equation can be solved with the method of separation of variables.

The wave function $\Psi(z,t)$ is written as a product of two functions $\psi(z)$ and $T(t)$, one depending on the spatial coordinate z only and the other depending on the temporal coordinate t only, i.e.,

$$\Psi(z,t) = \psi(z)T(t) \ .$$
(1.73)

Inserting (1.73) into the time-dependent wave equation given in (1.71) and dividing by $\psi(z)T(t)$ we get

$$-\frac{\hbar^2}{2m}\frac{1}{\psi(z)}\frac{\partial^2\psi(z)}{\partial z^2} + V(z) = i\hbar\frac{1}{T(t)}\frac{\partial T(t)}{\partial t} \ .$$
(1.74)

Equation (1.74) can be valid in general only if both sides, the left hand side that depends on z only and the right hand side that depends on t only, are equal to a constant, referred to as the separation constant Λ. We now have two ordinary differential equations: one for the spatial coordinate z and the other for the temporal coordinate t given as follows:

$$-\frac{\hbar^2}{2m}\frac{d^2\psi(z)}{dz^2} + V(z)\psi(z) = \Lambda\psi(z)$$
(1.75)

and

$$\frac{dT(t)}{dt} = -\frac{i\Lambda}{\hbar}T(t) \ .$$
(1.76)

The solution to the temporal equation is

$$T(t) = e^{-i\frac{\Lambda}{\hbar}t} \ ,$$
(1.77)

representing a simple oscillatory function of time with angular frequency $\omega = \Lambda/\hbar$. According to de Broglie and Planck the angular frequency must also be given as $E/\hbar$, where E is the total energy of the particle.

We can now conclude that the separation constant Λ equals the total particle energy E and obtain from (1.76) the following solution to the temporal equation

$$T(t) = e^{-i\frac{E}{\hbar}t} = e^{-i\omega t} \ ,$$
(1.78)

where we used Planck's relationship $\frac{E}{\hbar} = \omega$.

Recognizing that $\Lambda = E$ we can write (1.75) as

$$-\frac{\hbar^2}{2m}\frac{d^2\psi(z)}{dz^2} + V(z)\psi(z) = E\psi(z) \tag{1.79}$$

and obtain the so-called *time-independent Schrödinger wave equation* for the potential $V(z)$.

The essential problem in quantum mechanics is to find solutions to the time-independent Schrödinger equation for a given potential energy V, generally only depending on spatial coordinates. The solutions are given in the form of:

1. Physical wave functions $\psi(x, y, z)$ referred to as *eigenfunctions*.
2. Allowed energy states E referred to as *eigenvalues*.

The time-independent Schrödinger equation does not include the imaginary number i and its solutions, the eigenfunctions, are generally not complex. Since only certain functions (eigenfunctions) provide physical solutions to the time-independent Schrödinger equation, it follows that only certain values of E referred to as *eigenvalues* are allowed. This results in discrete energy values for physical systems and in energy quantization.

Many mathematical solutions are available as solutions to wave equations. However, to serve as a physical solution, an eigenfunction $\psi(z)$ and its derivative $d\psi/dz$ must be: (1) *finite*, (2) *single valued*, and (3) *continuous*.

Corresponding to each eigenvalue E_n is an eigenfunction $\psi_n(z)$ that is a solution to the time-independent Schrödinger equation for the potential $V_n(z)$. Each eigenvalue is also associated with a corresponding wave function $\Psi(z, t)$ that is a solution to the time-dependent Schrödinger equation and can be expressed as

$$\Psi(z, t) = \psi(z)e^{-i\frac{E}{\hbar}t} . \tag{1.80}$$

1.22.4 Measurable Quantities and Operators

As the term implies, a measurable quantity is any physical quantity of a particle that can be measured. Examples for measurable quantities are: position z, momentum p, kinetic energy E_K, potential energy V, total energy E, etc.

In quantum mechanics an operator is associated with each measurable quantity. The operator allows for a calculation of the average (expectation) value of the measurable quantity, provided that the wave function of the particle is known.

The *expectation value* (also referred to as the average or mean value) $\bar{Q}$ of a physical quantity Q, such as position z, momentum p, potential energy V, and total energy E of a particle is determined as follows provided that the particle's wave function $\Psi(z, t)$ is known

$$\bar{Q} = \int \Psi^*(z, t)[Q]\Psi(z, t)dz , \tag{1.81}$$

Table 1.5. Several measurable quantities and their associated operators used in quantum mechanics

Measurable quantity	Symbol	Associated operator	Symbol
Position	z	z	$[z]$
Momentum	p	$-i\hbar \frac{\partial}{\partial z}$	$[p]$
Potential energy	V	V	$[V]$
Kinetic energy	E_{K}	$-\frac{\hbar^2}{2m}\frac{\partial^2}{\partial z^2}$	$[E_{\mathrm{K}}]$
Hamiltonian	H	$-\frac{\hbar^2}{2m}\frac{\partial^2}{\partial z^2} + V$	$[H]$
Total energy	E	$i\hbar \frac{\partial}{\partial t}$	$[E]$

where $[Q]$ is the operator associated with the physical quantity Q. A listing of most common measurable quantities in quantum mechanics and their associated operators is given in Table 1.5.

The quantum uncertainty ΔQ for any measurable quantity Q is given as

$$\Delta Q = \sqrt{\overline{Q^2} - \bar{Q}^2} \, , \tag{1.82}$$

where $\bar{Q}^2$ is the square of the expectation value of the quantity Q and $\overline{Q^2}$ is the expectation value of Q^2.

- When $\Delta Q = 0$, the measurable quantity Q is said to be sharp and all measurements of Q yield identical results.
- In general $\Delta Q > 0$, and repeated measurements result in a distribution of measured points.

1.23 Uncertainty Principle

In classical mechanics the act of measuring the value of a measurable quantity does not disturb the quantity; therefore, the position and momentum of an object can be determined simultaneously and precisely. However, when the size of the object diminishes and approaches the dimensions of microscopic particles, it becomes impossible to determine with great precision at the same instant both the position and momentum of particles or radiation nor is it possible to determine the energy of a system in an arbitrarily short time interval.

Werner Heisenberg in 1927 proposed the *uncertainty principle* that limits the attainable precision of measurement results. The uncertainty principle covers two distinct components:

1. The *momentum-position uncertainty principle* deals with the simultaneous measurement of the position z and momentum p_z of a particle and

limits the attainable precision of z and p_z measurement to the following

$$\Delta z \Delta p_z \geq \frac{\hbar}{2} \, , \qquad (1.83)$$

where Δz is the uncertainty on z and Δp_z is the uncertainty on p_z. There are no limits on the precision of individual z and p_z measurements. However, in a simultaneous measurement of z and p_z the product of the two uncertainties cannot be smaller than $\hbar/2$, where $\hbar$ is the reduced Planck's constant ($\hbar = h/2\pi$). If z is known precisely ($\Delta z = 0$), then we cannot know p_z, since ($\Delta p_z = \infty$). The reverse is also true: if p_z is known exactly ($\Delta p_z = 0$), then we cannot know z, since $\Delta z = \infty$.

2. The other component (*energy-time uncertainty principle*) deals with the measurement of the energy E of a system and the time interval Δt required for the measurement. Similarly to the $(\Delta z, \Delta p_z)$ situation, Heisenberg uncertainty principle states the following

$$\Delta E \Delta t \geq \frac{\hbar}{2} \, , \qquad (1.84)$$

where ΔE is the uncertainty in the energy determination and Δt is the time interval taken for the measurement.

Classical mechanics sets no limits on the precision of measurement results and allows a deterministic prediction of the behavior of a system in the future. Quantum mechanics, on the other hand, limits the precision of measurement results and thus allows only probabilistic predictions of the system's behavior in the future.

1.24 Complementarity Principle

In 1928 *Niels Bohr* proposed the *principle of complementarity* postulating that any atomic scale phenomenon for its full and complete description requires that both its wave and particle properties be considered and determined, since the wave and particle models are complementary. This is in contrast to macroscopic scale phenomena where particle and wave characteristics (e.g., billiard ball vs. water wave) of the same macroscopic phenomenon are mutually incompatible rather than complementary.

Bohr's principle of complementarity is thus valid only for atomic size processes and asserts that these processes can manifest themselves either as waves or as particles (corpuscles) during a given experiment, but never as both during the same experiment. However, to understand and describe fully an atomic scale physical process the two types of properties must be investigated with different experiments, since both properties complement rather than exclude each other.

The most important example of this *particle-wave duality* is the photon, a mass-less particle characterized with energy, frequency and wavelength. How-

ever, in certain experiments such as in Compton effect the photon behaves like a particle; in other experiments such as double-slit diffraction it behaves like a wave.

Another example of the particle-wave duality are the wave-like properties of electrons as well as heavy charged particles and neutrons that manifest themselves through diffraction experiments (see, for example, Davisson-Germer experiment discussed in Sect. 1.21).

1.25 Tunneling

The particle-wave duality is highlighted in discussions of potential wells and potential barriers in quantum and wave mechanics; the potential wells attract and trap particles, potential barriers reflect or transmit them. While medical physics and clinical physics rarely deal with quantum and wave mechanics, there are several physical phenomena of importance to radiation physics and, by extension, to medical physics that can only be explained through wave-mechanical reasoning. *Tunneling*, for example, is a purely wave-mechanical phenomenon that is used in explaining two important effects in radiation physics: α decay and field emission. In addition, there are several other phenomena of importance in electronics that can be explained invoking tunneling such as, for example, in the periodic inversion of the ammonia molecule NH_3, used as standard in atomic clocks, and in a semiconductor device called tunnel diode that is used for fast switching in electronic circuits.

A *classical particle* incident on a square barrier will pass the barrier only if its kinetic energy E_K exceeds the barrier potential E_P. If $E_P > E_K$, the classical particle is reflected at the barrier and no transmission occurs because the region inside the barrier is forbidden to the classical particle.

A *quantum-mechanical particle* incident on a square barrier has access to regions on both sides of the barrier, irrespective of the relative magnitudes of the kinetic energy E_K and the barrier potential E_P. A matter wave is associated with the particle and it has a non-zero magnitude on both sides of the barrier as well as inside the barrier. The wave penetrates and traverses the barrier even when $E_P > E_K$, clearly contravening classical physics but conforming to the rules of wave mechanics. The wave function associated with a quantum-mechanical particle incident on a barrier must be continuous at the barrier, will exhibit an exponential decay inside the barrier, and will be continuous on the far side of the barrier. The non-zero probability for finding the particle on the opposite side of the barrier indicates that the particle may tunnel through the barrier or one may say that the particle undergoes the tunneling effect. In tunneling through a barrier, the particle behaves as a pure wave inside the barrier and as a pure particle outside the barrier.

1.25.1 Alpha Decay Tunneling

Alpha decay is considered a tunneling phenomenon in which α particles with kinetic energies between 4 MeV and 9 MeV tunnel through a potential barrier of the order of 30 MeV. The tunneling theory of the α decay was proposed by *George Gamow* in 1928. Inside the parent nucleus (atomic number Z) the α particle is free yet confined to the nuclear potential well by the strong nuclear force. The dimension of the well is of the order of few fm; once the α particle is beyond this distance from the center of the parent nucleus, it only experiences Coulomb repulsion between its charge $2e$ and the charge of the daughter nucleus $(Z-2)e$.

A classical α particle with kinetic energy $E_\mathrm{K} < 9$ MeV cannot overcome a potential barrier with $E_\mathrm{P} > 30$ MeV. On the other hand, a α particle with wave-like attributes may tunnel through the potential barrier and escape the parent nucleus through this purely quantum-mechanical phenomenon.

1.25.2 Field Emission Tunneling

Field emission is another interesting effect that is explained by the tunneling phenomenon. Here one relies on the wave phenomena of electrons to explain how electrons tunnel through a potential barrier (of the order of the work function) to escape the atoms of a metal through the application of a very strong electric field. This effect may be considered cold cathode emission in contrast to the well-known heated cathode emission that is used in the so-called Coolidge x-ray tubes, electron guns in linear accelerators, and many other instruments relying on the hot filament sources where electrons get "boiled-off" from the heated cathode. Modern application of field emission is in field emission microscope and in scanning tunneling microscope.

1.26 Maxwell's Equations

The basic laws of electricity and magnetism can be summarized by four basic Maxwell's equations on the assumption that no dielectric or magnetic material is present. Each of the four basic Maxwell's equations is also known under its own specific name honoring the physicist who derived the equation independently before Maxwell unified electric and magnetic forces under one umbrella. In radiation physics and in medical physics Maxwell's equations play an important role in the understanding of bremsstrahlung production, in waveguide theory of particle acceleration, and in the theory of ionization chamber operation.

Maxwell's equations may be expressed in integral form or in differential form and the two forms are linked through two theorems of vector calculus: the *Gauss's divergence theorem* and the *Stokes's theorem*. For a vector function $\vec{A}$ and volume V bounded by a surface S the two theorems are given as follows:

Gauss's theorem

$$\iiint_V \vec{\nabla} \cdot \vec{A} \, dV = \iiint_V \text{div} \vec{A} \, dV = \oiint_S \vec{A} \cdot dS \tag{1.85}$$

Stokes's theorem

$$\iint_S (\vec{\nabla} \times \vec{A}) \cdot d\vec{S} = \iint_S \text{curl} \vec{A} \cdot d\vec{S} = \oint_\ell \vec{A} \cdot d\vec{\ell} \tag{1.86}$$

Maxwell's equations (integral form on the left, differential form on the right) are given as follows:

$$\oiint \vec{\mathscr{E}} \cdot d\vec{S} = \frac{q}{\varepsilon_\text{o}} \qquad\qquad \vec{\nabla} \cdot \vec{\mathscr{E}} = \frac{\rho}{\varepsilon_\text{o}} \qquad\qquad \textit{Gauss's law}$$
$$\tag{1.87}$$

$$\oiint \vec{\mathscr{B}} \cdot d\vec{S} = 0 \qquad\qquad \vec{\nabla} \cdot \vec{\mathscr{B}} = 0 \qquad\qquad \textit{Gauss's law}$$
$$\tag{1.88}$$

$$\oint \vec{\mathscr{E}} \cdot d\vec{\ell} = -\frac{\partial}{\partial t} \iint \vec{\mathscr{B}} \cdot d\vec{S} \qquad \vec{\nabla} \times \vec{\mathscr{E}} = -\frac{\partial \vec{\mathscr{B}}}{\partial t} \qquad \textit{Faraday's law}$$
$$\tag{1.89}$$

$$\oint \vec{\mathscr{B}} \cdot d\vec{\ell} = \mu_\text{o} I + \frac{1}{c^2}\frac{\partial}{\partial t} \iint \vec{\mathscr{E}} \cdot d\vec{S}) \quad \vec{\nabla} \times \vec{\mathscr{B}} = \mu_\text{o}(\vec{j} + \frac{\partial \vec{\mathscr{B}}}{\partial t}) \quad \textit{Ampère's law,}$$
$$\tag{1.90}$$

where $\vec{\mathscr{E}}$ and $\vec{\mathscr{B}}$ are the electric and magnetic fields, respectively; ρ and $\vec{j}$ are the charge density and current density, respectively, ε_o and μ_o are the permittivity and permeability, respectively, of vacuum; q is the total charge; and I is the current.

Maxwell's equations combined with the *Lorentz force* and *Newton's second law of motion* provide a complete description of the classical dynamics of interacting charged particles and electromagnetic fields. The Lorentz force F_L for charge q moving in electric field $\vec{\mathscr{E}}$ and magnetic field $\vec{\mathscr{B}}$ with velocity $\vec{v}$ is given as follows:

$$F_\text{L} = q(\vec{\mathscr{E}} + \vec{v} \times \vec{\mathscr{B}}) \,. \tag{1.91}$$

Ernest Rutherford and Niels Bohr, Giants of Modern Physics

The photographs on the next page show stamps issued in honor of physicists *Ernest Rutherford* (1871–1937) and *Niels Bohr* (1885–1962), the two scientists credited with developing our current atomic model. According to the Rutherford-Bohr atomic model most of the atomic mass is concentrated in the positively charged nucleus and the negative electrons revolve in orbits about the nucleus. New Zealand issued the stamp for Rutherford and Denmark for Bohr, both countries honoring their respective native son. Both physicists received Nobel Prizes for their work: Rutherford in 1908 "for investigations into the disintegration of elements and the chemistry of radioactive substances", Bohr in 1922 for work on the structure of atoms.

Rutherford studied in New Zealand and England, but spent all his professional life first in Canada at McGill University in Montreal (1898–1907) and then in England at the University of Manchester (1908–1919) and the Cavendish Laboratory in Cambridge (1919–1937). During his nine years at McGill, Rutherford published some 70 papers and worked with Frederick Soddy on the disintegration theory of radioactivity. In his 12 years at the University of Manchester, Rutherford collaborated with Geiger and Marsden and, based on their experiments, proposed the nuclear model of the atom. In Cambridge, Rutherford continued using alpha particles from radium and polonium sources to probe the atom. He collaborated with James Chadwick who in 1932 discovered the neutron and with Charles Wilson, the developer of the "cloud chamber".

Rutherford is considered one of the most illustrious scientists of all time. His work on the atomic structure parallels Newton's work in mechanics, Darwin's work on evolution, Faraday's work in electricity and Einstein's work on relativity.

Bohr studied at the Copenhagen University and spent most of his professional life there, except for short intervals in 1912 and in 1914–1916 when he worked with Rutherford in Manchester. He built a renowned school of theoretical and experimental physics at the University of Copenhagen and became its first director from its inauguration in 1921 to his death in 1962. The school is now known as the Niels Bohr Institute. Bohr is best known for his introduction of the electron angular momentum quantization into the atomic model that is now referred to as the Rutherford-Bohr atom. He also made numerous other contributions to theoretical physics, most notably with his complementarity principle and the liquid drop nuclear model.

Bohr was also interested in national and international politics and advised Presidents Roosevelt and Truman as well as Prime Minister Churchill on scientific issues in general and nuclear matters in particular. Bohr enjoyed a tremendous esteem from physics colleagues, world leaders and the general public, and among the scientists of the 20th century only Albert Einstein and Marie Curie have reached the same level.

2 Rutherford–Bohr Atomic Model

This chapter is devoted to a discussion of the Rutherford–Bohr atomic model. First, it covers the intriguing Geiger–Marsden experiment of α-particle scattering on thin gold foils, the results of which lead to the Rutherford's ingenious conclusion that most of the atom is empty space and that most of the atomic mass is concentrated in an atomic nucleus. The kinematics of α-particle scattering is then discussed in some detail and the Bohr derivation of the hydrogen atom kinematics is presented. The simple hydrogen atom calculations are supplemented with corrections for the finite mass of the nucleus and the correspondence principle is introduced. Next, the concepts of one-electron atoms are expanded to multi-electron atoms through the Hartree approximation, and the exclusion principle and the periodic table of elements are introduced. The chapter concludes with a description of experiments that substantiate the Rutherford–Bohr atomic model and with a calculation of the ground state of the hydrogen atom based on the time-independent Schrödinger equation.
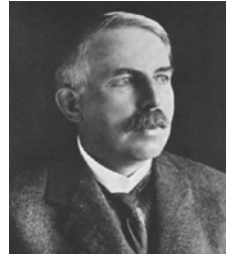
2.1 Geiger–Marsden Experiment

Hans Geiger and *Ernest Marsden* in 1909 carried out an experiment studying the scattering of 5.5 MeV α particles on a thin gold foil with a thickness of the order of 10^{-6} m. The α particles were obtained from radon-222, a natural α-particle emitter. The experiment, shown schematically in Fig. 2.1, seems rather mundane, however, its peculiar and unexpected results had a profound effect on modern physics in particular and on the humanity in general.

At the time of the Geiger–Marsden experiment Thomson's atomic model was the prevailing atomic model based on an assumption that the positive and the negative (electron) charges of an atom were distributed uniformly over the atomic volume ("plum-pudding" model).

It was *Ernest Rutherford* who concluded that the peculiar results of the Geiger–Marsden experiment did not support the Thomson's atomic model and proposed the currently accepted model in which:

1. mass and positive charge of the atom are concentrated in the nucleus the size of which is of the order of 10^{-15} m;
2. negatively charged electrons revolve about the nucleus.

The two competing atomic models are shown schematically in Fig. 2.2 (see Sect. 2.2.1); the *Thomson model* in part a, the *Rutherford model* in part b.

2.1.1 Parameters of the Geiger–Marsden Experiment

In the Geiger–Marsden experiment the kinetic energy of the α particles was 5.5 MeV and the radius of the gold–79 nucleus $^{197}_{79}\mathrm{Au}$ is determined as follows [see (1.14)]:

$$R = R_o \sqrt[3]{A} = 1.4 \text{ fm } \sqrt[3]{197} \approx 8 \text{ fm} . \tag{2.1}$$
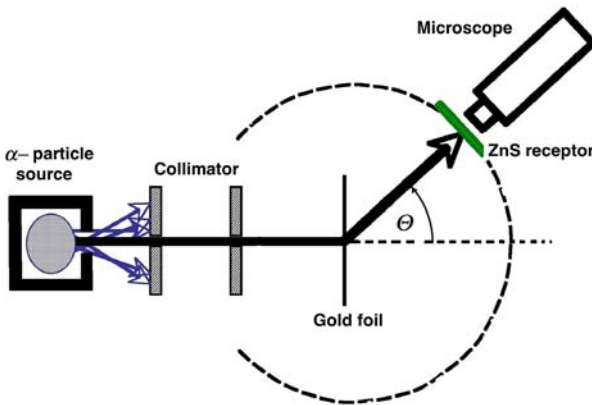
Fig. 2.1. Schematic diagram of the *Geiger–Marsden experiment* in the study of α-particle scattering on gold nuclei in a thin gold foil. Θ is the scattering angle

The distance of closest approach $D_{\alpha-\mathrm{N}}$ between the α particle and the nucleus is determined by equating E_{K}, the kinetic energy of the α particle at ∞, with E_{P}, the electric potential energy at $D_{\alpha-\mathrm{N}}$, and solving for $D_{\alpha-\mathrm{N}}$ to get

$$D_{\alpha-\mathrm{N}} = \frac{zZe^2}{4\pi\varepsilon_o} \frac{1}{E_K} = \frac{2 \times 79 \times e \times 1.6 \times 10^{-19} \text{ As Vm}}{4\pi \times 8.85 \times 10^{-12} \text{ As } 5.5 \times 10^6 \text{ eV}}$$

$$\approx 41 \text{ fm}. \tag{2.2}$$

Three important observations may now be made based on these parameters:

- For naturally occurring α particles interacting with nuclei of atoms the distance of closest approach $D_{\alpha-\mathrm{N}}$ exceeds the radius R of the nucleus. The α particle thus does not penetrate the nucleus.
- Nature provided Geiger and Marsden with ideal conditions to probe the nucleus. The radon-222 α particles have an energy of 5.5 MeV which is large enough to allow penetration of the atom but it is neither too large to cause nuclear penetration with associated nuclear reactions nor is it too large to require relativistic treatment of the α-particle velocity.
- Since artificial nuclear reactions and the relativistic mechanics were not understood at the time when the Geiger–Marsden experiment was carried out, Rutherford would not be able to solve with such elegance the atomic model question if the kinetic energy of the α particles used in the experiment was much larger or much smaller than 5.5 MeV.

The speed v_α of the α particles relative to the speed of light in vacuum c for 5.5 MeV α particles can be calculated using either the classical or the relativistic relationship (note that $m_\alpha c^2 \approx 4 \times 939$ MeV):

The *classical calculation* is done using the classical expression for the kinetic energy E_{K} of the α particle [see (1.45)]

$$E_{\mathrm{K}} = \frac{m_\alpha v_\alpha^2}{2} = \frac{1}{2} m_\alpha c^2 \left\{ \frac{v_\alpha^2}{c^2} \right\} . \tag{2.3}$$

Solve (2.3) for v_α/c to obtain

$$\frac{v_\alpha}{c} = \sqrt{\frac{2E_{\mathrm{K}}}{m_\alpha c^2}} = \sqrt{\frac{2 \times 5.5 \text{ } MeV}{4 \times 939 \text{ MeV}}} = 0.054 \tag{2.4}$$

The *relativistic calculation* using the relativistic expression for the kinetic energy E_{K} of the α particle

$$E_{\mathrm{K}} = \frac{m_\alpha c^2}{\sqrt{1 - \left(\frac{v_\alpha}{c}\right)^2}} - m_\alpha c^2 . \tag{2.5}$$

Solve (2.5) for v_α/c to obtain

$$\frac{v_\alpha}{c} = \sqrt{1 - \frac{1}{\left(1 + \frac{E_{\mathrm{K}}}{m_\alpha c^2}\right)^2}} = \sqrt{1 - \frac{1}{\left(1 + \frac{5.5}{4 \times 939}\right)^2}} = 0.054 . \tag{2.6}$$

The relativistic and classical calculations give identical results since the ratio of velocities $(v_\alpha/c) \ll 1$ for particles with kinetic energy E_K of the order of a few MeV. Rutherford's use of the simple classical relationship for the kinetic energy of the naturally occurring α particles was thus justified.

2.1.2 Thomson's Atomic Model

Joseph J. Thomson, who is also credited with the discovery of the electron in 1897, proposed an atomic model in which the negatively charged electrons were dispersed uniformly within a continuous spherical distribution of positive charge with a radius of the order of 1 Å. The electrons formed rings and each ring could accommodate a certain upper limit in the number of electrons and then other rings began to form. With this ring structure Thomson could in principle account for the periodicity of chemical properties of elements. A schematic representation of the Thomson's atomic model ("*plum-pudding model*") is given in Fig. 2.2a.

– In the ground state of the atom the electrons are fixed at their equilibrium positions and emit no radiation.
– In an excited state of the atom the electrons oscillate about their equilibrium positions and emit radiation through dipole oscillations by virtue of possessing charge and being continuously accelerated or decelerated (Larmor relationship).

According to the Thomson's atomic model the angular distribution of α particles scattered in the gold foil in the Geiger–Marsden experiment is
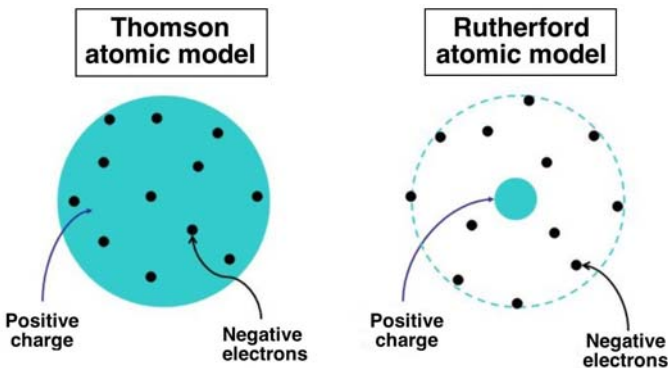
Fig. 2.2. Schematic diagram of two atomic models: **a** Thomson's "plum-pudding" model in which the electrons are uniformly distributed in the sea of positive atomic charge and **b** Rutherford's nuclear model in which the electrons revolve in empty space around the nucleus that is positively charged and contains most of the atomic mass

Gaussian and given by the following expression

$$N(\Theta)d\Theta = \frac{2I\Theta}{\overline{\Theta^2}}e^{-\Theta^2/\overline{\Theta^2}}d\Theta \ , \tag{2.7}$$

where

Θ	is the scattering angle of the α particle after it passes through the gold foil (the α particle undergoes $\sim 10^4$ interactions as a result of a foil thickness of 10^{-6} m and an approximate atomic diameter of 10^{-10} m),
$N(\Theta)d\Theta$	is the number of α particles scattered within the angular range of Θ to $\Theta + \mathrm{d}\Theta$,
I	is the number of α particles striking the gold foil,
$\overline{\Theta^2}$	is the mean square net deflection experimentally determined to be of the order of 3×10^{-4} rad^2, i.e., $(\overline{\Theta^2})^{1/2} = 1°$.

Geiger and Marsden found that more than 99% of the α particles incident on the gold foil were scattered at angles less than 3° and that their distribution followed a Gaussian distribution given in (2.7). However, Geiger and Marsden also found that one in $\sim 10^4$ α particles was scattered with a scattering angle $\Theta > 90°$ which implied a probability of 10^{-4} for scattering with $\Theta > 90°$, in drastic disagreement with the probability of 10^{-3500} predicted by the theory based on the Thomson's atomic model, as shown below.

According to the Thomson atomic model the probability for α-particle scattering with $\Theta > 90°$ (i.e., with a scattering angle Θ between $\pi/2$ and π) is calculated by integrating (2.7) as follows:

$$\frac{N(\Theta > \frac{\pi}{2})}{I} = \frac{\int\limits_{\pi/2}^{\pi} N(\Theta)d\Theta}{I} = -\int\limits_{\pi/2}^{\pi} e^{-\Theta^2/\overline{\Theta^2}}d(\Theta^2/\overline{\Theta^2}) = -\left. e^{-\frac{\Theta^2}{\overline{\Theta^2}}}\right|_{\pi/2}^{\pi}$$

$$= -e^{-\left\{\frac{180°}{1°}\right\}^2} + e^{-\left\{\frac{90°}{1°}\right\}^2} = e^{-90^2} \approx 10^{-3500} \ , \tag{2.8}$$

where we use the value of 1° for the root mean square angle $\sqrt{\overline{\Theta^2}}$.

2.2 Rutherford Atom and Rutherford Scattering

The theoretical result of 10^{-3500} for the probability of α-particle scattering with a scattering angle greater than 90° on a Thomson atom is an extremely small number in comparison with the result of 10^{-4} obtained experimentally by Geiger and Marsden. This highlighted a serious problem with the Thomson's atomic model and stimulated *Ernest Rutherford* to propose a completely new model that agreed with experimental results obtained by Geiger and Marsden.

2.2.1 Rutherford Model of the Atom

Contrary to Thomson's "plum-pudding" atomic model, depicted schematically in Fig. 2.2a, essentially all mass of the Rutherford atom is concentrated in the atomic nucleus that is also the seat of the positive charge of the atom and has a radius of the order of 10^{-15} m, as shown schematically in Fig. 2.2b. Electrons are distributed in a spherical cloud on the periphery of the Rutherford atom with a radius of the order of 10^{-10} m.

2.2.2 Kinematics of Rutherford Scattering

Based on his model and four additional assumptions, Rutherford derived the kinematics for the scattering of α particles on gold nuclei using basic principles of classical mechanics. The four additional assumptions are as follows.

1. the mass M of the gold nucleus is much larger than the mass of the α particle m_α, i.e., $M \gg m_\alpha$.
2. Scattering of α particles on atomic electrons is negligible because $m_\alpha \gg m_e$, where m_e is the electron mass.
3. The α particle does not penetrate the nucleus (no nuclear reactions).
4. The classical relationship for the kinetic energy E_K of the α particle, i.e., $E_K = m_\alpha v^2/2$, is valid, where v is the velocity of the α particle.

The interaction between the α particle (charge ze) and the nucleus (charge Ze) is a repulsive Coulomb interaction between two positive point charges, and, as a result, the α particle follows a hyperbolic trajectory, as shown schematically in Fig. 2.3.

As shown in Fig. 2.3, the nucleus is in the outer focus of the hyperbola because of the repulsive interaction between the α particle and the nucleus. The relationship between the impact parameter b and the scattering angle θ may be derived most elegantly by determining two independent expressions for the change in momentum Δp of the scattered α particle. Note that θ represents the scattering angle in a single α-particle interaction with one nucleus, whereas Θ represents the scattering angle resulting from the α particle traversing the thin gold foil and undergoing 10^4 interactions while traversing the foil.

The momentum transfer is along a line that bisects the angle $\pi - \theta$, as indicated in Fig. 2.3. The magnitude of the Coulomb force F_{coul} acting on the α particle is given by

$$F_{coul} = \frac{zZe^2}{4\pi\varepsilon_o}\frac{1}{r^2} \ , \tag{2.9}$$

where

r is the distance between the α particle and the nucleus M,
z is the atomic number of the α particle (for helium $z = 2$ and $A = 4$),
Z is the atomic number of the absorber (for gold $Z = 79$ and $A = 197$).
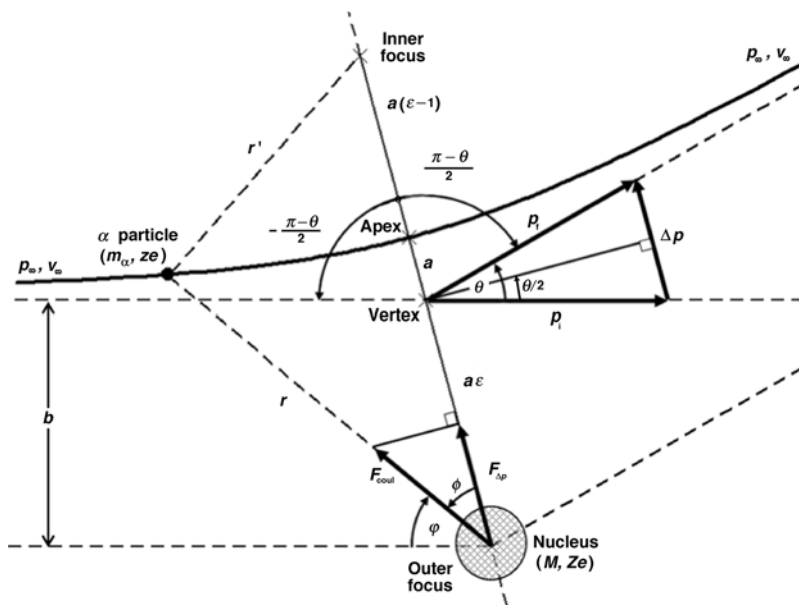
Fig. 2.3. Schematic diagram for scattering of an α particle on a nucleus: θ is the scattering angle; b the impact parameter; $\Delta\vec{p}$ the change in α-particle momentum; v_∞ the initial velocity of the α particle; and p_∞ the initial momentum of the α particle. The trajectory of the α particle is a hyperbola as a result of the repulsive Coulomb interaction between the α particle and the nucleus

Since the component of the force F_{coul} in the direction of the momentum transfer is $F_{\Delta p} = F_{\mathrm{coul}} \cos\phi$, the momentum transfer (impulse) Δp may be written as the time integral of the force component $F_{\Delta p}$, i.e.,

$$\Delta p = \int_{-\infty}^{\infty} F_{\Delta p} dt = \int_{-\infty}^{\infty} F_{\mathrm{coul}} \cos\phi \, d\phi$$

$$= \frac{zZe^2}{4\pi\varepsilon_\mathrm{o}} \int_{-\frac{\pi-\theta}{2}}^{\frac{\pi-\theta}{2}} \frac{\cos\phi}{r^2} \frac{dt}{d\phi} d\phi \ , \tag{2.10}$$

where ϕ is the angle between the radius vector r and the bisector, as also shown in Fig. 2.3.

Using the conservation of angular momentum L

$$L = m_\alpha v_\infty b = m_\alpha \omega \, r^2 \ , \tag{2.11}$$

where

m_α is the mass of the α particle,
b is the impact parameter,
r is the radius vector between the α particle and the nucleus,
v_∞ is the initial and final α-particle velocity before and after the interaction,
ω is the angular frequency equal to $d\phi/dt$,

we can now rewrite (2.10) in a simple form

$$\Delta p = \frac{zZe^2}{4\pi\varepsilon_o}\frac{1}{v_\infty b}\int\limits_{-\frac{\pi-\theta}{2}}^{\frac{\pi-\theta}{2}}\cos\phi\, d\phi = \frac{zZe^2}{4\pi\varepsilon_o}\frac{1}{v_\infty b}\left\{\sin\phi\right\}_{-(\pi-\theta)/2}^{+(\pi-\theta)/2}$$

$$= 2\frac{zZe^2}{4\pi\varepsilon_o}\frac{1}{v_\infty b}\cos\frac{\theta}{2} \ . \tag{2.12}$$

With the help of the momentum vector diagram, also given in Fig. 2.3, the momentum transfer Δp may also be written as

$$\Delta p = 2p_\infty\sin\frac{\theta}{2} = 2m_\alpha v_\infty\sin\frac{\theta}{2} \ . \tag{2.13}$$

Combining (2.12) and (2.13) we obtain the following expressions for the impact parameter b

$$b = \frac{zZe^2}{4\pi\varepsilon_o m_\alpha v_\infty^2}\cot\frac{\theta}{2} = \frac{1}{2}\frac{zZe^2}{4\pi\varepsilon_o}\frac{1}{E_K}\cot\frac{\theta}{2} = \frac{1}{2}D_{\alpha-N}\cot\frac{\theta}{2} \ , \tag{2.14}$$

with the use of:

1. the classical relationship for the kinetic energy of the α particle ($E_K = m_\alpha v_\infty^2/2$), since $v_\infty \ll c$,
2. the definition of $D_{\alpha-N}$ as the distance of closest approach between the α particle and the nucleus in a "direct-hit" head-on collision for which the impact parameter $b = 0$, the scattering angle $\theta = \pi$, and $D_{\alpha-N} = zZe^2/(4\pi\varepsilon_o E_K)$.

Hyperbolic Trajectory

Equations for the *hyperbolic trajectory* of an α particle interacting with a nucleus can be derived from the diagram given in Fig. 2.3 and the simple rule governing the hyperbola

$$r - r' = 2a \ , \tag{2.15}$$

where

a is the distance between the apex and the vertex of the hyperbola,
r is the distance between the point of interest on the hyperbola and the outer focus,

r' is the distance between the point of interest on the hyperbola and the inner focus.

The parameters of the hyperbola such as a, r, and r' are defined in Fig. 2.3 and the locations of the inner focus, outer focus, apex and vertex are also indicated in Fig. 2.3. Solving (2.15) for r' and squaring the result, we get the following expression for $(r')^2$

$$(r')^2 = r^2 - 4ar + 4a^2 \ . \tag{2.16}$$

Using the law of cosines in conjunction with Fig. 2.3, we express $(r')^2$ as

$$(r')^2 = r^2 - 4a\varepsilon r \cos\phi + 4a^2\varepsilon^2 \ , \tag{2.17}$$

where ε is the eccentricity of the hyperbola. Subtracting (2.17) from (2.16) and solving for $r(\phi)$, we now obtain the following general equation for the hyperbolic trajectory of the α particle

$$r(\phi) = \frac{a(\varepsilon^2 - 1)}{\varepsilon \cos\phi - 1} \ . \tag{2.18}$$

Three separate special conditions are of interest with regard to (2.18):

1. $r = \infty$ (for determining the eccentricity ε)
2. $\phi = 0$ (for determining the general distance of closest approach $R_{a-\mathrm{N}}$)
3. $\theta = \pi$ (for determining the distance of closest approach in a direct hit that results in the shortest distance of closest approach defined as $D_{\alpha-\mathrm{N}}$)

For $r = \infty$ the angle ϕ equals to $(\pi - \theta)/2$ and the denominator in (2.18) $[\varepsilon \cos((\pi - \theta)/2) - 1]$ must equal zero, resulting in the following relationship for the eccentricity ε

$$\varepsilon \cos\frac{\pi - \theta}{2} = \varepsilon \sin\frac{\theta}{2} = 1 \ \ \text{or} \ \ \varepsilon = \frac{1}{\sin\frac{\theta}{2}} \ . \tag{2.19}$$

The distance of closest approach $R_{\alpha-\mathrm{N}}$ between the α particle and the nucleus in a non-direct hit collision ($\theta < \pi$ and $\phi = 0$) is given as

$$R_{\alpha-\mathrm{N}} = r(\phi = 0) = \frac{a(\varepsilon^2 - 1)}{\varepsilon - 1} = a(1 + \varepsilon)$$

$$= a\left\{1 + \left(\sin\frac{\theta}{2}\right)^{-1}\right\} \ . \tag{2.20}$$

The distance of closest approach in a direct-hit collision ($\theta = \pi$) can now be written as

$$D_{\alpha-\mathrm{N}} = R_{\alpha-\mathrm{N}}(\theta = \pi) = 2a \ , \tag{2.21}$$

from where it follows that a, the distance between the apex and the vertex of the hyperbola, is equal to $D_{\alpha-\mathrm{N}}/2$.

Hyperbola in Polar Coordinates

In *polar coordinates* (r, φ) the hyperbolic α-particle trajectory may be expressed as

$$\frac{1}{r} = \frac{1}{b}\sin\varphi + \frac{a}{b^2}(\cos\varphi - 1) \ , \tag{2.22}$$

with parameters a, b, and φ defined in Fig. 2.3. Note that φ and ϕ are different angles and that the following relationship for angles φ, ϕ, and θ applies

$$\varphi + \phi = \left| \frac{\pi - \theta}{2} \right| \ . \tag{2.23}$$

It can be shown that the expressions of (2.18) and (2.22) for a hyperbola are equivalent.

2.2.3 Differential Cross-Section for Rutherford Scattering

The differential cross-section $d\sigma_{\mathrm{Ruth}}/d\Omega$ for Rutherford scattering into a solid angle $d\Omega = 2\pi \sin\theta\, d\theta$ that corresponds to an angular aperture between θ and $\theta + d\theta$ (equivalent to impact parameters between b and $b - db$), assuming the azimuthal distribution to be isotopic, is the area of a ring with mean radius b and width db

$$d\sigma_{Ruth} = 2\pi\, b\, db = 2\pi \sin\theta \frac{b}{\sin\theta} \left| \frac{db}{d\theta} \right| \, d\theta \ . \tag{2.24}$$

Recognizing that

$$d\Omega = 2\pi \sin\theta\, d\theta \ , \tag{2.25}$$

expressing $\sin\theta$ as

$$\sin\theta = 2\sin\frac{\theta}{2}\cos\frac{\theta}{2} \ , \tag{2.26}$$

and using (2.14) for the impact parameter b to determine $|db/d\theta|$ as

$$\left| \frac{db}{d\theta} \right| = \frac{D_{\alpha-N}}{4} \frac{1}{\sin^2(\theta/2)} \ , \tag{2.27}$$

we obtain the following expression for $d\sigma_{Ruth}/d\Omega$, the differential Rutherford cross section

$$\frac{d\sigma_{\mathrm{Ruth}}}{d\Omega} = \left(\frac{D_{\alpha-\mathrm{N}}}{4} \right)^2 \frac{1}{\sin^4\frac{\theta}{2}} \ . \tag{2.28}$$

At small scattering angles θ, where $\sin(\theta/2) \approx \theta/2$, (2.28) may be approximated as

$$\frac{d\sigma_{\mathrm{Ruth}}}{d\Omega} = \frac{D_{\alpha-\mathrm{N}}^2}{\theta^4} \ . \tag{2.29}$$

Since most of the Rutherford scattering occurs for $\theta \ll 1$ rad and even at $\theta = \pi/2$ the small angle result is within 30% of the Rutherford general expression, it is reasonable to use the small angle approximation of (2.29) at all angles for which the unscreened point-Coulomb field expression is valid.

2.2.4 Minimum and Maximum Scattering Angles

Departures from the point Coulomb field approximation appear for large and small angles θ, corresponding to small and large impact parameters b, respectively.

At large b (i.e., at small θ) the screening effects of the atomic orbital electrons cause the potential felt by the α particle to fall off more rapidly than the $1/r$ Coulomb point-source potential. It is convenient to account for electron screening of the nuclear potential with the Thomas-Fermi statistical model of the atom in which the *Thomas-Fermi atomic potential* is given as follows:

$$V_{\mathrm{TF}}(r) \approx \frac{Ze^2}{4\pi\varepsilon_{\mathrm{o}}} \frac{1}{r} e^{-r/a_{\mathrm{TF}}} . \tag{2.30}$$

In (2.30) a_{TF} is the Thomas-Fermi atomic radius expressed as

$$a_{\mathrm{TF}} \approx 1.4 a_{\mathrm{o}} Z^{-1/3} , \tag{2.31}$$

representing a fixed fraction of all atomic electrons or, more loosely, the radius of the atomic electron cloud that screens the nucleus ($a_{\mathrm{o}} = 0.5292$ Å is the Bohr radius, discussed in Sect. 2.3). This implies that with a decreasing scattering angle θ the scattering cross-section will flatten off at small angles θ to a finite value at $\theta = 0$ rather than increasing as θ^{-4} and exhibiting a singularity at $\theta = 0$.

The small angle result of (2.29) may then in general be written as

$$\frac{d\sigma_{\mathrm{Ruth}}}{d\Omega} \approx \frac{D_{\alpha-\mathrm{N}}^2}{\left(\theta^2 + \theta_{\mathrm{min}}^2\right)^2} \tag{2.32}$$

In contrast to (2.29) which is singular at $\theta = 0$ the relationship in (2.32) provides a finite value at $\theta = 0$ equal to

$$\left.\frac{d\sigma_{\mathrm{Ruth}}}{d\Omega}\right|_{\theta=0} = \frac{D_{\alpha-\mathrm{N}}^2}{\theta_{\mathrm{min}}^4} \tag{2.33}$$

For small angular deflections θ where $\Delta p \ll p$ and $\theta \approx 0$ we can write

$$\theta \approx \frac{\Delta p}{p_\infty} = \frac{2zZe^2}{4\pi\varepsilon_{\mathrm{o}} v_\infty b \, p_\infty} = \frac{D_{\alpha-\mathrm{N}}}{b} \tag{2.34}$$

using (2.2), (2.12), and (2.13)

Substituting a_{TF}, the Thomas-Fermi radius of the atom, for b into (2.34) we estimate θ_{min} as

$$\theta_{\mathrm{min}} = D_{\alpha-\mathrm{N}}/a_{\mathrm{TF}} , \tag{2.35}$$

while the quantum-mechanical result is

$$\theta_{\min} = \frac{\hbar}{pa_{\mathrm{TF}}} = \frac{\hbar c \sqrt[3]{Z}}{1.4 a_{\mathrm{o}} \sqrt{E_{\mathrm{K}}(E_{\mathrm{K}} + 2E_{\mathrm{o}})}} \tag{2.36}$$

using the expressions for p and a_{TF} given by (1.50) and (2.31), respectively.

At relatively large scattering angles θ the differential Rutherford cross section $d\sigma_{\mathrm{Ruth}}/d\Omega$ is smaller than that predicted by (2.28) because of the finite size of the nucleus. Approximating the charge distribution of the atomic nucleus by a volume distribution inside a sphere of radius R results in the following electrostatic potentials $V(r)$ for regions inside and outside the nucleus

$$V(r) = \frac{zZe^2}{4\pi\varepsilon_{\mathrm{o}}R}\left(\frac{3}{2} - \frac{1}{2}\frac{r^2}{R^2}\right) \qquad \text{for } r < R, \tag{2.37}$$

$$V(r) = \frac{3}{8}\frac{zZe^2}{\pi\varepsilon_{\mathrm{o}}R} \qquad \text{for } r = 0 , \tag{2.38}$$

$$V(r) = \frac{zZe^2}{4\pi\varepsilon_{\mathrm{o}}R} \qquad \text{for } r = R , \tag{2.39}$$

$$V(r) = \frac{zZe^2}{4\pi\varepsilon_{\mathrm{o}}r} \qquad \text{for } r > R . \tag{2.40}$$

The scattering is confined to angles smaller than $\theta_{\max} = \lambda/(2\pi R)$ where λ is the de Broglie wavelength of the incident particle. The maximum scattering angle $\theta_{\max}$ is then approximated as follows using the expressions for p of (1.50) and R: of (2.1)

$$\theta_{\max} = \frac{\hbar}{pR} = \frac{\hbar c}{\sqrt{E_{\mathrm{K}}(E_{\mathrm{K}} + 2E_{\mathrm{o}})}\, R_{\mathrm{o}} . \sqrt[3]{A}} . \tag{2.41}$$

Using (2.36) and (2.41) we obtain the following expression for $\theta_{\max}/\theta_{\min}$

$$\frac{\theta_{\max}}{\theta_{\min}} = \frac{a_{\mathrm{TF}}}{R} = \frac{1.4 a_{\mathrm{o}}}{R_{\mathrm{o}}\sqrt[3]{ZA}} , \tag{2.42}$$

ranging from $\sim 5 \times 10^4$ for low atomic number elements to $\sim 2 \times 10^3$ for high atomic number elements. Thus, we may conclude that $\theta_{\max}/\theta_{\min} \gg 1$ for all elements.

2.2.5 Total Rutherford Scattering Cross-Section

The total Rutherford scattering cross section can be approximated by using the small angle approximation and integrating (2.32) over the complete solid angle to obtain

$$\sigma_{\text{Ruth}} = \int \frac{d\sigma_{\text{Ruth}}}{d\Omega} d\Omega =$$

$$= 2\pi \int\limits_{0}^{\theta_{\max}} \frac{d\sigma_{\text{Ruth}}}{d\Omega} \sin\theta \, d\theta \approx 2\pi \, D_{\alpha-\text{N}}^2 \int\limits_{0}^{\theta_{\max}} \frac{\theta \, d\theta}{(\theta^2 + \theta_{\min}^2)^2} =$$

$$= \pi \, D_{\alpha-\text{N}}^2 \int\limits_{0}^{\theta_{\max}} \frac{d(\theta^2 + \theta_{\min}^2)}{(\theta^2 + \theta_{\min}^2)^2} =$$

$$= \pi \, D_{\alpha-\text{N}}^2 \left\{ \frac{1}{\theta_{\min}^2} - \frac{1}{\theta_{\max}^2 + \theta_{\min}^2} \right\} =$$

$$= \pi \, D_{\alpha-\text{N}}^2 \, \frac{1}{\theta_{\min}^2} \left\{ 1 - \frac{1}{1 + (\theta_{\max}^2 / \theta_{\min}^2)} \right\} . \tag{2.43}$$

In each Rutherford collision the angular deflections obey the Rutherford's expression with cut-offs at $\theta_{\min}$ and $\theta_{\max}$ given by (2.36) and (2.41), respectively. The typical value for $\hbar/p$ in the two expressions can be estimated for α particles with a typical kinetic energy of 5.5 MeV as follows:

$$\frac{\hbar}{p} = \frac{\hbar c}{m_\alpha c^2 (v/c)} \approx \frac{200 \text{ MeV} \cdot \text{fm}}{4 \times 10^3 \text{ MeV} \, 5 \times 10^{-2}} = 1 \text{ fm} . \tag{2.44}$$

Inserting the value for $\hbar/p$ into (2.36) and (2.41) for a typical α-particle kinetic energy E_{K} of 5.5 MeV combined with appropriate values for a_{TF} and R results in the following values for $\theta_{\min}$ and $\theta_{\max}$ in the gold atom

$$\theta_{\min} \approx \frac{\hbar}{p a_{\text{TF}}} \approx \frac{1 \text{ fm}}{2 \times 10^4 \text{ fm}} = 5 \times 10^{-5} \text{ rad} \tag{2.45}$$

$$\theta_{\max} \approx \frac{\hbar}{pR} \approx \frac{1 \text{ fm}}{10 \text{ fm}} = 10^{-1} \text{ rad} . \tag{2.46}$$

Rutherford's condition stipulating that $\theta_{\min} \ll \theta_{\max} \ll 1$ is thus satisfied and, since also $\theta_{\max}/\theta_{\min} \gg 1$, the total cross section for Rutherford's scattering given in (2.43) can be simplified, after inserting (2.2) and (2.36), to read

$$\sigma_{\text{Ruth}} \approx \frac{\pi \, D_{\alpha-\text{N}}^2}{\theta_{\min}^2} = \pi a_{\text{TF}}^2 \left\{ \frac{2zZe^2}{4\pi\varepsilon_{\text{o}}\hbar v} \right\}^2 . \tag{2.47}$$

The parameters of (2.47) are as follows:

a_{TF} is the Thomas-Fermi atomic radius,
Z is the atomic number of the absorber foil,
z is the atomic number of the α particle,
v is the velocity of the α particle,
$D_{\alpha-\text{N}}$ is the distance of closest approach between the α particle and nucleus in a direct-hit collision ($b = 0$).

The differential Rutherford scattering cross section of (2.32) is plotted in Fig. 2.4 in the form $(1/D_{\alpha-\text{N}}^2)(dR_{\text{Ruth}}/d\Omega)$ against the scattering angle θ for
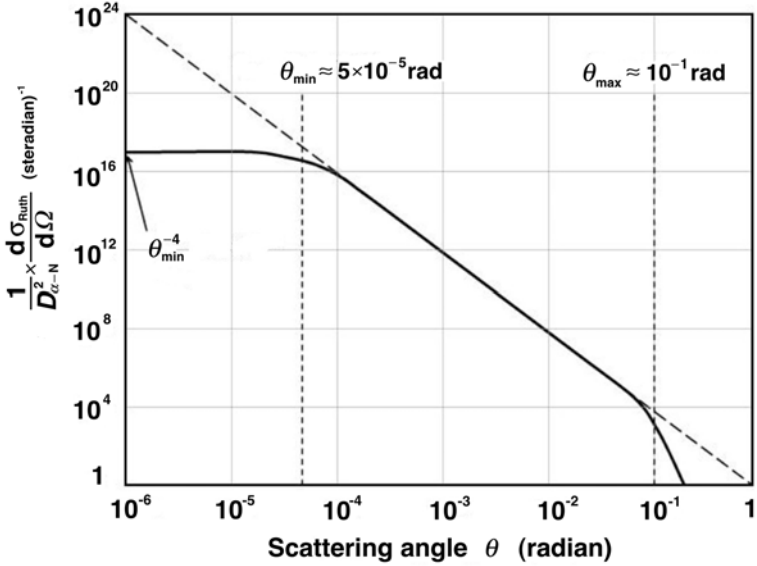
Fig. 2.4. Differential Rutherford scattering cross section $[(1/D^2_{\alpha-N}) \times (d\sigma_{\mathrm{Ruth}}/d\Omega)]$ plotted against the scattering angle θ for 5.5 MeV α particles interacting with gold. The minimum and maximum scattering angles $\theta_{\min} = 5 \times 10^{-5}$ rad and $\theta_{\max} = 10^{-1}$ rad, respectively, are identified. For $\theta \to 0$ the value of the ordinate approaches $(1/\theta^4_{\min}) \approx 1.6 \times 10^{17}$ $(\mathrm{rad})^{-4}$

scattering of 5.5-MeV α particles $[\theta_{\min} = 5 \times 10^{-5}$ rad, as given in (2.45) and $\theta_{\max} = 10^{-1}$ rad, as given in (2.46)] on gold nuclei.

The solid curve of Fig. 2.4 represents the differential Rutherford scattering cross section and contains the following components:

1. For $\theta_{\min} < \theta < \theta_{\max}$ the simple differential Rutherford scattering expression given by (2.29) applies resulting in a straight line on the log-log plot in Fig. 2.4.
2. For $\theta < \theta_{\min}$ (2.32) applies since it accounts for the screening of the nuclear potential by orbital electrons and provides a finite value of $1/\theta^4_{\min} = 1.6 \times 10^{17}$ rad^{-4} for $\theta = 0$ in Fig. 2.4.
3. For $\theta > \theta_{\max}$ the finite size of the nuclear potential must be considered and this lowers the value of the differential cross section from the value predicted by the simple Rutherford result of (2.29).

2.2.6 Mean Square Scattering Angle for Single Rutherford Scattering

Rutherford scattering is confined to very small angles and for energetic α particles $\theta_{\max} \ll 1$ rad. An α particle traversing a gold foil will undergo

a large number of small angle θ scatterings and emerge from the foil with a small cumulative angle Θ that represents a statistical superposition of a large number of small angle deflections.

Large angle scattering events, on the other hand, are rare and a given α particle will undergo at most only one such rare scattering event while traversing the gold foil. As discussed in Sect. 2.1.2, Geiger and Marsden found that only about 1 in 10^4 α particles traverses the 1 μm thick gold foil with a scattering angle Θ exceeding $90°$. The range of Rutherford angular scattering is thus divided into two distinct regions:

1. Single scattering events with large angle θ.
2. Multiple scattering events resulting in a small cumulative angle Θ.

In the multiple-scatter region, the mean square angle for single scattering $\overline{\theta^2}$ is

$$\overline{\theta^2} = \frac{\int \theta^2 \frac{d\sigma_{\mathrm{Ruth}}}{d\Omega} d\Omega}{\int \frac{d\sigma_{\mathrm{Ruth}}}{d\Omega} d\Omega} = \frac{\int \theta^2 \frac{d\sigma_{\mathrm{Ruth}}}{d\Omega} d\Omega}{\sigma_{\mathrm{Ruth}}} \ . \tag{2.48}$$

The denominator in (2.48) is the total Rutherford scattering cross section σ_{Ruth} given in (2.47). It is proportional to the square of the distance of closest approach $(D_{\alpha-N})^2$ and inversely proportional to $\theta_{\min}^2$.

The integral in the numerator of (2.48) is in the small angle approximation $(\sin\theta \approx \theta)$ calculated as follows:

$$\int \theta^2 \frac{d\sigma_{\mathrm{Ruth}}}{d\Omega} d\Omega = 2\pi D_{\alpha-N}^2 \int\limits_0^{\theta_{\max}} \frac{\theta^2 \sin\theta d\theta}{(\theta^2 + \theta_{\min}^2)^2}$$

$$\approx 2\pi D_{\alpha-N}^2 \int\limits_0^{\theta_{\max}} \frac{\theta^3 d\theta}{(\theta^2 + \theta_{\min}^2)^2}$$

$$= \pi D_{\alpha-N}^2 \int\limits_0^{\theta_{\max}} \frac{(\theta^2 + \theta_{\min}^2)d(\theta^2 + \theta_{\min}^2)}{(\theta^2 + \theta_{\min}^2)^2}$$

$$- \pi D_{\alpha-N}^2 \int\limits_0^{\theta_{\max}} \frac{\theta_{\min}^2 d(\theta^2 + \theta_{\min}^2)}{(\theta^2 + \theta_{\min}^2)^2}$$

$$= \pi D_{\alpha-N}^2 \left\{ \ln(\theta^2 + \theta_{\min}^2) + \frac{\theta_{\min}^2}{\theta^2 + \theta_{\min}^2} \right\}_0^{\theta_{\max}}$$

$$= \pi D_{\alpha-N}^2 \left\{ \ln\left(1 + \frac{\theta_{\max}^2}{\theta_{\min}^2}\right) + \frac{\theta_{\min}^2}{\theta_{\max}^2 + \theta_{\min}^2} - 1 \right\} \ . \tag{2.49}$$

The mean square angle $\overline{\theta^2}$ of (2.48) for a single scattering event, after incorporating the Rutherford total scattering cross section given in (2.47), is then

given by the following relationship:

$$
\begin{aligned}
\overline{\theta^2} &= \theta_{\min}^2 \ln\left(1 + \frac{\theta_{\max}^2}{\theta_{\min}^2}\right) - \frac{\theta_{\min}^2 \theta_{\max}^2}{\theta_{\min}^2 + \theta_{\max}^2} \\
&= \theta_{\min}^2 \ln\left(1 + \frac{\theta_{\max}^2}{\theta_{\min}^2}\right) - \left(\frac{1}{\theta_{\min}^2} + \frac{1}{\theta_{\max}^2}\right)^{-1} .
\end{aligned}
\tag{2.50}
$$

The expression in (2.50) can be simplified using the Rutherford scattering condition stipulating that $\theta_{\min} \ll \theta_{\max} \ll 1$ to obtain

$$
\overline{\theta^2} \approx 2\,\theta_{\min}^2 \ln \frac{\theta_{\max}}{\theta_{\min}} .
\tag{2.51}
$$

2.2.7 Mean Square Scattering Angle
for Multiple Rutherford Scattering

Since the successive scattering collisions are independent events, the *central-limit theorem* of statistics (see Sect. 4.4.6) shows that for a large number $n > 20$ of such collisions, the distribution in angle will be Gaussian around the forward direction [see (2.7)] with a cumulative mean square angle $\overline{\Theta^2}$ related to the mean square angle $\overline{\theta^2}$ for a single scattering event given in (2.51).

The cumulative mean square angle $\overline{\Theta^2}$ and the mean square angle $\overline{\theta^2}$ for a single scattering event are related as follows:

$$
\overline{\Theta^2} = n\overline{\theta^2} ,
\tag{2.52}
$$

where n, the number of scattering events, is given as follows:

$$
n = \frac{N_a}{V} \sigma_{\text{Ruth}} t = \rho \frac{N_A}{A} \sigma_{\text{Ruth}} t = \pi \rho \frac{N_A}{A} \frac{D_{\alpha-N}^2}{\theta_{\min}^2} t .
\tag{2.53}
$$

In (2.53) the parameters are as follows:

σ_{Ruth} is the total Rutherford cross-section given by (2.47),
N_a/V is the number of atoms per volume equal to $\rho N_A/A$,
ρ is the density of the foil material,
t is the thickness of the foil,
A is the atomic mass number,
N_A is the Avogadro's number ($N_A = 6.023 \times 10^{23}$ atom/gramatom),
$D_{\alpha-N}$ is the distance of closest approach between the α particle and the nucleus in a direct hit interaction where $b = 0$ [see (2.2)],
$\theta_{\min}$ is the cut-off angle defined in (2.36).

The mean square angle $\overline{\Theta^2}$ of the Gaussian distribution after combining (2.51), (2.52) and (2.53) is then given by

$$
\overline{\Theta^2} = 2\pi \rho \frac{N_A}{A} t D_{\alpha-N}^2 \ln \frac{\theta_{\max}}{\theta_{\min}} ,
\tag{2.54}
$$

indicating that the mean square angle $\overline{\Theta^2}$ for multiple Rutherford scattering increases linearly with the foil thickness t. Inserting the expressions for

$\theta_{\min}$ and $\theta_{\max}$ of (2.36) and (2.41), respectively, into (2.54), we now get the following expression for the mean square angle $\overline{\Theta^2}$ in Rutherford scattering

$$
\begin{aligned}
\overline{\Theta^2} &= 2\pi \, \rho \frac{N_A}{A} t D_{\alpha-N}^2 \ln \frac{1.4 a_o}{R_o \sqrt[3]{AZ}} \\
&= 2\pi \, \rho \frac{N_A}{A} t \left\{ \frac{zZe^2}{4\pi\varepsilon_o E_K} \right\}^2 \ln \frac{1.4 a_o}{R_o \sqrt[3]{AZ}} \ ,
\end{aligned}
\tag{2.55}
$$

where $a_o = 0.5292$ Å and $R_o = 1.2$ fm are the Bohr radius constant of (2.58) below and the nuclear radius constant of (1.14), respectively.

2.3 Bohr Model of the Hydrogen Atom

Niels Bohr in 1913 combined Rutherford's concept of the nuclear atom with Planck's idea of the quantized nature of the radiative process and developed an atomic model that successfully deals with one-electron structures such as the hydrogen atom, singly ionized helium, doubly ionized lithium, etc. The model, known as the Bohr model of the atom, is based on four postulates that combine classical mechanics with the concept of angular momentum quantization.

The *four Bohr postulates* are stated as follows.

1. **Postulate 1:** Electrons revolve about the Rutherford nucleus in well-defined, allowed orbits (often referred to as shells). The Coulomb force of attraction $F_{\text{coul}} = Ze^2/(4\pi\varepsilon_o r^2)$ between the electrons and the positively charged nucleus is balanced by the centripetal force $F_{\text{cent}} = mv^2/r$, where Z is the number of protons in the nucleus (atomic number); r the radius of the orbit or shell; m_e the electron mass; and v the velocity of the electron in the orbit.
2. **Postulate 2:** While in orbit, the electron does not lose any energy despite being constantly accelerated (this postulate is in contravention of the basic law of nature which states that an accelerated charged particle will lose part of its energy in the form of radiation).
3. **Postulate 3:** The angular momentum $L = m_e v r$ of the electron in an allowed orbit is quantized and given as $L = n\hbar$, where n is an integer referred to as the principal quantum number and $\hbar = h/(2\pi)$ is the reduced Planck's constant with h the Planck's constant. The simple quantization of angular momentum stipulates that the angular momentum can have only integral multiples of a basic value ($\hbar$).
4. **Postulate 4:** An atom or ion emits radiation when an electron makes a transition from an initial allowed orbit with quantum number n_i to a final allowed orbit with quantum number n_f for $n_i > n_f$.

The angular momentum quantization rule simply means that $\hbar$ is the lowest angular momentum available to the electron ($n = 1$, ground state) and that

higher n orbits ($n > 1$, excited states) can only have integer values of $\hbar$ for the magnitude of the orbital angular momentum, where n is the *principal quantum number* or the shell number. One-electron atomic structures are now referred to as the Bohr atom.

2.3.1 Radius of the Bohr Atom

Assuming that $M_{\text{nucleus}} \approx \infty$ and that $M_{\text{nucleus}} \gg m_{\text{electron}}$, equating the centrifugal force and the Coulomb force on the electron [see Fig. 2.5a]

$$\frac{m_e v^2}{r_n} = \frac{1}{4\pi\varepsilon_0}\frac{Ze^2}{r_n^2} \tag{2.56}$$

and inserting the quantization relationship for the angular momentum of the electron (third Bohr postulate)

$$L = m_e v_n r_n = m_e \omega_n r_n^2 = n\hbar, \tag{2.57}$$

we get the following relationship for r_n, the radius of the n-th allowed Bohr orbit

$$r_n = \frac{4\pi\varepsilon_0}{e^2}\frac{(\hbar c)^2}{m_e c^2}\left(\frac{n^2}{Z}\right) = a_0 \left(\frac{n^2}{Z}\right) = (0.5292\ \text{Å}) \times \left(\frac{n^2}{Z}\right), \quad (2.58)$$

where a_0 is called the Bohr radius of a one electron atom ($a_0 = 0.5292$ Å).

2.3.2 Velocity of the Bohr Electron

Inserting the expression for r_n of (2.58) into (2.57) we obtain the following expression for v_n/c, where v_n is the velocity of the electron in the n-th allowed
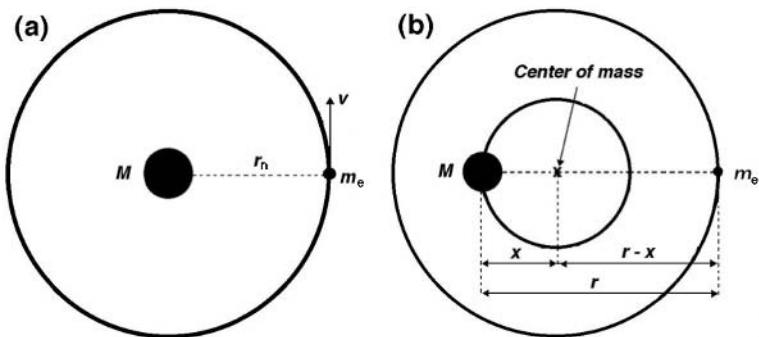
Fig. 2.5. Schematic diagram of the Rutherford–Bohr atomic model. In **a** the electron revolves about the center of the nucleus M where the nuclear mass $M \to \infty$, in **b** the nuclear mass M is finite and both the electron as well as the nucleus revolve about their common center-of-mass

Bohr orbit

$$\frac{v_n}{c} = \frac{n\,\hbar c}{m_e c^2 r_n} = \frac{e^2}{4\pi\varepsilon_\mathrm{o}}\frac{1}{\hbar c}\left(\frac{Z}{n}\right)$$

$$= \alpha\left(\frac{Z}{n}\right) \approx \frac{1}{137}\left(\frac{Z}{n}\right) \approx (7\times 10^{-3})\times\left(\frac{Z}{n}\right)\ , \tag{2.59}$$

where α is the so-called fine structure constant ($\sim 1/137$).

Since, as evident from (2.59), the electron velocity in the ground state ($n = 1$) orbit of hydrogen is less than 1% of the speed of light c, the use of classical mechanics in one-electron Bohr atom is justifiable. Both Rutherford and Bohr used classical mechanics in their momentous discoveries of the atomic structure and the kinematics of electronic motion, respectively. On the one hand, nature provided Rutherford with an atomic probe (naturally occurring α particles) having just the appropriate energy (few MeV) to probe the atom without having to deal with relativistic effects and nuclear penetration. On the other hand, nature provided Bohr with the hydrogen one-electron atom in which the electron can be treated with simple classical relationships.

2.3.3 Total Energy of the Bohr Electron

The total energy E_n of the electron when in one of the allowed orbits (shells) with radius r_n is the sum of the electron's kinetic energy E_K and potential energy E_P

$$E_\mathrm{n} = E_\mathrm{K} + E_\mathrm{P} = \frac{m_e v_\mathrm{n}^2}{2} + \frac{Ze^2}{4\pi\varepsilon_\mathrm{o}}\int_{\infty}^{r_\mathrm{n}}\frac{dr}{r^2} = \frac{1}{2}\frac{Ze^2}{4\pi\varepsilon_\mathrm{o}}\frac{1}{r_\mathrm{n}} - \frac{Ze^2}{4\pi\varepsilon_\mathrm{o}}\frac{1}{r_\mathrm{n}} =$$

$$= -\frac{1}{2}\frac{Ze^2}{4\pi\varepsilon_\mathrm{o}}\frac{1}{r_n} = -\frac{1}{2}\left(\frac{e^2}{4\pi\varepsilon_\mathrm{o}}\right)^2\frac{m_e c^2}{(\hbar c)^2}\left(\frac{Z}{n}\right)^2 = -E_\mathrm{R}\left(\frac{Z}{n}\right)^2 =$$

$$= (-13.61\ \text{eV})\times\left(\frac{Z}{n}\right)^2\ . \tag{2.60}$$

Equation (2.60) represents the energy quantization of allowed bound electronic states in a one-electron atom. This energy quantization is a direct consequence of the simple angular momentum quantization $L = n\hbar$ introduced by Bohr. E_R is called the Rydberg energy ($E_\mathrm{R} = 13.61$ eV).

By convention the following conditions apply:

- A stationary free electron, infinitely far from the nucleus has zero energy.
- An electron bound to the nucleus can only attain discrete allowed negative energy levels, as predicted by (2.60).
- An electron with a positive energy is free and moving in a continuum of kinetic energies.

- The five lowest bound energy levels ($n = 1$ through $n = 5$) of the hydrogen atom according to (2.60) are: -13.6 eV, -3.4 eV, -1.51 eV, -0.85 eV, and -0.54 eV.

The energy level diagram for a hydrogen atom is shown in Fig. 2.6. It provides an excellent example of energy level diagrams for one-electron structures such as hydrogen, singly ionized helium atom, or doubly ionized lithium atom. The energy levels for hydrogen were calculated from (2.60) using $Z = 1$. The following features can be easily identified:

- The negative energy levels of the electron represent discrete allowed electron states bound to the nucleus with a given binding energy.
- The positive energy levels represent a free electron in a continuum of allowed kinetic energies.
- The zero energy level separates the discrete allowed bound electron states from the continuum of kinetic energies associated with a free electron.
- Electron in $n = 1$ state is said to be in the ground state; an electron in a state with $n > 1$ is said to be in an excited state.
- Energy must be supplied to an electron in the ground state of a hydrogen atom to move it to an excited state. An electron cannot remain in an
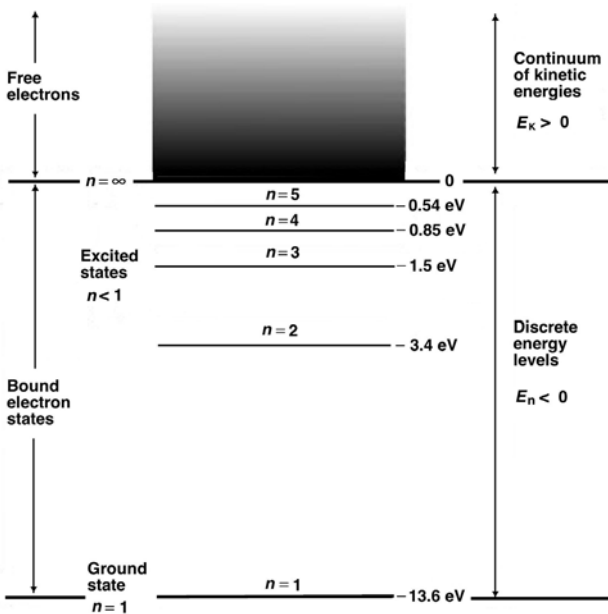
Fig. 2.6. Energy level diagram for the hydrogen atom as example of energy level diagrams for one-electron structures. In the ground state ($n = 1$) the electron is bound to the nucleus with a binding energy of 13.6 eV

excited state; rather it will move to a lower level shell and the transition energy will be emitted in the form of a photon.

2.3.4 Transition Frequency and Wave Number

The energy $h\nu$ of a photon emitted as a result of an electronic transition from an initial allowed orbit with $n = n_i$ to a final allowed orbit with $n = n_f$, where $n_i > n_f$, is given by

$$h\nu = E_i - E_f = -E_R Z^2 \left[\frac{1}{n_i^2} - \frac{1}{n_f^2} \right] . \tag{2.61}$$

The wave number of the emitted photon is then given by

$$k = \frac{1}{\lambda} = \frac{\nu}{c} = \frac{E_R}{2\pi\hbar c} Z^2 \left[\frac{1}{n_f^2} - \frac{1}{n_i^2} \right] = R_\infty Z^2 \left[\frac{1}{n_f^2} - \frac{1}{n_i^2} \right] =$$
$$= (109\,737 \text{ cm}^{-1}) \times Z^2 \left[\frac{1}{n_f^2} - \frac{1}{n_i^2} \right] , \tag{2.62}$$

where R_∞ is the so-called Rydberg constant ($109\,737$ cm^{-1}).

2.3.5 Atomic Spectra of Hydrogen

Photons emitted by excited atoms are concentrated at a number of discrete wavelengths (lines). The hydrogen spectrum is relatively simple and results from transitions of a single electron in the hydrogen atom. Table 2.1 gives a listing for the first five known series of the hydrogen emission spectrum. It also provides the limit in eV and Å for each of the five series.

Table 2.1. Characteristics of the first five emission series of the hydrogen atom

Name of series	Spectral range	Final orbit n_f	Initial orbit n_i	Limit of series (eV)	Limit of series (Å)
Lyman	ultraviolet	1	2,3,4 …∞	13.6	912
Balmer	visible	2	3,4,5 …∞	3.4	3646
Paschen	infrared	3	4,5,6 …∞	1.5	8265
Brackett	infrared	4	5,6,7 …∞	0.85	14584
Pfund	infrared	5	6,7,8 …∞	0.54	22957

2.3.6 Correction for Finite Mass of the Nucleus

A careful experimental study of the hydrogen spectrum has shown that the Rydberg constant for hydrogen is 109 678 cm^{-1} rather than the $R_\infty = 109\,737$ cm^{-1} value that Bohr derived from first principles. This small discrepancy of the order of one part in 2000 arises from Bohr's assumption that the nuclear mass (proton in the case of hydrogen atom) M is infinite and that the electron revolves about a point at the center of the nucleus, as shown schematically in Fig. 2.5a on page 60.

When the finite mass of the nucleus M is taken into consideration, both the electron and the nucleus revolve about their common center-of-mass, as shown schematically in Fig. 2.5b. The total angular momentum L of the system is given by the following expression:

$$L = m_e(r - x)^2\omega + Mx^2\omega \,, \tag{2.63}$$

where

r is the distance between the electron and the nucleus,
x is the distance between the center-of-mass and the nucleus,
$r - x$ is the distance between the center-of-mass and the electron.

After introducing the relationship

$$m_e(r - x) = Mx \tag{2.64}$$

into (2.63), the angular momentum L for the atomic nucleus/electron system may be written as

$$L = Mx^2\omega + m_e(r - x)^2\omega = \frac{m_e M}{m_e + M}r^2\omega = \mu r^2\omega \,, \tag{2.65}$$

where μ is the so-called *reduced mass* of the nucleus/electron system given as

$$\mu = \frac{m_e M}{m_e + M} = \frac{m_e}{1 + \frac{m_e}{M}} \,. \tag{2.66}$$

All Bohr relationships, given above for one-electron structures in (2.58) through (2.62) with a nuclear mass $M \to \infty$, are also valid for finite nuclear masses M as long as the electron rest mass m_e in these relationships is replaced with the appropriate reduced mass μ.

For the hydrogen atom $\mu = m_e/(1 + m_e/M_{\text{proton}}) = 0.9995\ m_e$ and the Rydberg constant R_H is

$$R_H = \frac{\mu}{m_e}R_\infty = \frac{1}{1 + \frac{m_e}{M_{\text{proton}}}}R_\infty = \frac{109\,737\ \text{cm}^{-1}}{1 + \frac{1}{1837}} = 109\,677\ \text{cm}^{-1} \,, \tag{2.67}$$

representing a 1 part in 2000 correction, in excellent agreement with the experimental result.

2.3.7 Positronium

The positronium "atom" (Ps) is a semi-stable, hydrogen-like configuration consisting of a positron and electron revolving about their common center-of-mass before the process of annihilation occurs. The lifetime of the positronium is about 10^{-7} s. The reduced mass μ for the positronium "atom" is $m_e/2$; the Rydberg constant $R_{\mathrm{Ps}} = R_\infty/2$; the radius of orbits $(r_{\mathrm{Ps}})_n = 2a_o n^2$; and the ground state energy $(E_{\mathrm{Ps}})_n = E_R/(2n^2)$.

2.3.8 Muonic Atom

A muonic atom consists of a nucleus of charge Ze and a negative muon revolving about it. The muonic mass M_{muon} is $207m_e$. The reduced mass for a muonic atom with $Z = 1$ is $186m_e$; the Rydberg constant $R_{\mathrm{muon}} = 186R_\infty$; and the ground state energy $E_{\mathrm{muon}} = 186E_R$.

2.3.9 Quantum Numbers

Bohr's atomic theory predicts quantized energy levels for the one-electron hydrogen atom that depend only on n, the principal quantum number, since $E_n = -E_R/n^2$, where E_R is the Rydberg energy.

In contrast, the solution of the Schrödinger's equation in spherical coordinates for the hydrogen atom gives three quantum numbers for the hydrogen atom: $n, \ell,$ and m_ℓ, where:

n is the *principal quantum number* with allowed values $n = 1, 2, 3 \ldots$, giving the electron binding energy in shell n as $E_n = -E_R/n^2$,

ℓ is the *orbital angular momentum quantum number* with the following allowed values $\ell = 0, 1, 2, 3, \ldots n - 1$, giving the electron orbital angular momentum $L = \hbar\sqrt{\ell(\ell+1)}$,

m_ℓ is referred to as the *magnetic quantum number* giving the z component of the orbital angular momentum $L_z = m_\ell \hbar$ and has the following allowed values: $m_\ell = -\ell, -\ell + 1, -\ell + 2, \ldots \ell - 2, \ell - 1, \ell$.

Experiments by *Otto Stern* and *Walter Gerlach* in 1921 have shown that the electron, in addition to its orbital angular momentum $\vec{L}$, possesses an intrinsic angular momentum. This intrinsic angular momentum is referred to as the *spin* $\vec{S}$ and is specified by two quantum numbers: $s = 1/2$ and m_s that can take two values ($1/2$ or $-1/2$). The electron spin is given as $S = \hbar\sqrt{s(s+1)} = \hbar\sqrt{3}/2$ and its z component as $S_z = m_s\hbar$.

- The orbital and spin angular momenta of an electron actually interact with one another. This interaction is referred to as the *spin-orbit coupling* and results in a total electronic angular momentum $\vec{J}$ that is the vector sum of the orbital and intrinsic spin components, i.e., $\vec{J} = \vec{L} + \vec{S}$. The total angular momentum $\vec{J}$ has the value $J = \hbar\sqrt{j(j+1)}$ where the possible

values of the quantum number j are:

$|\ell - s|, |\ell - s + 1|, \ldots |\ell + s|$, with $s = 1/2$ for all electrons.

- The z component of the total angular momentum has the value $J_z = m_j \hbar$, where the possible values of m_j are: $-j, -j+1, -j+2, \ldots j-2, j-1, j$.
- The state of an atomic electron is thus specified with a set of four quantum numbers:
  - n, ℓ, m_ℓ, m_s when there is *no spin-orbit interaction*
  or
  - n, ℓ, j, m_j when there is *spin-orbit interaction*.

2.3.10 Successes and Limitations of the Bohr Atomic Model

With his four postulates and the innovative idea of angular momentum quantization Bohr provided an excellent extension of the Rutherford atomic model and succeeded in explaining quantitatively the photon spectrum of the hydrogen atom and other one-electron structures such as singly ionized helium, doubly ionized lithium, etc.

According to the Bohr atomic model, each of the five known series of the hydrogen spectrum arises from a family of electronic transitions that all end at the same final state n_f. The Lyman ($n_f = 1$), Brackett ($n_f = 4$), and Pfund ($n_f = 5$) series were not known at the time when Bohr proposed his model; however, the three series were discovered soon after Bohr predicted them with his model.

In addition to its tremendous successes, the Bohr atomic model suffers two severe limitations:

- The model does not predict the relative intensities of the photon emission in characteristic orbital transitions
- The model does not work quantitatively for multi-electron atoms.

2.3.11 Correspondence Principle

Niels Bohr postulated that the smallest change in angular momentum L of a particle is equal to $\hbar$ where $\hbar$ is the reduced Planck's constant ($2\pi\hbar = h$). This is seemingly in drastic disagreement with classical mechanics where the angular momentum as well as the energy of a particle behave as continuous functions. In macroscopic systems the angular momentum quantization is not noticed because $\hbar$ represents such a small fraction of the angular momentum; on the atomic scale, however, $\hbar$ may be of the order of the angular momentum making the $\hbar$ quantization very noticeable.

The *correspondence principle* proposed by *Niels Bohr* in 1923 states that for large values of the principal quantum number n (i.e., for $n \to \infty$) the quantum and classical theories must merge and agree. In general, the correspondence principle stipulates that the predictions of the quantum theory for

any physical system must match the predictions of the corresponding classical theory in the limit where the quantum numbers specifying the state of the system are very large. This principle can be used to confirm the Bohr angular momentum quantization ($L = n\hbar$) postulate as follows:

Consider an electron that makes a transition from an initial orbit $n_\mathrm{i} = n$ to a final orbit $n_\mathrm{f} = n - \Delta n$, where n is large and $\Delta n \ll n$. The transition energy ΔE and the transition frequency ν_trans of the emitted photon are given as follows:

$$\Delta E = E_\mathrm{initial} - E_\mathrm{final} \tag{2.68}$$

and

$$\nu_\mathrm{trans} = \frac{\Delta E}{2\pi\hbar} . \tag{2.69}$$

Since n is large, we can calculate ΔE from the derivative with respect to n of the total orbital energy E_n given in (2.60) to obtain

$$\frac{dE_\mathrm{n}}{dn} = 2E_\mathrm{R}\frac{Z^2}{n^3} . \tag{2.70}$$

To get ΔE we express (2.70) as follows:

$$\Delta E = 2E_\mathrm{R}Z^2\frac{\Delta n}{n^3} , \tag{2.71}$$

resulting in the following expression for the transition frequency ν_trans

$$\nu_\mathrm{trans} = \frac{\Delta E}{2\pi\hbar} = \frac{2E_\mathrm{R}Z^2}{2\pi\hbar}\frac{\Delta n}{n^3} = \left\{\frac{Ze^2}{4\pi\varepsilon_\mathrm{o}}\right\}^2 \frac{m_\mathrm{e}}{2\pi\hbar^3}\frac{\Delta n}{n^3} . \tag{2.72}$$

Recognizing that the velocity υ and angular velocity ω are related through $\upsilon = \omega r$, we get from (2.56) the following expression

$$\frac{Ze^2}{4\pi\varepsilon_\mathrm{o}} = m_\mathrm{e}\upsilon^2 r = m_\mathrm{e}\omega^2 r^3, \quad \text{resulting in} \quad \left\{\frac{Ze^2}{4\pi\varepsilon_\mathrm{o}}\right\}^2 = m_\mathrm{e}^2\omega^4 r^6 . \tag{2.73}$$

The angular momentum was given in (2.57) as

$$L = n\hbar = m_\mathrm{e}\upsilon r = m_\mathrm{e}\omega r^2, \quad \text{resulting in} \quad n^3\hbar^3 = m_\mathrm{e}^3\omega^3 r^6 . \tag{2.74}$$

Combining (2.73) and (2.74) with (2.72), we get the following expression for the transition frequency ν_trans

$$\nu_\mathrm{trans} = \left\{\frac{Ze^2}{4\pi\varepsilon_\mathrm{o}}\right\}^2 \frac{m_\mathrm{e}}{2\pi\hbar^3}\frac{\Delta n}{n^3} = \frac{m_\mathrm{e}^2\omega^4 r^6 m_\mathrm{e}\Delta n}{2\pi m_\mathrm{e}^3\omega^3 r^6} = \frac{\omega}{2\pi}\Delta n . \tag{2.75}$$

After incorporating expressions for r_n and υ_n given in (2.58) and (2.59), respectively, the classical orbital frequency ν_orb for the orbit n is given as

$$\nu_\mathrm{orb} = \frac{\omega_\mathrm{n}}{2\pi} = \frac{\upsilon_\mathrm{n}}{2\pi r_\mathrm{n}} = \frac{\alpha c}{2\pi a_\mathrm{o}n^3} . \tag{2.76}$$

We note that ν_{trans} of (2.75) equals to ν_{orb} of (2.76) for large values of n and $\Delta n = 1$, confirming the correspondence between quantum and classical physics for $n \to \infty$.

We now compare the transition frequency ν_{trans} and orbital frequency ν_{orb} for a small n transition from $n_{\mathrm{i}} = 2$ to $n_{\mathrm{f}} = 1$ in a hydrogen atom $(Z = 1)$ and obtain

$$\nu_{\mathrm{orb}}(n = 2) = \frac{v_2}{2\pi r_2} = \frac{\alpha c}{16\pi a_{\mathrm{o}}} = 8.24 \times 10^{14} \ \mathrm{s}^{-1} \tag{2.77}$$

and

$$\nu_{\mathrm{trans}} = \frac{E_2 - E_1}{2\pi \hbar} = \frac{E_{\mathrm{R}}}{2\pi \hbar} \left\{ 1 - \frac{1}{4} \right\} = \frac{3 E_{\mathrm{R}}}{8\pi \hbar} = \frac{3 \alpha c}{16\pi a_{\mathrm{o}}}$$
$$= 24.7 \times 10^{14} \ \mathrm{s}^{-1} = 3 \nu_{\mathrm{orb}} \tag{2.78}$$

From (2.77) and (2.78) we note that for low values of n the orbital and transition frequencies are different, in contrast to the situation at large n where $\nu_{\mathrm{trans}} = \nu_{\mathrm{orb}}$, as shown by (2.75) and (2.76). Thus at large n there is agreement between quantum and classical physics, as predicted by the correspondence principle enunciated by *Niels Bohr*, while for low n quantum and classical physics give different results.

2.4 Multi-electron Atoms

A multielectron atom of atomic number Z contains a nucleus of charge $+Ze$ surrounded by Z electrons, each of charge $-e$ and revolving in an orbit about the nucleus. The kinematics of electron motion and energy levels of electrons in a multi-electron atom are governed by

1. kinetic energy of orbital electron,
2. attractive Coulomb force between the electron and the nucleus,
3. repulsive Coulomb force exerted on the electron by the other $Z-1$ atomic electrons,
4. weak interactions involving orbital and spin angular momenta of orbital electrons,
5. minor interactions between the electron and nuclear angular momenta,
6. relativistic effects and the effect of the finite nuclear size.

2.4.1 Exclusion Principle

Wolfgang Pauli in 1925 eloquently answered the question on the values of quantum numbers assigned to individual electrons in a multi-electron atom. Pauli's exclusion principle that states: "*In a multielectron atom there can never be more than one electron in the same quantum state*" is important for the understanding of the properties of multi-electron atoms and the periodic table of elements.

- According to Pauli's exclusion principle in a multi-electron atom no two electrons can have all four quantum numbers identical.
- The energy and position of each electron in a multi-electron atom are most affected by the principal quantum number n. The electrons that have the same value of n in an atom form a *shell*.
- Within a shell, the energy and position of each electron are affected by the value of the orbital angular momentum quantum number ℓ. Electrons that have the same value of ℓ in a shell form a *sub-shell*.
- The specification of quantum numbers n and ℓ for each electron in a multi-electron atom is referred to as the *electronic configuration* of the atom.
- Pauli's exclusion principle confirms the shell structure of the atom as well as the sub-shell structure of individual atomic shells:
  - Number of electrons in sub-shells that are labeled with quantum numbers n, ℓ, m_ℓ: $\qquad\qquad 2(2\ell + 1)$
  - Number of electrons in sub-shells that are labeled with quantum numbers n, ℓ, j: $\qquad\qquad (2j + 1)$
  - Number of electrons in a shell: $\qquad 2\sum_{\ell=0}^{n-1}(2\ell + 1) = 2n^2$

The main characteristics of atomic shells and sub-shells are given in Tables 2.2 and 2.3, respectively. The spectroscopic notation for electrons in the K, L, and M shells and associated sub-shells is given in Table 2.4.

Table 2.2. Main characteristics of atomic shells

Principal quantum number n	1	2	3	4	5
Spectroscopic notation	K	L	M	N	O
Maximum number of electrons	2	8	18	32	–

Table 2.3. Main characteristics of atomic subshells

Orbital quantum number ℓ	0	1	2	3
Spectroscopic notation	s	p	d	f
Maximum number of electrons	2	6	10	14

Table 2.4. Notation for electrons in the K, L, M shells of a multi-electron atom

Principal quantum number n	Orbital angular momentum ℓ and total angular momentum j of electron					
	$s_{1/2}$	$p_{1/2}$	$p_{3/2}$	$d_{3/2}$	$d_{5/2}$	f
1	K					
2	L_I	L_{II}	L_{III}			
3	M_I	M_{II}	M_{III}	M_{IV}	M_V	

2.4.2 Hartree's Approximation for Multi-electron Atoms

Bohr's theory works well for one-electron structures (hydrogen atom, singly ionized helium, doubly ionized lithium, etc.) but does not apply directly to multi-electron atoms because of the repulsive Coulomb interactions among electrons constituting the atom. These interactions disrupt the attractive Coulomb interaction between an orbital electron and the nucleus and make it impossible to predict accurately the potential that influences the kinematics of the orbital electron. *Douglas Hartree* proposed an approximation that predicts the energy levels and radii of multi-electron atoms reasonably well despite its inherent simplicity.

Hartree assumed that the potential seen by a given atomic electron is given by

$$V(r) = -\frac{Z_{\text{eff}}\, e^2}{4\pi\varepsilon_{\text{o}}}\frac{1}{r} \; , \tag{2.79}$$

where

Z_{eff} is the effective atomic number,

$Z_{\text{eff}}e$ is an effective charge that accounts for the nuclear charge Ze as well as for the effects of all other atomic electrons.

Hartree's calculations show that in multi-electron atoms the effective atomic number Z_{eff} for K-shell electrons $(n = 1)$ has a value of about $Z - 2$. Charge distributions of all other atomic electrons produce a charge of about $-2e$ inside a sphere with the radius of the K shell, partially shielding the K-shell electron from the nuclear charge $+Ze$ and producing an effective charge $Z_{\text{eff}}e = (Z - 2)e$.

For outer shell electrons Hartree's calculations show that the effective atomic number Z_{eff} approximately equals n, where n specifies the principal quantum number of the outermost filled shell of the atom in the ground state.

Based on Bohr's one-electron atom model, Hartree's relationships for the radii r_{n} of atomic orbits (shells) and the energy levels E_{n} of atomic orbits are given as follows:

$$r_{\text{n}} = \frac{a_{\text{o}} n^2}{Z_{\text{eff}}} \tag{2.80}$$

and

$$E_{\text{n}} = -E_{\text{R}} \left(\frac{Z_{\text{eff}}}{n}\right)^2 . \tag{2.81}$$

Hartree's approximation for the K-shell $(n = 1)$ electrons in multi-electron atoms then results in the following expressions for the K-shell radius and K-shell binding energy

$$r_1 = r_K = \frac{a_{\text{o}}}{Z - 2} \tag{2.82}$$

and

$$E_1 = E(\mathrm{K}) = -E_\mathrm{R}(Z-2)^2 \,, \tag{2.83}$$

showing that the K-shell radii are inversely proportional to $Z-2$ and the K-shell binding energies increase as $(Z-2)^2$.

- K-shell radii range from a low of 0.5×10^{-2} Å for very high atomic number elements to 0.5 Å for hydrogen.
- K-shell binding energies (ionization potentials of K shell) range from 13.6 eV for hydrogen to 9 keV for copper, 33 keV for iodine, 69.5 keV for tungsten, 88 keV for lead, and 115 keV for uranium. For $Z > 30$, (2.83) gives values in good agreement with measured data. For example, the calculated and measured K-shell binding energies for copper are 9.9 keV and 9 keV, respectively, for tungsten 70.5 keV and 69 keV, respectively, and for lead 87 keV and 88 kev, respectively.

Hartree's approximation for outer shell electrons in multi-electron atoms with $(Z_\mathrm{eff} \approx n)$ predicts the following outer shell radius (radius of atom) and binding energy of outer shell electrons (ionization potential of atom)

$$r_\mathrm{outershell} \approx na_\mathrm{o} = n \times (0.53 \text{ Å}) \tag{2.84}$$

and

$$E_\mathrm{outer\ shell} \approx -E_\mathrm{R} = -13.6 \text{ eV} \,. \tag{2.85}$$

The radius of the K-shell constricts with an increasing Z; the radius of the outermost shell (atomic radius), on the other hand, increases slowly with Z, resulting in a very slow variation of the atomic size with the atomic number Z.

A comparison between Bohr's relationships for one-electron atoms and Hartree's relationships for multi-electron atoms is given in Table 2.5. The table compares expressions for the radii of shells, velocities of electrons in shells, energy levels of shells, and wave-number for electronic transitions between shells.

A simplified energy level diagram for tungsten, a typical multi-electron atom of importance in medical physics for its use as target material in x-ray tubes, is shown in Fig. 2.7. The K, L, M, and N shells are completely filled with their normal allotment of electrons $(2n^2)$, the O shell has 12 electrons and the P shell has 2 electrons.

The $n > 1$ shells are actually split into subshells, as discussed in Sect. 3.1.1. In Fig. 2.7 the fine structure of shells is represented by only one energy level that is equal to the average energy of all subshells for a given n.

- A vacancy in a shell with a low quantum number n will result in high-energy transitions in the keV range referred to as *x-ray transitions*.
- A vacancy in a shell with a high quantum number n will result in relatively low-energy transitions (in the eV range) referred to as *optical transitions*.

Table 2.5. Expressions for the radius, velocity, energy and wave-number of atomic structure according to Bohr's one-electron model and Hartree's multi-electron model

	One-electron atom Bohr theory	Multi-electron atom Hartree approximation
		Z_{eff} (for $n = 1$) $\approx Z - 2$ Z_{eff} (for outer shell) $\approx n$
Radius r_n	$r_n = a_o \frac{n^2}{Z}$ $r_1 = \frac{a_o}{Z}$ $a_o = 0.53$ Å	$r_n = a_o \frac{n^2}{Z_{eff}}$ $r_1 = r_K \approx \frac{a_o}{Z-2}$ $r_{outer\ shell} \approx n a_o$
Velocity v_n	$v_n = \alpha c \frac{Z}{n}$ $v_1 = \alpha c Z$ $\alpha = \frac{1}{137}$	$v_n = \alpha c \frac{Z_{eff}}{n}$ $v_1 = v_K \approx \alpha c (Z - 2)$ $v_{outer\ shell} \approx \alpha c$
Energy E_n	$E_n = -E_R \left\{ \frac{Z}{n} \right\}^2$ $E_1 = -E_R Z^2$ $E_R = 13.6$ eV	$E_n = -E_R \left\{ \frac{Z_{eff}}{n} \right\}^2$ $E_1 = E_K \approx -E_R (Z - 2)^2$ $E_{outer\ shell} \approx -E_R$
Wave-number k	$k = R_\infty Z^2 \left\{ \frac{1}{n_f^2} - \frac{1}{n_i^2} \right\}$ $R_\infty = 109\,737$ cm^{-1}	$k = R_\infty Z_{eff}^2 \left\{ \frac{1}{n_f^2} - \frac{1}{n_i^2} \right\}$ $Z_{eff}(K_\alpha) \approx Z - 1$ $k(K_\alpha) \approx \frac{3}{4} R_\infty (Z - 1)^2$

2.4.3 Periodic Table of Elements

The chemical properties of atoms are periodic functions of the atomic number Z and are governed mainly by electrons with the lowest binding energy, i.e., by outer shell electrons commonly referred to as valence electrons. The periodicity of chemical and physical properties of elements (periodic law) was first noticed by *Dmitry Mendeleyev*, who in 1869 produced a periodic table of the then-known elements.

Since Mendeleyev's time the periodic table of elements has undergone several modifications as the knowledge of the underlying physics and chemistry expanded and new elements were discovered and added to the pool. However, the basic principles elucidated by Mendeleyev are still valid today.

In a modern periodic table of elements each element is represented by its chemical symbol and its atomic number. The periodicity of properties of
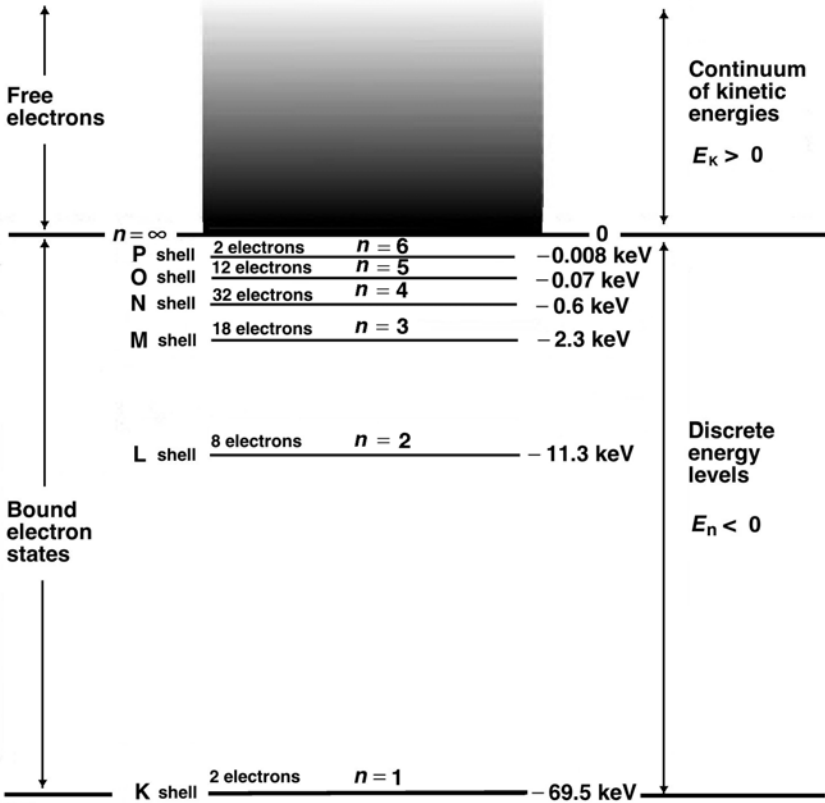
Fig. 2.7. A simplified energy level diagram for the tungsten atom, a typical example of a multi-electron atom

elements is caused by the periodicity in electronic structure that follows the rules of the Pauli exclusion principle (see Sect. 2.4.1).

The periodic table of elements is now most commonly arranged in the form of 7 horizontal rows or *periods* and 8 vertical columns or *groups*. Elements with similar chemical and physical properties are listed in the same column.

The *periods* in the periodic table are of increasing length as follows:

- Period 1 has two elements: hydrogen and helium.
- Periods 2 and 3 have 8 elements each.
- Periods 4 and 5 have 18 elements each.
- Period 6 has 32 elements condensed into 18 elements and the series of 14 lanthanons with atomic numbers Z from 57 through 71 is listed separately. Synonyms for lanthanon are lanthanide, lanthanoid, rare earth, and rare-earth element.

- Period 7 is still incomplete and the series of 14 actinons with atomic numbers Z from 89 through 103 is listed separately. Synonyms for actinon are actinide and actinoid.

The *groups* in the periodic table are arranged into 8 distinct groups, each group split into subgroups A and B. Each subgroup has a complement of electrons in the outermost atomic shell (in the range from 1 to 8) that determines its valence, i.e., chemical property.

Table 2.6 gives a simplified modern periodic table of elements with atomic numbers Z ranging from 1 (hydrogen) to 109 (meitnerium). Several groups of elements have distinct names, such as alkali elements (group I.A), alkali earth elements (group II.A), halogens (group VII.A) and noble gases (group VIII.A). Elements of other groups are grouped into transition metals, non-transition metals, non-metals (including halogens of group VII.A), lanthanons and actinons.

2.4.4 Ionization Potential of Atoms

The ionization potential (IP) of an atom is defined as the energy required for removal of the least bound electron (i.e., the outer shell or valence electron) from the atom. The E_R value predicted by Hartree [see (2.85)] is only an approximation and it turns out, as shown in Fig. 2.8, that the ionization potentials of atoms vary periodically with Z from hydrogen at 13.6 eV to a high value of 24.6 eV for helium down to about 4.5 eV for alkali elements that have only one outer shell (valence) electron.

The highest atomic ionization potential in nature is the ionization potential of the helium atom at 24.6 eV. In contrast, the ionization potential of a singly ionized helium atom (He^+) can be calculated easily from the Bohr's theory using (2.60) with $Z = 2$ and $n = 1$ to obtain an IP of 54.4 eV. This value is substantially higher than the IP for a helium atom because of the two-electron repulsive interaction that lowers the IP in the neutral helium atom.

A plot of the ionization potential IP against atomic number Z, shown in Fig. 2.8, exhibits peaks and valleys in the range from 4.5 eV to 24.6 eV, with the peaks occurring for noble gases (outer shell filled with 8 electrons) and valleys for alkali elements (one solitary electron in the outer shell). *Note*: the ionization potential of lead is a few eV in contrast to the ionization potential of the K shell in lead that is 88 keV.

2.5 Experimental Confirmation of the Bohr Atomic Model

The Bohr atomic model postulates that the total energy of atomic electrons bound to the nucleus is quantized. The binding energy quantization follows

Table 2.6. Simplified periodic table of elements covering 109 known elements and consisting of 7 periods 8 groups, each group divided into subgroups A and B

	I.A	II.A	III.B	IV.B	V.B	VI.B	VII.B	VIII.B			I.B	II.B	III.A	IV.A	V.A	VI.A	VII.A	VIII.A
1	1 H																	2 He
2	3 Li	4 Be											5 B	6 C	7 N	8 O	9 F	10 Ne
3	11 Na	12 Mg											13 Al	14 Si	15 P	16 S	17 Cl	18 Ar
4	19 K	20 Ca	21 Sc	22 Ti	23 V	24 Cr	25 Mn	26 Fe	27 Co	28 Ni	29 Cu	30 Zn	31 Ga	32 Ge	33 As	34 Se	35 Br	36 Kr
5	37 Rb	38 Sr	39 Y	40 Zr	41 Nb	42 Mo	43 Tc	44 Ru	45 Rh	46 Pd	47 Ag	48 Cd	49 In	50 Sn	51 Sb	52 Te	53 I	54 Xe
6	55 Cs	56 Ba	57-71 La	72 Hf	73 Ta	74 W	75 Re	76 Os	77 Ir	78 Pt	79 Au	80 Hg	81 Tl	82 Pb	83 Bi	84 Po	85 At	86 Rn
7	87 Fr	88 Ra	89-103 Ac	104 Rf	105 Db	106 Sg	107 Bh	108 Hs	109 Mt									

Alkali metals (group I.A) with one electron in the outer atomic shell
Lithium (Li-3); Sodium (Na-11); Potassium (K-19); Rubidium (Rb-37); Cesium (Cs-55); Francium (Fr-87)

Alkali earth metals (group II.A) with 2 electrons in the outer atomic shell
Beryllium (Be-4); Magnesium (Mg-12); Calcium (Ca-20); Strontium (Sr-38); Barium (Ba-56); Radium (88)

Transition metals with 1 or 2 electrons in the outer atomic shell

Non-transition metals with 3, 4, 5, or 6 electrons in the outer atomic shell

Non-metals with 3, 4, 5, 6, or 7 electrons in the outer atomic shell

Halogens (group VII.A) with 7 electrons in the outer atomic shell
Fluorine (F-9); Chlorine (Cl-17); Bromine (Br-35); Iodine (I-53); Astatine (At-85)

Noble (Inert) gases (group VIII.A) with 8 electrons in the outer atomic shell
Helium (He-4); Neon (Ne-10); Argon (Ar-18); Krypton (Kr-36); Xenon (Xe-54); Radon (Rn-86)

Lanthanons (lanthanide series from $Z = 57$ to $Z = 71$)
Lanthanum (La-57); Cerium (Ce-58); Praseodymium (Pr-59); Neodymium (Nd-60); Promethium (Pm-61); Samarium (Sm-62); Europium (Eu-63); Gadolinium (Gd-64); Terbium (Tb-65); Dysprosium (Dy-66); Holmium (Ho-67); Erbium (Er-68); Thulium (Tm-69); Ytterbium (Yb-70); Lutetium (71)

Actinons (actinide series from $Z = 89$ to $Z = 103$)
Actinium (Ac-89); Thorium (Th-90); Protactinium (Pr-91); Uranium (U-92); Neptunium (Np-93); Plutonium (Pu-94); Americium (Am-95); Curium (Cm-96); Berkelium (Bk-97); Californium (Cf-98); Einsteinium (Es-99); Fermium (Fm-100); Mendelevium (Md-101); Nobelium (No-102); Lawrencium (Lr-103)
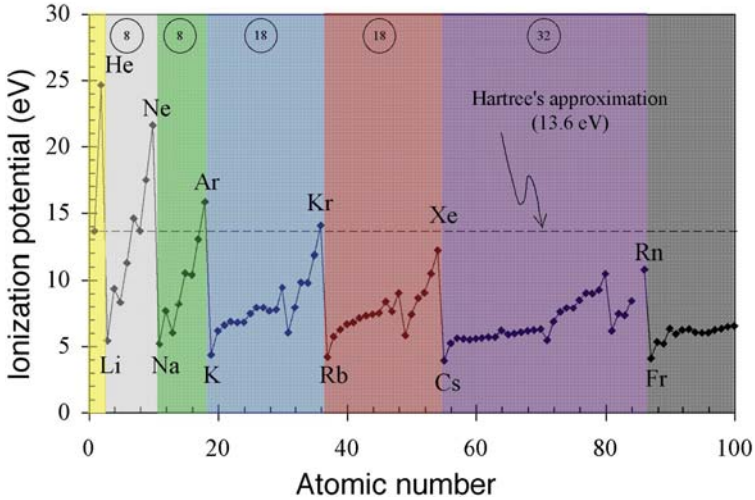
Fig. 2.8. Ionization potential (ionization energy) of atoms against atomic number Z. The noble gases that contain the most stable electronic configurations and the highest ionization potentials are identified, as are the alkali elements that contain the least stable electronic configurations and the lowest ionization potentials with only one valence electron in the outer shell. The circled numbers indicate the number of atoms in a given period

from the simple quantization of the electron angular momentum $L = n\hbar$. Direct confirmation of the electron binding energy quantization was obtained from the following three experiments:

1. Measurement of *absorption and emission spectra* of mono-atomic gases.
2. *Moseley's experiment.*
3. *Franck-Hertz experiment.*

2.5.1 Emission and Absorption Spectra of Mono-Atomic Gases

In contrast to the continuous spectra emitted from the surface of solids at high temperatures, the spectra emitted by free excited atoms of gases consist of a number of discrete wavelengths. An electric discharge produces excitations in the gas, and the radiation is emitted when the gas atoms return to their ground state. Correct prediction of line spectra emitted or absorbed by mono-atomic gases, especially hydrogen, serves as an important confirmation of the Bohr atomic model.

- The *emission spectrum* is measured by first collimating the emitted radiation by a slit, and then passing the collimated slit-beam through an optical prism or a diffraction grating. The prism or grating breaks the beam into its wavelength spectrum that is recorded on a photographic

plate. Each kind of free atom produces its own characteristic emission line, making spectroscopy a useful complement to chemical analysis.

- In addition to the emission spectrum, it is also possible to study the *absorption spectrum* of gases. The experimental technique is similar to that used in measurement of the emission spectrum except that in the measurement of the absorption spectrum a continuous spectrum is made to pass through the gas under investigation. The photographic plate shows a set of unexposed lines that result from the absorption by the gas of distinct wavelengths of the continuous spectrum.

- For every line in the absorption spectrum of a given gas there is a corresponding line in the emission spectrum; however, the reverse is not true. The lines in the absorption spectrum represent transitions to excited states that all originate in the ground state. The lines in the emission spectrum, on the other hand, represent not only transitions to the ground state but also transitions between various excited states. The number of lines in an emission spectrum will thus exceed the number of lines in the corresponding absorption spectrum.

2.5.2 Moseley's Experiment

Henry Moseley in 1913 carried out a systematic study of K_α x rays produced by all then-known elements from aluminum to gold using the Bragg technique of x-ray scattering from a crystalline lattice of a potassium ferrocyanide crystal. The characteristic K_α x rays (electronic transition from $n_i = 2$ to $n_f = 1$; see Sect. 3.1.1) were produced by bombardment of the targets with energetic electrons. The results of Moseley's experiments serve as an excellent confirmation of the Bohr atomic theory.

From the relationship between the measured scattering angle ϕ and the known crystalline lattice spacing d (Bragg's law: $2d \sin \phi = m\lambda$, where m is an integer) Moseley determined the wavelengths λ of K_α x rays for various elements and observed that the $\sqrt{\nu}$ where ν is the frequency ($\nu = c/\lambda$) of the K_α x rays was linearly proportional to the atomic number Z. He then showed that all x-ray data could be fitted by the following relationship

$$\sqrt{\nu} = \sqrt{a}(Z - b) , \tag{2.86}$$

where a and b are constants.

The same $\sqrt{\nu}$ versus Z behavior also follows from the Hartree-type approximation that in general predicts the following relationship for the wavenumber k

$$k = \frac{1}{\lambda} = \frac{\nu}{c} = R_\infty Z_{\text{eff}}^2 \left(\frac{1}{n_f^2} - \frac{1}{n_i^2} \right) \tag{2.87}$$

or

$$\sqrt{\nu} = Z_{\text{eff}} \sqrt{cR_\infty \left(\frac{1}{n_f^2} - \frac{1}{n_i^2} \right)} . \tag{2.88}$$

For K_α characteristic x rays, where $n_i = 2$ and $n_f = 1$, Hartree's expression gives

$$k(K_\alpha) = \frac{3}{4} R_\infty Z_{\text{eff}}^2 = \frac{3}{4} R_\infty (Z-1)^2 \; . \tag{2.89}$$

Note that in the K_α emission $Z_{\text{eff}} = Z - 1$ rather than $Z_{\text{eff}} = Z - 2$ which is the Z_{eff} predicted by Hartree for neutral multi-electron atoms. In the K_α emission there is a vacancy in the K shell and the L-shell electron making the K_α transition actually sees an effective charge $(Z-1)e$ rather than an effective charge $(Z-2)e$, as is the case for K-shell electrons in neutral atoms.

2.5.3 Franck-Hertz Experiment

Direct confirmation that the internal energy states of an atom are quantized came from an experiment carried out by *James Franck* and *Gustav Hertz* in 1914. The experimental set up is shown schematically in Fig. 2.9a.

- An evacuated vessel containing three electrodes (cathode, anode and plate) is filled with mercury vapor.
- Electrons are emitted thermionically from the heated cathode and accelerated toward the perforated anode by a potential V applied between cathode and anode.
- Some of the electrons pass through the perforated anode and travel to the plate, provided their kinetic energy upon passing through the perforated anode is sufficiently high to overcome a small retarding potential V_{ret} that is applied between the anode and the plate.
- The experiment involves measuring the electron current reaching the plate as a function of the accelerating voltage V.
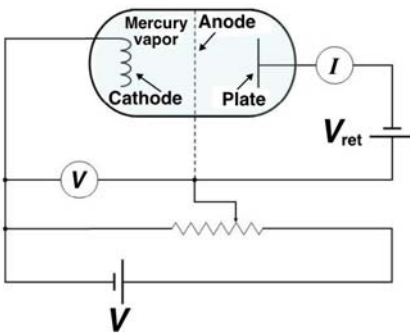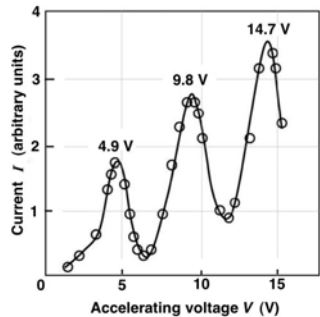
Fig. 2.9. a Schematic diagram of the Franck-Hertz experiment; **b** Typical result of the Franck-Hertz experiment using mercury vapor

- With an increasing potential V the current at the plate increases with V until, at a potential of 4.9 V, it abruptly drops, indicating that some interaction between the electrons and mercury atoms suddenly appears when the electrons attain a kinetic energy of 4.9 eV. The interaction was interpreted as an excitation of mercury atoms with a discrete energy of 4.9 eV; the electron raising an outer shell mercury electron to its first excited state and, in doing so, losing its kinetic energy and its ability to overcome the retarding potential V_{ret} between the anode and the plate.
- The sharpness of the current drop at 4.9 V indicates that electrons with energy below 4.9 eV cannot transfer their energy to a mercury atom, substantiating the existence of discrete energy levels for the mercury atom.
- With voltage increase beyond 4.9 V the current reaches a minimum and then rises again until it reaches another maximum at 9.8 V, indicating that some electrons underwent two interactions with mercury atoms. Other maxima at higher multiples of 4.9 V were observed with careful experiments. Typical experimental results are shown in Fig. 2.9b.
- In contrast to the minimum excitation potential of the outer shell electron in mercury of 4.9 eV, the ionization potential of mercury is 10.4 eV.
- A further investigation showed a concurrent emission of 2536 Å ultraviolet rays that, according to Bohr model, will be emitted when the mercury atom reverts from its first excited state to the ground state through a 4.9 eV optical transition.
- The photon energy $E_\nu = 4.9$ eV is given by the standard relationship

$$E_\nu = h\nu = 2\pi\hbar c/\lambda \, , \tag{2.90}$$

from which the wavelength of the emitted photon can be calculated as

$$\lambda = \frac{2\pi\hbar c}{E_\nu} = \frac{2\pi\,197.4 \times 10^6 \text{ eV } 10^{-5} \text{ Å}}{4.9 \text{ eV}} = 2536 \text{ Å} \, . \tag{2.91}$$

Ultraviolet photons with a wavelength of 2536 Å were actually observed accompanying the Franck-Hertz experiment, adding to the measured peaks in the current versus voltage diagram of Fig. 2.9b another means for the confirmation of the quantization of atomic energy levels.

2.6 Schrödinger Equation for the Ground State of Hydrogen

In solving the Schrödinger equation for a hydrogen or hydrogen-like one-electron atom, a 3-dimensional approach must be used to account for the electron motion under the influence of a central force. The Coulomb potential binds the electron to the nucleus and the coordinate system is chosen such that its origin coincides with the center of the nucleus. To account for the motion of the nucleus we use the reduced mass μ of (2.66) rather than the pure electron rest mass m_{e} in the calculation.

The time-independent Schrödinger wave equation was given in (1.79) as

$$-\frac{\hbar^2}{2\mu}\nabla^2\psi + V(r)\psi = E\psi \ , \tag{2.92}$$

where

$V(r)$ is the potential energy of the particle,
E is the total energy of the particle
∇^2 is the Laplacian operator in Cartesian, cylindrical or spherical coordinates,
μ is the reduced mass of the electron/proton system given in (2.66).

For the hydrogen atom, the potential $V(r)$ is represented by the spherically-symmetric Coulomb potential as follows:

$$V(r) = -\frac{1}{4\pi\varepsilon_{\mathrm{o}}}\frac{e^2}{r} \ . \tag{2.93}$$

The Schrödinger wave equation is separable in spherical coordinates (r, θ, ϕ) and for the hydrogen atom it is written by expressing the Laplacian operator in spherical coordinates as follows:

$$-\frac{\hbar^2}{2\mu}\left\{\frac{1}{r^2}\frac{\partial}{\partial r}\left(r^2\frac{\partial}{\partial r}\right) + \frac{1}{r^2\sin\theta}\frac{\partial}{\partial\theta}\left(\sin\theta\frac{\partial}{\partial\theta}\right) + \frac{1}{r^2\sin^2\theta}\frac{\partial^2}{\partial\phi^2}\right\}$$
$$\psi(r, \theta, \phi) - \frac{e^2}{4\pi\varepsilon_{\mathrm{o}}}\frac{1}{r}\psi(r, \theta, \phi) = E\psi(r, \theta, \phi) \ , \tag{2.94}$$

with (r, θ, ϕ) the spherical coordinates of the electron.

The boundary conditions stipulate that $|\psi|^2$ must be an integrable function. This implies that the wave function $\psi(r, \theta, \phi)$ vanishes as $r \to \infty$, i.e., the condition that $\lim_{r\to\infty}\psi(r, \theta, \phi) = 0$ must hold.

Equation (2.94) can be solved with the method of separation of variables by expressing the function $\psi(r, \theta, \phi)$ as a product of three functions: $R(r)$, $\Theta(\theta)$, and $\Phi(\phi)$; each of the three functions depends on only one of the three spherical variables, i.e.,

$$\psi(r, \theta, \phi) = R(r)\Theta(\theta)\Phi(\phi) \ . \tag{2.95}$$

Inserting (2.95) into (2.94) and dividing by $R(r)\Theta(\theta)\Phi(\phi)$ we get the following expression

$$-\frac{\hbar^2}{2\mu}\left\{\frac{1}{r^2}\frac{1}{R}\frac{\partial}{\partial r}\left(r^2\frac{\partial R}{\partial r}\right) + \frac{1}{r^2\sin\theta}\frac{1}{\Theta}\frac{\partial}{\partial\theta}\left(\sin\theta\frac{\partial\Theta}{\partial\theta}\right) + \frac{1}{r^2\sin^2\theta}\frac{1}{\Phi}\frac{\partial^2\Phi}{\partial\phi^2}\right\}$$
$$-\frac{e^2}{4\pi\varepsilon_{\mathrm{o}}}\frac{1}{r} = E \ , \tag{2.96}$$

Separation of variables then results in the following three ordinary differential equations

$$\frac{d^2\Phi}{d\phi^2} = -m_\ell\Phi \ , \tag{2.97}$$

$$-\frac{1}{\sin\theta}\frac{d}{d\theta}\left(\sin\theta\frac{d\Theta}{d\theta}\right) + \frac{m_\ell^2\Theta}{\sin^2\theta} = \ell(\ell+1)\Theta \ , \qquad (2.98)$$

and

$$\frac{1}{r^2}\frac{d}{dr}\left(r^2\frac{dR}{dr}\right) + \frac{2\mu}{\hbar^2}\left(E + \frac{e^2}{4\pi\varepsilon_o}\right)R = \ell(\ell+1)\frac{R}{r^2} \ , \qquad (2.99)$$

with separation constants m_ℓ and $\ell(\ell+1)$, where m_ℓ and ℓ are referred to as the magnetic and orbital quantum numbers, respectively.

Equation (2.99) for $R(r)$ gives physical solutions only for certain values of the total energy E. This indicates that the energy of the hydrogen atom is quantized, as suggested by the Bohr theory, and predicts energy states that are identical to those calculated for the Bohr model of the hydrogen atom. The energy levels E_n calculated from the Schrödinger wave equation, similarly to those calculated for the Bohr atom, depend only on the principal quantum number n; however, the wave function solutions depend on three quantum numbers: n (principal), ℓ (orbital) and m_ℓ (magnetic). All quantum numbers are integers governed by the following rules:

$$n = 1, 2, 3\ldots, \quad \ell = 0, 1, 2, \ldots n-1,$$
$$m_\ell = -\ell, -\ell+1, \ldots (\ell-1), \ell \ . \qquad (2.100)$$

Equation (2.94) is generally quite complex yielding wave functions for the ground state $n = 1$ of the hydrogen atom as well as for any of the excited states with associated values of quantum numbers ℓ and m_ℓ.

The ground state of the hydrogen atom can be calculated in a simple fashion as follows. Since $V(r)$ is spherically symmetric, we assume that solutions to the Schrödinger equation for the ground state of hydrogen will be spherically symmetric which means that the wave function $\psi(r, \theta, \phi)$ does not depend on θ and φ, it depends on r alone, and we can write for the spherically symmetric solutions that $\psi(r, \theta, \phi) = R(r)$.

The Schrödinger equation then becomes significantly simpler and after some rearranging of terms it is given as follows:

$$\frac{d^2R(r)}{dr^2} + \frac{2}{r}\left\{\frac{dR(r)}{dr} + \frac{\mu}{\hbar^2}\frac{e^2}{4\pi\varepsilon_o}R(r)\right\} + \frac{2\mu E}{\hbar^2}R(r) = 0 \ . \qquad (2.101)$$

We can now simplify the Schrödinger equation further by recognizing that for large r the $(1/r)$ term will be negligible and we obtain

$$\frac{d^2R(r)}{dr^2} - \left(-\frac{2\mu E}{\hbar^2}\right)R(r) \approx 0 \ . \qquad (2.102)$$

Next we define the constant $-2\mu E/\hbar^2$ as λ^2 and recognize that the total energy E_1 for the ground state of hydrogen will be negative

$$\lambda^2 = -\frac{2\mu E_1}{\hbar^2} \ . \qquad (2.103)$$

The simplified Schrödinger equation is now given as follows:

$$\frac{d^2R(r)}{dr^2} - \lambda^2 R(r) = 0 . \tag{2.104}$$

Equation (2.104) is recognized as a form of the Helmholtz differential equation in one dimension that leads to exponential functions for $\lambda^2 > 0$, to a linear function for $\lambda = 0$, and to trigonometric functions for $\lambda < 0$. Since the total energy E is negative for bound states in hydrogen, λ^2 is positive and the solutions to (2.104) will be exponential functions. The simplest exponential solution is

$$R(r) = Ce^{-\lambda r} , \tag{2.105}$$

with the first derivative expressed as

$$\frac{dR(r)}{dr} = -\lambda Ce^{-\lambda r} = -\lambda R(r) . \tag{2.106}$$

The second derivative of the function $R(r)$ of (2.105) is given as follows:

$$\frac{d^2R(r)}{dr^2} = \lambda^2 Ce^{-\lambda r} = \lambda^2 R(r) . \tag{2.107}$$

Inserting (2.105) and (2.107) into (2.104) shows that (2.105) is a valid solution to (2.104). We now insert (2.105), (2.106) and (2.107) into (2.101) and get the following expression

$$\lambda^2 R(r) + \frac{2}{r} \left\{ -\lambda + \frac{\mu}{\hbar^2} \frac{e^2}{4\pi\varepsilon_{\mathrm{o}}} \right\} R(r) + \frac{2\mu E_1}{\hbar^2} R(r) = 0 . \tag{2.108}$$

The first and fourth terms of (2.108) cancel out because λ^2 is defined as $(-2\mu E_1/\hbar^2)$ in (2.103). Since (2.108) must be valid for any $\psi(r)$, the term in curly brackets equals zero and provides another definition for the constant λ as follows:

$$\lambda = \frac{\mu}{\hbar^2} \frac{e^2}{4\pi\varepsilon_{\mathrm{o}}} = \frac{\mu c^2}{(\hbar c)^2} \frac{e^2}{4\pi\varepsilon_{\mathrm{o}}} . \tag{2.109}$$

We recognize (2.109) for λ as the inverse of the Bohr radius a_{o} that was given in (2.58). Therefore, we express $1/\lambda$ as follows:

$$\frac{1}{\lambda} = a_{\mathrm{o}} = \frac{(\hbar c)^2}{\mu c^2} \frac{4\pi\varepsilon_{\mathrm{o}}}{e^2} = 0.5292 \text{ Å} . \tag{2.110}$$

Combining (2.103) and (2.109) for the constant λ we now express the ground state energy E_1 as

$$E_1 = -\frac{1}{2} \frac{\hbar^2}{\mu} \frac{1}{a_{\mathrm{o}}^2} = -\frac{1}{2} \left(\frac{e^2}{4\pi\varepsilon_{\mathrm{o}}} \right)^2 \frac{\mu c^2}{(\hbar c)^2} = -13.61 \text{ eV} . \tag{2.111}$$

The wave function $R(r)$ for the ground state of hydrogen is given in (2.105) in general terms with constants C and λ. The constant λ was established in (2.110) as the inverse of the Bohr radius a_{o}; the constant C we determine from

the normalization condition of (1.62) that is given by the following expression

$$\iiint |\psi(r)|^2 \, dV = 1 \, , \tag{2.112}$$

with the volume integral extending over all space.

The constant C is determined after inserting $\psi(r, \theta, \phi) = R(r)$ given by (2.105) into (2.112) to obtain

$$\iiint |\psi(r)|^2 \, dV = C^2 \int_0^{2\pi} \int_0^{\pi} \int_0^{\infty} e^{-\frac{2r}{a_\mathrm{o}}} r^2 \, d\phi \sin\theta d\theta dr$$

$$= 4\pi C^2 \int_0^{\infty} r^2 e^{-\frac{2r}{a_\mathrm{o}}} \, dr = 4\pi C^2 \frac{1}{4a_\mathrm{o}^3} = 1 \, , \tag{2.113}$$

where the last integral over r is determined from the following recursive formula

$$\int x^n e^{ax} dx = \frac{1}{a} x^n e^{ax} - \frac{n}{a} \int x^{n-1} e^{ax} dx \, . \tag{2.114}$$

The integral over r in (2.113) is equal to $1/(4a_\mathrm{o}^3)$ and the constant C is now given as follows:

$$C = \pi^{-1/2} a_\mathrm{o}^{-3/2} \, , \tag{2.115}$$

resulting in the following expression for the wave function $R(r)$ for the ground state of the hydrogen atom

$$\psi_{\mathrm{n},\ell,\mathrm{m}_\ell}(r, \theta, \phi) = \psi_{100} = R_1(r) = \frac{1}{\pi^{1/2} a_\mathrm{o}^{3/2}} e^{-\frac{r}{a_\mathrm{o}}} \, . \tag{2.116}$$

The probability density of (1.60) can now be modified to calculate the radial probability density dP/dr as follows:

$$\frac{dP}{dV} = \psi^*(r, \theta, \phi) \psi(r, \theta, \phi) = |\psi(r, \theta, \phi)|^2 \tag{2.117}$$

and

$$\frac{dP}{dr} = 4\pi r^2 |\psi(r, \theta, \phi)|^2 \, , \tag{2.118}$$

since $dV = 4\pi r^2 dr$ for the spherical symmetry governing the ground state ($n = 1$) of the hydrogen atom.

The radial probability density dP/dr for the ground state is given as follows, after inserting (2.116) into (2.118):

$$\frac{dP}{dr} = \frac{4r^2}{a_\mathrm{o}^3} e^{-\frac{2r}{a_\mathrm{o}}} \, . \tag{2.119}$$

A plot of unit-less $a_\mathrm{o}(dP/dr)$ given as $4(r/a_\mathrm{o})^2 \exp(-2r/a_\mathrm{o})$ against (r/a_o) for the ground state of the hydrogen atom is shown in Fig. 2.10. The following observations can be made based on data shown in Fig. 2.10:
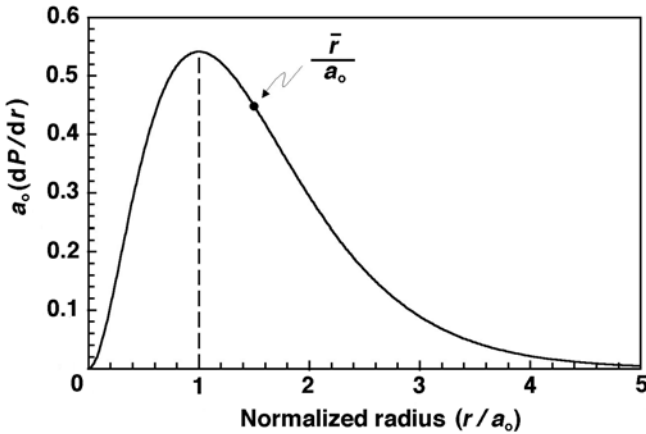
Fig. 2.10. The radial probability density multiplied with the Bohr radius a_o against normalized radius r for the ground state electron of hydrogen

1. $dP/dr = 0$ for $r = 0$ and $r = \infty$.
2. dP/dr reaches its maximum at $r = a_o$ highlighting Schrödinger's theory prediction that the ground state electron in hydrogen is most likely to be found at $r = a_o$ where a_o is the Bohr radius given in (2.58). One can also obtain this result by calculating d^2P/dr^2 and setting the result equal to zero at $r = r_{\max}$. Thus, the most probable radius r_p for the electron in the ground state of hydrogen is equal to a_o.
3. Contrary to Bohr theory that predicts the electron in a fixed orbit with $r = a_o$, Schrödinger's theory predicts that there is a finite probability for the electron to be anywhere between $r = 0$ and $r = \infty$. However, the most probable radius for the electron is $r = a_o$.

To illustrate Schrödinger's theory better a few simple calculations will now be made for the ground state of hydrogen:

1. The probability that the orbital electron will be found inside the first Bohr radius a_o is calculated by integrating (2.119) from $r = 0$ to $r = a_o$ to get

$$P = \frac{4}{a_o^3} \int_0^{a_o} r^2 e^{-2r/a_o} dr = \left\{ \frac{4e^{-2r/a_o}}{a_o^3} \left[-\frac{a_o r^2}{2} - \frac{a_o^2 r}{2} - \frac{a_o^3}{4} \right] \right\}_{r=0}^{r=a_o}$$

$$= -\left\{ e^{-2r/a_o} \left[2 \left(\frac{r}{a_o} \right)^2 + 2 \left(\frac{r}{a_o} \right) + 1 \right] \right\}_{r=0}^{r=a_o} = 1 - 5e^{-2} = 0.323$$

$$(2.120)$$

2. The probability that the orbital electron will be found with radius exceeding a_o is similarly calculated by integrating (2.119) from $r = a_o$ to $r = \infty$

$$
\begin{aligned}
P &= \frac{4}{a_o^3} \int_0^{a_o} r^2 e^{-2r/a_o} dr = \left\{ \frac{4e^{-2r/a_o}}{a_o^3} \left[-\frac{a_o r^2}{2} - \frac{a_o^2 r}{2} - \frac{a_o^3}{4} \right] \right\}_{r=a_o}^{r=\infty} \\
&= -\left\{ e^{-2r/a_o} \left[2\left(\frac{r}{a_o}\right)^2 + 2\left(\frac{r}{a_o}\right) + 1 \right] \right\}_{r=a_o}^{r=\infty} = 5e^{-2} = 0.677
\end{aligned}
\tag{2.121}
$$

3. The probability that the orbital electron will be found inside the nucleus (proton) is calculated by integrating (2.119) from $r = 0$ to $r = R$ where R is the proton radius estimated from (1.14) as $R \approx 1.2$ fm. Using $R/a_o = 2.4 \times 10^{-5}$ we get the following probability

$$
\begin{aligned}
P &= \frac{4}{a_o^3} \int_0^{a_o} r^2 e^{-2r/a_o} dr = \left\{ \frac{4e^{-2r/a_o}}{a_o^3} \left[-\frac{a_o r^2}{2} - \frac{a_o^2 r}{2} - \frac{a_o^3}{4} \right] \right\}_{r=0}^{r=R} \\
&= -\left\{ e^{-2r/a_o} \left[2\left(\frac{r}{a_o}\right)^2 + 2\left(\frac{r}{a_o}\right) + 1 \right] \right\}_{r=0}^{r=R} \\
&= 1 - e^{-2R/a_o} \left[2\left(\frac{R}{a_o}\right)^2 + 2\left(\frac{R}{a_o}\right) + 1 \right] \approx 2.3 \times 10^{-9}
\end{aligned}
\tag{2.122}
$$

4. The average electron radius $\bar{r}$ is calculated from (1.81) to get

$$
\bar{r} = \int \int \int r \left[R(r) \right]^2 dV = \frac{4}{a_o^3} \int_0^\infty r^3 e^{-\frac{2r}{a_o}} dr = \frac{4a_o^4 3!}{16a_0^3} = \frac{3}{2} a_o
\tag{2.123}
$$

The most probable radius $r_p = a_o$ and the /average radius $\bar{r} = 1.5a_o$ are not identical because the radial probability density distribution is not symmetrical about its maximum at a_o, as shown in Fig. 2.10. As calculated in (2.120) and (2.121), the area under the dP/dr curve between $r = 0$ and $r = a_o$ is exactly one half the area under the curve between $r = a_o$ and $r = \infty$. As shown in (2.122), the probability for the electron to venture inside the proton nucleus is very small but not negligible.

Linear Accelerator Waveguide

The photograph on the next page shows a cut-away view of a simple standing wave accelerating waveguide used in a medical linear accelerator to accelerate electrons to a kinetic energy of 6 MeV that corresponds to a velocity of 99.7% of the speed of light in vacuum.

In contrast to x-ray tubes that use an electrostatic potential between the anode (target) and the cathode (filament) for acceleration of electrons to a given kinetic energy of the order of 100 keV, a medical linear accelerator (linac) uses an accelerating waveguide in which electrons are accelerated with electromagnetic fields to much higher kinetic energies in the range from 4 MeV to 25 MeV.

Waveguides are evacuated or gas-filled structures of rectangular or circular cross sections used in transmission of microwaves. Two types of waveguides are used in linacs: radiofrequency power transmission waveguides (usually gas-filled) and accelerating waveguides (always evacuated). The power transmission waveguides transmit the radiofrequency power from the power source to the accelerating waveguide in which electrons are accelerated. The electrons are accelerated in the accelerating waveguide by means of energy transfer from the high power microwave field that is set up in the accelerating waveguide and produced by the radiofrequency power generator.

The simplest accelerating waveguide is obtained from a cylindrical uniform waveguide by adding a series of irises (disks) with circular holes at the center and placed at equal distances along the uniform waveguide. These irises divide the waveguide into a series of cylindrical cavities that form the basic structure of the accelerating waveguide. The phase velocity of radiofrequency in a uniform waveguide exceeds that of the speed of light in vacuum and one of the roles of the irises is to slow down the radiofrequency below the speed of light to allow electron acceleration. The irises also couple the cavities, distribute microwave power from one cavity to another, and provide a suitable electric field pattern for acceleration of electrons in the accelerating waveguide.

The waveguide cavities are clearly visible on the photograph of the waveguide; the accelerating cavities are on the central axis of the waveguide, the radiofrequency coupling cavities are offside. The source of electrons (electron gun) is on the left, the x-ray target on the right, both permanently embedded into the waveguide structure. The electron gun is a simple electrostatic accelerator that produces electrons thermionically in a heated filament and accelerates them to a typical energy of 20 keV. The target is made of metal thicker than the 6 MeV electron range in the target material. The 6 MeV electrons are stopped in the target and a small portion of their energy is transformed into bremsstrahlung x rays that form a spectrum ranging in photon energies from 0 to 6 MeV and have an effective energy of about 2 MeV. The bremsstrahlung x-ray beam produced by 6 MeV electrons striking a target is referred to as a 6 MV beam.

3 Production of X Rays

This chapter is devoted to a study of the production of the two known types of x rays: *characteristic radiation* and *bremsstrahlung*. Both types of x rays are important in medical physics, since both are used extensively in diagnostic imaging and in external beam radiotherapy. *Characteristic x-rays* are produced by electronic transitions in atoms triggered by vacancies in inner electronic shells of the absorber atom. *Bremsstrahlung*, on the other hand, is produced by Coulomb interactions between an energetic light charged particle and the nucleus of the absorber atom. Vacancies in electronic shells of atoms can be produced by various means such as Coulomb interactions, photon interactions, nuclear decay, positron annihilation and Auger effect; however, x-rays used in medicine are produced only through Coulomb interactions of energetic electrons with orbital electrons and nuclei of an x-ray target.

This chapter provides a discussion of theoretical and practical aspects of x-ray production, briefly introduces Čerenkov radiation and synchrotron radiation, both of some interest in nuclear and medical physics, and concludes with a brief discussion of various accelerators of interest in medicine.
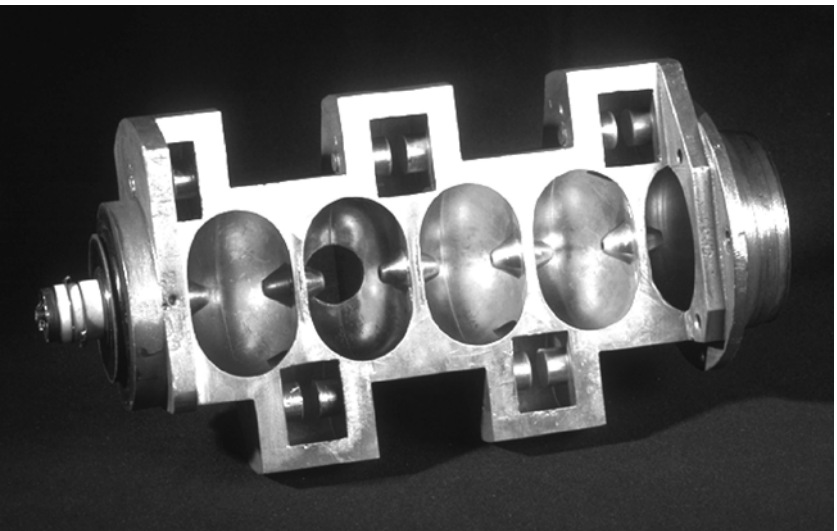
3.1 X-Ray Line Spectra (Characteristic Radiation)

A vacancy in an atomic shell plays an important role in physics and chemistry. Defined as an electron missing from the normal complement of electrons in a given atomic shell, a vacancy can be produced by eight different effects or interactions ranging from various photon-atom interactions through charge particle-atom interactions to nuclear effects. Depending on the nature and energy of the interaction, the vacancy may occur in the outer shell or in one of the inner shells of the atom. The list of the 8 effects for production of shell vacancy in an atom is as follows:

1. *Photoelectric effect* (see Sect. 7.5)
2. *Compton scattering* (see Sect. 7.3)
3. *Triplet production* (see Sect. 7.6.1)
4. *Charged particle Coulomb interaction* with an atom (see Sect. 5.3.1)
5. *Internal conversion* (see Sect. 8.9.3)
6. *Electron capture* (see Sect. 8.8.4)
7. *Positron annihilation* (see Sect. 7.6.7)
8. *Auger effect* (see Sect. 3.1.2)

An atom with a vacancy in its inner shell is in a highly excited state and returns to its ground state through a series of electronic transitions. Electrons from higher atomic shells will fill the shell vacancies and the energy difference in binding energies between the initial and final shell or sub-shell will be emitted from the atom in one of two ways:

1. Radiatively in the form of *characteristic (fluorescent) radiation*.
2. Non-radiatively in the form of *Auger electrons, Coster-Kronig electrons* or *super Coster-Kronig electrons*.

3.1.1 Characteristic Radiation

Radiative transitions result in emission of photons that are called *characteristic radiation*, since the wavelength λ and energy $h\nu$ of the emitted photon are characteristic of the atom in which the photon originated. An older term, *fluorescent radiation*, is occasionally used to describe the characteristic photons. The set of radiative transition photons emitted from a given atom is referred to as the *line spectrum* of the atom. *Charles G. Barkla* is credited with the discovery of characteristic x rays.

Energy level diagrams for high atomic number x-ray targets are usually drawn using the n, ℓ, j and m_j quantum numbers, as shown in Fig. 3.1. In addition to dependence on n (main structure), the energy level diagram also exhibits dependence on ℓ and j (fine structure). However, only certain allowed transitions, fulfilling specific selection rules, result in x rays. In Fig. 3.1 only transitions from the M and L to the K shell are shown; allowed transitions with solid lines and a forbidden transition with a dotted line.
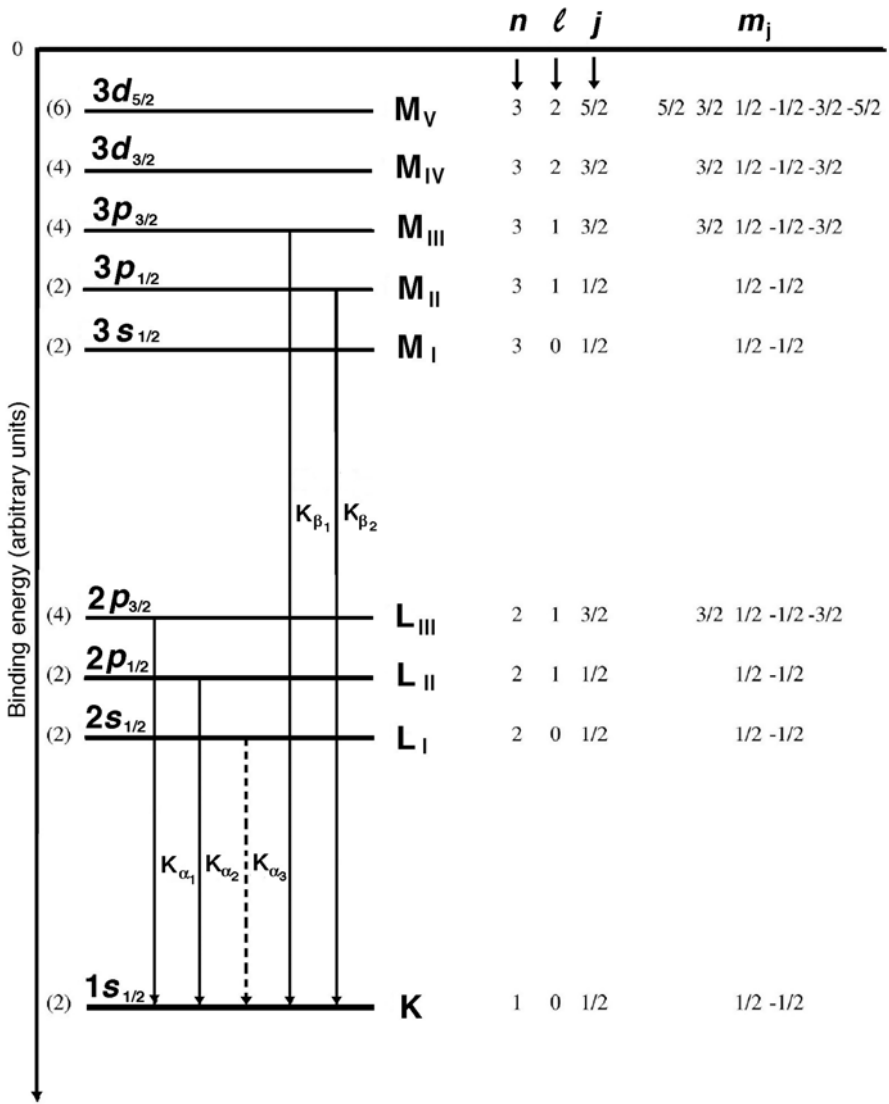
Fig. 3.1. Typical energy level diagram for a high atomic number element showing the K, L, and M shells with associated sub-shells. The *numbers in brackets* indicate the maximum possible number of electrons in a given sub-shell equal to $(2j+1)$. K_α and K_β transitions are also shown. The allowed K_α and K_β transitions are shown with *solid lines*, the forbidden K_{α_3} transition is shown with a *dashed line*

The selection rules for allowed characteristic transitions are:

$$\Delta\ell = \pm 1 \qquad \text{and} \qquad \Delta j = 0 \text{ or } \pm 1 \,, \tag{3.1}$$

with the proviso that transitions from $j = 0$ to $j = 0$ are forbidden.

- The energies released through an electronic transition are affected by the atomic number Z of the absorbing atom and by the quantum numbers of the atomic shells involved in the electronic transition.
- Transitions between outer shell electrons may result in optical photons and are referred to as *optical transitions* ($h\nu$ of the order of a few eV); transitions between inner shells of high atomic number elements may result in x rays and are referred to as *x-ray transitions* ($h\nu$ of the order of 10 to 100 keV).

In general the following conventions are used in atomic physics:

1. Transitions to the K shell are referred to as the K lines, to the L shell as L lines, to the M shell as M lines, etc.
2. Transitions from the nearest neighbor shell are designated as α transitions, from the second nearest neighbor shell β transitions, etc.
3. Transitions from one shell to another do not all have the same energy because of the fine structure (sub-shells) in the shell levels. The highest energy transition between two shells is usually designated with number 1, second highest with number 2, etc.
4. In Fig. 3.1 the transition K_{α_3} represents a forbidden transition ($\Delta\ell = 0$) from the L to the K shell ($2s_{1/2} \to 1s_{1/2}$ with $\Delta\ell = 0$ and $\Delta j = 0$).
5. The transition K_{β_1} represents an allowed transition from the M to the K shell ($3p_{3/2} \to 1s_{1/2}$ with $\Delta\ell = 1$ and $\Delta j = 1$).

3.1.2 Auger Effect and Fluorescent Yield

The allowed transitions between electronic shells or orbits do not necessarily result in characteristic x rays, they may also result in an *Auger effect*. Electrons may undergo transitions that violate the selection rules applicable for production of characteristic radiation; however, the energy difference is then transferred to other orbital electrons that are ejected from the atom as Auger electrons, Coster-Kronig electrons or super Coster-Kronig electrons, as shown schematically in Fig. 3.2. The kinetic energy of these electrons is equal to the energy released through the primary electronic transition less the binding energy of the ejected Auger electron. Emission of Auger electrons from an atom is referred to as the Auger effect.

In Auger effect the primary transition occurs between two shells, in the Coster-Kronig and super Coster-Kronig effects the primary transition occurs within two sub-shells of a shell.

1. In the Coster-Kronig effect the transition energy is transferred to an electron in another shell and the emitted electron is called a Coster-Kronig electron.
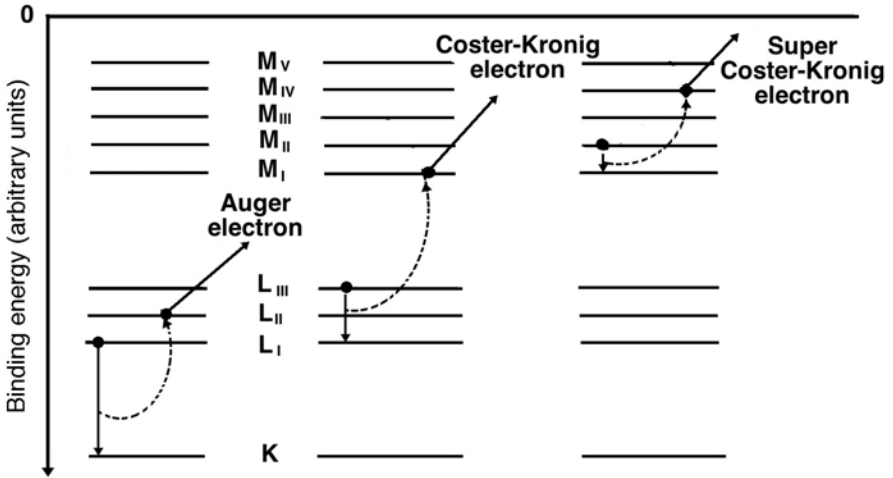
Fig. 3.2. Schematic representation of the Auger effect, the Coster-Kronig effect and the super Coster-Kronig effect. In the Auger effect the electron makes an intershell transition and the transition energy is transferred to the Auger electron. In the Coster-Kronig effect the electron makes an intrashell transition and the transition energy is transferred to an electron in a higher shell. In the super Coster-Kronig effect the electron makes an intrashell transition and the energy is transferred to an electron in the same shell

2. In the super Coster-Kronig effect the energy is transferred to a sub-shell electron within the shell in which the primary transition occurred and the emitted electron is called a super Coster-Kronig electron.

The *fluorescent yield* ω for a given shell gives the number of characteristic (fluorescent) photons emitted per vacancy in the given shell, as shown in Fig. 3.3 for the K and L shells versus the atomic number Z of the absorber.

The exact mechanism of energy transfer in the Auger effect is difficult to calculate numerically. In the past, the effect was often considered an internal atomic photoelectric effect and the explanation makes sense energetically. However, two experimental facts contradict this assumption:

1. Auger effect often results from forbidden radiative transitions, i.e., transitions that violate the selection rules for the radiative fluorescent process.

2. Fluorescent yield ω for high atomic number materials is significantly larger than that for low atomic number materials; contrary to the well-known photoelectric effect Z dependence that follows a Z^3 behavior (see Sect. 7.5).
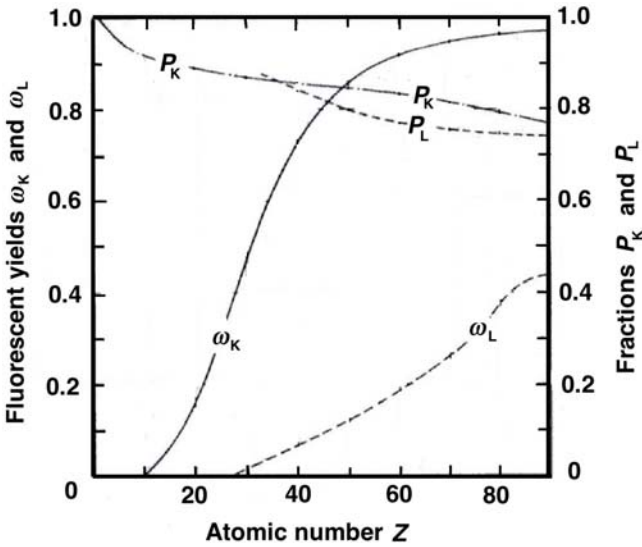
Fig. 3.3. Fluorescent yields ω_K for $h\nu > (E_B)_K$ and ω_L for $(E_B)_L < h\nu < (E_B)_K$ as well as fractions P_K for $h\nu > (E_B)_K$ and P_L for $(E_B)_L < h\nu < (E_B)_K$ against atomic number Z. Data are obtained from F.H. Attix, "Introduction to Radiological Physics and Radiation Dosimetry"

3.2 Emission of Radiation by Accelerated Charged Particle (Bremsstrahlung Production)

Charged particles are characterized by their rest mass, charge, velocity and kinetic energy. With regard to their rest mass, charged particles of interest to medical physics and dosimetry are classified into two groups:

- *light charged particles*: electrons e^- and positrons e^+,
- *heavy charged particles*: protons p, deuterons d, alpha particles α, heavier ions such as Li^+, Be^+ C^+, Ne^+, etc.

3.2.1 Velocity of Charged Particles

With regard to its velocity $\vec{v}$ a charged particle is:

1. stationary with $\vec{v} = 0$,
2. moving with a uniform velocity $\vec{v} = \text{constant}$,
3. accelerated with an acceleration $\vec{a} = d\vec{v}/dt$.

Stationary Charged Particle

A *stationary charged particle* has an associated electric field $\vec{\mathscr{E}}$ whose energy density ρ is given by

$$\rho = \frac{1}{2}\varepsilon_{\mathrm{o}}\mathscr{E}^2 \ , \tag{3.2}$$

where ε_{o} is the dielectric constant (permittivity) of vacuum ($\varepsilon_{\mathrm{o}} = 8.85 \times 10^{-12}$ A $\cdot$ s/V $\cdot$ m).

This energy is stored in the field and is not radiated away by the charged particle. The electric field $\mathscr{E}(r)$ produced by a stationary charged particle of charge q follows the inverse square law and is isotropic

$$E(r) = \frac{1}{4\pi\varepsilon_{\mathrm{o}}}\frac{q}{r^2}. \tag{3.3}$$

Charged Particle Moving with a Uniform Velocity

A charged particle moving with a *uniform velocity* $\vec{v}$ has an associated magnetic field $\vec{\mathscr{B}}$ as well as an electric field $\vec{\mathscr{E}}$. The energy density ρ is then given by

$$\rho = \frac{1}{2}\varepsilon_{\mathrm{o}}\mathscr{E}^2 + \frac{1}{2\mu_{\mathrm{o}}}\mathscr{B}^2 \ , \tag{3.4}$$

where μ_{o} is the magnetic permeability of vacuum ($\mu_{\mathrm{o}} = 4\pi \times 10^{-7}$ V$\cdot$s/A$\cdot$m).

This energy is stored in the field, moves along with the charged particle, and is not radiated away by the charged particle.

At low (classical) velocities $\vec{v}$ the electric field $\vec{\mathscr{E}}$ produced by the charged particle is isotropic and follows the inverse square law. However, as the velocity of the charged particle increases and approaches c, the speed of light in vacuum, the electric field decreases in the forward and backward direction and increases in a direction at right angles to the motion. As shown in Fig. 3.4, the electric field is contracted by a factor $(1 - \beta^2)$ in the direction of the flight of the particle, whereas it is enhanced by a factor $\gamma = 1/\sqrt{1 - \beta^2}$ in the transverse direction.

The electric field distortion for moving charged particles is of importance in collision stopping power calculations. As a charged particle passes through an absorber, it sweeps out a cylinder throughout which its field is capable of transferring energy to orbital electrons of the absorber. The radius of this cylinder increases with increasing parameter γ as the charged particle velocity v increases allowing more orbital electrons to be affected by the charged particle, thereby increasing the energy loss, i.e., the stopping power, for the charged particle.
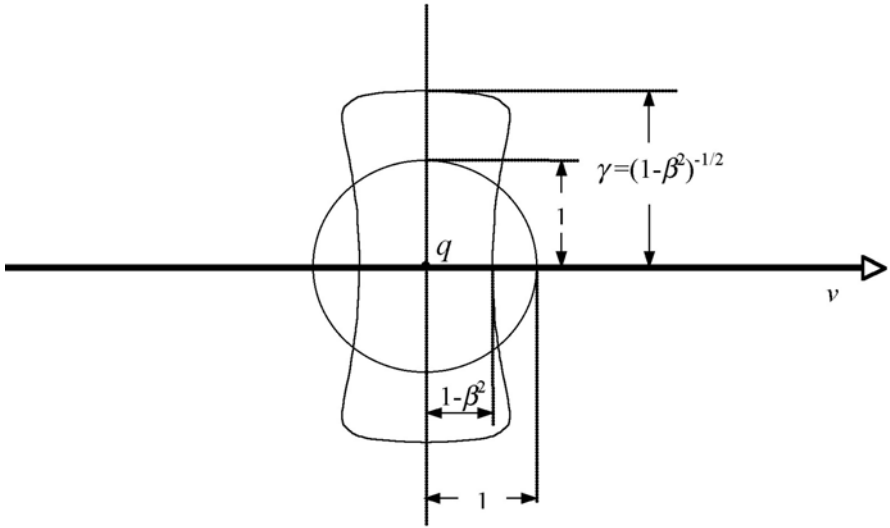
Fig. 3.4. Electric field produced by a charged particle q moving with uniform velocity v in vacuum. The field is shown for two velocities: $\beta = v/c \approx 0$ (classical physics) and $\beta = v/c \to 1$. The electric field for $\beta \to 0$ is isotropic, for relativistic velocities it is distorted; contracted by a factor $(1 - \beta^2)$ in the direction of motion and opposite to the direction of motion, and expanded by a factor $\gamma = 1/\sqrt{1 - \beta^2}$ in directions perpendicular to the direction of motion

Accelerated Charged Particle

For an *accelerated charged particle* the non-static electric and magnetic fields cannot adjust themselves in such a way that no energy is radiated away from the charged particle. As a result, an accelerated or decelerated charged particle emits some of its kinetic energy in the form of photons (bremsstrahlung radiation), as discussed below.

3.2.2 Electric and Magnetic Fields Produced by Accelerated Charged Particles

Electric and magnetic fields associated with accelerated charged particles are calculated from Lienard-Wiechert potentials. To determine the fields at time t the potentials must be evaluated for an earlier time (called the retarded time), with the charged particle at a retarded position on its trajectory.

The electric and the magnetic field of an accelerated charged particle have two components:

1. *local* (or near) *velocity field* component which falls off as $1/r^2$,
2. *far* (or radiation) *acceleration field* component which falls off as $1/r$.

At large distances r of interest in medical physics and dosimetry the $1/r$ radiation component dominates and the $1/r^2$ near field component may be ignored, since it approaches zero much faster than the $1/r$ component. The energy loss by radiation is thus determined by the far field components of the electric field $\vec{\mathscr{E}}$ and the magnetic field $\vec{\mathscr{B}}$. The far field components of $\vec{\mathscr{E}}$ and $\vec{\mathscr{B}}$ are given as follows

$$\vec{\mathscr{E}} = \frac{q}{4\pi\varepsilon_{\mathrm{o}}}\frac{\vec{r} \times (\vec{r} \times \dot{\vec{v}})}{r^3} \qquad \text{or} \qquad \mathscr{E} = \frac{1}{4\pi\varepsilon_{\mathrm{o}}}\frac{q}{c^2}\frac{\dot{v}\sin\theta}{r} \tag{3.5}$$

and

$$\vec{\mathscr{B}} = \frac{\mu_{\mathrm{o}}}{4\pi}\frac{q}{c}\frac{\dot{\vec{v}} \times r}{r^2} \qquad \text{or} \qquad \mathscr{B} = \frac{\mu_{\mathrm{o}}}{4\pi}\frac{q}{c}\frac{\dot{v}\sin\theta}{r} = \frac{\mathscr{E}}{c} \ , \tag{3.6}$$

where

$\vec{r}$ is the radius vector connecting the charged particle with the point of observation,

$\dot{\vec{v}}$ is the acceleration of the charged particle,

q is the charge of the charged particle,

θ is the angle between $\vec{r}$ and $\vec{v}$,

c is the speed of light in vacuum.

The $\vec{\mathscr{E}}$ and $\vec{\mathscr{B}}$ fields propagate outward with velocity c and form the electromagnetic (EM) radiation (bremsstrahlung) emitted by the accelerated charged particle.

3.2.3 Energy Density of the Radiation Emitted by Accelerated Charged Particle

The energy density ρ of the emitted radiation is given by

$$\rho = \frac{1}{2}\varepsilon_{\mathrm{o}}\mathscr{E}^2 + \frac{1}{2\mu_{\mathrm{o}}}\mathscr{B}^2 = \varepsilon_{\mathrm{o}}\mathscr{E}^2 \ , \tag{3.7}$$

noting that $\mathscr{B} = \mathscr{E}/c$ from (3.6) and $c^2 = 1/\varepsilon_{\mathrm{o}}\mu_{\mathrm{o}}$.

3.2.4 Intensity of the Radiation Emitted by Accelerated Charged Particle

The intensity of the emitted radiation $\mathscr{I}(r,\theta)$, i.e., the energy flow per unit area A, is given by the vector product $\vec{\mathscr{E}} \times \vec{\mathscr{B}}/\mu_{\mathrm{o}}$, known as the Poynting vector $\vec{S}$, where

$$\vec{S} = \vec{\mathscr{E}} \times \vec{\mathscr{B}}/\mu_{\mathrm{o}} \ , \tag{3.8}$$

or, after using (3.5) and (3.6) and recognizing that $\vec{\mathscr{E}}$ and $\vec{\mathscr{B}}$ are perpendicular to one another

$$\left|\vec{S}\right| = \mathscr{I}(r,\theta) = \frac{\mathscr{E}\mathscr{B}}{\mu_{\mathrm{o}}} = \varepsilon_{\mathrm{o}}c\mathscr{E}^2 = \frac{1}{16\pi\varepsilon_{\mathrm{o}}}\frac{q^2a^2}{c^3}\frac{\sin^2\theta}{r^2} \ . \tag{3.9}$$

- The emitted radiation intensity $\mathscr{I}(r,\theta)$ is linearly proportional to:
  - q^2, the square of particle's charge
  - a^2, the square of particle's acceleration,
  - $\sin^2\theta$
- The emitted radiation intensity $\mathscr{I}(r,\theta)$ is inversely proportional to r^2, reflecting an inverse square law behavior.
- The emitted radiation intensity $\mathscr{I}(r,\theta)$ exhibits a maximum at right angles to the direction of motion where $\theta = \pi/2$. No radiation is emitted in the forward direction ($\theta = 0$) or in the backward direction ($\theta = \pi$).

3.2.5 Power Emitted by Accelerated Charged Particle Through Electromagnetic Radiation (Classical Larmor Relationship)

The power P (energy per unit time) emitted by the accelerated charged particle in the form of bremsstrahlung radiation is obtained by integrating the intensity $\mathscr{I}(r,\theta)$ over the area A. Recognizing that $dA = r^2 d\Omega = 2\pi r^2 \sin\theta\, d\theta$ we obtain

$$P = \frac{dE}{dt} = \int \mathscr{I}(r,\theta)dA = \int \mathscr{I}(r,\theta)r^2 d\Omega = 2\pi \int\limits_0^{\pi} \mathscr{I}(r,\theta)r^2\sin\theta d\theta$$

$$= \frac{2\pi}{16\pi^2\varepsilon_{\mathrm{o}}}\frac{q^2a^2}{c^3}\int\limits_0^{2\pi}\sin^3\theta d\theta = \frac{1}{6\pi\varepsilon_{\mathrm{o}}}\frac{q^2a^2}{c^3} \ . \tag{3.10}$$

Equation (3.10) is the classical Larmor relationship predicting that the power P emitted in the form of bremsstrahlung radiation by an accelerated charged particle is proportional to:

- q^2, the square of particle's charge
- a^2, the square of particle's acceleration.

The Larmor's result represents one of the basic laws of nature and is of great importance to radiation physics. It can be expressed as follows:

> "Any time a charged particle is accelerated or decelerated it emits part of its kinetic energy in the form of bremsstrahlung photons."

As shown by the Larmor relationship of (3.10), the power emitted in the form of radiation depends on $(qa)^2$ where q is the particle charge and a is its acceleration. The question arises on the efficiency of x-ray production for various charged particles of mass m and charge ze. As charged particles

interact with an absorber, they experience Coulomb interactions with orbital electrons (charge e) and nuclei (charge Ze) of the absorber. Bremsstrahlung is only produced through inelastic Coulomb interactions between a charged particle and the nucleus of the absorber.

The acceleration a produced in this type of Coulomb interaction can be evaluated through equating the Newton force with the Coulomb force, i.e.,

$$ma = \frac{zeZe}{4\pi\varepsilon_{\mathrm{o}}r^2} \ , \tag{3.11}$$

from where it follows that

$$a \propto \frac{zZe^2}{m} \ , \tag{3.12}$$

i.e., the acceleration a experienced by a charged particle interacting with absorbed nuclei is linearly proportional with: (1) the charge of the charged particle (ze) and (2) the charge of the absorber nucleus (Ze), and inversely proportional to: (1) the mass m of the charged particle and (2) the square of the distance between the two interacting particles r^2.

Since it is proportional to a^2, as shown in (3.10), the power of bremsstrahlung production is inversely proportional to m^2. Thus a proton, by virtue of its relatively large mass m_{p} in comparison with the electron mass m_{e}, ($m_p/m_e = 1836$) will produce much less bremsstrahlung radiation than does an electron, specifically about $(m_p/m_e)^2 \approx 4 \times 10^6$ times less. The radiative stopping power for electrons in comparison to that for protons is over six orders of magnitude greater at the same velocity.

- As a result of the inverse m^2 dependence, *heavy charged particles* traversing a medium lose energy only through ionization (collision) losses and their radiative losses are negligible. These collision losses occur in interactions of the heavy charged particles with orbital electrons of the medium. The total stopping power for heavy charged particles is then given by the collision stopping power and their radiative stopping power is ignored, i.e., $S_{\mathrm{tot}} = S_{\mathrm{col}}$.

- *Light charged particles*, on the other hand, undergo collision as well as radiative losses, since they interact with both the orbital electrons and the nuclei of the absorber. The total stopping power for light charged particles is then a sum of the collision stopping power and the radiative stopping power, i.e., $S_{\mathrm{tot}} = S_{\mathrm{col}} + S_{\mathrm{rad}}$.

- As established in 1915 by *William Duane* and *Franklin L. Hunt*, the incident light particle can radiate an amount of energy which ranges from zero to the incident particle kinetic energy E_{K}

$$E_{\mathrm{K}} = h\nu_{\max} = 2\pi\frac{\hbar c}{\lambda_{\min}} \ , \tag{3.13}$$

producing a sharp cut-off at the short-wavelength end of the continuous bremsstrahlung spectrum (*Duane-Hunt law*).

3.2.6 Relativistic Larmor Relationship

Recognizing that $\vec{a} = \dot{\vec{v}} = \dot{\vec{p}}/m$ we can extend the classical Larmor result to relativistic velocities and obtain

$$P = \frac{dE}{dt} = \frac{1}{6\pi\varepsilon_{\mathrm{o}}} \frac{q^2}{m^2 c^3} \left| \frac{d\vec{p}}{dt} \right| \cdot \left| \frac{d\vec{p}}{dt} \right| . \tag{3.14}$$

For the special case of a linear motion (e.g., in a linear accelerator waveguide) the emitted power P is given as follows

$$P = \frac{dE}{dt} = \frac{1}{6\pi\varepsilon_{\mathrm{o}}} \frac{q^2}{m^2 c^3} \left(\frac{dp}{dt} \right)^2 = \frac{1}{6\pi\varepsilon_{\mathrm{o}}} \frac{q^2}{m^2 c^3} \left(\frac{dE}{dx} \right)^2 , \tag{3.15}$$

noting that the rate of change of momentum (dp/dt) is equal to the change in energy of the particle per unit distance (dE/dx).

3.2.7 Relativistic Electric Field Produced by Accelerated Charged Particle

The velocity $\vec{v}$ of the charged particle affects the electric field $\mathscr{E}$ and, as $\beta = v/c$ increases, the electric field $\mathscr{E}$ becomes tipped forward and increases in magnitude as predicted by an expression differing from the classical result of (3.5) by a factor $1/(1 - \beta\cos\theta)^{5/2}$

$$\mathscr{E}(r,\theta) = \frac{1}{4\pi\varepsilon_{\mathrm{o}}} \frac{q}{c^2} \frac{\dot{v}}{r} \frac{\sin\theta}{(\sqrt{1 - \beta\cos\theta})^5} . \tag{3.16}$$

As a result, the emitted radiation intensity $\mathscr{I}(r,\theta)$ also becomes tipped forward

$$S(r,\theta) = \mathscr{I}(r,\theta) = \varepsilon_{\mathrm{o}} c \mathscr{E}^2 = \frac{1}{16\pi\varepsilon_{\mathrm{o}}} \frac{q^2 a^2}{c^3 r^2} \frac{\sin^2\theta}{(1 - \beta\cos\theta)^5} . \tag{3.17}$$

Note that at classical velocities where $\beta \to 0$, (3.16) and (3.17) revert to the classical relationships, given in (3.5) and (3.9), respectively.

- Equation (3.17) shows that the intensity $\mathscr{I}(r,\theta)$ is in general proportional to $\sin^2\theta/(1 - \beta\cos\theta)^5$. In classical mechanics where $\beta \to 0$, the radiation intensity is proportional to $\sin^2\theta$ and the maximum intensity occurs at $\theta = \pi/2$.
- As β increases the radiation intensity becomes more and more forward-peaked; however, the intensities for the forward direction $(\theta = 0)$ and the backward direction $(\theta = \pi)$ are still equal to zero, similarly to the classical situation.
- The function $\sin^2\theta/(1 - \beta\cos\theta)^5$ that governs the radiation intensity distribution $\mathscr{I}(r,\theta)$ of (3.17) is plotted in Fig. 3.5 for $\beta = 0.006$ (classical result for $v \to 0$) and for $\beta = 0.941$. For electrons $(m_{\mathrm{e}}c^2 = 0.511 \text{ MeV})$ these two β values correspond to kinetic energies of 10 eV and 1 MeV, respectively.
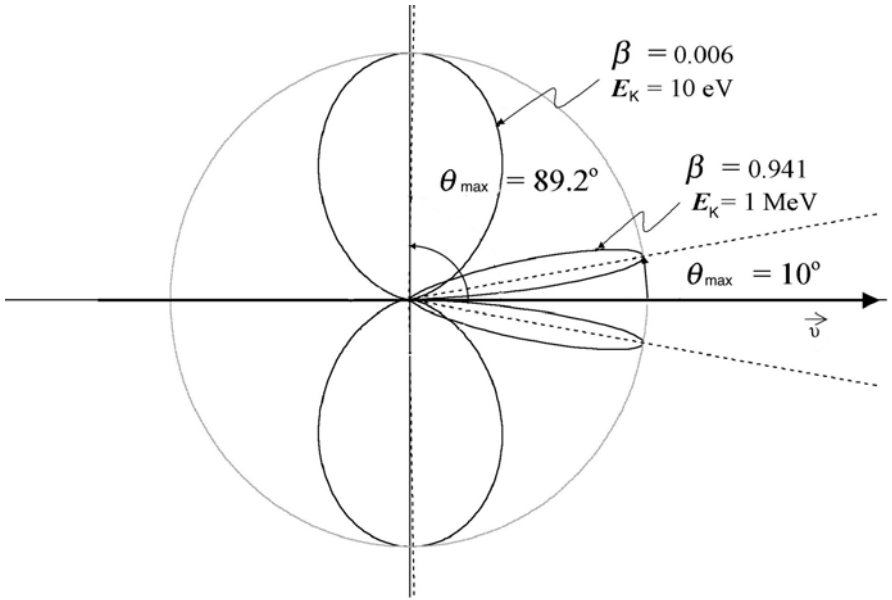
Fig. 3.5. Radiation intensity distributions for two accelerated electrons; one with $\beta = 0.006$ corresponding to an electron kinetic energy of 10 eV and $\theta_{\max}$ of 89.2° and the other with $\beta = 0.941$ corresponding to an electron kinetic energy of 1 MeV and $\theta_{\max}$ of 10°. Both distributions are normalized to 1 at θ_{max}. The actual ratio of radiation intensities at $\theta_{\max} = 89.2°$ and $\theta_{\max} = 10°$ is 1 vs. 1.44×10^4, as shown in Table 3.1

- Note that in Fig. 3.5 the maximum values of both β distributions are normalized to 1. In reality, as shown in Table 3.1, if the maximum value for the $\beta = 0.006$ distribution is 1, then, for the $\beta = 0.941$ distribution, it is more than four orders of magnitude larger at 1.44×10^4.

3.2.8 Characteristic Angle $\theta_{\mathbf{max}}$

It is evident that, as β increases, the emitted radiation intensity $\mathscr{I}(r, \theta)$ becomes more forward-peaked, and its peak intensity that occurs at a characteristic angle $\theta_{\max}$ also increases. The characteristic angle $\theta_{\max}$ is determined as follows:

Set $d\mathscr{I}(r, \theta)/d\theta\,|_{\theta=\theta_{\max}} = 0$, where $\mathscr{I}(r, \theta)$ is given in (3.17), to obtain

$$\frac{2 \sin \theta_{\max} \cos \theta_{\max}}{(1 - \beta \cos \theta_{\max})^5} - \frac{5\beta \sin^3 \theta_{\max}}{(1 - \beta \cos \theta_{\max})^6} = 0 \ . \tag{3.18}$$

Equation (3.18) yields a quadratic equation for $\cos \theta_{\max}$, given as follows

$$3\beta \cos^2 \theta_{\max} + 2 \cos \theta_{\max} - 5\beta = 0 \ . \tag{3.19}$$

Table 3.1. Various parameters for bremsstrahlung production by electrons with kinetic energy E_K

E_K (MeV)	$\beta^{(a)}$	$\gamma^{(b)}$	$\theta^{(c)}_{\max}$	$C\mathscr{I}(r, \theta_{\max})^{(d)}$
10^{-5}	0.006	1.00002	89.2°	1.0000
10^{-4}	0.020	1.0002	87.2°	1.0025
10^{-3}	0.063	1.002	81.2°	1.024
10^{-2}	0.195	1.02	64.4°	1.263
10^{-1}	0.548	1.20	35.0°	6.47
1	0.941	2.96	10.0°	1.44×10^4
10	0.999	20.4	1.4°	1.62×10^{11}
10^2	0.9999	70.71	0.4°	1.64×10^{15}

(a) $\beta = \frac{v}{c} = \sqrt{1 - \frac{1}{\left(1 + \frac{E_K}{m_e c^2}\right)^2}}$, where $m_e c^2 = 0.511$ MeV for electrons and positrons

(b) $\gamma = \frac{1}{\sqrt{1 - \beta^2}}$

(c) $\theta_{\max} = \arccos\left\{ \frac{1}{3\beta} \left(\sqrt{1 + 15\beta^2} - 1 \right) \right\}$, where β is given in (a)

(d) $C\mathscr{I}(r, \theta_{\max}) = \frac{\sin^2 \theta_{\max}}{(1 - \beta \cos \theta_{\max})^5}$, where $C = \left(\frac{e^2 a^2}{16\pi^2 \varepsilon_o c^3 r^2} \right)^{-1}$

The physically acceptable solution of the quadratic equation is $\cos\theta_{\max} = \frac{1}{3\beta}(\sqrt{1 + 15\beta^2} - 1)$, resulting in the following expression for $\theta_{\max}$:

$$\theta_{\max} = \arccos\left\{ \frac{1}{3\beta}(\sqrt{1 + 15\beta^2} - 1) \right\} . \tag{3.20}$$

- The limiting values for $\theta_{\max}$ of (3.20) are as follows:
    - *Classical region*: as $\beta \to 0$; $\theta_{\max} \to \pi/2$.
    - *Relativistic region*: as $\beta \to 1$; $\theta_{\max} \to 0$.
    - In the *extreme relativistic region* the following approximation holds:

$$\theta_{\max} \approx 1/(2\gamma) . \tag{3.21}$$

- The characteristic angle $\theta_{\max}$ drops rapidly from 90° as β increases.
- Even for $\beta = 0.5$, corresponding to a γ of 1.155 and a relatively low electron kinetic energy of 80 keV, the characteristic angle $\theta_{\max}$ is 38.2°.
- In the relativistic region $\theta_{\max}$ is very small being of the order of $1/2\gamma$, i.e., of the order of the ratio of the particle's rest energy E_o to its total energy E.
- Table 3.1 lists parameters β, γ, $\theta_{\max}$ and $\mathscr{I}(r, \theta_{\max})$ for bremsstrahlung production by electrons and positrons with kinetic energies between 10^{-5} MeV and 10^2 MeV.
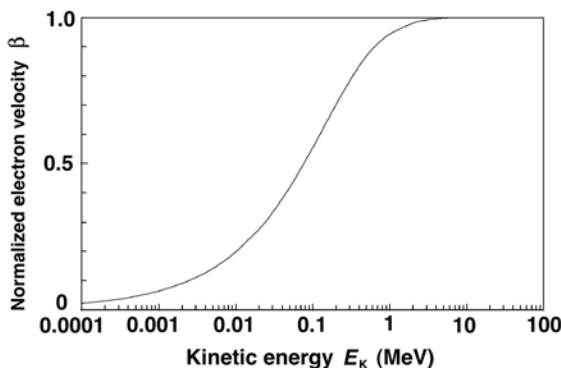
Fig. 3.6. Normalized electron velocity β against the kinetic energy E_K of the electron
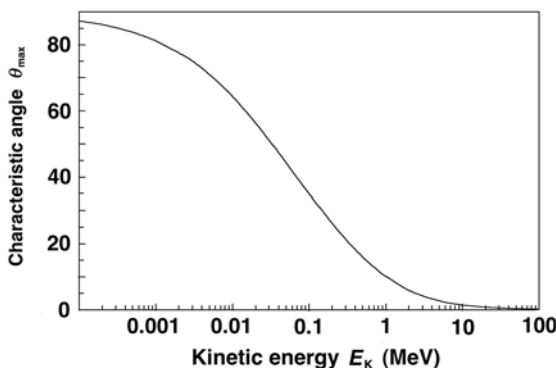
Fig. 3.7. Characteristic angle $\theta_{\max}$ against kinetic energy E_K of the electron

The entry $C\mathcal{I}(r, \theta_{\max})$ in Table 3.1 highlights the significant increase in the bremsstrahlung photon distribution at $\theta = \theta_{\max}$ and confirms the rapid increase in x-ray production efficiency with an increase in electron (or positron) kinetic energy.

Parameters β and $\theta_{\max}$, given in Table 3.1, are also plotted against the electron kinetic energy E_K in Figs. 3.6 and 3.7, respectively. For very low kinetic energies E_K (classical region) $\beta \approx 0$ and $\theta_{\max} \approx 90°$. As E_K increases, β rises and asymptotically approaches 1 for very high E_K, while $\theta_{\max}$ decreases with increasing E_K and asymptotically approaches $0°$ for very high E_K. In the orthovoltage x-ray range $\theta_{\max} \approx 40°$; in the megavoltage x-ray range $\theta_{\max} \approx 5°$.

3.3 Synchrotron Radiation

Synchrotron radiation refers to electromagnetic radiation emitted by charged particles following a curved trajectory in free space under the influence of a magnetic field. The phenomenon was first observed in 1947 in synchrotrons (hence the term synchrotron radiation); accelerators that accelerate charged particles in circular orbits to very high relativistic energies. Since the effect occurs under the influence of a magnetic field that keeps the particles in a circular trajectory, it is sometimes called *magnetic bremsstrahlung.*

Electrons as well as heavier charged particles may produce the synchrotron radiation. The radiation can be considered: (1) an unnecessary nuisance causing energy losses when the objective is to attain high kinetic energies of charged particles in circular accelerators or (2) an extraordinary dedicated source of intense, short duration, x ray or ultraviolet pulses that can be exploited as a tool to study structure of matter on an atomic, molecular and cellular scale or to devise ultra fast imaging studies in cardiology. Originally, research on synchrotron radiation was conducted as a sideline to particle acceleration, recently, however, special sources of synchrotron radiation called storage rings were built with the specific purpose to produce and exploit synchrotron radiation.

The magnetic field exerts a Lorentz force on the charged particle perpendicularly to the particle's direction of motion causing particle's acceleration and, according to the Larmor relationship of (3.10), emission of photons. Larmor relationship of (3.10) for power P radiated by particle of charge q accelerated with acceleration a is given as follows

$$P = \frac{1}{6\pi\varepsilon_{\mathrm{o}}} \frac{q^2 a^2}{c^3} \ . \tag{3.22}$$

For a classical particle in circular motion with radius R, the acceleration is simply the centripetal acceleration v^2/R, where v is the velocity of the particle.

For a relativistic particle with velocity $v \to c$ and mass $m = \gamma m_{\mathrm{o}}$, where m_{o} is the particle's rest mass, in circular motion in a circular accelerator with radius R, the acceleration is similarly obtained from

$$F = m_{\mathrm{o}} a = \frac{dp}{dt'} \ , \tag{3.23}$$

where

p is the relativistic momentum of the particle: $p = mv = \gamma m_{\mathrm{o}} v$,
t' is the proper time in the particle's reference frame given as: $t' = t/\gamma = t\sqrt{1 - \beta^2}$.

Neglecting the rate of change of γ with time t, the acceleration a can now be written as

$$a = \frac{1}{m_{\mathrm{o}}} \frac{dp}{dt'} = \frac{\gamma}{m_{\mathrm{o}}} \frac{d(\gamma m_{\mathrm{o}} v)}{dt} = \gamma^2 \frac{dv}{dt} = \gamma^2 \frac{v^2}{R} \ . \tag{3.24}$$

The power radiated from a relativistic particle according to Larmor relationship is as follows

$$P = \frac{1}{6\pi\varepsilon_o}\frac{q^2 a^2}{c^3} = \frac{q^2\gamma^4}{6\pi\varepsilon_o c^3}\frac{v^4}{R^2} = \frac{cq^2\beta^4\gamma^4}{6\pi\varepsilon_o R^2}\ . \tag{3.25}$$

Since we know that the particle total energy E is given as $E = \gamma m_o c^2 = \gamma E_o$, where E_o is the particle rest energy, we write (3.25) as follows

$$P = \frac{cq^2\beta^4}{6\pi\varepsilon_o R^2}\left(\frac{E}{E_o}\right)^4\ . \tag{3.26}$$

For highly relativistic particles, $v \to c$ and the energy loss rate is governed by $\gamma^4 = (E/E_o)^4$ when R is fixed for a given accelerator. Equation (3.26) suggests that the larger is the accelerator radius R the smaller is the rate of energy loss.

The radiation loss ΔE during one complete revolution of a highly relativistic particle ($\beta \approx 1$) is calculated by first determining the duration τ of one revolution as

$$\tau = \frac{2\pi R}{v} \approx \frac{2\pi R}{c}\ . \tag{3.27}$$

The radiation loss in one revolution is then

$$\Delta E = P\tau = \frac{cq^2}{6\pi\varepsilon_o R^2}\left(\frac{E}{E_o}\right)^4\frac{2\pi R}{c} = \frac{q^2}{3\varepsilon_o R}\left(\frac{E}{E_o}\right)^4\ . \tag{3.28}$$

The radiation energy loss per turn is inversely proportional to the radius R of the orbit and linearly proportional to $(E/E_o)^4$.

For electrons ($q = e$ and $m_o = m_e = 0.511$ MeV) we get the following expression for ΔE:

$$\Delta E = \frac{e^2}{3\varepsilon_o(m_e c^2)^4}\frac{E^4}{R} = \left\{8.8 \times 10^{-8}\frac{\text{eV}\cdot\text{m}}{(\text{MeV})^4}\right\}\frac{E^4}{R}\ . \tag{3.29}$$

The energy is radiated in a cone centered along the instantaneous velocity of the particle. The cone has a half angle θ_{syn} approximated as (E_o/E). For highly relativistic particles the cone is very narrow and the radiation is emitted in the forward direction similarly to the situation with the bremsstrahlung loss by relativistic particles, discussed in Sect. 3.2.8.

The wavelength distribution of synchrotron radiation follows a continuous spectrum in the x-ray, ultraviolet and visible region, with the peak emitted wavelength linearly proportional to R and $(E_o/E)^3$.

3.4 Čerenkov Radiation

As discussed in Sect. 3.2, a charged particle radiates energy in free space only if accelerated or decelerated; a charged particle in rectilinear uniform

velocity motion in free space does not lose any of its kinetic energy in the form of photon radiation. However, if a charged particle moves with uniform rectilinear motion through a transparent dielectric material, part of its kinetic energy is radiated in the form of electromagnetic radiation if the particle velocity v exceeds the phase velocity of light c_n in the particular medium, i.e.,

$$v > c_n = \frac{c}{n} \, , \tag{3.30}$$

where n is the index of refraction of light in the particular medium.

The phenomenon of visible light emission under these conditions is referred to as Čerenkov radiation and was discovered by *Pavel A. Čerenkov* and *Sergei I. Vavilov* in 1934.

The emitted Čerenkov radiation does not come directly from the charged particle. Rather, the emission of Čerenkov radiation involves a large number of atoms of the dielectric medium that become polarized by the fast charged particle moving with uniform velocity through the medium. The orbital electrons of the polarized atoms are accelerated by the fields of the charged particle and emit radiation coherently when $v > c_n = c/n$.

- Čerenkov radiation is emitted along the surface of a forward directed cone centered on the charged particle direction of motion. The cone is specified with the following relationship:

$$\cos \theta_{cer} = \frac{c_n}{v} = \frac{1}{\beta n} \, , \tag{3.31}$$

  where θ_{cer} is the Čerenkov angle defined as the angle between the charged particle direction of motion and the envelope of the cone.
- Equation (3.31) suggests that there is a threshold velocity v_{thr} below which no Čerenkov radiation will occur for a given charged particle and absorbing dielectric

$$v_{thr} = \frac{c}{n} = c_n \tag{3.32}$$

$$\beta_{thr} = 1/n \, . \tag{3.33}$$

  – For $v > v_{thr}$ the Čerenkov radiation is emitted with the Čerenkov angle θ_{cer}.
  – For $v < v_{thr}$ no Čerenkov photons are produced.
  – The velocity threshold for Čerenkov radiation in water is $v_{thr} = (1/1.33)c = 0.75c$.
  – The velocity threshold of $0.75c$ for water corresponds to an energy threshold

$$(E_K)_{thr} = \frac{m_e c^2}{\sqrt{1 - \left(\frac{v_{thr}}{c}\right)^2}} = \frac{n m_e c^2}{\sqrt{n^2 - 1}} = 0.775 \text{ MeV.} \tag{3.34}$$

Thus, Čerenkov radiation occurs in water for electrons with kinetic energies exceeding 0.775 MeV.

- Čerenkov radiation is independent of charged particle mass but depends on particle charge and particle velocity v.
- Equation (3.31) also shows that there is a maximum angle of emission $(\theta_{\mathrm{cer}})_{\max}$ in the extreme relativistic limit where $\beta \to 1$

$$(\theta_{\mathrm{cer}})_{\max} = \arccos(1/n) \ .$$

Thus, for relativistic electrons ($\beta \to 1$) in water ($n = 1.33$), $(\theta_{\mathrm{cer}})_{\max} = 41.2°$.

- Čerenkov radiation frequencies appear in the high frequency visible and near visible regions of the electromagnetic spectrum, but do not extend into the x-ray region because for x rays $n < 1$.
- Since the refraction index n depends on the wavelength λ of the emitted radiation, the emission angle θ_{cer} for Čerenkov radiation also depends on the frequency of the Čerenkov radiation in addition to depending on the charged particle velocity v.
- For emission of Čerenkov radiation, the number of quanta per wavelength interval $\Delta\lambda$ is proportional to $1/\lambda^2$, favoring the blue end of the visible spectrum. This explains the characteristic bluish glow surrounding the fission core of a swimming-pool nuclear reactor or surrounding the high activity cobalt-60 sources stored in water-filled storage tanks prior to their installation in teletherapy machines. The Čerenkov radiation results from Compton electrons that propagate through water with velocities v exceeding $c/n = 0.75c$.
- As the charged particle moves through a dielectric, the total amount of energy appearing as Čerenkov radiation is very small compared to the total energy loss by a charged particle through collision (ionization) and radiative (bremsstrahlung) losses. For example, electrons in water lose about 2 MeV/cm through collision and radiative losses and only about 400 eV/cm through Čerenkov radiation losses, i.e., about a factor of 5000 times less. It is obvious that Čerenkov radiation is negligible as far as radiation dosimetry is concerned.
- The Čerenkov-Vavilov effect is used in Čerenkov detectors not only to detect fast moving charged particles but also to determine their energy through a measurement of the Čerenkov angle.

3.5 Practical Considerations in Production of Radiation

The sections above dealt with general classical and relativistic relationships governing the emission of radiation by accelerated charged particles, including *bremsstrahlung* as the most important means and two more-specialized phenomena: the *synchrotron radiation* and the *Čerenkov radiation*.

In principle, all charged particles can emit radiation under certain conditions. In practice, however, the choice of charged particles that can produce measurable amounts of radiation of interest in medical physics and medicine is limited to light charged particles (electrons and positrons) that can undergo the following interactions:

1. Rapid deceleration of energetic electrons in targets through inelastic Coulomb collisions of electrons with nuclei of the target resulting in superficial, orthovoltage, or megavoltage x rays (bremsstrahlung) for use in diagnosis (imaging) and treatment (radiotherapy) of disease.

2. Deceleration of electrons in retarding potentials resulting in microwave radiation. This process is used in magnetrons to produce radiofrequency photons and in klystrons to amplify radiofrequency photons. The radiofrequency used in standard clinical linear accelerators is 2856 MHz (S band); in miniature linear accelerator waveguides (tomotherapy and robotic arm mounting) it is at 10^4 MHz (X band).

3. Deceleration of electrons resulting in bremsstrahlung production in patients irradiated with photon or electron beams producing unwanted dose to the total body of the patient.

4. Acceleration of electrons in a linac waveguide (rectilinear motion of electrons) resulting in unwanted leakage radiation.

5. Circular motion of electrons in circular accelerators resulting in synchrotron radiation (sometimes referred to as magnetic bremsstrahlung) produced in high-energy circular accelerators and in storage rings. When charged particles pass through transverse magnetic fields, they experience an acceleration that, according to Larmor's relationship, results in emission of radiation that is typically of lower energy than bremsstrahlung. In comparison with synchrotron radiation, the accelerations in production of bremsstrahlung are random and also much larger. Production of synchrotron radiation is still a very expensive undertaking, as it involves very expensive and sophisticated circular accelerators.

6. Deceleration of positrons (slowing down before annihilation) in positron emission tomography (PET) imaging studies of human organs resulting in unwanted stray radiation.

7. Atomic polarization effects when electrons move through transparent dielectric materials with a uniform velocity that exceeds the speed of light in the dielectric material result in visible light referred to as Čerenkov radiation. The efficiency for production of Čerenkov radiation is several orders of magnitude lower than the efficiency for bremsstrahlung production.

8. High energy electrons striking a nucleus may precipitate nuclear reactions (e,n) or (e,p) and transform the nucleus into a radioactive state thereby activating the treatment room and also the patient.

3.6 Particle Accelerators

Numerous types of accelerators have been built for basic research in nuclear and high-energy physics, and most of them have been modified for at least some limited use in radiotherapy. Irrespective of the accelerator type two basic conditions must be met for particle acceleration:

1. *Particle to be accelerated must be charged.*
2. *Electric field must be provided in the direction of particle acceleration.*

The various types of accelerators differ in the way they produce the accelerating electric field and in how the field acts on the particles to be accelerated.

As far as the accelerating electric field is concerned there are two main classes of accelerators: *electrostatic* and *cyclic*.

In *electrostatic accelerators* the particles are accelerated by applying an electrostatic electric field through a voltage difference, constant in time, whose value fixes the value of the final kinetic energy of the particle. Since the electrostatic fields are conservative, the kinetic energy that the particle can gain depends only on the point of departure and point of arrival and, hence, cannot be larger than the potential energy corresponding to the maximum voltage drop existing in the machine. The energy that an electrostatic accelerator can reach is limited by the discharges that occur between the high voltage terminal and the walls of the accelerator chamber when the voltage drop exceeds a certain critical value (typically 1 MV).

The electric fields used in *cyclic accelerators* are variable and non-conservative, associated with a variable magnetic field and resulting in some close paths along which the kinetic energy gained by the particle differs from zero. If the particle is made to follow such a closed path many times over, one obtains a process of gradual acceleration that is not limited to the maximum voltage drop existing in the accelerator. Thus, the final kinetic energy of the particle is obtained by submitting the charged particle to the same, relatively small, potential difference a large number of times, each cycle adding a small amount of energy to the total kinetic energy of the particle.

Examples of electrostatic accelerators used in medicine are: *superficial* and *orthovoltage x-ray tubes* and *neutron generators*. The best known example of a cyclic accelerator is the *linear accelerator (linac)*; other examples are *microtrons, betatrons* and *cyclotrons*.

3.6.1 Betatron

The betatron was developed in 1940 by *Donald W. Kerst* as a cyclic electron accelerator for basic physics research; however, its potential for use in radiotherapy was realized soon thereafter.

- The machine consists of a magnet fed by an alternating current of frequency between 50 and 200 Hz. The electrons are made to circulate in a
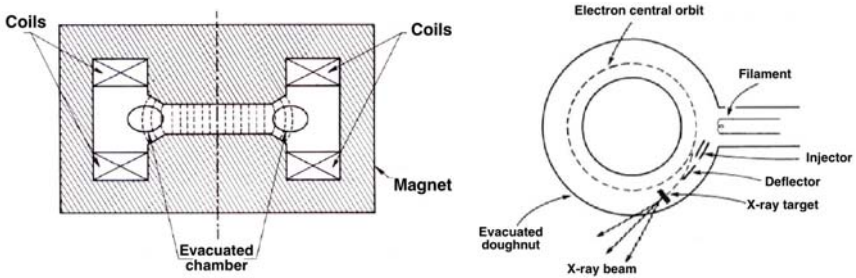
Fig. 3.8. Schematic diagram of a betatron. *Left:* vertical cross section; *right:* top view

toroidal vacuum chamber (doughnut) that is placed into the gap between two magnet poles. A schematic diagram of a betatron is given in Fig. 3.8.

- Conceptually, the betatron may be considered an analog of a transformer: the primary current is the alternating current exciting the magnet and the secondary current is the electron current circulating in the vacuum chamber (doughnut).
- The electrons are accelerated by the electric field induced in the doughnut by the changing magnetic flux in the magnet; they are kept in a circular orbit by the magnetic field present in the doughnut.
- In the 1950s betatrons played an important role in megavoltage radio-therapy. However, the development of linacs pushed them into oblivion because of the numerous advantages offered by linacs over betatrons, such as: much higher beam output (up to 10 Gy/min for linacs vs 1 Gy/min for betatrons); larger field size; full isocentric mounting; more compact design; and quieter operation.

3.6.2 Cyclotron

The cyclotron was developed in 1930 by *Ernest O. Lawrence* for acceleration of ions to a kinetic energy of a few MeV. Initially, the cyclotron was used for basic nuclear physics research but has later on found important medical uses in production of radionuclides for nuclear medicine as well as in production of proton and neutron beams for radiotherapy. The recent introduction of the PET/CT machines for use in radiotherapy has dramatically increased the importance of cyclotrons in medicine. The PET/CT machines rely on glucose labeled with positron-emitting fluorine-18 that is produced by proton cyclotrons.

- In a cyclotron the particles are accelerated along a spiral trajectory guided inside two evacuated half-cylindrical electrodes (referred to as "dees" be-cause of their D-shape form) by a uniform magnetic field (1 tesla) that is produced between the pole pieces of a large magnet. A schematic diagram of the cyclotron is given in Fig. 3.9.
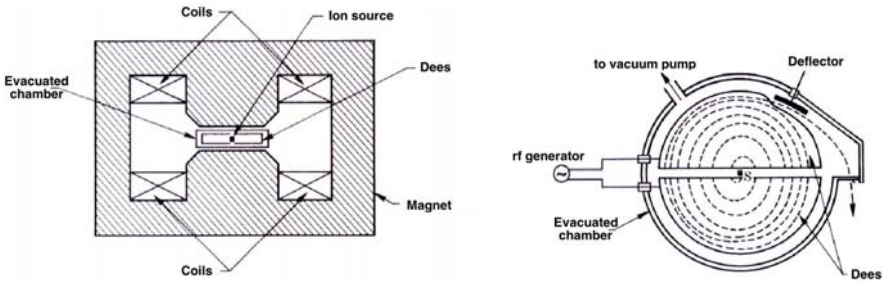
Fig. 3.9. Schematic diagram of a cyclotron. *left:* vertical cross section, *right:* top view

- A radiofrequency voltage with a constant frequency between 10 and 30 MHz is applied between the two electrodes and the charged particle is accelerated while crossing the gap between the two electrodes.
- Inside the electrodes there is no electric field and the particle drifts under the influence of the magnetic field in a semicircular orbit with a constant speed, until it crosses the gap again. If, in the meantime, the electric field has reversed its direction, the particle will again be accelerated across the gap, gain a small amount of energy, and drift in the other electrode along a semicircle of a larger radius than the former one, resulting in a spiral orbit and a gradual increase in kinetic energy after a large number of gap crossings.

3.6.3 Microtron

The microtron is an electron accelerator, which combines the features of a linac and a cyclotron. The concept of the microtron was developed by *Vladimir I. Veksler* in 1944 and the machine is used in modern radiotherapy, albeit to a much smaller extent than are linacs.

Two types of microtrons were developed: *circular* and *racetrack*.

- In the circular microtron the electron gains energy from a microwave resonant cavity and describes circular orbits of increasing radius in a uniform magnetic field. To keep the particle in phase with the microwave power, the cavity voltage, frequency, and magnetic field are adjusted in such a way that after each passage through the cavity, the electrons gain an energy increment resulting in an increase in the transit time in the magnetic field equal to an integral number of microwave cycles.
- In the racetrack microtron the magnet is split into two D-shaped pole pieces that are separated to provide greater flexibility in achieving efficient electron injection and higher energy gain per orbit through the use of multi-cavity accelerating structures similar to those used in linacs. The electon orbits consist of two semicircular and two straight sections.

3.7 Linear Accelerator

During the past few decades medical linear accelerators (linacs) have become the predominant machine in treatment of cancer with ionizing radiation. In contrast to linacs used for high-energy physics research, medical linacs are compact machines mounted isocentrically so as to allow practical radiation treatment aiming the beam toward the patient from various directions.

Medical linacs are cyclic accelerators which accelerate electrons to kinetic energies from 4 MeV to 25 MeV using non-conservative microwave radiofrequency (RF) fields in the frequency range from 10^3 MHz (L band) to 10^4 MHz (X band), with the vast majority running at 2856 MHz (S band).

In a linear accelerator the electrons are accelerated following straight trajectories in special evacuated structures called accelerating waveguides. Electrons follow a linear path through the same, relatively low, potential difference several times; hence, linacs also fall into the class of cyclic accelerators.

Various types of linacs are available for clinical use. Some provide x rays only in the low megavoltage range (4 MV or 6 MV), others provide both x rays and electrons at various megavoltage energies. A typical modern high-energy linac will provide two photon energies (e.g., 6 MV and 18 MV) and several electron energies (e.g., 6, 9, 12, 16, 22 MeV)

3.7.1 Linac Generations

During the past 40 years, medical linacs have gone through five distinct generations, making the contemporary machines extremely sophisticated in comparison with the machines of the 1960s. Each generation introduced the following new features:

- *Low energy photons (4–8 MV):*
  straight-through beam; fixed flattening filter; external wedges; symmetric jaws; single transmission ionization chamber; isocentric mounting.
- *Medium energy photons (10–15 MV) and electrons:*
  bent beam; movable target and flattening filter; scattering foils; dual transmission ionization chamber; electron cones.
- *High energy photons (18–25 MV) and electrons:*
  dual photon energy and multiple electron energies; achromatic bending magnet; dual scattering foils or scanned electron pencil beam; motorized wedge; asymmetric or independent collimator jaws.
- *High energy photons and electrons:*
  computer-controlled operation; dynamic wedge; electronic portal imaging device; multileaf collimator.
- *High energy photons and electrons:*
  photon beam intensity modulation with multileaf collimator; full dynamic conformal dose delivery with intensity modulated beams produced with a multileaf collimator; on-board imaging for use in adaptive radiotherapy.

3.7.2 Components of Modern Linacs

The linacs are usually mounted isocentrically and the operational systems are distributed over five major and distinct sections of the machine:

1. *gantry;*
2. *gantry stand or support;*
3. *modulator cabinet;*
4. *patient support assembly, i.e., treatment couch;*
5. *control console.*

A schematic diagram of a typical modern S-band medical linac is shown in Fig. 3.10. Also shown are the connections and relationships among the various linac components, listed above. The diagram provides a general layout of linac components; however, there are significant variations from one commercial machine to another, depending on the final electron beam kinetic energy as well as on the particular design used by the manufacturer. The length of the accelerating waveguide depends on the final electron kinetic energy, and ranges from ∼30 cm at 4 MeV to ∼150 cm at 25 MeV.

The *beam-forming components* of medical linacs are usually grouped into six classes:
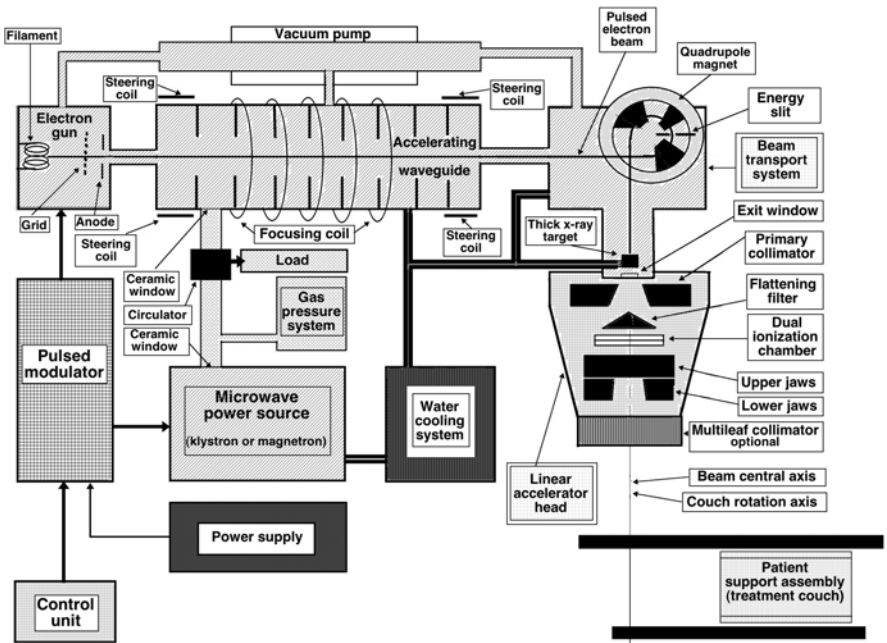
Fig. 3.10. Schematic diagram of a medical linear accelerator (linac)

1. *injection system;*
2. *RF power generation system;*
3. *accelerating waveguide;*
4. *auxiliary system;*
5. *beam transport system; and*
6. *beam monitoring system and beam collimation.*

The *injection system* is the source of electrons, essentially a simple electrostatic accelerator called an electron gun. Two types of electron gun are in use: diode type and triode type, both containing a heated cathode (at a negative potential of the order of -25 kV) and a perforated grounded anode. In addition, triode type gun also incorporates a grid placed between the cathode and the anode. Electrons are thermionically emitted from the heated cathode, focused into a pencil beam and accelerated toward the perforated anode through which they drift into the accelerating waveguide.

The *radiofrequency (RF) power generating system* produces the high power microwave radiation used for electron acceleration in the accelerating waveguide and consists of two components: the RF power source and the pulsed modulator. The RF power source is either a magnetron or a klystron in conjunction with a low power RF oscillator. Both devices use electron acceleration and deceleration in vacuum for production of the high power RF fields. The pulsed modulator produces the high voltage, high current, short duration pulses required by the RF power source and the electron injection system.

Electrons are accelerated in the *accelerating waveguide* by means of an energy transfer from the high power RF field which is setup in the accelerating waveguide and produced by the RF power generator. The accelerating waveguide is in principle obtained from a cylindrical uniform waveguide by adding a series of disks (irises) with circular holes at the center, positioned at equal intervals along the tube. These disks divide the waveguide into a series of cylindrical cavities that form the basic structure of the accelerating waveguide in a linac.

The *auxiliary system* of a linac consists of several basic systems that are not directly involved with electron acceleration, yet they make the acceleration possible and the linac viable for clinical operation. These systems are: the vacuum-pumping system, the water-cooling system, the air-pressure system, and the shielding against leakage radiation.

The *electron beam transport system* brings the pulsed high-energy electron beam from the accelerating waveguide onto the target in the x-ray therapy mode and onto the scattering foil in the electron therapy mode.

The *beam monitoring and beam collimation system* forms an essential system in a medical linac ensuring that radiation dose may be delivered to the patient as prescribed, with a high numerical and spatial accuracy.

3.7.3 Linac Treatment Head

The linac head contains several components, which influence the production, shaping, localizing, and monitoring of the clinical photon and electron beams. Electrons, originating in the electron gun, are accelerated in the accelerating waveguide to the desired kinetic energy and then brought, in the form of a pencil beam, through the beam transport system into the linac treatment head, where the clinical photon and electron beams are produced. The important components found in a typical head of a modern linac include:

1. several *retractable x-ray targets*;
2. *flattening filters* and *electron scattering foils* (also referred to as scattering filters);
3. *primary* and *adjustable secondary collimators*;
4. *dual transmission ionization chambers*;
5. *field defining light* and *range finder*;
6. optional *retractable wedges* or full *dynamic wedges*;
7. *multileaf collimator* (MLC).

Clinical photon beams are produced in medical linear accelerators with a target/flattening filter combination. The electron beam accelerated to a given kinetic energy in the accelerating waveguide is brought by the beam transport system onto an x-ray target in which a small fraction (of the order of 10%) of the electron pencil beam kinetic energy is transformed into bremsstrahlung x rays. The intensity of the x ray beam produced in the target is mainly forward peaked and a flattening filter is used to flatten the beam and make it useful for clinical applications. Each clinical photon beam produced by a given electron kinetic energy has its own specific target/flattening filter combination.

Photon beam collimation in a typical modern medical linac is achieved with three collimation devices: the primary collimator, the secondary movable beam defining collimator, and the multileaf collimator (MLC). The primary collimator defines a maximum circular field which is further truncated with the adjustable rectangular collimator consisting of two upper and two lower independent jaws and producing rectangular or square fields with a maximum dimension of 40×40 cm^2 at the linac isocenter, 100 cm from the x-ray target.

The MLCs are a relatively new addition to modern linac dose delivery technology. In principle, the idea behind an MLC is simple. It allows production of irregularly shaped radiation fields with accuracy and efficiency and is based on an array of narrow collimator leaf pairs, each leaf controlled with its own miniature motor. The building of a reliable MLC system presents a substantial technological challenge and current models incorporate up to 120 leaves (60 pairs) covering radiation fields up to 40×40 cm^2 and requiring 120 individually computer-controlled motors and control circuits.

Clinical electron beams are produced in a medical linac by retracting the target and flattening filter from the electron pencil beam and either scattering the electron pencil beam with a scattering foil or deflecting and scanning the pencil beam magnetically to cover the field size required for electron beam treatment. Special cones (applicators) are used to collimate the clinical electron beams.

Dose monitoring systems in medical linacs are based on transmission ionization chambers permanently imbedded in the linac clinical photon and electron beams. The chambers are used to monitor the beam output (patient dose) continuously during the patient treatment. In addition to dose monitoring the chambers are also used for monitoring the radial and transverse flatness of the radiation beam as well as its symmetry and energy. For patient safety, the linac dosimetry system usually consists of two separately sealed ionization chambers with completely independent biasing power supplies and readout electrometers. If the primary chamber fails during patient treatment, the secondary chamber will terminate the irradiation, usually after an additional dose of only a few percent above the prescribed dose has been delivered.

3.7.4 Configuration of Modern Linacs

At megavoltage electron energies the bremsstrahlung photons produced in the x-ray target are mainly forward-peaked and the clinical photon beam is produced in the direction of the electron beam striking the target.

In the simplest and most practical configuration, the electron gun and the x-ray target form part of the accelerating waveguide and are aligned directly with the linac isocentre, obviating the need for a beam transport system. A straight-through photon beam is produced and the RF power source is also mounted in the gantry. The simplest linacs are isocentrically mounted 4 or 6 MV machines with the electron gun and target permanently built into the accelerating waveguide, thereby requiring no beam transport nor offering an electron therapy option.

Accelerating waveguides for intermediate (8–15 MeV) and high (15–30 MeV) electron energies are too long for direct isocentric mounting, so they are located either in the gantry, parallel to the gantry axis of rotation, or in the gantry stand. A beam transport system is then used to transport the electron beam from the accelerating waveguide to the x-ray target. The RF power source in the two configurations is commonly mounted in the gantry stand. Various design configurations for modern isocentric linear accelerators are shown in Fig. 3.11.
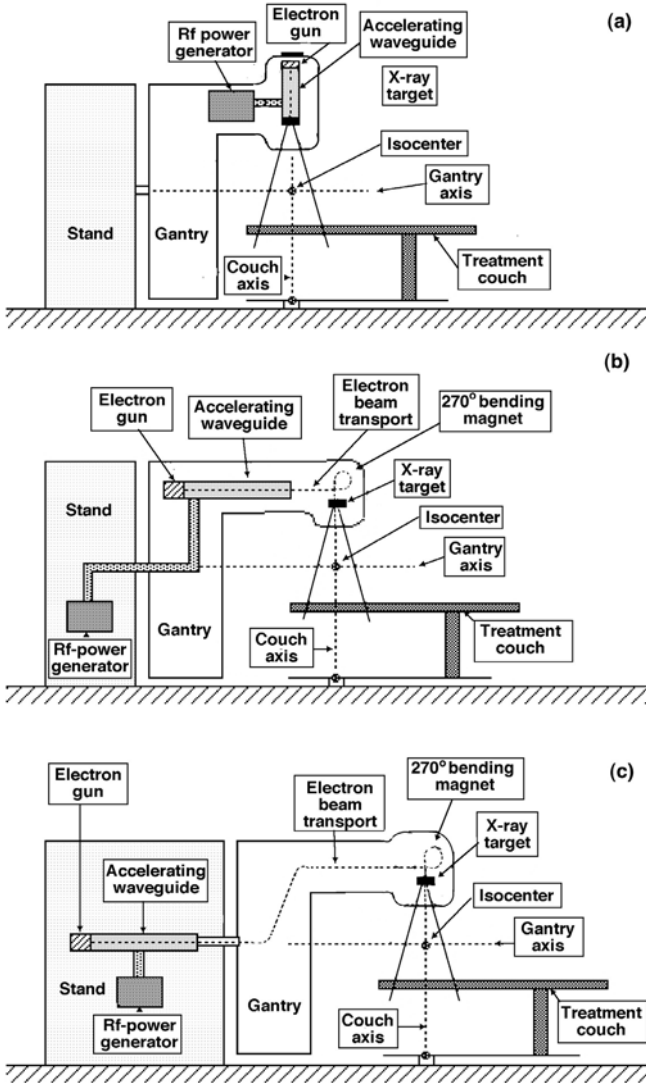
Fig. 3.11. Design configurations for isocentric medical linacs. **a** Straight-through beam design; the electron gun and target are permanently embedded into the accelerating waveguide; machine produces only x rays with energies of 4–6 MV; the rf-power generator is mounted in the gantry. **b** Accelerating waveguide is in the gantry parallel to the isocenter axis; electrons are brought to the movable target through a beam transport system; the rf-power generator is located in the gantry stand; machine can produce megavoltage x rays as well as electrons. **c** Accelerating waveguide and rf-power generator are located in the gantry stand; electrons are brought to the movable target through a beam transport system; machine can produce megavoltage x rays as well as electrons

An Electron Pencil Beam Penetrating into Water

The photograph on the next page represents a 1 MeV electron pencil beam consisting of 50 electrons penetrating into a water phantom. The distribution is calculated with the EGS-nrc Monte Carlo code that traces the trajectories of the individual incident electrons through their various Coulomb interactions with the orbital electrons and nuclei of the water molecules.

Interactions of incident electrons with orbital electrons result in collision (ionization) losses of the incident electrons; interactions with nuclei result in scattering (change in direction of motion) and may also result in radiative (bremsstrahlung) losses. The jagged paths in the figure represent incident electron tracks in water; the two straight traces represent two bremsstrahlung photons, both escaping the phantom. A careful observer will also be able to discern the tracks of secondary electrons (δ electrons) that are liberated in water by the primary electrons and given sufficient kinetic energies to be able to ionize matter in their own right.

Monte Carlo calculations are a statistical process and their accuracy depends on the number of events included in the calculation. The larger is this number, the better is the accuracy of the calculation and, of course, the longer is the calculation time. With the ever-increasing power and speed of computers, Monte Carlo techniques are becoming of practical importance in radiation dosimetry and in calculations of dose distributions in patients treated with x rays, gamma rays, or particle beams.

While the current treatment planning techniques are based on a set of measurements carried out in water phantoms, practical Monte Carlo-based treatment planning algorithms that are currently under development in many research centers will base the calculations directly on data for a particular patient, thereby, in principle, significantly improving the accuracy of dose distribution calculations.

Recently patient-specific Monte Carlo-based treatment planning systems have become commercially available; however, their routine implementation in radiotherapy clinics still hinges on many factors, such as adequate modeling of radiation sources; solving several experimental problems involving tissue inhomogeneities; answering many important clinical questions; updating the dose calculation algorithms; and improving the computing hardware. It is expected that in the near future incorporation of predictive biological models for tumor control and normal tissue complication into Monte Carlo-based dose calculation engines will form the standard approach to radiotherapy treatment planning.

Photograph: Courtesy of Jan P. Seuntjens, Ph.D., McGill University, Montréal. Reproduced with Permission.

4 Two-Particle Collisions

This chapter deals with two-particle collisions characterized by an energetic projectile striking a stationary target. Three categories of projectiles of interest in medical physics are considered: *light charged particles* such as electrons and positrons, *heavy charged particles* such as protons and α particles, and *neutral particles* such as neutrons. The targets are either atoms as a whole, atomic nuclei, or atomic orbital electrons. The collisions are classified into three categories: nuclear reactions; elastic collisions; and inelastic collisions.

The many types of interacting particles as well as the various possible categories of interactions result in a wide range of two-particle collisions of interest in medical physics. Several parameters, such as the Q value and energy threshold in nuclear reactions, and energy transfer, scattering angle and angular scattering power in elastic scattering, used in characterization of two-particle collisions, are defined in this chapter. Many of these parameters play an important role in radiation dosimetry through their effects on stopping powers, as discussed in Chap. 5. They also play an important role in the production of radioactive nuclides (nucleosynthesis), as discussed in Chap. 8.
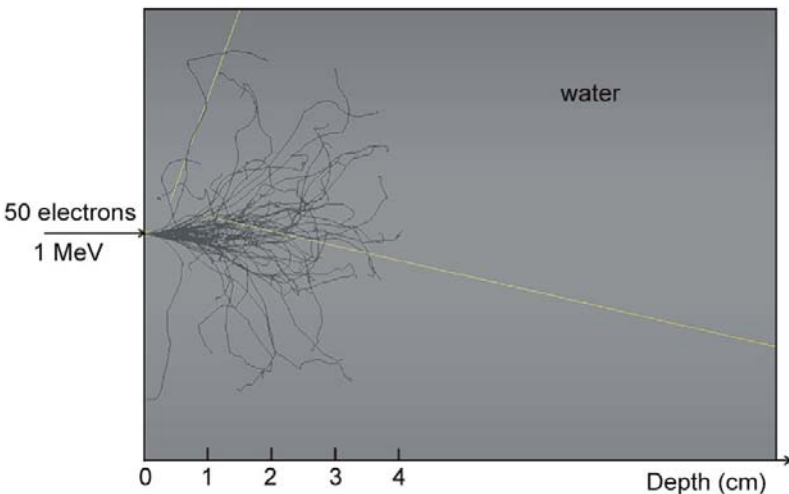
4.1 Collisions of Two Particles: General Aspects

A common problem in nuclear physics and radiation dosimetry is the collision of two particles in which a projectile with mass m_1, velocity v_1 and kinetic energy $(E_K)_1$ strikes a stationary target with mass m_2 and velocity $v_2 = 0$.

As shown schematically in Fig. 4.1, the collision in the most general case results in an intermediate compound that decays into two reaction products: one of mass m_3 ejected with velocity v_3 at an angle θ to the incident projectile direction, and the other of mass m_4 ejected with velocity v_4 at an angle ϕ to the incident projectile direction.

The probability or cross section for a particular collision as well as the collision outcome depend on the physical properties of the projectile (mass, charge, velocity, kinetic energy) and the stationary target (mass, charge).

Projectiles of interest in medical physics fall into one of three categories, each category characterized by its own specific mechanism for the interaction between the projectile and the target. The three categories of projectiles are: (i) *heavy charged particles*, (ii) *light charged particles*, and (iii) *neutrons*.
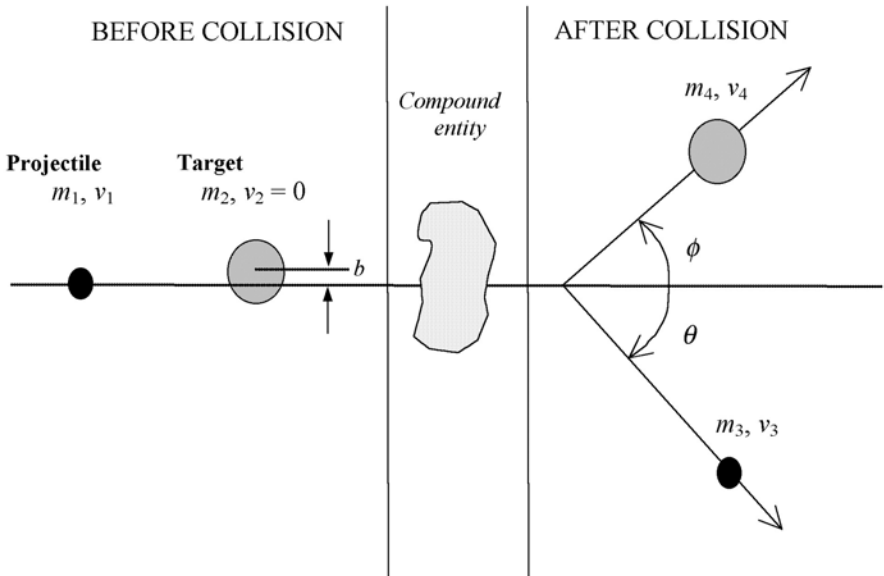
Fig. 4.1. Schematic representation of a two-particle collision of a projectile with mass m_1, velocity v_1 and kinetic energy $(E_K)_1$ striking a stationary target with mass m_2 and velocity $v_2 = 0$. An intermediate compound entity is produced temporarily that decays into two reaction products, one of mass m_3 ejected with velocity v_3 at an angle θ to the incident projectile direction, and the other of mass m_4 ejected with velocity v_4 at an angle ϕ to the incident projectile direction

1. *Heavy charged particles*, such as protons, α particles or heavy ions, interact with the target through Coulomb interactions. Typical targets for heavy charged particles are atomic nuclei and atomic orbital electrons.
2. *Light charged particles,* such as electrons or positrons, interact with the target through Coulomb interactions. Typical targets for light charged particles are either atomic nuclei or atomic orbital electrons.
3. *Neutrons* interact with the target through direct collisions with the target. Typical targets for neutrons are atomic nuclei.

Targets are either atoms as a whole, atomic nuclei, or atomic orbital electrons. *Two-particle collisions* are classified into three categories: (1) *nuclear reactions*, (2) *elastic collisions*, and (3) *inelastic collisions*.

1. *Nuclear reactions*, shown schematically in Fig. 4.1 and discussed in Sect. 4.2, represent the most general case of a two-particle collision of a projectile m_1 with a target m_2 resulting in two reaction products, m_3 and m_4, that differ from the initial products m_1 and m_2.
   - In any nuclear reaction a number of physical quantities must be conserved, most notably: *charge*; *linear momentum* and *mass-energy.*
   - In addition, the sum of atomic numbers Z and the sum of atomic mass numbers A for before and after the collision must also be conserved, i.e.,

$$\Sigma Z \quad \text{(before collision)} = \Sigma Z \quad \text{(after collision)}$$

and

$$\Sigma A \quad \text{(before collision)} = \Sigma A \quad \text{(after collision)}.$$

2. *Elastic scattering* is a special case of a two-particle collision in which:
   - The products after the collision are identical to the products before the collision, i.e., $m_3 = m_1$ and $m_4 = m_2$.
   - The total kinetic energy and momentum before the collision are equal to the total kinetic energy and momentum, respectively, after the collision.
   - A small fraction of the initial kinetic energy of the projectile is transferred to the target.

   Two-particle elastic scattering is shown schematically in Fig. 4.2 (p. 125). The energy transfer in elastic collisions is discussed in Sect. 4.3; the cross sections for single and multiple elastic scattering of two charged particles are discussed in Sect. 4.4.

3. In *inelastic scattering* of the projectile m_1 on the target m_2, similarly to elastic scattering, the reaction products after collision are identical to the initial products, i.e., $m_3 = m_1$ and $m_4 = m_2$; however, the incident projectile transfers a portion of its kinetic energy to the target in the form of not only kinetic energy but also in the form of an intrinsic excitation energy E^*.

The excitation energy E^* may represent:
- Nuclear excitation of the target.
- Atomic excitation or ionization of the target.
- Emission of bremsstrahlung by the projectile.

As a result of the various types of projectiles and targets as well as several categories of two-particle collisions, many different two-particle interactions are possible. The interactions of interest in medical physics and radiation dosimetry are summarized in Table 4.1.

Table 4.1. Collisions between various projectiles and targets of interest in medical physics and radiation dosimetry

Projectile	Heavy charged particle		Light charged particle		Neutron	
Target	Nucleus	Electron	Nucleus	Electron	Nucleus	Electron
Nuclear reaction $m_2(m_1, m_3)m_4$	Yes[a]	No	Yes[e]	No	Yes[j]	No
Elastic scattering $m_2(m_1,m_1)m_2$	Yes[b]	No	Yes[f]	Yes[h]	Yes[k]	No
Inelastic scattering $m_2(m_1,m_1)m_2*$	Yes[c]	Yes[d]	Yes[g]	Yes[i]	Yes[l]	No

Heavy charged particle interactions with nuclei of the target

(a) *Nuclear reaction* precipitated by a heavy charged particle projectile m_1 striking a nucleus m_2 resulting in products m_3 and m_4.
   Example: Deuteron bombarding nitrogen-14
$$^{14}_7\text{N}(\text{d},\text{p})^{15}_7\text{N}$$
(b) *Elastic Coulomb collision* of heavy charged particle with atomic nucleus
   Example: Rutherford scattering of α particle on gold nucleus,
$$^{197}_{79}\text{Au}(\alpha,\alpha)^{197}_{79}\text{Au}$$
(c) *Inelastic collision* of heavy charged particle with nucleus
   Example: Nuclear excitation,
$$^A_Z\text{X}(\alpha,\alpha)^A_Z\text{X}^* \Rightarrow {}^A_Z\text{X}^* \rightarrow {}^A_Z\text{X} + \gamma$$
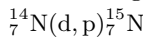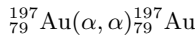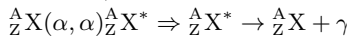
Heavy charged particle interactions with orbital electrons of the target

(d) *Inelastic collision* of heavy charged particle with atomic orbital electron
   Example: Excitation or ionization of an atom

Light charged particle interactions with nuclei of the target

(e) *Nuclear reaction* precipitated by an energetic light charged particle striking the nucleus
    Examples: (e,n) and (e,p) nuclear reactions

(f) *Elastic collision* between a light charged particle and atomic nucleus
    Example: Non-radiative scattering of electrons on the nuclei of the target

(g) *Inelastic collision* between a light charged particle and atomic nucleus
    Example: Bremsstrahlung production by electrons or positrons undergoing a Coulomb interaction with an atomic nucleus (radiative loss)

Light charged particle interactions with orbital electrons of the target

(h) *Elastic collision* between a light charged particle and an orbital electron
    Example: Ramsauer effect in which an electron of very low kinetic energy (below 100 eV) undergoes an elastic collision with an atomic orbital electron

(i) *Inelastic collision* between a light charged particle and atomic orbital electron
    Example 1:   Electron-orbital electron interaction resulting in atomic excitation or ionization (hard and soft collisions)
    Example 2:   Positron annihilation leaving atom in an ionized state coinciding with emission of two γ annihilation quanta.

Neutron interactions with nuclei of the target

(j) *Nuclear reaction* caused by neutron colliding with atomic nucleus
    Example: 1:   Neutron capture or neutron activation (see Sect. 8.4)
$$_{27}^{59}\text{Co}(\text{n},\gamma)_{27}^{60}\text{Co}$$
    Example 2:   Spallation and nuclear fission for high atomic number targets

(k) *Elastic collision* between neutron and atomic nucleus (see Sect. 6.2.1)

(l) *Inelastic collision* between neutron and atomic nucleus (see Sect. 6.2.2)
    Example: Nuclear excitation
$$_{Z}^{A}\text{X}(\text{n},\text{n})_{Z}^{A}\text{X}^{*} \Rightarrow {}_{Z}^{A}\text{X}^{*} \rightarrow {}_{Z}^{A}\text{X} + \gamma$$
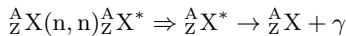
4.2 Nuclear Reactions

Two-particle collisions between the projectile m_1 and target m_2 resulting in products m_3 and m_4 are referred to as *nuclear reactions* and are governed by conservation of total energy and momentum laws. As shown in Table 4.1, the projectile can be a heavy charged particle, a light charged particle or a neutron.

The collision leading to a nuclear reaction is shown schematically in Fig. 4.1 with the projectile m_1 moving with velocity υ_1 and kinetic energy $(E_\text{K})_1$ striking a stationary target m_2. An intermediate compound entity is produced temporarily that decays into two reaction products, m_3 and m_4, ejected with velocities υ_3 at angle θ and υ_4 at angle ϕ, respectively.

4.2.1 Conservation of Momentum in Nuclear Reactions

The conservation of momentum in a two-particle nuclear collision is expressed through the vector relationship

$$m_1\vec{v}_1 = m_3\vec{v}_3 + m_4\vec{v}_4 \,, \tag{4.1}$$

that can be resolved into a component along the incident direction and a component perpendicular to the incident direction to obtain

$$m_1 v_1 = m_3 v_3 \cos\theta + m_4 v_4 \cos\phi \tag{4.2}$$

and

$$0 = m_3 v_3 \sin\theta - m_4 v_4 \sin\phi \,, \tag{4.3}$$

where the angles θ and ϕ are defined in Fig. 4.1 on page 118.

4.2.2 Conservation of Energy in Nuclear Reactions

The total energy of the projectile m_1 and target m_2 before the interaction (collision) must equal to the total energy of products m_3 and m_4 after the collision, i.e.,

$$\begin{aligned}
\{m_{1\mathrm{o}}c^2 + (E_\mathrm{K})_1\} + (m_{2\mathrm{o}}c^2 + 0) = \\
\{m_{3\mathrm{o}}c^2 + (E_\mathrm{K})_3\} + \{m_{4\mathrm{o}}c^2 + (E_\mathrm{K})_4\} \,,
\end{aligned} \tag{4.4}$$

where

$m_{1\mathrm{o}}c^2$	is the rest energy of the projectile;
$m_{2\mathrm{o}}c^2$	is the rest energy of the target;
$m_{3\mathrm{o}}c^2$	is the rest energy of the reaction product m_3;
$m_{4\mathrm{o}}c^2$	is the rest energy of the reaction product m_4;
$(E_\mathrm{K})_1$	is the initial kinetic energy of the projectile;
$(E_\mathrm{K})_3$	is the kinetic energy of the reaction product m_3;
$(E_\mathrm{K})_4$	is the kinetic energy of the reaction product m_4.

Inserting into (4.4) the so-called Q value for the collision in the form

$$Q = (m_{1\mathrm{o}}c^2 + m_{2\mathrm{o}}c^2) - (m_{3\mathrm{o}}c^2 + m_{4\mathrm{o}}c^2) \,, \tag{4.5}$$

we get the following relationship for the conservation of energy

$$E_{\mathrm{K}_1} + Q = E_{\mathrm{K}_3} + E_{\mathrm{K}_4} \,. \tag{4.6}$$

Each two-particle collision possesses a characteristic Q value that can be either positive, zero, or negative.

- For $Q > 0$, the collision is *exothermic* and results in release of energy.
- For $Q = 0$, the collision is termed *elastic*.
- For $Q < 0$, the collision is termed *endothermic* and, to take place, it requires an energy transfer from the projectile to the target.

4.2.3 Threshold Energy E_{thr} for Nuclear Reactions

An exothermic reaction can occur spontaneously; an endothermic reaction cannot take place unless the projectile has a kinetic energy exceeding a *threshold energy.*

- The threshold is defined as the smallest total energy E_{thr} or the smallest kinetic energy $(E_{\text{K}})_{\text{thr}}$ of the projectile at which an endothermic collision can still occur.
- The threshold energy for an endothermic collision is determined through the use of the so-called invariant

$$E^2 - p^2 c^2 = invariant \,, \tag{4.7}$$

  where

  E is the total energy before and the total energy after the collision;
  p is the total momentum before and the total momentum after the collision;

The invariant is valid for both the *laboratory coordinate system* and for the *center-of-mass coordinate system* and, for convenience, the conditions before the collision are written for the laboratory system while the conditions after the collision are written for the center-of-mass system.

The conditions for before and after the collision are written as follows:

- *total energy before:* $E_{\text{thr}} + m_{2\text{o}}c^2 = \sqrt{m_{1\text{o}}^2 c^4 + p_1^2 c^2} + m_{2\text{o}}c^2 \,,$ (4.8)

  where E_{thr} is the total threshold energy of the projectile;
- *total momentum before:* p_1;
- *total energy after* in the center-of-mass system: $m_{3\text{o}}c^2 + m_{4\text{o}}c^2$;
- *total momentum after* in the center-of-mass system: 0.

The invariant of (4.7) for before and after the collision then gives

$$\left(\sqrt{m_{1\text{o}}^2 c^4 + p_1^2 c^2} + m_{2\text{o}}c^2\right)^2 - p_1^2 c^2 = \left(m_{3\text{o}}c^2 + m_{4\text{o}}c^2\right)^2 - 0 \,. \tag{4.9}$$

Solving for $E_{\text{thr}} = \sqrt{m_{1\text{o}}^2 c^4 + p_1^2 c^2}$ results in the following expression for the total threshold energy

$$E_{\text{thr}} = \frac{\left(m_{3\text{o}}c^2 + m_{4\text{o}}c^2\right)^2 - \left(m_{1\text{o}}^2 c^4 + m_{2\text{o}}^2 c^4\right)}{2 m_{2\text{o}}c^2} \,. \tag{4.10}$$

Noting that $E_{\text{thr}} = (E_{\text{K}})_{\text{thr}} + m_{1\text{o}}c^2$, where $(E_{\text{K}})_{\text{thr}}$ is the threshold kinetic energy of the projectile, we get the following expression for $(E_{\text{K}})_{\text{thr}}$

$$(E_{\text{K}})_{\text{thr}} = \frac{\left(m_{3\text{o}}c^2 + m_{4\text{o}}c^2\right)^2 - \left(m_{1\text{o}}c^2 + m_{2\text{o}}c^2\right)^2}{2 m_{2\text{o}}c^2} \,. \tag{4.11}$$

The threshold kinetic energy $(E_{\text{K}})_{\text{thr}}$ of the projectile may now be written in terms of the nuclear reaction Q value [(4.5)] as follows:

– we note that from (4.5) for the Q value we can write

$$\left(m_{3o}c^2 + m_{4o}c^2\right)^2 = \left(m_{1o}c^2 + m_{2o}c^2\right)^2 \\ + Q^2 - 2Q\left(m_{1o}c^2 + m_{2o}c^2\right) . \qquad (4.12)$$

– Inserting the relationship of (4.12) into (4.11) we obtain

$$(E_K)_{thr} = -Q\left[\frac{m_{1mo}c^2 + m_{2o}c^2}{m_{2o}c^2} - \frac{Q}{2m_{2o}c^2}\right]$$

$$\approx -Q\left(1 + \frac{m_{1o}}{m_{2o}}\right) , \qquad (4.13)$$

where, since $Q \ll m_{2o}c^2$, we can ignore the $Q/(2m_{2o}c^2)$ term in (4.13).

In (4.13) the threshold kinetic energy $(E_K)_{thr}$ of the projectile exceeds the $|Q|$ value by a relatively small amount to account for conservation of both energy and momentum in the collision.

As a special case the invariant of (4.7) may also be used to calculate the threshold photon energy $(E_\gamma)_{thr}$ for pair production (see Sect. 7.6.2)

– In the field of nucleus of rest mass m_A (pair production) as

$$(E_\gamma^p)_{thr} = 2m_e c^2\left(1 + \frac{m_e}{m_A}\right) . \qquad (4.14)$$

– In the field of orbital electron of rest mass m_e (triplet production) as

$$(E_\gamma^t)_{thr} = 4m_e c^2 . \qquad (4.15)$$

4.3 Two-Particle Elastic Scattering: Energy Transfer

Elastic scattering in a two-particle collision is a special case of a nuclear collision between a projectile m_1 and target m_2:

1. The initial and final products are identical (i.e., $m_3 = m_1$ and $m_4 = m_2$), however, the projectile changes its direction of motion (i.e., is scattered) and the target recoils.
2. The Q value for the collision, as given in (4.7), equals zero, i.e., $Q = 0$.
3. A certain amount of kinetic energy (ΔE_K) is transferred from the projectile m_1 to the target m_2. The amount of energy transfer is governed by conservation of the kinetic energy and momentum, and depends on the scattering angle θ of the projectile and the recoil angle ϕ of the target.

Two-particle elastic scattering between projectile m_1 moving with velocity v_1 and a stationary target m_2 is shown schematically in Fig. 4.2, with θ the scattering angle of the projectile, ϕ the recoil angle of the target, and b the impact parameter. After the collision particle m_1 continues with velocity u_1 and the target recoils with velocity u_2.
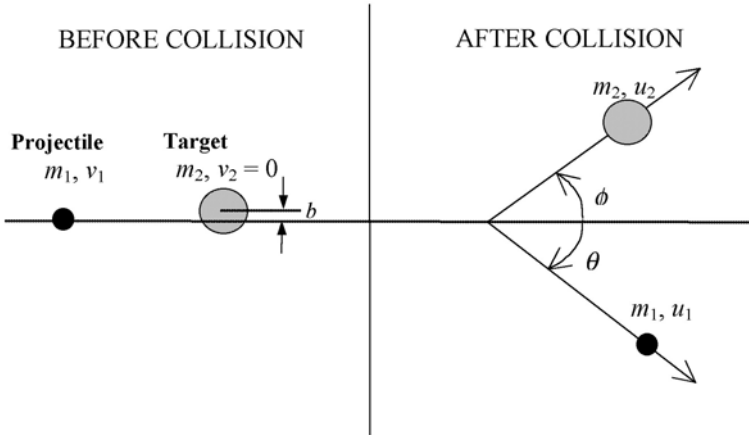
Fig. 4.2. Schematic diagram of an elastic collision between a projectile with mass m_1 and velocity v_1 striking a stationary target m_2. The projectile is scattered with a scattering angle θ; the target recoils with a recoil angle ϕ. The impact parameter is b. After the collision the velocity of the projectile m_1 is u_1; the velocity of the target m_2 is u_2

4.3.1 General Energy Transfer from Projectile m_1 to Target m_2 in Elastic Scattering

The kinetic energy transfer ΔE_K from projectile m_1 to the target m_2 is determined classically using the conservation of kinetic energy and momentum laws as follows:

- *Conservation of kinetic energy:*

$$(E_K)_1 = \frac{1}{2}m_1 v_1^2 = \frac{1}{2}m_1 u_1^2 + \frac{1}{2}m_2 u_2^2 , \tag{4.16}$$

  where $(E_K)_1$ is the initial kinetic energy of the projectile m_1.
- *Conservation of momentum:*

$$m_1 v_1 = m_1 u_1 \cos\theta + m_2 u_2 \cos\phi \tag{4.17}$$

$$0 = m_1 u_1 \sin\theta - m_2 u_2 \sin\phi , \tag{4.18}$$

  where
  v_1 is the initial velocity of the projectile m_1,
  u_1 is the final velocity of the projectile m_1,
  u_2 is the final velocity of the target m_2 ,
  θ is the scattering angle of the projectile m_1 ,
  ϕ is the recoil angle of the target m_2.

Equations (4.17) and (4.18) can be written as follows:

$$(m_1 v_1 - m_2 u_2 \cos\phi)^2 = m_1^2 u_1^2 \cos^2\theta \tag{4.19}$$

and

$$m_1^2 u_1^2 \sin^2 \theta = m_1^2 u_1^2 - m_1^2 u_1^2 \cos^2 \theta = m_2^2 u_2^2 \sin^2 \phi \ , \qquad (4.20)$$

respectively.

Inserting (4.19) into (4.20) gives

$$m_2^2 u_2^2 = m_1^2 u_1^2 - m_1^2 v_1^2 + 2 m_1 v_1 m_2 u_2 \cos \phi \ , \qquad (4.21)$$

which, after inserting (4.16) multiplied by $2m_1$, reads

$$m_2^2 u_2^2 = 2 m_1 v_1 m_2 u_2 \cos \phi - m_1 m_2 u_2^2 \qquad \text{or}$$
$$2 m_1 v_1 \cos \phi = (m_1 + m_2) \, u_2 \ . \qquad (4.22)$$

Since $\Delta E_{\mathrm{K}} = \frac{m_2 u_2^2}{2}$, we get the following classical general expression for the kinetic energy transfer ΔE_{K} from the projectile m_1 to the target m_2

$$\Delta E_{\mathrm{K}} = E_{\mathrm{K}_1} \frac{4 m_1 m_2}{\left(m_1 + m_2\right)^2} \cos^2 \phi \ , \qquad (4.23)$$

where ϕ is the recoil angle of the target m_2, defined graphically in Fig. 4.2.

4.3.2 Energy Transfer in a Two-Particle Elastic Head-On Collision

A head-on (direct hit) elastic collision between two particles is a special elastic collision in which the impact parameter b equals to zero. This results in a maximum possible momentum transfer $\Delta p_{\max}$ and maximum possible energy transfer $(\Delta E_{\mathrm{K}})_{\max}$ from the projectile m_1 to the target m_2. The head-on two-particle elastic collision is characterized as follows:

1. The impact parameter $b = 0$.
2. The target recoil angle $\phi = 0$.
3. The projectile scattering angle θ is either 0 or π depending on the relative magnitudes of masses m_1 and m_2

    –   for $m_1 > m_2$, $\theta = 0$ (forward scattering),
    –   for $m_1 < m_2$, $\theta = \pi$ (back-scattering),
    –   for $m_1 = m_2$, the projectile stops and target recoils with $\phi = 0$.

Classical Relationships for a Head-On Collision

Before collision		After collision	
$\circ \ \rightarrow$	$\circ$	$\circ \ \rightarrow$	$\circ \ \rightarrow$
m_1, v_1	$m_2, v_2 = 0$	m_1, u_1	m_2, u_2

Conservation of Momentum: $m_1 v_1 + 0 = m_1 u_1 + m_2 u_2 \qquad (4.24)$

Conservation of Energy: $\dfrac{m_1 v_1^2}{2} + 0 = \dfrac{m_1 u_1^2}{2} + \dfrac{m_2 u_2^2}{2}$ (4.25)

- The *maximum momentum transfer* $\Delta p_{\max}$ from the projectile m_1 to the target m_2 is given by:

$$\Delta p_{\max} = m_1 v_1 - m_1 u_1 = \frac{2m_1 m_2}{m_1 + m_2} v_1 = \frac{2m_2}{m_1 + m_2} p_1 \ , \qquad (4.26)$$

where p_1 is the initial momentum of the projectile m_1.

- The *maximum energy transfer* $\Delta E_{\max}$ from the projectile m_1 to the stationary target m_2 is given by

$$\Delta E_{\max} = \frac{m_1 v_1^2}{2} - \frac{m_1 u_1^2}{2} = \frac{m_2 u_2^2}{2} = \frac{4m_1 m_2}{(m_1 + m_2)^2} E_{K_1} \ , \qquad (4.27)$$

where E_{K_1} is the initial kinetic energy of the projectile m_1. The same result can be obtained from the general relationship given in (4.23) after inserting $\phi = 0$ for the target recoil angle.

Special Cases for the Classical Energy Transfer in a Head-On Collision

- $m_1 \gg m_2 \rightarrow \Delta E_{\max} = \dfrac{4m_1 m_2}{(m_1 + m_2)^2} E_{K_1}$

$$\approx 4 \frac{m_2}{m_1} E_{K_1} = 2m_2 v_1^2 \qquad (4.28)$$

Example: proton colliding with orbital electron: $m_p \gg m_e$

$$\Delta E_{\max} = \frac{4m_e m_p}{(m_e + m_p)^2} E_{K_1} \approx 4 \frac{m_e}{m_p} E_{K_1} = 2m_e v_1^2 \qquad (4.29)$$

Since $4m_e/m_p = 4/1836 \approx 0.002$, we see that in a direct hit between a proton and an electron only about 0.2% of the proton kinetic energy is transferred to the target electron in a single collision.

- $m_1 \ll m_2 \rightarrow \Delta E_{\max} = \dfrac{4m_1 m_2}{(m_1 + m_2)^2} E_{K_1} \approx 4 \dfrac{m_1}{m_2} E_{K_1}$ (4.30)

Example 1: α *particle colliding with gold nucleus* (Au-207): $m_\alpha \ll m_{Au}$ (*Rutherford scattering*, see Sect. 2.2)

$$\Delta E_{\max} = 4 \frac{m_a m_{Au}}{(m_\alpha + m_{Au})^2} E_{K_1} \approx 4 \frac{m_\alpha}{m_{Au}} E_{K_1} \ . \qquad (4.31)$$

Since $4m_\alpha/m_{Au} \approx 0.08$, we see that in a single direct hit head-on collision only about 8% of the incident α-particle kinetic energy is transferred to the gold target.

Example 2: Neutron colliding with lead nucleus (Pb-207):

$m_\text{neutron} \ll m_\text{lead nucleus}$

$$\Delta E_\text{max} = 4\frac{m_\text{n}m_\text{Pb}}{(m_\text{n} + m_\text{Pb})^2}E_{\text{K}_1} \approx 4\frac{m_\text{n}}{m_\text{Pb}}E_{\text{K}_1} \ . \tag{4.32}$$

Since $4m_\text{n}/m_\text{Pb} \approx 1/50 = 0.02$, we see that in a direct hit only about 2% of the incident neutron kinetic energy is transferred to the lead target. This shows that lead is a very inefficient material for slowing down neutrons; low atomic number materials are much more suitable for this purpose. Of practical importance here is the use of polyethylene as shielding material for doors in high-energy linac bunkers to shield against neutrons produced in the linac.

- $m_1 = m_2 \rightarrow \Delta E_\text{max} = \dfrac{4m_1 m_2}{(m_1 + m_2)^2}E_{\text{K}_1} = E_{\text{K}_1}$ (4.33)

  Example: Interaction between two *distinguishable particles* such as *positron colliding with orbital electron* or *neutron colliding with hydrogen atom:*

  In a direct hit between two distinguishable particles of equal mass the whole kinetic energy of the incident particle is transferred to the target in a single hit.

- $m_1 = m_2 \rightarrow \Delta E_\text{max} = \dfrac{1}{2}E_\text{K}$ (4.34)

  Example: Interaction between two *indistinguishable particles* such as *electron colliding with orbital electron:*

  After the interaction, the particle with the larger kinetic energy is assumed to be the incident particle; therefore the maximum possible energy transfer is $E_\text{K}/2$.

Relativistic Relationships for a Head-On Collision

The relationship for ΔE_max in (4.27) was calculated classically. The relativistic result given below is similar to the classical result, with $m_{1\text{o}}$ and $m_{2\text{o}}$ standing for the rest masses of the projectile m_1 and target m_2.

Before collision		After collision	
$\circ \ \rightarrow$	$\circ$	$\circ \ \rightarrow$	$\circ \ \rightarrow$
$m_{1\text{o}}, v_1$	$m_{2\text{o}}, v_2 = 0$	$m_{1\text{o}}, u_1$	$m_{2\text{o}}, u_2$

Conservation of Momentum:

$$\gamma\beta m_{1\text{o}}c^2 + 0 = \gamma_1\beta_1 m_{1\text{o}}c^2 + \gamma_2\beta_2 m_{2\text{o}}c^2 \tag{4.35}$$

Conservation of Energy:

$$\gamma m_{1\mathrm{o}}c^2 + m_{2\mathrm{o}}c^2 = \gamma_1 m_{1\mathrm{o}}c^2 + \gamma_2 m_{2\mathrm{o}}c^2 \qquad (4.36)$$

with
$\beta = v/c;\ \beta_1 = u_1/c;\ \beta_2 = u_2/c;\ \gamma = \frac{1}{\sqrt{1-\beta^2}};\ \gamma_1 = \frac{1}{\sqrt{1-\beta_1^2}};\ \gamma_2 = \frac{1}{\sqrt{1-\beta_2^2}}.$

- The *maximum momentum transfer* $\Delta p_{\max}$ from the projectile $m_{1\mathrm{o}}$ to the target $m_{2\mathrm{o}}$ is given by

$$\Delta p_{\max} = \frac{2(\gamma m_{1\mathrm{o}} + m_{2\mathrm{o}})m_{2\mathrm{o}}}{m_{1\mathrm{o}}^2 + m_{2\mathrm{o}}^2 + 2\gamma m_{1\mathrm{o}}m_{2\mathrm{o}}}p_1 \ , \qquad (4.37)$$

  where p_1 is the initial momentum of the projectile $m_{1\mathrm{o}}$.

- The *maximum energy transfer* $\Delta E_{\max}$ from the projectile $m_{1\mathrm{o}}$ to the target $m_{2\mathrm{o}}$ is given by

$$\Delta E_{\max} = \frac{2(\gamma + 1)m_{1\mathrm{o}}m_{2\mathrm{o}}}{m_{1\mathrm{o}}^2 + m_{2\mathrm{o}}^2 + 2\gamma m_{1\mathrm{o}}m_{2\mathrm{o}}}E_{\mathrm{K}_1} \ , \qquad (4.38)$$

  where E_{K_1} is the initial kinetic energy of the projectile $m_{1\mathrm{o}}$.

- The relativistic equations for the maximum momentum transfer of (4.37) and maximum energy transfer of (4.38) transform into the classical equations [(4.26) and (4.27), respectively], for small velocities of the projectile where $\beta \to 0$, corresponding to $\gamma = (1 - \beta^2)^{-1/2} \to 1$.

Special Cases for the Relativistic Energy Transfer in a Head-On Collision

- $m_{1\mathrm{o}} \gg m_{2\mathrm{o}}$

$$\Delta E_{\max} = \frac{2(\gamma + 1)(m_{2\mathrm{o}}/m_{1\mathrm{o}})}{1 + (m_{2\mathrm{o}}/m_{1\mathrm{o}})^2 + 2\gamma(m_{2\mathrm{o}}/m_{1\mathrm{o}})}E_{\mathrm{K}_1}$$

$$\approx 2(\gamma^2 - 1)\frac{m_{2\mathrm{o}}}{m_{1\mathrm{o}}}m_{1\mathrm{o}}c^2 = 2m_{2\mathrm{o}}c^2\frac{\beta^2}{1 - \beta^2} \ , \qquad (4.39)$$

  with the kinetic energy of the projectile given as follows:

$$E_{\mathrm{K}_1} = m_{1\mathrm{o}}c^2(1/\sqrt{1-\beta^2} - 1) = m_{1\mathrm{o}}c^2(\gamma - 1). \qquad (4.40)$$

  Example: Heavy charged particle (e.g., proton) colliding with an orbital electron

- $m_{1\mathrm{o}} = m_{2\mathrm{o}}$ (Collision between two *distinguishable particles*)

$$\Delta E_{\max} = \frac{2(\gamma + 1)m_{1\mathrm{o}}m_{2\mathrm{o}}}{m_{1\mathrm{o}}^2 + m_{2\mathrm{o}}^2 + 2\gamma m_{1\mathrm{o}}m_{2\mathrm{o}}}E_{\mathrm{K}_1}$$

$$= \frac{2(\gamma + 1)m_{1\mathrm{o}}^2}{2(\gamma + 1)m_{1\mathrm{o}}^2} = E_{\mathrm{K}_1} \qquad (4.41)$$

Example: positron colliding with an orbital electron

- $m_{1o} = m_{2o}$ (Collision between two *indistinguishable particles*)

$$\Delta E_{\max} = \frac{1}{2} E_{K_1} \tag{4.42}$$

Example: electron colliding with an orbital electron (collision between two indistinguishable particles – after the interaction, the particle with larger kinetic energy is assumed to be the incident particle).

4.4 Cross Sections for Elastic Scattering of Charged Particles

Most interactions of energetic charged particles as they traverse an absorber can be characterized as elastic Coulomb scattering between the energetic charged particle and the atoms of the absorber. The charged particles of interest in medical physics are either light charged particles such as electrons and positrons or heavy charged particles such as protons, α particles, and heavier ions.

Charged particles can have elastic scattering interactions with orbital electrons as well as with nuclei of the absorber atoms. The Coulomb force between the charged particle and the orbital electron or the nucleus of the absorber governs the elastic collisions. The Coulomb force is either attractive or repulsive depending on the polarity of the interacting charged particles. In either case the trajectory of the projectile is a hyperbola: for an attractive Coulomb force the target is in the inner focus of the hyperbola, for a repulsive Coulomb force the target is in the outer focus of the hyperbola. An elastic collision between an α particle and a nucleus of an absorber is shown schematically in Fig. 2.3 (Rutherford scattering); an elastic collision between a heavy charged particle and an orbital electron is shown schematically in Fig. 5.3 (p. 146).

Various investigators worked on theoretical aspects of elastic scattering of charged particles, most notably *Rutherford* on α particle scattering, *Mott* on electron-nucleus scattering as well as on non-relativistic electron-orbital electron scattering, and *Møller* on relativistic electron-orbital electron scattering.

The particle interactions in absorbers are characterized by various parameters that describe single and multiple scattering events.

- For *single scattering* we define the differential and total scattering cross section, effective characteristic distance, and mean square scattering angle.
- For *multiple scattering* we define the mean square scattering angle and the mass angular scattering power.

4.4.1 Differential Scattering Cross Section
for a Single Scattering Event

The differential scattering cross section $d\sigma/d\Omega$ for a single scattering event between two charged particles was discussed in relation to Rutherford scattering in Sect. 2.2.3. In the small scattering angle θ approximation where $\sin(\theta/2) \approx \theta/2$, the differential scattering cross section is generally expressed as

$$\frac{d\sigma}{d\Omega} = \frac{D_{\mathrm{eff}}^2}{\left(\theta^2 + \theta_{\min}^2\right)^2} \ , \tag{4.43}$$

where

$\theta_{\min}$ is a cut-off angle; a minimum angle below which the unscreened point Coulomb field expression is no longer valid;

D_{eff} is an effective characteristic distance (e.g., distance of closest approach $D_{\alpha-\mathrm{N}}$ in Rutherford scattering).

4.4.2 Effective Characteristic Distance

The effective characteristic distance D_{eff} depends on the nature of the specific scattering event as well as on the physical properties of the scattered particle and the scattering material.

The differential scattering cross section of (2.32) was derived for Rutherford scattering of α particles on gold nuclei in Sect. 2.2.3 and is a good approximation for both heavy and light charged particles as long as the appropriate effective characteristic distance D_{eff} is used in the calculations.

In *Rutherford scattering* of an α particle on a nucleus the effective characteristic distance D_{eff} is the distance of closest approach $D_{\alpha-\mathrm{N}}$ between the α particle and the nucleus in a direct-hit (head on) collision ($b = 0$, $\theta = \pi$).

$$D_{\mathrm{eff}}(\alpha - \mathrm{N}) = D_{\alpha-\mathrm{N}} = \frac{zZe^2}{4\pi\varepsilon_{\mathrm{o}}} \frac{1}{E_{\mathrm{K}}} \ , \tag{4.44}$$

where

z is the atomic number of the α particle;
Z is the atomic number of the absorber atom;
E_{K} is the initial kinetic energy of the α particle.

In *electron-nucleus elastic scattering* the effective characteristic distance D_{eff} is as follows:

$$D_{\mathrm{eff}}(\mathrm{e} - \mathrm{N}) = D_{\mathrm{e-n}} = \frac{Ze^2}{4\pi\varepsilon_{\mathrm{o}}\frac{mv^2}{2}} = \frac{2Ze^2\sqrt{1-\beta^2}}{4\pi\varepsilon_{\mathrm{o}}(m_{\mathrm{e}}c^2\beta^2)}$$

$$= \frac{2Zr_{\mathrm{e}}\sqrt{1-\beta^2}}{\beta^2} \ , \tag{4.45}$$

where

m is the total mass of the electron, i.e., $m = m_e/\sqrt{1-\beta^2}$,
m_e is the rest mass of the electron,
β is the velocity of the electron normalized to c, i.e., $\beta = v/c$,
v is the velocity of the electron,
Z is the atomic number of the absorber,
r_e is the classical radius of the electron (2.82 fm)

In *electron-orbital electron scattering* the effective characteristic distance $D_{\mathrm{eff}}(e-e)$ is given by

$$
\begin{aligned}
D_{\mathrm{eff}}(e-e) = D_{e-e} &= \frac{e^2}{4\pi\varepsilon_o \frac{mv^2}{2}} \\
&= \frac{2e^2\sqrt{1-\beta^2}}{4\pi\varepsilon_o(m_e c^2\beta^2)} = \frac{2r_e\sqrt{1-\beta^2}}{\beta^2} ,
\end{aligned}
\tag{4.46}
$$

where

m is the total mass of the electron, i.e., $m = m_e/\sqrt{1-\beta^2}$
m_e is the rest mass of the electron
β is the velocity of the electron normalized to c, i.e., $\beta = v/c$
v is the velocity of the electron
Z is the atomic number of the absorber
r_e is the classical radius of the electron (2.82 fm)

The *total effective characteristic distance* D_{eff} for electron scattering on absorber atoms has two components: the *electron–nucleus* (e–n) component and the *electron–orbital electron* (e–e) component.

- The differential cross section for elastic electron scattering on atoms of an absorber consists of a sum of the differential electron-nucleus cross section and Z times the differential electron-orbital electron cross section, i.e.,

$$
\left.\frac{d\sigma}{d\Omega}\right|_{e-a} = \left.\frac{d\sigma}{d\Omega}\right|_{e-n} + Z\left.\frac{d\sigma}{d\Omega}\right|_{e-e} = \frac{D_{e-a}^2}{(\theta^2+\theta_{\min}^2)^2} ,
\tag{4.47}
$$

  where D_{e-a} is the effective distance for *electron-atom* elastic scattering.
- $D_{\mathrm{eff}}(e-a)$ is then given as follows:

$$
\begin{aligned}
D_{\mathrm{eff}}(e-a) = D_{e-a} &= \sqrt{D_{e-n}^2 + ZD_{e-e}^2} = \frac{2\sqrt{Z(Z+1)}e^2}{4\pi\varepsilon_o mv^2} \\
&= \frac{2r_e\sqrt{Z(Z+1)}\sqrt{1-\beta^2}}{\beta^2} ,
\end{aligned}
\tag{4.48}
$$

  where
  m is the total mass of the electron, i.e., $m = m_e/\sqrt{1-\beta^2}$,
  m_e is the rest mass of the electron,
  β is the velocity of the electron normalized to c, i.e., $\beta = v/c$,

υ is the velocity of the electron,
Z is the atomic number of the absorber,
r_e is the classical radius of the electron (2.82 fm).

4.4.3 Minimum and Maximum Scattering Angles

The minimum and maximum scattering angles $\theta_{\min}$ and $\theta_{\max}$, respectively, are angles where the deviation from point Coulomb nuclear field becomes significant. These departures from the point Coulomb field approximation appear at very small and very large angles θ, corresponding to very large and very small impact parameters b, respectively.

At very small angles θ the screening of the nuclear charge by atomic orbital electrons decreases the differential cross section and at large angles θ the finite nuclear size or nuclear penetration by the charged particle decreases the differential cross section.

As is evident from Figs. 2.3 and 5.3, the relationship governing the change of momentum Δp in elastic scattering is given as follows:

$$\sin(\theta/2) = \Delta p/(2p_\infty) \; , \tag{4.49}$$

where

θ is the scattering angle,
p_∞ is the particle momentum at a large distance from the scattering interaction.

In a small angle θ approximation we get a relationship

$$\theta \approx \Delta p/p_\infty \; ,$$

that results in the following quantum-mechanical expressions for $\theta_{\min}$ and $\theta_{\max}$ [see (2.36) and (2.41)]

$$\theta_{\min} \approx \frac{\Delta p}{p_\infty} \approx \frac{\hbar}{p_\infty a_{\mathrm{TF}}} = \frac{\hbar c \sqrt[3]{Z}}{1.4\sqrt{E_\mathrm{K}(E_\mathrm{K} + 2E_\mathrm{o})}\, a_\mathrm{o}}$$

$$\approx \frac{2.7 \times 10^{-3} \text{ MeV } \sqrt[3]{Z}}{\sqrt{E_\mathrm{K}(E_\mathrm{K} + 2E_\mathrm{o})}} \tag{4.50}$$

and

$$\theta_{\max} \approx \frac{\Delta p}{p_\infty} \approx \frac{\hbar}{p_\infty R} = \frac{\hbar c \sqrt[3]{Z}}{\sqrt{E_\mathrm{K}(E_\mathrm{K} + 2E_\mathrm{o})}\, R_\mathrm{o} \sqrt[3]{A}}$$

$$\approx \frac{1.4 \times 10^2 \text{ MeV}}{\sqrt{E_\mathrm{K}(E_\mathrm{K} + 2E_\mathrm{o})}\, \sqrt[3]{A}} \; , \tag{4.51}$$

where

a_{TF} is the Thomas-Fermi atomic radius equal to $1.4 a_\mathrm{o} Z^{-1/3}$ with a_o the Bohr radius and Z the atomic number of the absorber,

a_o is the Bohr radius [see (2.58)],

R is the radius of the nucleus equal to $R_o A^{1/3}$ with R_o a constant ($R_o = 1.4$ fm),

E_K is the kinetic energy of the charged particle,

E_o is the rest energy of the charged particle,

A is the atomic mass number of the absorber.

The ratio $\theta_{\max}/\theta_{\min}$ is then given as [see (2.42)]

$$\frac{\theta_{\max}}{\theta_{\min}} = \frac{1.4 \times 10^2}{2.7 \times 10^{-3} \sqrt[3]{AZ}} = 0.52 \times 10^5 (AZ)^{-1/3} \ . \tag{4.52}$$

Using (4.50) and (4.51) we find:

- For Rutherford scattering of 5.5 MeV α particles on gold Au-197 (Geiger-Marsden experiment) a $\theta_{\min}$ of 5×10^{-5} rad, as given in (2.45), and $\theta_{\max}$ of 10^{-1} rad, as given in (2.46) in agreement with the general condition that $\theta_{\min} \ll \theta_{\max} \ll 1$.
- For 10 MeV electrons scattered on gold-197, on the other hand, we find considerably larger $\theta_{\min}$ and $\theta_{\max}$ at 1.6×10^{-3} rad and 2.5 rad, respectively. However, we may still assume that $\theta_{\min} \ll \theta_{\max}$.
- For $\theta_{\max}$ larger than unity, $\theta_{\max}$ is usually set equal to 1.

4.4.4 Total Cross Section for a Single Scattering Event

The total cross section σ for a single scattering event is approximated as follows using the small angle approximation $\sin \theta \approx \theta$:

$$\sigma = \int \frac{d\sigma}{d\Omega} d\Omega \approx 2\pi D_{\text{eff}}^2 \int\limits_0^{\theta_{\max}} \frac{\theta \, d\theta}{(\theta^2 + \theta_{\min}^2)^2} = \pi D_{\text{eff}}^2 \int\limits_0^{\theta_{\max}} \frac{d(\theta^2 + \theta_{\min}^2)}{(\theta^2 + \theta_{\min}^2)^2}$$

$$= -\pi D_{\text{eff}}^2 \left[\frac{1}{\theta^2 + \theta_{\min}^2} \right]_0^{\theta_{\max}} = \pi D_{\text{eff}}^2 \left\{ \frac{1}{\theta_{\min}^2} - \frac{1}{\theta_{\max}^2 + \theta_{\min}^2} \right\}$$

$$= \pi D_{\text{eff}}^2 \frac{1}{\theta_{\min}^2} \left\{ 1 - \frac{1}{1 + (\theta_{\max}/\theta_{\min})^2} \right\} \ . \tag{4.53}$$

Since $\theta_{\max}/\theta_{\min} \gg 1$ even for very high atomic number materials, we can simplify the expression for total cross section σ to read

$$\sigma \approx \frac{\pi D_{\text{eff}}^2}{\theta_{\min}^2} \ . \tag{4.54}$$

4.4.5 Mean Square Angle for a Single Scattering Event

The mean square angle for a single scattering event $\overline{\theta^2}$ is defined by the following relationship

$$\overline{\theta^2} = \frac{\int\limits_0^{\theta_{\max}} \theta^2 \frac{d\sigma}{d\Omega} d\Omega}{\int\limits_0^{\theta_{\max}} \frac{d\sigma}{d\Omega} d\Omega} = \frac{2\pi}{\sigma} \int\limits_0^{\theta_{\max}} \theta^2 \frac{d\sigma}{d\Omega} \sin\theta \, d\theta \, , \tag{4.55}$$

where

$d\sigma/d\Omega$ is the differential cross section for the single scattering event, given
          in (4.47),
σ is the total cross section for the single scattering event [see (4.53)
          and (4.54)],
θ is the scattering angle for the single scattering event,
$\theta_{\max}$ is the maximum scattering angle taken as the smaller value of either
          π which represents the maximum possible scattering angle or $\theta_{\max}$
          calculated for the given interaction (see below).

The mean square angle $\overline{\theta^2}$ for a single scattering event may be approximated in the small angle approximation as follows:

$$\overline{\theta^2} = \frac{2\pi \, D_{\text{eff}}^2}{\sigma} \int\limits_0^{\theta_{\max}} \frac{\theta^3 d\theta}{(\theta^2 + \theta_{\min}^2)^2}$$

$$= \frac{\pi \, D_{\text{eff}}^2}{\sigma} \int\limits_0^{\theta_{\max}} \frac{(\theta^2 + \theta_{\min}^2) d(\theta^2 + \theta_{\min}^2)}{(\theta^2 + \theta_{\min}^2)^2} - \frac{\pi D_{\text{eff}}^2}{\sigma} \int\limits_0^{\theta_{\max}} \frac{\theta_{\min}^2 d(\theta^2 + \theta_{\min}^2)}{(\theta^2 + \theta_{\min}^2)^2}$$

$$= \frac{\pi D_{\text{eff}}^2}{\sigma} \left\{ \ln\left(1 + \frac{\theta_{\max}^2}{\theta_{\min}^2}\right) - \frac{1}{1 + (\theta_{\min}/\theta_{\max})^2} \right\} \, , \tag{4.56}$$

or, after inserting the expression for σ given in (4.54)

$$\overline{\theta^2} = \theta_{\min}^2 \left\{ \ln\left(1 + \frac{\theta_{\max}^2}{\theta_{\min}^2}\right) - \frac{1}{1 + (\theta_{\min}/\theta_{\max})^2} \right\}$$

$$= \theta_{\min}^2 \ln\left(1 + \frac{\theta_{\max}^2}{\theta_{\min}^2}\right) - \frac{\theta_{\min}^2 \theta_{\max}^2}{\theta_{\min}^2 + \theta_{\max}^2} \, . \tag{4.57}$$

4.4.6 Mean Square Angle for Multiple Scattering

The thicker is the absorber and the larger is its atomic number Z, the greater is the likelihood that the incident particle will undergo several single scattering events. For a sufficiently thick absorber the mean number of successive encounters rises to a value that permits a statistical treatment of the process. Generally 20 collisions are deemed sufficient and we then speak of multiple

Coulomb scattering that is characterized by a large succession of small angle deflections symmetrically distributed about the incident particle direction.

The mean square angle for multiple Coulomb scattering $\overline{\Theta^2}$ is calculated from the mean square angle for single scattering $\overline{\theta^2}$ with the help of the *central limit theorem* that states the following:

> *"For a large number N of experiments that measure some stochastic variable X, the probability distribution of the average of all measurements is Gaussian and is centered at $\overline{X}$ with a standard deviation $1/\sqrt{N}$ times the standard deviation of the probability density of X".*

Since the successive single scattering collisions in the absorber are independent events, the central limit theorem shows that for a large number $n > 20$ of such collisions the distribution in angle will be Gaussian around the forward direction with a mean square angle $\overline{\Theta^2}$ given as

$$\overline{\Theta^2} = n\overline{\theta^2} \ , \tag{4.58}$$

where

$\overline{\theta^2}$ is the mean square angle for single scattering,
n is the number of scattering events calculated as follows:

$$n = \frac{N_a}{V}\sigma t = \rho\frac{N_A}{A}\sigma t \ , \tag{4.59}$$

where

N_a/V is number of atoms per volume equal to $\rho N_A/A$,
σ is the total cross section for a single scattering event,
t is thickness of the absorber,
ρ is density of the absorber,
N_A is the Avogadro's number,
A is the atomic mass number of absorber.

Incorporating the value for the mean square angle for single scattering $\overline{\theta^2}$ from (4.57) into (4.58) and using (4.59), the mean square angle for multiple scattering $\overline{\Theta^2}$ can be written as

$$\overline{\Theta^2} = \pi\rho\frac{N_A}{A}tD_{\text{eff}}^2\left\{\ln\left(1 + \frac{\theta_{\max}^2}{\theta_{\min}^2}\right) - \frac{1}{1 + \theta_{\min}^2/\theta_{\max}^2}\right\} \ , \tag{4.60}$$

where $\theta_{\min}$ and $\theta_{\max}$ are the minimum and maximum scattering angles, respectively, defined in Sect. 4.4.3, and D_{eff} is the effective characteristic distance for a particular scattering event defined in Sect. 4.4.2.

Equation (4.60) for $\theta_{\max}/\theta_{\min} \gg 1$ simplifies to

$$\overline{\Theta^2} = 2\pi\rho\frac{N_A}{A}tD_{\text{eff}}^2\ln\left(\frac{\theta_{\max}}{\theta_{\min}}\right) \ . \tag{4.61}$$

4.5 Mass Angular Scattering Power for Electrons

As shown in (4.60), $\overline{\Theta^2}$ increases linearly with the absorber thickness t. A mass angular scattering power T/ρ can thus be defined for electrons as follows:

1. either the mean square angle for multiple scattering $\overline{\Theta^2}$ per mass thickness ρt,
2. the increase in the mean square angle $\overline{\Theta^2}$ per unit mass thickness ρt to obtain

$$
\frac{T}{\rho} = \frac{\overline{\Theta^2}}{\rho t} = \frac{d\overline{\Theta^2}}{d(\rho t)}
$$

$$
= \pi \frac{N_A}{A} D_{\text{eff}}^2 \left\{ \ln\left(1 + \frac{\theta_{\max}^2}{\theta_{\min}^2}\right) - \frac{1}{1 + \theta_{\min}^2/\theta_{\max}^2} \right\} , \tag{4.62}
$$

or, as usually given in the literature (ICRU #35),

$$
\frac{T}{\rho} = \pi \frac{N_A}{A} D_{\text{eff}}^2 \left\{ \ln\left(1 + \frac{\theta_{\max}^2}{\theta_{\min}^2}\right) - 1 + \left[1 + \frac{\theta_{\max}^2}{\theta_{\min}^2}\right]^{-1} \right\} , \tag{4.63}
$$

with D_{eff}, the effective characteristic distance, given in (4.48).

The term $\sqrt{1 - \beta^2}/\beta^2$ in (4.48) for D_{eff} can be expressed in terms of the electron kinetic energy E_K and electron rest energy $m_e c^2$. We first define the ratio $E_K/(m_e c^2)$ as τ and then use the standard relativistic relationship for the total energy of the electron, i.e.,

$$
m_e c^2 + E_K = \frac{m_e c^2}{\sqrt{1 - \beta^2}} \tag{4.64}
$$

to obtain

$$
\sqrt{1 - \beta^2} = \frac{1}{1 + \tau} \tag{4.65}
$$

and

$$
\beta^2 = \frac{\tau(2 + \tau)}{(1 + \tau)^2} , \tag{4.66}
$$

resulting in the following expression for the term $\sqrt{1 - \beta^2}/\beta^2$

$$
\frac{\sqrt{1 - \beta^2}}{\beta^2} = \frac{1 + \tau}{\tau(2 + \tau)} . \tag{4.67}
$$

The mass angular scattering power T/ρ may then be expressed as follows:

$$
\frac{T}{\rho} = 4\pi \frac{N_A}{A} r_e^2 Z(Z + 1) \left[\frac{1 + \tau}{\tau(2 + \tau)}\right]^2
$$

$$
\left\{ \ln\left(1 + \frac{\theta_{\max}^2}{\theta_{\min}^2}\right) - 1 + \left[1 + \frac{\theta_{\max}^2}{\theta_{\min}^2}\right]^{-1} \right\} . \tag{4.68}
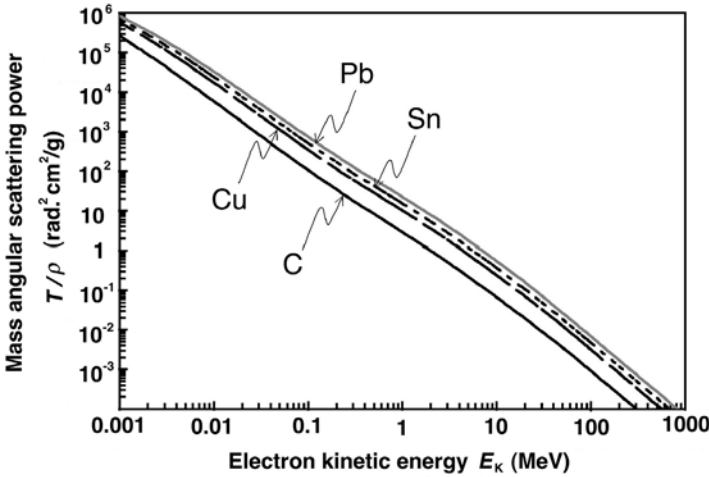$$

Fig. 4.3. Mass angular scattering power T/ρ against electron kinetic energy E_K for various materials of interest in medical physics

Two features of the mass angular scattering power T/ρ can be identified:

- T/ρ is roughly proportional to Z. This follows from the $Z(Z+1)/A$ dependence recognizing that $A \approx 2Z$ to obtain $T/\rho \propto Z$.
- T/ρ for large electron kinetic energies E_K, i.e., $\tau \gg 1$, is proportional to $1/E_K^2$. This follows from $(1+\tau)^2/\{\tau(2+\tau)\}^2 \approx 1/\tau^2$ for $\tau \gg 1$.

A plot of the mass angular scattering power T/ρ for electrons in various materials of interest in medical physics in the electron kinetic energy range from 1 keV to 1000 MeV is given in Fig. 4.3. The mass angular scattering power T/ρ consists of two components: the electron–nucleus (e–n) scattering and the electron–orbital electron (e–e) scattering.

The plot of T/ρ against electron kinetic energy E_K for kinetic energies in the megavoltage energy range is essentially linear on a log-log plot resulting in the $T/\rho \propto 1/E_K^2$ dependence. The steady $1/E_K^2$ drop of T/ρ as a function of increasing E_K suggests a relatively simple means for electron kinetic energy determination from a measurement of the mass angular scattering power T/ρ in a given medium.

The propagation of an electron pencil beam in a medium is described by a distribution function that is given by the Fermi-Eyges solution to the Fermi differential equation. The Fermi-Eyges theory predicts that the dose distribution in a medium on a plane perpendicular to the incident direction of the pencil electron beam is given by a Gaussian distribution with a spatial spread proportional to the variance of the Gaussian distribution.

In air the square of the spatial spread of the electron pencil beam, A_2, is related to T/ρ and z, the thickness of the air layer from the pencil beam origin through the following expression

$$A_2(z) = \frac{T}{\rho}\frac{\rho z^3}{3} \ . \tag{4.69}$$

In deriving (4.69) the following assumptions are made:

1. Only small angle scattering events are considered.
2. The air layer z is much smaller than the electron range in air.
3. Secondary electrons, set in motion by the electron incident pencil beam, are ignored.
4. The bremsstrahlung contamination of the electron pencil beam is ignored.

Function $A_2(z)$ given in (4.69) is a linear function of z^3 with the slope proportional to the mass angular scattering power T/ρ, which in turn is a function of electron beam kinetic energy E_K through function τ given in (4.68). Thus, from a measurement of $A_2(z)$, the spatial spread of an electron pencil beam in air, at several distances z from the pencil beam origin, one first determines T/ρ through (4.69) and then determines the electron beam kinetic energy E_K with data tabulated for air or data calculated for air from (4.68).

Lichtenberg Figures

Images on the next page are so-called *Lichtenberg figures:* in part (a) calculated using the fractal geometry technique and in part (b) produced by 10 MeV electrons deposited in a Lucite (acrylic) block.

The first Lichtenberg figures were actually two-dimensional patterns formed in dust on a charged plate in the laboratory of their discoverer, *Georg Christoph Lichtenberg,* an 18th century German physicist. The basic principles involved in the formation of these early figures are also fundamental to the operation of modern copy machines and laser printers.

Fractal geometry is a modern invention in comparison to the over 2000 year-old Euclidean geometry. Man-made objects usually follow Euclidean geometry shapes and are defined by simple algebraic formulas. In contrast, objects in nature often follow the rules of fractal geometry defined by iterative or recursive algorithms. *Benoit B. Mandelbrot*, a Polish-American mathematician is credited with introducing the term and techniques of fractal geometry during the 1970s. The most striking feature of fractal geometry is the so-called self-similarity implying that the fractal contains smaller components that replicate the whole fractal when magnified. In theory a fractal is composed of an infinite number of ever diminishing components, all of the same shape.

High-voltage electrical discharges on the surface or inside of insulating materials often result in Lichtenberg figures or patterns. Lucite is usually used as the medium for capturing the Lichtenberg figures, because it has an excellent combination of optical (it is transparent), dielectric (it is an insulator), and mechanical (it is strong, yet easy to machine) properties suitable for highlighting the Lichtenberg effect. Electrons accelerated in a linear accelerator (linac) to a speed close to the speed of light in vacuum are made to strike a Lucite block. They penetrate into the block and come to rest inside the block. The electron space charge trapped in the block is released either spontaneously or through mechanical stress, and the discharge paths within the Lucite leave permanent records of their passage as they melt and fracture the plastic along the way. The charge exit point appears as a small hole at the surface of the Lucite block. Similar breakdown, albeit on a much larger scale, occurs during a lightning flash as the electrical discharge drains the highly charged regions within storm clouds; however, the discharge in air leaves behind no permanent record of the passage through air.

The fractal tree shown in (a) is a typical example of fractal geometry use in calculating the shape of a natural object. An example of a frozen Lichtenberg discharge in Lucite is shown in (b). The similarity between the calculated and the measured "tree" is striking.

(a) *Courtesy of Prof. Volkhard Nordmeier, Technische Universität, Berlin.*
(b) *Courtesy of Bert Hickman, Stoneridge Engineering*, `www.teslamania.com`

5 Interactions of Charged Particles with Matter

In this chapter we discuss interactions of charged particle radiation with matter. A charged particle is surrounded by its Coulomb electric force field that interacts with orbital electrons (collision loss) and the nucleus (radiative loss) of all atoms it encounters as it penetrates into matter. The energy transfer from the charged particle to matter in each individual atomic interaction is generally small, so that the particle undergoes a large number of interactions before its kinetic energy is spent. Stopping power is the parameter used to describe the gradual loss of energy of the charged particle as it penetrates into an absorbing medium. Two classes of stopping powers are known: *collision (ionization) stopping power* that results from charged particle interaction with orbital electrons of the absorber and *radiative stopping power* that results from charged particle interaction with nuclei of the absorber.

Stopping powers play an important role in radiation dosimetry. They depend on the properties of the charged particle such as its mass, charge, velocity and energy as well as on the properties of the absorbing medium such as its density and atomic number. In addition to stopping powers, other parameters of charged particle interaction with matter, such as the range, energy transfer, mean ionization potential, and radiation yield, are also discussed in this chapter.

(a)

(b)

5.1 General Aspects of Stopping Power

As a *charged particle* travels through an absorber, it experiences Coulomb interactions with the nuclei and the orbital electrons of the absorber atoms. These interactions can be divided into three categories depending on the size of the classical impact parameter b compared to the classical atomic radius a:

1. Coulomb force interaction of the charged particle with the external nuclear field (*bremsstrahlung production*) for $b \ll a$.
2. Coulomb force interaction of the charged particle with orbital electron for $b \approx a$ (*hard collision*).
3. Coulomb force interaction of the charged particle with orbital electron for $b \gg a$ (*soft collision*).

Generally, the charged particle experiences a large number of interactions before its kinetic energy is expended. In each interaction the charged particle's path may be altered (*elastic* or *inelastic scattering*) and it may lose some of its kinetic energy that will be transferred to the medium (*collision loss*) or to photons (*radiative loss*).

Radiative, hard and soft collisions are shown schematically in Fig. 5.1, with b the impact parameter and a the atomic radius.

• The rate of energy loss per unit of path length by a charged particle in a medium is called the linear *stopping power* (dE/dx).
• The stopping power is typically given in units $\mathrm{MeV} \cdot \mathrm{cm}^2/\mathrm{g}$ and then referred to as the mass stopping power S equal to the linear stopping power divided by the density ρ of the absorbing medium.
• The stopping power is a property of the material in which a charged particle propagates.
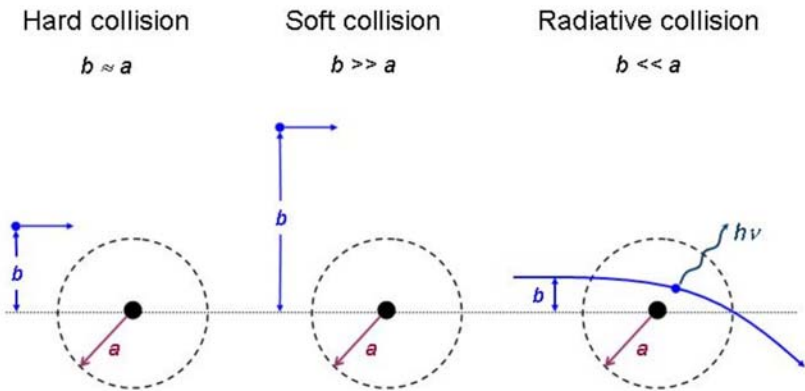

Fig. 5.1. Three different types of collisions of a charged particle with an atom, depending on the relative sizes of the impact parameter b and atomic radius a. Hard collision for $b \approx a$; soft collision for $b \gg a$; and radiative collision for $b \ll a$

Two types of stopping powers are known:

1. *Radiative stopping power* that results from charged particle Coulomb interaction with the nuclei of the absorber. Only light charged particles (electrons and positrons) experience appreciable energy losses through these interactions that are usually referred to as bremsstrahlung interactions.

2. *Collision (ionization) stopping power* that results from charged particle Coulomb interactions with orbital electrons of the absorber. Both heavy and light charged particles experience these interactions that result in energy transfer from the charged particle to orbital electrons, i.e., excitation and ionization of absorber atoms.

The total stopping power S_{tot} for a charged particle of energy E_{K} traveling through an absorber of atomic number Z is the sum of the radiative and collision stopping power, i.e.,

$$S_{\mathrm{tot}} = S_{\mathrm{rad}} + S_{\mathrm{col}} . \tag{5.1}$$

5.2 Radiative Stopping Power

The rate of bremsstrahlung production by light charged particles (electrons and positrons) traveling through an absorber is expressed by the mass radiative stopping power S_{rad} (in $\mathrm{MeV \cdot cm^2}/g$) which is given as follows:

$$S_{\mathrm{rad}} = N_{\mathrm{a}} \sigma_{\mathrm{rad}} E_{\mathrm{i}} , \tag{5.2}$$

where

N_{a} is the number of atoms per unit mass: $N_{\mathrm{a}} = N/m = N_{\mathrm{A}}/A$,

σ_{rad} is the total cross section for bremsstrahlung production given for various energy ranges in Table 5.1,

E_{i} is the initial total energy of the light charged particle, i.e., $E_{\mathrm{i}} = E_{\mathrm{K_i}} + m_e c^2$,

$E_{\mathrm{K_i}}$ is the initial kinetic energy of the light charged particle.

Inserting σ_{rad} for non-relativistic particles from Table 5.1 into (5.2) we obtain the following expression for S_{rad}:

$$S_{\mathrm{rad}} = \alpha r_{\mathrm{e}}^2 Z^2 \frac{N_{\mathrm{A}}}{A} B_{\mathrm{rad}} E_{\mathrm{i}} , \tag{5.3}$$

where B_{rad} is a slowly varying function of Z and E_{i}, also given in Table 5.1 and determined from $\sigma_{\mathrm{rad}}/(\alpha r_{\mathrm{e}}^2 Z^2)$. The parameter B_{rad} has a value of $16/3$ for light charged particles in the non-relativistic energy range ($E_{\mathrm{K}} \ll m_e c^2$); about 6 at $E_{\mathrm{K}} = 1$ MeV; 12 at $E_{\mathrm{K}} = 10$ MeV; and 15 at $E_{\mathrm{K}} = 100$ MeV.

The mass radiative stopping power S_{rad} is proportional to:

- $(N_{\mathrm{A}} Z^2/A)$, that, by virtue of $Z/A \approx 0.5$ for all elements with the exception of hydrogen, indicates a proportionality with the atomic number of the absorber Z.

Table 5.1. Total cross section for bremsstrahlung production and parameter B_{rad} for various ranges of electron kinetic energies

Energy range	σ_{rad} (cm^2/nucleon)	$B_{\mathrm{rad}} = \sigma_{\mathrm{rad}}/(\alpha\, r_{\mathrm{e}}^2 Z^2)$	
Non-relativistic $E_{\mathrm{K_i}} \ll m_{\mathrm{e}}c^2$	$\dfrac{16}{3}\alpha\, r_{\mathrm{e}}^2 Z^2$	$\dfrac{16}{3}$	(5.4)
Relativistic $E_{\mathrm{K_i}} \approx m_{\mathrm{e}}c^2$	complicated power series	—	(5.5)
High-relativistic $m_{\mathrm{e}}c^2 \ll E_{\mathrm{K_i}} \ll \dfrac{m_{\mathrm{e}}c^2}{\alpha Z^{1/3}}$	$8\alpha r_{\mathrm{e}}^2 Z^2 \left[\ln\left(\dfrac{E_{\mathrm{i}}}{m_{\mathrm{e}}c^2}\right) - \dfrac{1}{6}\right]$	$8\left[\ln\left(\dfrac{E_{\mathrm{i}}}{m_{\mathrm{e}}c^2}\right) - \dfrac{1}{6}\right]$	(5.6)
Extreme relativistic $E_{\mathrm{K_i}} \gg \dfrac{m_{\mathrm{e}}c^2}{\alpha\, Z^{1/3}}$	$4\alpha r_{\mathrm{e}}^2 Z^2 \left[\ln\dfrac{183}{Z^{1/3}} + \dfrac{1}{18}\right]$	$4\left[\ln\dfrac{183}{Z^{1/3}} + \dfrac{1}{18}\right]$	(5.7)

- Total energy E_{i} (or kinetic energy E_{Ki} for $E_{\mathrm{Ki}} \gg m_{\mathrm{e}}c^2$)) of the light charged particle.
- Equation (5.3) was derived theoretically by *Hans Bethe* and *Walter Heitler*. *Martin Berger* and *Stephen Seltzer* have provided extensive tables of S_{rad} for a wide range of absorbing materials

Figure 5.2 shows the mass radiative stopping power S_{rad} for electrons in water, aluminum and lead based on tabulated data obtained from the *National Institute of Standards and Technology* (NIST) in Washington, D.C., USA. The S_{rad} data are shown with solid curves, mass collision stopping powers S_{col} (discussed in Sect. 5.3) are shown dotted for comparison. The radiative stopping power S_{rad} clearly shows an approximate proportionality to the atomic number Z of the absorber and kinetic energy E_{K} of light charged particles with kinetic energies above 2 MeV.

5.3 Collision Stopping Power for Heavy Charged Particles

In the energy range below 10 MeV, the energy transfer from energetic heavy charged particles to a medium (absorber) they traverse occurs mainly through Coulomb interactions of the charged particle with orbital electrons of the absorber atoms. As shown schematically in Fig. 5.1, these interactions (collisions) fall into two categories depending on the relative magnitude of the impact parameter b and the atomic radius a of the absorber:

1. *soft collisions* for $b \gg a$
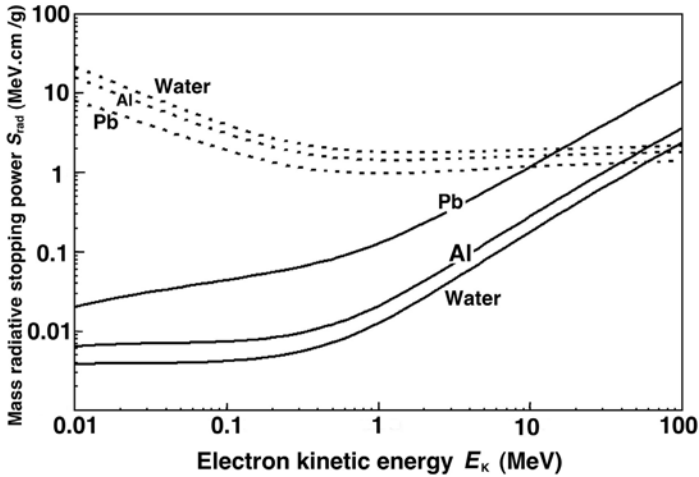2. *hard collisions* for $b \approx a$

Fig. 5.2. Mass radiative stopping power for electrons in water, aluminum and lead shown with *solid curves* against the electron kinetic energy. Mass collision stopping powers for the same materials are shown with *dotted curves* for comparison. Data were obtained from the NIST

5.3.1 Momentum Transfer from Heavy Charged Particle to Orbital Electron

The classical derivation of the *mass collision stopping power* S_{col} of a heavy charged particle, such as a proton, is based on the calculation of the momentum change Δp of the heavy charged particle colliding with an orbital electron. The Coulomb interaction between the heavy charged particle (charge ze and mass M) and the orbital electron (charge e and mass m_e) is shown schematically in Fig. 5.3. The situation here appears similar to that depicted in Fig. 2.3 for Rutherford scattering between an α particle m_α and gold nucleus M. We must note, however, that in Rutherford scattering $m_\alpha \ll M$, while the case here is reversed as we have a heavy charged particle M interacting with an orbital electron m_e where $M \gg m_e$.

The momentum transfer Δp is along a line that bisects the angle $\pi - \theta$, as indicated in Fig. 5.3, and the magnitude of Δp is calculated as follows:

$$\Delta p = \int F_{\Delta p} dt = \int_{-\infty}^{\infty} F_{\text{coul}} \cos \phi \, dt . \tag{5.8}$$

The magnitude of the Coulomb force F_{coul} between the heavy charged particle and the electron is

$$F_{\text{coul}} = \frac{ze^2}{4\pi\varepsilon_o} \frac{1}{r^2} , \tag{5.9}$$
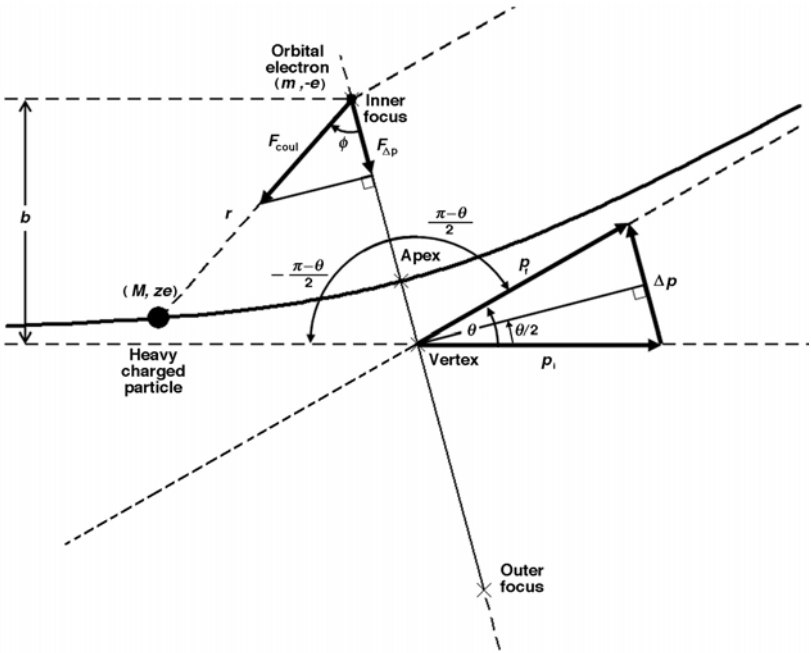
where r is the distance between the two particles.

Fig. 5.3. Schematic diagram of a collision between a heavy charged particle M and an orbital electron m_e. Since $M \gg m_e$, the scattering angle $\theta \approx 0°$. The scattering angle is shown larger than $0°$ to highlight the principles of the Coulomb collision and aid in the derivation of Δp. The electron is in the inner focus of the hyperbola because of the attractive Coulomb force between the positive charged particle and the negative electron

Incorporating the expression for the Coulomb force into (5.8), the momentum transfer Δp can now be written as

$$\Delta p = \frac{ze^2}{4\pi\varepsilon_o} \int\limits_{-\frac{\pi-\theta}{2}}^{\frac{\pi-\theta}{2}} \frac{\cos\phi}{r^2} \frac{dt}{d\phi} d\phi , \tag{5.10}$$

where ϕ is the angle between the radius vector r and the bisector, as shown in Fig. 5.3.

The angular momentum L for the collision process is defined as follows:

$$L = Mv_\infty b = M\omega r^2 , \tag{5.11}$$

where

M is the mass of the heavy charged particle,
v_∞ is the initial velocity of the heavy charged particle (i.e., velocity before the interaction),
ω is the angular frequency equal to $d\phi/dt$.

Using the conservation of angular momentum, we can now write (5.10) in a simpler form:

$$\Delta p = \frac{ze^2}{4\pi\varepsilon_{\mathrm{o}}} \frac{1}{\upsilon_\infty b} \int\limits_{-\frac{\pi-\theta}{2}}^{\frac{\pi-\theta}{2}} \cos\phi \, d\phi = \frac{ze^2}{4\pi\varepsilon_{\mathrm{o}}} \frac{1}{\upsilon_\infty b} \left\{\sin\phi\right\}_{-(\pi-\theta)/2}^{(\pi-\theta)/2}$$

$$= 2\frac{ze^2}{4\pi\varepsilon_{\mathrm{o}}} \frac{1}{\upsilon_\infty b} \cos\frac{\theta}{2} \ . \tag{5.12}$$

Equation (5.12) is identical to Rutherford's expression for Δp in (2.12). However, in the case of a heavy charged particle (ze) interacting with a stationary orbital electron (e) the scattering angle $\theta \approx 0$, and thus results in a simplified expression for Δp since $\cos(\theta/2) \approx 1$

$$\Delta p = 2\frac{ze^2}{4\pi\varepsilon_{\mathrm{o}}} \frac{1}{\upsilon_\infty b} \ . \tag{5.13}$$

The energy transferred to the orbital electron from the heavy charged particle for a single interaction with an impact parameter b is

$$\Delta E(b) = \frac{(\Delta p)^2}{2m_{\mathrm{e}}} = 2\left(\frac{e^2}{4\pi\varepsilon_{\mathrm{o}}}\right)^2 \frac{z^2}{m_{\mathrm{e}}\upsilon_\infty^2 b^2} \ , \tag{5.14}$$

using the classical expression between kinetic energy $E_{\mathrm{K}} = mv_\infty^2/2$ and momentum $p = mv_\infty$

$$E_{\mathrm{K}} = \frac{mv_\infty^2}{2} = \frac{p^2}{2m}. \tag{5.15}$$

Note that in (5.14) m_{e} is the rest mass of the electron (target) and υ_∞ is the velocity of the heavy charget particle (projectile).

5.3.2 Linear Collision Stopping Power

The total energy loss of the charged particle in the absorber per unit path length dE/dx is defined as the *linear stopping power*. It is calculated by integrating $\Delta E(b)$ over all possible impact parameters b ranging from $b_{\min}$ to $b_{\max}$ and accounting for all electrons available for interaction to obtain

$$-\frac{dE}{dx} = \int\limits_{b_{\min}}^{b_{\max}} \Delta E(b)\frac{\Delta n}{\Delta x} \ . \tag{5.16}$$

The mass collision stopping power S_{col} is calculated from the linear collision stopping power with the standard relationship

$$S_{\mathrm{col}} = -\frac{1}{\rho}\frac{dE}{dx} \ . \tag{5.17}$$

In (5.16) $\Delta n/\Delta x$ is the number of electrons per unit path length in a thin annual cylinder with inner radius b and outer radius $b + db$. The cylinder's axis is aligned with the trajectory of the heavy charged particle.

Intuitively we may consider integration in (5.16) over all possible impact parameters from 0 to ∞; however, we must account for two physical limitations affecting the energy transfer from a heavy charged particle to orbital electrons:

1. Minimum possible energy transfer is governed by the ionization and excitation potentials of orbital electrons resulting in a maximum impact parameter $b_{\max}$ beyond which energy transfer becomes impossible.
2. Maximum possible energy transfer in a head-on collision between the heavy charged particle and the orbital electron was discussed in Sect. 4.3 and results in a minimum impact parameter $b_{\min}$.

The number of electrons Δn contained in the annual cylinder with radii b and $b + db$ is

$$\Delta n = N_e dm = (ZN_A/A)dm \ , \tag{5.18}$$

where

N_e is the number of electrons per unit mass (ZN_A/A) in the absorber,
dm is the mass contained in the annual cylinder between b and $b+db$ equal to

$$dm = \rho dV = \rho\pi(b + db)^2 \Delta x - \rho\pi b^2 \Delta x$$
$$= \rho\pi \Delta x[b^2 + 2b(db) + (db)^2 - b^2] \approx 2\pi\,\rho\,b\,db\,\Delta x \ . \tag{5.19}$$

Ignoring the $(db)^2$ term in (5.19) we express $\Delta n/\Delta x$ as follows:

$$\Delta n/\Delta x = 2\pi\,\rho(ZN_A/A)b\,db \ . \tag{5.20}$$

The mass collision stopping power S_{col} is then equal to

$$S_{\text{col}} = -\frac{1}{\rho}\frac{dE}{dx} = 4\pi N_e \left(\frac{e^2}{4\pi\varepsilon_o}\right)^2 \frac{z^2}{m_e v_\infty^2} \int\limits_{b_{\min}}^{b_{\max}} \frac{db}{b}$$

$$= 4\pi N_e \left(\frac{e^2}{4\pi\varepsilon_o}\right)^2 \frac{z^2}{m_e v_\infty^2} \ln\frac{b_{\max}}{b_{\min}} \ . \tag{5.21}$$

$$= 4\pi \frac{Z}{A} N_A \left(\frac{e^2}{4\pi\varepsilon_o}\right)^2 \frac{z^2}{m_e v_\infty^2} \ln\frac{b_{\max}}{b_{\min}} \ . \tag{5.22}$$

The mass collision stopping power exhibits: (1) *linear proportionality with z^2*, the atomic number of the heavy charged particle (projectile) and (2) *inverse proportionality with v_∞^2*, the initial velocity of the projectile. This implies, for example, that mass collision stopping powers of an absorbing medium will differ by: (1) factor of 4 in the case of protons and α particles of same velocities; (2) factor of 16 in the case of protons and α particles of same kinetic energies.

Since Z/A varies from substance to substance within quite a narrow range (it falls from 0.5 for low Z elements to $\sim$0.4 for high Z elements, with one notable exception of hydrogen for which $Z/A \approx 1$), we note that the mass collision stopping power varies very slightly from substance to substance. This means that the energy losses of a given charged particle passing through layers of equal thickness in g/cm^2 are about the same for all substances.

5.3.3 Minimum Energy Transfer and Mean Ionization-Excitation Potential

For large impact parameters b the energy transfer $\Delta E(b)$, calculated from (5.14), may be smaller than the binding energy of the orbital electron or smaller than the minimum excitation potential of the given orbital electron. Thus, no energy transfer is possible for $b > b_{max}$ where b_{max} corresponds to a minimum energy transfer ΔE_{min}, referred to as the *mean ionization-excitation potential I* of the absorber atom. This potential depends only on the stopping medium but not on the type of the charged particle. It is always larger than the ionization potential of the atom since it accounts for all possible atomic ionizations as well as atomic excitations.

The mean ionization-excitation potential I corresponds to the minimum amount of energy ΔE_{min} that can be transferred on the average to an absorber atom in a Coulomb interaction between the charged particle and an orbital electron. Using (5.14), ΔE_{min} is written as

$$\Delta E_{min} = 2 \left(\frac{e^2}{4\pi\varepsilon_o} \right)^2 \frac{z^2}{m_e v_\infty^2 b_{max}^2} = I \tag{5.23}$$

showing that $b_{max} \propto 1/\sqrt{I}$.

In general, the mean ionization-excitation potential I cannot be calculated from the atomic theory; however, it may be estimated from the following empirical relationships:

$$I(\text{in eV}) \approx 11.5 \, Z \,, \tag{5.24}$$

or, to a better approximation,

$$I(\text{in eV}) = 9.1 Z \left(1 + 1.9 \, Z^{-2/3} \right) . \tag{5.25}$$

Some typical values for I are as follows (from the ICRU Report 37): hydrogen: 14.9 eV; carbon: 78 eV; aluminum: 167 eV; copper: 322 eV; water: 75 eV; air: 86 eV.

5.3.4 Maximum Energy Transfer

For small impact parameters b the energy transfer is governed by the maximum energy ΔE_{max} that can be transferred in a single head-on collision, as discussed in Sect. 4.3.2. Classically ΔE_{max} for a head-on collision between a

heavy charged particle M with kinetic energy E_K and an electron with mass m_e is given by

$$\Delta E_{\max} = \frac{4m_e M}{(m_e + M)^2} E_K \approx 4\frac{m_e}{M} E_K = 4\frac{m_e}{M}\frac{Mv_\infty^2}{2} = 2m_e v_\infty^2 \ . (5.26)$$

Equation (5.26) shows that only a very small fraction $(4m_e/M)$ of the heavy charged particle kinetic energy can be transferred to an orbital electron in a single collision (note that $M \gg m_e$).

The classical relationship between $\Delta E_{\max}$ and the minimum impact parameter $b_{\min}$ that allows the maximum energy transfer from a heavy charged particle to an orbital electron is

$$\Delta E_{\max} = 2 \left(\frac{e^2}{4\pi\varepsilon_o}\right)^2 \frac{z^2}{m_e v_\infty^2 b_{\min}^2} = 2m_e v_\infty^2 \ , \tag{5.27}$$

resulting in $\Delta E_{\max} \propto 1/b_{\min}^2$ or $b_{\min} \propto 1/\sqrt{\Delta E_{\max}}$.

5.4 Mass Collision Stopping Power

The energy transfer $\Delta E(b)$ from a heavy charged particle to an orbital electron ranges from $\Delta E_{\min}(b_{\max}) = I$ to $\Delta E_{\max}(b_{\min}) = 2m_e v_\infty^2$; i.e.,

$$I \leq \Delta E(b) \leq 2m_e v_\infty^2 \ . \tag{5.28}$$

The ratio $b_{\max}/b_{\min}$, after combining (5.23) and (5.27), is given as

$$\frac{b_{\max}}{b_{\min}} = \sqrt{\frac{\Delta E_{\max}}{\Delta E_{\min}}} = \sqrt{\frac{2m_e v_\infty^2}{I}} \ . \tag{5.29}$$

- The *classical mass collision stopping power* of (5.22) for a heavy charged particle (*Niels Bohr* 1913) colliding with orbital electrons is then given with the following approximation:

$$S_{\text{col}} = 4\pi \frac{Z}{A} N_A \left(\frac{e^2}{4\pi\varepsilon_o}\right)^2 \frac{z^2}{m_e v_\infty^2} \ln \sqrt{\frac{2m_e v_\infty^2}{I}} \ . \tag{5.30}$$

- The *non-relativistic quantum-mechanical* expression for the mass stopping power of heavy charged particles was derived by *Hans Bethe* and *Felix Bloch* and it differs from Bohr's expression of (5.30) only in the occurrence of the power $1/2$ in the Bohr's logarithmic term. The Bethe-Bloch mass stopping power is

$$S_{\text{col}} = 4\pi \frac{Z}{A} N_A \left(\frac{e^2}{4\pi\varepsilon_o}\right)^2 \frac{z^2}{m_e v_\infty^2} \ln \frac{2m_e v_\infty^2}{I} \ . \tag{5.31}$$

- Bethe's *relativistic quantum-mechanical* expression for the mass collision stopping power of heavy charged particles accounts for relativistic effects to get

$$S_{\text{col}} = 4\pi \frac{Z}{A} N_A \left(\frac{e^2}{4\pi\varepsilon_o} \right)^2 \frac{z^2}{m_e v_\infty^2}$$
$$\left\{ \ln \frac{2m_e c^2}{I} + \ln \beta^2 - \ln(1 - \beta^2) - \beta^2 \right\} , \qquad (5.32)$$

where β is the normalized incident particle velocity ($\beta = v/c$) and the relativistic expression for ΔE_{max} of (4.38) is used.

  - Two corrections were subsequently incorporated into Bethe's expression for the mass collision stopping power:
  - *Correction* C_K/Z to account for non-participation of bound K-shell electrons in the slowing-down process. This correction reduces the collision stopping power but is only effective at low kinetic energies of the charged particle.
  - *Polarization (density effect) correction* δ also lowers the collision stopping power. It is applied to condensed media (liquids and solids) for which the dipole distortion of the atoms near the track of the charged particle weakens the Coulomb force field experienced by the more distant atoms, thus decreasing their participation in the slowing down process.
  - The polarization correction does not apply for gases, because in gases the atoms are spaced sufficiently far apart to act independently of one another. The correction is also negligible for heavy charged particles at energies of interest in medical physics, but is significant for light charged particles (electrons and positrons).

- Incorporating the K-shell correction C_K/Z and the polarization correction δ into Bethe's relativistic quantum-mechanical expression results in the following relationship for the mass collision stopping power S_{col} for heavy charged particles:

$$S_{\text{col}} = 4\pi \frac{Z}{A} N_A \left(\frac{e^2}{4\pi\varepsilon_o} \right)^2 \frac{z^2}{m_e v_\infty^2}$$
$$\left\{ \ln \frac{2m_e c^2}{I} + \ln \beta^2 - \ln(1 - \beta^2) - \beta^2 - \frac{C_K}{Z} - \delta \right\} . \qquad (5.33)$$

- Considering the various expressions stated above for the mass collision stopping power S_{col} of heavy charged particles, we can write S_{col} in general terms as follows:

$$S_{\text{col}} = 4\pi \frac{N_A}{A} \left(\frac{e^2}{4\pi\varepsilon_o} \right)^2 \frac{z^2}{m_e c^2 (v_\infty/c)^2} B_{\text{col}} . \qquad (5.34)$$

Table 5.2. Expressions for the atomic stopping number B_{col} for various energy ranges of heavy charged particle energy

Derivation	B_{col}	
Classical (Bohr)	$Z \ln \sqrt{\frac{2m_e v^2}{I}}$	(5.36)
Non-relativistic, quantum-mechanical (Bethe-Bloch)	$Z \ln \frac{2m_e v^2}{I}$	(5.37)
Relativistic, quantum-mechanical (Bethe)	$Z \left[\ln \frac{2m_e c^2}{I} + \ln \beta^2 - \ln(1 - \beta^2) - \beta^2 \right]$	(5.38)
Relativistic, quantum-mechanical with K-shell and polarization correction	$Z \left[\ln \frac{2m_e c^2}{I} + \ln \beta^2 - \ln(1 - \beta^2) \right.$ $\left. -\beta^2 - \frac{C_K}{Z} - \delta \right]$	(5.39)

After inserting into (5.34) the appropriate values for the constants N_A, e, ε_o, and $m_e c^2$ and using $\beta = v_\infty / c$ we obtain the following expression for the mass collision stopping power S_{col}:

$$S_{col} = 0.3070 \frac{\text{MeV} \cdot \text{cm}^2}{(\text{gram} - \text{atom})} \frac{z^2}{A\beta^2} B_{col} , \qquad (5.35)$$

where B_{col} is called the *atomic stopping number*.

- The atomic stopping number B_{col} is a function of the atomic number Z of the absorber (through the mean ionization-excitation potential I) and of the velocity of the charged particle. The form of the expression for B_{col} also depends on the specific approach taken in its derivation, as indicated in Table 5.2.

The units of S_{col} in (5.35) are MeV $\cdot$ cm^2/g; the constant in (5.35) has units of MeV $\cdot$ cm^2/(gram-atom). Since the units of A are g/(gram-atom), incorporating an appropriate value for A into (5.35) results in proper units for S_{col} in MeV $\cdot$ cm^2/g.

From the general expression for the mass collision stopping power given in (5.33) we note that the mass collision stopping power S_{col} for a heavy charged particle traversing an absorber *does not depend on charged particle mass* but depends upon:

1. *Atomic number Z, atomic mass A*, and *mean ionization-excitation potential I* in the form [Z/A and $(-\ln I)$] of the absorber. As Z increases, Z/A and $-\ln I$ decrease resulting in a decrease of S_{col}.
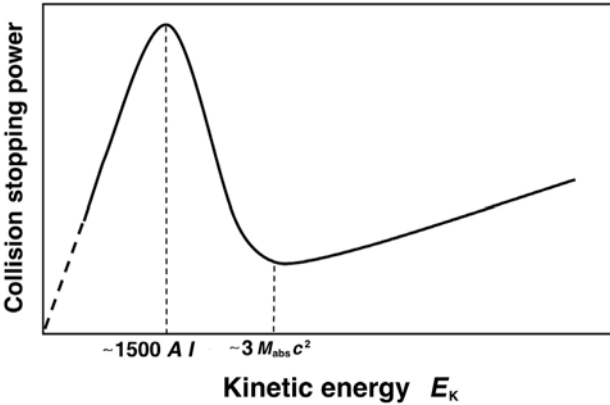
Fig. 5.4. Schematic representation of the shape of the collision stopping power curve as a function of the charged particle kinetic energy E_K. Three regions are shown as the energy increases: (1) the rise of stopping power at low energies to reach a maximum at about $1500AI$; (2) fall-off as $1/E_K$ or $1/v^2$ beyond the maximum to reach a minimum, and (3) slow relativistic rise at relativistic energies where $v \approx c$

2. *Particle velocity* v. For increasing non-relativistic velocities S_{col} first increases, reaches a maximum, then decreases as $1/v^2$, reaches a broad minimum and then slowly rises with the relativistic term $\{\ln \beta^2 - \ln(1 - \beta^2) - \beta^2\}$ as v becomes relativistic and approaches c.
3. *Particle charge ze.* S_{col} increases as z^2, i.e., a doubly charged particle experiences 4 times the collision stopping power of a singly charged particle of the same velocity v moving through the same absorber.

As shown schematically in Fig. 5.4, the collision stopping power against E_K goes through three distinct regions as the kinetic energy E_K increases:

1. At low kinetic energies, S_{col} rises with energy and reaches a peak at $2.78IM/(4m_e)$, where M is the mass of the heavy charged particle and m_e the mass of the electron. The kinetic energy $(E_K)_{max}$ at which the peak in S_{col} occurs can be estimated from the non-relativistic Bethe-Bloch equation [(5.31)] as follows:

$$S_{col} = 4\pi \frac{Z}{A} N_A \left(\frac{e^2}{4\pi\varepsilon_o}\right)^2 \frac{z^2}{m_e v^2} \ln \frac{2m_e v^2}{I}$$
$$= const \frac{1}{E_K} \ln \left(\frac{4}{I} \frac{m_e}{M} E_K\right) , \tag{5.40}$$

where

E_K is the classical kinetic energy of the heavy charged particle; $E_K = Mv^2/2$,

M is the mass of the heavy charged particle,

v is the velocity of the heavy charged particle.

$(E_K)_{max}$ is determined by setting $dS_{col}/dE_K|_{E_K=(E_K)_{max}} = 0$ and solving for $(E_K)_{max}$

$$\left.\frac{dS_{col}}{dE_K}\right|_{E_K=E_{Kmax}} = 0 = -\frac{const}{[(E_K)_{max}]^2}\ln\left(\frac{4}{I}\frac{m_e}{M}(E_K)_{max}\right) + \frac{const}{[(E_K)_{max}]^2}$$

$$= \frac{const}{[(E_K)_{max}]^2}\left[1 - \ln\left(\frac{4}{I}\frac{m_e}{M}(E_K)_{max}\right)\right] . \quad (5.41)$$

Equation (5.41) results in the following expression for $(E_K)_{max}$:

$$(E_K)_{max} = \left(\frac{4}{I}\frac{m_e}{M}\right)^{-1} e \approx 1500 \, A\, I \, , \quad (5.42)$$

where we use $M \approx M_p A$ for the mass of the heavy charged particle, with M_p the proton mass and A the atomic mass number of the heavy charged particle; $M_p/m_e \approx 2000$; and $e \approx 3$.

2. Beyond the peak, S_{col} decreases as $1/v^2$ or $1/E_K$ of the charged particle until it reaches a broad minimum around $3M_{absorber}c^2$, where $M_{absorber}$ is the rest mass of the absorber.
3. Beyond the broad minimum the mass collision stopping power S_{col} rises slowly with kinetic energy E_K as a result of the relativistic terms $\left\{\ln\beta^2 - \ln(1-\beta^2) - \beta^2\right\}$

5.5 Collision Stopping Power for Light Charged Particles

Electron interactions (collisions) with orbital electrons of an absorber differ from those of heavy charged particles in three important aspects:

1. Relativistic effects become important at relatively low kinetic energies.
2. Collisions with orbital electrons may result in large energy transfers of up to 50% of the incident electron kinetic energy. They may also result in elastic and inelastic electron scattering.
3. Collisions of electrons with nuclei of the absorber may result in bremsstrahlung production (radiative loss).

For electrons and positrons, energy transfers due to soft collisions are combined with those due to hard collisions using the Møller (for electrons) and Bhabba (for positrons) cross sections for free electrons. The complete mass collision stopping power for electrons and positrons, according to the ICRU Report 37, is

$$S_{col} = 2\pi r_e^2 \frac{Z}{A} N_A \frac{m_e c^2}{\beta^2}\left[\ln\frac{E_K}{I} + \ln(1+\tau/2) + F^{\pm}(\tau) - \delta\right] , \quad (5.43)$$

In (5.43) the function $F^-(\tau)$ is given for electrons as

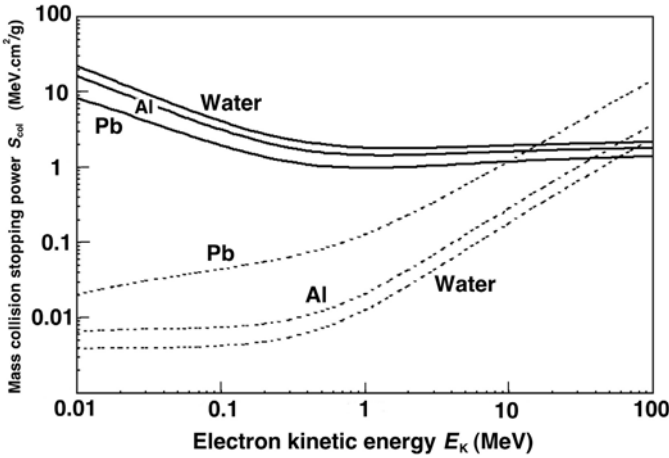$$F^-(\tau) = (1-\beta^2)\left[1 + \tau^2/8 - (2\tau+1)\ln 2\right] \quad (5.44)$$

Fig. 5.5. Mass collision stopping power for electrons in water, aluminum and lead against electron kinetic energy. The collision stopping power data are shown with *solid curves;* the radiative stopping power data of Fig. 5.2 are shown with *dotted curves* for comparison. Data were obtained from the NIST

The function $F^+(\tau)$ for positrons is given as

$$F^+(\tau) = 2\ln 2 - (\beta^2/12)$$
$$\left[23 + 14/(\tau+2) + 10/(\tau+2)^2 + 4/(\tau+2)^3\right] , \quad (5.45)$$

where

τ is the electron or positron kinetic energy normalized to $m_e c^2$, i.e., $\tau = E_K/m_e c^2$,

β is the electron or positron velocity normalized to c, i.e., $\beta = \upsilon/c$.

Figure 5.5 shows mass collision stopping powers S_{col} for electrons in water, aluminum and lead with solid lines. For comparison, mass radiative stopping powers of Fig. 5.2 are shown with dotted lines. The data show that higher atomic number absorbers have lower S_{col} than lower atomic number absorbers at same electron energies. The dependence of S_{col} on stopping medium results from two factors in the stopping power expressions given by (5.33) and (5.43), both lowering S_{col} with an increasing Z of the stopping medium:

1. The factor Z/A makes S_{col} dependent on the number of electrons per unit mass of the absorber. Z/A is 1 for hydrogen; 0.5 for low Z absorbers; then gradually drops to ∼0.4 for high Z absorbers.
2. The $-\ln I$ term decreases S_{col} with increasing Z, since I increases almost linearly with increasing Z, as shown in (5.24) and (5.25).

5.6 Total Mass Stopping Power

Generally, the total mass stopping power S_{tot} of charged particles is given by the sum of two components: the *radiative stopping power* S_{rad} and the *collision stopping power* S_{col}, i.e.,

$$S_{\text{tot}} = S_{\text{rad}} + S_{\text{col}} . \tag{5.46}$$

For heavy charged particles the radiative stopping power is negligible ($S_{\text{rad}} \approx 0$), thus $S_{\text{tot}} = S_{\text{col}}$

For light charged particles both components contribute to the total stopping power. Within a broad range of kinetic energies below 10 MeV collision (ionizational) losses are dominant ($S_{\text{col}} > S_{\text{rad}}$); however, the situation is reversed at high kinetic energies where $S_{\text{rad}} > S_{\text{col}}$.

The crossover between the two modes occurs at a *critical kinetic energy* $(E_{\text{K}})_{\text{crit}}$ where the two stopping powers are equal, i.e., $S_{\text{rad}} = S_{\text{col}}$ for a given absorber with atomic number Z. The critical kinetic energy $(E_{\text{K}})_{\text{crit}}$ can be estimated from the following empirical relationship:

$$(E_{\text{K}})_{\text{crit}} \approx \frac{800 \text{ MeV}}{Z} , \tag{5.47}$$

that for water, aluminum and lead amounts to ~105 MeV, ~61 MeV and ~10 MeV, respectively.

–   For high Z absorbers the dominance of radiative losses over collision losses starts at lower kinetic energies than in low Z absorbers. However, even in high Z media such as lead and uranium $(E_{\text{K}})_{\text{crit}}$ is at ~10 MeV, well in the relativistic region.
–   The ratio of collision to radiative stopping power ($S_{\text{col}}/S_{\text{rad}}$) at a given electron kinetic energy may be estimated from the following:

$$\frac{S_{\text{col}}}{S_{\text{rad}}} = \frac{800 \text{ MeV}}{Z \, E_{\text{K}}} = \frac{(E_{\text{K}})_{\text{crit}}}{E_{\text{K}}} . \tag{5.48}$$

Figure 5.6 shows the total mass stopping power of electrons (solid curves) in water, aluminum and lead against the electron kinetic energy. For comparison the radiative and collision components of the total stopping power of Figs. 5.2 and 5.5 are also shown.

5.7 Bremsstrahlung (Radiation) Yield

The bremsstrahlung yield $B(E_{\text{Ko}})$ of a charged particle with initial kinetic energy E_{Ko} striking an absorber is defined as that fraction of the initial kinetic energy that is emitted as bremsstrahlung radiation through the slowing down process of the particle in the absorber.
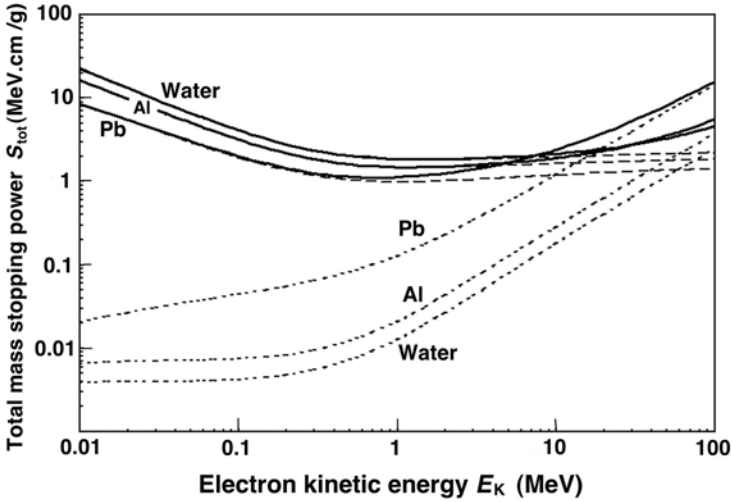
Fig. 5.6. Total mass stopping power S_{tot} for electrons in water, aluminum and lead against the electron kinetic energy shown with *solid curves*. The mass collision and mass radiative stopping powers are shown with *dotted curves* for comparison. The total stopping power of a given material is the sum of the radiative and collision stopping powers. Data were obtained from the NIST

- For heavy charged particles $B(E_{Ko}) \approx 0$.
- For light charged particles (electrons and positrons) the bremsstrahlung yield $B(E_{Ko})$ is determined from stopping power data as follows:

$$B(E_{Ko}) = \frac{\int\limits_{0}^{E_{Ko}} \frac{S_{rad}(E)}{S_{tot}(E)} dE}{\int\limits_{0}^{E_{Ko}} dE} = \frac{1}{E_{Ko}} \int\limits_{0}^{E_{Ko}} \frac{S_{rad}(E)}{S_{tot}(E)} dE \ . \tag{5.49}$$

- For positron interactions, annihilation-in-flight also produces photons; however, the effect is generally ignored in calculation of the bremsstrahlung yield $B(E_{Ko})$.
- The energy E_{rad} radiated per charged particle is

$$E_{rad} = E_{Ko} B(E_{Ko}) = \int\limits_{0}^{E_{Ko}} \frac{S_{rad}(E)}{S_{tot}(E)} dE \ , \tag{5.50}$$

while the energy E_{col} lost through ionization per charged particle is

$$E_{col} = E_{Ko} - E_{rad} = E_{Ko} [1 - B(E_{Ko})] = \int\limits_{0}^{E_o} \frac{S_{col}(E)}{S_{tot}(E)} dE \ . \tag{5.51}$$
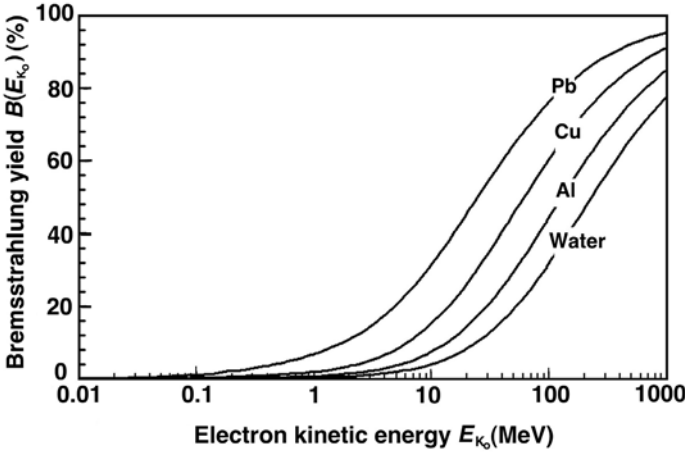
Fig. 5.7. Bremsstrahlung yield $B(E_{Ko})$ for electrons in water, aluminum, copper and lead against the incident electron kinetic energy. Data were obtained from the National Institute of Standards and Technology (NIST), Washington, D.C.

- Bremsstrahlung yield $B(E_{Ko})$ for water, aluminum, copper and lead is plotted against incident electron kinetic energy E_{Ko} in Fig. 5.7.
- In radiation dosimetry a quantity referred to as the *radiative fraction* $\bar{g}$ is defined as the average fraction of the energy that is transferred from photons to electrons and positrons and subsequently lost by these particles to radiative processes that are predominantly bremsstrahlung interactions but can also include annihilation-in-flight interactions by positrons. The quantity $\bar{g}$ appears in the following expressions:

$$\frac{\mu_{ab}}{\rho} = \frac{\mu_{tr}}{\rho}(1 - \bar{g}) \tag{5.52}$$

and

$$K_{col} = K(1 - \bar{g}) , \tag{5.53}$$

where

μ_{ab}/ρ is the mass energy absorption coefficient for a photon beam,
μ_{tr}/ρ is the mass energy transfer coefficient for a photon beam,
K_{col} is the collision kerma,
K is the total kerma.

- The radiative fraction $\bar{g}$ is the average value of $B(E_{K_i})$ for all electrons and positrons of various initial energies E_{K_i} present in the spectrum of light charged particles produced in a medium by either monoenergetic photons or a photon spectrum.
- $B(E_{Ko})$ is the bremsstrahlung yield defined for monoenergetic electrons with initial energy E_{Ko}, while $\bar{g}$ is the radiative fraction calculated for a spectrum of electrons and positrons produced in the medium by photons.

5.8 Range of Charged Particles

In traversing matter charged particles lose their energy in ionizing and radiative collisions that may also result in significant deflections. In addition, charged particles suffer a large number of deflections as a result of elastic scattering. These effects are much more pronounced for light charged particles (electrons and positrons) in comparison to heavy charged particles.

- *Heavy charged particles* do not experience radiative losses, transfer only small amounts of energy in individual ionizing collisions with orbital electrons, and mainly suffer small angle deflections in elastic collisions. Their path through an absorbing medium is thus essentially rectilinear, as shown schematically in Fig. 5.8.
- *Electrons* with kinetic energy E_K, on the other hand, can lose energy up to $E_K/2$ in individual ionizing collisions and energy up to E_K in individual radiative collisions. Since they can also be scattered with very large scattering angles, their path through the absorbing medium is very tortuous, as shown schematically in Fig. 5.8.
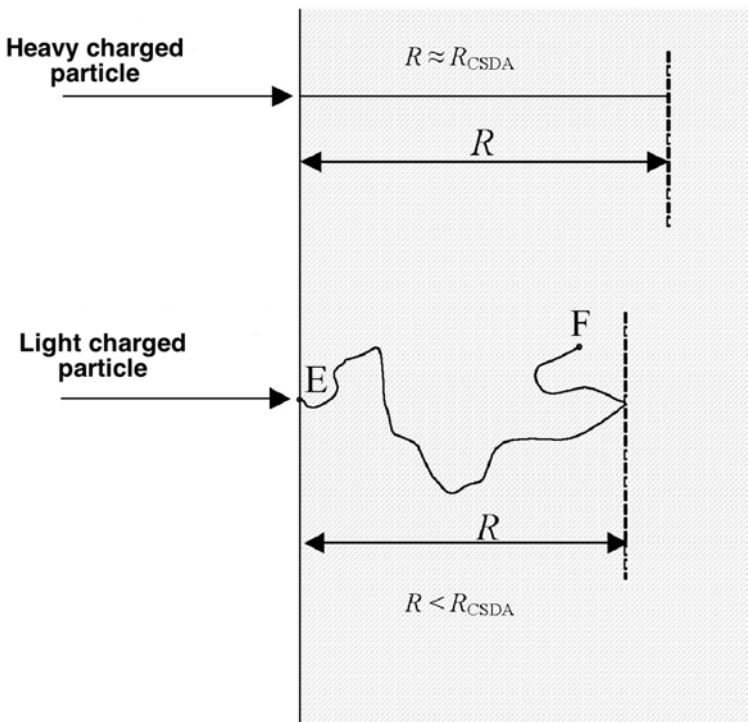
Fig. 5.8. Schematic diagram of charged particle penetration into a medium. *Top:* Heavy charged particle; *bottom:* light charged particle (electron or positron)

- The range R of a charged particle in a particular absorbing medium is an experimental concept providing the thickness of an absorber that the particle can just penetrate. It depends on the particle's kinetic energy, mass as well as charge, and on the composition of the absorbing medium. Various definitions of range that depend upon the method employed in the range determination are in common use.

- Generally, the concepts of range R must be distinguished from the concept of the path-length ℓ of a charged particle. This path-length simply provides the total path-length of the charged particle in the absorber and can be calculated, as suggested by *Martin Berger* and *Stephen Seltzer* in 1983, using the continuous slowing down approximation (CSDA) as follows:

$$R_{\mathrm{CSDA}} = \int\limits_{0}^{E_{\mathrm{K_i}}} \frac{dE}{S_{\mathrm{tot}}(E)} \ , \tag{5.54}$$

where

R_{CSDA} is the CSDA range (mean path-length) of the charged particle in the absorber,

$E_{\mathrm{K_i}}$ is the initial kinetic energy of the charged particle,

$S_{\mathrm{tot}}(E)$ is the total stopping power of the charged particle as a function of the kinetic energy E_{K}.

- For heavy charged particles, R_{CSDA} is a very good approximation to the average range $\bar{R}$ of the charged particle in the absorbing medium, because of the essentially rectilinear path of the charged particle (see Fig. 5.8) in the absorber.

- For light charged particles R_{CSDA} is up to twice the range of charged particles in the absorber, because of the very tortuous path that the light charged particles experience in the absorbing medium (see Fig. 5.8).

5.9 Mean Stopping Power

In radiation dosimetry the main interest is in the energy absorbed per unit mass of the absorbing medium governed by collision losses of charged particles. It is often convenient to characterize a given radiation beam with electrons of only one energy rather than with an electron spectrum $d\phi/dE$ that is present in practice.

For example, monoenergetic electrons set in motion with an initial kinetic energy E_{Ko} in an absorbing medium will through their own slowing down process produce a spectrum of electrons in the medium ranging in energy from E_{Ko} down to zero. The electron spectrum $d\phi/dE$, when ignoring any possible hard collisions, is given as

$$\frac{d\phi(E)}{dE} = \frac{N}{S_{\mathrm{tot}}(E)} \ , \tag{5.55}$$

where

N is the number of monoenergetic electrons of energy E_{Ko} produced per unit mass in the absorbing medium,

$S_{\text{tot}}(E)$ is the total stopping power.

For this electron spectrum, produced by monoenergetic electrons, we can define a *mean collision stopping power* $\bar{S}_{\text{col}}$ as follows:

$$\overline{S}_{\text{col}}(E_{\text{Ko}}) = \frac{\int\limits_0^{E_{\text{Ko}}} \frac{d\phi}{dE} S_{\text{col}}(E) dE}{\int\limits_0^{E_{\text{Ko}}} \frac{d\phi}{dE} dE} \ . \tag{5.56}$$

Using (5.54) and (5.55) the integral in the denominator of (5.56) is determined as follows:

$$\int\limits_0^{E_{\text{Ko}}} \frac{d\phi}{dE} dE = N \int\limits_0^{E_{\text{Ko}}} \frac{dE}{S_{tot}(E)} = N\, R_{\text{CSDA}} \ . \tag{5.57}$$

Using (5.50) and (5.55), the numerator of (5.56) is determined as follows:

$$\int\limits_0^{E_{\text{Ko}}} \frac{d\phi}{dE} S_{\text{col}}(E) dE = N \int\limits_0^{E_{\text{Ko}}} \frac{S_{\text{col}}(E)}{S_{\text{tot}}(E)} dE$$

$$= N \int\limits_0^{E_{\text{Ko}}} \frac{S_{\text{tot}}(E) - S_{\text{rad}}(E)}{S_{\text{tot}}(E)} dE$$

$$= N E_{\text{Ko}} - N E_{\text{Ko}} B(E_{\text{Ko}}) \ . \tag{5.58}$$

The mean collision stopping power $\overline{S}_{\text{col}}(E_{\text{K}_i})$ of (5.58) can now be written as

$$\overline{S}_{\text{col}}(E_{\text{Ko}}) = E_{\text{Ko}} \frac{1 - B(E_{\text{Ko}})}{R_{\text{CSDA}}} \ . \tag{5.59}$$

The relationship for $\overline{S}_{\text{col}}(E_{\text{Ko}})$ above could also be stated intuitively by noting that an electron with an initial kinetic energy E_{Ko} will, through traveling the path-length ℓ equal to R_{CSDA}, in the absorbing medium lose an energy $E_{\text{Ko}}B(E_{\text{Ko}})$ to bremsstrahlung and deposit an energy $E_{\text{Ko}}[1 - B(E_{\text{Ko}})]$ in the medium.

5.10 Restricted Collision Stopping Power

In radiation dosimetry one is interested in determining the energy transferred to a localized region of interest; however, the use of the mass collision stopping power S_{col} for this purpose may overestimate the dose because S_{col} incorporates both hard and soft collisions. The δ rays resulting from hard

collisions may be energetic enough to carry their kinetic energy a significant distance from the track of the primary particle thereby escaping from the region of interest. The concept of restricted mass collision stopping power L_Δ has been introduced to address this issue by excluding the δ rays with energies exceeding a suitable threshold value Δ.

The choice of the energy threshold Δ depends on the problem at hand. For dosimetric measurements involving air-filled ionization chambers with a typical electrode separation of 2 mm a frequently used threshold value is 10 keV (Note, the range of a 10 keV electron in air is of the order of 2 mm). For microdosimetric studies, on the other hand, one usually takes 100 eV as a reasonable threshold value.

Of course, to be physically relevant Δ must not exceed $\Delta E_{\max}$, the maximum possible energy transfer to orbital electron from the incident particle with kinetic energy E_K in a direct-hit collision. As shown in Sect. 4.3.2, $\Delta E_{\max}$ equals to $E_K/2$ for electrons, E_K for positrons, and $2m_e c^2 \beta^2/(1-\beta^2)$ for heavy charged particles [see (4.42), (4.41), and (4.39), respectively].

For a given kinetic energy E_K of the primary particle the restricted collision stopping power L_Δ is in general smaller than the unrestricted collision stopping power S_{col}; the smaller is Δ, the larger is the discrepancy. As Δ increases from a very small value, the discrepancy diminishes until at $\Delta = \Delta E_{\max}$ the restricted and unrestricted collision stopping powers become equal, i.e., $L_{\Delta = \Delta E_{\max}} = S_{col}$, irrespective of E_K.

Figure 5.9 displays the unrestricted collision mass stopping power as well as the restricted collision mass stopping powers with $\Delta = 10$ keV and $\Delta = 100$ keV against kinetic energy E_K for electrons in carbon based on data in the ICRU Report 37.

The following observations can now be made:

1. Since energy transfers to secondary electrons are limited to $E_K/2$, the unrestricted and restricted mass stopping powers are identical for kinetic energies lower than or equal to 2Δ. This is indicated in Fig. 5.9 with vertical lines at 20 keV and 200 keV for the threshold values $\Delta = 10$ keV and $\Delta = 100$ keV, respectively.
2. For a given $E_K > 2\Delta$, the smaller is Δ, the larger is the discrepancy between the unrestricted and restricted stopping powers.
3. For a given Δ and $E_K > 2\Delta$, the larger is E_K, the larger is the discrepancy between the unrestricted and restricted stopping powers.

5.11 Bremsstrahlung Targets

Bremsstrahlung production is of great importance in radiation oncology physics, since most of the radiation beams used for external beam radiotherapy are produced through bremsstrahlung interactions of monoenergetic electrons with solid targets. These targets are components of x-ray machines
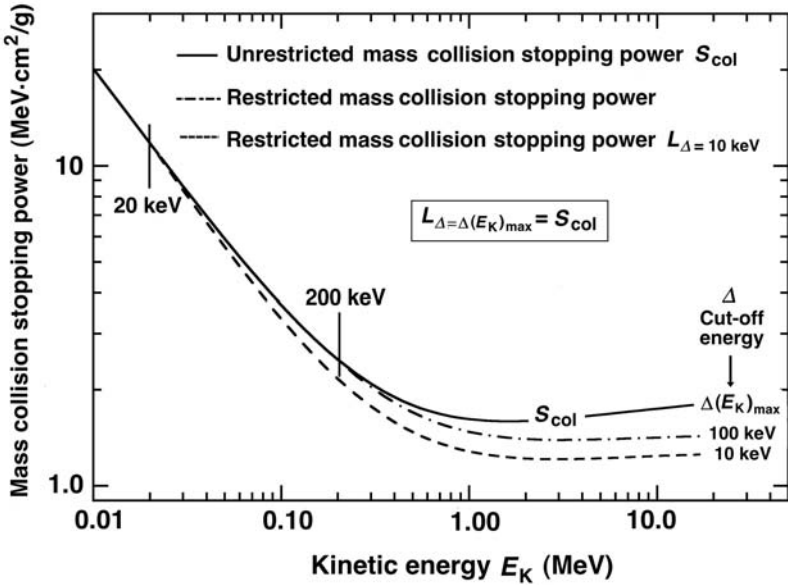
Fig. 5.9. Unrestricted and restricted ($\Delta = 10$ keV and $\Delta = 100$ keV) collision mass stopping powers for electrons in carbon against kinetic energy. Data are based on the ICRU Report 37

and linear accelerators; the most commonly used radiation-emitting machines for diagnosis and treatment of disease.

An electron that strikes the target with a given kinetic energy will undergo several different interactions with target atoms before it comes to rest and dissipates all of its kinetic energy in the target. As discussed in Sect. 5.1, there are two classes of electron interactions with a target atom:

1. with orbital electrons of the target atoms
2. with nuclei of the target atoms

Incident electron interaction with orbital electron of a target atom results mainly in collision loss and ionization of the target atom that may be accompanied by an energetic electron referred to as a delta ray. The collision loss will be followed by emission of characteristic x rays and Auger electrons.

Incident electron interaction with the nucleus of a target atom results mainly in elastic scattering events but may also result in radiative loss accompanied with bremsstrahlung production.

While bremsstrahlung is the major contributor to the x-ray spectrum at superficial and orthovoltage energies, it is essentially the sole contributor to the x-ray spectrum at megavoltage energies.

With regard to their thickness compared to the range of electrons in the target material, x-ray targets are either *thin* or *thick*. As discussed in

Sect. 3.2.8, the peak x-ray intensity occurs at a characteristic angle θ_{max} that depends on the kinetic energy of the incident electrons:

1. In the diagnostic energy range (50 kVp to 120 kVp) θ_{max} is 90º.
2. In the megavoltage radiotherapy range θ_{max} is $\sim$ 0º and the target is referred to as a *transmission target.*

5.11.1 Thin X-ray Targets

Thin x-ray targets are mainly of theoretical interest and their thickness is very small compared to the range of electrons of given kinetic energy in the target material. By definition, a thin target is so thin that electrons:

1. Lose no energy by atomic ionizations
2. Suffer no significant elastic collisions
3. Experience only one bremsstrahlung interaction while traversing the target.

The radiation emitted by accelerated or decelerated electrons of kinetic energy E_K has an intensity I [(energy per photon) $\times$ (number of photons)] that is constant for all photon energies and experiences a sharp cut-off at $h\nu_{max} = E_K$ (Duane-Hunt law).

The shape of the spectral distribution of a thin x-ray target is independent of the target atomic number Z.

5.11.2 Thick X-ray Targets

Thick x-ray targets have thicknesses of the order of the range of electrons R in the target material. In practice, typical thicknesses are equal to about 1.1 R to satisfy two opposing conditions:

1. To ensure that no electrons that strike the target can traverse the target
2. To minimize the attenuation of the bremsstrahlung beam in the target.

Thick target radiation is much more difficult to handle theoretically than thin target radiation; however, in practice most targets used in bremsstrahlung production are of the thick target variety. Main characteristics of thick target radiation are as follows:

- The spectral distribution of thick-target bremsstrahlung is essentially a super-position of contributions from a large number of thin targets, each thin target traversed by a lower energy monoenergetic electron beam having a lower $h\nu_{max}$.
- The integrated intensity of thick-target bremsstrahlung depends linearly on the atomic number Z of the target material. This implies that high Z targets will be more efficient for x-ray production that low Z targets.

- In megavoltage radiotherapy only photons in the narrow cone in the forward direction are used for the clinical beams and the x-ray yield in the forward direction is essentially independent of the atomic number Z of the target.
- The average energy E_{rad} radiated by an electron of initial energy E_{Ko} in being stopped in a thick target was given in (5.50) as

$$E_{\mathrm{rad}} = E_{\mathrm{Ko}} B(E_{\mathrm{Ko}}) = \int\limits_0^{E_{\mathrm{Ko}}} \frac{S_{\mathrm{rad}}(E)}{S_{\mathrm{tot}}(E)} dE \tag{5.60}$$

- In the diagnostic energy range, where $E_{\mathrm{Ko}} \ll m_e c^2$, the mass radiative stopping power S_{rad} is independent of the kinetic energy of the electron and, from (5.3) combined with Table 5.1, given as

$$\begin{aligned} S_{\mathrm{rad}} &= (N_A/A)\sigma_{\mathrm{rad}} E_{\mathrm{Ko}} = (16/3)\alpha\, r_e^2 Z^2 E_{\mathrm{Ko}} \\ &= (16/3)\alpha\, r_e^2 (N_A/A) Z^2 (E_{\mathrm{Ko}} + m_e c^2). \end{aligned} \tag{5.61}$$

- For $E_{\mathrm{Ko}} \ll m_e c^2$ the mass radiative stopping power S_{rad} of (5.61) is independent of the kinetic energy of the electron and may then be simplified to read

$$\begin{aligned} E_{\mathrm{rad}} &= S_{\mathrm{rad}} \int\limits_0^{E_{\mathrm{Ko}}} \frac{dE}{S_{\mathrm{tot}}(E)} \\ &= S_{\mathrm{rad}} R_{\mathrm{CSDA}} = \mathrm{const}\frac{N_A}{A} Z^2 R_{\mathrm{CSDA}} \ . \end{aligned} \tag{5.62}$$

- Since in this energy range $S_{\mathrm{tot}} \approx S_{\mathrm{col}}$ and $S_{\mathrm{col}} \propto N_A Z/A$, we note that $R_{\mathrm{CSDA}} \propto (N_A Z/A)^{-1}$ and the average energy radiated by the electron stopped in a thick target is linearly proportional to the atomic number Z of the target, i.e.,

$$E_{\mathrm{rad}} \propto Z f(E_{\mathrm{K_i}}, Z) \ , \tag{5.63}$$

where $f(E_{\mathrm{K_i}}, Z)$ is a slowly varying function of Z.
- The thick target bremsstrahlung is linearly proportional to the atomic number of the target in the diagnostic energy range where $E_{\mathrm{Ko}} \ll m_e c^2$. This rule will fail when E_{Ko} becomes large enough for the radiative losses to no longer be negligible in comparison with collision losses.

5.11.3 Practical Aspects of Megavoltage X-ray Targets

Traditionally, the requirements for target properties, established during the early days of x-ray technology, were quite straightforward:

1. High atomic number Z to maximize efficiency for x-ray production.
2. High melting point to minimize damage to the target from the electron beam.

Tungsten satisfies both conditions and is thus the material of choice in most x-ray tubes. With the advent of megavoltage linear accelerators (linacs), it seemed prudent to adopt tungsten as the target material in linacs. The approach worked well for linac energies below 15 MV; however, at energies above 15 MV high Z targets did not prove optimal. This was established in the early 1970s with 25 MV linacs that incorporated tungsten target/tungsten flattening filter combinations. A flattening filter is an important component of the clinical x-ray beam forming assembly in linacs and betatrons, producing a flat, clinically useful megavoltage photon beam.

The tungsten target/tungsten flattening filter combination in the 25 MV linac produced an x-ray beam with tissue-penetrating properties that matched betatron beams that were operated at 16 MV. This was a significant energy difference considering the extra cost in building a linac running at 25 MV rather than at 16 MV.

The cause of the discrepancy between the linac beam and the betatron beam was traced to the target/flattening filter design and atomic number in the two machines. By virtue of its design, the betatron uses a thin target that inherently produces a more penetrating photon beam in comparison to linac's thick transmission target. It also used an aluminum flattening filter in comparison to linac's tungsten filter, and aluminum with its low atomic number will soften the megavoltage x-ray beam less than the high atomic number target.

A thin target may be used in betatrons because the target is immersed in a strong magnetic field that engulfs the doughnut and sweeps the transmitted electrons into the doughnut wall before they can strike the flattening filter and produce unwanted off-focus x-rays. In linacs the targets are not immersed in a strong magnetic field so they are of the thick variety to prevent any electrons from traversing the target.

The 25 MV linac beam was thus formed with a thick high Z target and a high Z flattening filter, while the betatron beam was formed with a thin target and a low Z flattening filter. A study of unfiltered linac x-ray beams has shown that a low Z thick target produces the same quality x-ray beam as a thin betatron target at beam energies above 15 MeV. Thus, a conclusion can be made that x-ray targets in this energy range should be made of low atomic number materials to produce the most penetrating photon beams.

- The low Z target recommendation goes against the target high Z requirement for maximizing the x-ray production; however, it turns out that in the megavoltage energy range the x-ray production in the forward direction is actually independent of target atomic number and for practical radiotherapy one uses only photons projected in the forward direction.
- Even though the x-ray yield depends on Z of the target (the higher is Z, the higher is the yield), this yield is stated for the 4π geometry and in radiotherapy one uses only the forward direction for which the yield is essentially independent of Z. It is actually advantageous to have a lower

x-ray yield in regions outside the useful radiotherapy beam, because this lowers the required shielding against leakage radiation produced by the linac.

- The traditional target requirement on a high melting point is not as stringent for high-energy linacs in comparison with diagnostic x-ray tubes. At high photon energies used in radiotherapy, the efficiency for x-ray production is of the order of 10% to 20% rather than below 1% as is the case with diagnostic x-ray tubes. Therefore, the electron beam energy deposition and target cooling are of much less concern in megavoltage linacs as compared to diagnostic range x-ray tubes.

- Since for the same electron kinetic energy (above 15 MeV) the effective energy of the radiation beam in the forward direction is actually larger for low Z targets in comparison with high Z targets, a conclusion can be made that low atomic number targets should be used in high-energy linear accelerators. The practical problem with this stipulation unfortunately is that it is difficult to find a low Z target that also has a high density (i.e., has a relatively short range of electrons) to make it compact for use in linacs. For example, the required target thickness for 25 MeV electrons is 1 cm of lead ($Z = 82$, $\rho = 11.3$ g/cm^{-3}), 0.5 cm of tungsten ($Z = 74$, $\rho = 19.25$ g/cm^{-3}), and 4 cm of aluminum ($Z = 13$, $\rho = 2.7$ g/cm^{-3}). From the atomic number point of view aluminum is an excellent choice of target material, however, its low density precludes its use as a practical target material in high-energy linear accelerators.

- As far as flattening filters are concerned, low atomic number materials are preferable in the range above 15 MV because they cause less beam softening than high atomic number materials; however, similarly to the situation with target materials, space constraints in linac heads limit the practical choices available. Thus, aluminum was a good choice for flattening the betatron beam, since the field size produced by the machine was limited to a 20×20 cm^2 field. Modern linear accelerators, however, must deliver fields up to 40×40 cm^2 at 100 cm from the target and these field sizes cannot be supported by aluminum flattening filters because of the associated required large size of the filter.

- The mass angular scattering power that depends linearly on the atomic number of the flattening filter material, as discussed in Sect. 4.5, also must be considered when the choice of flattening filter material is made.

Čerenkov Radiation in a Nuclear Reactor

The photograph on the next page shows *Čerenkov blue radiation* from the reactor core during operation of a TRIGA Mark II nuclear reactor at Kansas State University (KSU) in Manhattan, Kansas.

The KSU reactor, in operation since 1962, is a swimming pool reactor, so called because it sits near the bottom of a large concrete pool of water. Currently licensed to operate at 250 kW thermal power, it serves as an excellent tool for nuclear research, education and training. It also provides special services, such as nucleosynthesis, neutron activation analysis, neutron radiography and material irradiation.

Nuclear reactors are based on fission chain reactions that are self-sustained by using some of the fission-produced neutrons to induce new fissions. Each fission event liberates energy of the order of 200 MeV that is distributed among the fission fragments, fission neutrons, beta particles from the beta decay of radioactive fission fragments, and gamma rays.

The important components of a reactor core are: reactor fuel, most commonly uranium-235; moderator that slows down to thermal energies the fission-produced fast neutrons; and control rods that very efficiently absorb neutrons. The position of the control rods in the reactor core affects the number of neutrons available to induce fission thereby controlling the fission rate, reactor power, and reactor shut down.

While no particle can exceed the speed of light in vacuum, in a given medium it is quite possible for charged particles to propagate with velocities that are larger than the speed of light in that medium. When a nuclear reactor is in operation, many fission products emit high-energy beta particles (electrons and positrons) and these particles may travel in water surrounding the reactor core at velocities larger than the speed of light in water. Water molecules line up along the path of beta particles, and, as they return to their normal random orientations, energy is released in the form of visible and ultraviolet photons. This type of radiation, produced only when a particle moves faster than speed of light in medium, is called Čerenkov radiation and is named after the Russian scientist who in 1934 was the first to study the phenomenon in depth.

Unlike fluorescence and atomic emission spectra that have characteristic spectral peaks, Čerenkov radiation is continuous and its intensity is proportional to the frequency (inversely proportional to wavelength), resulting in the predominantly blue emission visible to the naked eye and even more emission in the ultraviolet region of the photon spectrum, invisible to the human eye. The Čerenkov effect is analogous to the sonic boom in acoustics when an object exceeds the speed of sound in air.

Photograph: Courtesy of Kansas State University, TRIGA Mark II Nuclear Reactor, Reproduced with Permission.

6 Interactions of Neutrons with Matter

Neutrons, by virtue of their neutrality, are indirectly ionizing radiation exhibiting a quasi-exponential penetration into an absorber and depositing energy in the absorber through a two-step process: (1) energy transfer to heavy charged particles and (2) energy deposition in the absorber through Coulomb interactions of the charged particles with atoms of the absorber. As they penetrate into matter, neutrons may undergo elastic and inelastic scattering as well as nuclear reactions, such as capture, spallation or fission. Two distinct categories of neutrons are of importance in medical physics: *thermal neutrons* used in boron-neutron capture therapy (BNCT) and *fast neutrons* used in external beam radiotherapy.

Several parameters used for describing neutron fields and neutron dose deposition in absorbers are defined and discussed in this chapter. Also discussed are several radiotherapy techniques based on neutron beams, machines for production of neutron beams in radiotherapy, and an efficient source of neutrons for brachytherapy, the californium-252.
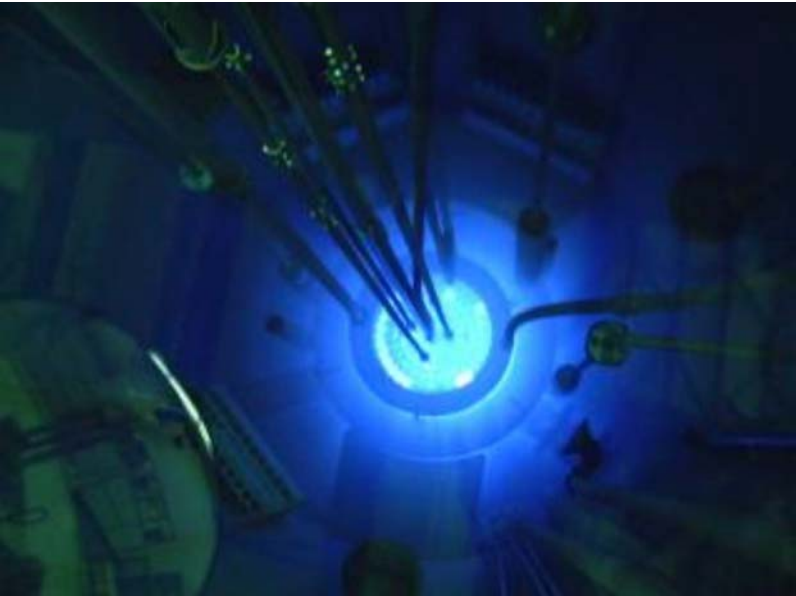
6.1 General Aspects of Neutron Interactions with Absorbers

Neutrons, similarly to photons, may penetrate an absorber without interacting or they may undergo various interactions with the absorber. In contrast to photons, however, neutrons interact mostly with the nuclei of the absorber and have only weak interactions with orbital electrons of the absorber.

Neutron beams, similarly to photon beams, belong to the category of indirectly ionizing radiation beams, both types transferring energy to absorbing medium through an intermediate step in which energy is transferred to a charged particle (protons and heavier nuclei in the case of neutrons; electrons and positrons in the case of photons).

The secondary heavy charged particles released in a medium traversed by neutrons have a very short range in the medium ensuring charged particle equilibrium. Since no bremsstrahlung x rays are generated by the charged particles, the absorbed dose for neutron beams is equal to kerma at any point in the neutron field.

In terms of their kinetic energy E_{K}, neutrons are classified into several categories:

1. *Ultracold neutrons* with $E_{\mathrm{K}} < 2 \times 10^{-7}$ eV
2. *Very cold neutrons* with 2×10^{-7}eV $\leq E_{\mathrm{K}} \leq 5 \times 10^{-5}$ eV
3. *Cold neutrons* with 5×10^{-5} eV $\leq E_{\mathrm{K}} \leq 0.025$ eV
4. *Thermal neutrons* with $E_{\mathrm{K}} \approx 0.025$ eV,
5. *Epithermal neutrons* with 1 eV $< E_{\mathrm{K}} < 1$ keV,
6. *Intermediate neutrons* with 1 keV $< E_{\mathrm{K}} < 0.1$ MeV,
7. *Fast neutrons* with $E_{\mathrm{K}} > 0.1$ MeV.

Note that the velocity of an ultracold neutron with kinetic energy of 2×10^{-7} eV is ~ 6 m/s ($v/c \approx 2 \times 10^{-8}$); of a thermal neutron with kinetic energy of 0.025 eV it is ~ 2200 m/s ($v/c \approx 7 \times 10^{-6}$); and of a fast neutron with kinetic energy of 2.5 MeV it is $\sim 1.4 \times 10^{7}$ m/s ($v/c \approx 0.05$).

There are five principal processes by which neutrons interact with the nuclei of the absorber:

1. *Elastic scattering,*
2. *Inelastic scattering,*
3. *Neutron capture,*
4. *Spallation,*
5. *Fission.*

The probability (cross section) for these different types of interactions varies with the kinetic energy of the neutron and with the properties of the absorber.

6.2 Neutron Interactions with Nuclei of the Absorber

6.2.1 Elastic Scattering

In elastic scattering a neutron collides with a nucleus of mass M that recoils with an angle ϕ with respect to the neutron initial direction of motion, as shown schematically in Fig. 4.2 and discussed in Sect. 4.3. Kinetic energy and momentum are conserved in the interaction.

For a neutron with mass m_n and initial kinetic energy E_{Ki}, the kinetic energy ΔE_K transferred to the nucleus is in general given as (see Sect. 4.3.1)

$$\Delta E_K = E_{Ki} \frac{4m_n M}{(m_n + M)^2} \cos^2 \phi \, . \tag{6.1}$$

The maximum possible energy transfer $(\Delta E_K)_{max}$ is attained in a head-on collision for which $\phi = 180°$ (see Sect. 4.3.1)

$$(\Delta E_K)_{max} = E_{Ki} \frac{4m_n M}{(m_n + M)^2}. \tag{6.2}$$

The average kinetic energy $\overline{\Delta E_K}$ transferred to the recoil nucleus is

$$\overline{\Delta E_K} = \frac{1}{2} E_{Ki} \frac{4m_n M}{(m_n + M)^2} = 2E_{Ki} \frac{m_n M}{(m_n + M)^2} \, . \tag{6.3}$$

The kinetic energy of the scattered neutron, E_{Kf}, in a head-on collision is equal to

$$E_{Kf} = E_{Ki} - (\Delta E_K)_{max} = E_{Ki} \left(\frac{m_n - M}{m_n + M} \right)^2 \, , \tag{6.4}$$

while $\overline{E}_{Kf}$, the average energy attained by the scattered neutron, is

$$\overline{E}_{Kf} = E_{Ki} - \overline{\Delta E_K} = E_{Ki} \frac{m_n^2 + M^2}{(m_n + M)^2} \, . \tag{6.5}$$

Thus, for example, if the target nucleus is hydrogen (nucleus is a proton with mass m_p), then $M = m_p \approx m_n$ and the neutron will transfer on the average one half of its initial kinetic energy to the proton [see (6.5)]. The maximum energy transferred to the proton equals to the initial neutron energy E_{Ki} [see (6.2)]. The recoil proton will then travel a short distance through the absorbing medium and rapidly transfer its kinetic energy to the medium through Coulomb interactions with the nuclei and orbital electrons of the medium.

The transfer of the neutron's energy to the absorbing medium is much less efficient when $m_n \ll M$; the larger is M, the less efficient is the energy transfer, as evident from (6.2).

6.2.2 Inelastic Scattering

In inelastic scattering the neutron n is first captured by the nucleus and then re-emitted with a lower energy and in a direction that is different from the incident neutron direction. The nucleus is left in an excited state and will de-excite by emitting high energy gamma rays. This process is illustrated by the following relationship:

$$n + {}^{A}_{Z}X \rightarrow {}^{A+1}_{Z}Y^* \rightarrow {}^{A}_{Z}X^* + n \;\Rightarrow\; {}^{A}_{Z}X^* \rightarrow {}^{A}_{Z}X + \gamma \,, \tag{6.6}$$
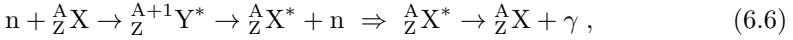
where

$\quad {}^{A}_{Z}X$ is the target nucleus,

$\quad {}^{A+1}_{Z}Y^*$ is an unstable compound nucleus,

$\quad {}^{A}_{Z}X^*$ is an excited target nucleus.

6.2.3 Neutron Capture

Neutron capture is a term used to describe a nuclear reaction in which a thermal neutron bombards a nucleus leading to the emission of a proton or gamma ray. Two of these interactions are of particular importance in tissue: ${}^{14}N(n,p){}^{14}C$ and ${}^{1}H(n,\gamma){}^{2}H$ and one interaction, ${}^{113}Cd(n,\gamma){}^{114}Cd$, is of importance in shielding against thermal neutrons.

A cadmium filter with a thickness of 1 mm absorbs essentially all incident thermal neutrons with energies below 0.5 eV, but readily transmits neutrons with energies exceeding 0.5 eV. The cross section for neutron capture plotted against neutron kinetic energy exhibits a broad resonance with a peak at 0.178 eV. At the resonance peak energy the cross section for neutron capture by natural cadmium (12% abundance of cadmium-113) is 7800 b, while pure cadmium-113 has a cross section of $\sim 64 \times 10^3$ b.

Often neutron bombardment of a stable target is carried out in a nuclear reactor with the intent of producing a radioactive isotope for industrial or medical purposes. When the main interest in the reaction is the end product, the reaction is termed neutron activation. Of interest in medical physics is the neutron activation process in general and in particular when it is used for production of cobalt-60 sources for radiotherapy, iridium-192 sources for brachytherapy, and molybdenum radionuclides for nuclear medicine diagnostic procedures. The neutron activation process is discussed in greater detail in Sect. 8.4.

6.2.4 Spallation

Spallation occurs when a fast neutron n penetrates the nucleus and adds sufficient energy to the nucleus so that it disintegrates into many small residual components such as α particles and protons p. An example of spallation is as follows:

$$ {}^{16}_{8}0 + n \rightarrow 3\alpha + 2p + 3n \,. \tag{6.7}$$

Most of the energy released from the spallation process is carried away by the heavier fragments that deposit their energy in the absorber locally. On the other hand, neutrons and de-excitation gamma rays produced in spallation carry their energy to a remote location.

6.2.5 Fission Induced by Neutron Bombardment

Fission is a particular type of neutron interaction produced by the bombardment of certain very high atomic number nuclei by thermal neutrons. The residual particles are nuclei of lower atomic number and usually more than one fast neutron is produced by the reaction. The discovery of fission is attributed to *Otto Hahn*, *Fritz Strassman*, *Lise Meitner* and *Otto Frisch* in 1939.

Materials that can undergo the fission reaction are called *fissile* or *fissionable materials*. The most important fissionable materials are:

– *Uranium*-235 (0.7% of naturally occurring uranium)
– *Plutonium*-239 produced from uranium-238
– *Uranium*-233 produced from thorium-232

• Uranium-238 and thorium-232 are called *fertile nuclides*; they do not undergo fission themselves; however, they transform into fissionable nuclides upon bombardment with neutrons in a nuclear reactor.
• As fissionable nuclides undergo the fission process, lighter, generally radioactive, nuclides called *fission fragments* are formed. Fission fragments combined with the nuclides subsequently formed through radioactive decay of fission fragments are called *fission products*.

A general equation for fission of uranium-235 is as follows:

$$^{235}_{92}\text{U} + \text{n} \rightarrow ^{236}_{92}\text{U} \rightarrow ^{b}_{a}\text{X} + ^{c}_{d}\text{Y} + f\text{n} , \tag{6.8}$$
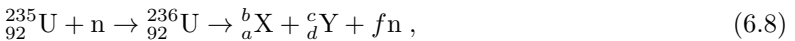
where the nucleus $^{235}_{92}\text{U}$ has been penetrated by a thermal neutron n to produce a compound nucleus $^{236}_{92}\text{U}$. The compound nucleus $^{236}_{92}\text{U}$ is unstable and divides by the fission process into two generally unstable nuclei of smaller atomic number and atomic mass number such that $a+c = 92$ and $b+d+f = 236$, with f the number of fast neutrons produced by the fission process.

Fission reactions always result in the release of a large amount of energy. On the average, the energy released is about 200 MeV per fission of $^{235}_{92}\text{U}$ and the number of new neutrons produced is, on the average, 2.5 per fission.

The new neutrons can be used to produce fission in other uranium-235 nuclei leading to an exponential increase in the number of neutrons and resulting in a *nuclear chain reaction*. The kinetic energy acquired by fission fragments is converted into heat that can be used in nuclear reactors in a controlled fashion for peaceful purposes in electric power generation. Unfortunately, uncontrolled chain reactions can be used for destructive purposes

either directly in atomic bombs or indirectly as detonators of fusion-based hydrogen bombs.

In a nuclear reactor the nuclear chain reactions are controlled in such a way that, following each fission, only one new neutron is used for continuing the chain reaction. The first nuclear reactor was constructed in 1942 in Chicago under the scientific leadership of *Enrico Fermi.* Since then several hundred nuclear reactors have been constructed around the world, mainly for electric power generation but also for research purposes and for production of radionuclides used in industry and medicine.

The principal component of any reactor is the *core* that contains the fissionable fuel, most commonly uranium oxide with uranium-235 enriched to 2–4% in contrast to its natural abundance of 0.7%.

Fission occurs in the nuclear fuel and the fission energy in the form of kinetic energy of fission fragments and new neutrons is rapidly converted into heat. A *coolant* (usually water) is used to maintain a stable temperature in the reactor core. The coolant exits the core either as steam or as hot pressurized water, subsequently used to drive turbines connected to electric power generators. The neutron fluence rate in the reactor core is controlled by movable *control rods* that are made of material with high cross section for absorption of neutrons, such as cadmium or boron compounds.

The fission efficiency is the highest for thermal neutrons, but the new neutrons are produced with relatively large kinetic energies. *Moderators* are used to slow down the new neutrons through elastic scattering events between neutrons and nuclei of the moderator. Water serves as *moderator* material in most reactors; however, some reactors may use the so-called heavy water (D_2O, where D stands for deuterium), graphite or beryllium for the purposes of moderation. Heavy water has a smaller probability for neutron absorption through the (n, γ) reaction than water. Graphite also does not absorb many neutrons and scatters neutrons well. Beryllium is an excellent solid moderator with its low neutron absorption cross section and a high neutron scattering cross section.

6.3 Neutron Kerma

Neutron fields are usually described in terms of fluence $\varphi(E_K)$ rather than energy fluence $\psi(E_K)$ as is usually the case with photon fields. For a monoenergetic neutron beam of fluence φ in cm^{-2} undergoing a specific type of interaction i with a particular atom at a point in medium, the kerma K_i in a small mass m is expressed as

$$K_i = \varphi \, \sigma_i \frac{N}{m} (\overline{\Delta E}_K)_i \tag{6.9}$$

where

φ is the neutron fluence in cm^{-2}

σ_i is the cross section for the particular interaction i,

N is the number of target atoms in mass m with $N/m = N_A/A$,

$(\overline{\Delta E_K})_i$ is the mean energy transferred from neutrons to charged particles through the particular interaction i.

The product $\sigma_i N/m$ summed over all possible neutron interactions is the mass attenuation coefficient μ/ρ for neutrons in the absorbing medium.

Following the convention used for photon beams, we define the mass energy transfer coefficient μ_{tr}/ρ for neutrons as follows:

$$\frac{\mu_{tr}}{\rho} = \frac{\mu}{\rho} \frac{\overline{\Delta E_K}}{E_K} \;, \tag{6.10}$$

where $\overline{\Delta E_K}/E_K$ is the fraction of the neutron energy transferred to charged particles.

The total kerma K accounting for all possible interactions is

$$K = \varphi \; \sigma_i \frac{N}{m} \overline{\Delta E_K} = \varphi \; \frac{\mu}{\rho} \overline{\Delta E_K} = \varphi \frac{\mu_{tr}}{\rho} E_K \;, \tag{6.11}$$

where E_K is the kinetic energy of the monoenergetic neutron beam.

6.4 Neutron Kerma Factor

The product $(\mu_{tr}/\rho)E_K$, defined as the *neutron kerma factor* F_n with units of J $\cdot$ cm^2/g, is tabulated for neutrons instead of the mass energy transfer coefficient. Figure 6.1 provides the neutron kerma factor F_n against neutron kinetic energy for various materials of interest in medical physics (hydrogen, water, tissue, carbon, oxygen, and nitrogen).

For *monoenergetic neutrons* we get the following expression for the neutron kerma K:

$$K = \varphi \; (F_n)_{E_K,Z} \;, \tag{6.12}$$

where

φ is the fluence of monoenergetic neutrons of kinetic energy E_K,

$(F_n)_{E_K,Z}$ is the neutron kerma factor F_n in J $\cdot$ cm^2/g for neutrons of kinetic energy E_K in the irradiated absorber with atomic number Z.

For neutron beams characterized with an *energy spectrum* $\varphi'(E_K)$ of particle fluence, kerma is expressed as follows:

$$K = \int_0^{(E_K)_{max}} \varphi'(E_K)(F_n)_{E_K,Z} dE_K \;, \tag{6.13}$$

where $(E_K)_{max}$ is the maximum neutron kinetic energy in the continuous neutron spectrum with the differential fluence distribution $\varphi'(E_K)$.
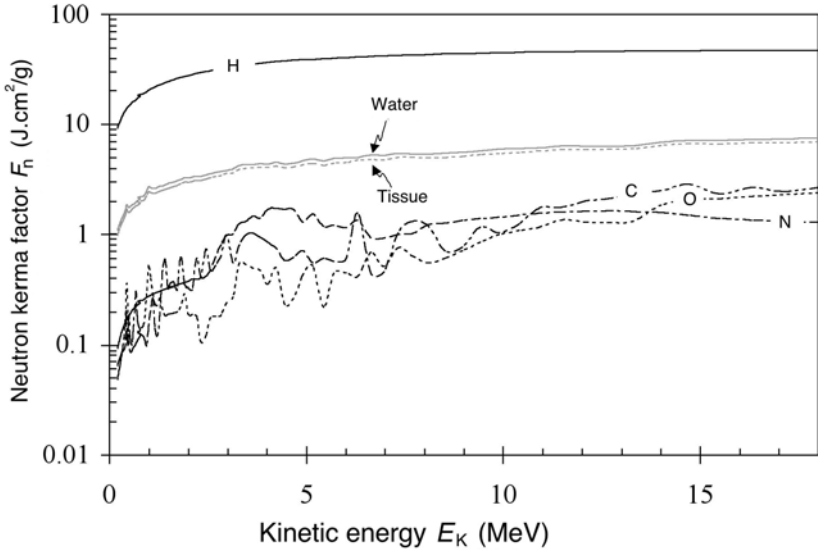
Fig. 6.1. Neuton kerma factor F_n against neutron kinetic energy E_K for various materials of interest in medical physics. Data were obtained from the NIST

An average value for the neutron kerma factor F_n for the spectrum of neutrons $\varphi'(E_\mathrm{K})$ is given as

$$(\overline{F_\mathrm{n}})_{\varphi'(E_\mathrm{K}),\mathrm{Z}} = \frac{K}{\varphi} = \frac{\displaystyle\int_0^{(E_\mathrm{K})_{\max}} \varphi'(E_\mathrm{K})(F_\mathrm{n})_{E_\mathrm{K},\mathrm{Z}}\,dE_\mathrm{K}}{\displaystyle\int_0^{E_{\mathrm{K}_{\max}}} \varphi'(E_\mathrm{K})\,dE_\mathrm{K}}\ . \tag{6.14}$$

6.5 Neutron Dose Deposition in Tissue

By virtue of their neutrality, neutrons, similarly to photons, deposit dose in tissue through a two-step process:

1. Energy transfer to heavy charged particles, such as protons and heavier nuclei in tissue.
2. Energy deposition in tissue by heavy charged particles through Coulomb interactions of the charged particles with atoms of tissue.

Similarly to photons, the nature of neutron interactions with tissue depends on the kinetic energy of neutrons; however, the options available for neutron interactions are not as varied as those for photons (see Chap. 7). For neutrons there are only two kinetic energy ranges to consider:

1. *Thermal neutron energy* of the order of 0.025 eV.
2. *Epithermal*, *intermediate* and *fast neutrons* with kinetic energy >0.025 eV.

6.5.1 Thermal Neutron Interactions in Tissue

Thermal neutrons undergo two possible interactions with nuclei of tissue:

1. *Neutron capture by nitrogen-14* ($^{14}_{7}$N) nucleus that produces carbon-14 ($^{14}_{6}$C) and a proton. The cross section for the $^{14}_{7}$N(n,p)$^{14}_{6}$C reaction is $\sigma_{\text{N}-14} = 1.84$ b/atom.
2. *Neutron capture by hydrogen-1* ($^{1}_{1}$H) nucleus that produces a deuterium nucleus and a γ photon. The cross section for reaction $^{1}_{1}$H(n,γ)$^{2}_{1}$H is $\sigma_{\text{H}-1} = 0.33$ b/atom.

According to the ICRU and the ICRP the human tissue composition in percent by mass is: $\sim 10\%$ for hydrogen-1 and $\sim 3\%$ for nitrogen-14. The data for oxygen-16 and carbon-12, the other two abundant constituents of tissue, are $\sim 75\%$ and $\sim 12\%$, respectively.

The kerma deposited in muscle tissue per unit neutron fluence φ is from (6.9) given as follows:

$$\frac{K}{\varphi} = \sigma \left(\frac{N_\text{t}}{m} \right) \overline{\Delta E}_\text{K} \; , \tag{6.15}$$

where

σ is the thermal neutron cross section for the specific nuclear reaction,
$\overline{\Delta E}_\text{K}$ is the average energy transfer in the nuclear reaction,
(N_t/m) is the number of specific nuclei, such as nitrogen-14 or hydrogen-1, per unit mass of tissue.

Thermal Neutron Capture in Nitrogen-14 in Tissue

The kinetic energy released by thermal neutron capture in nitrogen-14 is determined by calculating the change in total nuclear binding energy between the nitrogen-14 nucleus ($E_\text{B} = 104.66$ MeV) and the carbon-14 nucleus ($E_\text{B} = 105.29$ MeV). Since the total binding energy of carbon-14 exceeds that of nitrogen-14 by 0.63 MeV, we note that the energy released to charged particles in thermal neutron capture by the nitrogen-14 nucleus is 0.63 MeV. This energy is shared as kinetic energy between the proton and the carbon-14 nucleus in the inverse proportion of their masses, since both nuclei carry away the same momenta, but in opposite directions. Thus, the proton receives a kinetic energy of 0.58 MeV; the carbon-14 atom a kinetic energy of 0.05 MeV.

The number of nitrogen-14 atoms per gram of tissue, $(N_\text{t}/m)_{\text{N}-14}$, is determined as follows:

1. 1 gram-atom of N-14 contains N_A atoms of N-14.
2. 1 g of N-14 contains (N_A/A) atoms of N-14, where $A = 14.01$ g/gram-atom.

3. 1 g of tissue contains 0.03 g of N-14 atoms, i.e., $0.03 \times (N_A/A)$ atoms of N-14, therefore $(N_t/m)_{N-14} = 1.3 \times 10^{21}$ atom/g.

The kerma K per unit thermal neutron fluence φ for the $^{14}_{7}$N(n,p)$^{14}_{6}$C reaction is thus equal to

$$\frac{K}{\varphi} = \sigma \left(\frac{N_t}{m}\right)_{N-14} \overline{\Delta E_K}$$

$$= 1.84 \times 10^{-28} \ \frac{m^{-2}}{atom} \times 1.3 \times 10^{21} \frac{atom}{g} \times 0.63 \ MeV$$

$$= 2.4 \times 10^{-17} \ Gy \cdot m^{-2}/neutron. \tag{6.16}$$

Thermal Neutron Capture in Hydrogen-1 in Tissue

Despite a lower cross section for capture in hydrogen compared to nitrogen, thermal neutrons have a much larger probability for being captured by hydrogen than by nitrogen in tissue because in the number of atoms per gram of tissue (concentration) hydrogen surpasses nitrogen with a ratio of ~ 45 to 1.

In the $^1_1$H(n, γ) $^2_1$H reaction a γ photon is produced and the binding energy difference between a proton $E_B = 0$ and deuteron ($E_B = 2.22$ MeV) is 2.22 MeV. Neglecting the recoil energy of the deuteron, we assume that the γ photon receives the complete available energy of 2.22 MeV, i.e., $E_\gamma = 2.22$ MeV.

The number of hydrogen-1 atoms per gram of tissue, $(N_t/m)_{H-1}$ is determined as follows:

1. 1 gram-atom of H-1 contains N_A atoms of H-1.
2. 1 g of H-1 contains (N_A/A) atoms of H-1.
3. 1 g of tissue contains 0.1 g of H-1 atoms, i.e., $0.1 \times (N_A/A)$ atoms of H-1, therefore $(N_t/m)_{H-1} = 6 \times 10^{22}$ atom/g $\approx 45 \times (N_t/m)_{N-14}$.

The energy transfer to γ photons per unit thermal neutron fluence φ and per unit mass of tissue m for the $^1_1$H(n,γ)$^2_1$H nuclear reaction is given as follows, again using (6.9):

$$\frac{E_\gamma}{\varphi m} = \sigma_{H-1} \left(\frac{N_t}{m}\right)_{H-1} \Delta E_\gamma$$

$$= 0.33 \times 10^{-28} \ \frac{m^{-2}}{atom} \times 6 \times 10^{22} \frac{atom}{g} \times 2.22 \ MeV$$

$$= 7 \times 10^{-16} \ J \cdot kg^{-1} \cdot m^{-2}/neutron. \tag{6.17}$$

The result of (6.17) represents the energy per unit neutron fluence and per unit mass of tissue that is transferred to γ photons. The amount of this energy that actually contributes to the kerma in tissue depends on the fraction of this energy that is transferred from the γ photons to electrons in tissue. This fraction depends on the size of the tissue mass: for a small size mass most of the γ photons may escape; for a large mass all photons might be absorbed.

The human body is intermediate in size, so most of the γ photons produced through the ${}_1^1\mathrm{H}(\mathrm{n},\gamma){}_1^2\mathrm{H}$ reaction are absorbed in the body, making the ${}_1^1\mathrm{H}(\mathrm{n},\gamma){}_1^2\mathrm{H}$ reaction the main contributor to kerma and dose delivered to humans from thermal neutrons. The ${}_1^1\mathrm{H}(\mathrm{n},\gamma){}_1^2\mathrm{H}$ reaction also dominates the kerma production in tissue for epithermal neutrons, since the body acts as a moderator for thermalizing the neutrons.

6.5.2 Interactions of Intermediate and Fast Neutrons with Tissue

For neutrons with kinetic energies above 100 eV (upper end epithermal, intermediate and fast neutrons) by far the most important interaction is the elastic scattering with nuclei of tissue, most importantly with hydrogen-1.

As given in Sect. 4.3, the following expressions govern the elastic collisions by two particles:

1. The *kinetic energy transfer* ΔE_K from the neutron with mass m_n to tissue nucleus with mass M, as given in (4.23), is

$$\Delta E_\mathrm{K} = \frac{4 m_\mathrm{n} M}{(m_\mathrm{n} + M)^2} (E_\mathrm{K})_\mathrm{n} \cos^2 \phi \,, \tag{6.18}$$

   where
   $(E_\mathrm{K})_\mathrm{n}$ is the kinetic energy of the incident neutron,
   ϕ is the recoil angle of the target M nucleus.
2. The *maximum kinetic energy transfer* $(\Delta E_\mathrm{K})_\mathrm{max}$, occurs for $\phi = 0$ and is given as

$$(\Delta E_\mathrm{K})_\mathrm{max} = \frac{4 m_\mathrm{n} M}{(m_\mathrm{n} + M)^2} (E_\mathrm{K})_\mathrm{n} \,. \tag{6.19}$$

3. The *average energy transfer* by elastic scattering from a neutron to tissue nucleus M is given as follows:

$$\overline{\Delta E}_\mathrm{K} = \frac{4 m_\mathrm{n} M}{(m_\mathrm{n} + M)^2} (E_\mathrm{K})_\mathrm{n} \overline{\cos^2 \phi}$$

$$= \frac{2 m_\mathrm{n} M}{(m_\mathrm{n} + M)^2} (E_\mathrm{K})_\mathrm{n} = \frac{1}{2} (\Delta E_\mathrm{K})_\mathrm{max} \,. \tag{6.20}$$

The average energy $\overline{\Delta E}_\mathrm{K}$ transferred to recoil nucleus M in tissue in elastic scattering depends on the nuclear mass M and ranges from $0.5(E_\mathrm{K})_\mathrm{n}$ for hydrogen-1; through $0.14(E_\mathrm{K})_\mathrm{n}$ for carbon-12; $0.12(E_\mathrm{K})_\mathrm{n}$ for nitrogen-14, to $0.11(E_\mathrm{K})_\mathrm{n}$ for oxygen-16. Of the possible contributors to energy transfer to nuclei in tissue, hydrogen-1 is the most efficient, since it not only provides the largest number of atoms per tissue mass, it also transfers the largest amount of energy (50%) from the neutron to the scattering nucleus per each elastic scattering event, as shown in Table 6.1.

Table 6.1. Parameters of tissue constituents relevant to neutron absorption and scattering

	Abundance (% by mass)	Abundance $\dfrac{\#atoms}{\text{g of tissue}}$	Abundance (relative to hydrogen)	$\overline{\Delta E_{\mathrm{K}}}$ % of $(E_{\mathrm{K}})_{\mathrm{n}}$
Hydrogen-1	10	6.0×10^{22}	1	50
Carbon-12	75	3.8×10^{22}	0.63	14
Nitrogen-14	3	1.3×10^{21}	0.022	12
Oxygen-16	12	4.5×10^{21}	0.075	11

Table 6.2. Two predominant interactions of neutrons depositing dose in tissue and their regions of predominance

	Reaction	$\overline{\Delta E_{\mathrm{K}}}$ (MeV)	K/φ (Gy per $neutron/\mathrm{m}^2$)
$E_{\mathrm{Kn}} < 100$ eV	$^{14}_{7}\mathrm{N}(\mathrm{n,p})^{14}_{6}\mathrm{C}$	0.63	2.4×10^{-17}
$E_{\mathrm{Kn}} > 100$ eV	$^{1}_{1}\mathrm{H}(\mathrm{n,n'})^{1}_{1}\mathrm{H'}$	$0.5 E_{\mathrm{Kn}}$	$0.5 \sigma_{\mathrm{el}} E_{\mathrm{Kn}}$

4. The dependence of the neutron kerma factor (K/φ, kerma per unit fluence) on neutron energy is essentially split into two regions, one for neutron energy below 100 eV and the other for neutron energy above 100 eV, as summarized in Table 6.2.

6.6 Neutron Beams in Medicine

Of the seven energy categories of neutrons (ultracold, very cold, cold, thermal, epithermal, intermediate and fast, as listed in Sect. 6.1) three categories: thermal, epithermal and fast neutrons are used in radiotherapy; thermal and epithermal neutrons for *boron neutron capture therapy* (BNCT) and fast neutrons for *external beam radiotherapy*.

6.6.1 Boron Neutron Capture Therapy (BNCT)

The BNCT irradiation technique relies on the exceptionally high thermal neutron cross section ($\sigma = 3840$ barn) of the boron-10 nuclide.

Exposed to thermal neutrons, boron-10 undergoes the following nuclear reaction:

$$^{10}_{5}\mathrm{B} + \mathrm{n} \rightarrow {}^{7}_{3}\mathrm{Li} + \alpha + Q(2.79 \text{ MeV}) , \tag{6.21}$$
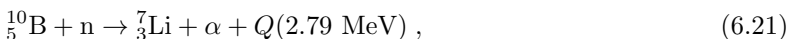
where n represents a thermal neutron, α an alpha particle, and $^{7}_{3}\mathrm{Li}$ the lithium-7 nucleus. The nuclear masses M and binding energies E_{B} for the nuclides of (6.21) are given in Table 6.3 (p. 185).

The Q value for the reaction of (6.21) is calculated either from the nuclear rest energies for the nuclei of (6.21) or from the total binding energies for the nuclei of (6.21) as follows:

$$Q = M(^{10}_5B) \times 931.5 \text{ MeV/u} + M_n c^2 -$$
$$\left\{ M(^7_3Li) + M(\alpha) \right\} \times 931.5 \text{ MeV/u} = 2.79 \text{ MeV} \qquad (6.22)$$

or

$$Q = E_B(^7_3Li) + E_B(\alpha) - E_B(^{10}_5B) = 2.79 \text{ MeV} , \qquad (6.23)$$

where $M_n c^2$ is the neutron rest energy equal to 939.5654 MeV.

Both methods give a reaction Q value of 2.79 MeV that is shared between a gamma photon (0.48 MeV) produced by an excited lithium-7 nucleus and reaction products lithium-7 and the α particle. The 2.31 MeV kinetic energy (2.79 MeV–0.48 MeV) is shared between the two reaction products in the inverse proportion of their masses, i.e., lithium-7 carries away an energy of 0.84 MeV; the α particle 1.47 MeV. The range of these reaction products in tissue is of the order of 6 μm. By virtue of their relatively large masses, both reaction products are densely ionizing particles that can produce significant radiation damage on the cellular level during their short travel through tissue. In addition, the cellular damage produced by these densely ionizing particles depends much less on the presence of oxygen than is the case with standard sparsely ionizing beams, such as x rays, gamma rays, and electrons.

The basic premise behind the BNCT is that if boron-10 can be selectively concentrated in a tumor and the tumor is exposed to thermal neutrons, a higher dose will be delivered to the tumor than to the adjacent normal tissue because the tumor contains the boron-10 nuclide, while the surrounding tissues do not, at least not at the same concentration.

In theory the idea behind the BNCT is logical and simple; however, in practice the technique is still considered in an experimental stage despite more than 50 years that was spent on its development by various research groups. Most attempts with the use of the BNCT are concentrated on treatment of malignant brain tumors, and essentially all practical aspects of dose delivery are wrought with difficulties. The most serious difficulties are:

- Boron-10 is difficult to concentrate in the tumor.
- Thermal neutrons of sufficient fluence rate (of the order of 10^{12} cm^{-2}·s^{-1}) can only be obtained from a nuclear reactor and reactors are not readily available for this kind of purpose.
- Thermal neutrons have very poor penetration into tissue, exhibiting negligible skin sparing and a rapid dose fall-off with depth in tissue (50% dose at ~ 2 cm depth in tissue).
- The thermal neutron beam produced in a nuclear reactor is contaminated with gamma photons and the dosimetry of the mixed neutron/gamma ray fields is problematic.

Despite difficulties there are several research groups around the world working with great enthusiasm on making the BNCT more clinically useful, yet so far the success was limited.

6.6.2 Radiotherapy with Fast Neutron Beams

In contrast to the BNCT, radiotherapy with fast neutrons is quite advanced, practiced in several centers around the world, and accepted as a viable, albeit uncommon, alternative to standard radiotherapy with photon and electron beams. In comparison with photon and electron beams, the main attraction of fast neutron beams is their much lower oxygen enhancement ratio (OER); the main drawback is their significantly more difficult and more expensive means of production.

The OER is defined as the ratio of doses without and with oxygen (hypoxic vs. well-oxygenated cells) to produce the same biological effect. The OER for electrons and photons (sparsely ionizing radiation) is about 2 to 3, while for neutrons (densely ionizing radiation) it is only about 1.5. This means that treatment of anoxic tumors is much less affected by the absence of oxygen than is the standard treatment with photons or electrons.

The depth dose distributions produced in tissue by fast neutron beams exhibit similar characteristics to those of photon beams (see Sect. 1.11 and Fig. 1.2). The dose maximum occurs at a depth beneath the surface and depends on beam energy; the larger is the energy, the larger is the depth of dose maximum and the more penetrating is the neutron beam. The skin sparing effect is present, yet less pronounced than in photon beams of similar penetration.

As a rough comparison one can state that in terms of tissue penetration, a 14 MeV neutron beam is equivalent to a cobalt-60 gamma ray beam and a 70 MeV neutron beam is equivalent to an 8 MV megavoltage x-ray beam.

6.6.3 Machines for Production of Clinical Fast Neutron Beams

Two types of machine are used for production of clinical fast neutron beams:

1. *neutron generator*
2. *cyclotron*

Deuterium-Tritium (DT) Generator

In a neutron DT generator a beam of deuterons (d) is accelerated to a few hundred keV and directed onto a tritium ($_1^3$H) target thereby producing the following nuclear reaction:

$$d + _1^3H \rightarrow _2^4He + n + Q(17.6 \text{ MeV}) . \tag{6.24}$$
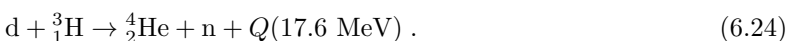
The Q value for the reaction $Q_{\text{d-t}}$ is calculated in the simplest manner by using the binding energies given for the nuclides of (6.24) in Table 6.3. The calculation is as follows:

$$Q_{\text{d-t}} = E_{\text{B}}(\alpha) - \left\{E_{\text{B}}(\text{d}) + E_{\text{B}}(^3_1\text{H})\right\}$$
$$= 28.2957 \text{ MeV} - \{2.2246 + 8.4818\} \text{ MeV} = 17.6 \text{ MeV} . \quad (6.25)$$

The same result can be obtained by accounting for nuclear masses for the nuclei in (6.24) as follows:

$$Q_{\text{d-t}} = \left\{ \left[M(\text{d}) + M(^3_1\text{H})\right] - \left[M(^4_2\text{He}) + M_{\text{n}}\right]\right\} c^2$$
$$= \{[1875.61 + 2808.92] - [3727.38 + 939.56]\} \text{ MeV}$$
$$= 17.6 \text{ MeV}. \quad (6.26)$$

The reaction energy $Q_{\text{d-t}}$ of 17.6 MeV is shared between the neutron n and the α particle in inverse proportions to their masses, resulting in a neutron kinetic energy of 14 MeV. The atomic masses, nuclear masses and binding energies for the nuclides discussed in this chapter are given in Table 6.3 (p. 185).

DT neutron generators are relatively inexpensive; however, they have difficulties producing stable beams of sufficient intensity because of problems with the tritium target. Since at their best, the DT neutron generators produce beams that are only equivalent in penetration to cobalt-60 gamma ray beams and have significantly lower outputs than a standard cobalt unit, they are not serious contenders for delivery of routine radiotherapy treatments.

Fast Neutron Beams from Cyclotrons

Cyclotrons were briefly discussed in Sect. 3.6.2. In addition to their use in production of clinical heavy charged particle beams and in production of radionuclides for use in industry and medicine, they provide very practical means for production of clinical neutron beams.

The most common approach in neutron production with cyclotrons is to accelerate protons (p) or deuterons (d) onto a beryllium target and this results in neutron spectra that are characteristic of the particular nuclear reaction used.

The maximum neutron energy in the spectrum is given as the sum of the incident particle kinetic energy and the reaction Q value for the particular nuclear reaction that produces the neutrons. The two nuclear reactions are as follows:

$$\text{p} + {}^9_4\text{Be} \rightarrow {}^9_5\text{B} + \text{n} + Q(-1.85 \text{ MeV}) \quad (6.27)$$

$$\text{d} + {}^9_4\text{Be} \rightarrow {}^{10}_5\text{B} + \text{n} + Q(4.36 \text{ MeV}) . \quad (6.28)$$
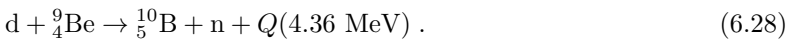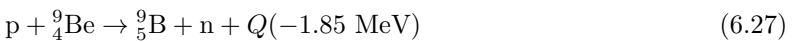
The reaction Q values for the two reactions can be determined either by subtracting the binding energies for the products before the interaction from

those for after the interaction, similarly to the procedure with regard to (6.25) or by subtracting the rest energies for the products after the interaction from the rest energies for before the interaction, similarly to the procedure with regard to (6.26).

6.6.4 Californium-252 Neutron Source

The californium-252 (Cf-252) radionuclide is an efficient neutron source that can be readily encapsulated into portable sealed sources for use in science, industry and medicine. It is commonly produced as a transuranium radionuclide in a nuclear reactor by irradiating a suitable target with a very high neutron fluence rate of the order of 10^{15} cm$^{-1} \cdot$ s^{-1} and was found useful in many areas such as neutron activation analysis, neutron radiography, nuclear reactor start up, and brachytherapy treatment of cancer.

- Cf-252 decays with a half-life of 2.65 y through α decay into curium-248.
- The specific activity of Cf-252 is 2×10^7 Bq/μg (540 Ci/g).
- About 3% of all Cf-252 decays occur through spontaneous fission (see Sect. 8.14) with 3.8 neutrons produced on the average per fission, amounting to a neutron production rate of 2.35×10^6 μg$^{-1} \cdot$ s^{-1}.
- The neutron spectrum emitted by Cf-252 has a Maxwellian energy distribution with an average energy of 2.1 MeV and most probable energy of $\sim$0.7 MeV.

Industrial sources contain up to 50 mg of Cf-252 emitting of the order of 10^{11} neutrons per second. High dose rate (HDR) brachytherapy requires about 500 μg of Cf-252 per source and emits $\sim 10^9$ neutrons per second. Current technology results in source diameters of the order of 3 mm; adequate for intracavitary brachytherapy but not suitable for interstitial brachytherapy. Smaller dimension (miniature) sources are likely to be produced in the near future, making the Cf-252 brachytherapy more practical and more widely available. Standard HDR brachytherapy is carried out with iridium-192 sources that emit a spectrum of gamma rays with an effective energy of ~ 400 keV. The advantage of neutron irradiation is that neutron therapy is significantly more effective than conventional photon therapy in treatment of hypoxic (oxygen deficient) malignant disease.

6.7 Neutron Radiography

X-ray and gamma ray radiography became indispensable imaging tools in medicine, science and industry; however, radiography with more exotic particles such as protons and neutrons is also being developed.

Neutron radiography (NR) is a non-invasive imaging technique similar to the industrial gamma radiography except that instead of x ray or gamma ray transmission through an object, it uses attenuation of a neutron beam in

an object. While the transmission of photons through an absorber is charac-
terized by photon interactions with orbital electrons of the absorber and is
governed by the atomic number, density and thickness of the absorber, the
transmission of neutrons through an absorber is characterized by neutron in-
teractions with the nuclei of the absorber and governed by the neutron cross
sections of the absorber nuclei. In contrast to x rays, neutrons are attenuated
strongly by some low atomic number materials such as hydrogen, lithium,
boron and cadmium but penetrate many high atomic number materials with
relative ease.

Elements with similar atomic numbers will exhibit very similar x-ray at-
tenuation and yet may have markedly different neutron attenuation charac-
teristics. Organic materials and water are clearly visible in neutron radio-
graphs because of their hydrogen content, while many structural materials
such as aluminum and iron or shielding materials such as lead are nearly
transparent.

Neutron radiography can be carried out with neutrons of any energy rang-
ing from cold to fast neutrons, but the results depend strongly on the neutron
cross sections of elements comprising the test object. Most applications of NR
are now found in industry but research in medical use is also carried out. Be-
cause of their large hydrogen content, biological objects can be imaged only
by fast neutrons and, since the equivalent doses required for clinical imaging
are relatively large, the procedure can be justified only for patients undergo-
ing neutron radiotherapy.

Table 6.3. Main attributes of nuclides presented in this chapter. Data are from
the NIST

	Symbol	Z	A	ATOMIC MASS $m(u)$	NUCLEAR MASS Mc^2 (MeV)	BINDING ENERGY E_B (MeV)	Decay mode	E_B (MeV) nucleon	Half-life
Deuterium	D	1	2	2.01410178	1875.612809	2.224579715	-	1.1123	Stable
Tritium	T	1	3	3.01604927	2808.920927	8.481821847	β^-	2.8273	12.3 y
Helium	He	2	3	3.01602931	2808.391338	7.718080337	-	2.5727	Stable
Helium	He	2	4	4.00260325	3727.379086	28.29569225	-	7.0739	Stable
Lithium	Li	3	7	7.016004	6533.832935	39.24459209	-	5.6064	Stable
Beryllium	Be	4	8	8.00530509	7454.850008	56.49954794	-	7.0624	Stable
Beryllium	Be	4	9	9.0121821	8392.749945	58.16497109	-	6.4628	Stable
Boron	B	5	9	9.0133288	8393.30709	56.31449479	-	6.2572	Stable
Boron	B	5	10	10.012937	9324.436174	64.75077116	-	6.4751	Stable

Computerized Tomography Images and Leonardo Da Vinci

The center image on the next page is a famous sketch of a man by *Leonardo Da Vinci* (1452–1519). While other great men and women that humanity produced in arts and science generally excelled in only one specific area of art or science, Leonardo da Vinci was a man of enormous talents covering most areas of human endeavor, whether in arts or science; a truly versatile renaissance man. He was active as sculptor, painter, musician, architect, engineer, inventor, and researcher of human body. Many of Leonardo Da Vinci's drawings of the human body helped doctors understand better the layout of muscle and bone structures within the human body.

The left and right images on the next page are examples of *computerized tomography* (CT) images of the human body, representing the most important development resulting from *Wilhelm Roentgen's* discovery of x rays in 1895. A CT scanner is a machine that uses an x-ray beam rotating about a specific area of a patient to collect x-ray attenuation data for patient's tissues. It then manipulates these data with special mathematical algorithms to display a series of transverse slices through the patient. The transverse CT data can be reconstructed so as to obtain sagittal sections (shown in the right image on the next page) and coronal sections (shown in the left image on the next page) through the patient's organs or to obtain digitally reconstructed radiographs. The excellent resolution obtained with a modern CT scanner provides an extremely versatile "non-invasive" diagnostic tool. CT scanners have been in clinical and industrial use since the early 1970s and evolved through five generations, each generation becoming increasingly more sophisticated and faster.

Three types of detectors are used in CT scanners: (1) scintillation detectors (sodium iodide or calcium fluoride) in conjunction with a photomultiplier tube; (2) gas filled (xenon or krypton) ionization chamber; and (3) semiconductor detectors (cesium iodide) in conjunction with a p–n junction photodiode.

Three-dimensional images can be obtained through three techniques: (1) multiple 2D acquisitions (based on a series of sequential scans); (2) spiral (helical) CT (the x-ray source rotates continuously around the patient while simultaneously the patient is translated through the gantry); and (3) cone-beam CT (a 2D detector array is used in order to measure the entire volume-of-interest during one single orbit of the x-ray source.

Allan Cormack (1924–1998), a South African-American physicist, developed the theoretical foundations that made computerized tomography possible and published his work during 1963–64. His work generated little interest until *Godfrey Hounsfield* (1919–2004), a British electrical engineer, developed a practical model of a CT scanner in the early 1970s. Hounsfield and Cormack received the 1979 Nobel Prize in Psychology and Medicine for their independent invention of the CT scanner.

7 Interactions of Photons with Matter

In this chapter we discuss the various types of photon interactions with absorbing media. Photons are indirectly ionizing radiation and they deposit energy in the absorbing medium through a two-step process: (1) energy transfer to an energetic light charged particle (electron or positron) and (2) energy deposition in medium by the charged particle. Some of the interactions are only of theoretical interest and help in the understanding of the general photon interaction phenomena, others are of great importance in medical physics since they play a fundamental role in imaging, radiotherapy as well as radiation dosimetry. Depending on their energy and the atomic number of the absorber, photons may interact with an absorber atom as a whole, with the nucleus of an absorber atom or with an orbital electron of the absorber atom. The probability of a particular interaction to occur depends on the photon energy as well as on the density and atomic number of the absorber, and is generally expressed in the form of an interaction cross section.

In this chapter we first discuss in detail the individual photon interactions of importance to medical physics and then concentrate on the general aspects of photon interactions with absorbers including the mass energy transfer coefficients and mass energy absorption coefficients for use in radiation dosimetry. Also discussed are the various effects that follow the individual photon interactions.
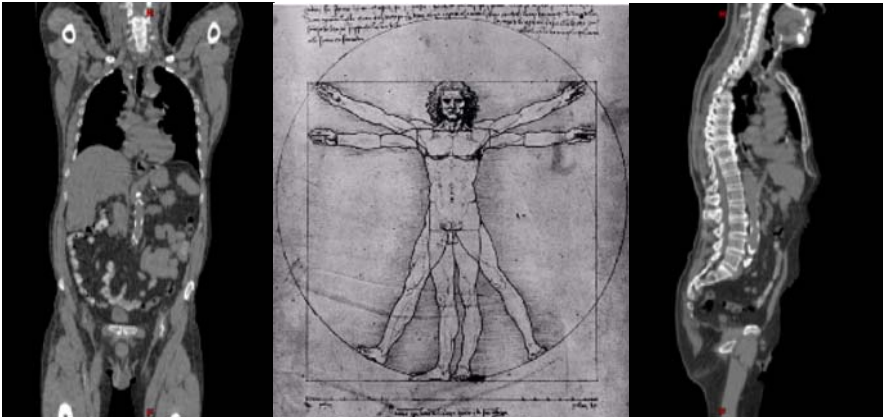
7.1 General Aspects of Photon Interactions
with Absorbers

In penetrating an absorbing medium, photons may experience various inter-actions with the atoms of the medium. These interactions with atoms may involve either the *nuclei* of the absorbing medium or the *orbital electrons* of the absorbing medium.

The interactions with nuclei may be direct *photon-nucleus* interactions (*photodisintegration*) or interactions between the photon and the electrostatic field of the nucleus (*pair production*).

The *photon-orbital electron* interactions are characterized as interactions between the photon and either (i) a loosely bound electron (*Thomson scat-tering, Compton effect, triplet production*) or (ii) a tightly bound electron (*photoelectric effect*).

- A *loosely bound electron* is an electron whose binding energy E_B is small in comparison with the photon energy $h\nu$, i.e., $E_B \ll h\nu$. An interaction between a photon and a loosely bound electron is considered to be an interaction between a photon and a free (unbound) electron.
- A *tightly bound electron* is an electron whose binding energy E_B is compa-rable to, larger than, or slightly smaller than the photon energy $h\nu$. For a photon interaction to occur with a tightly bound electron, the binding en-ergy E_B of the electron must be of the order of, but slightly smaller, than the photon energy, i.e., $E_B \lesssim h\nu$. An interaction between a photon and a tightly bound electron is considered an interaction between a photon and the atom as a whole.

As far as the photon fate after the interaction with an atom is concerned there are two possible outcomes:

1. *Photon disappears* (i.e., is absorbed completely) and a portion of its en-ergy is transferred to light charged particles (electrons and positrons).
2. *Photon is scattered* and two outcomes are possible:
   a) The resulting photon has the same energy as the incident photon and no light charged particle is released in the interaction.
   b) The resulting scattered photon has a lower energy than the incident photon and the energy excess is transferred to a light charged particle (electron).

The light charged particles produced in the absorbing medium through pho-ton interactions will:

1. either deposit their energy to the medium through Coulomb interactions with orbital electrons of the absorbing medium (collision loss also referred to as ionization loss), as discussed in detail in Sect. 5.3.

2. or radiate their kinetic energy away through Coulomb interactions with the nuclei of the absorbing medium (radiative loss), as discussed in detail in Sect. 5.2.

7.2 Thomson Scattering

The scattering of low energy photons ($h\nu \ll m_e c^2$) by loosely bound, i.e., essentially free electrons is described adequately by non-relativistic classical theory of *Joseph J. Thomson.*

Thomson assumed that the incident photon beam sets a quasi-free electron of the atom into a forced resonant oscillation. He then used classical theory to calculate the cross section for the re-emission of the electromagnetic (EM) radiation as a result of induced dipole oscillation of the electrons. This type of photon elastic scattering is now called *Thomson scattering.*

The electric fields $\mathscr{E}_{in}$ for the harmonic incident radiation and $\mathscr{E}_{out}$ for the emitted scattered electromagnetic waves [far field, see (3.5)] are given, respectively, by

$$\mathscr{E}_{in} = \mathscr{E}_o \sin \omega t \tag{7.1}$$

and

$$\mathscr{E}_{out} = \frac{e}{4\pi\varepsilon_o} \frac{\ddot{x} \sin\Theta}{c^2 r} \ , \tag{7.2}$$

where

$\mathscr{E}_o$ is the amplitude of the incident harmonic oscillation,
Θ is the angle between the direction of emission $\vec{r}$ and the polarization vector of the incident wave $\vec{\mathscr{E}}_{in}$,
$\ddot{x}$ is the acceleration of the electron.

The equation of motion for the accelerated electron vibrating about its equilibrium position is

$$m_e \ddot{x} = e\vec{\mathscr{E}} = e\vec{\mathscr{E}}_o \sin\omega t \ . \tag{7.3}$$

Inserting $\ddot{x}$ from the equation of motion for the accelerated electron into (7.2), we get the following expression for $\mathscr{E}_{out}$:

$$\mathscr{E}_{out} = \frac{e^2}{4\pi\varepsilon_o} \frac{\mathscr{E}_o}{m_e c^2} \frac{\sin\omega t \sin\Theta}{r} = r_e \mathscr{E}_o \frac{\sin\omega t \sin\Theta}{r} \ , \tag{7.4}$$

where r_e is the so-called classical radius of the electron ($r_e = 2.818$ fm).

The electronic differential cross section $d_e\sigma_{Th}$ for re-emission of radiation into a solid angle $d\Omega$ is by definition given as follows:

$$d_e\sigma_{Th} = \frac{\bar{S}_{out}}{\bar{S}_{in}}dA = \frac{\bar{S}_{out}}{\bar{S}_{in}}r^2 d\Omega \quad \text{or} \quad \frac{d_e\sigma_{Th}}{d\Omega} = r^2 \frac{\bar{S}_{out}}{\bar{S}_{in}} \ . \tag{7.5}$$

The incident and emitted wave intensities are expressed as follows by the time averages of the corresponding Poynting vectors $\bar{S}_{out}$ and $\bar{S}_{in}$, respectively [see (3.9)]:

$$\bar{S}_{in} = \varepsilon_o c \overline{\mathcal{E}_{in}^2} = \varepsilon_o c \mathcal{E}_o^2 \overline{\sin^2 \omega t} = \frac{1}{2}\varepsilon_o c \mathcal{E}_o^2 \tag{7.6}$$

and

$$\bar{S}_{out} = \varepsilon_o c \overline{\mathcal{E}_{out}^2} = \varepsilon_o c \frac{r_e^2 \mathcal{E}_o^2 \overline{\sin^2 \omega t} \ \overline{\sin^2 \Theta}}{r^2} = \frac{\varepsilon_o c r_e^2 \mathcal{E}_o^2}{2} \frac{\overline{\sin^2 \Theta}}{r^2} \ , \tag{7.7}$$

recognizing that $\overline{\sin^2 \omega t} = \frac{1}{2}$.

Inserting $\bar{S}_{in}$ and $\bar{S}_{out}$ into (7.5) we get the following expression for $d_e\sigma_{Th}/d\Omega$

$$\frac{d_e\sigma_{Th}}{d\Omega} = r_e^2 \overline{\sin^2 \Theta} \ . \tag{7.8}$$

The average value of $\sin^2 \Theta$ for unpolarized radiation may be evaluated using the following relationships:

$$\cos\Theta = \frac{a}{r}; \qquad \sin\theta = \frac{b}{r}; \qquad \text{and} \qquad \cos\psi = \frac{a}{b} \ , \tag{7.9}$$

where the angles θ, Θ and ψ as well as the parameters a and b are defined in Fig. 7.1.

Combining the expressions given in (7.9) we obtain

$$\cos\Theta = \sin\theta \, \cos\psi \ , \tag{7.10}$$

where

θ is the scattering angle defined as the angle between the incident photon and the scattered photon, as shown in Fig. 7.1,

ψ is the polarization angle.

$\overline{\sin^2 \Theta}$ is now determined by integration over the polarization angle ψ from 0 to 2π

$$\overline{\sin^2 \Theta} = \int_0^{2\pi} \sin^2 \Theta \, d\psi \Big/ \int_0^{2\pi} d\psi = \frac{1}{2\pi} \int_0^{2\pi} (1 - \cos^2 \Theta) d\psi$$

$$= 1 - \frac{\sin^2 \theta}{2\pi} \int_0^{2\pi} \cos^2 \psi \, d\psi$$

$$= 1 - \frac{1}{2}\sin^2 \theta = \frac{1}{2}(1 + \cos^2 \theta). \tag{7.11}$$
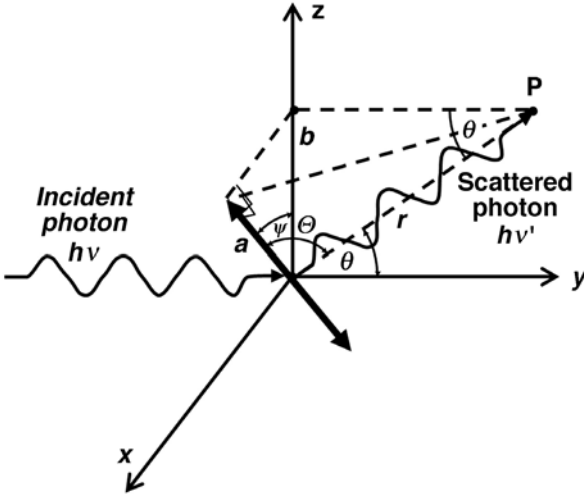
Fig. 7.1. Schematic diagram of Thomson scattering where the incident photon with energy $h\nu$ is scattered and emitted with a scattering angle θ. Note that angles θ and Θ are not coplanar (i.e., they are not in the same plane)

The differential electronic cross section per unit solid angle for Thomson scattering $d_e\sigma_{Th}/d\Omega$ is from (7.8) and (7.11) expressed as follows:

$$\frac{d_e\sigma_{Th}}{d\Omega} = \frac{r_e^2}{2}(1 + \cos^2\theta) \tag{7.12}$$

and drawn in Figs. 7.2 and 7.3 against the scattering angle θ in the range from 0 to π. The graph in Fig. 7.2 is plotted in the Cartesian coordinate system; that in Fig. 7.3 shows the same data in the polar coordinate system. Both graphs show that $d_e\sigma_{Th}/d\Omega$ ranges from 39.7 mb/electron.sterad at $\theta = \pi/2$ to 79.4 mb/electron.sterad for $\theta = 0°$ and $\theta = \pi$.

The differential electronic cross section per unit angle for Thomson scattering $d_e\sigma_{Th}/d\theta$ gives the fraction of the incident energy that is scattered into a cone contained between θ and $\theta + d\theta$. The function, plotted in Fig. 7.4 against the scattering angle θ, is expressed as follows, noting that $d\Omega = 2\pi\sin\theta\,d\theta$:

$$\frac{d_e\sigma_{Th}}{d\theta} = \frac{d_e\sigma_{Th}}{d\Omega}\frac{d\Omega}{d\theta} = 2\pi\sin\theta\frac{d_e\sigma_{Th}}{d\Omega} = \pi r_e^2\sin\theta(1 + \cos^2\theta)\,. \tag{7.13}$$

As shown in Fig. 7.4, $d_e\sigma_{Th}/d\theta$ is zero at $\theta = 0$ and $\theta = 180°$, reaches maxima at $\theta = 55°$ and $\theta = 125°$ and attains a non-zero minimum at $\theta = 90°$. The two maxima and the non-zero minimum are determined after setting $d^2\sigma_{Th}/d\theta^2 = 0$ and solving the result for θ.

The total electronic cross section $_e\sigma_{Th}$ for Thomson scattering is obtained by determining the area under the $d_e\sigma_{Th}/d\theta$ curve of Fig. 7.4 or by integrating
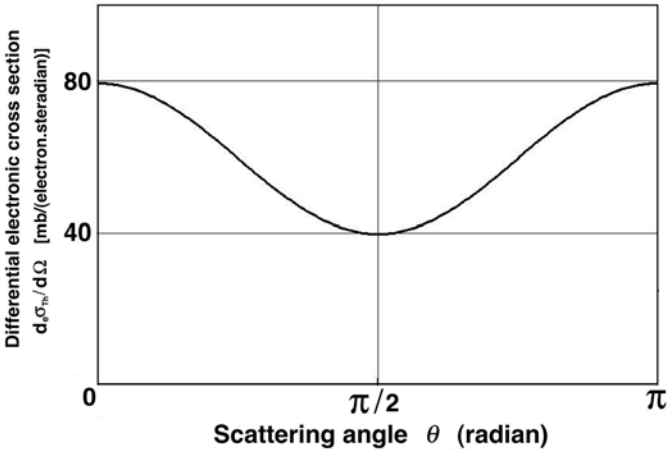
Fig. 7.2. Differential electronic cross section $d_e\sigma_{\mathrm{Th}}/d\Omega$ per unit solid angle plotted against the scattering angle θ for Thomson scattering, as given by (7.12)
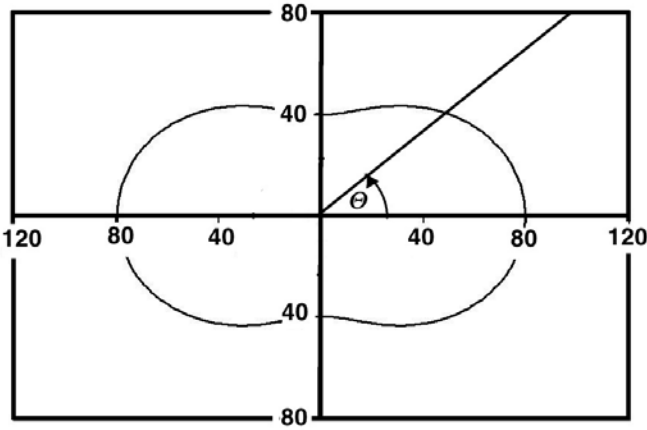
Fig. 7.3. Differential Thomson electronic cross section $d_e\sigma_{\mathrm{Th}}/d\Omega$ per unit solid angle plotted against the scattering angle θ in polar coordinate system. The units shown are mb/electron.steradian

(7.13) over all scattering angles θ from 0 to π to obtain

$$_e\sigma_{\mathrm{Th}} = \int \frac{d_e\sigma_{\mathrm{Th}}}{d\Omega} d\Omega = \frac{r_e^2}{2} \int\limits_0^\pi (1+\cos^2\theta)2\pi\sin\theta\, d\theta$$

$$= \frac{8\pi}{3} r_e^2 = 0.665 \text{ b}. \tag{7.14}$$
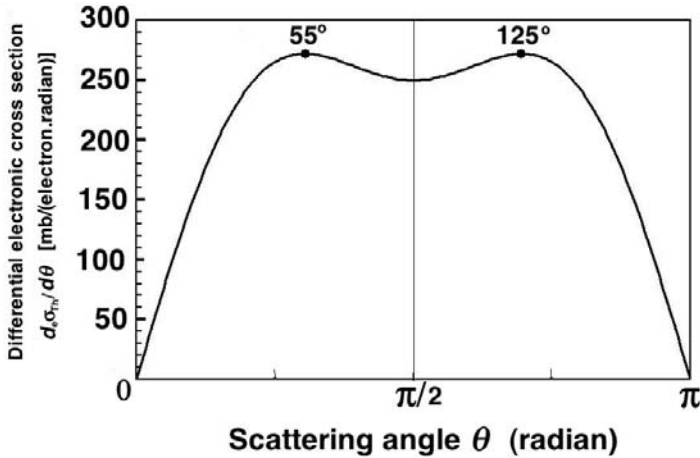
Fig. 7.4. Differential electronic cross section $d_e\sigma_{\mathrm{Th}}/d\theta$ per unit angle θ plotted against the scattering angle θ

This is a noteworthy result in that it contains no energy-dependent terms and predicts no change in energy upon re-emission of the electromagnetic radiation. The cross section $_e\sigma_{\mathrm{Th}}$ is called the Thomson classical cross section for a free electron and has the same value (0.665 b) for all incident photon energies.

The atomic cross section $_a\sigma_{\mathrm{Th}}$ is in terms of the electronic cross section $_e\sigma_{\mathrm{Th}}$ given as follows:

$$_a\sigma_{\mathrm{Th}} = Z\,_e\sigma_{\mathrm{Th}}\;, \tag{7.15}$$

showing a linear dependence upon atomic number Z, as elucidated for low atomic number elements by *Charles Glover Barkla*, an English physicist who received the Nobel Prize in Physics for his discovery of characteristic x rays.

For photon energies $h\nu$ exceeding the electron binding energy but small in comparison with $m_e c^2$, i.e., $E_B \ll h\nu \ll m_e c^2$, the atomic cross section measured at small θ approaches the Thomson's value of (7.15). At larger θ and larger photon energies $(h\nu \rightarrow m_e c^2)$, however, Thomson's classical theory breaks down and the intensity of coherently scattered radiation on free electrons diminishes in favor of incoherently Compton-scattered radiation.

7.3 Compton Scattering (Compton Effect)

An interaction of a photon of energy $h\nu$ with a loosely bound orbital electron of an absorber is called Compton effect (Compton scattering) in honor of *Arthur Compton* who made the first measurements of photon-"*free electron*" scattering in 1922.
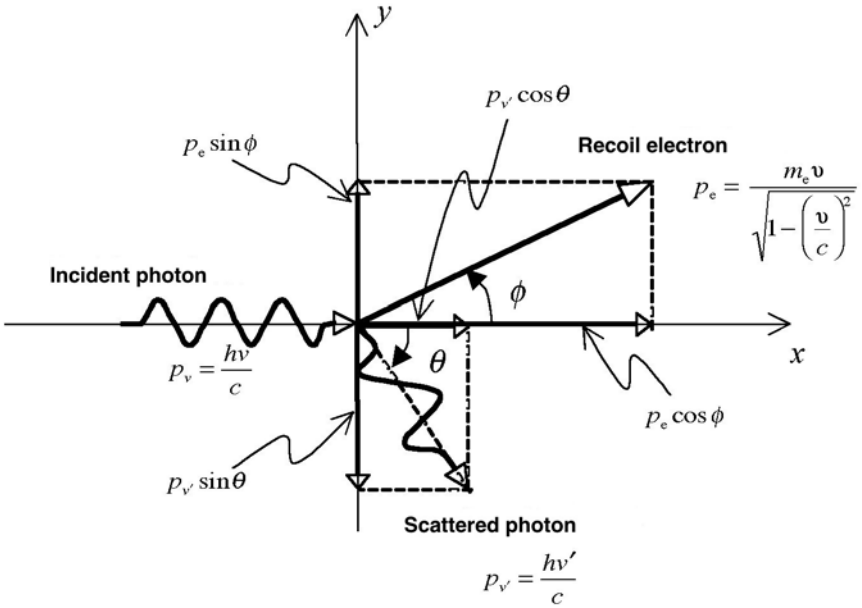
Fig. 7.5. Schematic diagram of the Compton effect. An incident photon with energy $h\nu$ interacts with a stationary and free electron. A photon with energy $h\nu'$ is produced and scattered with a scattering angle $\theta = 60°$. The difference between the incident photon energy $h\nu$ and the scattered photon energy $h\nu'$ is given as kinetic energy to the recoil electron

In theoretical studies of the Compton effect an assumption is made that the photon interacts with a free and stationary electron. A photon, referred to as scattered photon with energy $h\nu'$ that is smaller than the incident photon energy $h\nu$, is produced and an electron, referred to as the Compton (recoil) electron, is ejected from the atom with kinetic energy E_K.

A typical Compton effect interaction is shown schematically in Fig. 7.5 for a 1 MeV photon scattered on a "free" (loosely bound) electron with a scattering angle $\theta = 60°$. The scattering angle θ is the angle between the incident photon direction and the scattered photon direction and can range from $\theta = 0°$ (forward scattering) through $90°$ (side scattering) to $\theta = 180°$ (back scattering). The recoil electron angle ϕ is the angle between the incident photon direction and the direction of the recoil Compton electron.

The corpuscular nature of the photon is assumed and relativistic conservation of total energy and momentum laws are used in the derivation of the well-known Compton wavelength shift relationship

$$\Delta\lambda = \lambda' - \lambda = \lambda_c(1 - \cos\theta) \,, \tag{7.16}$$

where

λ is the wavelength of the incident photon: $\lambda = 2\pi\hbar c/(h\nu)$,
λ' is the wavelength of the scattered photon; $\lambda' = 2\pi\hbar c/(h\nu')$,
$\Delta\lambda$ is the difference between the scattered and incident photon wavelength,
     i.e., $\Delta\lambda = \lambda' - \lambda$,
λ_c is the so-called Compton wavelength of the electron defined as

$$\lambda_c = h/(m_e c) = 2\pi\hbar c/(m_e c^2) = 0.0243 \text{ Å} . \qquad (7.17)$$

The following three relativistic relationships can be written for the conservation of total energy and momentum in a Compton interaction:

1. *Conservation of total energy*

$$h\nu + m_e c^2 = h\nu' + m_e c^2 + E_K \qquad (7.18)$$

   that results in

$$h\nu = h\nu' + E_K . \qquad (7.19)$$

2. *Conservation of momentum* in the direction of the incident photon $h\nu$:
   x axis

$$p_\nu = p_{\nu'} \cos\theta + p_e \cos\phi . \qquad (7.20)$$

3. *Conservation of momentum* in the direction normal to that of the incident
   photon $h\nu$: *y axis*

$$0 = -p_{\nu'} \sin\theta + p_e \sin\phi , \qquad (7.21)$$

   where
   E_K is the kinetic energy of the recoil electron,
   p_ν is the momentum of the incident photon: $p_\nu = h\nu/c$,
   $p_{\nu'}$ is the momentum of the scattered photon: $p_{\nu'} = h\nu'/c$,
   p_e is the momentum of the recoil electron: $p_e = m_e \upsilon/\sqrt{1 - (\upsilon/c)^2}$.

Using the relativistic expression for momentum p of (1.30) in conjunction with the three basic conservation relationships above, one can eliminate any two parameters from the three equations to obtain the Compton wavelength shift equation for $\Delta\lambda$ of (7.16) which in turn leads to relationships for the energy of the scattered photon $h\nu'$ and the energy of the recoil electron E_K as a function of the incident photon energy $h\nu$ and scattering angle θ

$$\Delta\lambda = \lambda' - \lambda = \frac{c}{\nu'} - \frac{c}{\nu} = \frac{h}{m_e c}(1 - \cos\theta) \qquad \text{or}$$
$$\frac{1}{h\nu'} - \frac{1}{h\nu} = \frac{1}{m_e c^2}(1 - \cos\theta) . \qquad (7.22)$$

From (7.22) we obtain the following expressions for $h\nu'$ and E_K, respectively:

$$h\nu' = h\nu \frac{1}{1 + \varepsilon(1 - \cos\theta)} , \qquad (7.23)$$
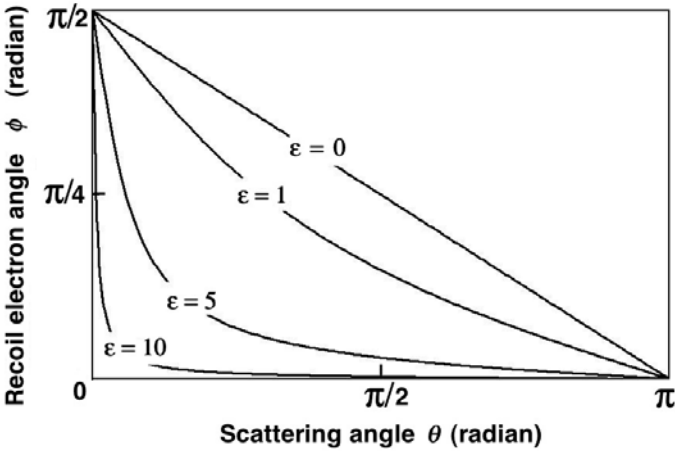
Fig. 7.6. Relationship between the electron recoil angle ϕ and photon scattering angle θ

and

$$E_{\mathrm{K}} = h\nu \frac{\varepsilon(1 - \cos\theta)}{1 + \varepsilon(1 - \cos\theta)} \ , \tag{7.24}$$

where $\varepsilon = h\nu/m_{\mathrm{e}}c^2$ represents the incident photon energy $h\nu$ normalized to the electron rest energy $m_{\mathrm{e}}c^2$.

7.3.1 Relationship Between the Scattering Angle θ and the Recoil Angle ϕ

The scattering angle θ and the recoil electron angle ϕ (see Fig. 7.5) are related as follows:

$$\cot\phi = (1 + \varepsilon)\tan(\theta/2) \ . \tag{7.25}$$

The ϕ vs θ relationship is plotted in Fig. 7.6 for various values of $\varepsilon = h\nu/(m_{\mathrm{e}}c^2)$ showing that for a given θ, the higher is the incident photon energy $h\nu$ or the higher is ε, the smaller is the recoil electron angle ϕ.

Equation (7.25) and Fig. 7.6 also show that the range of the scattering angle θ is from 0 to π, while the corresponding range of the recoil electron angle ϕ is limited from $\pi/2$ to 0, respectively.

7.3.2 Scattered Photon Energy $h\nu'$ as a Function of $h\nu$ and θ

The relationship between $h\nu'$ and $h\nu$ of (7.23) is plotted in Fig. 7.7 for various scattering angles θ between $0°$ (forward scattering) and π (backscattering). The following conclusions can now be made:
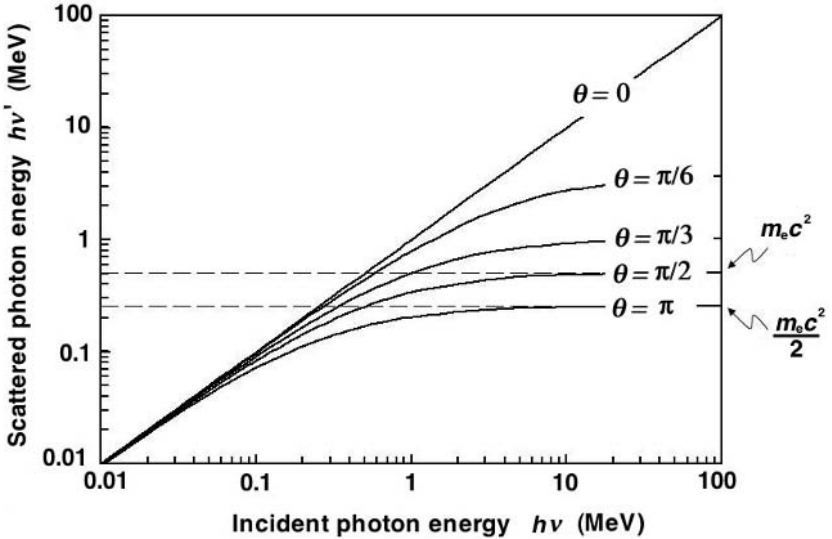
Fig. 7.7. Scattered photon energy $h\nu'$ against the incident photon energy $h\nu$ for various scattering angles θ in the range from $0°$ to$180°$

- For $\theta = 0$, the energy of the scattered photon $h\nu'$ equals the energy of the incident photon $h\nu$, irrespective of $h\nu$. Since in this case no energy is transferred to the electron, we are dealing here with classical Thomson scattering.
- For $\theta > 0$ the energy of the scattered photon saturates at high values of $h\nu$; the larger is the scattering angle θ, the lower is the saturation value of $h\nu'$ for $h\nu \to \infty$.
- For example, the saturation values of $h\nu'$ at $\theta = \frac{\pi}{2}$ and $\theta = \pi$ for $h\nu \to \infty$ are

$$h\nu'_{\mathrm{sat}}(\theta = \frac{\pi}{2}) = \lim_{h\nu \to \infty} \frac{h\nu}{1 + \varepsilon}$$
$$= \lim_{h\nu \to \infty} \frac{h\nu}{1 + \frac{h\nu}{m_e c^2}} = m_e c^2 = 0.511 \text{ MeV} \qquad (7.26)$$

and

$$h\nu'_{\mathrm{sat}}(\theta = \pi) = \lim_{h\nu \to \infty} \frac{h\nu}{1 + 2\varepsilon}$$
$$= \lim_{h\nu \to \infty} \frac{h\nu}{1 + \frac{2h\nu}{m_e c^2}} = \frac{m_e c^2}{2} = 0.255 \text{ MeV}, \qquad (7.27)$$

respectively, as shown in Fig. 7.7. These results show that photons scattered with angles θ larger than $\pi/2$ cannot exceed 511 keV no matter how

high is the incident photon energy $h\nu$. This finding is of great practical importance in design of shielding barriers for linear accelerator installations.

- For a given $h\nu$ the scattered photon energy $h\nu'$ will be in the range between $h\nu/(1 + 2\varepsilon)$ for $\theta = \pi$ and $h\nu$ for $\theta = 0$, i.e.,

$$\left.\frac{h\nu}{1 + 2\varepsilon}\right|_{\theta=\pi} \leq h\nu' \leq h\nu|_{\theta=0} . \tag{7.28}$$

- As shown in (7.22), the Compton shift in wavelength $\Delta\lambda$ is independent of the energy of the incident photon $h\nu$.
- The Compton shift in energy, on the other hand, depends strongly on the incident photon energy $h\nu$. Low-energy photons are scattered with minimal change in energy, while high-energy photons suffer a very large change in energy. The shift in photon energy $h\nu - h\nu'$ is equal to the kinetic energy E_K transferred to the Compton recoil electron.

7.3.3 Energy Transfer to the Compton Recoil Electron

The Compton (recoil) electron gains its kinetic energy E_K from the incident photon of energy $h\nu$, as given in (7.24)

$$E_K = h\nu - h\nu' = h\nu\frac{\varepsilon(1 - \cos\theta)}{1 + \varepsilon(1 - \cos\theta)} . \tag{7.29}$$

The maximum kinetic energy transfer $(E_K)_{\max}$ to recoil electron for a given $h\nu$ occurs at $\theta = \pi$ (photon backscattering) which corresponds to electron recoil angle $\phi = 0$, as shown in Fig. 7.8 with a plot of $(E_K)_{\max}/(h\nu)$ against $h\nu$. The maximum fraction of the incident photon energy $h\nu$ given to the recoil electron, $(E_K)_{\max}/(h\nu)$, is also given in Table 7.1 for photon energies in the range from 0.01 MeV to 100 MeV. In general $(E_K)_{\max}/(h\nu)$ is given as follows:

$$\frac{(E_K)_{\max}}{h\nu} = \frac{E_K(\theta = \pi)}{h\nu} = \frac{2\varepsilon}{1 + 2\varepsilon}. \tag{7.30}$$

The expression of (7.29) can be solved for $h\nu$ after inserting $\varepsilon = h\nu/(m_ec^2)$ to obtain a quadratic equation for $h\nu$ with the following solution:

$$h\nu = \frac{1}{2}(E_K)_{\max}\left\{1 + \sqrt{1 + \frac{2m_ec^2}{(E_K)_{\max}}}\right\} . \tag{7.31}$$

For a given incident photon energy $h\nu$ the kinetic energy E_K of the recoil electron is in the range from 0 at $\theta = 0°$ to $2h\nu\varepsilon/(1 + 2\varepsilon)$ at $\theta = \pi$, i.e.,

$$0 \leq E_K \leq 2h\nu\varepsilon/(1 + 2\varepsilon) = (E_K)_{\max} . \tag{7.32}$$

From the dosimetric point of view, the most important curve given in Fig. 7.8 is the one showing $\overline{E}_K^\sigma/(h\nu)$, the mean fraction of the incident photon energy $h\nu$ transferred to recoil electrons. Data for $\overline{E}_K^\sigma/(h\nu)$ are also given in
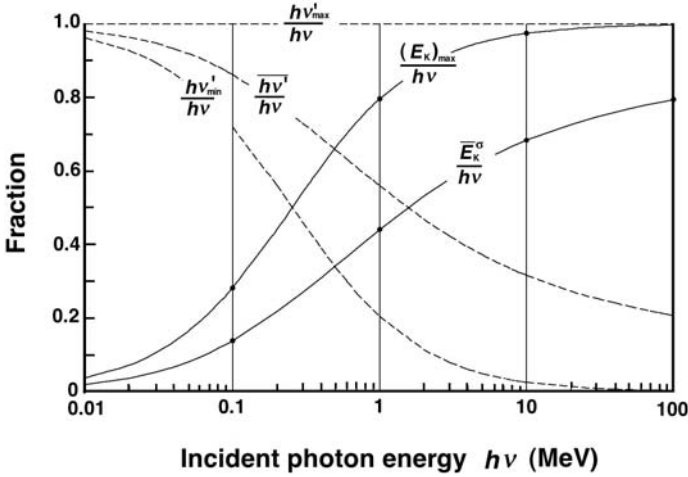
Fig. 7.8. Fraction of incident photon energy $h\nu$ transferred in Compton effect to:
- Maximum energy of recoil electron: $(E_K)_{max}/(h\nu)$; $\theta = \pi$ [see (7.30)]
- Mean energy of recoil electron: $\overline{E}_K^\sigma/(h\nu)$ [see (7.54) below]
- Maximum energy of scattered photon: $h\nu'_{max}/(h\nu)$; $\theta = 0°$ [see (7.33)]
- Mean energy of the scattered photon: $\overline{h\nu'}/(h\nu)$ [see (7.34)]
- Minimum energy of the scattered photon: $h\nu'_{min}/(h\nu)$; $\theta = \pi$ [see (7.35)]

Table 7.1, showing that the fractional energy transfer to recoil electrons is quite low at low photon energies (0.02 at $h\nu = 0.01$ MeV) and then slowly rises to become 0.44 at $h\nu = 1$ MeV and 0.796 at $h\nu = 100$ MeV. The mean fraction $\overline{E}_K^\sigma/(h\nu)$ is discussed further in (7.53) and (7.54) below.

Figure 7.8 and Table 7.1 also show the *maximum*, *mean* and *minimum* fractions ($h\nu'_{max}/h\nu$, $\overline{h\nu'}/h\nu$, $h\nu'_{min}/h\nu$, respectively) of the incident photon energy $h\nu$ given to the scattered photon. The fractions are calculated as follows:

$$\frac{h\nu'_{max}}{h\nu} = \frac{h\nu'|_{\theta=0}}{h\nu} = 1 \ , \tag{7.33}$$

$$\frac{\overline{h\nu'}}{h\nu} = 1 - \frac{\bar{E}_K}{h\nu} \ , \tag{7.34}$$

$$\frac{h\nu'_{min}}{h\nu} = \frac{h\nu'|_{\theta=\pi}}{h\nu} = \frac{1}{1+2\varepsilon} = 1 - \frac{(E_K)_{max}}{h\nu} \ , \tag{7.35}$$

where $\varepsilon = h\nu/(m_e c^2)$.

7.3.4 Differential Cross Section for Compton Scattering $d_e\sigma_c^{KN}/d\Omega$

The probability or cross section for a Compton interaction between a photon and a "free electron" is given by an expression derived by *Oskar Klein* and

Table 7.1. Fractions of the incident phoyton energy transferred through Compton effect to the maximum electron kinetic energy $(E_K)_{max}/(h\nu)$; mean electron kinetic energy $\overline{E}_K^\sigma/(h\nu)$; maximum scatterd photon energy $h\nu'_{max}/(h\nu)$; mean scattered photon energy $\overline{h\nu'}/(h\nu)$; and minimum scattered photon energy $h\nu'_{min}/(h\nu)$

$h\nu$ (MeV)	0.01	0.1	1.0	10.0	100.0
$(E_K^\sigma)_{max}/(h\nu)$	0.04	0.29	0.80	0.95	0.995
$\overline{E}_K^\sigma/(h\nu)$	0.02	0.14	0.44	0.68	0.796
$h\nu'_{max}/(h\nu)$	1.0	1.0	1.0	1.0	1.0
$\overline{h\nu'}/(h\nu)$	0.98	0.86	0.56	0.32	0.21
$h\nu'_{min}/(h\nu)$	0.96	0.71	0.20	0.05	0.005

Yoshio Nishina in 1929. The differential electronic cross section for Compton effect is given as follows:

$$
\begin{aligned}
\frac{d_e\sigma_c^{KN}}{d\Omega} &= \frac{r_e^2}{2}\left(\frac{\nu'}{\nu}\right)^2\left\{\frac{\nu'}{\nu} + \frac{\nu}{\nu'} - \sin^2\theta\right\} \\
&= \frac{r_e^2}{2}(1 + \cos^2\theta)\, F_{KN} = \frac{d_e\sigma_{Th}}{d\Omega}F_{KN}\ ,
\end{aligned} \tag{7.36}
$$

where

$d_e\sigma_c^{KN}/d\Omega$ is the differential Klein-Nishina electronic cross section for the Compton effect,
ν is the frequency of the incident photon,
ν' is the frequency of the scattered photon,
θ is the scattering angle,
r_e is the classical radius of the electron (2.82 fm),
F_{KN} is the Klein-Nishina form factor,
$d_e\sigma_{Th}/d\Omega$ is the differential cross section for Thomson scattering.

The Klein-Nishina form factor F_{KN} for a free electron is given as follows:

$$
F_{KN} = \frac{1}{[1 + \varepsilon(1 - \cos\theta)]^2}\left\{1 + \frac{\varepsilon^2(1 - \cos\theta)^2}{[1 + \varepsilon(1 - \cos\theta)](1 + \cos^2\theta)}\right\}, \tag{7.37}
$$

where again $\varepsilon = h\nu/(m_ec^2)$.

The Klein-Nishina form factor F_{KN} is plotted in Fig. 7.9 against the scattering angle θ for various values of the energy parameter ε. For $\varepsilon = 0$ the form factor is 1 irrespective of the scattering angle θ.

As shown in (7.37) and in Fig. 7.9, the form factor F_{KN} is a complicated function of the scattering angle θ and parameter ε. However, it is easy to show that:
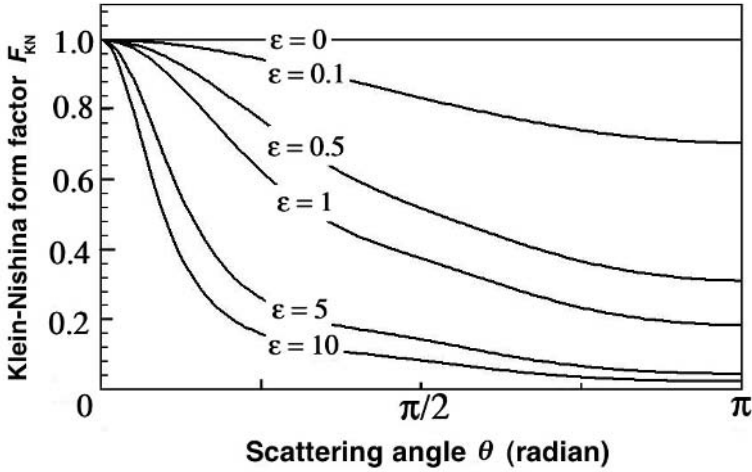
Fig. 7.9. Atomic form factor for Compton effect F_{KN} against scattering angle θ

- $F_{KN} \leq 1$ for all θ and ε.   (7.38)
- $F_{KN} = 1$ for $\theta = 0$ at any ε.   (7.39)
- $F_{KN} = 1$ for $\varepsilon = 0$ at any θ (Thomson scattering).   (7.40)

The differential electronic cross section for the Compton effect $d_e\sigma_c^{KN}/d\Omega$ when $F_{KN} = 1$ is equal to the Thomson electronic differential cross section $d_e\sigma_{Th}/d\Omega$ given in (7.12)

$$\frac{d_e\sigma_c^{KN}}{d\Omega}\Big|_{F_{KN}=1} = \frac{d_e\sigma_{Th}}{d\Omega} = \frac{r_e^2}{2}\left(1 + \cos^2\theta\right) . \tag{7.41}$$

The differential Compton electronic cross section $d_e\sigma_c^{KN}/d\Omega$ is given in Fig. 7.10 against the scattering angle θ for various values of ε ranging from $\varepsilon \approx 0$ which results in $F_{KN} = 1$ for all θ, (i.e., Thomson scattering) to $\varepsilon = 10$ for which the F_{KN} causes a significant deviation from the Thomson electronic cross section for all angles θ except for $\theta = 0$.

The data of Fig. 7.10 are replotted in Fig. 7.11 in a polar coordinate system that gives a better illustration of the Compton scattering phenomenon.

- At low ε the probabilities for forward scattering and back scattering are equal and amount to 79.4 mb (Thomson scattering).
- As the energy $h\nu$ increases the probability for back scattering decreases and the probability for forward scattering remains constant at 79.4 mb.
- The polar diagram of Fig. 7.11 is sometimes colloquially referred to as the "peanut diagram" to help students remember its shape.

At low incident photon energies (Thomson limit) the probabilities for forward scattering and back scattering are equal and twice as large as the probability
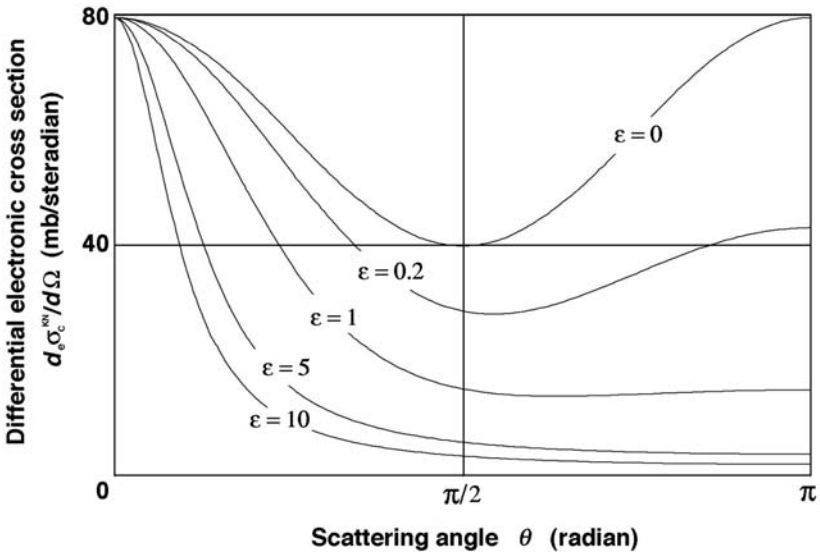
Fig. 7.10. Differential electronic cross section for Compton effect $d_e\sigma_c^{KN}/d\Omega$ against scattering angle θ for various values of $\varepsilon = h\nu/(m_ec^2)$, as given by (7.36). The differential electronic cross section for Compton effect $d_e\sigma_c^{KN}/d\Omega$ for $\varepsilon = 0$ is equal to the differential electronic cross section for Thomson scattering $d_e\sigma_{Th}/d\Omega$ (see Fig. 7.2)
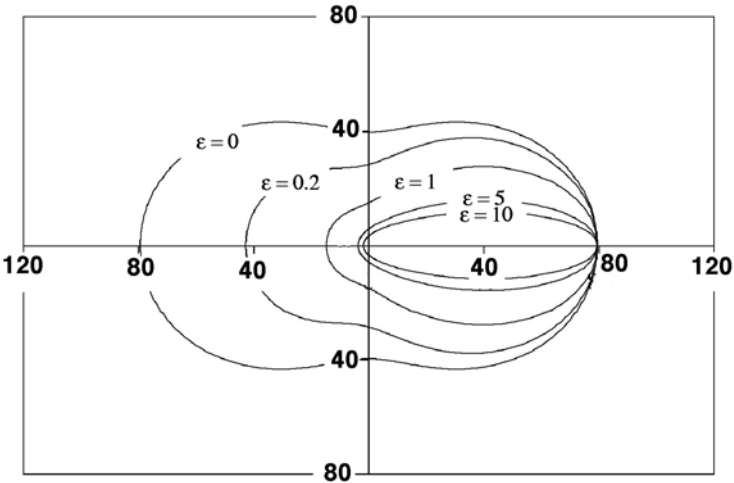
Fig. 7.11. Polar representation of the angular dependence of the differential electronic cross section $d_e\sigma_c^{KN}/d\Omega$ for Compton scattering, as given by (7.36) and plotted for various values of $\varepsilon = h\nu/(m_ec^2)$. The differential electronic cross section for Compton effect $d_e\sigma_c^{KN}/d\Omega$ for $\varepsilon = 0$ is equal to the differential electronic cross section for Thomson scattering $d_e\sigma_{Th}/d\Omega$ (see Fig. 7.3)

for side scattering. As the incident photon energy, i.e., ε, increases, the scattering becomes increasingly more forward peaked and backscattering rapidly diminishes.

7.3.5 Differential Energy Transfer Cross Section $(d_e\sigma_c^{KN})_{tr}/d\Omega$

The differential energy transfer coefficient $(d_e\sigma_c^{KN})_{tr}/d\Omega$ for the Compton effect is determined from the differential electronic cross section $d_e\sigma_c/d\Omega$ given in (7.36) as follows:

$$\frac{(d_e\sigma_c^{KN})_{tr}}{d\Omega} = \frac{d_e\sigma_c^{KN}}{d\Omega}\frac{\overline{E}_K}{h\nu} = \frac{r_e^2}{2}\left(\frac{\nu'}{\nu}\right)^2\left\{\frac{\nu'}{\nu}+\frac{\nu}{\nu'}-\sin^2\theta\right\}\left(\frac{\nu-\nu'}{\nu}\right)$$

$$= \frac{d_e\sigma_{Th}}{d\Omega}F_{KN}\frac{\overline{E}_K^\sigma}{h\nu} = \frac{r_e^2}{2}(1+\cos^2\theta)\frac{\varepsilon(1-\cos\theta)}{[1+\varepsilon(1-\cos\theta)]^3}$$

$$\left\{1+\frac{\varepsilon^2(1-\cos\theta)^2}{[1+\varepsilon(1-\cos\theta)](1+\cos^2\theta)}\right\}\frac{\overline{E}_K^\sigma}{h\nu}, \quad (7.42)$$

where $\overline{E}_K^\sigma/(h\nu)$ is given in Fig. 7.8 and in Table 7.1 for incident photon energies in the range $0.01\text{ MeV} \le h\nu \le 100\text{ MeV}$.

7.3.6 Energy Distribution of Recoil Electrons $d_e\sigma_c^{KN}/dE_K$

The differential electronic Klein-Nishina cross section $d_e\sigma_c^{KN}/dE_K$ expressing the initial energy spectrum of Compton recoil electrons averaged over all scattering angles θ is calculated from the general Klein-Nishina relationship for $d_e\sigma_c^{KN}/d\Omega$ as follows:

$$\frac{d_e\sigma_c^{KN}(E_K)}{dE_K} = \frac{d_e\sigma_c^{KN}}{d\Omega}\frac{d\Omega}{d\theta}\frac{d\theta}{dE_K} =$$

$$= \frac{\pi r_e^2}{\varepsilon h\nu}\left\{2-\frac{2E_K}{\varepsilon(h\nu-E_K)}+\frac{E_K^2}{\varepsilon^2(h\nu-E_K)^2}+\frac{E_K^2}{h\nu(h\nu-E_K)}\right\},$$

$$(7.43)$$

where

$d_e\sigma_c^{KN}/d\Omega$ is given in (7.36),
$d\Omega/d\theta$ is $2\pi\sin\theta$,
$d\theta/dE_K$ is $(dE_K/d\theta)^{-1}$ with $E_K(\theta)$ given in (7.29).

The differential electronic cross section $d_e\sigma_c^{KN}/dE_K$ is plotted in Fig. 7.12 against the kinetic energy E_K of the recoil electron for various values of the incident photon energy $h\nu$. The following features can now be recognized:

- The distribution of kinetic energies given to the Compton recoil electrons is essentially flat from zero almost up to the maximum electron kinetic energy $(E_K)_{max}$ where a higher concentration occurs.
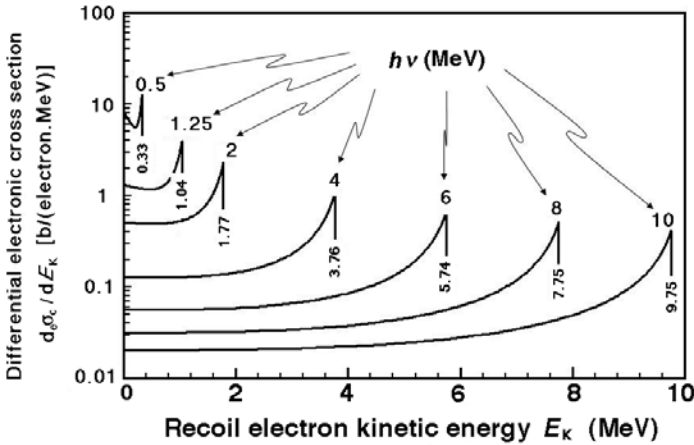
Fig. 7.12. Differential electronic Klein-Nishina cross section per unit kinetic energy $d_e\sigma_c^{KN}/dE_K$ calculated from (7.43) and plotted against the kinetic energy of the Compton recoil electron E_K for various incident photon energies $h\nu$. For a given photon energy the maximum kinetic energy of the recoil electron, calculated from (7.44), is indicated on the graph

- $(E_K)_{max}$ is calculated from

$$(E_K)_{max} = 2h\nu\varepsilon/(1 + 2\varepsilon) = h\nu - h\nu'_{min} , \qquad (7.44)$$

as given by (7.30). Since, as shown in (7.27), $h\nu'_{min}$ approaches $m_ec^2/2$ for high $h\nu$, we note that $(E_K)_{max}$ approaches $h\nu - (m_ec^2/2)$.

7.3.7 Total Electronic Klein-Nishina Cross Section for Compton Scattering $_e\sigma_c^{KN}$

The total cross section for the Compton scattering on a free electron $_e\sigma_c^{KN}$ is calculated by integrating the differential cross section $d_e\sigma_c^{KN}/d\Omega$ of (7.36) over the whole solid angle

$$\begin{aligned}
_e\sigma_c^{KN} &= \int \frac{d_e\sigma_c^{KN}}{d\Omega}d\Omega \\
&= 2\pi r_e^2 \left\{ \frac{1+\varepsilon}{\varepsilon^2} \left[\frac{2(1+\varepsilon)}{1+2\varepsilon} - \frac{\ln(1+2\varepsilon)}{\varepsilon} \right] + \frac{\ln(1+2\varepsilon)}{2\varepsilon} - \frac{1+3\varepsilon}{(1+2\varepsilon)^2} \right\}.
\end{aligned}$$
$$(7.45)$$

The numerical value of $_e\sigma_c^{KN}$ can also be obtained through a determination of the area under the $d_e\sigma_c^{KN}/d\theta$ curve for a given ε. For $\varepsilon = 0$ the area is equal to the Thomson result of 0.665 b [see (7.14)].

Two extreme cases are of special interest, since they simplify the expression for $_e\sigma_c^{KN}$:
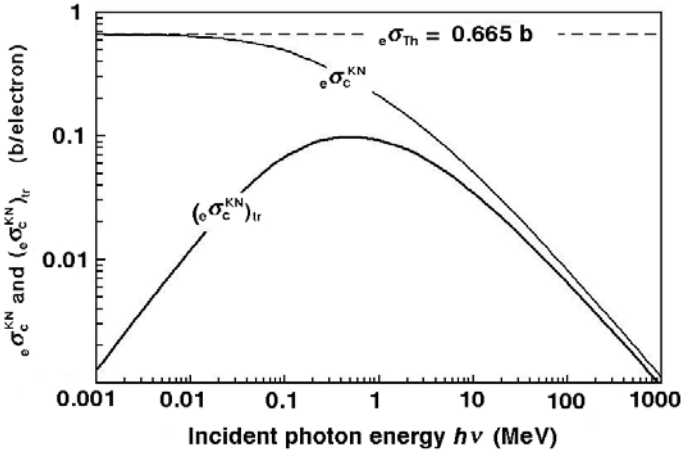
Fig. 7.13. Compton electronic cross section $_e\sigma_c^{KN}$ and electronic energy transfer cross section $(_e\sigma_c^{KN})_{tr}$ for a free electron against incident photon energy $h\nu$ in the energy range from 0.001 MeV to 1000 MeV, determined from Klein-Nishina Eqs. (7.45) and (7.51), respectively. For very low photon energies $_e\sigma_c^{KN} = {}_e\sigma_{Th} = 0.665$ b

- For small incident photon energies $h\nu$ we get the following relationship:

$$_e\sigma_c^{KN} = \frac{8\pi}{3}r_e^2(1 - 2\varepsilon + \frac{26}{5}\varepsilon^2 - \frac{133}{10}\varepsilon^3 + \frac{1144}{35}\varepsilon^4 - \ldots) , \quad (7.46)$$

which for $\varepsilon \to 0$ approaches the classical Thomson result of (7.14), i.e.,

$$_e\sigma_c^{KN}\big|_{\varepsilon \to 0} \approx {}_e\sigma_{Th} = \frac{8\pi}{3}r_e^2 = 0.665 \text{ b} . \quad (7.47)$$

- For very large incident photon energies $h\nu$, i.e., $\varepsilon \gg 1$, we get

$$_e\sigma_c^{KN} \approx \pi r_e^2 \frac{1 + 2\ln\varepsilon}{2\varepsilon} . \quad (7.48)$$

Figure 7.13 shows the Compton electronic cross section $_e\sigma_c^{KN}$ as determined by the Klein-Nishina relationship of (7.45) against the incident photon energy $h\nu$ in the energy range from 0.001 MeV to 1000 MeV. The following features can be identified:

- At low photon energies $_e\sigma_c^{KN}$ is approximately equal to the classical Thomson cross section $_e\sigma_{Th}$ which, with its value of 0.665 b, is independent of photon energy.
- For intermediate photon energies $_e\sigma_c^{KN}$ decreases gradually with photon energy to read 0.46 b at $h\nu = 0.1$ MeV, 0.21 b at $h\nu = 1$ MeV, 0.05 b at $h\nu = 10$ MeV, and 0.08 b at $h\nu = 100$ MeV.
- At very high photon energies $h\nu$, the Compton electronic cross section $_e\sigma_c^{KN}$ attains $1/(h\nu)$ dependence, as shown in (7.48).

- The Compton electronic cross section $_e\sigma_c^{KN}$ is independent of atomic number Z of the absorber, since in the Compton theory the electron is assumed free and stationary, i.e., the electron's binding energy to the atom is assumed to be negligible.

The Compton atomic cross section $_a\sigma_c^{KN}$ is determined from the electronic cross section of (7.45) using the standard relationship

$$_a\sigma_c^{KN} = Z \, _e\sigma_c^{KN} \, , \tag{7.49}$$

where Z is the atomic number of the absorber.

The Compton mass attenuation coefficient σ_c^{KN}/ρ is given as follows:

$$\frac{\sigma_c^{KN}}{\rho} = \frac{N_A}{A} \, _a\sigma_c^{KN} = \frac{ZN_A}{A} \, _e\sigma_c^{KN} \approx \frac{1}{2} N_A \, _e\sigma_c^{KN} \, . \tag{7.50}$$

The atomic Compton cross section (attenuation coefficient) $_a\sigma_c^{KN}$ is linearly proportional to Z, while the Compton mass attenuation coefficient σ_c^{KN}/ρ is essentially independent of Z insofar as Z/A is independent of Z. In reality Z/A ranges from 1 for hydrogen, to 0.5 for low atomic number elements down to 0.4 for high Z, allowing us to make the approximation $Z/A \approx 0.5$.

7.3.8 Energy Transfer Cross Section for Compton Effect $(_e\sigma_c^{KN})_{tr}$

The electronic energy transfer cross section $(_e\sigma_c^{KN})_{tr}$ is obtained by integrating the differential energy cross section $d(_e\sigma_c^{KN})_{tr}/d\Omega$ of (7.42) over all photon scattering angles θ from $0°$ to $180°$ to get

$$(_e\sigma_c^{KN})_{tr} =$$

$$2\pi r_e^2 \left\{ \frac{2(1+\varepsilon)^2}{\varepsilon^2(1+2\varepsilon)} - \frac{1+3\varepsilon}{(1+2\varepsilon)^2} - \right.$$
$$\left. - \frac{(1+\varepsilon)(2\varepsilon^2 - 2\varepsilon - 1)}{\varepsilon^2(1+2\varepsilon)^2} - \frac{4\varepsilon^2}{3(1+2\varepsilon)^3} - \left[\frac{1+\varepsilon}{\varepsilon^3} - \frac{1}{2\varepsilon} + \frac{1}{2\varepsilon^3} \right] \ln(1+2\varepsilon) \right\} \, . \tag{7.51}$$

In addition to the Compton electronic cross section $_e\sigma_c^{KN}$, Fig. 7.13 also shows the energy transfer cross section for the Compton effect $(_e\sigma_c^{KN})_{tr}$ calculated with (7.51) and plotted against the incident photon energy $h\nu$ in the energy range from 0.001 MeV to 1000 MeV.

Since $(_e\sigma_c^{KN})_{tr}$ and $_e\sigma_c^{KN}$ are related through the following relationship:

$$(_e\sigma_c^{KN})_{tr} = {}_e\sigma_c^{KN} \overline{E}_{tr}^\sigma/(h\nu) \, , \tag{7.52}$$

where $\overline{E}_{tr}^\sigma/h\nu$ is the mean fraction of the incident photon energy transferred to the kinetic energy of the Compton recoil electron, we can calculate

$\overline{E}_{\mathrm{K}}^{\sigma}/h\nu$ as

$$\frac{\overline{E}_{\mathrm{K}}^{\sigma}}{h\nu} = \frac{({}_{\mathrm{e}}\sigma_{\mathrm{c}}^{\mathrm{KN}})_{\mathrm{tr}}}{{}_{\mathrm{e}}\sigma_{\mathrm{c}}^{\mathrm{KN}}} \ , \tag{7.53}$$

with $({}_{\mathrm{e}}\sigma_{\mathrm{c}}^{\mathrm{KN}})_{\mathrm{tr}}$ and ${}_{\mathrm{e}}\sigma_{\mathrm{c}}^{\mathrm{KN}}$ given in (7.51) and (7.45), respectively.

Inserting (7.45) and (7.51) into (7.53) gives the following result for the mean fraction of the incident photon energy transferred to the kinetic energy of the recoil electron in Compton effect $\overline{E}_{\mathrm{K}}^{\sigma}/h\nu$:

$$\frac{\overline{E}_{\mathrm{K}}^{\sigma}}{h\nu} =$$

$$\frac{\left\{ \frac{2(1+\varepsilon)^2}{\varepsilon^2(1+2\varepsilon)} - \frac{1+3\varepsilon}{(1+2\varepsilon)^2} - \frac{(1+\varepsilon)(2\varepsilon^2-2\varepsilon-1)}{\varepsilon^2(1+2\varepsilon)^2} - \frac{4\varepsilon^2}{3(1+2\varepsilon)^3} - \left[\frac{1+\varepsilon}{\varepsilon^3} - \frac{1}{2\varepsilon} + \frac{1}{2\varepsilon^3}\right] \ln(1+2\varepsilon) \right\}}{\left\{ \frac{1+\varepsilon}{\varepsilon^2}\left[\frac{2(1+\varepsilon)}{1+2\varepsilon} - \frac{\ln(1+2\varepsilon)}{\varepsilon}\right] + \frac{\ln(1+2\varepsilon)}{2\varepsilon} - \frac{1+3\varepsilon}{(1+2\varepsilon)^2} \right\}} \ . \tag{7.54}$$

At first glance (7.54) looks very cumbersome; however, it is simple to use once the appropriate value for ε at a given photon energy $h\nu$ has been established. For example, an incident photon of energy $h\nu = 1.02$ MeV results in $\varepsilon = 2$ that, when inserted into (7.54), gives $\overline{E}_{\mathrm{K}}^{\sigma}/(h\nu) = 0.440$ or $\overline{E}_{\mathrm{K}}^{\sigma} = 0.440$ MeV. The energy of the corresponding scattered photon is $h\nu' = h\nu - \overline{E}_{\mathrm{K}}^{\sigma} = 0.660$ MeV.

$\overline{E}_{\mathrm{K}}^{\sigma}/(h\nu)$ is plotted in Fig. 7.8 (the "Compton Graph") in the incident photon energy $h\nu$ range between 0.01 MeV and 100 MeV. Table 7.1 gives several values of $\overline{E}_{\mathrm{K}}^{\sigma}/(h\nu)$ in the same energy range.

The plot of $\overline{E}_{\mathrm{K}}^{\sigma}/(h\nu)$ against incident photon energy $h\nu$ of Fig. 7.8 shows that when low energy photons interact in a Compton process, very little energy is transferred to recoil electrons and most energy goes to the scattered photon. On the other hand, when high energy photons ($h\nu > 10$ MeV) interact in a Compton process, most of the incident photon energy is given to the recoil electron and very little is given to the scattered photon.

7.3.9 Binding Energy Effects and Corrections

The Compton electronic cross section ${}_{\mathrm{e}}\sigma_{\mathrm{c}}^{\mathrm{KN}}$ and energy transfer coefficient $({}_{\mathrm{e}}\sigma_{\mathrm{c}}^{\mathrm{KN}})_{\mathrm{tr}}$ were calculated with Klein-Nishina relationships for free electrons and are plotted in Fig. 7.13 with solid curves. At very low incident photon energies the assumption of free electrons breaks down and the electronic binding energy E_{B} affects the Compton atomic cross sections; the closer is the photon energy $h\nu$ to E_{B}, the larger is the deviation of the atomic cross section ${}_{\mathrm{a}}\sigma_{\mathrm{c}}$ from the calculated free-electron Klein-Nishina cross sections ${}_{\mathrm{e}}\sigma_{\mathrm{c}}^{\mathrm{KN}}$.

This discrepancy is evident from Fig. 7.14 that displays, for various absorbers ranging from hydrogen to lead, the atomic cross sections ${}_{\mathrm{a}}\sigma_{\mathrm{c}}$ (solid curves) and the calculated Klein-Nishina atomic cross sections ${}_{\mathrm{a}}\sigma_{\mathrm{c}}^{\mathrm{KN}}$. Note that ${}_{\mathrm{a}}\sigma_{\mathrm{c}}^{\mathrm{KN}} = Z \, {}_{\mathrm{e}}\sigma_{\mathrm{c}}^{\mathrm{KN}}$, where ${}_{\mathrm{e}}\sigma_{\mathrm{c}}^{\mathrm{KN}}$ is calculated with (7.45). It is also shown
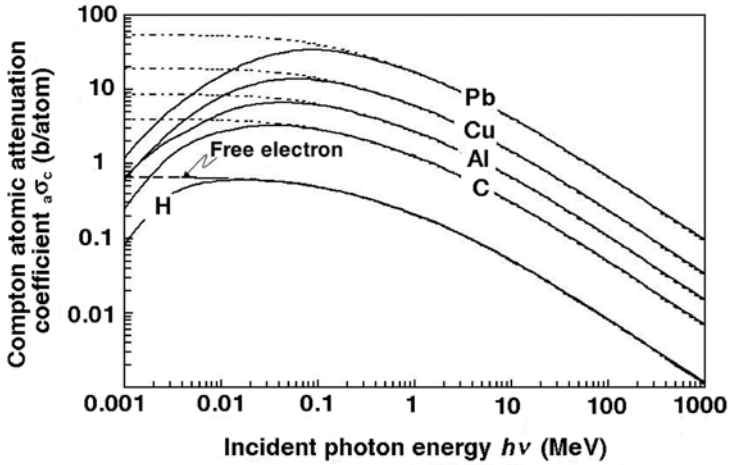
Fig. 7.14. Compton atomic cross sections $_a\sigma_c$ plotted against incident photon energy $h\nu$ for various absorbers, ranging from hydrogen to lead. The *dotted curves* represent $_a\sigma_c^{KN}$ data calculated with Klein-Nishina free-electron relationships; the *solid curves* represent the $_a\sigma_c$ data that incorporate the binding effects of the orbital electrons. The *dashed curve* represents the Klein-Nishina free electron coefficients $_e\sigma_c^{KN}$ for the Compton effect

in Fig. 7.14 that at low incident photon energies $h\nu$, the larger is the atomic number Z of the absorber, the more pronounced is the discrepancy and the higher is the energy at which $_a\sigma_c$ and $_a\sigma_c^{KN}$ begin to coincide.

Various theories have been developed to account for electronic binding energy effects on Compton atomic cross sections. Most notable is the method developed by *John Hubbell* from the National Institute for Science and Technology (NIST) in Washington, USA, who treated the binding energy corrections to the Klein-Nishina relationships in the impulse approximation taking into account all orbital electrons of the absorber atom. This involves applying a multiplicative correction function $S(x, Z)$, referred to as the *incoherent scattering function*, to the Klein-Nishina atomic cross sections as follows:

$$\frac{d_a\sigma_c}{d\Omega} = \frac{d_a\sigma_c^{KN}}{d\Omega} S(x, Z) , \tag{7.55}$$

where x, the *momentum transfer variable*, stands for $\sin(\theta/2)/\lambda$.

The total Compton atomic cross section $_a\sigma_c$ is obtained from the following integral:

$$_a\sigma_c = \int_{\theta=0}^{\theta=\pi} S(x, Z) \, d_e\sigma_c^{KN}(\theta) , \tag{7.56}$$
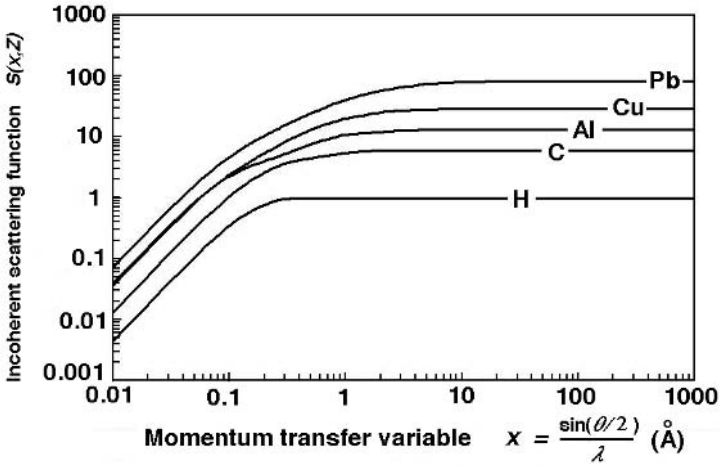
Fig. 7.15. Incoherent scattering function $S(x, Z)$ plotted against the momentum transfer variable x for various absorbers in the range from hydrogen to lead

where the incoherent scattering function $S(x, Z)$ relates to the properties of the absorber atom and is important for collisions in which the electron momentum p_e is small enough so that the electron has a finite probability for not escaping from the atom.

From Fig. 7.5, in conjunction with the application of the law of cosines on the triangle $(\vec{p}_\nu, \vec{p}_{\nu'}, \vec{p}_e)$, we obtain the following relationship for p_e^2:

$$p_e^2 = p_\nu^2 + p_{\nu'}^2 - 2p_\nu p_{\nu'} \cos\theta \tag{7.57}$$

or

$$p_e = \sqrt{\left(\frac{h\nu}{c}\right)^2 + \left(\frac{h\nu'}{c}\right)^2 - 2\frac{h\nu}{c}\frac{h\nu'}{c}\cos\theta} \,. \tag{7.58}$$

For small $h\nu$ we know that $h\nu' \approx h\nu$ (see Fig. 7.7) and p_e of (7.58) is approximated as follows:

$$p_e \approx \frac{h\nu}{c}\sqrt{2(1 - \cos\theta)} = \frac{h\nu}{c}\sqrt{4\sin^2\frac{\theta}{2}} = 2h\frac{\sin\frac{\theta}{2}}{\lambda} = 2hx \,, \tag{7.59}$$

where $x = (\sin\theta/2)/\lambda$ is defined as the *momentum transfer variable* with λ the wavelength of the incident photon.

Hubbell also compiled extensive tables of the incoherent scattering function $S(x, Z)$. Figure 7.15 presents Hubbell's data for $S(x, Z)$ plotted against $x = \sin(\theta/2)/\lambda$ for several absorbers in the range from hydrogen to lead. The figure shows that $S(x, Z)$ saturates at Z for relatively large values of x; the higher is Z, the larger is x at which the saturation sets in. With decreasing

x, the function $S(x, Z)$ decreases and attains at $x = 0.01$ a value that is less than 1% of its saturation Z value. The following features can be recognized:

- The electron binding correction is effective only when $S(x, Z) < Z$.
- For $S(x, Z) = Z$ there is no correction and the Klein-Nishina coefficients $_e\sigma_c^{KN}$ provide correct values for the atomic cross sections $_a\sigma_c$ through the simple relationship $_a\sigma_c = Z(_e\sigma_c^{KN})$.
- The binding energy correction is only important at photon energies of the order of E_B, and this occurs in the photon energy region where photoeffect and Rayleigh scattering are much more probable than the Compton effect. Thus, ignoring the binding correction on Compton cross sections will not adversely affect the determination of the total cross section for photon interactions at relatively low photon energies, since, at these low energies, effects other than the Compton effect make a much larger contribution to the total attenuation coefficient than does the Compton effect.

The effects of binding energy corrections on Klein-Nishina differential atomic cross sections per unit angle $d_a\sigma_c^{KN}/d\theta$ are shown in Fig. 7.16 for various incident photon energies in the range from 1 keV to 10 MeV, for hydrogen in part (a), carbon in part (b), and lead in part (c). The data points are for Klein-Nishina expressions $d_a\sigma_c^{KN}/d\theta = Z\, d_e\sigma_c^{KN}/d\theta$, the solid curves represent the Klein-Nishina results corrected with the incoherent scattering function $S(x, Z)$, i.e., $d_a\sigma_c/d\theta = S(x, Z)\, d_e\sigma_c^{KN}/d\theta$.

The following conclusions may be made from Fig. 7.16:

- For a given absorber Z, the binding energy correction is more significant at lower photon energies. For example, in lead the uncorrected and corrected 1 keV curves differ considerably, the 10 keV curves differ less, the 0.1 MeV curves even less, while the 1 MeV and 10 MeV curves are identical.
- For a given photon energy $h\nu$, the binding energy correction is more significant at higher atomic numbers Z. For example, the uncorrected and corrected 0.1 MeV curves in hydrogen are identical, for carbon they are almost identical, and for lead they are significantly different.

7.3.10 Mass Attenuation Coefficient for Compton Effect

The Compton mass attenuation coefficient σ_c/ρ is calculated from the Compton atomic cross section $_a\sigma_c$ with the standard relationship as follows:

$$\frac{\sigma_c}{\rho} = \frac{N_A}{A}\,_a\sigma_c \ . \tag{7.60}$$

In the energy region not affected by electron binding effects the following relationships hold:

$$_a\sigma_c = Z(_e\sigma_c^{KN}) \tag{7.61}$$
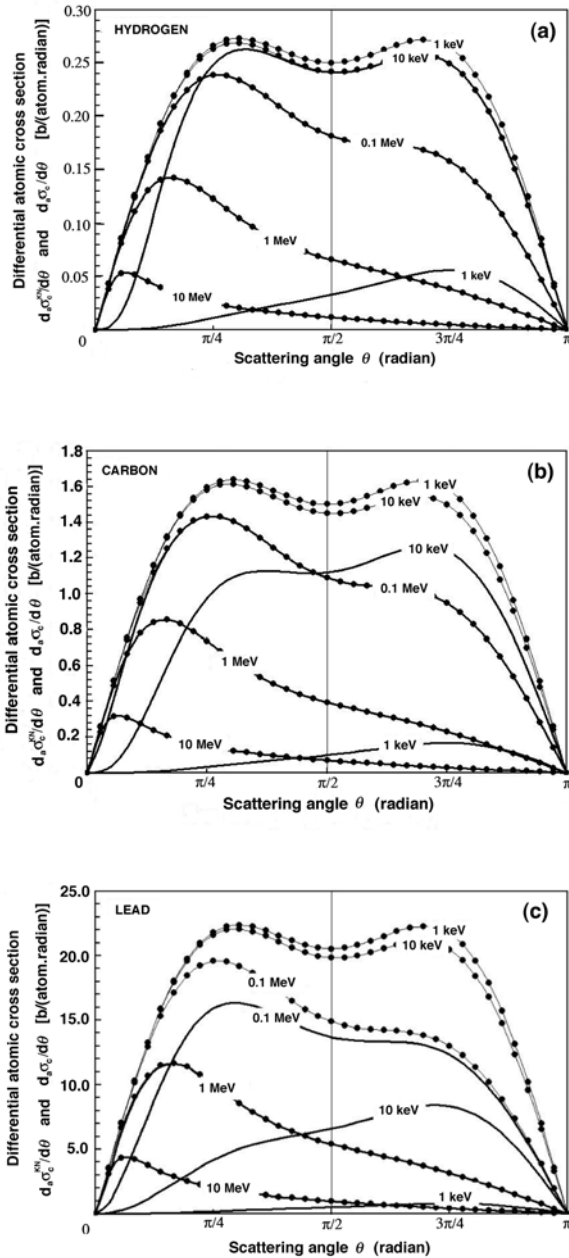
Fig. 7.16. Differential atomic cross-section per unit angle for Compton effect, $d_a\sigma_c/d\theta$, against scattering angle θ for hydrogen in part **a**, carbon in part **b**, and lead in part **c**. The *dotted curves (data points)* are for Klein-Nishina data, the *solid lines* represent the Klein-Nishina data corrected with the incoherent scattering function $S(x, Z)$

and

$$\frac{\sigma_c}{\rho} = \frac{ZN_A}{A} {}_e\sigma_c^{KN} \approx \frac{N_A}{2} {}_e\sigma_c^{KN}, \tag{7.62}$$

where Z and A are the atomic number and atomic mass, respectively, of the absorber and their ratio Z/A is of the order of 0.5.

The following conclusions may now be drawn from (7.62):

1. Since ${}_e\sigma_c^{KN}$ is given for free electrons, it is independent of Z. This makes ${}_a\sigma_c$ linearly dependent on Z.
2. Since $Z/A \approx 0.5$ for all elements with the exception of hydrogen for which $Z/A = 1$, σ_c/ρ is essentially independent of Z. In reality, as often stated before, $Z/A = 0.5$ for low atomic number absorbers but with increasing Z the ratio Z/A gradually falls to $Z/A = 0.4$ for high atomic number absorbers.

Since the Compton atomic coefficient ${}_a\sigma_c$ is linearly proportional to the atomic number Z of the absorber, as shown in (7.61), the mass attenuation coefficient σ_c/ρ is essentially independent of Z, as shown in (7.62), insofar as Z/A is considered independent of Z.

Tables 7.2 and 7.3 list the Compton atomic cross section ${}_a\sigma_c$ and mass attenuation coefficient σ_c/ρ, respectively, for 10 keV and 1 MeV photons interacting with various absorbers in the range from hydrogen to lead. Columns (5) display the atomic cross sections ${}_a\sigma_c$ incorporating binding energy corrections, while columns (6) display the Klein-Nishina atomic cross sections ${}_a\sigma_c^{KN} = Z({}_e\sigma_c^{KN})$. The two coefficients (${}_a\sigma_c$ and ${}_a\sigma_c^{KN}$) agree well for the photon energy of 1 MeV; however, the discrepancy between the two is significant for the photon energy of 10 keV, as also shown in Fig. 7.14.

We also note that at $h\nu = 1$ MeV, the σ_c/ρ values follow straight from the Klein-Nishina electronic cross sections and are affected only by the specific value for Z/A. This is not the case for σ_c/ρ at 10 keV that are affected not only by Z/A but also by the electronic binding effects that are significant in this energy range for all Z; the larger is Z, the larger is the binding effect, as shown in columns (5) and (6) of Table 7.2.

7.3.11 Compton Mass Energy Transfer Coefficient

The Compton mass energy transfer coefficient $(\sigma_c/\rho)_{tr}$ is calculated from the mass attenuation coefficient σ_c/ρ using the standard relationship

$$\left(\frac{\sigma_c}{\rho}\right)_{tr} = \frac{\sigma_c}{\rho}\frac{\overline{E}_K^\sigma}{h\nu}, \tag{7.63}$$

where $\overline{E}_K^\sigma$ is the average energy transferred to the kinetic energy of recoil electrons in the Compton effect. $\overline{E}_K^\sigma$ is given by (7.54) and in Table 7.1. It is plotted as "*The Compton Graph*" in Fig. 7.8. $\overline{E}_K^\sigma/(h\nu)$ is the average fraction of the incident photon energy that is transferred to the recoil (Compton)

Table 7.2. Compton atomic cross sections $_a\sigma_c$ and mass attenuation coefficients σ_c/ρ at photon energy of 10 keV for various absorbers

(1) Element	(2) Symbol	(3) Atomic number Z	(4) Atomic mass A	(5) (a) $_a\sigma_c$ (b/atom)	(6) (b) $Z\,_e\sigma_c^{KN}$ (b/atom)	(7) (c) σ_c/ρ (cm^2/g)
Hydrogen	H	1	1.008	0.60	0.64	0.0358
Carbon	C	6	12.01	2.70	3.84	0.0135
Aluminum	Aℓ	13	26.98	4.74	8.33	0.0106
Copper	Cu	29	63.54	8.15	18.57	0.0176
Tin	Sn	50	118.69	12.00	32.03	0.0607
Lead	Pb	82	207.2	15.60	52.52	0.0153

(a) Data are from the NIST

(b) $_e\sigma_c^{KN}(h\nu = 10 \text{ keV}) = 0.6405 \times 10^{-24}$ cm^2/electron $= 0.6405$ b/electron

(c) $\dfrac{\sigma_c}{\rho} = \dfrac{N_A}{A}\,_a\sigma_c = \dfrac{ZN_A}{A}\,_e\sigma_c^{KN} \approx \dfrac{N_A}{2}\,_e\sigma_c^{KN} = 0.193$ cm^2/g   (7.64)

Table 7.3. Compton atomic cross sections $_a\sigma_c$ and mass attenuation coefficients σ_c/ρ at photon energy of 1 MeV for various absorbers

(1) Element	(2) Symbol	(3) Atomic number Z	(4) Atomic mass A	(5) (a) $_a\sigma_c$ (b/atom)	(6) (b) $Z\,_e\sigma_c^{KN}$ (b/atom)	(7) (c) σ_c/ρ (cm^2/g)
Hydrogen	H	1	1.008	0.211	0.211	0.1261
Carbon	C	6	12.01	1.27	1.27	0.0636
Aluminum	Aℓ	13	26.98	2.75	2.75	0.0613
Copper	Cu	29	63.54	6.12	6.12	0.0580
Tin	Sn	50	118.69	10.5	10.56	0.0534
Lead	Pb	82	207.2	17.19	17.32	0.0500

(a) Data are from the NIST

(b) $_e\sigma_c^{KN}(h\nu = 1 \text{ MeV}) = 0.2112 \times 10^{-24}$ cm^2/electron $= 0.2112$ b/electron

(c) $\dfrac{\sigma_c}{\rho} = \dfrac{N_A}{A}\,_a\sigma_c = \dfrac{ZN_A}{A}\,_e\sigma_c^{KN} \approx \dfrac{N_A}{2}\,_e\sigma_c^{KN} = 0.0636$ cm^2/g   (7.65)

electron. As shown in Fig. 7.8, this average fraction increases with increasing energy from a low value of 0.01 at 10 keV, through 0.44 at 1 MeV, to reach a value of 0.8 at 100 MeV.

- For low incident photon energies $(\sigma_c/\rho)_{tr} \ll \sigma/\rho$.
- For high incident photon energies $(\sigma_c/\rho)_{tr} \approx \sigma/\rho$.

Figure 7.17 shows the $_a\sigma_c$ and $_a\sigma_c^{KN}$ data for lead from Fig. 7.14 and in addition, it also shows the binding energy effect on the Compton atomic energy transfer coefficients of lead by displaying $(_a\sigma_c)_{tr}$ and $(_a\sigma_c^{KN})_{tr}$ both obtained by multiplying the $_a\sigma_c$ and $_a\sigma_c^{KN}$ data, respectively, with the appropriate
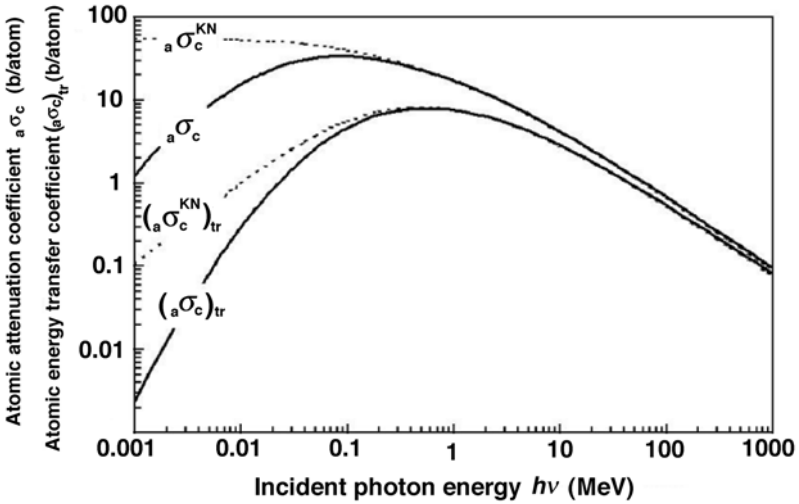
Fig. 7.17. The Compton atomic cross section for lead of Fig. 7.14 and the Compton atomic energy transfer coefficients for lead; *dashed curves* are Klein-Nishina data for free unbound electrons; *solid curves* are data incorporating electronic binding effects. Data are from the NIST

average kinetic energy transferred to the recoil electron given by (7.54) and plotted in Fig. 7.8.

7.4 Rayleigh Scattering

Rayleigh scattering is a photon interaction process in which photons are scattered by bound atomic electrons. The atom is neither excited nor ionized and after the interaction the bound electrons revert to their original state. The atom as a whole absorbs the transferred momentum but its recoil energy is very small and the incident photon scattered with scattering angle θ has essentially the same energy as the original photon. The scattering angles are relatively small because the recoil imparted to the atom must not produce atomic excitation or ionization.

The Rayleigh scattering is named after the physicist *John W. Rayleigh* who in 1900 developed a classical theory for scattering of electromagnetic radiation by atoms. The effect occurs mostly at low photon energies $h\nu$ and for high atomic number Z of the absorber, in the energy region where electron binding effects severely diminish the Compton Klein-Nishina cross sections. As a result of a coherent contribution of all atomic electrons to the Rayleigh (i.e., coherent) atomic cross section, the Rayleigh cross section exceeds the Compton cross section in this energy region.

7.4.1 Differential Atomic Cross Sections for Rayleigh Scattering

The differential Rayleigh atomic cross section $d_a\sigma_R/d\Omega$ per *unit solid angle* is given as follows:

$$\frac{d_a\sigma_R}{d\Omega} = \frac{d_e\sigma_{Th}}{d\Omega}\left\{F(x,Z)\right\}^2 = \frac{r_e^2}{2}(1+\cos^2\theta)\left\{F(x,Z)\right\}^2 , \qquad (7.66)$$

where

$d_e\sigma_{Th}/d\Omega$ is the differential Thomson electronic cross section,

$F(x,Z)$ is the so-called *atomic form factor* with the momentum transfer variable $x = \sin(\theta/2)/\lambda$, as given in (7.59),

λ is the wavelength of the incident photon,

Z is the atomic number of the absorber.

The differential Rayleigh atomic cross section $d_a\sigma_R/d\theta$ per *unit scattering angle* θ is

$$\frac{d_a\sigma_R}{d\theta} = \frac{d_a\sigma_R}{d\Omega}\frac{d\Omega}{d\theta} = \frac{r_e^2}{2}(1+\cos^2\theta)\left\{F(x,Z)\right\}^2 2\pi\sin\theta =$$
$$= \pi r_e^2 \sin\theta(1+\cos^2\theta)\left\{F(x,Z)\right\}^2 . \qquad (7.67)$$

7.4.2 Form Factor $F(x,Z)$ for Rayleigh Scattering

Calculations of the atomic form factor $F(x,Z)$ are difficult and, since they are based on atomic wavefunctions, they can be carried out analytically only for the hydrogen atom. For all other atoms the calculations rely on various approximations and atomic models, such as the Thomas-Fermi, Hartree, or Hartree-Fock.

The atomic form factor $F(x,Z)$ is equal to Z for small scattering angles θ and approaches zero for large scattering angles θ. Its values are plotted in Fig. 7.18 against the momentum transfer variable $x = \sin(\theta/2)/\lambda$ for various absorbers ranging in atomic number Z from 1 to 82.

Figure 7.19 is a plot of the differential Rayleigh atomic cross section $d_a\sigma_R/d\theta$ against the scattering angle θ for hydrogen and carbon, respectively, consisting of a product of the differential Thomson electronic cross section $d_e\sigma_{Th}/d\theta$ given in (7.13) and the square of the atomic form factor $F(x,Z)$, as given in (7.67). For comparison the differential Thomson atomic cross section $d_a\sigma_{Th}/d\theta$ is also shown in Fig. 7.19. For hydrogen $d_a\sigma_{Th}/d\theta = d_e\sigma_{Th}/d\theta$, while for carbon $d_a\sigma_{Th}/d\theta = 6\,d_e\sigma_{Th}/d\theta$, with both curves symmetrical about $\theta = \pi/2$.

The $d_a\sigma_R/d\theta$ curves for various energies shown in Fig. 7.19 are not symmetrical about $\theta = \pi/2$ because of the peculiar shape of the atomic form factor $F(x,Z)$ that causes a predominance in forward Rayleigh scattering; the larger the photon energy, the more asymmetrical is the $d_a\sigma_R/d\theta$ curve and the more forward peaked is the Rayleigh scattering. The area under each $d_a\sigma_R/d\theta$ curve gives the total Rayleigh atomic cross-section $_a\sigma_R$ for a given photon energy.
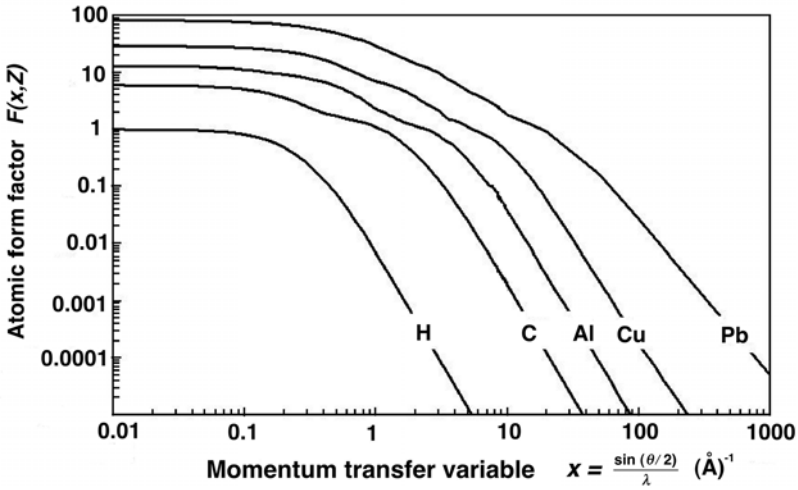
Fig. 7.18. Atomic form factor $F(x, Z)$ plotted against the momentum transfer variable $x = \sin(\theta/2)/\lambda$

7.4.3 Scattering Angles in Rayleigh Scattering

The angular spread of Rayleigh scattering depends on the photon energy $h\nu$ and the atomic number Z of the absorber. It can be estimated from the following relationship:

$$\theta_{\mathrm{R}} \approx 2 \arcsin\left(\frac{0.026 Z^{1/3}}{\varepsilon}\right) , \tag{7.68}$$

where

θ_{R} is the characteristic angle for Rayleigh scattering, representing the opening half angle of a cone that contains 75% of the Rayleigh-scattered photons,

Z is the atomic number of the absorber,

ε is the reduced photon energy, *i.e.*, $\varepsilon = h\nu/(m_{\mathrm{e}}c^2)$.

As suggested by (7.68), the angle θ_{R} increases with increasing Z of the absorber for the same $h\nu$ and decreases with increasing photon energy $h\nu$ for the same Z. Table 7.4 lists the characteristic angle θ_{R} for Rayleigh scattering for photon energies in the range from 100 keV to 10 MeV and various absorbers (carbon, copper and lead), calculated from (7.68).

- At high photon energies ($h\nu > 1$ MeV) Rayleigh scattering is confined to small angles for all absorbers.
- At low energies, particularly for high Z absorbers, the angular distribution of Rayleigh-scattered photons is much broader. In this energy range the Rayleigh atomic cross section $_{\mathrm{a}}\sigma_{\mathrm{R}}$ exceeds the Compton atomic cross
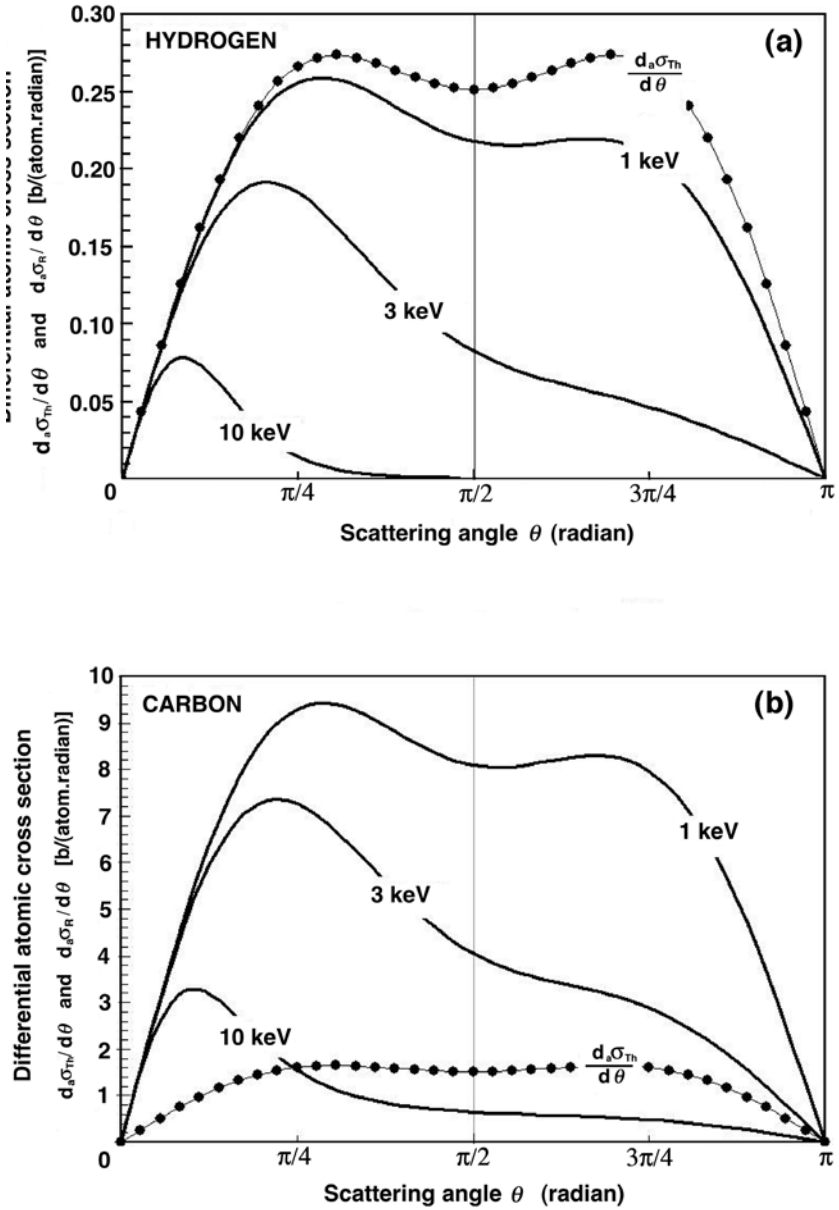
Fig. 7.19. Differential atomic cross section per unit angle for Rayleigh scattering $d_a\sigma_R/d\theta$, given by (7.67), for incident photon energies of 1, 3, and 10 keV for hydrogen in part **a** and carbon in part **b**. The differential Thomson cross-section $d_a\sigma_{Th}/d\theta$ for the two absorbing materials is shown by the *dotted curves* (data points) for comparison

Table 7.4. The characteristic angle θ_R for Rayleigh scattering for various absorber materials and photon energies in the range from 100 keV to 10 MeV

Absorber	Symbol	Z	Photon energy (MeV)				
			0.1	0.5	1	5	10
Carbon	C	6	28°	6°	3°	0.6°	0.3°
Copper	Cu	29	48°	9°	5°	0.9°	0.5°
Lead	Pb	82	70°	13°	7°	1.3°	0.7°

section $_a\sigma_c$ but is nonetheless very small in comparison with the photo-electric atomic cross section $_a\tau$. The atomic Rayleigh cross section $_a\sigma_R$ is therefore often ignored in gamma ray transport as well as in shielding barrier calculations.

- Rayleigh scattering plays no role in radiation dosimetry, since no energy is transferred to charged particles through Rayleigh scattering.

7.4.4 Atomic Cross Sections for Rayleigh Scattering $_a\sigma_R$

The Rayleigh atomic cross section $_a\sigma_R$ can be obtained by determining the area under the appropriate $d_a\sigma_R/d\theta$ curve plotted against θ, as shown in Fig. 7.19, or it can be calculated by integrating the differential cross section $d_a\sigma_R/d\theta$ of (7.67) over all possible scattering angles θ from 0 to π, i.e.,

$$_a\sigma_R = \pi r_e^2 \int_0^\pi \sin\theta (1 + \cos^2\theta) \left[F(x, Z)\right]^2 d\theta \ . \tag{7.69}$$

Rayleigh atomic cross section $_a\sigma_R$ is shown with solid curves against incident photon energy $h\nu$ in the range from 1 keV to 1000 MeV in Fig. 7.20. For comparison, the figure also shows the Compton atomic cross-section $_a\sigma_c$ of Fig. 7.14 in the same energy range. The following conclusions may be reached from Fig. 7.20:

- At low photon energies $_a\sigma_R$ exceeds $_a\sigma_c$; the higher is the atomic number of the absorber, the larger is the difference. However, at low photon energies both $_a\sigma_R$ and $_a\sigma_c$ are negligible in comparison with the atomic cross section for the photoelectric effect $_a\tau$, so both are usually ignored in calculations of the total atomic cross section $_a\mu$ for a given absorber at very low photon energies.
- The photon energy $h\nu_{eq}$ at which the atomic cross sections for Rayleigh and Compton scattering are equal, i.e., $_a\sigma_R = _a\sigma_c$, is proportional to the atomic number Z of the absorber. From Fig. 7.20 we also note that for photon energies exceeding $h\nu_{eq}$ the Rayleigh atomic cross section $_a\sigma_R$ is inversely proportional to $(h\nu)^2$; i.e.,

$$_a\sigma_R \propto (1/h\nu)^2 \ . \tag{7.70}$$
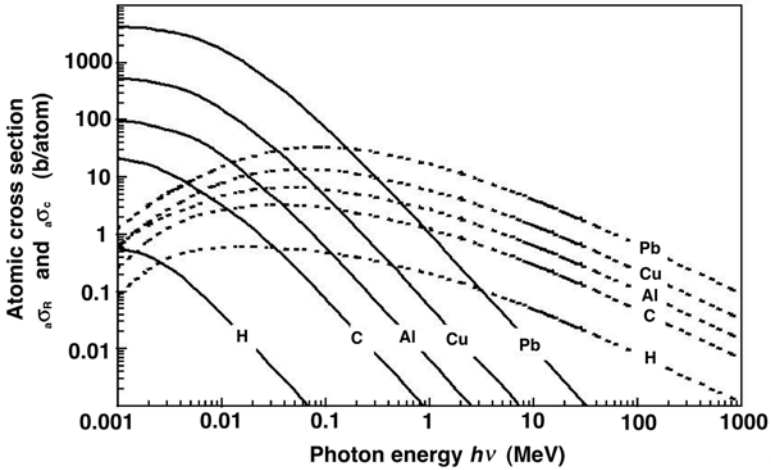
Fig. 7.20. Atomic cross sections for Rayleigh scattering $_a\sigma_R$ and Compton scattering $_a\sigma_c$ against incident photon energy $h\nu$ in the range from 1 keV to 1000 MeV for various absorbers ranging from hydrogen to lead. $_a\sigma_R$ is shown by *solid curves;* $_a\sigma_c$ is shown by *dashed curves* for comparison. For very low photon energies the $_a\sigma_R$ *curves* exhibit a plateau with a value of $_e\sigma_{Th} Z^2$ where $_e\sigma_{Th}$ is the energy independent Thomson cross-section and Z is the atomic number of the absorber (note that $F(x, Z) \to Z$ for low $h\nu$, i.e., large λ). Data are from the NIST

- In general, as evident from Fig. 7.20, we may also state that $_a\sigma_R$ is proportional to Z^2, where Z is the atomic number of the absorber.

7.4.5 Mass Attenuation Coefficient for Rayleigh Scattering

The Rayleigh mass attenuation coefficient σ_R/ρ is determined through the standard relationship

$$\frac{\sigma_R}{\rho} = \frac{N_A}{A} {}_a\sigma_R \ . \tag{7.71}$$

- Since $_a\sigma_R \propto Z^2/(h\nu)^2$ and $A \approx 2Z$, we conclude that $\sigma_R/\rho \propto Z/(h\nu)^2$, where Z and A are the atomic number and atomic mass, respectively, of the absorber.
- Since no energy is transferred to charged particles in Rayleigh scattering, the energy transfer coefficient for Rayleigh scattering is zero.

7.5 Photoelectric Effect

An interaction between a photon and a tightly bound orbital electron of an absorber atom is called *photoelectric effect* (photoeffect). In the interaction

Before interaction

After interaction

$h\nu$

e^-
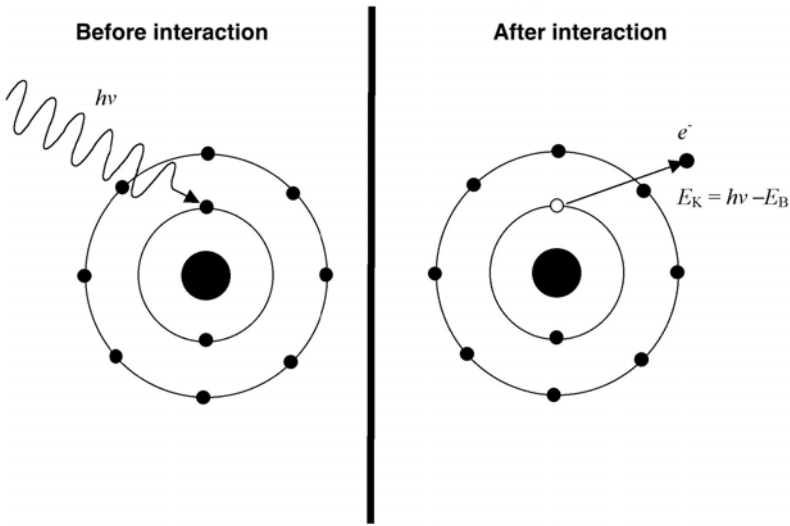
$E_K = h\nu - E_B$

Fig. 7.21. Schematic diagram of the photoelectric effect. A photon with energy $h\nu$ interacts with a K-shell electron. The photon is absorbed completely and the K-shell electron is ejected as photoelectron from the atom with a kinetic energy $E_K = h\nu - E_B(K)$, where $E_B(K)$ is the binding energy of the K-shell electron. The vacancy in the K shell will subsequently be filled with a higher orbit electron and the energy of the electronic transition will be emitted either in the form of a characteristic (fluorescent) photon or in the form of an Auger electron

the photon is absorbed completely and the orbital electron is ejected with kinetic energy E_K. The ejected orbital electron is referred to as a *photoelectron*. The photoelectric interaction between a photon of energy $h\nu$ and a K-shell atomic electron is shown schematically in Fig. 7.21.

Conservation of energy and momentum considerations show that the photoelectric effect can only occur on a tightly bound electron rather than on a "free electron", so that the atom as a whole picks up the difference between the momentum of the photon ($p_\nu = h\nu/c$) and that of the photoelectron ($p_e = \sqrt{E^2 - E_o^2}/c$), where E and E_o are the total energy and rest energy, respectively, of the photoelectron.

Figure 7.22 shows that energy and momentum cannot be conserved simultaneously in a photon-free electron interaction. In part (a) the total energy is conserved but, as a result of total energy conservation, the total momentum is not conserved. In part (b) the total momentum is conserved but, as a result of total momentum conservation, the total energy is not conserved. Thus, an extra interaction partner must absorb the extra momentum and this is achieved when the electron is tightly bound to the nucleus, so that the whole atom picks up the extra momentum
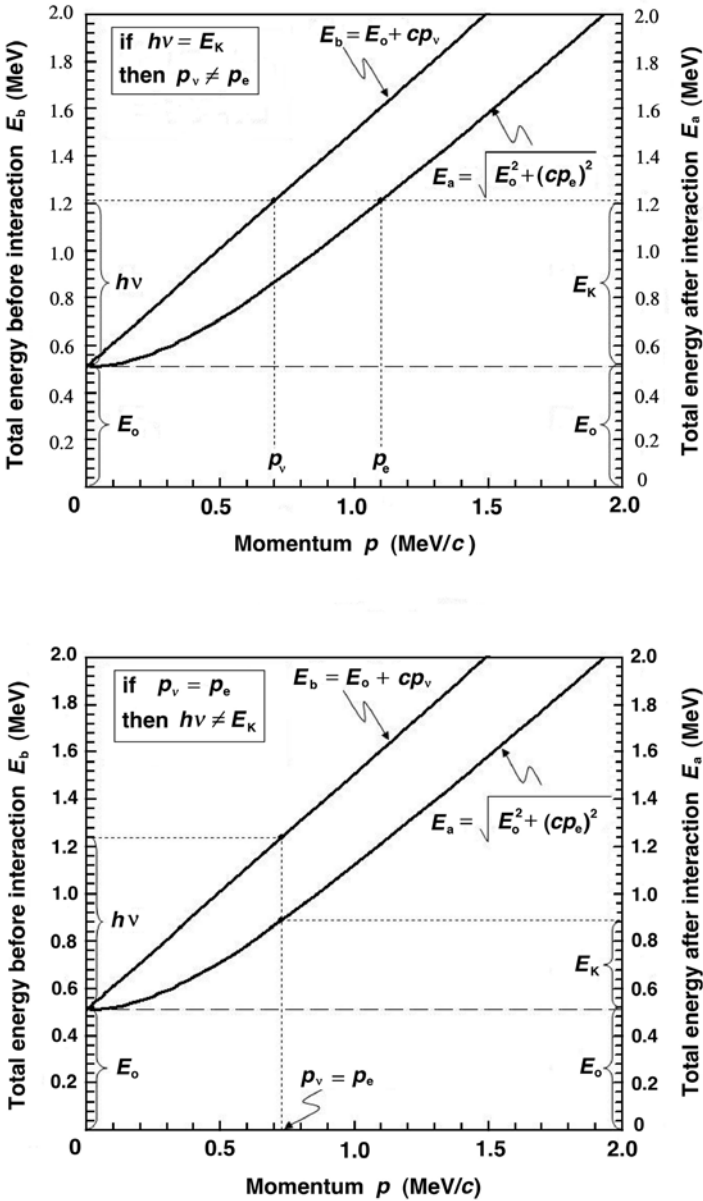
Fig. 7.22. Energy and momentum conservation considerations in photoelectric effect occurring on a free electron. In part **a** the total energy is conserved ($E_b = E_a$) but not the momentum; in part **b** the total momentum is conserved ($p_\nu = p_e$) but not the total energy

- Because of the relatively large nuclear mass, the atomic recoil energy is exceedingly small and may be neglected. The kinetic energy E_K of the ejected photoelectron then equals the incident photon energy $h\nu$ less the binding energy E_B of the orbital electron, i.e.,

$$E_K = h\nu - E_B \ . \tag{7.72}$$

- When the photon energy $h\nu$ exceeds the K-shell binding energy $E_B(K)$ of the absorber, i.e., $h\nu > E_B(K)$, about 80% of all photoelectric absorptions occur with the K-shell electrons of the absorber.
- The energy uptake by the photoelectron may be insufficient to bring about its ejection from the atom (ionization), but may be sufficient to raise it to a higher orbit (excitation).
- The vacancy that results from the emission of the photoelectron will be filled by a higher shell electron and the transition energy will be emitted either as a characteristic (fluorescent) photon or as an Auger electron, the probability for each governed by the fluorescent yield (see Sect. 3.1).

7.5.1 Atomic Cross Section for Photoelectric Effect

The atomic cross section for the photoelectric effect $_a\tau$ as a function of the incident photon energy $h\nu$ exhibits a characteristic sawtooth structure in which the sharp discontinuities (absorption edges) arise whenever the photon energy coincides with the binding energy of a particular electron shell. Since all shells except for the K shell exhibit a fine structure, the $_a\tau$ curve plotted against the incident photon energy $h\nu$ also exhibits a fine structure in the L, M, ... etc. absorption edges.

Three distinct energy regions characterize the atomic cross section $_a\tau$: (1) *Region in the immediate vicinity of absorption edges*; (2) *Region at some distance from the absorption edge*; and (3) *Region in the relativistic region far from the K absorption edge*.

1. Theoretical predictions for $_a\tau$ in region (1) are difficult and uncertain.

2. For region (2) the atomic attenuation coefficient (cross section) for K-shell electrons $_a\tau_K$ is given as follows:

$$_a\tau_K = \alpha^4 \, _e\sigma_{Th} Z^n \sqrt{\frac{32}{\varepsilon^7}} \ , \tag{7.73}$$

where

ε is the usual normalized photon energy, *i.e.*, $\varepsilon = h\nu/(m_e c^2)$,

α is the fine structure constant (1/137),

Z is the atomic number of the absorber,

$_e\sigma_{Th}$ is the total Thomson electronic cross section given in (7.14),

n is the power for the Z dependence of $_a\tau_K$ ranging from $n = 4$ at relatively low photon energies to $n = 4.6$ at high photon energies,
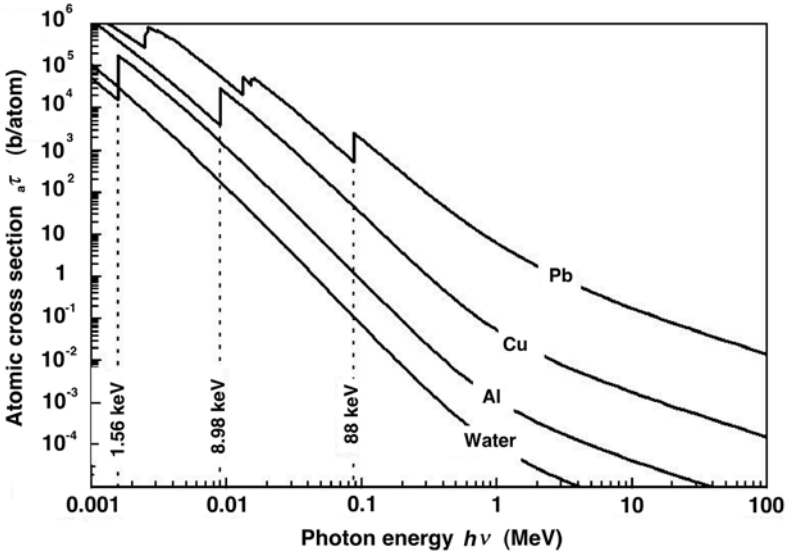
Fig. 7.23. Photoelectric atomic cross section $_a\tau$ against photon energy $h\nu$ for various absorbers. Energies of K-absorption edges are also indicated. Data are from the NIST

3. In the relativistic region ($\varepsilon \gg 1$), $_a\tau_K$ is given as follows:

$$_a\tau_K = \frac{1.5}{\varepsilon}\alpha^4 Z^5 {}_e\sigma_{Th} . \tag{7.74}$$

The following conclusions may be reached with regard to energy and atomic number dependence of $_a\tau_K$:

- The energy dependence of $_a\tau_K$ is assumed to go as $(1/h\nu)^3$ at low photon energies $h\nu$ gradually transforming into $1/h\nu$ at high $h\nu$.
- The energy dependences for regions (2) and (3) can be identified from Fig. 7.23 that displays the atomic cross section for the photoeffect against incident photon energy for various absorbers ranging from water to lead. Absorption edges are clearly shown in Fig. 7.23, the K absorption edges are identified for aluminum (1.56 eV), copper (8.98 eV) and lead (88 keV). The fine structures of the L and M absorption edges are also shown.
- The atomic number Z dependence ($_a\tau \propto Z^n$) of $_a\tau$, where n ranges from 4 to 5, is also evident from Fig. 7.23.

7.5.2 Angular Distribution of Photoelectrons

The angular distribution of photoelectrons depends on the incident photon energy $h\nu$. At low $h\nu$ photoelectrons tend to be emitted at $90°$ to the incident photon direction. As $h\nu$ increases, however, the photoelectron emis-

sion peak moves progressively to more forward photoelectron emission an-
gles, somewhat akin to the emission of bremsstrahlung photons in electron
bremsstrahlung interaction.

7.5.3 Energy Transfer to Photoelectrons in Photoelectric Effect

The photoelectron attains a kinetic energy of $E_K = h\nu - E_B$ as it leaves the
atom but also leaves behind a vacancy in a shell that is most often a K-shell
for $h\nu > E_B(K)$, where $E_B(K)$ is the binding energy of the K-shell electron.
The vacancy is filled with an upper shell electron and the transition energy
is emitted either in the form of a characteristic (fluorescent) photon or in
the form of an Auger electron depending on the fluorescent yield ω for the
particular interaction.

Because of the presence of Auger electrons, the mean energy transfer to
electrons in a photoelectric effect $\overline{E}_{tr}^{\tau}$ for $h\nu > E_B(K)$ is in general between
$h\nu - E_B(K)$ and $h\nu$.

- $\overline{E}_{tr}^{\tau} = h\nu - E_B(K)$ when $\omega_K \approx 1$, i.e., no Auger electrons are produced as
  a result of the photoelectric effect and the emission of a photoelectron.
- $\overline{E}_{tr}^{\tau} = h\nu$ when $\omega_K = 0$, i.e., no characteristic photons are produced as a
  result of the photoelectric effect and emission of a photoelectron.
- $h\nu - E_B(K) < \overline{E}_{tr}^{\tau} < h\nu$ is the general case in which a combination of
  characteristic photons and Auger electrons is released.

The general relationship for $\overline{E}_{tr}^{\tau}$ is given as follows:

$$\overline{E}_{tr}^{\tau} = h\nu - P_K\,\omega_K\,\overline{h\nu}_K \; , \tag{7.75}$$

where

P_K is the fraction of all photoelectric interactions that occur in the K-shell
for photons $h\nu > E_B(K)$. Typical values of P_K are of the order of 0.8
or larger, as shown in Fig. 3.3;

ω_K is the fluorescent yield for the K-shell, as discussed in Sect. 3.1.2 and
displayed in Fig. 3.3;

$\overline{h\nu}_K$ is a K-shell weighted mean value of all possible fluorescent transition
energies, ranging from the L $\rightarrow$ K transition through the M $\rightarrow$ K
transition, etc. to a limit $E_B(K)$. Since the K_α transitions are the most
probable fluorescent transitions for the K shell, the value of $\overline{h\nu}_K$ is
weighted toward the energy of the K_α transition and typically amounts
to about 86% of the $E_B(K)$ value for a given Z of the absorber.

Figure 7.24 provides a plot of the K-shell binding energy $E_B(K)$, the K-
shell weighted mean fluorescence energy $\overline{h\nu}_K \approx 0.86E_B(K)$, and the average
energy emitted in the form of K fluorescent photons $P_K\omega_K\overline{h\nu}_K$ against the
atomic number Z of the absorber. The range of the K-shell binding energies in
nature is from 13.6 eV for hydrogen to about 150 keV for the highest atomic
number elements. $E_B(K)$ can be estimated from the Hartree relationship
given in (2.83).
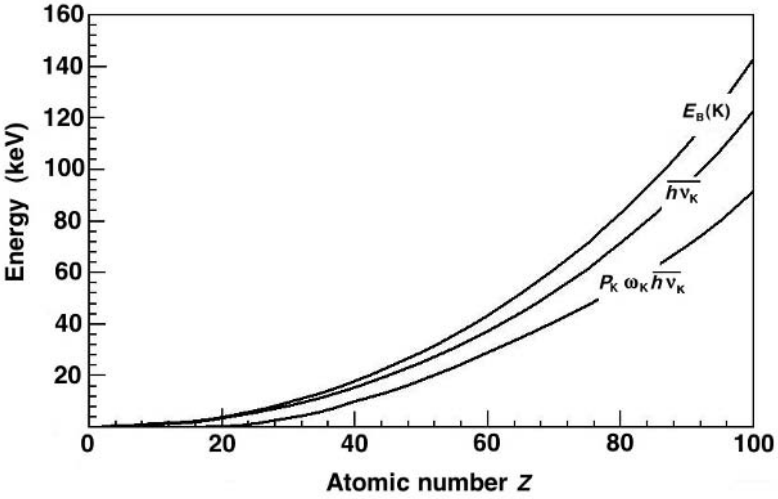
Fig. 7.24. The electron binding energy in the K shell, $E_B(K)$; the weighted mean characteristic x-ray energy for the K shell, $\overline{h\nu}_K$; and the mean energy emitted in the form of K-shell characteristic photons, $P_K\omega_K\overline{h\nu}_K$ against the atomic number Z of the absorber

7.5.4 Mass Attenuation Coefficient for the Photoelectric Effect

The mass attenuation coefficient for the photoelectric effect τ/ρ is calculated from the atomic cross section $_a\tau$ with the standard relationship

$$\frac{\tau}{\rho} = \frac{N_A}{A}\,_a\tau \ , \tag{7.76}$$

where A and ρ are the atomic mass and density, respectively, of the absorber.

7.5.5 Mass Energy Transfer Coefficient for the Photoelectric Effect

The mass energy transfer coefficient for the photoelectric effect $(\tau_K/\rho)_{tr}$ for incident photon energy $h\nu$ that exceeds the K-shell binding energy $E_B(K)$, i.e., $h\nu \geq E_B(K)$ is calculated from the relationship

$$\left(\frac{\tau_K}{\rho}\right)_{tr} = \frac{\tau_K}{\rho}\frac{\overline{E}_{tr}^\tau}{h\nu} = \frac{\tau_K}{\rho}\frac{h\nu - P_K\,\omega_K\,\overline{h\nu}_K}{h\nu}$$
$$= \frac{\tau_K}{\rho}\left(1 - \frac{P_K\,\omega_K\,\overline{h\nu}_K}{h\nu}\right) = \frac{\tau_K}{\rho}\bar{f}^\tau \ , \tag{7.77}$$

where $\bar{f}^\tau = 1 - P_K\,\omega_K\,\overline{h\nu}_K/(h\nu)$ is the mean fraction of energy $h\nu$ transferred to electrons.

Table 7.5. Parameters for photoelectric effect in various absorbers for photon energies $h\nu$ exceeding the K-shell binding energy $E_B(K)$

Element	Z	ω_K	P_K	$E_B(K)$ (keV)	$\overline{h\nu}_K$ (keV)	$P_K\omega_K\overline{h\nu}_K$ (keV)	$\bar{f}^\tau(E_B(K))$
C	6	0	0.95	0.28	0.24	0	1.0
Cu	29	0.50	0.87	9.0	7.7	3.35	0.62
Sn	50	0.85	0.85	29.2	25.0	18.1	0.38
Pb	82	0.97	0.78	88.0	75.7	64.6	0.27

Table 7.5 gives the fluorescent yield ω_K, the fraction P_K, the K-shell binding energy $E_B(K)$, the mean K-shell characteristic radiation energy $\overline{h\nu}_K$, the product $P_K\omega_K\overline{h\nu}_K$; and $\bar{f}^\tau(E_B(K))$, the mean fraction of the photon energy transferred to electrons in photoelectric effect for photons of energy $h\nu = E_B(K)$.

The fraction $\bar{f}^\tau$, plotted against photon energy $h\nu$ for various elements in Fig. 7.25, starts at its lowest value at $h\nu = E_B(K)$ and then gradually approaches 1 with increasing photon energy. For $f^\tau = 1$, the incident photon energy $h\nu$ is transferred to electrons in full: the photoelectron receives a kinetic energy $h\nu - E_B(K)$ and the available energy $E_B(K)$ either goes to Auger electrons for low Z absorbers or is essentially negligible in comparison to $h\nu$ for all absorbers at very high photon energies $h\nu$.

The formalism that was used above for K-shell electrons when $h\nu > E_B(K)$ will apply for L-shell electrons when $E_B(L) < h\nu < E_B(K)$, etc. The tightest bound electron available for a photoelectric interaction is by far
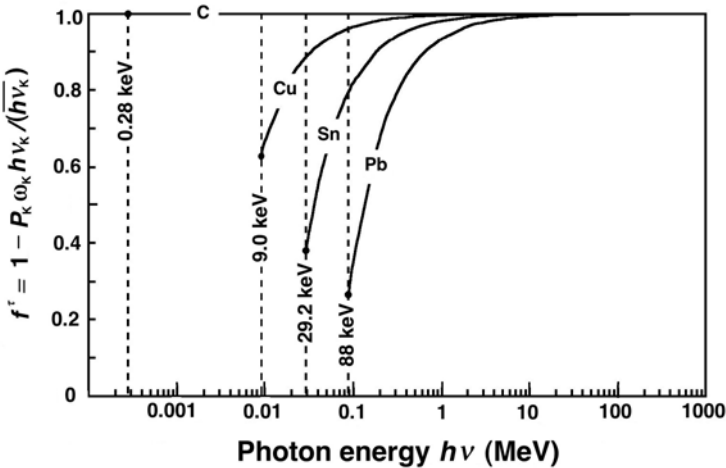
Fig. 7.25. The photoelectric fraction $\bar{f}^\tau_K$, the mean fraction of photon energy $h\nu$ transferred to electrons in a K-shell photoelectric effect interaction in carbon, copper, tin, and lead, against photon energy $h\nu$

the most likely to have a photoelectric interaction with the photon; thus only electrons most likely to have an interaction are considered in calculation of the photoelectric coefficients.

7.6 Pair Production

When the photon energy $h\nu$ exceeds $2m_ec^2 = 1.02$ MeV, the production of an electron-positron pair in conjunction with a complete absorption of the photon becomes energetically possible. For the effect to occur, three quantities must be conserved: *energy*, *charge* and *momentum*.

For $h\nu > 2m_ec^2$, energy and charge can be conserved even if pair production occurs in free space. However, to conserve the linear momentum the effect cannot occur in free space; it can only occur in the Coulomb field of a collision partner (either atomic nucleus or orbital electron) that can take up a suitable fraction of the momentum carried by the photon.

The pair production and triplet production interactions are shown schematically in Fig. 7.26.

7.6.1 Conservation of Energy, Momentum and Charge for Pair Production in Free Space

Before the pair production interaction there is photon energy $E_\nu = h\nu > 2m_ec^2$ and photon momentum $p_\nu = h\nu/c$. In the interaction an electron-positron pair is produced with a total energy $E_{\text{pair}} = 2\gamma m_ec^2$ and total momentum $p_{\text{pair}} = 2\gamma m_e\upsilon$.

- *Conservation of Energy:*
  $E_\nu = h\nu \equiv E_{\text{pair}} = 2\gamma m_ec^2$
- *Conservation of Momentum:*
  $$p_\nu = \frac{h\nu}{c} \equiv p_{\text{pair}} = 2\gamma m_e\upsilon \rightarrow 2\gamma m_ec^2\frac{\upsilon}{c^2} = E_\nu\frac{\upsilon}{c^2} = p_\nu\frac{\upsilon}{c}$$

  Since the particle velocity υ is always smaller than c, it follows that p_ν, the momentum before the pair production interaction, is always larger than p_{pair}, the total momentum after the pair production interaction. Thus, the photon possesses momentum excess that is not absorbed by the electron-positron pair. This momentum excess must be absorbed by a collision partner, be it the atomic nucleus or an orbital electron of an absorber. Therefore, pair production interaction cannot occur in free space (vacuum) where no collision partner is available.
- When the extra momentum is absorbed by the atomic nucleus of the absorber, the recoil energy, as a result of the relatively large nuclear mass, is exceedingly small and the effect is described as the standard pair production (usually referred to as *pair production*). Two particles (electron and positron) leave the interaction site.
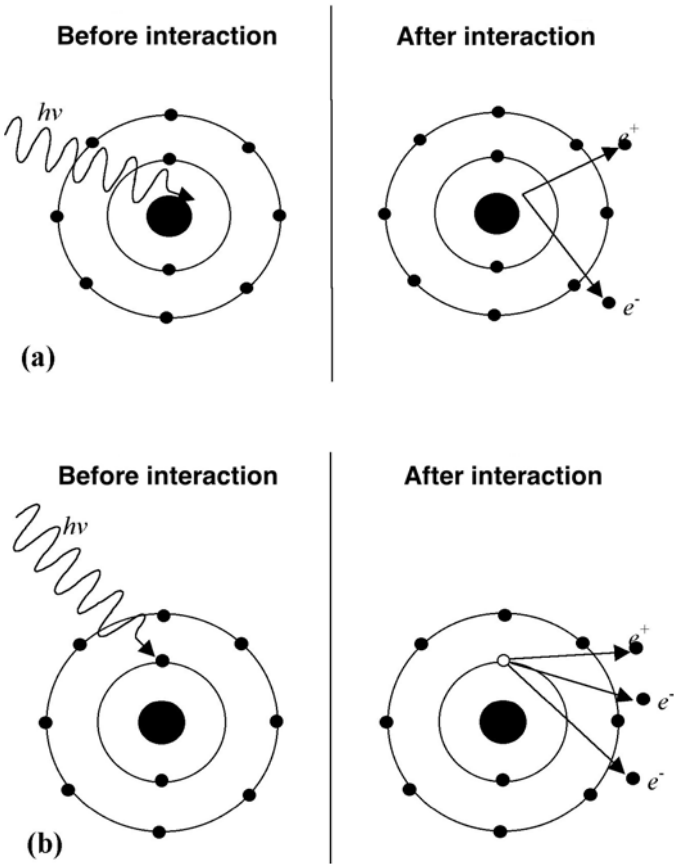
Fig. 7.26. Schematic representation of pair production (**a**) in the Coulomb field of a nucleus and (**b**) triplet production (in the Coulomb field of an orbital electron)

- When an orbital electron of the absorber picks up the extra momentum, the recoil energy of the orbital electron may be significant and the effect is described as the pair production in the Coulomb field of electron, i.e., *triplet production.* Three particles (two electrons and a positron) leave the interaction site.
- *Conservation of Charge:*
  The total charge before the interaction is zero and the total charge after the interaction is also zero.

7.6.2 Threshold Energy for Pair Production and Triplet Production

In contrast to other common photon interactions, such as photoelectric effect, Rayleigh scattering and Compton scattering, pair production exhibits a

threshold energy below which the effect cannot happen. The threshold energy is derived following the procedure described in detail in Section 4.2.3 that is based on the invariant: $E^2 - p^2c^2 = inv$ where E and p are the total energy and total momentum, respectively, before and after the interaction.

For *pair production* in the field of the nucleus the conditions for before the interaction (in the laboratory system) and for after the interaction (in the center-of-mass system) are written as follows:

* *Total energy before:* $(h\nu)_{\text{thr}}^{\text{PP}} + m_A c^2$, where $m_A c^2$ is the rest mass of the nucleus, the interaction partner.
* *Total momentum before:* $(h\nu)_{\text{thr}}^{\text{PP}}/c$.
* *Total energy after:* $(m_A c^2 + 2m_e c^2)$.
* *Total momentum after:* 0

The invariant for before and after the pair production event is

$$\left\{(h\nu)_{\text{thr}}^{\text{PP}} + m_A c^2\right\}^2 - \left(\frac{(h\nu)_{\text{thr}}^{\text{PP}}}{\text{c}}\right)^2 c^2 = (m_A c^2 + 2m_e c^2)^2 - 0 \,, \quad (7.78)$$

resulting in the following expression for pair production threshold $E_{\text{thr}}^{\text{PP}} = (h\nu)_{\text{thr}}^{\text{PP}}$

$$E_{\gamma\text{thr}}^{\text{PP}} = (h\nu)_{\text{thr}}^{\text{PP}} = 2m_e c^2 \left(1 + \frac{m_e c^2}{m_A c^2}\right)$$

$$= (1.022 \text{ MeV}) \times \left(1 + \frac{m_e c^2}{m_A c^2}\right) . \quad (7.79)$$

In the first approximation we can use $(h\nu)_{\text{thr}}^{\text{PP}} \approx 2m_e c^2$, since the ratio $m_e c^2/m_A c^2$ is very small, indicating that the recoil energy of the nucleus is exceedingly small.

For *triplet production* the conditions for before the interaction (in the laboratory system) and for after the interaction (in the center-of-mass system) are written as follows:

* *Total energy before:* $(h\nu)_{\text{thr}}^{\text{tp}} + m_e c^2$, where $m_e c^2$ is the rest mass of the orbital electron, the interaction partner.
* *Total momentum before:* $(h\nu)_{\text{thr}}^{\text{tp}}/c$.
* *Total energy after:* $3m_e c^2$, accounting for rest energies of the orbital electron as well as for the electron-positron pair.
* *Total momentum after:* 0.

The invariant for before and after the triplet production event is

$$\left\{(h\nu)_{\text{thr}}^{\text{tp}} + m_e c^2\right\}^2 - [(h\nu)_{\text{thr}}^{\text{tp}}]^2 = (3m_e c^2)^2 - 0 \,, \quad (7.80)$$

resulting in the following expression for the triplet production threshold:

$$E_{\gamma\text{thr}}^{\text{tp}} = (h\nu)_{\text{thr}}^{\text{tp}} = 4m_e c^2 = 2.044 \text{ MeV} . \quad (7.81)$$

7.6.3 Energy Transfer to Charged Particles in Pair Production

The total kinetic energy transferred to charged particles (electron and positron) in pair production is

$$(E_K^\kappa)_{tr} = h\nu - 2m_e c^2 \ , \tag{7.82}$$

ignoring the minute recoil energy of the nucleus.

Generally, the electron and the positron do not receive equal kinetic energies but their average is given as

$$\overline{E}_K^{pp} = \frac{h\nu - 2m_e c^2}{2} \ . \tag{7.83}$$

The exact energy distribution of electrons and positrons in pair production is a complex function of photon energy $h\nu$ and atomic number Z of the absorber. In the first approximation we assume that all distributions of the available energy $(h\nu - 2m_e c^2)$ are equally probable, except for the extreme case where one particle obtains all the available energy and the other particle obtains none.

7.6.4 Angular Distribution of Charged Particles

The angular distribution of the electrons and positrons produced in pair production is peaked increasingly in the forward direction with increasing incident photon energy $h\nu$. For very high energies ($\varepsilon = h\nu/(m_e c^2) \gg 1$) the mean angle $\bar{\theta}$ of positron and electron emission is of the order of $\theta \approx 1/\varepsilon$.

7.6.5 Nuclear Screening

For very high photon energies ($h\nu > 20$ MeV) significant contribution to the pair production cross section may come from interaction points that lie outside the orbit of K shell electrons. The Coulomb field in which the pair production occurs is thus reduced because of the screening of the nucleus by the two K-shell electrons, thereby requiring a screening correction in theoretical calculations.

7.6.6 Atomic Cross Sections for Pair Production

The theoretical derivations of atomic cross sections for pair production $_a\kappa$ are very complicated, some based on Born approximation, others not, some accounting for nuclear screening and others not.

In general the atomic cross sections for pair production in the field of a nucleus or orbital electron appear as follows:

$$_a\kappa = \alpha r_e^2 Z^2 P(\varepsilon, Z) \ , \tag{7.84}$$

Table 7.6. Characteristics of atomic cross section for pair production in the field of the nucleus or in the field of an orbital electron

Field	Energy range	$P(\varepsilon, Z)$	Comment	
nucleus	$1 \ll \varepsilon \ll 1/(\alpha Z^{1/3})$	$\dfrac{28}{9} \ln 2\varepsilon - \dfrac{218}{27}$	no screening	(7.85)
nucleus	$\varepsilon \gg 1/(\alpha Z^{1/3})$	$\dfrac{28}{9} \ln \dfrac{183}{Z^{1/3}} - \dfrac{2}{27}$	complete screening	(7.86)
nucleus	outside the limits above but $\varepsilon > 4$	$\dfrac{28}{9} \ln 2\varepsilon - \dfrac{218}{27} - 1.027$	no screening	(7.87)
electron	$\varepsilon > 4$	$\dfrac{1}{Z}\left(\dfrac{28}{9} \ln 2\varepsilon - 11.3\right)$	no screening	(7.88)

where

α	is the fine structure constant ($\alpha = 1/137$),
r_{e}	is the classical electron radius [$r_{\mathrm{e}} = e^2/(4\pi\varepsilon_{\mathrm{o}} m_{\mathrm{e}} c^2) = 2.818$ fm],
Z	is the atomic number of the absorber,
$P(\varepsilon, Z)$	is a complicated function of the photon energy $h\nu$ and atomic number Z of the absorber, as given in Table 7.6.

It is evident from (7.83) through (7.88) and from Table 7.6, that the atomic cross section for pair production $_{\mathrm{a}}\kappa_{\mathrm{pp}}$ is proportional to Z^2, while the atomic cross section for triplet production $_{\mathrm{a}}\kappa_{\mathrm{tp}}$ is linearly proportional to Z. In general, the relationship between $_{\mathrm{a}}\kappa_{\mathrm{pp}}$ and $_{\mathrm{a}}\kappa_{\mathrm{tp}}$ is given as follows:

$$_{\mathrm{a}}\kappa_{\mathrm{pp}}/_{\mathrm{a}}\kappa_{\mathrm{tp}} = \eta Z \ , \tag{7.89}$$

where η is a parameter, depending only on $h\nu$, and, according to *Robley Evans*, equal to 2.6 at $h\nu = 6.5$ MeV, 1.2 at $h\nu = 100$ MeV, and approaching unity as $h\nu \to \infty$. This indicates that the atomic cross section for triplet production $_{\mathrm{a}}\kappa_{\mathrm{tp}}$ is at best about 30% of the pair production cross section $_{\mathrm{a}}\kappa_{\mathrm{pp}}$ for $Z = 1$ and less than 1% for high Z absorbers.

Since the atomic cross section for pair production in the field of the atomic nucleus exceeds significantly the atomic cross section for triplet production, as shown in Fig. 7.27 for two absorbing materials: carbon with $Z = 6$ and lead with $Z = 82$, both the pair production and the triplet production contributions are usually given under the header of general pair production as follows:

$$_{\mathrm{a}}\kappa = {}_{\mathrm{a}}\kappa_{\mathrm{pp}} + {}_{\mathrm{a}}\kappa_{\mathrm{tp}} = {}_{\mathrm{a}}\kappa_{\mathrm{pp}} \{1 + 1/(\eta Z)\} \ , \tag{7.90}$$

where the electronic effects (triplet production) are accounted for with the correction term $1/(\eta Z)$. This term is equal to zero for $h\nu < 4m_{\mathrm{e}}c^2$, where $4m_{\mathrm{e}}c^2$ is the threshold energy for triplet production.
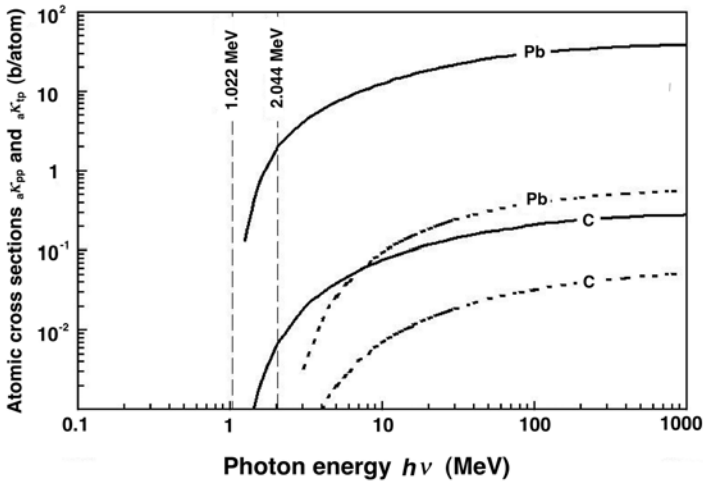
Fig. 7.27. Atomic cross sections for pair production $_a\kappa_{pp}$ (*solid curves*) and for triplet production $_a\kappa_{tp}$ (*dotted curves*) against incident photon energy $h\nu$ for carbon and lead. Data are from the NIST
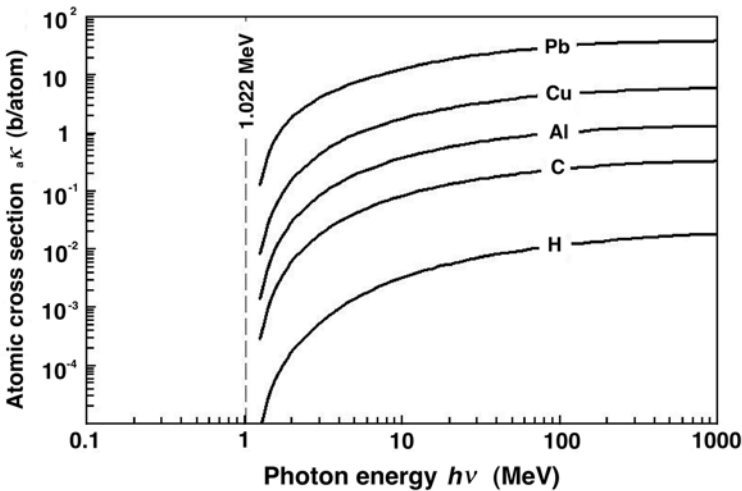
Fig. 7.28. Atomic cross section for pair production (including triplet production) $_a\kappa$ against incident photon energy $h\nu$ for various absorbers in the range from hydrogen to lead. Data are from the NIST

The atomic cross sections for general pair production $_a\kappa$ are plotted in Fig. 7.28 for various absorbers ranging from hydrogen to lead. The increase of $_a\kappa$ with incident photon energy $h\nu$ and with atomic number Z of the absorber is evident.

7.6.7 Mass Attenuation Coefficient for Pair Production

The mass attenuation coefficient for pair production κ/ρ is calculated from the atomic cross section $_\mathrm{a}\kappa$ with the standard relationship

$$\frac{\kappa}{\rho} = \frac{N_\mathrm{A}}{A}{}_\mathrm{a}\kappa \; , \tag{7.91}$$

where A and ρ are the atomic mass and density, respectively, of the absorber.

7.6.8 Mass Energy Transfer Coefficient for Pair Production

The mass energy transfer coefficient for pair production $(\kappa/\rho)_\mathrm{tr}$ for incident photon energy $h\nu$ that exceeds the threshold energy of 1.02 MeV for pair production is calculated from the relationship

$$\left(\frac{\kappa}{\rho}\right)_\mathrm{tr} = \frac{\kappa}{\rho}\frac{h\nu - 2m_\mathrm{e}c^2}{h\nu} = \frac{\kappa}{\rho}\left(1 - \frac{2m_\mathrm{e}c^2}{h\nu}\right) = \bar{f}^{\kappa}\frac{\kappa}{\rho} \; , \tag{7.92}$$

where $\bar{f}^{\kappa}$ is the average fraction of the incident photon energy $h\nu$ that is transferred to charged particles (electron and positron) in pair production.

The pair production fraction $\bar{f}^{\kappa}$ is plotted against photon energy $h\nu$ in Fig. 7.29. The fraction $\bar{f}^{\kappa}$ is 0 for $h\nu \leq 2m_\mathrm{e}c^2$, rises gradually with increasing energy above $2m_\mathrm{e}c^2$, and approaches $\bar{f}^{\kappa} = 1$ asymptotically, showing that at large $h\nu$ the following relationship holds $(\kappa/\rho)_\mathrm{tr} \approx (\kappa/\rho)$. Figure 7.30 shows a comparison between the mass attenuation coefficient κ/ρ and mass energy transfer coefficient $(\kappa/\rho)_\mathrm{tr}$ against photon energy for carbon and lead. Both coefficients are related through $\bar{f}^{\kappa}$, as given by (7.92).
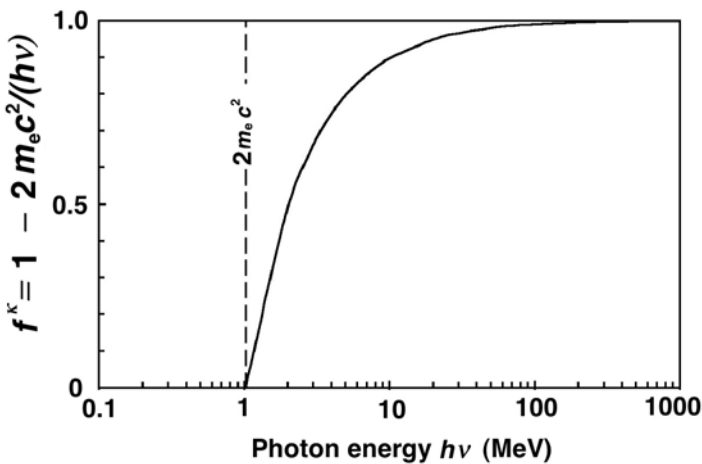
Fig. 7.29. The average pair production fraction $\bar{f}^{\kappa}$ against photon energy $h\nu$
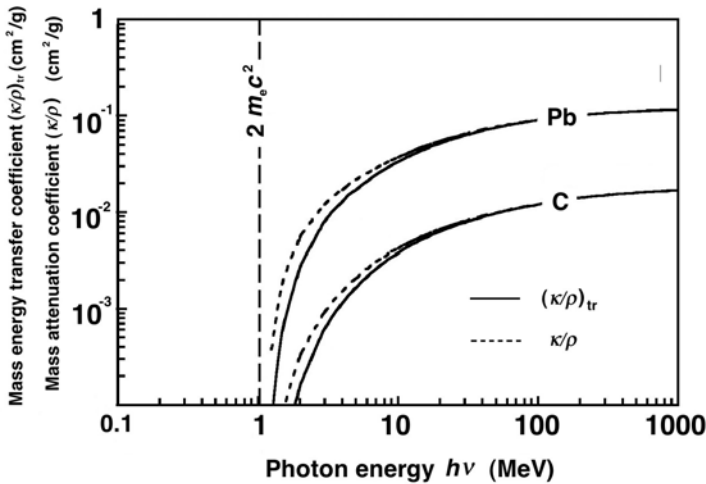
Fig. 7.30. Mass energy transfer coefficient $(\kappa/\rho)_{\mathrm{tr}}$ (*solid curves*) and mass attenuation coefficient κ/ρ (*dashed curves*) for pair production against photon energy $h\nu$ for carbon and lead. Data are from the NIST

7.6.9 Positron Annihilation

The positron is an antiparticle to an electron. The two have identical rest masses: $m_{\mathrm{e}}c^2 = 0.511$ MeV and opposite signs: electrons are negative, positrons positive. The positron was discovered in 1932 by *Carl Anderson* during his study of cosmic ray tracks in a Wilson cloud chamber.

Of interest in medical physics are positrons produced by:

1. Energetic photons undergoing pair production or triplet production (important in radiation dosimetry and health physics)
2. β^+ decay used in positron emission tomography (PET) imaging.

Energetic positrons move through an absorbing medium and experience collisional and radiative losses of their kinetic energy through Coulomb interactions with orbital electrons and nuclei, respectively, of the absorber.

Eventually, positron collides with an electron and the two annihilate directly or they annihilate through an intermediate step forming a metastable hydrogen-like structure (see Sect. 2.3.7) called positronium (Ps). The positron and electron of the positronium revolve about their common center-of-mass in discrete orbits that are subjected to Bohr quantization rules with the reduced mass equal to one half of the electron rest mass and the lowest state with a binding energy of $(1/2)E_{\mathrm{R}} = 6.8$ eV.

The process of positron-electron annihilation is an inverse to pair production with the total mass before annihilation transformed into one, two, or three photons.

- The most common electron-positron annihilation occurs when the positron loses all of its kinetic energy and then undergoes annihilation with a "stationary and free" electron. The annihilation results in two photons (annihilation quanta) of energy $m_e c^2 = 0.511$ MeV each and moving in opposite directions (at nearly 180° to one another) ensuring conservation of total charge (zero), total energy ($2m_e c^2 = 1.02$ MeV) and total momentum (zero).
- A less common event (of the order of 2% of all annihilation interactions) is the annihilation-in-flight between a positron with non-zero kinetic energy E_K and either a tightly bound electron or a "free" electron.
  - When the electron is tightly bound to the nucleus, the nucleus can pick up the recoil momentum, and annihilation-in-flight produces only one photon with essentially the total positron energy (sum of rest energy and kinetic energy).
  - When the electron is essentially free, the annihilation-in-flight results in two photons, one of energy $h\nu_1$ and the other of energy $h\nu_2$. It can be shown that, for energetic positrons where $E_K \gg m_e c^2$, the following relationships hold: $h\nu_1 = E_K + (3/2)m_e c^2$ and $h\nu_2 = (1/2)m_e c^2$.

7.7 Photonuclear Reactions (Photodisintegration)

Photonuclear reaction is a direct interaction between an energetic photon and an absorber nucleus. Two other names are often used for the effect: *photodisintegration* and "*nuclear photoeffect*". Neutrons produced in photonuclear reactions are referred to as *photoneutrons*.

In photonuclear reactions the nucleus absorbs a photon and the most likely result of such an interaction is the emission of a single neutron through a (γ, n) reaction, even though emissions of charged particles, gamma rays, more than one neutron, or fission fragments (photofission) are also possible but much less likely to occur.

The most notable feature of the cross section for nuclear absorption of energetic photons is the so-called "giant resonance" exhibiting a broad peak in the cross section centered at about 24 MeV for low atomic number Z absorbers and at about 12 MeV for high Z absorbers. The only exceptions to the high photon energy rule are the two reactions $^2\mathrm{H}(\gamma, \mathrm{n})^1\mathrm{H}$ and $^9\mathrm{Be}(\gamma, \mathrm{n})2\alpha$ that have giant resonance peaks at much lower photon energies.

The full-width-at-half-maximum (FWHM) in the giant resonance cross sections typically ranges from about 3 MeV to 9 MeV. The FWHM depends on the detailed properties of absorber nuclei.

Table 7.7 provides various parameters for the "giant (γ, n) resonance" cross section for selected absorbers.

- The threshold energy represents the separation energy of a neutron from the nucleus that is of the order of 8 MeV or more, except for the deuteron

Table 7.7. Photonuclear (γ, n) giant resonance cross section parameters for selected absorbers

Absorber	Threshold energy (MeV)	Resonance peak energy $h\nu_{max}$(MeV)	Resonance FWHM (MeV)	% of total electronic cross section at $h\nu_{max}$
^{12}C	18.7	23.0	3.6	5.9
^{27}Aℓ	13.1	21.5	9.0	3.9
^{63}Cu	10.8	17.0	8.0	2.0
^{208}Pb	7.4	13.6	3.8	2.7

$(^2$H) and berillium-9 (^{9}Be) where it is at 2.22 MeV and 1.67 MeV, respectively.

- The resonance peak energy steadily decreases from 23 MeV for carbon-12 (^{12}C) with increasing Z.
- The magnitude of the atomic cross section for photodisintegration $_a\sigma_{PN}$, even at the resonance peak energy $h\nu_{max}$, is relatively small in comparison with the sum of competing "electronic" cross sections and amounts to only a few percent of the total "electronic" cross section. As a result, $_a\sigma_{PN}$ is usually neglected in photon attenuation studies in medical physics.

While the photonuclear reactions do not play a role in general photon attenuation studies, they are of considerable importance in shielding calculations whenever photon energies exceed the photonuclear reaction threshold. Neutrons produced through the (γ, n) photonuclear reactions are usually far more penetrating than the photons that produced them. In addition, the daughter nuclei resulting from the (γ, n) reaction may be radioactive and the neutrons, through subsequent neutron capture, may produce radioactivity in the irradiation facility, adding to radiation hazard in the facility. This raises concern over the induced radioactivity in clinical high-energy linear accelerator installations (above 10 MV) and results in choice of appropriate machine components to decrease the magnitude and half-life of the radioactivation as well as adequate treatment room ventilation to expel the nitrogen-13 and oxygen-15 produced in the room (typical air exchanges in treatment rooms are of the order of six to eight per hour).

7.8 General Aspects of Photon Interaction with Absorbers

The most important parameter used for characterization of x-ray or gamma ray penetration into absorbing media is the linear attenuation coefficient μ. This coefficient depends on energy $h\nu$ of the photon and atomic number Z of the absorber, and may be described as the probability per unit path length that a photon will have an interaction with the absorber.

7.8.1 Narrow Beam Geometry

The attenuation coefficient μ is determined experimentally using the so-called *narrow beam geometry* technique that implies a narrowly collimated source of monoenergtic photons and a narrowly collimated detector. As shown in Fig. 7.31a, a slab of absorber material of thickness x is placed between the source and detector. The absorber decreases the detector signal (intensity) from $I(0)$ that is measured without the absorber in place to $I(x)$ that is measured with absorber thickness x in the beam.

A layer of thickness dx' within the absorber reduces the beam intensity by dI and the fractional reduction in intensity, $-dI/I$, is proportional to

- attenuation coefficient μ
- layer thickness dx'

The relationship for $-dI/I$ can thus be written as follows:

$$-dI/I = \mu dx' \tag{7.93}$$

or, after integration from 0 to x, as

$$\int_{I(0)}^{I(x)} \frac{dI}{I} = -\int_0^x \mu dx', \qquad \text{or} \qquad I(x) = I(0)e^{-\int_0^x \mu dx'}. \tag{7.94}$$

For a homogeneous medium $\mu = $ const and (7.94) reduces to the standard exponential relationship valid for monoenergetic photon beams

$$I(x) = I(0)e^{-\mu x} . \tag{7.95}$$
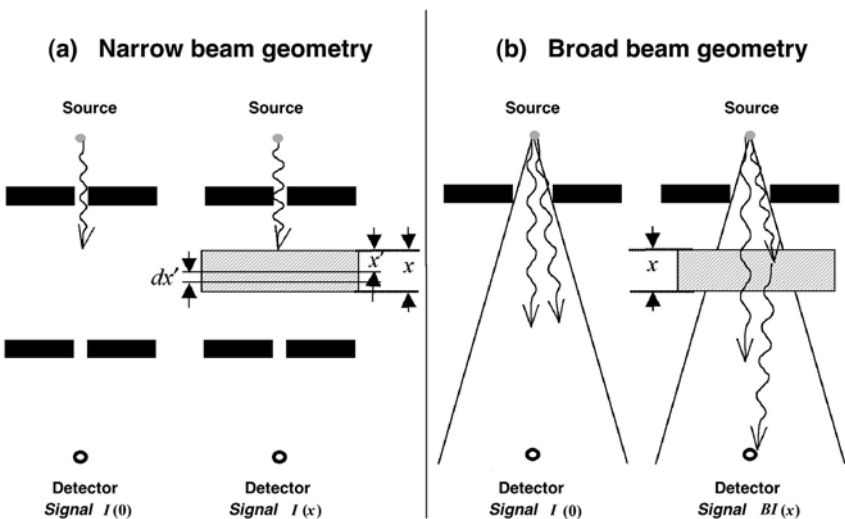
Fig. 7.31. Measurement of photon attenuation in absorbing material. Part **a** is for narrow beam geometry; part **b** is for broad beam geometry

7.8.2 Characteristic Absorber Thicknesses

Several thicknesses of special interest are defined as parameters for monoenergetic photon beam characterization in narrow beam geometry:

1. *First Half-Value Layer* (HVL_1 or $x_{1/2}$) is the thickness of a homogeneous absorber that attenuates the narrow beam intensity $I(0)$ to one half (50%) of the original intensity, i.e., $I(x_{1/2}) = 0.5I(0)$. Half-value layers are often used for characterization of superficial and orthovoltage x-ray beams. The absorbing materials used for this purpose are usually aluminum (for the superficial energy range) and copper (for the orthovoltage energy range).
2. *Mean Free Path* (MFP or $\bar{x}$) is the thickness of a homogeneous absorber that attenuates the beam intensity $I(0)$ to $1/e = 0.368$ (36.8%) of its original intensity, i.e., $I(\bar{x}) = 0.368I(0)$. The photon mean free path is the average distance a photon of energy $h\nu$ travels through a given absorber before undergoing an interaction.
3. *Tenth-Value Layer* (TVL or $x_{1/10}$) is the thickness of a homogeneous absorber that attenuates the beam intensity $I(0)$ to one tenth (10%) of its original intensity, i.e., $I(x_{1/10}) = 0.1I(0)$. Tenth-value layers are often used in radiation protection in treatment room shielding calculations.
4. *Second Half-Value Layer* (HVL_2), measured with the same homogeneous absorber material as the first half value layer (HVL_1), is defined as the thickness of the absorber that attenuates the narrow beam intensity from $0.5I(0)$ to $0.25I(0)$. The ratio between HVL_1 and HVL_2 is called the homogeneity factor χ of the photon beam.
   - When $\chi = 1$, the photon beam is monoenergetic such as a cobalt-60 beam with energy of 1.25 MeV or cesium-137 beam with energy of 0.662 MeV.
   - When $\chi \neq 1$, the photon beam possesses a spectral distribution.
   - For $\chi < 1$ the absorber is hardening the photon beam, i.e., preferentially removing low-energy photons from the spectrum (photoelectric effect region).
   - For $\chi > 1$ the absorber is softening the photon beam, i.e., preferentially removing high-energy photons from the spectrum (pair production region).

In terms of $x_{1/2}$, $\bar{x}$, and $x_{1/10}$ the linear attenuation coefficient μ may be expressed as

$$\mu = \frac{\ln 2}{x_{1/2}} = \frac{1}{\bar{x}} = \frac{\ln 10}{x_{1/10}} \ , \tag{7.96}$$

resulting in the following relationships among the characteristic thicknesses:

$$x_{1/2} = (\ln 2)\bar{x} = \frac{\ln 2}{\ln 10}x_{1/10} \equiv 0.301x_{1/10} \ . \tag{7.97}$$

The various characteristic thicknesses and their effects on photon beam intensity are summarized in Table 7.8.

Table 7.8. Characteristic absorber thicknesses and their effects upon beam intensity attenuation

Absorber thickness	$\frac{I(x)}{I(0)}$	$100\frac{I(x)}{I(0)}$	Name	Symbol
$(\ln 2)/\mu$	0.500	50.0%	Half-Value Layer	$HVL = x_{1/2}$
$1/\mu$	0.368	36.8%	Mean Free Path	$MFP = \bar{x}$
$(\ln 10)/\mu$	0.100	10.0%	Tenth-Value Layer	$TVL = x_{1/10}$
$3/\mu$	0.050	5.0%	—	—
$5/\mu$	0.0067	$\sim 0.7\%$	—	—
$7/\mu$	0.0009	$\sim 0.1\%$	—	—
$9/\mu$	0.00012	$\sim 0.012\%$	—	—

7.8.3 Other Attenuation Coefficients and Cross Sections

In addition to the *linear attenuation coefficient* μ, other related coefficients and cross sections are in use for describing photon beam attenuation characteristics, such as

- *mass attenuation coefficient* μ_m
- *atomic cross section* ${}_a\mu$
- *electronic cross section* ${}_e\mu$
- *energy transfer coefficient* μ_{tr}
- *energy absorption coefficient* μ_{ab}

The relationship among the various attenuation coefficients and cross sections is given as follows:

$$\mu = \rho\mu_m = n^{\square}{}_a\mu = Z\,n^{\square}\,({}_e\mu)\;, \tag{7.98}$$

where

ρ is the density of the absorber:
$n^{\square}$ is the number of atoms N_a per volume V of the absorber, i.e., $n^{\square} = N_a/V$, and $N_a/V = \rho N_a/m = \rho N_A/A$ with N_A the Avogadro's number of atoms per gram-atom and A the atomic mass of the absorber in g/gram-atom;
Z is the atomic number of the absorber.

Two other coefficients are in use to account for

1. the energy transferred from photons to charged particles (electrons and positrons) in a photon-atom interaction (*energy transfer coefficient* μ_{tr});
2. the energy actually absorbed by the medium (*energy absorption coefficient* μ_{ab}, often labeled as μ_{en} in the literature).

The *energy transfer coefficient* μ_{tr} is defined as follows:

$$\mu_{tr} = \mu\overline{E}_{tr}/(h\nu)\;, \tag{7.99}$$

where $\overline{E}_{tr}$ is the average energy transferred from the primary photon with energy $h\nu$ to kinetic energy of charged particles (electrons and positrons).

The *energy absorption coefficient* μ_{ab} is similarly defined as

$$\mu_{ab} = \mu\overline{E}_{ab}/(h\nu) , \tag{7.100}$$

where $\overline{E}_{ab}$ is the average energy absorbed in the volume-of-interest in the medium.

The average energy absorbed in the volume-of-interest in the medium is equal to

$$\bar{E}_{ab} = \bar{E}_{tr} - \bar{E}_{rad} , \tag{7.101}$$

where $\bar{E}_{rad}$ is the average energy component of $\bar{E}_{tr}$ that the charged particles lose in the form of radiative collisions and is thus not absorbed in the volume-of-interest.

- The energy absorption coefficient μ_{ab} can now be written in terms of the energy transfer coefficient μ_{tr} as follows:

$$\mu_{ab} = \mu\frac{\bar{E}_{ab}}{h\nu} = \mu\frac{\bar{E}_{tr} - \bar{E}_{rad}}{h\nu} = \mu_{tr} - \mu_{tr}\frac{\bar{E}_{rad}}{\bar{E}_{tr}} = \mu_{tr}(1-\bar{g}) , \tag{7.102}$$

  where $\bar{g}$ represents the so-called *radiative fraction*, i.e., the average fraction of the energy lost in radiative interactions by the secondary charged particles as they travel through the absorbing medium. These radiative interactions are the bremsstrahlung production (for electrons and positrons) and in-flight annihilation (for positrons).
- The in-flight annihilation is usually ignored and the radiative fraction is often referred to as the bremsstrahlung fraction. As discussed in Sect. 5.7, the radiative fraction $\bar{g}$ is the average value of the radiation yields $B(E_{Ko})$ for the spectrum of all electrons and positrons of various starting energies E_{Ko} produced or released in the medium by primary photons.

Table 7.9 lists the various attenuation coefficients and cross-sections, their relationship to the linear attenuation coefficient and their units.

7.8.4 Broad Beam Geometry

In contrast to the narrow beam geometry that is used in determination of the various attenuation coefficients and cross sections for photon beam attenuation, one can also deal with broad beam geometry in which the detector reading is not only decreased through attenuation of the primary photon beam in the absorber, it is also increased by the radiation scattered from the absorber into the detector. The geometry for a broad beam experiment on photon attenuation in an absorber is shown in Fig. 7.31b.

Table 7.9. Attenuation coefficients and cross sections used in photon attenuation studies

	Symbol	Relationship to μ	Units
Linear attenuation coefficient	μ	μ	cm^{-1}
Mass attenuation coefficient	μ_m	μ/ρ [a]	cm^2/g
Atomic cross-section	$_a\mu$	$\mu/n^{\square}$ [b]	$cm^2/atom$
Electronic cross-section	$_e\mu$	$\mu/(Zn^{\square})$ [c]	$cm^2/electron$

[a] ρ is the density of the absorber,
[b] $n^{\square}$ is the number of atoms per unit volume of the absorber, i.e., $n^{\square} = \rho N_A/A$,
[c] $Zn^{\square}$ is the number of electrons per unit volume of absorber, i.e., $Zn^{\square} = \rho Z N_A/A$.

The signal measured by the detector for an absorber thickness x is then equal to $BI(x)$ where:

$I(x)$ is the narrow beam geometry signal for absorber thickness x,
B is the so-called *build-up factor* that accounts for the secondary photons that are scattered from the absorber into the detector.

Broad beam geometry is used in radiation protection for design of treatment room shielding and in beam transport studies.

7.8.5 Classification of Photon Interactions

As discussed in previous sections and summarized in Table 7.10, there are numerous options available to photons for interacting with matter. The photon interactions may be classified according to the *type of target* and *type of event.*

- As shown in Table 7.11, according to the *type of target* there are two possibilities for photon interaction with an atom:
  – photon/orbital electron interaction,

Table 7.10. Most important photon interactions with atoms of the absorber

Interaction	Symbol for electronic cross section	Symbol for atomic cross section	Symbol for linear attenuation coefficient
Thomson scattering	$_e\sigma_{Th}$	$_a\sigma_{Th}$	σ_{Th}
Rayleigh scattering	-	$_a\sigma_R$	σ_R
Compton scattering	$_e\sigma_c$	$_a\sigma_c$	σ_C
Photoelectric effect	-	$_a\tau$	τ
Pair production	-	$_a\kappa_{pp}$	κ_p
Triplet production	$_e\kappa_{tp}$	$_a\kappa_{tp}$	κ_t
Photodisintegration	-	$_a\sigma_{pn}$	σ_{pn}

Table 7.11. Types of targets in photon interactions with atoms

Photon-orbital electron interactions	Photon-nucleus interactions
— with bound electrons	— with nucleus directly
Photoelectric effect	*Photodisintegration*
Rayleigh scattering	
— with "free" electrons	— with Coulomb field of nucleus
Thomson scattering	*Pair production*
Compton scattering	
— with Coulomb field of electron	
Triplet production	

Table 7.12. Types of photon-atom interactions

Complete absorption of photon	Photon scattering
Photoelectric effect	Thomson scattering
Pair production	Rayleigh scattering
Triplet production	Compton scattering
Photodisintegration	

–   photon/nucleus interaction.

•   As shown in Table 7.12, according to the *type of event* there are two
    possibilities for photon interaction with an atom:
    –   complete absorption of the photon,
    –   scattering of the photon.

As far as medical physics is concerned, photon interactions are classified into
four categories:

1. *Interactions of major importance:*
    –   Photoelectric effect
    –   Compton scattering by free electron
    –   Pair production (including triplet production)

2. *Interactions of moderate importance:*
    –   Rayleigh scattering
    –   Thomson scattering by free electron

3. *Interactions of minor importance:*
    –   Photonuclear reactions

4. *Negligible interactions:*
    –   Thomson scattering by the nucleus
    –   Compton scattering by the nucleus

– Meson production
– Delbrück scattering

7.8.6 Mass Attenuation Coefficient of Compounds and Mixtures

The mass attenuation coefficient μ/ρ for a compound or mixture is approximated by a summation of a weighted average of its constituents, i.e.,

$$\frac{\mu}{\rho} = \sum_i w_i \frac{\mu_i}{\rho} \;, \tag{7.103}$$

where

w_i is the proportion by weight of the i-th constituent,
μ_i/ρ is the mass attenuation coefficient of the i-th constituent.

7.8.7 Tabulation of Attenuation Coefficients

The attenuation coefficients and cross sections listed in Table 7.10 have specific values for a given photon energy $h\nu$ and absorber atomic number Z, and these values represent a sum of values for all individual interactions that a photon may have with an atom (photonuclear reactions are usually neglected).

Thus, for an absorber with density ρ, atomic number Z, and atomic mass A, we write the following relationships for the linear attenuation coefficient μ, mass attenuation coefficient μ_m, atomic cross section $_a\mu$, and electronic cross-section $_e\mu$:

$$\mu = \tau + \sigma_R + \sigma_c + \kappa \;, \tag{7.104}$$

$$\mu_m = \mu/\rho = (\tau + \sigma_R + \sigma_c + \kappa)/\rho \;, \tag{7.105}$$

$$\begin{aligned} _a\mu &= \frac{\mu}{\rho}\frac{A}{N_A} = \frac{1}{\rho}\frac{A}{N_A}(\tau + \sigma_R + \sigma_c + \kappa) \\ &= {}_a\tau + {}_a\sigma_R + {}_a\sigma_c + {}_a\kappa \;, \end{aligned} \tag{7.106}$$

$$_e\mu = \frac{\mu}{\rho}\frac{A}{ZN_A} = \frac{1}{\rho}\frac{A}{ZN_A}(\tau + \sigma_R + \sigma_c + \kappa) \;, \tag{7.107}$$

where

τ is the linear attenuation coefficient for photoelectric effect,
σ_R is the linear attenuation coefficient for Rayleigh scattering,
σ_c is the linear attenuation coefficient for Compton effect,
κ is the linear attenuation coefficient for pair production (including triplet).

In Fig. 7.32 we show the total mass attenuation coefficients μ/ρ for carbon in part a and lead in part b, plotted against the photon energy $h\nu$. In addition to μ/ρ that represents the sum of the individual coefficients for the photo-electric effect, Rayleigh scattering, Compton scattering and pair production, the coefficients for the individual components are also shown. Also shown are the absorption edges for the lead attenuator; the absorption edges for the carbon attenuator are not visible, because they occur off-scale at energies below 1 keV.

Figure 7.33 is a plot on a $(Z, h\nu)$ diagram of the relative predominance of the three major photon interactions with atoms: photoelectric effect, Compton scattering, and pair production for various absorbers with $Z = 1$ to $Z = 100$. The *two curves* on the graph represent the loci of points in the $(Z, h\nu)$ diagram for which either $_a\tau = {_a\sigma_c}$ or $_a\sigma_c = {_a\kappa}$, i.e., the *left hand curve* represents $(Z, h\nu)$ points for which the photoelectric atomic cross section $_a\tau$ equals the Compton atomic cross section $_a\sigma_c$ and the *right hand curve* represents $(Z, h\nu)$ points for which the Compton atomic cross section $_a\sigma_c$ equals the pair production atomic cross section $_a\kappa$.

From Figs. 7.32 and 7.33 the following conclusions may be made:

- At low photon energies ($h\nu < 100$ keV) and high atomic numbers Z the photoeffect mass coefficient τ/ρ predominates and makes the largest contribution to the total mass attenuation coefficient μ/ρ.
- At intermediate photon energies and low atomic numbers Z the Compton effect mass coefficient σ_c/ρ predominates and makes the largest contribution to the total mass attenuation coefficient μ/ρ.
- The width of the region of Compton scattering predominance depends on the atomic number Z of the absorber; the lower is Z, the broader is the Compton scattering predominance region. For water and tissue this region ranges from $\sim$20 keV up to $\sim$20 MeV, indicating that for most of radiotherapy the most important interaction of photon beams with tissues is the Compton scattering.
- The pair production dominates at photon energies $h\nu$ above 10 MeV and at high atomic numbers Z of the absorber.
- In all energy regions the Rayleigh scattering mass coefficient σ_R/ρ plays only a secondary role in comparison with the other three coefficients.

7.8.8 Energy Transfer Coefficient

The energy transfer coefficient μ_{tr} consist of three components, each of them representing a photon-atom interaction in which all or part of the photon energy $h\nu$ is transferred to charged particles (electrons or positrons). Rayleigh scattering transfers no energy to charged particles in the absorber and the interactions that generally result in energy transfer to charged particles are the photoelectric effect, Compton scattering and pair production. The energy transfer coefficient μ_{tr} is the sum of the energy transfer coefficients for the
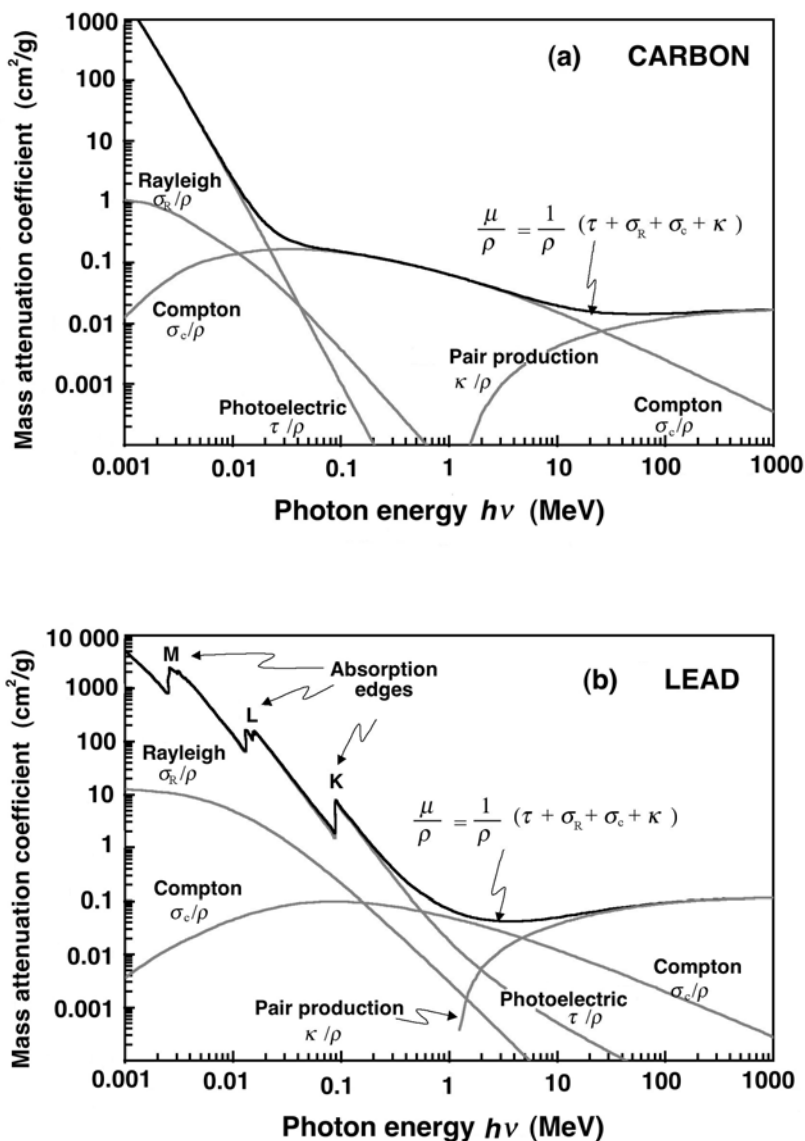
Fig. 7.32. Mass attenuation coefficient μ/ρ against photon energy $h\nu$ in the range from 1 keV to 1000 MeV for carbon in part **a** and lead in part **b**. In addition to the total coefficient μ/ρ, the individual coefficients for photoelectric effect, Rayleigh scattering, Compton scattering, and pair production (including triplet production) are also shown. The mass attenuation coefficient μ/ρ is the sum of the coefficients for individual effects, i.e., $\mu/\rho = (\tau + \sigma_{\mathrm{R}} + \sigma_{\mathrm{c}} + \kappa)/\rho$
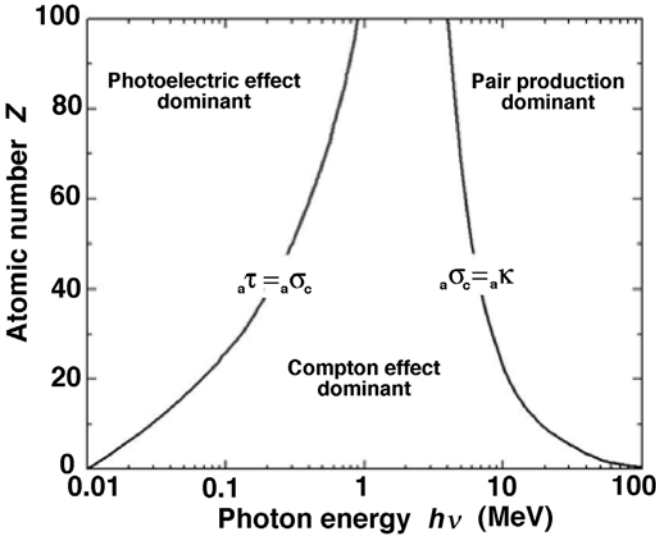
Fig. 7.33. Regions of relative predominance of the three main processes of photon interactions with an absorber: photoelectric effect, Compton scattering, and pair production. The *left curve* represents the loci of points on the $(Z, h\nu)$ diagram where the atomic cross section for photoelectric effect equals the atomic cross section for Compton scattering, i.e., $_a\tau = {_a\sigma_c}$. The *right curve* represents the loci of points on the $(Z, h\nu)$ diagram where the atomic cross section for Compton scattering equals the atomic cross section for pair production, i.e., $_a\sigma_c = {_a\kappa}$

three individual effects, i.e.,

$$
\begin{aligned}
\mu_{\text{tr}} &= \mu \frac{\overline{E}_{\text{tr}}}{h\nu} = \tau_{\text{tr}} + (\sigma_c)_{\text{tr}} + \kappa_{\text{tr}} = \\
&= \tau \frac{\overline{E}_{\text{tr}}^{\tau}}{h\nu} + \sigma_c \frac{\overline{E}_{\text{tr}}^{\sigma}}{h\nu} + \kappa \frac{\overline{E}_{\text{tr}}^{\kappa}}{h\nu} = f^{\tau}\tau + f^{\sigma}\sigma + f^{\kappa}\kappa = \\
&= \tau \left\{ 1 - \frac{P_K \omega_K \overline{h\nu}_K}{h\nu} \right\} + \sigma_c \frac{\overline{E}_{\text{tr}}^{\sigma}}{h\nu} + \kappa \left\{ 1 - \frac{2m_e c^2}{h\nu} \right\},
\end{aligned}
\tag{7.108}
$$

where

$\overline{E}_{\text{tr}}^{\tau}$ is the average energy transferred to electrons (photoelectron and Auger electrons) in a photoelectric effect process,

$\overline{E}_{\text{tr}}^{\sigma}$ is the average energy transferred to recoil electron in a Compton effect process,

$\overline{E}_{\text{tr}}^{\kappa}$ is the average energy transferred to electron and positron in a pair production process (including triplet production).

$\bar{f}^{\tau} = 1 - P_K \omega_K \overline{h\nu}_K / (h\nu)$ is the average fraction of the photon energy given to the photoelectron and Auger electrons in a pho-
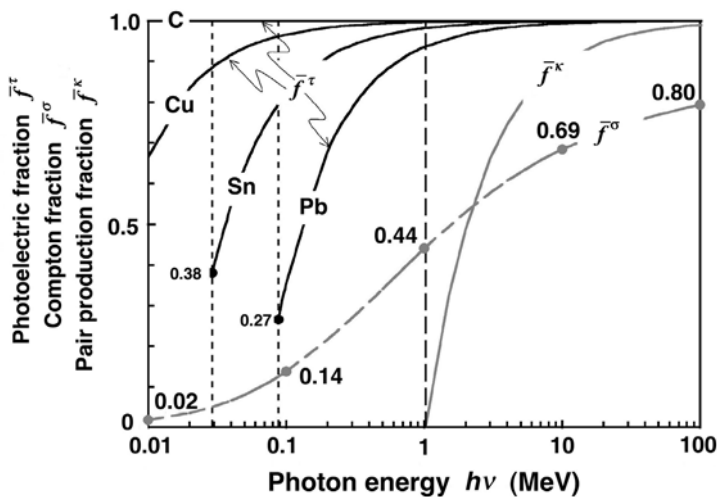
Fig. 7.34. Average energy transfer fractions $\bar{f}^{\tau}$, $\bar{f}^{\sigma}$, and $\bar{f}^{\kappa}$ for photoelectric effect, Compton effect and pair production, respectively, for carbon, copper, tin, and lead. Only the photoeffect fraction $\bar{f}^{\tau}$ depends on the atomic number Z of the absorber; the Compton effect and pair production fractions are independent of Z and depend only on photon energy $h\nu$

	toelectric effect interaction (for photons with energy above the K edge of the absorbing medium).
$\bar{f}^{\sigma} = \overline{E}_{\mathrm{tr}}^{\sigma}/(h\nu)$	is the average fraction of the photon energy given to the recoil (Compton) electron in a Compton interaction (see Fig. 7.8).
$\bar{f}^{\kappa} = 1 - 2m_{e}c^{2}/(h\nu)$	is the average fraction of the photon energy given to the electron/positron pair in a pair production interaction (including triplet production).

Figure 7.34 summarizes the three energy fractions $\bar{f}^{\tau}$, $\bar{f}^{\sigma}$, and $\bar{f}^{\kappa}$ for energy transfer in an absorber from photon to charged particles in photoelectric effect, Compton scattering, and pair production, respectively.

- All three fractions depend upon photon energy $h\nu$, increase with increasing photon energy $h\nu$, and converge to 1 at large $h\nu$.
- The photoelectric fraction $\bar{f}^{\tau}$ also depends on the atomic number Z of the absorber; the higher is Z, the lower is $\bar{f}^{\tau}$ in the vicinity of the absorption edge and the slower is the convergence to 1. The photoelectric fraction $\bar{f}^{\tau}$ was given in Fig. 7.25.
- The Compton Klein-Nishina fraction $\bar{f}^{\sigma}$ and the pair production fraction $\bar{f}^{\kappa}$ are independent of Z and depend on photon energy $h\nu$ only. The Compton Klein-Nishina fraction $\bar{f}^{\sigma}$ and the pair production fraction $\bar{f}^{\kappa}$ are given in Figs. 7.8 and 7.29, respectively.

From (7.108) we note that $\overline{E}_{tr}$, the average energy transferred to charged particles, is in general given as

$$\overline{E}_{tr} = h\nu\frac{\mu_{tr}}{\mu} = \sum_i w_i \overline{E}_{tr}^i = \frac{\tau}{\mu}\overline{E}_{tr}^\tau + \frac{\sigma_c}{\mu}\overline{E}_{tr}^\sigma + \frac{\kappa}{\mu}\overline{E}_{tr}^\kappa$$

$$= w_\tau \overline{E}_{tr}^\tau + w_\sigma \overline{E}_{tr}^\sigma + w_\kappa \overline{E}_{tr}^\kappa$$

$$= \frac{\tau}{\mu}(h\nu - P_K\omega_K\overline{h\nu}_K) + \frac{\sigma_c}{\mu}\overline{E}_{tr}^\sigma + \frac{\kappa}{\mu}(h\nu - 2m_e c^2) , \qquad (7.109)$$

where

i   refers to a particular interaction of the photon with an atom of the absorber,

w_i is the weight of the particular interaction i of photon with absorber atoms.

Figure 7.35 gives a plot of the mass energy transfer coefficient μ_{tr}/ρ for carbon and lead in the photon energy range from 1 keV to 100 MeV. The mass attenuation coefficient μ/ρ is shown with dashed curves for comparison.

- For lead the K, L, and M absorption edges are visible, for carbon they are not because they all occur below the lower 1 keV limit of the graph.
- At photon energies between 1 keV and 10 keV in the photoeffect region $\mu/\rho \approx \mu_{tr}/\rho \approx \mu_{ab}/\rho$.
- At intermediate photon energies in the Compton region the Compton fraction $\bar{f}^\sigma$ correction to μ/ρ is very effective (see Fig. 7.34) and clearly separates μ/ρ from μ_{tr}/ρ.
- At very high photon energies in the pair production region the pair production fraction is 1 and $\mu/\rho \approx \mu_{tr}/\rho$ (see Fig. 7.34).

7.8.9 Energy Absorption Coefficient

The energy absorption coefficient μ_{ab} is related to the energy transfer coefficient μ_{tr} by

$$\mu_{ab} = \mu_{tr}(1 - \bar{g}) , \qquad (7.110)$$

with $\bar{g}$ representing the so-called *radiative fraction*, i.e., the average fraction of secondary charged particle energy lost in radiative interactions that the secondary charged particles experience in their travel through the absorbing medium. These radiative interactions are the bremsstrahlung production (for electrons and positrons) and in-flight annihilation (for positrons).

- For low absorber atomic number Z and low photon energies $h\nu$ the radiative fraction $\bar{g}$ approaches zero and $\mu_{tr} \approx \mu_{ab}$.
- For increasing Z or $h\nu$ the radiative fraction $\bar{g}$ increases gradually, so that, for example, in lead at $h\nu = 10$ MeV, $\bar{g} = 0.26$ and $\mu_{ab} = 0.74\,\mu_{tr}$.

Figure 7.35 also shows, in addition to the mass attenuation coefficient μ/ρ and mass energy transfer coefficient μ_{tr}/ρ, the mass energy absorption
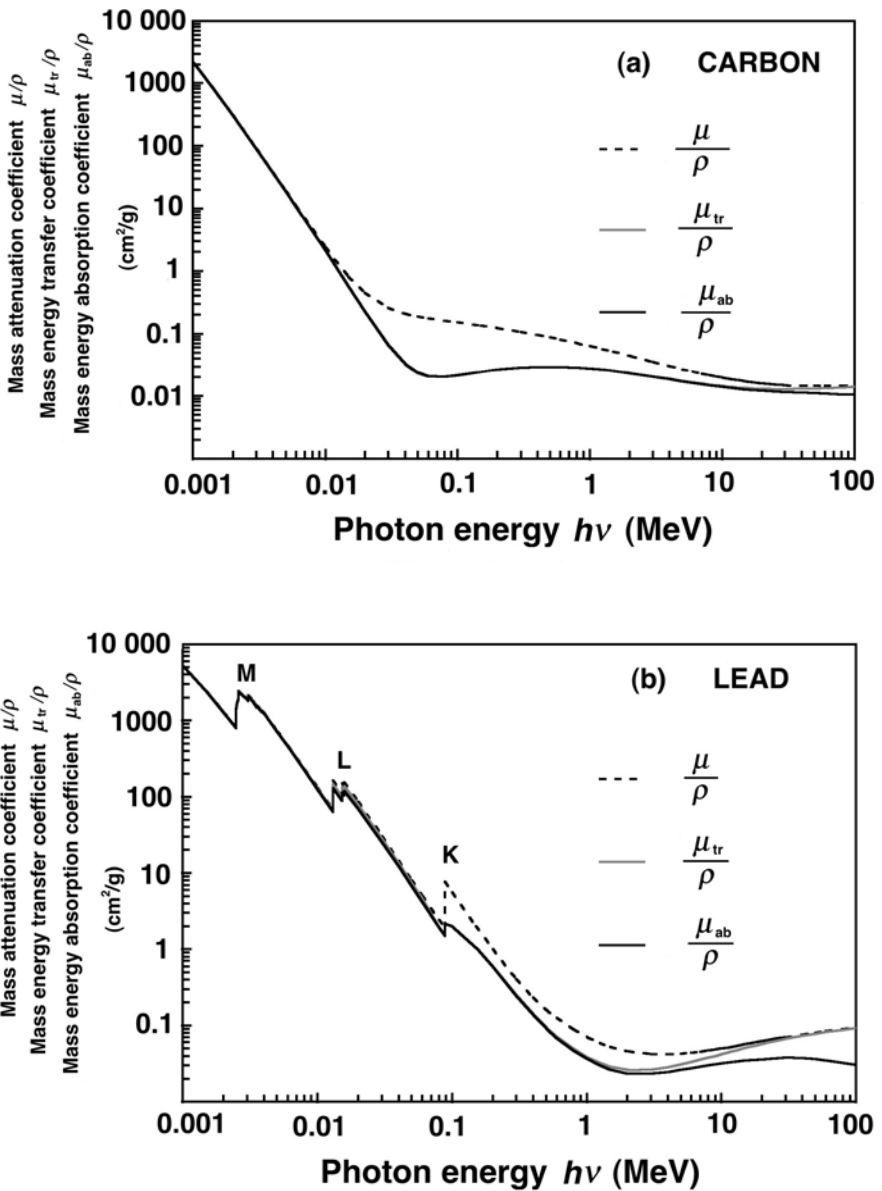
Fig. 7.35. Mass energy transfer coefficient μ_{tr}/ρ (*dark solid curves*), mass attenuation coefficient μ/ρ (*dashed curves*) and mass energy absorption coefficient μ_{ab}/ρ (*light solid curves*) against photon energy $h\nu$ for carbon in part **a** and lead in part **b**

coeffecient μ_{ab}/ρ for carbon and lead in the photon energy range from 1 keV to 100 MeV.

The following interesting observations can be made:

- The K, L, and M absorption edges are clearly visible in the plots for lead. The plots for carbon, on the other hand, do not exhibit any absorption edges because the edges occur below 1 keV in the energy range that is not shown.
- Up to a photon energy of a few MeV, $\mu_{tr}/\rho \approx \mu_{ab}/\rho$.
- At photon energies above 10 MeV, μ_{ab}/ρ diverges from μ_{tr}/ρ because of the radiative loss $\bar{g}$ of charged particles released in the medium by the high-energy photons. With an increasing photon energy the radiative fraction $\bar{g}$ increases and so does the difference between μ_{ab}/ρ and μ_{tr}/ρ.
- The radiative fraction $\bar{g}$ also depends on the atomic number Z of the absorber; the higher is Z, the higher is $\bar{g}$ for the same photon energy, as indicated in Fig. 7.35. For example, at a photon energy of 10 MeV, $\bar{g} = 0.035$ for carbon and $\bar{g} = 0.26$ for lead; at 100 MeV, $\bar{g} = 0.25$ for carbon and $\bar{g} = 0.67$ for lead.

7.8.10 Effects Following Photon Interactions

In photoelectric effect, Compton effect, and triplet production vacancies are produced in atomic shells through the ejection of orbital electrons.

- For orthovoltage and megavoltage photons used in diagnosis and treatment of disease with radiation, the shell vacancies occur mainly in inner atomic shells of the absorber.
- Pair production, Rayleigh scattering and photodisintegration do not produce shell vacancies.
- Vacancies in inner atomic shells are not stable; they are followed by emission of characteristic x rays or Auger electrons depending on the fluorescent yield of the absorbing material and cascade to the outer shell of the ion. The ion eventually attracts an electron from its surroundings and becomes a neutral atom.
- Pair production and triplet production are followed by the annihilation of the positron with an orbital electron of the absorber, most commonly producing two annihilation quanta of 0.511 MeV each and moving at approximately 180º to each other. Annihilation of a positron before it expanded all of its kinetic energy is referred to as annihilation-in-flight and may produce photon exceeding 0.511 MeV.

7.9 Summary of Photon Interactions

As is evident from discussions in this chapter, photons have numerous options for interaction with absorbers. The probabilities for interaction in general depend on the incident photon energy $h\nu$ and the atomic number Z of

the absorber. While over a dozen different photon interactions are known in nuclear physics, four of these are of importance to medical physics because they govern: (1) the transfer of energy from photons to light charged particles and the ultimate absorption of energy in irradiated tissues (radiation dosimetry) and (2) the attenuation and scattering of photons by tissues (imaging physics). The four important photon interactions are:

1. Photoelectric effect
2. Rayleigh scattering
3. Compton effect
4. Pair production

Photoelectric Effect

- The photoelectric effect (sometimes also referred to as photoeffect) is an interaction between a photon with energy $h\nu$ and a tightly bound orbital electron of an absorber atom. The interaction is thus between a photon and an absorber atom as a whole. The electron is ejected from the atom and referred to as a photoelectron.
- A tightly bound orbital electron is defined as an orbital electron with binding energy E_B either larger than $h\nu$ or of the order of $h\nu$. For $E_B > h\nu$ the photoeffect cannot occur; for $h\nu > E_B$ the photoelectric effect is possible. The closer is $h\nu$ to E_B, the larger is the probability for photoelectric effect to happen, provided, of course, that $h\nu$ exceeds E_B. At $h\nu = E_B$ the probability abruptly drops and exhibits the so-called absorption edge.
- When the photon energy $h\nu$ exceeds the K-shell binding energy E_B (K) of the absorber atoms, the photoelectric effect is most likely to occur with a K-shell electron in comparison with higher shell electrons. Over 80% of all photoelectric interactions occur with K-shell electrons when $h\nu \geq E_B(K)$.
- With increasing incident photon energy $h\nu$, the atomic, linear, and mass photoelectric attenuation coefficients decrease from their absorption edge value approximately as $1/(h\nu)^3$.
- The atomic photoelectric attenuation coefficient $_a\tau$ varies approximately as Z^5 for low Z absorbers and as Z^4 for high Z absorbers.
- The mass photoelectric attenuation coefficient $\tau_m = \tau/\rho$ varies approximately as Z^4 for low Z absorbers and as Z^3 for high Z absorbers.
- In water and tissue $\bar{E}_{tr}^\tau$, the average energy transferred to electrons (photoelectrons and Auger electrons) is equal to $\bar{E}_{ab}^\tau$, the average energy absorbed in the medium because the radiative fraction $\bar{g}$ is negligible; i.e., $\bar{g} \approx 0$.
- Furthermore, in water and tissue $\bar{E}_{tr}^\tau$ is approximately equal to the photon energy $h\nu$ because the fluorescent yield ω_K is approximately equal to zero. Thus in water and tissue the following relationship holds for the photoelectric effect: $\bar{E}_{tr}^\tau = \bar{E}_{ab}^\tau \approx h\nu$.

Rayleigh Scattering

- Rayleigh scattering is an interaction between a photon with energy $h\nu$ and the whole atom. All orbital electrons contribute to the scattering event and the phenomenon is referred to as coherent scattering because the photon is scattered by the constructive action of the tightly bound electrons of the whole atom.
- The photon leaves the point of interaction with the incident energy $h\nu$ intact but is redirected through a small scattering angle. Since no energy is transferred to charged particles, Rayleigh scattering plays no role in radiation dosimetry; however, it is of some importance in imaging physics because the scattering event has an adverse effect on image quality.
- The atomic Rayleigh attenuation coefficient $_a\sigma_R$ decreases approximately as $1/(h\nu)^2$ and is approximately proportional to Z^2 of the absorber.
- Even at very small incident photon energies $h\nu$, the Rayleigh component of the total attenuation coefficient is small and amounts to only a few percent.

Compton Effect

- Compton effect (often referred to as Compton scattering) is an interaction between a photon with energy $h\nu$ and a free orbital electron.
- A free electron is defined as an orbital electron whose binding energy E_B is much smaller than the photon energy $h\nu$; i.e., $h\nu \gg E_B$.
- In each Compton interaction a scattered photon and a free electron (referred to as Compton or recoil electron) are produced. The sum of the scattered photon energy $h\nu'$ and the Compton recoil electron kinetic energy E_K is equal to the incident photon energy $h\nu$. The relative distribution of the two energies depends on the incident photon energy $h\nu$ and on the angle of emission (scattering angle θ) of the scattered photon.
- The electronic and mass Compton attenuation coefficients $_e\sigma_c$ and σ_c/ρ, respectively, are essentially independent of the atomic number Z of the absorber.
- The atomic Compton attenuation coefficient $_a\sigma_c$ is linearly proportional to the atomic number Z of the absorber.
- The atomic and mass Compton attenuation coefficients $_a\sigma_c$ and σ_c/ρ, respectively, decrease with increasing incident photon energy $h\nu$.
- The average fraction of the incident photon energy $h\nu$ transferred to recoil electron increases with $h\nu$ (see *The Graph* in Fig. 7.8). At low photon energies the Compton energy transfer coefficient $(\sigma_c)_{tr}$ is much smaller than the Compton attenuation coefficient σ_c; i.e., $(\sigma_c)_{tr} \ll \sigma_c$. At high photon energies, on the other hand, $(\sigma_c)_{tr} \approx \sigma_c$.
- In water and tissue the Compton process is the predominant mode of photon interaction in the wide photon energy range from $\sim$100 keV to $\sim$10 MeV (see Fig. 7.33).

Pair Production

- Pair production is an interaction between a photon with energy $h\nu$ exceeding $2m_\mathrm{e}c^2 = 1.02$ MeV and the Coulomb field of a nucleus. The photon disappears and an electron-positron pair is produced. The process is an example of mass-energy equivalence and is sometimes referred to as materialization.
- Pair production in the Coulomb field of an orbital electron of the absorber is referred to as triplet production. The process is much less probable than nuclear pair production and has threshold energy of $4m_\mathrm{e}c^2 = 2.044$ MeV. The photon disappears and three light charged particles are released: the orbital electron and the electron-positron pair.
- The probability for pair production increases rapidly with the incident photon energy $h\nu$ for photon energies above the threshold energy.
- The atomic pair production attenuation coefficient $_\mathrm{a}\kappa$ varies approximately as Z^2 of the absorber.
- The mass pair production coefficient $\kappa_\mathrm{m} = \kappa/\rho$ varies approximately linearly with the atomic number Z of the absorber.
- The average energy transferred from the incident photon $h\nu$ to charged particles, $\bar{E}_\mathrm{tr}^\kappa$, is $h\nu - 2m_\mathrm{e}c^2$.

Table 7.13 provides a summary of the main characteristics for the photoelectric effect, Rayleigh scattering, Compton effect, and pair production.

7.10 Example 1: Interaction of 2 MeV Photons with Lead

For *2 MeV photons in lead* ($Z = 82$; $A = 207.2$ g/g-atom; $\rho = 11.36$ g/cm^3) the photoeffect, coherent scattering, Compton effect, and pair production linear attenuation coefficients are: $\tau = 0.055$ cm^{-1}, $\sigma_\mathrm{R} = 0.008$ cm^{-1}, $\sigma_\mathrm{c} = 0.395$ cm^{-1}, and $\kappa = 0.056$ cm^{-1}. The average energy transferred to charged particles $\bar{E}_\mathrm{tr} = 1.13$ MeV and the average energy absorbed in lead is $\bar{E}_\mathrm{ab} = 1.04$ MeV.

Calculate the linear attenuation coefficient μ; mass attenuation coefficient μ_m; atomic attenuation coefficient $_\mathrm{a}\mu$; mass energy transfer coefficient μ_tr; mass energy absorption coefficient μ_ab; and radiative fraction $\bar{g}$.

$$\begin{aligned}\mu &= \tau + \sigma_\mathrm{R} + \sigma_\mathrm{c} + \kappa = (0.055 + 0.008 + 0.395 + 0.056) \text{ cm}^{-1}\\ &= 0.514 \text{ cm}^{-1}\end{aligned} \tag{7.111}$$

$$\mu_\mathrm{m} = \frac{\mu}{\rho} = \frac{0.514 \text{ cm}^{-1}}{11.36 \text{ g/cm}^3} = 0.0453 \text{ cm}^2/\text{g} \tag{7.112}$$

Table 7.13. Main characteristics of photoelectric effect, Rayleigh scattering, Compton effect, and pair production

	Photoeffect	Rayleigh scattering	Compton effect	Pair production
Photon interaction	With whole atom (bound electron)	With bound electrons	With free electron	With nuclear Coulomb field
Mode of photon interaction	Photon disappears	Photon scattered	Photon scattered	Photon disappears
Energy dependence	$\dfrac{1}{(h\nu)^3}$	$\dfrac{1}{(h\nu)^2}$	Decreases with energy	Increases with energy
Threshold	Shell binding energy	No	Shell binding energy	$\sim 2m_ec^2$
Linear attenuation coefficient	τ	σ_R	σ_c	κ
Atomic coefficient dependence on Z	$_a\tau \propto Z^4$	$_a\sigma_R \propto Z^2$	$_a\sigma_c \propto Z$	$_a\kappa \propto Z^2$
Mass coefficient dependence on Z	$\dfrac{\tau}{\rho} \propto Z^3$	$\dfrac{\sigma_R}{\rho} \propto Z$	Independent of Z	$\dfrac{\kappa}{\rho} \propto Z$
Particles released in absorber	Photoelectron	None	Compton (recoil) electron	Electron-positron pair
Average energy transferred to charged part's	$h\nu - P_K\omega_K\overline{h\nu}_K$	0	$\overline{E}_{tr}^{\sigma}$ (see Fig. 7.8)	$h\nu - 2m_ec^2$
Fraction of energy $h\nu$ transferred	$1 - \dfrac{P_K\omega_K\overline{h\nu}_K}{h\nu}$	0	$\dfrac{\overline{E}_{tr}^{\sigma}}{h\nu}$	$1 - \dfrac{2m_ec^2}{h\nu}$
Subsequent effect	Characteristic x ray, Auger effect	None	Characteristic x ray, Auger effect	Annihilation radiation
Significant energy region for water	<20 keV	<20 keV	20 keV–10 MeV	>10 MeV
Significant energy region for lead	<500 keV	<100 keV	500 keV–3 MeV	>3 MeV

$$_{a}\mu = \left\{\frac{\rho N_A}{A}\right\}^{-1} \mu = \frac{207.2 \text{ (g/g-atom) } 0.514 \text{ cm}^{-1}}{11.36 \text{ g/cm}^3 \ 6.022 \times 10^{23} \text{ (atom/g-atom)}}$$

$$= 1.56 \times 10^{-23} \text{ cm}^2/\text{atom} \tag{7.113}$$

$$\frac{\mu_{tr}}{\rho} = \frac{\bar{E}_{tr}}{h\nu}\frac{\mu}{\rho} = \frac{1.13 \text{ MeV } 0.0453 \text{ cm}^2/\text{g}}{2 \text{ MeV}} = 0.0256 \text{ cm}^2/\text{g} \tag{7.114}$$

$$\frac{\mu_{ab}}{\rho} = \frac{\mu_{en}}{\rho} = \frac{\bar{E}_{ab}}{h\nu}\frac{\mu}{\rho}$$

$$= \frac{1.04 \text{ MeV} 0.0453 \text{ cm}^2/\text{g}}{2 \text{ MeV}} = 0.0236 \text{ cm}^2/\text{g} \tag{7.115}$$

$$\bar{g} = \frac{\bar{E}_{tr} - \bar{E}_{ab}}{\bar{E}_{tr}} = 1 - \frac{\bar{E}_{ab}}{\bar{E}_{tr}} = 1 - \frac{1.04 \text{ MeV}}{1.13 \text{ MeV}} = 0.08 \tag{7.116}$$

or

$$\bar{g} = 1 - \frac{\mu_{ab}/\rho}{\mu_{tr}/\rho} = 1 - \frac{0.0236 \text{ cm}^2/\text{g}}{0.0256 \text{ cm}^2/\text{g}} = 0.08. \tag{7.117}$$

The mass energy transfer coefficient μ_{tr}/ρ can also be determined using (7.108) with the appropriate average energy transfer fractions, given in Fig. 7.34, as follows:

$$\bar{f}^{\tau} = (h\nu - P_K\omega_K\overline{h\nu}_K)/(h\nu) = 0.965 , \tag{7.118}$$

$$\bar{f}^{\sigma} = \bar{E}_{tr}^{\sigma}/(h\nu) = 0.53 , \tag{7.119}$$

$$\bar{f}^{\kappa} = (h\nu - 2\,m_ec^2)/(h\nu) = 0.50 . \tag{7.120}$$

The mass energy transfer coefficient μ_{tr}/ρ is now given as follows:

$$\frac{\mu_{tr}}{\rho} = \frac{1 \text{ cm}^3}{11.36 \text{ g}} \left(0.965 \times 0.055 + 0.53 \times 0.395 + 0.50 \times 0.056\right) \text{ cm}^{-1}$$

$$= 0.0256 \frac{\text{cm}^2}{\text{g}} \tag{7.121}$$

in good agreement with the result obtained in (7.114).

Thus, as shown schematically in Fig. 7.36, a *2 MeV photon* in lead will on the average:

- *Transfer 1.13 MeV* to charged particles (electrons and positrons)
- *0.87 MeV will be scattered* through Rayleigh and Compton scattering.

Of the 1.13 MeV of energy transferred,

- *1.04 MeV will be absorbed* in lead and
- *0.09 MeV will be re-emitted* through bremsstrahlung radiative loss.

The radiative fraction $\bar{g}$ for 2 MeV photons in lead is 0.08.
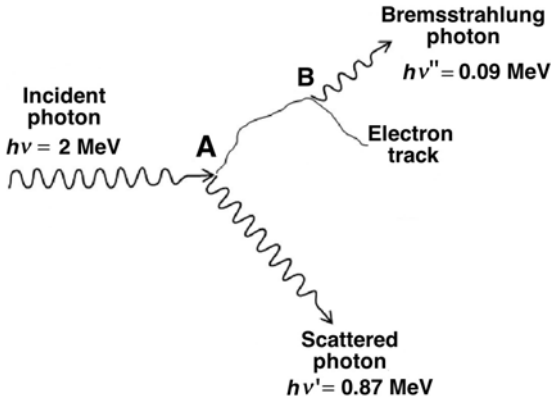
Fig. 7.36. Schematic diagram for general photon interactions with an atom. In this example a 2 MeV photon $h\nu$ interacts with a lead atom. An individual 2 MeV photon, as it encounters a lead atom at point A, may interact with the atom through photoelectric effect, Rayleigh scattering, Compton effect or pair production, or it may not interact at all. However, for a large number of 2 MeV photons striking lead, we may state that on the average:

- 1.13 MeV will be transferred at point A to charged particles (mainly to fast energetic electrons, but possibly also to positrons if the interaction is pair production);
- 0.87 MeV will be scattered through Rayleigh and Compton scattering $(h\nu')$

Of the 1.13 MeV transferred to charged particles:

- 1.04 MeV will be absorbed in lead over the fast charged particle tracks, and
- 0.09 MeV will be emitted in the form of bremsstrahlung photons $(h\nu'')$

7.11 Example 2: Interaction of 8 MeV Photons with Copper

Monoenergetic photons with energy $h\nu = 8$ MeV $(\varepsilon = 15.66)$ interact with a copper absorber $(Z = 29, A = 63.54$ g/g-atom; $\rho = 8.96$ g/cm^3). Using only the relationships and graphs given in this chapter, **determine**:

1. atomic cross section $_a\mu$
2. mass attenuation coefficient μ_m
3. linear attenuation coefficient μ
4. average energy transferred to charged particles $\overline{E}_{tr}$
5. mass energy transfer coefficient μ_{tr}/ρ
6. average radiative fraction $\bar{g}$
7. average energy absorbed in the copper absorber $\overline{E}_{ab}$
8. mass energy absorption coefficient μ_{ab}/ρ

1. To determine the total **atomic cross section $_a\mu$** we first calculate the individual atomic cross sections for photoelectric effect $_a\tau$, Compton scattering $_a\sigma_c$, and pair production $_a\kappa$. The total atomic cross section will be the sum of the three individual atomic cross sections. We ignore the atomic cross sections for Rayleigh scattering $_a\sigma_R$ and for photonuclear reactions $_a\sigma_{PN}$ because they are very small in comparison with the photoelectric, Compton and pair production cross sections.

Photoelectric Effect

Since $\varepsilon \gg 1$, we use (7.74) to estimate $_a\tau$ for K-shell electrons in copper

$$_a\tau_K = \frac{1.5}{\varepsilon}\alpha^4 Z^5 {}_e\sigma_{Th}$$

$$= \frac{1.5}{15.66}\frac{29^5}{137^4}0.665\,\frac{b}{atom} = 0.004 \text{ b/atom} \qquad (7.122)$$

Compton Effect

We use the Klein-Nishina relationship for the electronic cross section $_e\sigma_c^{KN}$, given in (7.45), and then calculate $_a\sigma_c^{KN}$ from $_a\sigma_c^{KN} = Z\,_e\sigma_c^{KN}$

$$_e\sigma_c^{KN}$$
$$= 2\pi r_e^2 \left\{ \frac{1+\varepsilon}{\varepsilon^2}\left[\frac{2(1+\varepsilon)}{1+2\varepsilon} - \frac{\ln(1+2\varepsilon)}{\varepsilon}\right] + \frac{\ln(1+2\varepsilon)}{2\varepsilon} - \frac{1+3\varepsilon}{(1+2\varepsilon)^2}\right\}$$
$$= 0.0599 \text{ b/electron} \qquad (7.123)$$

The atomic cross section is calculated from the electronic cross section as follows:

$$_a\sigma_c^{KN} = Z\,_e\sigma_c^{KN} = 29 \times 0.0599 \text{ b/atom} = 1.737 \text{ b/atom.} \quad (7.124)$$

Pair Production

Since the photon energy of 8 MeV is significantly above the nuclear pair production threshold of 1.02 MeV and also above the triplet production threshold of 2.04 MeV, both effects (pair production and triplet production) will occur and will contribute to the total atomic cross section $_a\mu$. To determine the atomic pair production cross-section we use (7.84)

$$_a\kappa_{pp} = \alpha r_e^2 Z^2 P_{pp}(\varepsilon, Z) . \qquad (7.125)$$

Since $1 \ll \varepsilon \ll \frac{1}{\alpha Z^{1/3}}$, where for our example $\varepsilon = 15.66$ and $1/(\alpha Z^{1/3}) = 44.6$, we use (7.84) to determine $P_{pp}(\varepsilon, Z)$ as follows:

$$P_{pp}(\varepsilon, Z) = \frac{28}{9}\ln(2\varepsilon) - \frac{218}{27} = 10.73 - 8.07 = 2.65 . \qquad (7.126)$$

The atomic cross-section for pair production $_a\kappa_{pp}$ is now calculated as follows:

$$_a\kappa_{pp} = \alpha r_e^2 Z^2 P_{pp}(\varepsilon, Z) = \frac{7.94 \times 10^{-2} \times 29^2 \times 2.65}{137} \frac{b}{atom}$$
$$= 1.292 \text{ b/atom.} \tag{7.127}$$

To account for the *triplet production* contribution we use (7.90) to get

$$_a\kappa = {}_a\kappa_{pp} \left\{ 1 + \frac{1}{\eta Z} \right\} = 1.292 \frac{b}{atom} \left\{ 1 + \frac{1}{2.5 \times 29} \right\}$$
$$= 1.310 \text{ b/atom.} \tag{7.128}$$

Two observations can now be made:
- For 8 MeV photons interacting with copper, triplet production contributes only of the order of 1.5% to the total atomic pair production cross section.
- The atomic cross-sections $_a\sigma_c$ and $_a\kappa$ for Compton scattering and pair production, respectively, are almost identical. This can actually be surmised from Fig. 7.33 that shows the loci of points $(Z, h\nu)$ for which $_a\tau = {}_a\sigma_c$ and $_a\sigma_c = {}_a\kappa$. The point $(Z = 29, h\nu = 8 \text{ MeV})$ is very close to the $_a\sigma_c = {}_a\kappa$ curve and thus must possess similar atomic cross-sections $_a\sigma_c$ and $_a\kappa$.

The total *atomic cross section* $_a\mu$ is the sum of the cross sections for individual non-negligible effects, as given in (7.106)

$$_a\mu = {}_a\tau + {}_a\sigma_R + \sigma_c + {}_a\kappa = (0.004 + 0 + 1.737 + 1.310)\text{b/atom}$$
$$= 3.051 \text{ b/atom .} \tag{7.129}$$

2. The **mass attenuation coefficient μ_m** is calculated, as suggested in (7.98), from

$$\mu_m = \frac{\mu}{\rho} = {}_a\mu \frac{N_A}{A} = 3.051 \frac{b}{atom} \frac{6.022 \times 10^{23} \text{ atom/g-atom}}{63.54 \text{ g/g-atom}}$$
$$= 0.0289 \frac{cm^2}{g} . \tag{7.130}$$

3. The **linear attenuation coefficient μ** is determined by multiplying μ_m with the absorber density ρ to get

$$\mu = \rho\mu_m = 8.96 \frac{g}{cm^3} \ 0.0289 \frac{cm^2}{g} = 0.259 \text{ cm}^{-1}. \tag{7.131}$$

4. The **average energy $\overline{E}_{tr}$ transferred** from photons to charged particles is determined using (7.109)

$$\overline{E}_{tr} = w_\tau \overline{E}_{tr}^\tau + w_\sigma \overline{E}_{tr}^\sigma + w_\kappa \overline{E}_{tr}^\kappa, \tag{7.132}$$

where

$$w_\tau = \frac{{}_\mathrm{a}\tau}{{}_\mathrm{a}\mu} = \frac{0.004}{3.051} = 1.3 \times 10^{-3}, \tag{7.133}$$

$$w_\sigma = \frac{{}_\mathrm{a}\sigma_\mathrm{c}}{{}_\mathrm{a}\mu} = \frac{1.737}{3.051} = 0.57, \tag{7.134}$$

$$w_\kappa = \frac{{}_\mathrm{a}\kappa}{{}_\mathrm{a}\mu} = \frac{1.310}{3.051} = 0.43, \tag{7.135}$$

$$\overline{E}_\mathrm{tr}^\tau = h\nu - P_\mathrm{K}\omega_\mathrm{K}\overline{h\nu}_\mathrm{K} = 8 \text{ MeV} - 0.5 \times 0.85 \times 7.7 \times 10^{-3} \text{ MeV}$$
$$\approx 8 \text{ MeV}, \tag{7.136}$$

(see Figs. 7.24 and 7.25 for values of P_K, ω_K, and $\overline{h\nu}_\mathrm{K}$)

$$\overline{E}_\mathrm{tr}^\sigma = 0.67 \times 8 \text{ MeV} \approx 5.36 \text{ MeV}, \tag{7.137}$$

(see "*The Compton Graph*" in Fig. 7.8)

$$\overline{E}_\mathrm{tr}^\kappa = h\nu - 2m_\mathrm{e}c^2 = 8 \text{ MeV} - 1.02 \text{ MeV} \approx 7 \text{ MeV}. \tag{7.138}$$

Inserting into (7.121) the weights w_i and the average energy transfers $\overline{E}_\mathrm{tr}^\mathrm{i}$ for the individual effects, we now calculate the average energy transferred from 8 MeV photons to charged particles in copper

$$\overline{E}_\mathrm{tr} = 1.3 \times 10^{-3} \times 8 \text{ MeV} + 0.57 \times 5.36 \text{ MeV} + 0.43 \times 7 \text{ MeV}$$
$$= 6.07 \text{ MeV}. \tag{7.139}$$

5. The **mass energy transfer coefficient $\mu_\mathbf{tr}/\rho$** is determined from the following:

$$\frac{\mu_\mathrm{tr}}{\rho} = \frac{\mu}{\rho}\frac{\overline{E}_\mathrm{tr}}{h\nu} = 0.0289 \text{ } \frac{\mathrm{cm}^2}{\mathrm{g}} \frac{6.07}{8} = 0.0219 \text{ cm}^2/\mathrm{g}. \tag{7.140}$$

6. The **radiative fraction $\bar{g}$** represents an average radiative yield $B(E_\mathrm{Ko})$ given in (5.49) for the spectrum of charged particles released by 8 MeV photons in the copper absorber. This charged particle spectrum is composed of recoil Compton electrons (average energy of 5.36 MeV) as well as electrons and positrons from the pair production (average energy of 0.5×7 MeV, i.e., 3.5 MeV).

The $\overline{E}_\mathrm{tr}$ exceeds $\overline{E}_\mathrm{o}$, the average of the initial energies acquired by charged particles that are set in motion in the absorber, because in pair production two charged particles with a combined energy of 7 MeV are set in motion and the initial average energy for each of the two charged particles is 3.5 MeV.

The *average initial energy* $\overline{E}_{\mathrm{o}}$ of all charged particles released in copper by 8 MeV photons is given as

$$\overline{E}_{\mathrm{o}} = \overline{E}_{\mathrm{tr}} \frac{_{\mathrm{a}}\sigma + _{\mathrm{a}}\kappa}{_{\mathrm{a}}\sigma + 2_{\mathrm{a}}\kappa} = 6.07 \text{ MeV} \frac{1.737 + 1.310}{1.737 + 2 \times 1.310}$$
$$= 4.25 \text{ MeV}. \tag{7.141}$$

The spectrum of charged particles released by 8 MeV photons in the copper absorber can only be determined reliably by Monte Carlo calculations.

In the first approximation, however, we assume that all charged particles are produced with monoenergetic initial energies $\overline{E}_{\mathrm{o}}$. Then the radiative yield $B(E_{\mathrm{Ko}})$, given in Fig. 5.7, can be equated with the radiative fraction $\bar{g}$ to get $\bar{g} \approx 0.1$.

The *average energy* $\overline{E}_{\mathrm{rad}}$ *radiated* by charged particles as bremsstrahlung is given by (5.50) as

$$\overline{E}_{\mathrm{rad}} = B(E_{\mathrm{Ko}})\overline{E}_{\mathrm{tr}} = 0.1 \times 6.07 \text{ MeV} = 0.61 \text{ MeV}. \tag{7.142}$$

7. The **average energy $\overline{E}_{\mathbf{ab}}$ absorbed** in the copper absorber is

$$\overline{E}_{\mathrm{ab}} = \overline{E}_{\mathrm{tr}} - \overline{E}_{\mathrm{rad}} = 6.07 \text{ MeV} - 0.61 \text{ MeV}$$
$$= 5.46 \text{ MeV}. \tag{7.143}$$

8. The **mass energy absorption coefficient $\mu_{\mathbf{ab}}/\rho$** is

$$\frac{\mu_{\mathrm{ab}}}{\rho} = \frac{\mu}{\rho}\frac{\overline{E}_{\mathrm{ab}}}{h\nu} = 0.0289 \frac{\mathrm{cm}^2}{\mathrm{g}}\frac{5.46}{8} = 0.0197 \text{ cm}^2/\mathrm{g} \tag{7.144}$$

The *mass energy absorption coefficient* μ_{ab}/ρ may also be calculated from the mass energy transfer coefficient μ_{tr}/ρ and the radiative fraction $\bar{g}$ as follows:

$$\frac{\mu_{\mathrm{ab}}}{\rho} = \frac{\mu_{\mathrm{tr}}}{\rho}(1 - \bar{g}) = 0.0219 \frac{\mathrm{cm}^2}{\mathrm{g}}(1 - 0.1)$$
$$= 0.0197 \text{ cm}^2/\mathrm{g}. \tag{7.145}$$

In summary, as shown schematicall in Fig. 7.37, we determined for 8 MeV photons interacting with a copper absorber that on the average:

(a) **6.07** MeV will be transferred to charged particles; **1.93** MeV will be scattered.
(b) **5.46** MeV will be absorbed in copper; **0.61** MeV will be radiated in the form of bremmstrahlung.
(c) The atomic cross-section $_{\mathrm{a}}\mu$, the mass attenuation coefficient μ_{m}, and the linear attenuation coefficient μ for 8 MeV photons in copper are: 3.051 b/atom; 0.0289 cm^2/g; and 0.259 cm^{-1}, respectively.

(d) The mass energy transfer coefficient μ_{tr}/ρ and mass energy absorption coefficient μ_{ab}/ρ are: 0.0219 cm^2/g and 0.0197 cm^2/g, respectively.
(e) The radiative fraction $\bar{g}$ for 8 MeV photons in copper is $\sim$0.1.
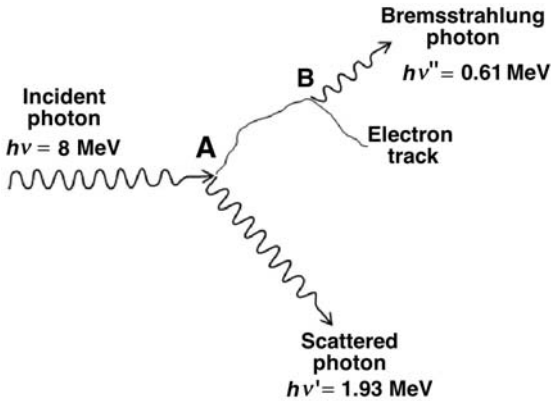
Fig. 7.37. Schematic diagram for general photon interactions with an atom. In this example an 8 MeV photon $h\nu$ interacts with a copper atom. An individual 8 MeV photon, as it encounters a copper atom at point A, may interact with the atom through photoelectric effect, Rayleigh scattering, Compton effect or pair production, or it may not interact at all. However, for a large number of 8 MeV photons striking copper, we may state that on the average:

- 6.07 MeV will be transferred at point A to charged particles (mainly to fast energetic electrons, but possibly also to positrons if the interaction is pair production);
- 1.93 MeV will be scattered through Rayleigh and Compton scattering $(h\nu')$

Of the 6.07 MeV transferred to charged particles:

- 5.46 MeV will be absorbed in copper over the fast charged particle tracks,
- 0.61 MeV will be emitted in the form of bremsstrahlung photons $(h\nu'')$
- The average energies transferred to charged particles in a photoelectric process, Rayleigh scattering, Compton scattering, and pair production are $\sim$8 MeV, 0, 5.36 MeV, and $\sim$7 MeV.

Teletherapy with a Cobalt-60 Source

The two figures on the next page depict a cobalt-60 teletherapy machine: actual modern machine on the left and a schematic diagram on the right. The machine is manufactured as "a megavoltage external beam therapy system using cobalt technology" by MDS Nordion in Ottawa, Canada. The schematic diagram of a cobalt machine was presented on a Canadian stamp issued in 1988 by the Canada Post Corporation in honor of *Harold E. Johns* (1915–1997), a Canadian medical physicist and the inventor of the *cobalt-60 teletherapy machine.*

The cobalt machine, shown schematically on the stamp, was developed in Canada in the 1950s for use in cancer therapy. It was the first truly practical and widely available megavoltage cancer therapy machine and incorporates a radioactive cobalt-60 source that is characterized with features suitable for external beam radiotherapy, such as high gamma ray energy, relatively long half-life, and high specific activity.

The cobalt-60 source is produced in a nuclear reactor by irradiating the stable cobalt-59 nuclide with thermal neutrons. The cobalt-60 source decays with a half-life of 5.26 years to nickel-60 with emission of beta particles (electrons) and two gamma rays (1.17 MeV and 1.33 MeV) per each disintegration, as shown schematically on the stamp.

Most modern cobalt machines are arranged on a gantry so that the source may rotate about a horizontal axis referred to as the machine isocenter axis. The source-axis distance typically is either 80 cm or 100 cm depending on the machine design. The isocentric source mounting allows the use of the isocentric treatment technique in which the radiation beam is directed toward the patient from various directions thereby concentrating the radiation dose in the target and spreading the dose to healthy tissues over a larger volume.

During the past two decades the linear accelerator (linac) eclipsed the cobalt unit and became the most widely used radiation source in modern radiotherapy. Compared to cobalt units linear accelerators offer higher beam energies that result in better skin sparing effect and more effective penetration into tissue; higher output dose rates that result in shorter treatment times; electron beams in addition to photon beams for treatment of superficial lesions; and a possibility for beam intensity modulation that provides optimal dose distributions in the target volume.

Despite the technological and practical advantages of linear accelerators over cobalt-60 machines, the latter still occupy an important place in the radiotherapy armamentarium, mainly because of considerably lower capital, installation and maintenance costs in comparison with linear accelerators. Moreover, the design of modern cobalt machines offers many of the features that until lately were in the domain of linear accelerators, such as large source-axis distance, high output, dynamic wedges, independent jaws, and a multileaf collimator. In the developing world, the cobalt-60 machines, owing to their relatively low costs as well as simpler design, maintenance, and operation, are likely to play an important role in cancer therapy for the foreseeable future.

8 Radioactivity

In this chapter we discuss various aspects of radioactivity of importance in medical physics. Natural radioactivity was discovered by *Henri Becquerel* in 1896, artificial radioactivity by *Frédéric Joliot* and *Irène Joliot-Curie* in 1934. Artificial production of radionuclides (nucleosynthesis) plays an important role in the treatment of cancer with teletherapy and brachytherapy as well as in nuclear medicine imaging. Radioactivity is a process by which an unstable parent nucleus decays into a more stable daughter nucleus that may or may not be stable. The unstable daughter nucleus will decay further until a stable nuclear configuration is reached. The radioactive decay is governed by the formalism based on the definition of activity and the radioactive decay constant.

We first discuss the decay of an unstable parent nucleus into a stable daughter nucleus, and then develop a formalism that deals with radioactive series decay and with the activation of radionuclides. A brief discussion of the origin of radioactive nuclides is then given, followed first by a discussion of general aspects of the radioactive decay and then by a detailed description of the various radioactive decay modes available to radioactive nuclides in their quest to attain a more stable configuration. Special emphasis is placed on aspects of radioactive decay of importance to medical physics.
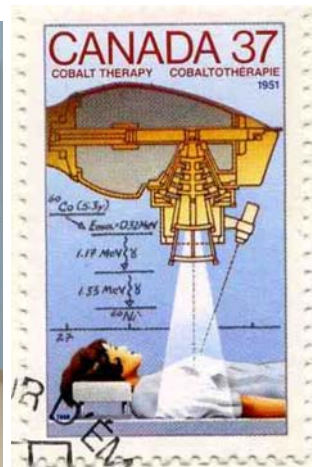
8.1 Introduction

Radioactivity, discovered in 1986 by *Henri Becquerel*, is a process by which an unstable parent nucleus transforms spontaneously into one or several daughter nuclei that are more stable than the parent nucleus by having larger binding energies per nucleon than does the parent nucleus. The daughter nucleus may also be unstable and will decay further through a chain of radioactive decays until a stable nuclear configuration is reached. Radioactive decay is usually accompanied by emission of energetic particles that may be used in science, industry, agriculture, and medicine.

- *Nuclear decay*, also called *nuclear disintegration*, *nuclear transformation* or *radioactive decay*, is a statistical phenomenon.
- The exponential laws that govern nuclear decay and growth of radioactive substances were first formulated by *Ernest Rutherford* and *Frederick Soddy* in 1902 and then refined by *Harry Bateman* in 1910.
- A radioactive substance containing atoms of same structure is often referred to as radioactive nuclide. Radioactive atoms, like any other atomic structure, are characterized by the atomic number Z and atomic mass number A.
- Radioactive decay involves a transition from the quantum state of the original nuclide (parent) to a quantum state of the product nuclide (daughter). The energy difference between the two quantum levels involved in a radioactive transition is referred to as the decay energy. The decay energy is emitted either in the form of electromagnetic radiation (usually gamma rays) or in the form of kinetic energy of the reaction products.
- The mode of radioactive decay depends upon the particular nuclide involved.
- All radioactive decay processes are governed by the same general formalism that is based on the definition of the activity $\mathscr{A}(t)$ and on a characteristic parameter for each radioactive decay process: the total radioactive *decay constant* λ with dimensions of reciprocal time, usually in s^{-1}.
- The decay constant λ is independent of the age of the radioactive atom and is essentially independent of physical conditions such as temperature, pressure, and chemical state of the atom's environment. Careful measurements have shown that λ can actually depend slightly on the physical environment. For example, at extreme pressure or at extremely low temperature the technetium-99m radio-nuclide shows a fractional change in λ of the order of 10^{-4} in comparison to the value at room temperature (293 K) and standard pressure (101.3 kPa).
- The total *radioactive decay constant* λ multiplied by a time interval that is much smaller than $1/\lambda$ represents the probability that any particular atom of a radioactive substance containing a large number $N(t)$ of identical radioactive atoms will decay (disintegrate) in that time interval. An assumption is made that λ is independent of the physical environment of a given atom.

- The *activity* $\mathscr{A}(t)$ of a radioactive substance containing a large number $N(t)$ of identical radioactive atoms represents the total number of decays (disintegrations) per unit time and is defined as a product between $N(t)$ and λ, i.e.,

$$\mathscr{A}(t) = \lambda N(t) \ . \tag{8.1}$$

- The *SI unit of activity* is the becquerel (Bq) given as 1 Bq = 1 s^{-1}. The becquerel and hertz both correspond to s^{-1}, but hertz expresses frequency of periodic motion, while becquerel expresses activity.
- The old unit of activity, the curie (Ci), was initially defined as the activity of 1 g of radium-226 and given as 1 Ci = 3.7×10^{10} s^{-1}. The activity of 1 g of radium-226 was subsequently measured to be 3.665×10^{10} s^{-1}; however, the definition of the curie was kept at 3.7×10^{10} s^{-1}. The current value of the activity of 1 g of radium-226 is thus 0.988 Ci or 3.665×10^{10} Bq.
- The becquerel (Bq) and the curie (Ci) are related as follows: 1 Bq = 2.703×10^{-11} Ci or 1 Ci = 3.7×10^{10} Bq.
- The *specific activity* a is defined as activity $\mathscr{A}$ per unit mass M, i.e.,

$$a = \frac{\mathscr{A}}{M} = \frac{\lambda N}{M} = \frac{\lambda N_A}{A} \ , \tag{8.2}$$

where N_A is the Avogadro's number (6.022×10^{23} atom/g-atom).
The specific activity a of a radioactive species depends on the decay constant λ and on the atomic mass number A of the radioactive atom. The units of specific activity are Bq/kg (SI unit) and Ci/g (old unit).

8.2 Decay of Radioactive Parent into a Stable Daughter

The simplest form of radioactive decay is characterized by a radioactive parent nucleus P decaying with decay constant λ_P into a stable daughter nucleus D, i.e.,

$$P \xrightarrow{\lambda_P} D \ . \tag{8.3}$$

The rate of depletion of the number of radioactive parent nuclei $N_P(t)$ is equal to the activity $\mathscr{A}_P(t)$ at time t, i.e.,

$$\frac{dN_P(t)}{dt} = -\mathscr{A}_P(t) = -\lambda_P N_P(t) \ . \tag{8.4}$$

The fundamental differential equation of (8.4) for $N_P(t)$ can be rewritten in general integral form to get

$$\int_{N_P(0)}^{N_P(t)} \frac{dN_P(t)}{N_P} = -\int_0^t \lambda_P dt \ , \tag{8.5}$$

where $N_P(0)$ is the number of radioactive nuclei at time $t = 0$.

Assuming that λ_P is constant, we can write (8.5) as follows:

$$\ln \frac{N_P(t)}{N_P(0)} = -\lambda_P t \tag{8.6}$$

or

$$N_P(t) = N_P(0)e^{-\lambda_P t} . \tag{8.7}$$

The activity of parent nuclei P at time t may now be expressed as follows:

$$\mathscr{A}_P(t) = \lambda_P N_P(t) = \lambda_P N_P(0)e^{-\lambda_P t} = \mathscr{A}_P(0)e^{-\lambda_P t} , \tag{8.8}$$

where $\mathscr{A}_P(0) = \lambda_P N_P(0)$ is the initial activity of the radioactive substance.

The decay law of (8.8) applies to all radioactive nuclides irrespective of their mode of decay; however, the decay constant λ_P is different for each radioactive nuclide P and is the most important defining characteristic of radioactive nuclides.

When more than one mode of decay is available to a radioactive nucleus (branching), the total decay constant λ is the sum of the partial decay constants λ_i applicable to each mode

$$\lambda = \sum_i \lambda_i . \tag{8.9}$$

Half life $(t_{1/2})_P$ of a radioactive substance P is that time during which the number of radioactive nuclei of the substance decays to half of the initial value $N_P(0)$ present at time $t = 0$. We can also state that in the time of one half life the activity of a radioactive substance diminishes to one half of its initial value, i.e.,

$$N_P[t = (t_{1/2})_P] = \frac{1}{2}N_P(0) = N_P(0)e^{-\lambda(t_{1/2})_P} . \tag{8.10}$$

From (8.10) we obtain the following relationship between the decay constant λ_P and the half-life $(t_{1/2})_P$:

$$\lambda_P = \frac{\ln 2}{(t_{1/2})_P} = \frac{0.693}{(t_{1/2})_P} . \tag{8.11}$$

The actual lifetime of any radioactive nucleus can vary from 0 to ∞, however, for a large number N_P of parent nuclei we can define the *average (mean) life* τ_P of a radioactive parent substance P that equals the sum of lifetimes of all individual atoms divided by the initial number of radioactive nuclei. The average (mean) life thus represents the average life expectancy of all nuclei in the radioactive substance P at time $t = 0$; i.e.,

$$\mathscr{A}_P(0)\tau_P = \mathscr{A}_P(0)\int_0^\infty e^{-\lambda_P t}dt = \frac{\mathscr{A}_P(0)}{\lambda_P} = N_P(0) , \tag{8.12}$$
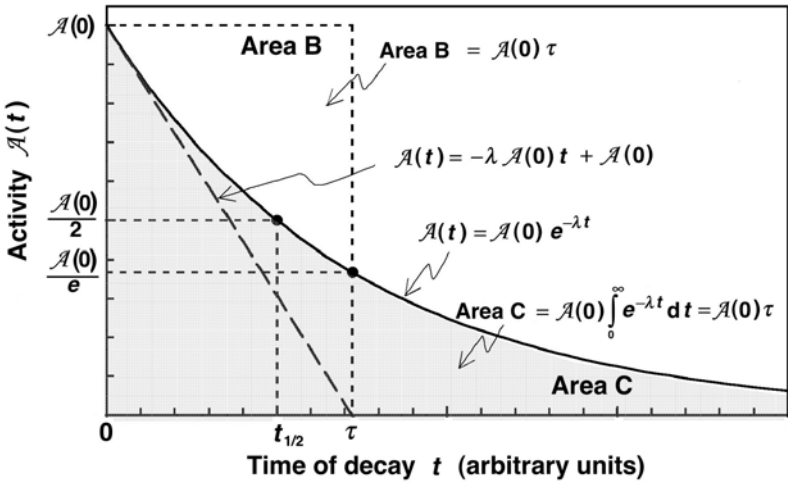
Fig. 8.1. Activity $\mathscr{A}(t)$ plotted against time t for a simple decay of a radioactive parent into a stable daughter. The activity follows the relationship given in (8.8) and (8.15). The concepts of half-life $t_{1/2}$ and mean-life τ are also illustrated. The area under the *exponential decay curve* from 0 to ∞ is equal to $\mathscr{A}(0)\tau$ where $\mathscr{A}(0)$ is the initial activity of the parent nuclei. The slope of the tangent to the *decay curve* at $t = 0$ is equal to $-\lambda\mathscr{A}_\mathrm{P}(0)$ and this tangent crosses the abscissa axis at $t = \tau$

The decay constant λ_P and mean life τ_P are related through the following expression:

$$\tau_\mathrm{P} = \frac{1}{\lambda_\mathrm{P}} \ . \tag{8.13}$$

The mean life τ_P can also be defined as the time required for the number of radioactive atoms or their activity to fall to $1/e = 0.368$ of its initial value $N_\mathrm{P}(0)$ or initial activity $\mathscr{A}_\mathrm{P}(0)$, respectively.

The mean life τ_P and half-life $(t_{1/2})_\mathrm{P}$ are related as follows:

$$\tau_\mathrm{P} = \frac{1}{\lambda_\mathrm{P}} = \frac{(t_{1/2})_\mathrm{P}}{\ln 2} = 1.44(t_{1/2})_\mathrm{P} \ . \tag{8.14}$$

A typical example of a radioactive decay for initial condition $\mathscr{A}_\mathrm{P}(t = 0) = \mathscr{A}_\mathrm{P}(0)$ is shown in Fig. 8.1 with a plot of parent activity $A_\mathrm{P}(t)$ against time t, i.e.,

$$\mathscr{A}_\mathrm{P}(t) = \mathscr{A}_\mathrm{P}(0)e^{-\lambda_\mathrm{P} t} \ . \tag{8.15}$$

The following properties of the radioactive decay curve are notable:

1. The area under the activity $\mathscr{A}_\mathrm{P}(t)$ vs. time t curve for $0 \leq t \leq \infty$ is given as

$$\int\limits_0^\infty \mathscr{A}_P(t)dt = \mathscr{A}_P(0)\int\limits_0^\infty -\lambda_P t\, dt$$

$$= \frac{\mathscr{A}_P(0)}{\lambda_P} = \mathscr{A}_P(0)\tau_P = N_P(0) , \tag{8.16}$$

and the result equals the initial number of radioactive nuclei at time $t = 0$.

2. The total number of radioactive nuclei present at any time $t > 0$ is simply the activity $\mathscr{A}_P(t)$ multiplied by the mean life τ_P.

3. The concept of half-life $(t_{1/2})_P$ is shown in Fig. 8.1 as the time in which the activity $\mathscr{A}_P(t)$ drops from $\mathscr{A}_P(0)$ to $0.5\,\mathscr{A}_P(0)$.

4. The concept of mean life τ_P is shown in Fig. 8.1 as the time in which the activity $\mathscr{A}_P(t)$ drops from $\mathscr{A}_P(0)$ to $0.368\mathscr{A}_P(0)$.

5. Area $\mathscr{A}_P(0)\tau_P$ is shown in Fig. 8.1 by a rectangle with sides $\mathscr{A}_P(0)$ and τ_P. If the initial activity $\mathscr{A}_P(0)$ could remain constant for mean life τ, all atoms would have been transformed and at time $t = \tau_P$ the activity would drop to zero.

6. In general, the slope of the tangent to the decay curve at time t is given as

$$\frac{d\mathscr{A}_P(t)}{dt} = -\lambda_P\mathscr{A}_P(0)e^{-\lambda_P t} , \tag{8.17}$$

while the initial slope at $t = 0$ is equal to $-\lambda_P\mathscr{A}_P(0)$.

7. The linear function, with the slope equal to $-\lambda_P\mathscr{A}_P(0)$ and the ordinate intercept at time $t = 0$ equal to $\mathscr{A}_P(0)$, is

$$\mathscr{A}_P(t) = -\lambda_P\mathscr{A}_P(0)t + \mathscr{A}_P(0) , \tag{8.18}$$

and represents the tangent to the decay curve at $t = 0$. It serves as a good approximation for the activity $\mathscr{A}_P(t)$ vs. t relationship when $t \ll \tau_P$, i.e.,

$$\mathscr{A}_P(t) \approx \mathscr{A}_P(0)\{1 - \lambda_P t\} = \mathscr{A}_P(0)\left\{1 - t/\tau_P\right\} \tag{8.19}$$

and results in $\mathscr{A}_P(t) = 0$ at $t = \tau_P$, in contrast to (8.15) that predicts $\mathscr{A}_P(t) = 0$ only at $t \to \infty$.

8.3 Radioactive Series Decay

8.3.1 Parent → Daughter → Granddaughter Relationships

Equations (8.7) and (8.15) describe the simple radioactive decay from an unstable parent P to a stable daughter D. A more complicated radioactive decay occurs when a radioactive parent P decays with a decay constant λ_P into a daughter D that in turn is radioactive and decays with a decay constant λ_D into a stable granddaughter G, i.e.,

$$P \xrightarrow{\lambda_P} D \xrightarrow{\lambda_D} G . \tag{8.20}$$

The rate of change dN_D/dt in the number of daughter nuclei D is equal to the supply of new daughter nuclei D through the decay of P given as $\lambda_P N_P(t)$ and the loss of daughter nuclei D from the decay of D to G given as $[-\lambda_D N_D(t)]$, i.e.,

$$dN_D/dt = \lambda_P N_P(t) - \lambda_D N_D(t) = \lambda_P N_P(0)\, e^{-\lambda_P t} - \lambda_D N_D(t) \ , \quad (8.21)$$

where $N_P(0)$ is the initial number of parent nuclei at time $t = 0$.

The parent P follows a straightforward radioactive decay process with the initial condition $N_P(t = 0) = N_P(0)$, as described by (8.7)

$$N_P(t) = N_P(0)\, e^{-\lambda_P t} \ . \quad (8.22)$$

We are now interested in obtaining the functional relationship for the number of daughter nuclei $N_D(t)$ assuming an initial condition that at $t = 0$ there are no daughter nuclei D present. The initial condition for the number of daughter nuclei N_D is thus as follows:

$$N_D(t = 0) = N_D(0) = 0 \ . \quad (8.23)$$

The general solution of the differential equation given by (8.21) will be of the form

$$N_D(t) = N_P(0) \left\{ p e^{-\lambda_P t} + d e^{-\lambda_D t} \right\} \ , \quad (8.24)$$

where p and d are constants to be determined using the following four steps:

1. Differentiate (8.24) with respect to time t to obtain

$$\frac{dN_D}{dt} = N_P(0) \left\{ -p\lambda_P e^{-\lambda_P t} - d\lambda_D e^{-\lambda_D t} \right\} . \quad (8.25)$$

2. Insert (8.24) and (8.25) into (8.21) and rearrange the terms to get

$$e^{-\lambda_P t} \left\{ -p\lambda_P - \lambda_P + p\lambda_D \right\} = 0 \ . \quad (8.26)$$

3. The factor in curly brackets of (8.26) must be equal to zero to satisfy the equation for all values of t, yielding the following expression for the constant p:

$$p = \frac{\lambda_P}{\lambda_D - \lambda_P} \ . \quad (8.27)$$

4. The coefficient d depends on the initial condition for N_D at time $t = 0$, i.e., $N_D(t = 0) = 0$ and may now be determined from (8.24) as

$$p + d = 0 \quad (8.28)$$

or after inserting (8.27)

$$d = -p = -\frac{\lambda_P}{\lambda_D - \lambda_P} \ . \quad (8.29)$$

The number of daughter nuclei $N_D(t)$ of (8.24) may now be written as follows:

$$N_D(t) = N_P(0) \frac{\lambda_P}{\lambda_D - \lambda_P} \left\{ e^{-\lambda_P t} - e^{-\lambda_D t} \right\} . \tag{8.30}$$

Recognizing that the activity of the daughter $\mathscr{A}_D(t)$ is $\lambda_D N_D(t)$ we now write $\mathscr{A}_D(t)$ as

$$
\begin{aligned}
\mathscr{A}_D(t) &= \frac{N_P(0)\lambda_P\lambda_D}{\lambda_D - \lambda_P} \left\{ e^{-\lambda_P t} - e^{-\lambda_D t} \right\} \\
&= \mathscr{A}_P(0) \frac{\lambda_D}{\lambda_D - \lambda_P} \left\{ e^{-\lambda_P t} - e^{-\lambda_D t} \right\} = \\
&= \mathscr{A}_P(0) \frac{1}{1 - \frac{\lambda_P}{\lambda_D}} \left\{ e^{-\lambda_P t} - e^{-\lambda_D t} \right\} \\
&= \mathscr{A}_P(t) \frac{\lambda_D}{\lambda_D - \lambda_P} \left\{ 1 - e^{-(\lambda_D - \lambda_P)t} \right\},
\end{aligned}
\tag{8.31}
$$

where

$\mathscr{A}_D(t)$ is the activity at time t of the daughter nuclei equal to $\lambda_D N_D(t)$,
$\mathscr{A}_P(0)$ is the initial activity of the parent nuclei present at time $t = 0$,
$\mathscr{A}_P(t)$ is the activity at time t of the parent nuclei equal to $\lambda_P N_P(t)$.

8.3.2 Characteristic Time

Equation (8.31) represents several general expressions for the activity $\mathscr{A}_D(t)$ of the daughter nuclei D and predicts a value of zero for $\mathscr{A}_D(t)$ at $t = 0$ (initial condition) and at $t = \infty$ (when all nuclei of the parent P and daughter D have decayed). This suggests that $\mathscr{A}_D(t)$ will pass through a maximum at a specified characteristic time $(t_{max})_D$ for $\lambda_P \neq \lambda_D$. The characteristic time $(t_{max})_D$ is determined by setting $d\mathscr{A}_D/dt = 0$ at $t = (t_{max})_D$ and solving for $(t_{max})_D$ to get

$$\lambda_P e^{-\lambda_P (t_{max})_D} = \lambda_D e^{-\lambda_D (t_{max})_D} \tag{8.32}$$

and

$$(t_{max})_D = \frac{\ln \frac{\lambda_P}{\lambda_D}}{\lambda_P - \lambda_D} . \tag{8.33}$$

Equation (8.33), governed by the initial conditions at $t = 0$

$$\mathscr{A}_P(t = 0) = \mathscr{A}_P(0) \quad \text{and} \quad \mathscr{A}_D(t = 0) = 0 \tag{8.34}$$

may also be expressed in terms of half-lives $(t_{1/2})_P$ and $(t_{1/2})_D$ as well as in terms of mean-lives τ_P and τ_D for the parent P nuclei and daughter D nuclei,

respectively, as

$$(t_{\max})_{\mathrm{D}} = \frac{\ln \frac{(t_{1/2})_{\mathrm{D}}}{(t_{1/2})_{\mathrm{P}}}}{\ln 2 \left\{ \frac{1}{(t_{1/2})_{\mathrm{P}}} - \frac{1}{(t_{1/2})_{\mathrm{D}}} \right\}}$$

$$= \frac{(t_{1/2})_{\mathrm{P}}(t_{1/2})_{\mathrm{D}}}{(t_{1/2})_{\mathrm{D}} - (t_{1/2})_{\mathrm{P}}} \frac{\ln \frac{(t_{1/2})_{\mathrm{D}}}{(t_{1/2})_{\mathrm{P}}}}{\ln 2} \tag{8.35}$$

and

$$(t_{\max})_{\mathrm{D}} = \frac{\ln \frac{\tau_{\mathrm{D}}}{\tau_{\mathrm{P}}}}{\frac{1}{\tau_{\mathrm{D}}} - \frac{1}{\tau_{\mathrm{P}}}} = \frac{\tau_{\mathrm{P}} \tau_{\mathrm{D}}}{\tau_{\mathrm{P}} - \tau_{\mathrm{D}}} \ln \frac{\tau_{\mathrm{P}}}{\tau_{\mathrm{D}}} \ . \tag{8.36}$$

8.3.3 General Form of Daughter Activity

Equations (8.33), (8.35) and (8.36) show that $(t_{\max})_{\mathrm{D}}$ is positive and real, irrespective of the relative values of λ_{P} and λ_{D}, except for the case of $\lambda_{\mathrm{P}} = \lambda_{\mathrm{D}}$ for which $\mathscr{A}_{\mathrm{D}}(t)$ in (8.31) is not defined.

At $t = (t_{\max})_{\mathrm{D}}$, we get from (8.31) that $\mathscr{A}_{\mathrm{P}}[(t_{\max})_{\mathrm{D}}] = \mathscr{A}_{\mathrm{D}}[(t_{\max})_{\mathrm{D}}]$, i.e., the activities of the parent and daughter nuclei are equal and the condition referred to as the *ideal equilibrium* is met. The term ideal equilibrium was introduced by *Robley Evans* to distinguish this instantaneous condition from other types of equilibrium (transient and secular) that are defined below for the relationship between the parent and daughter activity under certain special conditions.

- For $0 < t < (t_{\max})_{\mathrm{D}}$, the activity of parent nuclei $\mathscr{A}_{\mathrm{P}}(t)$ always exceeds the activity of the daughter nuclei $\mathscr{A}_{\mathrm{D}}(t)$, i.e., $\mathscr{A}_{\mathrm{D}}(t) < \mathscr{A}_{\mathrm{P}}(t)$.
- For $(t_{\max})_{\mathrm{D}} < t < \infty$, the activity of the daughter nuclei $\mathscr{A}_{\mathrm{D}}(t)$ always exceeds, or is equal to, the activity of the parent nuclei $\mathscr{A}_{\mathrm{P}}(t)$, i.e., $\mathscr{A}_{\mathrm{D}}(t) \gtrsim \mathscr{A}_{\mathrm{P}}(t)$.

Equation (8.31), describing the daughter activity $\mathscr{A}_{\mathrm{D}}(t)$, can be written in a general form covering all possible physical situations. This is achieved by introducing variables x, y_{P}, and y_{D} as well as a decay factor m defined as

1. x: time t normalized to half-life of parent nuclei $(t_{1/2})_{\mathrm{P}}$

$$x = \frac{t}{(t_{1/2})_{\mathrm{P}}} \ , \tag{8.37}$$

2. y_{P}: parent activity $\mathscr{A}_{\mathrm{P}}(t)$ normalized to $\mathscr{A}_{\mathrm{P}}(0)$, the parent activity at $t = 0$

$$y_{\mathrm{P}} = \frac{\mathscr{A}_{\mathrm{P}}(t)}{\mathscr{A}_{\mathrm{P}}(0)} = e^{-\lambda_{\mathrm{P}} t} \qquad [\text{see } (8.8) \text{ and } (8.22)] \ , \tag{8.38}$$

3. y_D: daughter activity $\mathscr{A}_D(t)$ normalized to $\mathscr{A}_P(0)$, the parent activity at $t = 0$

$$y_D = \frac{\mathscr{A}_D(t)}{\mathscr{A}_P(0)} , \tag{8.39}$$

4. m: *decay factor* defined as the ratio of the two decay constants, i.e., λ_P/λ_D

$$m = \frac{\lambda_P}{\lambda_D} = \frac{(t_{1/2})_D}{(t_{1/2})_P} , \tag{8.40}$$

Insertion of x, y_D, and m into (8.31) results in the following expression for y_D, the daughter activity $\mathscr{A}_D(t)$ normalized to the initial parent activity $\mathscr{A}_P(0)$

$$y_D = \frac{1}{1-m} \left\{ e^{-x \ln 2} - e^{-\frac{x}{m} \ln 2} \right\} = \frac{1}{1-m} \left\{ \frac{1}{2^x} - \frac{1}{2^{\frac{x}{m}}} \right\} . \tag{8.41}$$

Equation (8.41) for y_D as a function of x has physical meaning for all positive values of m except for $m = 1$ for which y_D is not defined. However, since (8.41) gives $y_D = 0/0$ for $m = 1$, we can apply the L'Hôpital's rule and determine the appropriate function for y_D as follows:

$$y_D(m = 1) = \lim_{m \to 1} \frac{\frac{d}{dm} \left\{ \frac{1}{2^x} - \frac{1}{2^{x/m}} \right\}}{\frac{d}{dm}(1 - m)}$$

$$= \lim_{m \to 1} \frac{-2^{-\frac{x}{m}} \ln 2 \left\{ \frac{x}{m^2} \right\}}{-1} = (\ln 2) \frac{x}{2^x} . \tag{8.42}$$

Similarly, (8.15) for the parent activity $\mathscr{A}_P(t)$ can be written in terms of variables x and y_P as follows:

$$y_P = e^{-\lambda_P t} = e^{-x \ln 2} = \frac{1}{2^x} , \tag{8.43}$$

where x was given in (8.37) as $x = t/(t_{1/2})_P$ and $y_P = \mathscr{A}_P(t)/\mathscr{A}_P(0)$ is the parent activity $\mathscr{A}_P(t)$ normalized to the parent activity $\mathscr{A}_P(0)$ at time $t = 0$.

The characteristic time $(t_{max})_D$ can now be generalized to x_{max} by using (8.37) to get the following expression:

$$(x_{max})_D = \frac{(t_{max})_D}{(t_{1/2})_P} . \tag{8.44}$$

Three different approaches can now be used to determine $(x_{max})_D$ for y_D in (8.41)

1. Set $(dy_D/dx) = 0$ at $x = (x_{max})_D$ and solve for $(x_{max})_D$ to get

$$\left. \frac{dy_D}{dx} \right|_{x=x_{max}} = \frac{\ln 2}{1-m} \left\{ -2^{-x} + \frac{1}{m} 2^{-\frac{x}{m}} \right\} \Bigg|_{x=x_{max}} = 0 . \tag{8.45}$$

Solving (8.45) for $(x_{max})_D$ we finally get

$$(x_{max})_D = \frac{m}{m-1} \frac{\log m}{\log 2} = \frac{m}{m-1} \frac{\ln m}{\ln 2} . \tag{8.46}$$
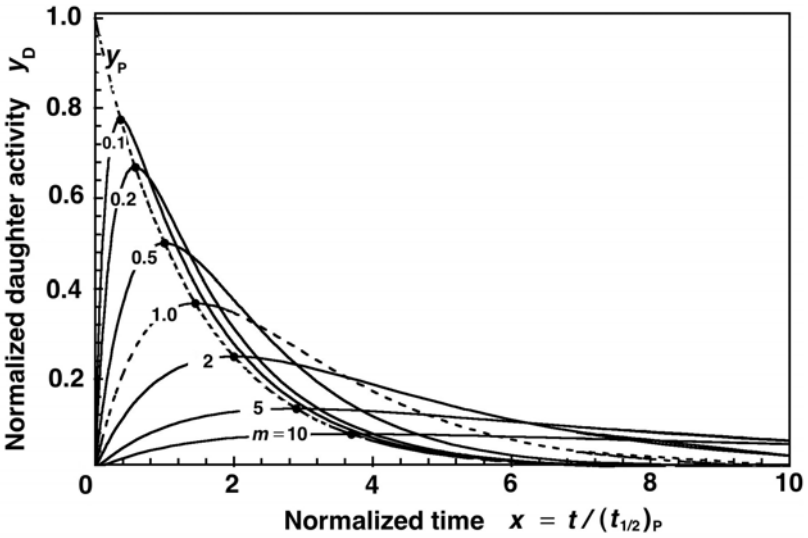
Fig. 8.2. Variable y_D of (8.41) against variable x for various values of decay parameter m. The *dashed curve* is for y_P of (8.43) against x. The parameter $(x_{max})_D$ shown by *dots on the y_P curve* is calculated from (8.46). Values for $(y_D)_{max}$ are obtained with (8.49)

For $m = 1$ (8.46) is not defined; however, since it gives $x_{max} = 0/0$, we can apply the L'Hopital's rule to get $(x_{max})_D|_{m \to 1}$ as follows:

$$(x_{max})_D|_{m \to 1} = \lim_{m \to 1} \frac{\frac{d(m \ln m)}{dm}}{\ln 2 \frac{d(m-1)}{dm}}$$

$$= \lim_{m \to 1} \frac{1 + \ln m}{\ln 2} = \frac{1}{\ln 2} = 1.44 \,, \qquad (8.47)$$

Thus, $(x_{max})_D$ is calculated from (8.46) for any positive m except for $m = 1$. For $m = 1$, (8.47) gives $x_{max} = 1.44$.

2. Insert (8.37) and (8.40) into (8.33) for $(t_{max})_D$ and solve for $(x_{max})_D$ to get the result given in (8.46).
3. Recognize that when $x = (x_{max})_D$ the condition of ideal equilibrium applies for (8.41), i.e., $y_P[(x_{max})_D] = y_D[(x_{max})_D]$. Insert $x = (x_{max})_D$ into (8.41) and (8.43), set $y_P[(x_{max})_D] = y_D[(x_{max})_D]$, and solve for $(x_{max})_D$ to get the result of (8.46).

In Fig. 8.2 we plot (8.41) for y_D against x using various values of the decay factor m in the range from 0.1 to 10.0. For comparison we also plot y_P of (8.43) against x (dotted curve).

The function plotted as a dashed curve for $m = 1$ in Fig. 8.2 is the function given in (8.42). The point of ideal equilibrium for this curve occurs at x_{max} given as $(1/\ln 2) = 1.44$ in (8.47) and at $y_D(x_{max}) = 1/e = 0.368$.

All y_D curves of Fig. 8.2 start at the origin at (0,0), rise with x, reach a peak at $(x_{max})_D$, as given in (8.46), and then decay with an increasing x. The smaller is m, the steeper is the initial rise of y_D, i.e., the larger is the initial slope of y_D. The initial slope and its dependence on m can be determined from the derivative dy_P/dx of (8.45) by setting $x = 0$ to get

$$\left.\frac{dy_D}{dx}\right|_{x=0} = \frac{\ln 2}{1-m}\left\{-2^{-x} + \frac{1}{m}2^{-\frac{x}{m}}\right\}\bigg|_{x=0} = \frac{\ln 2}{m} \ . \tag{8.48}$$

Noting that $x = t/(t_{1/2})_P$, $m = \lambda_P/\lambda_D$, and $y_D = \mathscr{A}_D(t)/\mathscr{A}_P(0)$, we can link the data of Fig. 8.2 with physical situations that occur in nature in the range $0.1 < m < 10$. Of course, the m region can be expanded easily to smaller and larger values outside the range shown in Fig. 8.2 as long as a different scale for the variable x is used.

As indicated with dots on the y_P curve in Fig. 8.2, $(y_{max})_D$, the maxima in y_D for a given m, occur at points $(x_{max})_D$ where the y_D curves cross over the y_P curve. The x_{max} values for a given m can be calculated from (8.46) and $(y_D)_{max}$ for a given m can be calculated simply by determining $y_P(x)$ at $x = x_{max}$ with $y_P(x)$ given in (8.43). We thus obtain the following expression for $(y_{max})_D$:

$$(y_{max})_D = y_P(x_{max})_D = 2^{\left(\frac{m}{1-m}\right)\frac{\ln m}{\ln 2}} = \frac{1}{2^{(x_{max})_D}} \equiv e^{\frac{m}{1-m}\ln m}$$
$$= e^{-(\ln 2)(x_{max})_D} \ , \tag{8.49}$$

where $(x_{max})_D$ was given by (8.46). Equation (8.49) is valid for all positive m with the exception of $m = 1$. We determine $(y_D)_{max}$ for $m = 1$ by applying the L'Hôpital's rule to (8.49) to get

$$(y_{max})_D|_{m=1} = \lim_{m\to 1} 2^{\frac{\frac{d}{dm}(m\ln m)}{\frac{d}{dm}(1-m)\ln 2}} = \lim_{m\to 1} 2^{\frac{\ln m+1}{-\ln 2}} = 2^{-\frac{1}{\ln 2}}$$
$$= e^{-1} = 0.368 \ . \tag{8.50}$$

As shown in (8.49), $(y_{max})_D$ and $(x_{max})_D$ are related through a simple exponential expression plotted in Fig. 8.3 and also given by (8.43) with $x = (x_{max})_D$ and $y_P = (y_{max})_D$. As shown in (8.49) the ideal equilibrium value $(y_{max})_D$ exhibits an exponential decay behavior starting at $(y_{max})_D = 1$ at $(x_{max})_D = 0$ through $(y_{max})_D = 0.5$ at $(x_{max})_D = 1$ to approach 0 at $(x_{max})_D \to \infty$.

Figures 8.4 and 8.5 show plots of $(y_{max})_D$ and $(x_{max})_D$, respectively, against m as given by (8.49) and (8.46), respectively, for positive m except for $m = 1$. The $m = 1$ values of $(x_{max})_D$ and $(y_{max})_D$, equal to $1/\ln 2$ and $1/e$, respectively, were calculated from (8.47) and (8.50), respectively. With increasing m, the parameter $(x_{max})_D$ starts at zero for $m = 0$, goes through $1/\ln 2 = 1.44$ at $m = 1$, and then increases as $\ln m$ for very large m. Parameter $(y_{max})_D$, on the other hand, starts at 1 for $m = 0$, goes through $1/e = 0.368$ at $m = 1$, and then decreases exponentially for very large m.
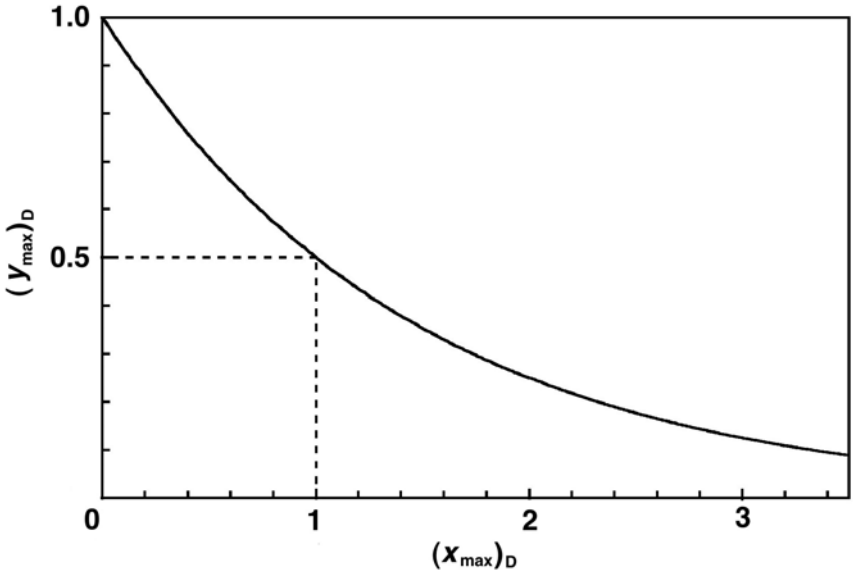
Fig. 8.3. Parameter $(y_{max})_D$ against parameter $(x_{max})_D$ as given in (8.49)
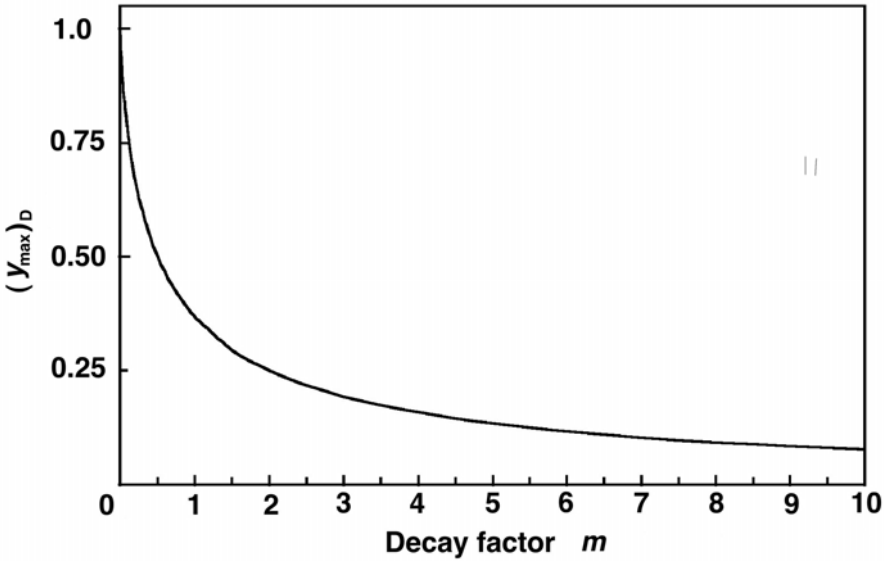
Fig. 8.4. Parameter $(y_{max})_D$ against decay factor m calculated from (8.49) for all $m > 0$ except for $m = 1$. The value of $(y_{max})_D$ for $m = 1$ is calculated from (8.50)
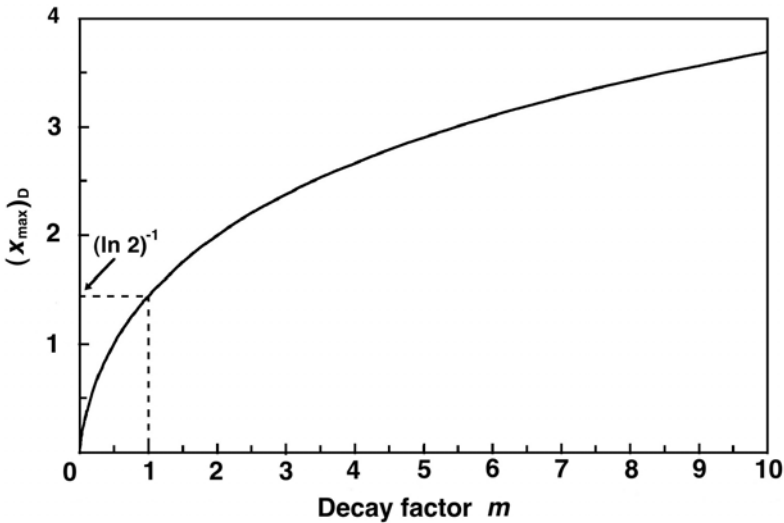
Fig. 8.5. Parameter $x_{\max}$ against decay factor m calculated from (8.46) for all $m > 0$ except for $m = 1$. The value of $(x_{\max})_{\mathrm{D}}$ for $m = 1$ is calculated from (8.47)

8.3.4 Equilibria in Parent-Daughter Activities

In many *parent→daughter→granddaughter* relationships after a certain time t the parent and daughter activities reach a constant ratio independent of a further increase in time t. This condition is referred to as *radioactive equilibrium* and can be analyzed further by examining the behavior of the activity ratio $\mathscr{A}_{\mathrm{D}}(t)/\mathscr{A}_{\mathrm{P}}(t)$ obtained from (8.31) as

$$\frac{\mathscr{A}_{\mathrm{D}}(t)}{\mathscr{A}_{\mathrm{P}}(t)} = \frac{\lambda_{\mathrm{D}}}{\lambda_{\mathrm{D}} - \lambda_{\mathrm{P}}} \left\{ 1 - e^{-(\lambda_{\mathrm{D}} - \lambda_{\mathrm{P}})t} \right\}$$

$$= \frac{1}{1 - \lambda_{\mathrm{P}}/\lambda_{\mathrm{D}}} \left\{ 1 - e^{-(\lambda_{\mathrm{D}} - \lambda_{\mathrm{P}})t} \right\} \tag{8.51}$$

for the two initial conditions:

1. $\mathscr{A}_{\mathrm{P}}(t = 0) = \mathscr{A}_{\mathrm{P}}(0) = \lambda_{\mathrm{P}} N_{\mathrm{P}}(0),$ $\hspace{2cm}$ (8.52)
2. $\mathscr{A}_{\mathrm{D}}(t = 0) = \mathscr{A}_{\mathrm{D}}(0) = 0.$ $\hspace{2cm}$ (8.53)

Inserting the decay factor m of (8.40) and variable x of (8.37) into (8.51) and defining parameter ξ as $\xi = \mathscr{A}_{\mathrm{D}}(t)/\mathscr{A}_{\mathrm{P}}(t) = y_{\mathrm{D}}/y_{\mathrm{P}}$, we write (8.51) as follows:

$$\xi = \frac{\mathscr{A}_{\mathrm{D}}(t)}{\mathscr{A}_{\mathrm{P}}(t)} = \frac{1}{1 - m} \left\{ 1 - e^{-(\ln 2)\frac{1-m}{m}x} \right\} \equiv \frac{1}{1 - m} \left\{ 1 - 2^{\frac{m-1}{m}x} \right\} .$$

$$\tag{8.54}$$

The $\xi(x)$ expression of (8.54) is valid for all positive m except for $m = 1$ for which it is not defined. However, we can determine the $\xi(x)$ functional
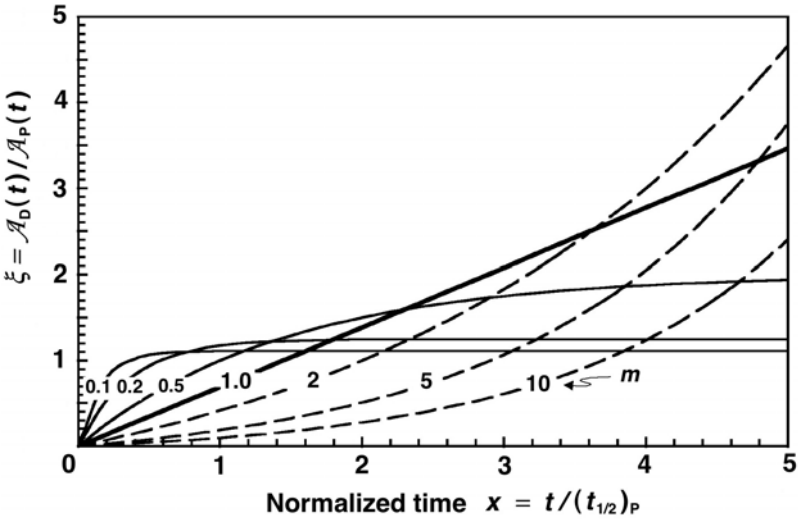
Fig. 8.6. Variable $\xi = \mathscr{A}_\mathrm{D}(t)/\mathscr{A}_\mathrm{P}(t) = y_\mathrm{D}/y_\mathrm{P}$ against x for several decay factors m in the range from 0.1 to 10 calculated from (8.54) except for $\xi(m=1)$ which gives a linear function calculated in (8.55)

relationship for $m = 1$ by applying the L'Hôpital's rule to get

$$\xi(m=1) = \lim_{m \to 1} \frac{\frac{d}{dm}\left\{1 - e^{\frac{m-1}{m}x \ln 2}\right\}}{d(1-m)/dm}$$

$$= \lim_{m \to 1} \frac{-e^{\frac{m-1}{m}x \ln 2}\left\{-\frac{x \ln 2}{m} - \frac{m-1}{m^2}x \ln 2\right\}}{-1} = (\ln 2)x \quad (8.55)$$

Equation (8.55) shows that $\xi(x)$ for $m = 1$ is a linear function of x, as shown in Fig. 8.6 in which we plot $\xi(x)$ for various values of m in the range from 0.1 to 10. The $m = 1$ linear equation actually separates two distinct regions for the variable ξ: (i) region where $m > 1$ and (ii) region where $0 < m < 1$.

1. For the $m > 1$ region, we write (8.54) as follows:

$$\xi = \frac{1}{m-1}\left\{e^{\frac{m-1}{m}x \ln 2} - 1\right\} . \quad (8.56)$$

Note that ξ rises exponentially with x, implying that the $\mathscr{A}_\mathrm{D}(t)/\mathscr{A}_\mathrm{P}(t)$ ratio also increases with time t and thus no equilibrium between $\mathscr{A}_\mathrm{P}(t)$ and $\mathscr{A}_\mathrm{D}(t)$ will ensue with an increasing time t. The exponential behavior of $\xi(x)$ is clearly shown in Fig. 8.6 with the dashed curves for $m > 1$ (in the range $1 < m < 10$).

2. For the $0 < m < 1$ region, (8.54) suggests that the exponential term diminishes with increasing x and exponentially approaches zero. This means that at large x the parameter ξ approaches a constant value that is independent of x and is equal to $1/(1-m)$. Under these conditions the parent activity $\mathscr{A}_P(t)$ and daughter activity $\mathscr{A}_D(t)$ are said to be in *transient equilibrium*, and are governed by the following relationship:

$$\xi = \frac{\mathscr{A}_D(t)}{\mathscr{A}_P(t)} = \frac{y_D}{y_P} = \frac{1}{1-m} = \frac{1}{1-\lambda_P/\lambda_D} = \frac{\lambda_D}{\lambda_D - \lambda_P} \ . \qquad (8.57)$$

After initially increasing, the daughter activity $\mathscr{A}_D(t)$ goes through a maximum and then decreases at the same rate as the parent activity $\mathscr{A}_P(t)$ and the two activities are related through (8.57). As m decreases, the daughter and parent activities at relatively large times t become increasingly more similar, since, as $m \to 0$, $\xi \to 1$. This represents a special case of transient equilibrium ($\lambda_D \gg \lambda_P$, i.e., $m \to 0$) and in this case the parent and daughter are said to be in *secular equilibrium*. Since in secular equilibrium $\xi = 1$, the parent and daughter activities are approximately equal, i.e., $\mathscr{A}_P(t) \approx \mathscr{A}_D(t)$ and the daughter decays with the same rate as the parent.

Equations (8.51) and (8.54) are valid in general, irrespective of the relative magnitudes of λ_P and λ_D; however, as indicated above, the ratio $\mathscr{A}_D(t)/\mathscr{A}_P(t)$ falls into four distinct categories that are clearly defined by the relative magnitudes of λ_P and λ_D. The four categories are:

(1) Daughter Longer-Lived Than Parent:

$(t_{1/2})_D > (t_{1/2})_P$, i.e., $\lambda_D < \lambda_P$.

We write the ratio $\mathscr{A}_D(t)/\mathscr{A}_P(t)$ of (8.51) as follows:

$$\frac{\mathscr{A}_D(t)}{\mathscr{A}_P(t)} = \frac{\lambda_D}{\lambda_P - \lambda_D} \left\{ e^{(\lambda_P - \lambda_D)t} - 1 \right\} \ . \qquad (8.58)$$

No equilibrium between the parent activity $\mathscr{A}_P(t)$ and the daughter activity $\mathscr{A}_D(t)$ will be reached for any t.

(2) Half-Lives of Parent and Daughter are Equal:

$(t_{1/2})_D = (t_{1/2})_P$, i.e., $\lambda_D = \lambda_P$.

The condition is mainly of theoretical interest as no such example has been observed in nature yet. The ratio $\mathscr{A}_D(t)/\mathscr{A}_P(t)$ is given as a linear function, as shown in (8.55).

(3) Daughter Shorter-Lived Than Parent:

$(t_{1/2})_D < (t_{1/2})_P$, *i.e.*, $\lambda_D > \lambda_P$

The activity ratio $\mathcal{A}_D(t)/\mathcal{A}_P(t)$ at large t becomes a constant equal to $\lambda_D/(\lambda_D - \lambda_P)$ and is then independent of t and larger than unity, i.e.,

$$\frac{\mathcal{A}_D(t)}{\mathcal{A}_P(t)} \approx \frac{\lambda_D}{\lambda_D - \lambda_P} > 1 \ . \tag{8.59}$$

The constancy of the ratio $\mathcal{A}_D(t)/\mathcal{A}_P(t)$ at large t implies a transient equilibrium between $\mathcal{A}_P(t)$ and $\mathcal{A}_D(t)$. The ratio $\mathcal{A}_D(t)/\mathcal{A}_P(t)$ of (8.51) can be written in terms of the characteristic time t_{max} inserting into (8.51) a new variable $t = nt_{max}$ with t_{max} given in (8.33) to get the following expression for $\mathcal{A}_D(t)/\mathcal{A}_P(t)$:

$$\frac{\mathcal{A}_D(t)}{\mathcal{A}_P(t)} = \frac{\lambda_D}{\lambda_D - \lambda_P} \left\{ 1 - e^{-(\lambda_D - \lambda_P)nt_{max}} \right\}$$

$$= \frac{\lambda_D}{\lambda_D - \lambda_P} \left\{ 1 - e^{-n \ln \frac{\lambda_D}{\lambda_P}} \right\} = \frac{\lambda_D}{\lambda_D - \lambda_P} \left\{ 1 - \left(\frac{\lambda_P}{\lambda_D} \right)^n \right\} \tag{8.60}$$

Equation (8.60) allows us to estimate the required value of n to bring the ratio $\mathcal{A}_D(t)/\mathcal{A}_P(t)$ to within a certain percentage p of the saturation value of $\lambda_D/(\lambda_D - \lambda_P)$ in transient equilibrium. This simply implies that the following relationship must hold:

$$(\lambda_P/\lambda_D)^n = p/100 \ , \tag{8.61}$$

or, after solving for n

$$n = \ln \frac{100}{p} \Big/ \ln \frac{\lambda_D}{\lambda_P} \ . \tag{8.62}$$

For example, the activity ratio $\xi = \mathcal{A}_D(t)/\mathcal{A}_P(t)$ will reach 90%, 98%, 99% and 99.9% of its saturation value; i.e., p is 10%, 2%, 1% and 0.1%, respectively, for values of n equal to $2.3/\ln(\lambda_D/\lambda_P)$; $3.9/\ln(\lambda_D/\lambda_P)$; $4.6/\ln(\lambda_D/\lambda_P)$; and $6.9/\ln(\lambda_D/\lambda_P)$.

(4) Daughter Much Shorter-Lived Than Parent:

$(t_{1/2})_D \ll (t_{1/2})_P$, i.e., $\lambda_D \gg \lambda_P$

The ratio of daughter activity $\mathcal{A}_D(t)$ and parent activity $\mathcal{A}_P(t)$, i.e., $\mathcal{A}_D(t)/\mathcal{A}_P(t)$ of (8.51) simplifies to

$$\frac{\mathcal{A}_D(t)}{\mathcal{A}_P(t)} \approx 1 - e^{-\lambda_D t} \ . \tag{8.63}$$

For relatively large time $t \gg t_{max}$, (8.63) becomes equal to unity, i.e.,

$$\mathcal{A}_D(t)/\mathcal{A}_P(t) \approx 1 \ . \tag{8.64}$$

The activity of the daughter $\mathcal{A}_D(t)$ very closely approximates that of its parent $\mathcal{A}_P(t)$, i.e., $\mathcal{A}_D(t) \approx \mathcal{A}_P(t)$, and they decay together at the rate of the parent. This special case of transient equilibrium in which the daughter and parent activities are essentially identical, i.e., $\mathcal{A}_D(t) \approx \mathcal{A}_P(t)$ is called *secular equilibrium*.

8.3.5 Bateman Equations

Equation (8.30) for the P $\to$ D $\to$ G relationship can be generalized to a chain of decaying nuclei of an arbitrary number of radioactive chain (series) links by using equations proposed by *Harry Bateman* in 1910. The radioactive chain is as follows:

$$N_1 \to N_2 \to N_3 \to \ldots \to N_{i-1} \to N_i \tag{8.65}$$

and the initial condition stipulates that at $t = 0$ only $N_1(0)$ parent nuclei are present, while all other descendent nuclei are not present yet, i.e.,

$$N_2(0) = N_3(0) = \ldots = N_{i-1}(0) = N_i(0) = 0 . \tag{8.66}$$

The number of nuclei $N_i(t)$ is given as follows

$$N_i(t) = C_1 e^{-\lambda_1 t} + C_2 e^{-\lambda_2 t} + C_3 e^{-\lambda_3 t} + \ldots + C_i e^{-\lambda_i t} , \tag{8.67}$$

where C_i are constants given as follows

$$C_1 = N_1(0) \frac{\lambda_1 \lambda_2 \ldots \lambda_{i-1}}{(\lambda_2 - \lambda_1)(\lambda_3 - \lambda_1) \ldots (\lambda_i - \lambda_1)} , \tag{8.68}$$

$$C_2 = N_1(0) \frac{\lambda_1 \lambda_2 \ldots \lambda_{i-1}}{(\lambda_1 - \lambda_2)(\lambda_3 - \lambda_2) \ldots (\lambda_i - \lambda_2)} , \tag{8.69}$$

$$\vdots$$

$$C_i = N_1(0) \frac{\lambda_1 \lambda_2 \ldots \lambda_{i-1}}{(\lambda_1 - \lambda_i)(\lambda_3 - \lambda_i) \ldots (\lambda_{i-1} - \lambda_i)} . \tag{8.70}$$

8.3.6 Mixture of Two or More Independently Decaying Radionuclides in a Sample

An unknown mixture of two or more radionuclides, each with its own half-life, will produce a composite decay curve that does not result in a straight line when plotted on a semi-logarithmic plot, unless, of course, all radionuclides have identical or very similar half-lives. The decay curves of the individual radionuclides can be resolved graphically, if their half-lives differ sufficiently and if at most three radioactive components are present.

Figure 8.7 illustrates this for a mixture of two radionuclides: nuclide A with short half-life and nuclide B with long half-life. *The solid curve* represents the measured decay curve (activity) for the mixture with the two components A and B. For large time t, the short-lived component A is essentially gone and the composite activity curve follows the decay of the long-lived radionuclide B.

The initial activities and half-lives of the nuclides A and B can be determined graphically as follows:
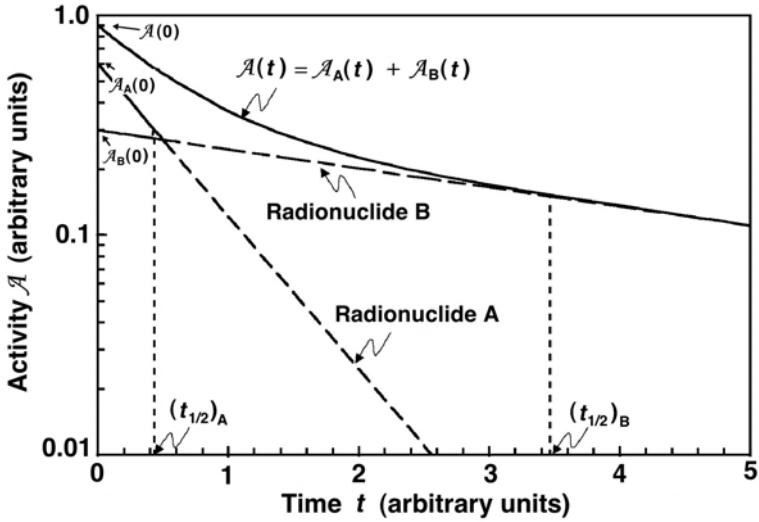
Fig. 8.7. Decay curves shown on a semi-logarithmic plot for a mixture of twora-dionuclides: short-lived A and long-lived B. The (*solid curve*) is the decay curve for the mixture of radionuclides A and B. The *dashed lines* are individual decay curves for radionuclide A and B

1. The first step is to carry out a linear extrapolation to time $t = 0$ of the long-time portion of the composite curve (region where the curve becomes linear on a semi-logarithmic plot). This gives the decay curve for nuclide B and the initial activity of nuclide B at $t = 0$.
2. The second step is to obtain the decay curve for the short-lived component A by subtracting the straight-line curve B from the composite curve. This results in another straight line on the semi-logarithmic plot, this time for nuclide A, and gives the initial activity of nuclide A at $t = 0$.
3. Half-lives for components A and B may be determined from the individual linear decay data for radionuclides A and B. The two radionuclides may then be identified through the use of tabulated half-lives for the known natural and artificial radionuclides.

8.4 Activation of Nuclides

8.4.1 Nuclear Reaction Cross Section

Particles of an incident beam striking a target can interact with the target nuclei through the following three processes:

1. *scattering,*
2. *absorption,*

3. *nuclear reaction.*

In traversing a target the beam is attenuated in

1. *intensity,*
2. *energy,*
3. *both intensity and energy.*

In a simplistic approach we might consider estimating the probability for a reaction between the incident particle and a target nucleus by treating the incident particles as points and the target nuclei as projecting an area πR^2 defined by the nuclear radius R.

- Any time an incident particle hits a nucleus, a reaction is assumed to happen; no reaction occurs when the particle misses the nucleus.
- This geometrical picture takes no account of the finite size of the incident particle nor does it consider the range of interaction forces that are in effect between the incident particle and the target nucleus.
- Rather than treating a geometrical cross sectional area πR^2 as a measure of interaction probability, we assign to the nucleus an effective area σ perpendicular to the incident beam such that a reaction occurs every time a bombarding particle hits any part of the effective disk area.
- This effective area is referred to as the reaction cross-section σ and is usually measured in barn, where 1 barn = 1 b = 10^{-24} cm^2. The cross section σ is proportional to the reaction probability P.
- The range of reaction cross sections σ in nuclear physics varies from a low of 10^{-19} b to a high of 10^6 b with the lower limit in effect for weak neutrino interactions with nuclei and the upper limit in effect for thermal neutron capture in certain nuclides.

The target of thickness x_o projects an area S to the incident particle beam. The target contains N nuclei each characterized with a reaction cross section σ. The density of nuclei $n^\square$ represents the number of nuclei N per volume of the target $V = Sx_o$.

To determine the reaction rate R (number of reactions per unit time) we consider two target options with regard to target thickness x_o: *thin targets* and *thick targets.*

Thin Targets
A *thin target* is thin enough so that no significant overlap between target nuclei occurs as the particle beam penetrates the target. This implies that negligible masking of target nuclei occurs in a thin target. The probability P for an incident particle to trigger a reaction in a thin target is the ratio of the effective area σN over the target area S, i.e.,

$$P = \frac{\sigma N}{S} = \frac{\sigma N x_o}{S x_o} = n^\square \sigma x_o \ . \tag{8.71}$$

If the number of incident particles per unit time is $\dot{N}_{\mathrm{o}}$, then R, the number of reactions per unit time is given as follows:

$$R = P\dot{N}_{\mathrm{o}} = \dot{N}_{\mathrm{o}}n^{\square}\sigma x_{\mathrm{o}} \ . \tag{8.72}$$

Thick Targets

In comparison with a thin target, a thick target has a thickness x_{o} that engenders considerable masking of target nuclei. In this case we assume that a thick target consists of a large number of thin targets. In each thin target layer of thickness dx the number of incident particles per unit time $\dot{N}$ diminishes by $d\dot{N}$ so that we can write $d\dot{N}(x)$ as

$$-d\dot{N}(x) = \dot{N}(x)n^{\square}\sigma dx \tag{8.73}$$

or

$$\int_{\dot{N}_{\mathrm{o}}}^{\dot{N}(t)} \frac{d\dot{N}(x)}{\dot{N}(x)} = -\int_{0}^{x_{\mathrm{o}}} n^{\square}\sigma dx \ , \tag{8.74}$$

where

$\dot{N}_{\mathrm{o}}$ is the number of particles per unit time striking the target.
$\dot{N}(x_{\mathrm{o}})$ is the number of particles per unit time that traverse the thick target of thickness x_{o}

The solution to (8.74) is

$$\dot{N}(x_{\mathrm{o}}) = \dot{N}_{\mathrm{o}}e^{-n^{\square}\sigma x_{\mathrm{o}}} \ . \tag{8.75}$$

The number of reactions per unit time in the thick target is now given by the following:

$$R = \dot{N}_{\mathrm{o}} - \dot{N}(x_{\mathrm{o}}) = \dot{N}_{\mathrm{o}}\left\{ 1 - e^{-n^{\square}\sigma x_{\mathrm{o}}} \right\} \ . \tag{8.76}$$

Equation (8.76) reduces to thin target relationship of (8.72) for small thicknesses x_{o}, as a consequence of the following approximation:

$$e^{-n^{\square}\sigma x_{\mathrm{o}}} \approx 1 - n^{\square}\sigma x_{\mathrm{o}} \ . \tag{8.77}$$

8.4.2 Neutron Activation

Stable nuclei may be transformed into unstable radioactive nuclei by bombardment with suitable particles or photons of appropriate energy. The process is known as *radioactivation* or *activation* and a variety of projectiles may be used for this purpose.

In practice the most commonly used activation process is triggered by *thermal neutrons* in a nuclear reactor, where a stable parent target P upon bombardment with neutrons is transformed into a radioactive daughter D

that decays with a decay constant λ_D into a granddaughter G, i.e.,

$$P \rightarrow D \rightarrow G . \tag{8.78}$$

The situation in radioactivation is similar to the *Parent→Daughter→Granddaughter* decay series discussed in Sect. 8.3, except that λ_P in neutron activation does not apply (the parent is stable) and is replaced by the product $\sigma_P \dot{\varphi}$ where:

σ_P is the probability for activation of parent nuclei governed by the activation cross section usually expressed in barn/atom where 1 barn = 1 b = 10^{-24} cm^2,

$\dot{\varphi}$ is the fluence rate of neutrons in the reactor usually expressed in neutrons per cm^2 per second, *i.e.*, cm$^{-2} \cdot$s^{-1}. Typical modern reactor fluence rates are of the order of 10^{11} to 10^{14} cm$^{-2} \cdot$s^{-1}. An assumption is made that the neutron fluence rate $\dot{\varphi}$ remains constant for the duration of the activation process, and this is not always easy to achieve in practice, especially for very long activation times.

8.4.3 Infinite Number of Parent Nuclei: Saturation Model

The daughter nuclei are produced at a rate of $\sigma_P \dot{\varphi} N_P(t)$ and they decay with a rate of $\lambda_D N_D(t)$. The number of daughter nuclei is $N_D(t)$ and the overall rate of change of the number of daughter nuclei is dN_D/dt obtained by combining the production rate of daughter nuclei $\sigma_P \dot{\varphi} N_P(t)$ with the decay rate of daughter nuclei $\lambda_D N_D(t)$ to get

$$\frac{dN_D(t)}{dt} = \sigma_P \dot{\varphi} N_P(t) - \lambda_D N_D(t) , \tag{8.79}$$

where $N_P(t)$ is the number of parent target nuclei.

An assumption is usually made that in neutron activation a negligible fraction of the parent atoms is transformed, so that the number of residual target atoms $N_P(t_o)$ equals to $N_P(0)$, the initial number of target atoms placed into the reactor for activation purposes at time $t = 0$. The time t_o is the total time the target is left in the reactor. The activation model that neglects the depletion of the number of target nuclei is referred to as the *saturation model*.

Another assumption is that the neutron fluence rate $\dot{\varphi}$ at the position of the sample is contributed from all directions. The sample in the form of pellets is irradiated in a "sea" of thermal neutrons and we may assume that the sample is a thin target that does not appreciably affect the neutron fluence inside the pellet.

For the initial conditions $N_P(t = 0) = N_P(0)$ and $N_D(t = 0) = N_D(0) = 0$ as well as the general condition that $N_P(t) = N_P(0) = $ const, the differential equation for dN_D/dt is written as

$$\frac{dN_D}{dt} = \sigma_P \dot{\varphi} N_P(0) - \lambda_D N_D(t) \tag{8.80}$$

or in the integral form as

$$\int\limits_{0}^{N_D(t)} \frac{d\left\{\sigma_P \dot{\varphi} N_P(0) - \lambda_D N_D\right\}}{\sigma_P \dot{\varphi} N_P(0) - \lambda_D N_D} = -\lambda_D \int\limits_{0}^{t} dt \ . \tag{8.81}$$

The solution of (8.81) is as follows:

$$N_D(t) = \frac{\sigma_P \dot{\varphi} N_P(0)}{\lambda_D} \left\{1 - e^{-\lambda_D t}\right\} \ . \tag{8.82}$$

The daughter activity $\mathscr{A}_D(t)$ equals to $\lambda_D N_D(t)$, thus we can write $\mathscr{A}_D(t)$ as

$$\mathscr{A}_D(t) = \sigma_P \dot{\varphi} N_P(0) \left\{1 - e^{-\lambda_D t}\right\} = (\mathscr{A}_{sat})_D \left\{1 - e^{-\lambda_D t}\right\} \ , \tag{8.83}$$

where $(\mathscr{A}_{sat})_D$, the saturation daughter activity that can be produced by bombardment of the parent target with neutrons, is equal to $\sigma_P \dot{\varphi} N_P(0)$.

Equation (8.83) is a simple exponential relationship and its initial slope $d\mathscr{A}_D(t)/dt$ at $t = 0$ is defined as the *radioactivation yield* Y_D of the daughter produced in the radioactivation process. The radioactivation yield represents the initial rate of formation of new daughter activity that depends upon the irradiation conditions as well as the decay constant of the daughter λ_D, as seen from the following expression:

$$Y_D = \left. \frac{d\mathscr{A}_D}{dt} \right|_{t=0} = \sigma_P \dot{\varphi} N_P(0) \lambda_D = \lambda_D (\mathscr{A}_{sat})_D = \frac{(\mathscr{A}_{sat})_D}{\tau_D} \ . \tag{8.84}$$

The build up of daughter activity $\mathscr{A}_D(t)$ in a target subjected to constant bombardment with neutrons in a reactor is illustrated in Fig. 8.8. The radioactivation yield Y_D is given by the initial slope of the growth curve at time $t = 0$. The extrapolation of the tangent to the growth curve at $t = 0$ intersects the asymptotic saturation activity line at a time $t = \tau_D = (t_{1/2})_D / \ln 2$, where $(t_{1/2})_D$ is the half-life of the daughter.

The following observations regarding the daughter activity growth curve, as given in (8.83), can now be made:

1. Initially at small t, where $\exp(-\lambda_D t) \approx 1 - \lambda_D t$, the growth of $\mathscr{A}_D(t)$ is rapid and almost linear with time, since

   $$\mathscr{A}_D(t) = (\mathscr{A}_{sat})_D \left\{1 - e^{-\lambda_D t}\right\} \approx (\mathscr{A}_{sat})_D \lambda_D t \ , \tag{8.85}$$

   but eventually at large times t the daughter activity $\mathscr{A}_D(t)$ becomes saturated (i.e., reaches a steady-state) at $(\mathscr{A}_{sat})_D$ and decays as fast as it is produced.
2. Equation (8.83) and Fig. 8.8 show that
   a. for an activation time $t = (t_{1/2})_D$, half the maximum activity $(\mathscr{A}_{sat})_D$ is produced;
   b. for $t = 2(t_{1/2})_D$, 3/4 of $(\mathscr{A}_{sat})_D$ is produced;
   c. for $t = 3(t_{1/2})_D$, 7/8 of $(\mathscr{A}_{sat})_D$ is produced, etc.
3. Because of the relatively slow approach to the saturation $(\mathscr{A}_{sat})_D$, it is generally accepted that in practice activation times beyond $2(t_{1/2})_D$ are not worthwhile.
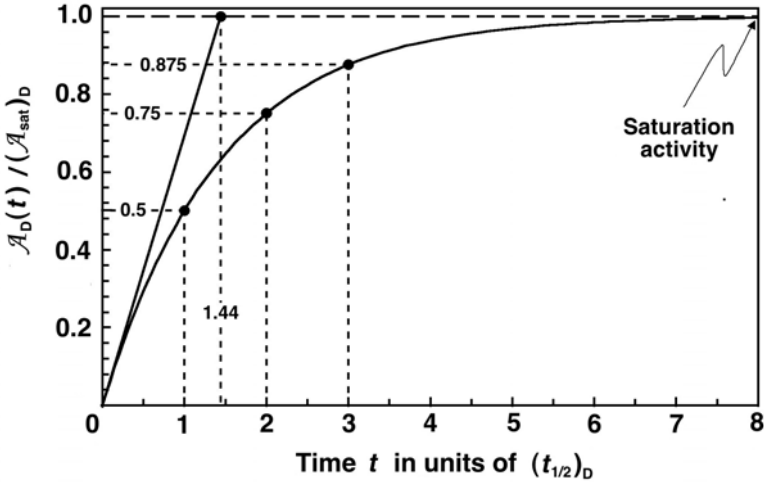
Fig. 8.8. Growth of daughter activity $\mathcal{A}_D(t)$ normalized to saturation activity $(\mathcal{A}_{\mathrm{sat}})_D$ plotted against time normalized to the half-life of the daughter $(t_{1/2})_D$. The slope of the tangent on the $\mathcal{A}_D(t)/(\mathcal{A}_{\mathrm{sat}})_D$ vs. t curve at $t = 0$, defined as the activation yield Y_D, is also shown

8.4.4 Finite Number of Parent Nuclei: Depletion Model

In situations where a measurable fraction of the target is consumed during the activation process, we can no longer assume that $N_P(t) = $ const. The fractional decrease in the number of parent atoms depends on the activation cross section σ_P and on the fluence rate $\dot{\varphi}$ of the reactor. The activation model that accounts for the depletion of the number of the target nuclei during the radioactivation process is called the *depletion model*.

In general, the rate of change in the number of parent atoms $N_P(t)$ with time t can be written as follows:

$$\frac{dN_P(t)}{dt} = -\sigma_P \dot{\varphi} N_P(t) , \tag{8.86}$$

similarly to the expression for radioactive decay given in (8.4) but replacing λ_P in (8.4) with the product $\sigma_P \dot{\varphi}$. The general solution for $N_P(t)$ of (8.86) is then

$$N_P(t) = N_P(0) e^{-\sigma_P \dot{\varphi} t} , \tag{8.87}$$

with $N_P(0)$ the initial number of parent nuclei placed into the reactor at time $t = 0$ and $N_P(t)$ the number of parent nuclei at time t.

The general expression for dN_D/dt, the rate of change in the number of daughter nuclei, is the number of parent nuclei transformed into daughter nuclei [governed by $N_P(t)$, σ_P, and $\dot{\varphi}$] minus the number of daughter nuclei that decay [governed by $N_D(t)$ and λ_P], or

$$\frac{dN_{\mathrm{D}}(t)}{dt} = \sigma_{\mathrm{P}}\dot{\varphi}N_{\mathrm{P}}(t) - \lambda_{\mathrm{D}}N_{\mathrm{D}}(t) , \tag{8.88}$$

with $N_{\mathrm{P}}(t)$ given in (8.81) in parallel to (8.22) for the $\mathrm{P} \to \mathrm{D} \to \mathrm{G}$ decay series.

The solution to (8.88), following the steps taken in the derivation of (8.30) for the $\mathrm{P} \to \mathrm{D} \to \mathrm{G}$ decay series and using the initial conditions:

$$N_{\mathrm{P}}(t = 0) = N_{\mathrm{P}}(0) \tag{8.89}$$

$$N_{\mathrm{D}}(t = 0) = N_{\mathrm{D}}(0) = 0 \tag{8.90}$$

is now as follows:

$$N_{\mathrm{D}}(t) = N_{\mathrm{P}}(0)\frac{\sigma_{\mathrm{P}}\dot{\varphi}}{\lambda_{\mathrm{D}} - \sigma_{\mathrm{P}}\dot{\varphi}} \left\{ e^{-\sigma_{\mathrm{P}}\dot{\varphi}t} - e^{-\lambda_{\mathrm{D}}t} \right\} . \tag{8.91}$$

Recognizing that $\mathscr{A}_{\mathrm{D}}(t) = \lambda_{\mathrm{D}}N_{\mathrm{D}}(t)$ and assuming the validity of the depletion model, we get the following general expression for the growth of the daughter activity $\mathscr{A}_{\mathrm{D}}(t)$:

$$\mathscr{A}_{\mathrm{D}}(t) = N_{\mathrm{P}}(0)\frac{\sigma_{\mathrm{P}}\dot{\varphi}\lambda_{\mathrm{D}}}{\lambda_{\mathrm{D}} - \sigma_{\mathrm{P}}\dot{\varphi}} \left\{ e^{-\sigma_{\mathrm{P}}\dot{\varphi}t} - e^{-\lambda_{\mathrm{D}}t} \right\} . \tag{8.92}$$

Since (8.92) for $\mathscr{A}_{\mathrm{D}}(t)$ in neutron activation is identical in form to (8.31) for a decay series, we use the analysis presented with regard to the decay series to obtain solutions for the general daughter growth in neutron activation. Generally, in neutron activation $\sigma_{\mathrm{P}}\dot{\varphi} < \lambda_{\mathrm{D}}$ and this results in transient equilibrium dynamics, as discussed for the decay series in Sect. 8.3.

When $\sigma_{\mathrm{P}}\dot{\varphi} \ll \lambda_{\mathrm{D}}$, we are dealing with a special case of transient equilibrium called secular equilibrium for which (8.92) will simplify to an expression that was given in (8.75) for the saturation model and was derived under the assumption that the fraction of nuclei transformed from parent to daughter in neutron activation is negligible in comparison to the initial number of parent atoms $N_{\mathrm{P}}(0)$. Equation (8.92) then reads

$$\mathscr{A}_{\mathrm{D}}(t) = \sigma_{\mathrm{P}}\dot{\varphi}N_{\mathrm{P}}(0)\left\{1 - e^{-\lambda_{\mathrm{D}}t}\right\} = (\mathscr{A}_{\mathrm{sat}})_{\mathrm{D}}\left\{1 - e^{-\lambda_{\mathrm{D}}t}\right\} , \tag{8.93}$$

where $(\mathscr{A}_{\mathrm{sat}})_{\mathrm{D}} = \sigma_{\mathrm{P}}\dot{\varphi}N_{\mathrm{P}}(0)$ is the saturation activity that is attainable by the target under the condition of secular equilibrium.

In the saturation model the activity $\mathscr{A}_{\mathrm{D}}(t)$ approaches the saturation activity $(\mathscr{A}_{\mathrm{sat}})_{\mathrm{D}}$ exponentially, as given in (8.93) and shown in Fig. 8.7. In saturation the production rate of the daughter equals the decay rate of the daughter resulting in a constant $N_{\mathrm{D}}(t)$ and constant saturation activity $(\mathscr{A}_{\mathrm{sat}})_{\mathrm{D}}$.

Usually, the growth of daughter in neutron activation is treated under the condition of secular equilibrium; however, with high enough reactor fluence rates $\dot{\varphi}$ and low enough daughter decay constants λ_{D}, this approximation may no longer be valid. The theoretical treatment then should recognize the radioactivation process as one of transient equilibrium for which account must be taken of the depletion of target nuclei, as given in (8.92).

- As discussed in detail in Section 8.3, the daughter activity $\mathcal{A}_D(t)$ in transient equilibrium cannot be assumed to reach saturation with increasing time t. Rather, the daughter activity $\mathcal{A}_D(t)$ is zero at time $t = 0$, and with increasing time first rises with t, reaches a maximum $(\mathcal{A}_{max})_D$ at time $t = (t_{max})_D$, and then drops as t increases further until at $t = \infty$ it becomes zero again.
- The daughter activity will reach its maximum $(\mathcal{A}_{max})_D = \mathcal{A}_D[(t_{max})_D]$ at the point of ideal equilibrium that occurs at a time $(t_{max})_D$ where $d\mathcal{A}_D(t_{max})/dt = 0$ and $\mathcal{A}_D[(t_{max})_D] = \sigma_P\dot{\varphi}N_P[(t_{max})_D]$. Note that in general $\mathcal{A}_D[(t_{max})_D] < (\mathcal{A}_{sat})_D$.
- The time $(t_{max})_D$ is given as

$$(t_{max})_D = \frac{\ln(\sigma_P\dot{\varphi}/\lambda_D)}{\sigma_P\dot{\varphi} - \lambda_D} . \tag{8.94}$$

Equation (8.94) with $\sigma_P\dot{\varphi}$ replaced by λ_P is identical in form to $(t_{max})_D$ that was calculated for a decay series in (8.33).

- Defining new parameters m, $(x_{max})_D$ and $(y_{max})_D$ as well as variables x, y_P, and y_D, similarly to the approach we took in Sect. 8.3.4 for the decay series, we can understand better the dynamics resulting from the saturation and depletion models of the neutron activation process. The parameters and variables are for neutron activation defined as follows, with m the so-called *activation factor*:

$$m = \frac{\sigma_P\dot{\varphi}}{\lambda_D}, \qquad\qquad \text{compare with (8.40)} \quad (8.95)$$

$$(x_{max})_D = \frac{m}{m-1}\frac{\ln m}{\ln 2}$$
$$\quad \text{for } m > 0 \text{ and } m \neq 1 \qquad\qquad \text{see (8.46)} \quad (8.96)$$
$$(x_{max})_D = 1/\ln 2 = 1.44 \qquad \text{for } m = 1 \qquad\qquad \text{see (8.47)} \quad (8.97)$$

$$(y_{max})_D = y_P(x_{max}) = 2^{\left(\frac{m}{1-m}\right)\frac{\ln m}{\ln 2}} = \frac{1}{2^{x_{max}}}$$
$$\equiv e^{\frac{m}{1-m}\ln m} = e^{-(\ln 2)(x_{max})_D},$$
$$\quad \text{for } m > 0, m \neq 1 \tag{8.98}$$

$$(y_{max})_D = 1/e = 0.368, \text{ for } m = 1 \qquad\qquad \text{see (8.50).} \quad (8.99)$$

$$x = \frac{\sigma_P\dot{\varphi}}{\ln 2}t = m\frac{\lambda_D}{\ln 2}t = m\frac{t}{(t_{1/2})_D}, \qquad \text{compare with (8.37).} \quad (8.100)$$

$$y_P = \frac{N_P(t)}{N_P(0)} = e^{-\sigma_P\dot{\varphi}t} = e^{-x\ln 2} = \frac{1}{2^x}, \qquad\qquad \text{see (8.43).} \quad (8.101)$$

$$y_D = \frac{\mathcal{A}_D(t)}{\sigma_P\dot{\varphi}N_P(0)}, \qquad\qquad \text{see (8.41) and (8.42).} \quad (8.102)$$
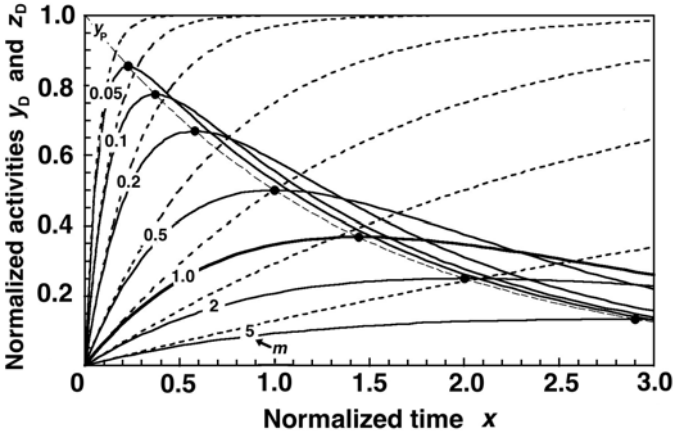
Fig. 8.9. Normalized daughter activities z_D of (8.105) for the saturation model (*dotted curves*) and y_D of (8.103) for the depletion model (*solid curves*) against the variable x for various decay factors m in the transient equilibrium region from 0.05 to 1.0 as well as for $m = 2$ and $m = 5$ in the non-equilibrium region where $m > 1$. The y_P curve is shown *dashed*. Points of ideal equilibrium specified for the depletion model by $(x_{max})_D$ and $(y_{max})_D$ are indicated with *heavy dots* on the y_P curve. Variables x and y_P are given by (8.100) and (8.101), respectively. Variables z_D for the saturation model and y_D for the depletion model $(m \neq 1)$ are given by (8.105) and (8.103), respectively. Variable y_D for the depletion model with $m = 1$ is given by (8.104). The activation m is defined in (8.95)

Similarly to (8.41), the variable $y_D(x)$ for the depletion model is given by the following function after inserting (8.95), (8.98), and (8.100) into (8.92) to get

$$y_D = \frac{1}{1-m}\left\{e^{-x\ln 2} - e^{-\frac{x}{m}\ln 2}\right\} = \frac{1}{1-m}\left\{\frac{1}{2^x} - \frac{1}{2^{x/m}}\right\} . \quad (8.103)$$

Equation (8.103) is valid for all positive m except for $m = 1$. For $m = 1$, $y_D(x)$ is given by the following function, as discussed in relation to (8.42):

$$y_D(m = 1) = (\ln 2)x/(2^x) . \quad (8.104)$$

For the saturation model, on the other hand, the normalized daughter activity z_D is given for any $m > 0$ as follows after inserting (8.95), (8.98) and (8.100) into (8.93)

$$z_D = \frac{\mathscr{A}_D(t)}{(\mathscr{A}_{sat})_D} = \frac{\mathscr{A}_D(t)}{\sigma_P\dot{\varphi}N_P(0)} = 1 - e^{-\lambda_D t}$$

$$= 1 - e^{-\frac{\lambda_D}{\sigma_P\dot{\varphi}}(\ln 2)x} = 1 - e^{-\frac{(\ln 2)x}{m}} = 1 - \frac{1}{2^{x/m}} . \quad (8.105)$$

To illustrate the general case of neutron activation for any m between zero (secular equilibrium) and 1 (start of non-equilibrium conditions) we show in Fig. 8.9 a plot of y_D and z_D against x for various m in the range from 0.05
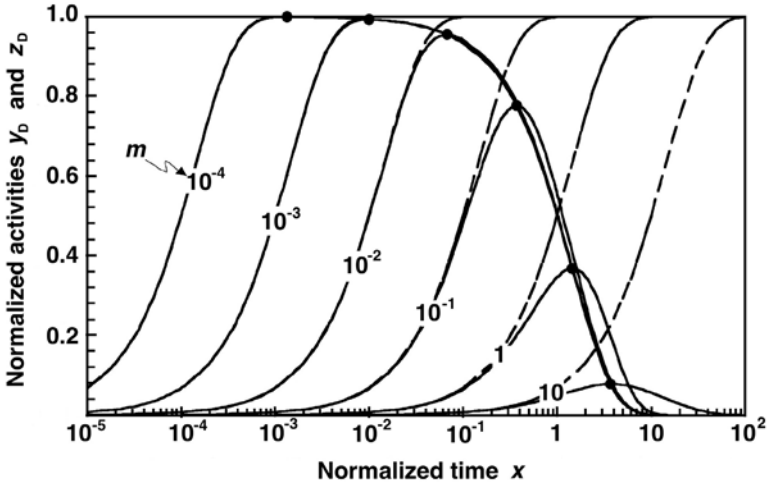
Fig. 8.10. Normalized daughter activities z_D of (8.105) for the saturation model (*dashed curves*) and y_D of (8.103) for the depletion model (*solid curves*) against the variable x for various activation factors m in the range from $m = 10^{-4}$ to $m = 10$. The *heavy dots* represent $(y_{max})_D$, the maxima of y_D for given m and follow the normalized parent activity y_P of (8.101). Variables x and y_P are given by (8.100) and (8.101), respectively. Variables z_D for the saturation model and y_D for the depletion model ($m \neq 1$) are given by (8.105) and (8.103), respectively. Variable y_D for the depletion model with $m = 1$ is given by (8.104). The decay factor m is defined in (8.95)

to 5 for both activation models: the saturation model of (8.105) with dashed curves and the depletion model of (8.103) with solid curves. For comparison we also show the y_P curve that indicates the depletion of the target nuclei during the neutron activation process.

The points of ideal equilibrium in the depletion model, where y_D reaches its maximum, are shown with dots on the y_P curve in Fig. 8.9. The expressions for $(x_{max})_D$ and $(y_{max})_D$ in terms of the activation factor $m \neq 1$ are given by (8.96) and (8.98), respectively, and for $m = 1$ by (8.97) and (8.99), respectively.

In Fig. 8.10 we plot the normalized daughter activities z_D for the saturation model and y_D for the depletion model from (8.105) and (8.103), respectively, against the variable x on a logarithmic scale to cover 6 orders of magnitude in the activation factor m ranging from 10^{-4} to 10. Some of the data presented in Fig. 8.10 have already been plotted in Fig. 8.9 that covers a much smaller range in m (from 0.05 to 5). The maxima $(y_{max})_D$ in depletion model curves are indicated with heavy dots that also follow a trace of y_P, the normalized number of parent nuclei given in (8.101).

The following conclusions can now be reached with regard to Figs. 8.9 and 8.10:

1. In practical neutron activation procedures the *activation factor* $m = \sigma_P \dot{\varphi}/\lambda_D$ is generally very small, justifying the use of the saturation model in studies of radioactivation dynamics. However, since m depends on the fluence rate $\dot{\varphi}$, neutron activation processes with very high fluence rates or relatively long activation times may invalidate the saturation model in favor of the depletion model.

2. The initial slope dy_D/dx at $t = 0$ is proportional to the activation yield Y defined for the saturation model in (8.77). A closer look at Figs. 8.9 and 8.10 reveals that both the saturation model and the depletion model predict y_D with the same initial slopes equal to $(\ln 2/m)$ irrespective of the magnitude of m. This result can be obtained by taking the derivative dy_D/dx at $x = 0$ of (8.105) for the saturation model and (8.103) for the depletion model.

3. For all m in the saturation model z_D approaches its saturation value of 1.0 exponentially, while in the depletion model y_D reaches its peak value $(y_{max})_D$ at $(x_{max})_D$ and then decreases with increasing x.

4. In the saturation model, for a given m, the normalized daughter activity z_D approaches exponentially the saturation value $(z_{sat})_D = 1$. The larger is m, the shallower is the initial slope, and the slower is the approach to saturation.

5. In the depletion model, for a given m, the normalized daughter activity y_D exhibits a maximum value $(y_{max})_D$ that is smaller than the saturation value $(z_{sat})_D = 1$. The larger is m the larger is the discrepancy between the two models and the smaller is $(y_{max})_D$ in comparison with $(z_{sat})_D = 1$.

6. Parameter $(y_{max})_D$ is the point of ideal equilibrium calculated from (8.98) and (8.99). It depends on $(x_{max})_D$, as shown in (8.98). Parameter $(x_{max})_D$ in turn depends on the activation factor m and is calculated from (8.46) and (8.96). As m decreases from $m = 1$ toward zero, $(x_{max})_D$ decreases and $(y_{max})_D$ increases, as shown by dots on the y_P curve in Figs. 8.9 and 8.10.

7. For $m > 10^{-3}$ parameter $(y_{max})_D$ decreases with increasing m. Thus, in this region of m the depletion model should be used for determination of the daughter activity.

8. For all $0 < m < 1$, variables y_P and y_D are said to be in transient equilibrium at $x \gg (x_{max})_D$. For $m \geq 1$ no equilibrium between y_P and y_D exists at any x.

9. For $m < 10^{-2}$, y_P and y_D are in the special form of transient equilibrium called secular equilibrium.

10. For $m < 10^{-3}$ the saturation model and the depletion model give identical results, *i.e.*, $y_D = z_D$, for $x \leq (x_{max})_D$ and attain a value of 1 at $x = (x_{max})_D$. However, for $x > (x_{max})_D$, z_D remains in saturation, while y_D decreases in harmony with y_P.

11. Using (8.102) we can now express $(A_{max})_D$, the maximum daughter activity in the depletion model, as follows:

$$(\mathscr{A}_{\mathrm{D}})_{\max} = (y_{\max})_{\mathrm{D}} \sigma_{\mathrm{P}} \dot{\varphi} N_{\mathrm{P}}(0) = \sigma_{\mathrm{P}} \dot{\varphi} N_{\mathrm{P}}(0)\, 2^{-(x_{\max})_{\mathrm{D}}}$$
$$= \sigma_{\mathrm{P}} \dot{\varphi} N_{\mathrm{P}}(0)\, e^{-\frac{m}{1-m} \ln m} \ . \tag{8.106}$$

12. Equation (8.106) shows that the maximum daughter activity $(\mathscr{A}_{\max})_{\mathrm{D}}$ depends on the saturation activity $(\mathscr{A}_{\mathrm{sat}})_{\mathrm{D}} = \sigma_{\mathrm{P}} \dot{\varphi} N_{\mathrm{P}}(0)$ and on $(y_{\max})_{\mathrm{D}}$ which approaches 1 for $m \to 0$, as shown in Fig. 8.4. However, as m increases toward 1, $(y_{\max})_{\mathrm{D}}$ decreases, resulting in $(\mathscr{A}_{\max})_{\mathrm{D}}$ that may be significantly smaller than $(\mathscr{A}_{\mathrm{sat}})_{\mathrm{D}}$.
13. Since the normalized daughter activity $y_{\mathrm{D}}(x)$ decreases with x for $x > (x_{\max})_{\mathrm{D}}$, it is obvious that activation times beyond $(x_{\max})_{\mathrm{D}}$ are counter-productive.

8.4.5 Maximum Attainable Specific Activities in Neutron Activation

As is evident from Fig. 8.10, $(y_{\max})_{\mathrm{D}}$, the maximum normalized daughter activity for the depletion model decreases with the activation factor $m = \sigma_{\mathrm{p}} \dot{\varphi}/\lambda_{\mathrm{D}}$. In practice this means that, for a given daughter radionuclide, $(y_{\max})_{\mathrm{D}}$ depends only on the particle fluence rate $\dot{\varphi}$, since the parameters σ_{p} and λ_{D} remain constant.

We now determine the maximum daughter specific activities $(a_{\max})_{\mathrm{D}}$ that can be attained during the activation process, as predicted by the saturation model and the depletion model.

For the *saturation model* we use (8.105) to get

$$(a_{\max})_{\mathrm{D}} = (a_{\mathrm{sat}})_{\mathrm{D}} = \frac{(\mathscr{A}_{\mathrm{sat}})_{\mathrm{D}}}{M_{\mathrm{P}}} = (z_{\max})_{\mathrm{D}} \sigma_{\mathrm{P}} \dot{\varphi} \frac{N_{\mathrm{P}}(0)}{M_{\mathrm{P}}} = \left(\sigma_{\mathrm{P}} \frac{N_{\mathrm{A}}}{A_{\mathrm{P}}}\right) \dot{\varphi} \ , \tag{8.107}$$

where M_{p} and A_{p} are the atomic mass and the atomic mass number of the parent nucleus, respectively, and the parameter $(z_{\max})_{\mathrm{D}}$ is equal to the saturation value of z_{D} equal to 1. Since $\sigma_{\mathrm{p}} N_{\mathrm{A}}/A_{\mathrm{p}}$ is constant for a given parent nucleus, we note that $(a_{\max})_{\mathrm{D}}$ is linearly proportional to $\dot{\varphi}$, the particle fluence rate. As $\dot{\varphi} \to \infty$ we get

$$\lim_{\dot{\varphi} \to \infty} (a_{\max})_{\mathrm{D}} = \infty \ , \tag{8.108}$$

This is obviously a problematic result, since we know that the maximum daughter specific activity produced through neutron activation cannot exceed the theoretical specific activity $(a_{\mathrm{theor}})_{\mathrm{D}}$, given for the daughter in (8.2) as

$$(a_{\mathrm{theor}})_{\mathrm{D}} = \frac{\mathscr{A}_{\mathrm{D}}}{M_{\mathrm{D}}} = \frac{\lambda_{\mathrm{D}} N_{\mathrm{D}}}{M_{\mathrm{D}}} = \frac{\lambda_{\mathrm{D}} N_{\mathrm{A}}}{A_{\mathrm{D}}} \ . \tag{8.109}$$

Equation (8.107) shows that the saturation model is useful as an approximation only for relatively low particle fluence rates $\dot{\varphi}$; at high fluence rates it breaks down and predicts a physically impossible result.

For the *depletion model* we use (8.102) to get

$$(a_{\max})_D = \frac{(\mathcal{A}_{\max})_D}{M_P} = (y_{\max})_D \sigma_P \dot{\varphi} \frac{N_P(0)}{M_P} = \left(\frac{\sigma_P N_A}{A_P}\right) (y_{\max})_D \dot{\varphi} \ .$$

(8.110)

This result is similar to $(a_{\max})_D$ given in (8.107) for the saturation model; however, it contains $(y_{\max})_D$, the normalized daughter activity that exhibits its own dependence on $\dot{\varphi}$, as shown in Fig. 8.10 and given in (8.98). Introducing the expression for $(y_{\max})_D$ of (8.98) into (8.112) and recognizing that the activation factor m is equal to $\sigma_p \dot{\varphi}/\lambda_D$, we get the following expression for the maximum daughter specific activity $(a_{\max})_D$:

$$(a_{\max})_D = \left(\frac{\sigma_P N_A}{A_P}\right) \dot{\varphi}\, e^{\frac{m}{1-m} \ln m} \ .$$

(8.111)

At first glance, it seems that the depletion model of (8.111) also suffers the same catastrophe with $\dot{\varphi} \to \infty$, as shown in (8.107) for the saturation model. However, a closer look at $\lim\limits_{\dot{\varphi} \to \infty} (a_{\max})_D$ for the depletion model produces a very logical result, namely that the maximum daughter specific activity $(a_{\max})_D$ will not exceed the theoretical specific activity a_{theor}, or

$$\lim_{\dot{\varphi} \to \infty} (a_{\max})_D = \left(\frac{\sigma_P N_A}{A_P}\right) \lim_{\dot{\varphi} \to \infty} \dot{\varphi}\, e^{-\frac{\sigma_P \dot{\varphi}/\lambda_D}{(\sigma_P \dot{\varphi}/\lambda_D)-1} \ln(\sigma_P \dot{\varphi}/\lambda_D)}$$
$$= \left(\frac{\sigma_P N_A}{A_P}\right) \lim_{\dot{\varphi} \to \infty} \dot{\varphi}\, e^{-\ln(\sigma_P \dot{\varphi}/\lambda_D)} = \frac{\lambda_D N_A}{A_P} \approx (a_{\text{theor}})_D$$

(8.112)

The result of (8.112) is independent of the particle fluence rate $\dot{\varphi}$, irrespective of the magnitude of $\dot{\varphi}$ and depends only on the decay constant λ_D of the daughter and the atomic mass number A_P of the parent. Recognizing that $A_p \approx A_D$ at least for large atomic number activation targets, we can state that $\lambda_D N_A / A_P \approx (a_{\text{theor}})_D$.

The depletion model, in contrast to the currently used saturation model, thus adequately predicts (a_{theor}) as the limit for the maximum attainable daughter specific activity in neutron activation and should be taken as the correct model for describing the parent/daughter kinematics in radioactivation in general, irrespective of the magnitude of the particle fluence rate $\dot{\varphi}$ used in the radioactivation.

The saturation model is valid as a special case of the depletion model under one of the following two conditions:

1. for the activation factor $m = \sigma_p \dot{\varphi}/\lambda_D < 10^{-3}$,
2. for the activation time t_a short compared to $(t_{\max})_D$, the time of ideal equilibrium between y_P and y_D.

The maximum attainable specific activities $(a_{\text{sat}})_D$ and $(a_{\max})_D$ are plotted against the neutron fluence rate $\dot{\varphi}$ in Fig. 8.11 for cobalt-60, iridium-192
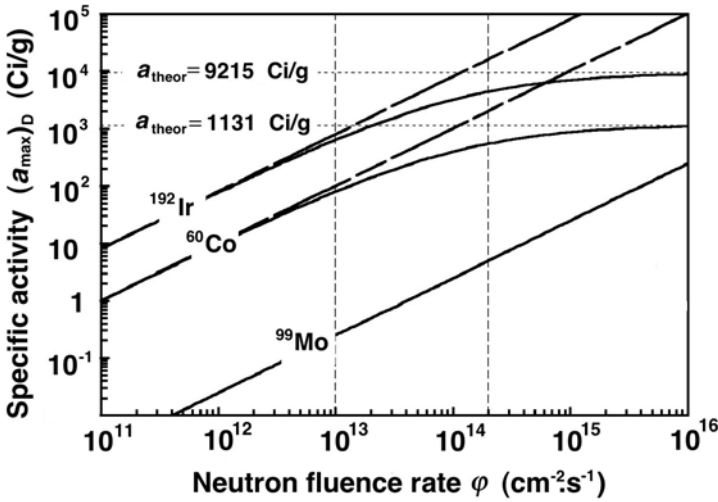
Fig. 8.11. Maximum attainable specific activities $(a_{sat})_D$ and $(a_{max})_D$ for the saturation model (*dashed curves*) and the depletion model (*solid curves*), respectively, plotted against neutron fluence rate $\dot{\varphi}$ for cobalt-60, iridium-192, and molybdenum-99 daughter products in neutron activation. The theoretical specific activities of cobalt-60 and iridium-192 are indicated with *horizontal dashed lines*. The *vertical dashed lines* at $\dot{\varphi} = 10^{13}$ cm$^{-2} \cdot$ s^{-1} and 2×10^{14} cm$^{-2} \cdot$ s^{-1} indicate data for the two neutron fluence rates of Table 8.2

and molybdenum-99. The theoretical specific activities $(a_{theor})_D$ for cobalt-60 and iridium-192 are also indicated in the figure. We note for iridium-192 and cobalt-60 that in the practical range from 10^{13} to 10^{15} cm$^{-2} \cdot$ s^{-1} the saturation model fails, while the depletion model approaches asymptotically the theoretical result. For molybdenum-99 in the neutron fluence range shown in Fig. 8.11, the maximum attainable specific activities are 5 to 6 orders of magnitude lower than $(a_{theor})_{MO}$, so that the saturation and depletion model give identical results as a consequence of $(\sigma_{MO}\dot{\varphi}/\lambda_{MO} < 10^{-3})$.

Table 8.1 lists the important characteristics of cobalt-60, iridium-192, and molybdenum-99. The theoretical specific activity $(a_{theor})_D$ is calculated from (8.2) assuming that the radioactive nuclide contains only the daughter nuclei, i.e., the source is carrier-free.

Table 8.2 lists the neutron activation characteristics for the saturation and depletion models applied to production of cobalt-60, iridium-192 and molybdenum-99 with two neutron fluence rates: $\dot{\varphi} = 10^{13}$ cm$^{-2} \cdot$ s^{-1} and $\dot{\varphi} = 2 \times 10^{14}$ cm$^{-2} \cdot$ s^{-1}. The two fluence rates are indicated with vertical dashed lines in Fig. 8.11 and are representative of rates used in activation processes with modern nuclear reactors. Of main interest in Table 8.2 are the maximum attainable specific activities $(a_{sat})_D$ and $(a_{max})_D$ predicted by the saturation model and the depletion model, respectively, and their comparison

Table 8.1. Characteristics of three radionuclides: cobalt-60, iridium-192, and molybdenum-99 produced by neutron activation in a nuclear reactor

Daughter nuclide	Cobalt-60	Iridium-192	Molybdenum-99
Half-life $(t_{1/2})_D$	5.27 y	73.8 d	66 h
Decay constant (s^{-1})	4.171×10^{-9}	1.087×10^{-7}	2.917×10^{-6}
Parent nuclide	Cobalt-59	Iridium-191	Molybdenum-98
Nuclear reaction	$^{59}_{27}Co(n,\gamma)^{60}_{27}Co$	$^{191}_{77}Ir(n,\gamma)^{191}_{77}Ir$	$^{98}_{42}Mo(n,\gamma)^{99}_{42}Mo$
Cross section (b)	37.2	954	0.13
a_{theor} [a] (Ci/g)	1.131×10^3	9.215×10^3	4.8×10^5
a_{pract} [b] (Ci/g)	~ 250	~ 450	~ 0.3
$\sigma_P N_A / A_P$ (cm^2/g)	0.38	3.01	8×10^{-4}

[a] Theoretical specific activity: $a_{theor} = \lambda_D N_A / A_D$, assuming a carrier-free source.
[b] Practical specific activity produced in a nuclear reactor.

to the theoretical values $(a_{theor})_D$ for the three daughter D products, also listed in the table.

Two interesting features of Fig. 8.11 and Table 8.2 are of note:

- For cobalt-60 $(a_{theor})_{Co} = 1131$ Ci/g, while at $\dot{\varphi} = 2 \times 10^{14}$ cm^{-2}·s^{-1} the saturation model for cobalt-60 production predicts $(a_{sat})_{Co} = 2054$ Ci/g, a physically impossible result. On the other hand, the depletion model predicts that $(a_{max})_{Co} = 550$ Ci/g which is a realistic result that can be substantiated with experiment.

- A study of iridium-192 results in conclusions similar to those for cobalt-60 and this is understood, since the activation factors m for the two radionuclides are essentially identical. The activation factor m for molybdenum-99 for practical fluence rates, on the other hand, is so small that both models predict identical specific activities, both a miniscule fraction of $(a_{theor})_{MO}$.

Of interest is also the activation time $(t_{max})_D$ required to obtain $(a_{max})_D$ using the depletion model. From (8.100) and (8.96) we obtain

$$\frac{(t_{max})_D}{(t_{1/2})_D} = \frac{x_{max}}{m} = \frac{\ln m}{(\ln 2)(m-1)} = \frac{\lambda_D \ln \frac{\sigma_P \dot{\varphi}}{\lambda_D}}{(\ln 2)(\sigma_P \dot{\varphi} - \lambda_D)} , \qquad (8.113)$$

with roughly an inverse proportionality with fluence rate $\dot{\varphi}$. Thus, the higher is the particle fluence rate $\dot{\varphi}$, the shorter is the time required to reach the maximum specific activity $(a_{max})_D$. For example, $(t_{max})_{Co}$ is 20.2 years at $\dot{\varphi} = 10^{13}$ cm^{-2}·s^{-1} and 5.61 years at $\dot{\varphi} = 2 \times 10^{14}$ cm^{-2}·s^{-1}, as also shown in Table 8.2.

The time $(t_{max})_D/(t_{1/2})_D$ of (8.113) is plotted against the neutron fluence rate $\dot{\varphi}$ for cobalt-60, iridium-192, and molybdenum-99 in Fig. 8.12. The curves

Table 8.2. Neutron activation characteristics for the saturation and depletion models applied to neutron activation of cobalt-59 into cobalt-60, iridium-191 into iridium-192, and molybdenum-98 into molybdenum-99 with neutron fluence rates of 10^{13} cm$^{-2}\cdot$s^{-1} and 2×10^{14} cm$^{-2}\cdot$s^{-1}

	Daughter nuclide	Cobalt-60		Iridium-192		Molybdenum-99	
(1)	$(a_{\text{theor}})_{\text{D}}$(Ci/g)	1131		9215		479604	
	$\dot{\varphi}$(cm$^{-2}\cdot$s^{-1})	10^{13}	2×10^{14}	10^{13}	2×10^{14}	10^{13}	2×10^{14}
(2)	$(a_{\text{sat}})_{\text{D}}$(Ci/g)	102.7	2054	813.5	16270	0.216	4.32
(3)	m	0.089	1.78	0.088	1.76	4.5×10^{-7}	8.9×10^{-6}
(4)	$x_{\max}$	0.341	1.90	0.338	1.89	9.4×10^{-6}	1.5×10^{-4}
(5)	$(y_{\max})_{\text{D}}$	0.789	0.268	0.791	0.270	1.00	1.00
(6)	$(a_{\max})_{\text{D}}$(Ci/g)	81.0	549.8	643.3	4398	0.22	4.32
(7)	$t_{\max}$	20.18 y	5.61 y	284.0 d	79.3 d	1392.4 h	1107.2 h

Footnotes:

(1) $\qquad (a_{\text{theor}})_{\text{D}} = \dfrac{\lambda_{\text{D}} N_{\text{A}}}{A_{\text{D}}}$ $\qquad\qquad$ see (8.109)

(2) $\qquad (a_{\text{sat}})_{\text{D}} = \dfrac{\sigma_{\text{P}} N_{\text{A}}}{A_{\text{P}}}\dot{\varphi}$ $\qquad\qquad$ see (8.107)

(3) $\qquad m = \dfrac{\sigma_{\text{P}}\dot{\varphi}}{\lambda_{\text{D}}}$ $\qquad\qquad$ see (8.95)

(4) $\qquad (x_{\max})_{\text{D}} = \dfrac{m}{(m-1)}\dfrac{\ln m}{\ln 2}$ $\qquad\qquad$ see (8.96)

(5) $\qquad (y_{\max})_{\text{D}} = \dfrac{1}{2^{x_{\max}}}$ $\qquad\qquad$ see (8.98)

(6) $\qquad (a_{\max})_{\text{D}} = \dfrac{\sigma_{\text{P}} N_{\text{A}}}{A_{\text{P}}}(y_{\max})_{\text{D}}\dot{\varphi}$ $\qquad\qquad$ see (8.112)

(7) $\qquad (t_{\max})_{\text{D}} = \dfrac{(t_{1/2})_{\text{D}}}{m}(x_{\max})_{\text{D}} = \dfrac{\ln 2}{m\lambda_{\text{D}}}(x_{\max})_{\text{D}}$

$\qquad\qquad = \dfrac{\ln 2}{\sigma_{\text{P}}\dot{\varphi}}(x_{\max})_{\text{D}} = \dfrac{\ln m}{\lambda_{\text{D}}(m-1)}$ $\qquad\qquad$ see (8.100)

for cobalt-60 and iridium-192 are essentially identical, because the activation factors m for the two radionuclides are very similar to one another as a result of similar ratios $\sigma_{\text{P}}/\lambda_{\text{D}}$ for the two radionuclides.

8.4.6 Examples of Parent Depletion: Neutron Activation of Cobalt-59, Iridium-191 and Molybdenum-98

Using the general data of Fig. 8.10 we plot in Fig. 8.13 the specific activity a_{D} of cobalt-60 in part (a) and of iridium-192 in part (b) against activation time t for various neutron fluence rates $\dot{\varphi}$ in the range from 10^{13} cm$^{-2}\cdot$s^{-1} to 2×10^{14} cm$^{-2}\cdot$s^{-1}. The specific activity a_{D} is calculated for the saturation model (dashed curves) given by (8.105) and the depletion model (solid curves) given in (8.103). Both equations are modified with incorporating (8.100) to obtain a plot of a_{D} against activation time t rather than against the general variable x. The heavy dots on the depletion model curves represent the time $(t_{\max})_{\text{D}}$ at which the maximum specific activity $(a_{\max})_{\text{D}}$ occurs. The theoretical specific
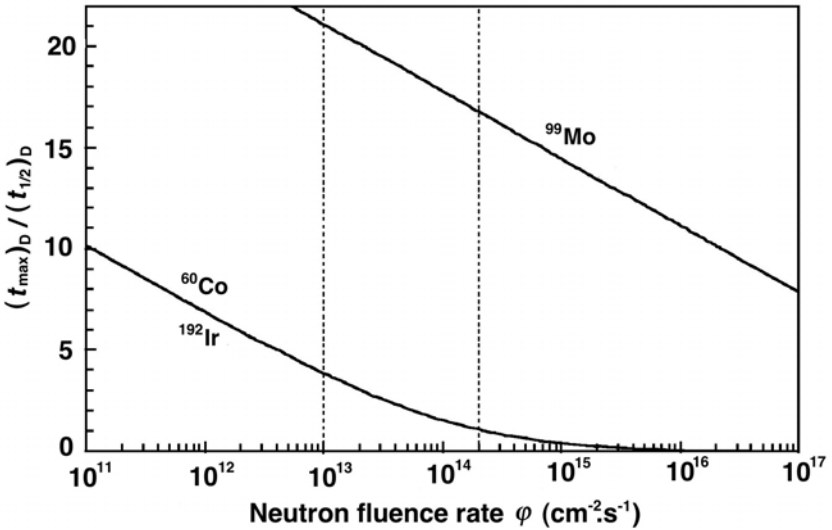
Fig. 8.12. Time $(t_{\max})_D/(t_{1/2})_D$ required for reaching the maximum specific activity $(a_{\max})_D$ plotted against neutron fluence rate $\dot\varphi$ for cobalt-60, iridium-192, and molybdenum-99. The data were calculated with the depletion model of radioactivation

activities a_{theor} of 1131 Ci/g and 9215 Ci/g for cobalt-60 and iridium-192, respectively, are indicated on the figure.

The discrepancy between the saturation and depletion model is evident, especially at high fluence rates and large activation times. An obvious break down of the saturation model occurs when it predicts a specific activity a_D that exceeds the theoretical specific a_{theor}.

Since both the saturation and the depletion model show identical initial slopes, i.e., activation yields [see (8.84) and Fig. 8.8], one may use the saturation model as a simple yet adequate approximation to the depletion model at activation times short in comparison with $t_{\max}$. However, when the goal is to obtain optimal specific activities in the daughter of the order of the theoretical specific activity for a given radionuclide, such as the cobalt-60 source for external beam radiotherapy or iridium-192 source for industrial radiography, the saturation model fails and the depletion model should be used for estimation of the required radioactivation times and specific activities expected.

Equation (8.111) gives a relationship between the maximum attainable specific activity $(a_{\max})_D$ and neutron fluence rate $\dot\varphi$ for the depletion model. We now calculate the fraction f of the theoretical specific activity $(a_{\text{theor}})_D$ that $(a_{\max})_D$ amounts to at a given fluence rate $\dot\varphi$. The functional relationship between f and $(a_{\max})_D$ will allow us to estimate the maximum possible
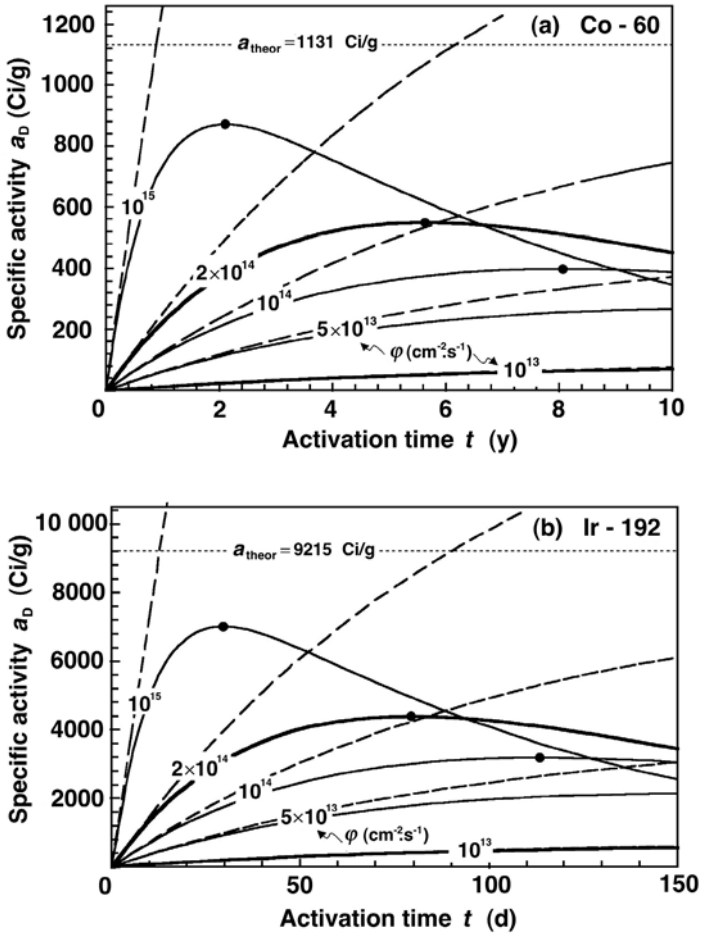
Fig. 8.13. Specific activity a_D of cobalt-60 in part **a** and of iridium-192 in part **b** plotted against activation time t for various neutron fluence rates. The specific activity a_D is calculated for the saturation model (*dashed curves*) given by (8.105) and the depletion model (*solid curves*) given in (8.103). Both equations are used in conjunction with (8.100) to obtain a plot of a_D against activation time t rather than against the variable x. The *heavy dots* on the depletion model curves represent the time $(t_{max})_D$ at which the maximum specific activity $(a_{max})_D$ occurs

specific activity for a given parent/daughter combination in a radioactivation process with a given fluence rate $\dot\varphi$. We write $(a_{max})_D$ as follows:

$$(a_{max})_D = f(a_{theor})_D = f\frac{\lambda_D N_A}{A_P} = \frac{\sigma_P N_A}{A_P}\dot\varphi\, e^{\frac{m}{1-m}\ln m}\,, \qquad (8.114)$$
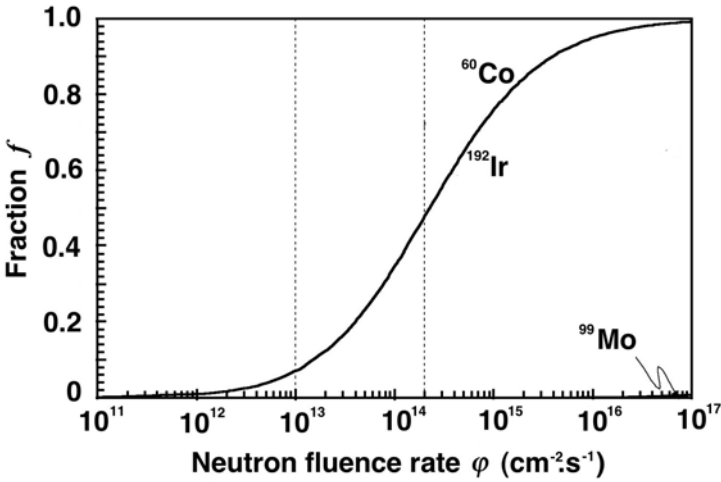
Fig. 8.14. Specific activity fraction f defined as $(a_{max})_D/(a_{theor})_D$ plotted against the neutron fluence rate $\dot{\varphi}$ for cobalt-60, iridium-192, and molybdenum-99. The data for molybdenum are visible only at very high fluence rates because the activation factor m at a given $\dot{\varphi}$ is several orders of magnitude smaller for molybdenum-99 in comparison with that of cobalt-60 and iridium-192

which gives

$$f = m \, e^{\frac{m}{1-m} \ln m} = m^{\frac{1}{1-m}}, \tag{8.115}$$

where we used the following relationships: $m = \sigma_P \dot{\varphi}/\lambda_D$ and $\mathscr{A}_D \approx \mathscr{A}_P$.

We then introduce $m = \alpha\dot{\varphi}$, where α is defined as $\alpha = \sigma_P/\lambda_D$, to obtain

$$f = (\alpha\dot{\varphi})^{1/(1-\alpha\dot{\varphi})} \tag{8.116}$$

and plot this expression in Fig. 8.14 for cobalt-60, iridium-192, and molybden-um-99 in the fluence rate range from 10^{11} cm$^{-2} \cdot$ s^{-1} to 10^{17} cm$^{-2} \cdot$ s^{-1}. Again, the data for cobalt-60 and iridium-192 are essentially the same for a given $\dot{\varphi}$, since, fortuitously, the ratio σ_P/λ_D is almost identical for the two radionuclides. The molybdenum-99 fraction f data, on the other hand, are extremely small in comparison to those of the other two radionuclides indicating very low practical specific activities in the practical fluence rate range from 10^{12} cm$^{-2} \cdot$ s^{-1} to 10^{15} cm$^{-2} \cdot$ s^{-1}.

Data from Fig. 8.14 show that for cobalt-60 and iridium-192 the fraction f is 0.07 at $\dot{\varphi} = 10^{13}$ cm$^{-2} \cdot$s^{-1} and 0.49 at $\dot{\varphi} = 2 \times 10^{14}$ cm$^{-2} \cdot$s^{-1}. Same results are provided in Table 8.2 with the ratio $(a_{max})_D/(a_{theor})_D$. Thus, to obtain a higher specific activity in a cobalt-60 or iridium-192 target, we would have to surpass the currently available reactor fluence rates $\dot{\varphi}$. For example, to reach $f = 0.75$, i.e., $(a_{max})_D = 850$ Ci/g for a cobalt-60 source and 6900 Ci/g for an iridium-192 source, a $\dot{\varphi}$ of 10^{15} cm$^{-2} \cdot$ s^{-1} would be required. This would result in an activation factor m of 8.8 and, as shown in Fig. 8.12 and given

by (8.113), the activation time t_{max} to reach this specific activity would be relatively short at 2.1 years for cobalt-60 and 30 days for iridium-192.

8.4.7 Neutron Activation of the Daughter: Depletion-Activation Model

In the discussion of neutron activation above we have tacitly assumed that the daughter nuclide is not affected by exposure to activation particles. In situations where this assumption does not hold, account must be taken of the activation of the daughter radionuclide into a granddaughter that may or may not be radioactive. Ignoring the possibility of the granddaughter radioactivity, we account for the daughter activation by subtracting $\sigma_D \dot{\varphi} N_D(t)$ from the differential equation for dN_D/dt given in (8.88) to obtain

$$\begin{aligned} \frac{dN_D}{dt} &= \sigma_D \dot{\varphi} N_D(t) - \lambda_D N_D(t) - \sigma_D \dot{\varphi} N_D(t) \\ &= \sigma_D \dot{\varphi} N_D(t) - \lambda_D^* N_D(t) \ , \end{aligned} \tag{8.117}$$

where σ_P and σ_D are cross sections for activation of parent and daughter nuclei, respectively; $N_P(t)$ and $N_D(t)$ are numbers of parent and daughter nuclei, respectively; and $\dot{\varphi}$ is the particle fluence rate. The modified decay constant λ_D^* is defined as follows:

$$\lambda_D^* = \lambda_D + \sigma_D \dot{\varphi} \ . \tag{8.118}$$

Using the same initial conditions as in (8.88), we get the following solution to (8.113):

$$N_D(t) = N_P(0) \frac{\sigma_P \dot{\varphi}}{\lambda_D^* - \sigma_P \dot{\varphi}} \left\{ e^{-\sigma_P \dot{\varphi} t} - e^{-\lambda_D^* t} \right\} \tag{8.119}$$

and the following expression for the daughter activity $\mathscr{A}_D(t)$

$$\begin{aligned} \mathscr{A}_D(t) &= \lambda_D N_D(t) = N_P(0) \frac{\sigma_P \dot{\varphi} \lambda_D}{\lambda_D^* - \sigma_P \dot{\varphi}} \left\{ e^{-\sigma_P \dot{\varphi} t} - e^{-\lambda_D^* t} \right\} = \\ &= \sigma_P \dot{\varphi} N_P(0) \frac{(\lambda_D/\lambda_D^*)}{1 - \sigma_P \dot{\varphi}/\lambda_D^*} \left\{ e^{-\sigma_P \dot{\varphi} t} - e^{-\lambda_D^* t} \right\} \ . \end{aligned} \tag{8.120}$$

To obtain a general expression for the daughter activity in the "*parent depletion-daughter activation model*" we now introduce new parameters and variables, similarly to the approach we took in the discussion of the decay series and the radioactivation depletion model, as follows:

$$k^* = \sigma_P/\sigma_D \tag{8.121}$$

$$\varepsilon^* = \frac{\lambda_D^*}{\lambda_D} = 1 + \frac{\sigma_D \dot{\varphi}}{\lambda_D} \tag{8.122}$$

$$m = \frac{\sigma_P \dot{\varphi}}{\lambda_D} \tag{8.123}$$

$$m^* = \frac{\sigma_P \dot{\varphi}}{\lambda_D^*} = \frac{m}{\varepsilon^*} \tag{8.124}$$

$$x = \frac{\sigma_P \dot{\varphi}}{\ln 2} t = \frac{m^* \lambda_D^*}{\ln 2} t \tag{8.125}$$

$$y_P = \frac{N_P(t)}{N_P(0)} = e^{-\sigma_P \dot{\varphi} t} = e^{-x \ln 2} = \frac{1}{2^x} \tag{8.126}$$

$$y_D^* = \frac{\mathscr{A}_D(t)}{\sigma_P \dot{\varphi} N_P(0)} = \frac{1}{\varepsilon(1 - m^*)} \left\{ \frac{1}{2^x} - \frac{1}{2^{x/m^*}} \right\} . \tag{8.127}$$

Equation (8.127) for the normalized daughter activity y_D^* of the depletion-activation model is similar to (8.103) for y_D of the depletion model, except for the factor ε^* which is larger than 1 and depends on $\dot{\varphi}$. In the depletion model $\sigma_D = 0$, $k^* = \infty$ and $\varepsilon^* = 1$, while for the depletion-activation model $\sigma_D \neq 0$ and $\varepsilon^* > 1$. Thus, y_D^* will behave similarly to the y_D in the depletion model: rise from 0 to reach a maximum $(y_{\max}^*)_D$ at $x = (x_{\max}^*)_D$ and then asymptotically decrease to zero at large x.

Similarly to (8.45) we find for $(x_{\max}^*)_D$

$$(x_{\max}^*)_D = \frac{m^* \ln m^*}{(m^* - 1) \ln 2} \tag{8.128}$$

and similarly to (8.49) we find for $(y_{\max}^*)_D$

$$(y_{\max}^*)_D = \frac{1}{\varepsilon 2^{x_{\max}^*}} = \frac{1}{\varepsilon} e^{-(\ln 2) x_{\max}^*} . \tag{8.129}$$

Similarly to (8.111), the maximum specific activity $(a_{\max}^*)_D$ of the daughter is expressed as

$$(a_{\max}^*)_D = \left(\frac{\sigma_P N_A}{A_P} \right) (y_{\max}^*)_D \dot{\varphi} = \left(\frac{\sigma_P N_A}{A_P} \right) \frac{\dot{\varphi}}{\varepsilon^*} e^{-\frac{m^* \ln m^*}{1 - m^*}} . \tag{8.130}$$

Since both ε^* and m^* depend on $\dot{\varphi}$, the question arises about the behavior of $(a_{\max}^*)_D$ in the limit as $\dot{\varphi} \to \infty$.

We determine $\lim\limits_{\dot{\varphi} \to \infty} (a_{\max}^*)_D$ as follows:

$$\lim_{\dot{\varphi} \to \infty} (a_{\max}^*)_D = \left(\frac{\sigma_P N_A}{A_P} \right) \lim_{\dot{\varphi} \to \infty} \frac{\dot{\varphi}}{\varepsilon^*} e^{-\frac{\sigma_P \dot{\varphi}/\lambda_D^*}{\sigma_P \dot{\varphi}/\lambda_D^* - 1} \ln(\sigma_P \dot{\varphi}/\lambda_D^*)}$$

$$= \left(\frac{\lambda_D N_A}{A_P} \right) \left\{ k e^{-\frac{k^* \ln k^*}{k^* - 1}} \right\} \approx g \times (a_{\text{theor}})_D , \tag{8.131}$$

where we define g as

$$g = k^* e^{-\frac{k^* \ln k^*}{1 - k^*}} . \tag{8.132}$$

A plot of the function g against the parameter k^* in the range from $k^* = 10^{-3}$ to $k^* = 10^3$ is given in Fig. 8.15. We note that in general at any k^*, as $\sigma_D \to 0$,
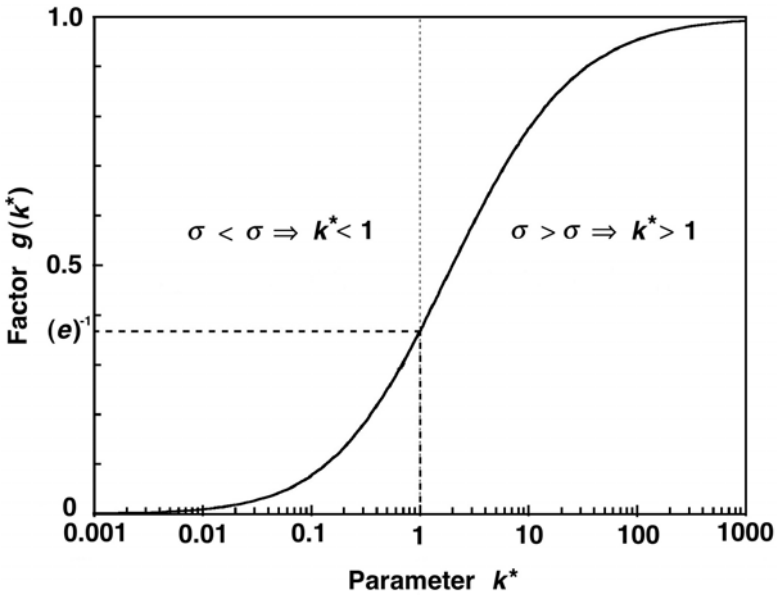
Fig. 8.15. A plot of function g of (8.132) against parameter $k^* = \sigma_P/\sigma_D$

$k^* \to \infty$, the function g approaches 1, and $(a^*_{max})_D$ transforms into $(a_{max})_D$ of (8.110).

In the limit for $\dot{\varphi} \to \infty$, the maximum specific activity $(a^*_{max})_D$ in the depletion-activation model thus approaches a limit $g(a_{theor})_D$ that is lower than the $(a_{theor})_D$ limit of the depletion model, since $g < 1$. The value $g = 1$ applies to the depletion model in which $\sigma_D = 0$, $\varepsilon = 1$ and $k^* = \infty$.

8.4.8 Example of Daughter Neutron Activation: Iridium-192

A closer investigation of the iridium radioactivation reveals a considerably more complicated picture than the one given in Sect. 8.4.5:

- Firstly, iridium has two stable isotopes: iridium-191 (Ir-191) with a natural abundance of 37.2% ($\sigma_P = \sigma_{191} = 954$ b) and iridium-193 with a natural abundance of 63.7% ($\sigma_P = \sigma_{193} = 100$ b). The Ir-191 isotope is of interest in industry and medicine, since iridium-192, the product of neutron activation has a reasonably long half-life of 73.8 days. In contrast, neutron activation of Ir-193 results in Ir-194 that decays with a short half-life of 19.3 hours. Since the Ir-192 radionuclide is produced through the neutron activation of the Ir-191 stable nuclide, the natural mixture of Ir-191 (37.3%) and Ir-193 (62.7%) in the activation target will result in a lower final specific activity of the Ir-192 source in comparison with activation of a pure Ir-191 target.
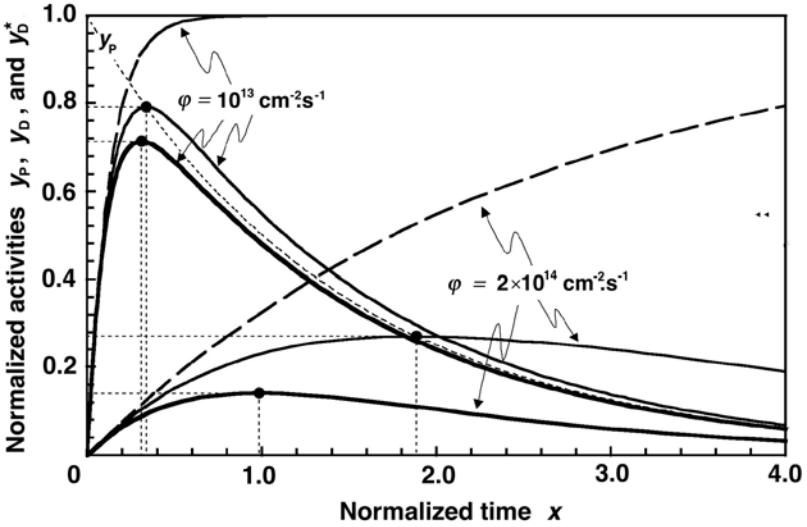
Fig. 8.16. A plot of normalized activity functions against x for iridium-191 neutron activation: z_D for the saturation model (*dashed curves*); y_D for the depletion model; and y_D^* for the depletion-activation model (*heavy solid curves*). The functions are plotted for two neutron fluence rates: $\dot{\varphi} = 10^{13}$ cm$^{-2}\cdot$s^{-1} and $\dot{\varphi} = 2\times10^{14}$ cm$^{-2}\cdot$s^{-1}

- Secondly, iridium-192, the daughter product of iridium-191 neutron activation, itself has a significant cross section for neutron activation $\sigma_D = \sigma_{192} = 1420$ b in contrast to the parent cross section $\sigma_P = \sigma_{191} = 954$ b. As shown in Sect. 8.4.5, the activation of the daughter product will affect the specific activity of the iridium-192 source.

In Fig. 8.16 we plot the normalized activity functions for iridium-191: z_D of (8.105) for the saturation model; y_D of (8.103) for the depletion model; and y_D^* of (8.127) for the depletion-activation model. The functions are plotted against the variable x of (8.100) for two neutron fluence rates: $\dot{\varphi} = 10^{13}$ cm$^{-2}\cdot$s^{-1} and $\dot{\varphi} = 2 \times 10^{14}$ cm$^{-2}\cdot$s^{-1}. The relevant parameters for these functions and three activation models are listed in Table 8.3.

The following features are of note:

1. For all three functions (z_D, y_D, and y_D^*) the initial slopes at $x = 0$ are identical and equal to $(\ln 2)/m$.
2. For the saturation model z_D saturates at 1; for the depletion model y_D reaches its maximum of $(y_{max})_D$ at $(x_{max})_D$; for the depletion-activation model y_D^* reaches its maximum of $(y_{max}^*)_D$ at $(x_{max}^*)_D$.
3. $(x_{max}^*)_D$ and $(y_{max}^*)_D$ for the depletion-activation model decrease in comparison to $(x_{max})_D$ and $(y_{max})_D$ for the depletion model, respectively. The larger is $\dot{\varphi}$, the larger is the discrepancy between the two parameters.
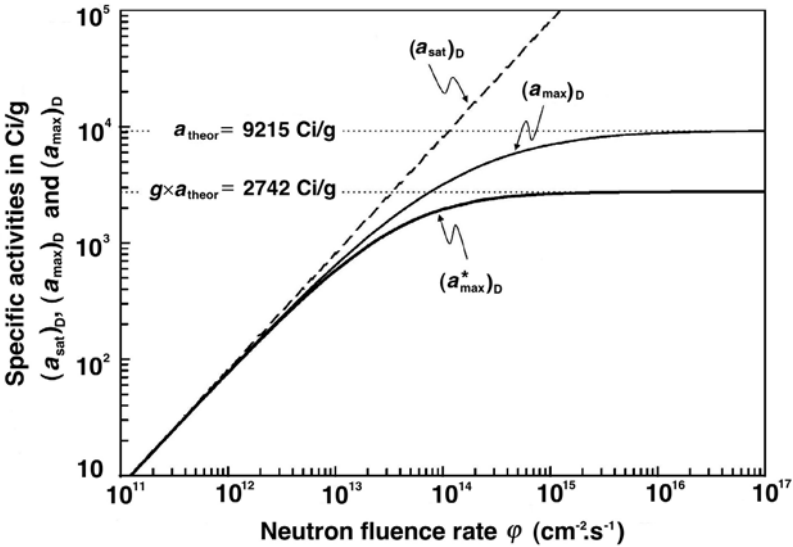
Fig. 8.17. Maximum attainable specific activity for iridium-192 against neutron fluence rate $\dot{\varphi}$ for the three activation models: saturation model (*dashed curve*); depletion model (*solid curve*); and depletion-saturation model (*heavy solid curve*). An assumption is made that the activation parent target contains pure iridium-191 rather than a natural mixture of iridium-191 and iridium-193 equal to 37.3% and 62.7%, respectively

4. $(y_{max}^*)_D$ no longer occurs at the point of ideal equilibrium where $y_P = y_D^*$, in contrast to $(y_{max})_D$ of the daughter in the depletion model that occurs at the point of ideal equilibrium.

Figure 8.17 shows a plot of the maximum attainable specific activity for iridium-192 against neutron fluence rate $\dot{\varphi}$ for the three activation models: saturation model with dashed curve; depletion model with solid curve; depletion-activation model with heavy solid curve. The saturation model saturates at $\sigma_P \dot{\varphi} N_A / A_P$, the depletion model saturates at the theoretical specific activity for iridium-192 at 9215 Ci/g, as also shown in Fig. 8.11, while the depletion-activation model saturates at $g \times (a_{theor})_{Ir-192} = 2742$ Ci/g, where $g = 0.3$, as given in (8.132) with k^* for iridium-192 equal to 0.672, as shown in Fig. 8.16 (Note: $k^* = \sigma_P / \sigma_D = 954/1420$).

Figure 8.17 shows that when large specific activities of iridium-192 are produced with fluence rates of the order of 10^{13} cm$^{-2} \cdot$ s^{-1} or higher, the best model for estimation of the specific activity of iridium-192 sample is the depletion-activation model.

In Fig. 8.18 we plot a_D, the specific activity of iridium-192, against activation time t normalized to $(t_{1/2})_D$, for the three radioactivation models (saturation model with dashed curve, depletion model with solid curve, and

Table 8.3. Parameters of the depletion model and the depletion-activation model applied to neutron activation of iridium-191 nuclide into iridium-192 nuclide

	Particle fluence		Definition
	$\dot\varphi =$ 10^{13} cm$^{-2}\cdot$s^{-1}	$\dot\varphi =$ 2×10^{14} cm$^{-2}\cdot$s^{-1}	
λ_D (s^{-1})	1.087×10^{-7}	1.087×10^{-7}	$\lambda_D = \ln 2/(t_{1/2})_D$
λ_D^* (s^{-1})	1.229×10^{-7}	3.927×10^{-7}	$\lambda_D^* = \lambda_D + \sigma_D\dot\varphi$ $^{(a)}$
ε	1.0	1.0	$\varepsilon = 1$
ε^*	1.13	3.61	$\varepsilon^* = \lambda_D^*/\lambda_D$
m	0.088	1.76	$m = \sigma_P\dot\varphi/\lambda_D$ $^{(b)}$
m^*	0.078	0.49	$m^* = \sigma_D\dot\varphi/\lambda_D^* = m/\varepsilon^*$
$(x_{max})_D$	0.338	1.89	$(x_{max})_D = m\ln m/[(m-1)\ln 2]$
$(x_{max}^*)_D$	0.311	0.98	$(x_{max}^*)_D = m^*\ln m^*/[(m^*-1)\ln 2]$
$(y_{max})_D$	0.793	0.270	$(y_{max})_D = 1/2^{(x_{max})_D}$
$(y_{max}^*)_D$	0.713	0.140	$(y_{max}^*)_D = 1/(\varepsilon^* 2^{(x_{max}^*)_D})$
$(a_{max})_D$	643.8	4398	$(a_{max})_D = (\sigma_P N_A/A_P)\dot\varphi(y_{max})_D$
$(a_{max}^*)_D$	580.0	2275	$(a_{max}^*)_D = (\sigma_P N_A/A_P)\dot\varphi(y_{max}^*)_D$
$(t_{max})_D/(t_{1/2})_D$	3.84	1.07	$(t_{max})_D/(t_{1/2})_D = (x_{max})_D/m$
$(t_{max}^*)_D/(t_{1/2})_D$	3.53	0.56	$(t_{max}^*)_D/(t_{1/2})_D = (x_{max}^*)_D/(m^*\varepsilon^*)$

$^{(a)}$ σ_D(Ir - 192) $= 1420$ b;
$^{(b)}$ σ_P(Ir - 191) $= 954$ b

depletion-activation model with heavy solid curve) and two fluence rates $\dot\varphi$: 10^{13} cm$^{-2}\cdot$s^{-1} in the top figure and 2×10^{14} cm$^{-2}\cdot$s^{-1} in the bottom figure. The appropriate values for the parameters $(a_{max})_D$, $(t_{max})_D$, $(a_{max}^*)_D$, and $(t_{max}^*)_D$ are given in Table 8.3. Note that an assumption is made that the iridium activation sample contains only the iridium-191 stable nuclide rather than a natural mixture of iridium-191 and iridium-193. Thus to get the specific activity for a natural sample of iridium, the natural abundance of iridium-191 in the sample would have to be taken into account.

Again we note that the activation of the daughter product iridium-192 has a significant effect on the daughter specific activity; this is especially pronounced at larger fluence rates, as shown in Fig. 8.18.

The following conclusions can now be made:

- The best model for description of radioactivation kinematics is the depletion model when the daughter product is not activated by the exposure to radioactivation particles. An example for the use of this model is the activation of cobalt-59 into cobalt-60.
- The best model for describing the radioactivation kinematics in situations where the daughter product is activated by the radioactivation particles is the depletion-activation model. An example for the use of this model is the neutron activation of iridium-191 into iridium-192.
- The saturation model is only an approximation to the other two models. It is valid only at very short activation times or when $\sigma_P\dot\varphi/\lambda_D < 10^{-3}$.
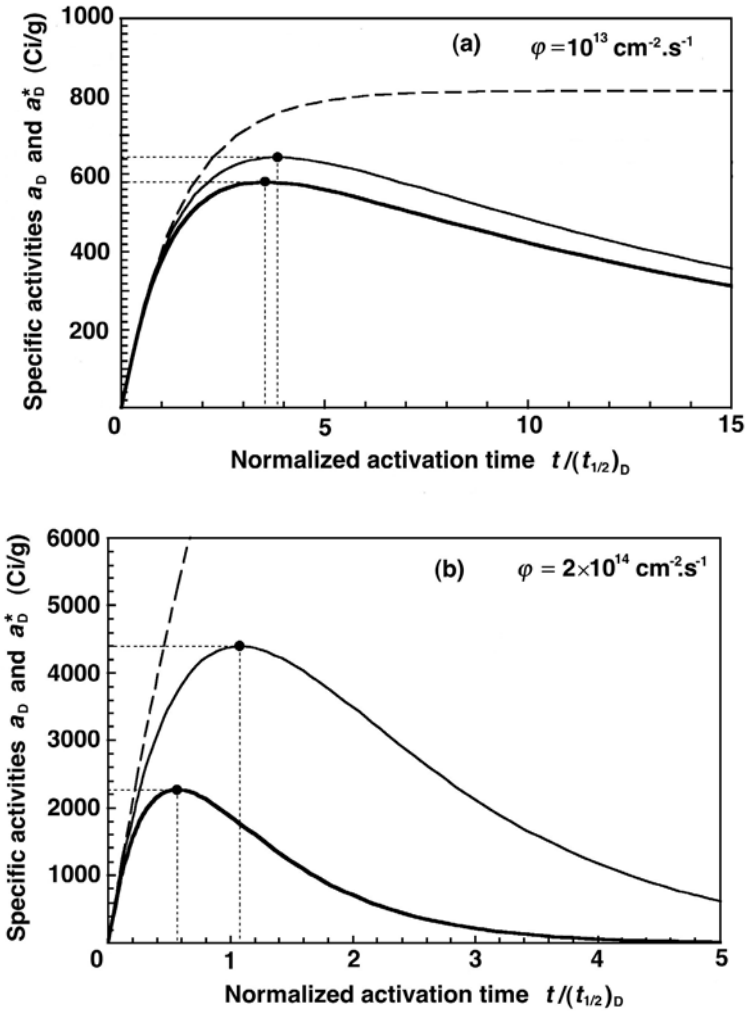
Fig. 8.18. Specific activity of iridium-192 against activation time t normalized to $(t_{1/2})_D$ for iridium-192 for three radio-activation models: saturation model with *dashed curves*; depletion model with *solid curves*; and depletion-activation model with *heavy solid curves*. Part **a** is for a fluence rate $\dot{\varphi}$ of 10^{13} cm$^{-2} \cdot$s^{-1}; part **b** is for a fluence rate $\dot{\varphi}$ of 2×10^{14} cm$^{-2} \cdot$s^{-1}. An assumption is made that the activation parent target contains pure iridium-191

An example for the use of this model is the neutron activation of molybdenum-98 into molybdenum-99.

8.4.9 Practical Aspects of Radioactivation

Currently, the list of known nuclides contains some 275 stable nuclides and over 3000 radioactive nuclides (radionuclides). Some 200 radionuclides are used in industry and medicine and most of them are produced through radioactivation.

A variety of particles may be used for radioactivation; however, most commonly radioactivation is achieved by bombarding stable target nuclei with neutrons produced by nuclear reactors or by protons produced by cyclotrons.

Nuclear reactors are the main source of radionuclides used in medicine. These radionuclides are produced either through neutron activation of stable target nuclei placed into the reactor or by separation from fission fragments resulting from the fission process of the nuclear fuel in which fuel nuclei split into two lighter fragments and two or three fission neutrons.

Activation with Thermal Neutrons

Thermal neutrons produced in nuclear reactors are the most common particles used for radioactivation. This type of the radioactivation process is then referred to as *neutron activation* or *neutron capture* and produces neutron-rich unstable isotopes that decay through β^- decay into more stable configurations. Two types of neutron activation processes occur commonly: (n, γ) and (n, p). The (n, γ) process results in emission of γ rays, while the (n, p) process results in emission of protons.

Sources produced by neutron activation in a nuclear reactor normally contain a mixture of stable parent nuclei in addition to radioactive daughter nuclei. The parent nuclei thus act as carriers of daughter nuclei and effectively decrease the specific activity of the source. For example, the practical specific activity of cobalt-60 sources is limited to about 300 Ci/g or $\sim 25\%$ of the carrier-free theoretical activity of 1133 Ci/g. This means that in a cobalt-60 teletherapy source $\sim 75\%$ of the source mass is composed of stable ^{59}Co nuclei and only $\sim 25\%$ is composed of radioactive ^{60}Co nuclei. The reactor-produced molybdenum-99, on the other hand, has a practical specific activity that is several orders of magnitude lower than the theoretical specific activity of molybdenum-99.

The (n, γ) reaction is much more common than the (n, p) reaction and usually produces radioactive products that are not carrier-free, while the (n, p) reaction can produce carrier-free sources. In non-carrier-free sources, a chemical separation of the daughter from the parent is not possible because the parent and daughter are isotopes of the same element; a physical separation, while possible, is too expensive.

- In a (n, γ) reaction the target nucleus $^A_Z X$ captures a neutron and is converted into an excited nucleus $^{A+1}_Z X^*$ that undergoes an immediate de-excitation to its ground state through emission of a γ ray. Note that $^A_Z X$

and $^{A+1}_{Z}X$ are isotopes of the same chemical element. The schematic representation of the reaction is as follows:

$$^{A}_{Z}X + n = {}^{A+1}_{Z}X^* + \gamma \qquad \text{or} \qquad {}^{A}_{Z}X(n, \gamma)^{A+1}_{Z}X . \qquad (8.133)$$
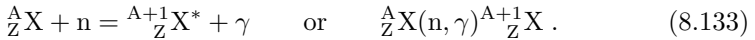
- In a (n, p) reaction the target nucleus $^{A}_{Z}X$ captures a neutron and promptly ejects a proton to become converted into a new nucleus $^{A}_{Z-1}Y$. Note that $^{A}_{Z}X$ and $^{A}_{Z-1}Y$ do not represent the same chemical element. Schematically the reaction is represented as follows:

$$^{A}_{Z}X + n = {}^{A}_{Z-1}Y + p \qquad \text{or} \qquad {}^{A}_{Z}X(n, p){}^{A}_{Z-1}Y . \qquad (8.134)$$
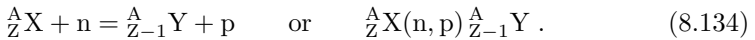
From a medical physics perspective the most important neutron activation processes are:

- Production of *cobalt-60 sealed sources* for use in external beam radiotherapy with typical initial source activity of the order of 370 TBq (10^4 Ci).
- Production of *iridium-192 sealed sources* for use in brachytherapy with typical activities of 0.37 TBq (10 Ci).
- Production of *molybdenum-99 radioisotope* for generating the technetium-99m (^{99m}Tc) radionuclide for use in nuclear medicine.

Activation with Protons or Heavier Charged Particles

Protons produced by cyclotrons are used in the production of proton-rich unstable radionuclides that decay through β^+ decay or electron capture into more stable configurations. When striking a target material, protons may cause nuclear reactions that produce radionuclides in a manner similar to neutron activation in a reactor. However, because of their positive charge, protons striking the target must have relatively high kinetic energies, typically 10–20 MeV, to penetrate the repulsive Coulomb barrier surrounding the positively charged nucleus. Many proton activation reactions are endoergic which means that energy must be supplied by the projectile for the reaction to occur. The minimum energy that will allow the reaction to occur is referred to as the threshold energy.

Proton capture by a target nucleus changes the atomic number from Z for the parent to $Z + 1$ for the daughter nucleus allowing production of carrier-free radionuclides for use in medicine, because a chemical separation of the newly produced daughter radionuclide from the remaining parent nuclide is possible. Positron emitters produced for use in medicine by proton activation in cyclotrons generally have much shorter half-lives than radionuclides produced for use in medicine by neutron activation in nuclear reactors.

Cyclotrons generally produce smaller quantities of radioactivity than do nuclear reactors because:

1. cross sections for proton capture are lower by several orders of magnitude than those for neutron capture and they are strongly energy dependent;
2. the proton beam is monodirectional and is attenuated in the target;

3. cyclotron particle fluence rates are generally lower than those produced by nuclear reactors.

The cyclotron-produced radionuclides are position emitters used in positron emission tomography (PET) scanners for diagnostic imaging. The four most important position emitting radionuclides used in medical PET imaging are: fluorine-18, carbon-11, nitrogen-13 and oxygen-15.

The *nuclear reaction energy* Q also known as the Q *value* for a nuclear reaction provides the energy release or energy absorption during the nuclear reaction. In general the Q value is determined in one of the following two manners:

1. The sum of nuclear rest energies of the reaction products (i.e., the total rest energy after reaction) is subtracted from the sum of nuclear rest energies of the reactants (i.e., the total rest energy before reaction).
2. The sum of nuclear binding energies of the reactants (i.e., the total binding energy before reaction) is subtracted from the sum of nuclear binding energies of reaction products (i.e., the total binding energy after reaction).

The Q value obtained with the two methods will be either positive or negative.

- For $Q > 0$ the reaction is called *exoergic* and the excess energy is shared between the two reaction products.
- For $Q < 0$ the reaction is called *endoergic* and for the reaction to occur, energy must be supplied in the form of the kinetic energy of the projectile.

As an example we calculate the nuclear reaction energy Q for the activation of oxygen-18 into flurorine-18 in a proton cyclotron. The reaction is as follows:

$$\,^{18}_{8}\mathrm{O} + \mathrm{p} \rightarrow \,^{18}_{9}\mathrm{F} + \mathrm{n} + Q(-2.44 \text{ MeV}) \tag{8.135}$$

and the Q value of -2.44 MeV is calculated with data from Table 8.6

Method 1:

$$Q = \left\{ \sum_i M_i c^2 \right\}_{\text{before}} - \left\{ \sum_i M_i c^2 \right\}_{\text{after}} =$$

$$= \left\{ M(\,^{18}_{8}\mathrm{O})c^2 + M_{\mathrm{p}}c^2 \right\} - \left\{ M(\,^{18}_{9}\mathrm{F})c^2 + M_{\mathrm{n}}c^2 \right\} =$$

$$= \left\{ 16762.0227 + 938.272 \right\} \text{ MeV} - \left\{ 16763.1673 + 939.5654 \right\} \text{ MeV} =$$

$$= -2.44 \text{ MeV}. \tag{8.136}$$

Method 2:

$$Q = \left\{ \sum_i (E_{\mathrm{B}})_i \right\}_{\text{after}} - \left\{ \sum_i (E_{\mathrm{B}})_i \right\}_{\text{before}} =$$

$$= 137.3693 \text{ MeV} - 139.8071 \text{ MeV} = -2.44 \text{ MeV}. \tag{8.137}$$

Both methods produce the same result: -2.44 MeV. The production of fluorine-18 in a cyclotron is thus an endoergic reaction and energy must be supplied for the reaction to occur.

In general, for endoergic reactions to occur the projectiles must have a certain minimum *threshold kinetic energy* $(E_K)_{thr}$ that exceeds the absolute value of Q, so that the total momentum for before and after the interaction is conserved. The general relationship for the threshold of endoergic reactions was derived in (4.13), and based on that result we write the threshold kinetic energy $(E_K)_{thr}$ for the proton with rest mass M_p, activating target nuclide of rest mass M_t, as

$$(E_K)_{thr} = -Q \left\{ 1 + \frac{M_p}{M_t} \right\} . \tag{8.138}$$

For example, the threshold energy for fluorine-18 production from oxygen-18 in a proton cyclotron at 2.58 MeV is slightly higher than the absolute value of $|Q| = 2.44$ MeV. The threshold energy of 2.58 MeV for fluorine-18 is determined from (8.138) as follows:

$$\begin{aligned}(E_K)_{thr} &= -Q \left\{ 1 + \frac{M_p c^2}{M(_8^{18}O)c^2} \right\} = \\ &= -(-2.44 \text{ MeV}) \left\{ 1 + \frac{938.272 \text{ MeV}}{16762.0227 \text{ MeV}} \right\} = 2.58 \text{ MeV}.\end{aligned} \tag{8.139}$$

For cyclotrons, rather than providing a fluence rate as is done for reactor produced neutrons, one provides a beam current, usually expressed in μA, where $1\,\mu A$ of current is equal to 6.25×10^{12} electronic charges per second, i.e., $6.25 \times 10^{12}\,e/s$. Thus, a proton beam of 1 μA corresponds to 6.25×10^{12} protons; a helium He^{2+} beam corresponds to 3.125×10^{12} helium ions.

Targets used in charged particle activation are either thin or thick.

- The thickness of a *thin target* is such that the target does not appreciably attenuate the charged particle beam.
- Charged particles traversing a *thick* target lose energy through Coulomb interactions with electrons of the target and this affects the activation yield, since the cross section for activation depends on charged particle energy. The particle beam is completely stopped in a thick target or it is degraded in energy to a level below the threshold energy for the particular nuclear reaction. Similarly to the approach that one takes with thick x-ray targets assuming they consist of many thin x-ray targets, one may assume that a thick target in charged particle activation (CPA) consists of a large number of thin targets, each one characterized by a given charged particle kinetic energy and reaction cross section. The kinetic energy for each slice is determined from stopping power data for the given charged particle in the target material.

- Target materials used in production of positron-emitting nuclides are either in a gaseous or liquid state.
- Cyclotron targets are most commonly of the thick target variety resulting in complete beam absorption in the target material.
- Essentially all energy carried into the target by the beam is transformed into heat because of charged particle Coulomb interactions with orbital electrons of the target atoms. Thus, targets are cooled with circulating helium gas.
- Only a small fraction of one percent of the charged particle beam is used up for induction of activation, the rest is dissipated as heat.

The derivations presented in Sect. 8.4 for neutron activation could in principle be generalized to charged particle activation (CPA); however, the issue of beam attenuation in thick targets that are routinely used for CPA of medical positron-emitting radionuclides complicates matters considerably. On the other hand, the specific activities produced by CPA are several orders of magnitude lower than specific activities produced in neutron activation, so that in general parent nuclide depletion is not of concern in CPA. In Sect. 8.4 it was established that the depletion model should be used for activation factors m exceeding 10^{-3}. Since typical values of m in CPA are of the order of 10^{-7}, it is obvious that daughter activation in CPA can be calculated using the simple saturation model that accounts for the daughter decay during the activation procedure.

Assuming that there is no charged particle beam attenuation in the target (thin target approximation), the daughter activity $\mathscr{A}_{\mathrm{D}}(t)$, similarly to the neutron activation case of (8.93), can be written as follows:

$$\mathscr{A}_{\mathrm{D}}(t) = In^{\square}\sigma_{\mathrm{P}}(1 - e^{-\lambda_{\mathrm{D}}t}) , \tag{8.140}$$

where

I is the intensity of the charged particle beam in particles per unit time,
$n^{\square}$ is the number of target nuclei per volume in cm^{-3},
x is the target thickness in cm,
σ_{P} is the reaction cross section of the parent nuclei at the energy of the charged particle beam in barn ($1\ \mathrm{b} = 10^{-24}\ \mathrm{cm}^2$).

Positron-emitting radionuclides are used in positron emission tomography (PET) scanning; a non-invasive imaging technique that provides a functional image of organs and tissues, in contrast to CT scanning and MRI scanning that provide anatomic images of organs and tissues. The positron-emitting radionuclides are attached to clinically useful biological markers that are used in studies involving various metabolic processes in cancer diagnosis and treatment (see Sect. 8.10). The main characteristics of the four most commonly used radionuclides in PET scanning are provided in Table 8.4.

Table 8.4. Main characteristics of four most common positron emitters produced in cyclotrons for use in medicine

Radionuclide	Specific activity	Target	Production reaction	Q value (MeV)	Half-life (minutes)
Carbon-11	8.4×10^8	Nitrogen-14	$_{7}^{14}\mathrm{N} + \mathrm{p} \rightarrow {}_{6}^{11}\mathrm{C} + \alpha$	-2.92	20.4
Nitrogen-13	1.4×10^9	Oxygen-16	$_{8}^{16}\mathrm{O} + \mathrm{p} \rightarrow {}_{7}^{13}\mathrm{N} + \alpha$	-5.22	10
Oxygen-15	6.0×10^9	Nitrogen-15	$_{7}^{15}\mathrm{N} + \mathrm{p} \rightarrow {}_{8}^{15}\mathrm{O} + \mathrm{n}$	-3.54	2.1
Fluorine-18	9.5×10^7	Oxygen-18	$_{8}^{18}\mathrm{O} + \mathrm{p} \rightarrow {}_{9}^{18}\mathrm{F} + \mathrm{n}$	-2.44	110

8.5 Origin of Radioactive Elements (Radionuclides)

Radioactive nuclides (radionuclides) are divided into two categories:

1. *Naturally-occurring,*
2. *Man-made or artificially produced.*

There is no essential physical difference between the two categories of radioactivity and the division is mainly historical.

Henri Becquerel discovered natural radioactivity in 1896 when he noticed that uranium spontaneously produced an invisible, penetrating radiation that affected photographic plates.

Irene Joliot-Curie and *Frédéric Joliot* discovered artificial radioactivity in 1934 during a series of experiments in which they bombarded boron samples with naturally occurring α particles and produced nitrogen that was unstable and emitted positrons (β^+ decay).

8.5.1 Man-Made (Artificial) Radionuclides

The man-made (artificial) radionuclides are manufactured by bombarding stable or very long-lived nuclides with energetic particles produced by machines of various kinds (mainly nuclear reactors, cyclotrons or linear accelerators). The process is referred to as radioactivation. Since Irene Joliot-Curie and Frédéric Joliot discovered artificial radioactivity in 1934 over 3000 different artificial radionuclides were synthesized and investigated. The production of new nuclides is referred to as nucleosynthesis.

8.5.2 Naturally-Occuring Radionuclides

The naturally occurring radioactive elements are almost exclusively members of one of four radioactive series that all begin with very long-lived parents that have half-lives of the order of the age of the earth.

Table 8.5. The four naturally occurring radioactive series

Name of series	Parent	First decay	n_α	Found in nature today	Half-life (10^9 y)	Stable end-product
Thorium	$^{232}_{90}\text{Th}$	$^{228}_{88}\text{Ra} + \alpha$	6	YES	14.05	$^{208}_{82}\text{Pb}$
Actinium	$^{235}_{92}\text{U}$	$^{231}_{90}\text{Th} + \alpha$	7	YES	0.704	$^{207}_{82}\text{Pb}$
Neptunium	$^{237}_{93}\text{Np}$	$^{233}_{91}\text{Pa} + \alpha$	7	NO	2.144×10^{-3}	$^{209}_{83}\text{Bi}$
Uranium	$^{238}_{92}\text{U}$	$^{234}_{90}\text{Th} + \alpha$	8	YES	4.47	$^{206}_{82}\text{Pb}$

The four naturally occurring series are named as follows:

- *Thorium series* originates with thorium-232,
- *Actinium series* originates with uranium-235,
- *Neptunium series* originates with neptunium-237,
- *Uranium series* originates with uranium-238.

The main characteristics of the four naturally occurring series are listed in Table 8.5. The series begin with a specific parent nucleus of very long half-life that decays through several daughter products to reach eventually a stable lead nuclide or a stable bismuth-203 isotope.

It is assumed that collapsing stars created all heavy radioactive elements in approximately equal proportions; however, these elements differ in their half-lives and this resulted in significant variations in today's abundance of heavy elements. Neptunium-237 has a significantly shorter half-life than the other three parent nuclei listed in Table 8.5. It does no longer occur naturally because it has completely decayed since the formation of the earth some 4.6×10^9 years ago. The other three parent nuclei (^{232}Th, ^{235}U, and ^{238}U) with much longer half-lives are still found in nature and serve as parents of their own series.

Cosmic ray protons continually produce small amounts of radioactive materials. The most notable example is carbon-14 that decays with a half-life of 5730 years and is used for the so-called carbon dating of once-living objects not older than some 50 000 years.

A few naturally-occurring complete radioactive elements lighter than lead, the endpoint of the three naturally occurring decay series, can be found in the earth. Most notably among them is potassium-40 (^{40}K) with a half-life of 1.277×10^9 years. Since it is present in all foods, it accounts for the greatest proportion of the naturally-occuring radiation load through ingestion among humans.

The existence of the four radioactive series with long-lived parent nuclei serves as the source of many short-lived daughters that are in transient or secular equilibrium with their parents. For example, radium-226 with its half-life of 1600 years would have disappeared long ago were it not for the uranium-238 decay series that provides constant replenishment of radium-226 in the environment.

8.5.3 Radionuclides in the Environment

Over 60 radionuclides can be found in the environment and some of them pose a health hazard to humans. They are grouped into three categories as follows:

1. *primordial* – originate from before the creation of the Earth;
2. *cosmogenic* – continually produced by cosmic radiation hitting the Earth;
3. *man-made* or *artificial* – produced through the process of radioactivation.

Pathways of radionuclides into environment:

1. *atmospheric pathway* (through human activity, radioactive decay, cosmogenic reactions),
2. *water pathway* (deposited in water from air or from ground through erosion, seepage, leaching, mining, etc.),
3. *food chain pathway* (radionuclides in water or air may enter the food chain).

Pathways of radionuclides into human body:

1. *ingestion,*
2. *inhalation,*
3. *through skin.*

8.6 General Aspects of Radioactive Decay Processes

Radioactive nuclides, either naturally occurring or artificially produced by nuclear reactions, are unstable and strive to reach more stable nuclear configurations through various processes of spontaneous radioactive decay that involve transformation to a more stable nuclide and emission of energetic particles. General aspects of spontaneous radioactive decay may be discussed using the formalism based on the definitions of activity $\mathscr{A}$ and decay constant λ without regard for the actual microscopic processes that underlie the radioactive disintegrations.

A closer look at radioactive decay processes shows that they are divided into six main categories:

1. α decay
2. β decay
3. γ decay
4. Spontaneous fission
5. Proton emission decay
6. Neutron emission decay.

The β decay actually encompasses three decay processes (β^+, β^-, and electron capture) and the γ decay encompasses two processes (γ decay and internal conversion).

There are many different spontaneous radioactive decay modes that an unstable nucleus may undergo in its quest for reaching a more stable nuclear configuration. On a microscopic scale the nine most important radioactive decay modes are:

1. α decay
2. β^- decay
3. β^+ decay
4. Electron capture
5. γ decay
6. Internal conversion
7. Spontaneous fission
8. Proton emission decay
9. Neutron emission decay

Nuclear transformations are usually accompanied by emission of energetic particles (charged particles, neutral particles, photons, etc.). The particles released in nuclear decay are as follows:

- α particles in α decay,
- electrons in β^- decay,
- positrons in β^+ decay,
- neutrinos in β^+ decay,
- antineutrinos in β^- decay,
- γ rays in γ decay,
- atomic orbital electrons in internal conversion,
- neutrons in spontaneous fission and in neutron emission decay,
- heavier nuclei in spontaneous fission,
- protons in proton emission decay.

In each nuclear transformation a number of physical quantities must be conserved. The most important of these quantities are:

1. *Total energy*
2. *Momentum*
3. *Charge*
4. *Atomic number*
5. *Atomic mass number (number of nucleons).*

The total energy of particles released by the transformation process is equal to the net decrease in the rest energy of the neutral atom, from parent P to daughter D. The disintegration (decay) energy, often referred to as the Q value for the radioactive decay, is thus defined as follows:

$$Q = \{M_{\mathrm{P}} - (M_{\mathrm{D}} + m)\}\, c^2 \,, \tag{8.141}$$

where M_{P}, M_{D}, and m are the nuclear rest masses (usually given in atomic mass units u) of the parent, daughter, and emitted particles, respectively. The energy equivalent of u is 931.5 MeV.

Often atomic masses rather than nuclear masses are used in calculations of Q values for radioactive decay. In many decay modes the electron masses cancel out, so that it makes no difference if atomic or nuclear masses are used in (8.141). On the other hand, there are situations where electron masses do not cancel out (e.g., β^+ decay) and there special care must be taken to account for all electrons involved when atomic rest masses are used in (8.141).

For radioactive decay to be energetically possible the Q value must be greater than zero. This means that spontaneous radioactive decay processes are exogenic. For $Q > 0$, the energy equivalent of the Q value is shared as kinetic energy between the particles emitted in the decay process and the daughter product. Since the daughter has a much larger mass than the other emitted particles, the kinetic energy acquired by the daughter is usually negligibly small.

In light (low atomic number) elements nuclear stability is achieved when the number of neutrons N and the number of protons Z is approximately equal ($N \approx Z$). As the atomic number increases, the N/Z ratio for stable nuclei increases from 1 at low Z elements to about 1.5 for heavy stable elements.

- If a nucleus has a N/Z ratio too high for stability, it has an excess of neutrons and is called neutron-rich. It decays through conversion of a neutron into a proton and emits an electron and anti-neutrino. This process is referred to as β^- decay. If the N/Z ratio is extremely high, a direct emission of a neutron is possible.
- If a nucleus has a N/Z ratio that is too low for stability, it has an excess of protons and is called proton-rich. It decays through conversion of a proton into a neutron and emits a positron and a neutrino (β^+ decay). Alternatively, the nucleus may capture an orbital electron, transform a proton into a neutron and emit a neutrino (electron capture). A direct emission of a proton is also possible, but less likely, unless the nuclear imbalance is very high.

8.7 Alpha Decay

Alpha (α) decay was the first mode of radioactive decay detected and investigated during the 1890s. It played a very important role in early modern physics experiments that led to the currently accepted Rutherford-Bohr atomic model (see Chap. 2) and is characterized by a nuclear transformation in which an unstable parent nucleus P attains a more stable nuclear configuration (daughter D) through ejection of an α particle. This α particle is a helium-4 nucleus that has, with a binding energy of 7 MeV/nucleon, a very stable configuration.

While α decay was well known since the discovery of natural radioactivity by *Henri Bequerel* in 1896 and α particles were already used as nuclear probes

by *Hans Geiger* and *Ernest Marsden* in 1909, its exact nature was finally unraveled much later in 1928 by *George Gamow*.

In α decay the number of protons and neutrons is conserved by producing a $^4_2$He nucleus (α particle) and lowering the parent's A and Z by 4 and 2, respectively, i.e.,

$$^A_Z P \rightarrow {}^{A-4}_{Z-2} D + {}^4_2 He . \tag{8.142}$$

- When an α particle is emitted by the parent (Z, A) nucleus, the atomic number of the parent decreases by 2 and it sheds two orbital electrons from its outermost shell to become a neutral daughter atom $(Z-2, A-4)$.
- The energetic α particle slows down in moving through the absorber medium and captures two electrons from its surroundings to become a neutral $^4_2$He atom.
- Typical kinetic energies of α particles released by naturally occurring radionuclides are between 4 MeV and 9 MeV, corresponding to a range in air of about 1 cm to 10 cm, respectively, and in tissue of about 10^{-3} cm and 10^{-2} cm, respectively.

The Coulomb barrier that an α particle experiences on the surface of the parent nucleus is of the order of 30 MeV; thus classically an α particle with a kinetic energy of 4 to 9 MeV cannot overcome the barrier. However, the quantum mechanical effect of tunneling gives the α particle a certain finite probability for tunneling through the potential barrier and escaping the parent nucleus P that transforms into the daughter nucleus D. Thus, positive decay energy Q_α and the quantum mechanical effect of tunneling (see Sect. 1.25) make the α decay possible.

8.7.1 Decay Energy in α Decay

The decay energy Q_α released in α decay appears as kinetic energy shared between the α particle and the daughter nucleus and is given as follows:

$$\begin{aligned} Q_\alpha &= \left\{ \mathcal{M}(P) - [\mathcal{M}(D) + \mathcal{M}(^4_2 He)] \right\} \\ &= \left\{ M(P) - [M(D) + M(\alpha)] \right\} c^2 , \end{aligned} \tag{8.143}$$

where $\mathcal{M}(P)$, $\mathcal{M}(D)$, and $\mathcal{M}(^4_2 He)$ are the *atomic rest masses* and $M(P)$, $M(D)$ and $M(\alpha)$ are the *nuclear rest masses* of the parent, daughter, and α particle, respectively.

Since neither the total number of protons nor the total number of neutrons changes in the α decay, Q_α can also be expressed in terms of binding energies E_B of the parent, daughter and helium nuclei, as follows:

$$Q_\alpha = E_B(D) + E_B(\alpha) - E_B(P) , \tag{8.144}$$

where

$E_B(D)$ is the total binding energy of the daughter D nucleus,

$E_B(\alpha)$ is the total binding energy of the α particle (28.3 MeV),
$E_B(P)$ is the total binding energy of the parent P nucleus.

The definition of nuclear binding energy E_B is given in (1.13). For α decay to be feasible, Q_α must be positive. This implies that the combined total binding energies of the daughter nucleus and the α particle nucleus must exceed the total binding energy of the parent nucleus. Or, similarly, this implies that the rest mass of the parent nucleus must exceed the combined rest masses of the daughter nucleus and the α particle.

Two entities are produced in α decay: the α particle and the daughter product. For decay of the parent nucleus at rest this implies that the α particle and the daughter will acquire momenta p equal in magnitude but opposite in direction and kinetic energies equal to $(E_K)_\alpha = p^2/(2m_\alpha)$ for the α particle and $(E_K)_D = p^2/(2M_D)$ for the daughter.

- α decay occurs commonly in nuclei with $Z > 82$ because in this range of atomic number Z, decay energies Q_α given by (8.143) or (8.144) are positive and of the order of ~ 4 MeV to ~ 9 MeV.
- The $Q_\alpha > 0$ results mainly from the high total binding energy of the $^4_2$He nucleus (28.3 MeV) that is significantly higher than for nuclei of $^3_2$He, $^3_1$H, and $^2_1$H for which spontaneous ejection from parent nuclei energetically is not feasible.
- Ejection of a heavy nucleus from the parent nucleus is energetically possible (large Q value); however, the effect of tunneling through the potential barrier is then also much more difficult for the heavy nucleus in comparison with tunneling for the α particle.
- Emission of heavy particles from parent nuclei with $Z > 92$ is possible and represents a mode of radioactive decay referred to as *spontaneous fission*, as discussed in Sect. 8.14.

The total decay energy Q_α must be positive for α decay to occur and is written as follows:

$$Q_\alpha = (E_K)_\alpha + (E_K)_D = \frac{p^2}{2m_\alpha} + \frac{p^2}{2M(D)} = \frac{p^2}{2m_\alpha}\left\{1 + \frac{m_\alpha}{M(D)}\right\}$$

$$= E_K)_\alpha \left\{1 + \frac{m_\alpha}{M(D)}\right\} . \tag{8.145}$$

Since $m_\alpha \ll M(D)$, the α particle recoils with a much higher kinetic energy than the daughter, i.e., the α particle acquires a much larger fraction of the total disintegration energy Q_α than does the daughter.

From (8.145) we determine $(E_K)_\alpha$, the kinetic energy of the α particle, as

$$(E_K)_\alpha = \frac{Q_\alpha}{1 + \frac{m_\alpha}{M(D)}} . \tag{8.146}$$

After inserting Q_α from (8.143) we get

$$(E_K)_\alpha = \frac{M(P)c^2 - M(D)c^2 - m_\alpha c^2}{1 + \frac{m_\alpha}{M_D}}$$

$$\approx \left\{ M(P)c^2 - M(D)c^2 - m_\alpha c^2 \right\} \left\{ \frac{A_P - 4}{A_P} \right\} = Q_\alpha \left\{ \frac{A_P - 4}{A_P} \right\},$$

(8.147)

where A_P is the atomic mass number of the parent nucleus; $(A_P - 4)$ is the atomic mass number of the daughter nucleus; and $m_\alpha / M(D) \approx 4/(A_P - 4)$.

The kinetic energy $(E_K)_D$ of the recoil daughter nucleus, on the other hand, is given as follows:

$$(E_K)_D = Q_\alpha - (E_K)_\alpha = \frac{4Q_\alpha}{A_P} .$$

(8.148)

8.7.2 Alpha Decay of Radium-226 into Radon-222

For historical reasons, the most important example of radioactive decay in general and α decay in particular is the decay of radium-226 with a half-life of 1600 years into radon-222 which in itself is radioactive and decays by α decay into polonium-218 with a half-life of 3.824 days:

$$^{226}_{88}\text{Ra} \rightarrow {}^{222}_{86}\text{Rn} + \alpha.$$

(8.149)

Radium-226 is the sixth member of the naturally occurring uranium series starting with uranium-238 and ending with stable lead-206. It was discovered in 1898 by *Marie Curie* and *Pierre Curie* and was used for therapeutic purposes almost immediately after its discovery, either as an external (sealed) source of radiation or as an internal (open) source.

The external use of radium-226 and radon-222 focused largely on treatment of malignant disease. In contrast, internal use of these two radionuclides was spread over the whole spectrum of human disease between 1905 through the 1930s and was based on ingestion of soluble radium salts, inhalation of radon gas or drinking water charged with radon.

When radium-226 is used as a sealed source, the radon-222 gas cannot escape and a build up occurs of the seven daughter products that form the radium-226 series. Some of these radionuclides undergo α decay, others β decay with or without emission of γ rays. The γ-ray spectrum consists of discrete lines ranging in energy from 0.18 MeV to 2.2 MeV producing a photon beam with an effective energy close to that of cobalt-60 (~ 1.25 MeV). The encapsulation of the source is thick enough to absorb all α and β particles emitted by radium-226 and its progeny; however, the encapsulation cannot stop the γ rays and this makes radium-226 sealed sources useful in treatment of cancer with radiation.

Before the advent of cobalt-60 and cesium-137 teletherapy machines in 1950s all external beam radiotherapy machines made use of radium-226.

They were called *teleradium* machines, contained 4 to 10 g of radium-226 and were very expensive because of the tedious radium-226 manufacturing process. They were also very inefficient because of the low inherent specific activity of radium-226 (0.988 Ci/g = 3.665×10^{10} Bq/g) and self-absorption of γ radiation in the source.

- Widespread availability of external beam radiotherapy only started in the 1950s with the invention of the cobalt-60 teletherapy machine in Canada. On the other hand, radium-226 proved very practical for use in brachytherapy where sources are placed into body cavities or directly implanted into malignant lesions for a specific time.
- While radium-based brachytherapy was very popular in the past century, modern brachytherapy is now carried out with other radionuclides (e.g., iridium-192, cesium-137, iodine-125, etc.) that do not pose safety hazards associated with the radon-222 gas that may leak through damaged radium-226 source encapsulation.

The decay energy Q_α for the α decay of radium-226 is calculated either using atomic rest masses $\mathcal{M}$ as given in (8.143) or nuclear rest masses M as given in (8.136) and (8.143) or nuclear binding energies E_B as given in (8.137). All required data are given in Table 8.6 on page 353.

With appropriate atomic rest masses $\mathcal{M}$ and (8.143) we get

$$Q_\alpha = \{\mathcal{M}(^{226}_{86}\mathrm{Ra}) - \mathcal{M}(^{222}_{86}\mathrm{Rn}) - \mathcal{M}(^4_2\mathrm{He})\}c^2 = 0.005232 \times 931.5 \text{ MeV}$$
$$= 4.87 \text{ MeV} > 0 , \tag{8.150}$$

while using appropriate binding energies E_B and (8.137) we get the same result, as follows:

$$Q_\alpha = \{E_\mathrm{B}(^{222}_{86}\mathrm{Rn}) + E_\mathrm{B}(^4_2\mathrm{He}) - E_\mathrm{B}(^{226}_{88}\mathrm{Ra})\}$$
$$= (1708.185 + 28.296 - 1731.610) \text{ MeV} = 4.87 \text{ MeV} . \tag{8.151}$$

Using appropriate nuclear rest energies Mc^2 in conjunction with (8.13) or (8.143) we also obtain $Q_\alpha = 4.87$ MeV.

The kinetic energy $(E_\mathrm{K})_\alpha$ of the α particle is given from (8.147) as

$$(E_\mathrm{K})_\alpha = Q_\alpha \left(\frac{A_\mathrm{P} - 4}{A_\mathrm{P}}\right) = 4.87 \text{ MeV} \frac{222}{226} = 4.78 \text{ MeV} , \tag{8.152}$$

while 0.09 MeV goes into the recoil kinetic energy $(E_\mathrm{K})_\mathrm{D}$ of the $^{222}_{86}\mathrm{Rn}$ atom, as calculated from (8.148)

$$(E_\mathrm{K})_\mathrm{D} = Q_\alpha - (E_\mathrm{K})_\alpha = 0.09 \text{ MeV}$$
$$= \frac{4Q_\alpha}{A_\mathrm{P}} = \frac{4 \times 4.87 \text{ MeV}}{226} = 0.09 \text{ MeV} . \tag{8.153}$$

Figure 8.19 shows an energy level diagram for radium-226 decaying through α decay into radon-222. A closer look at the decay scheme of $^{226}_{88}\mathrm{Ra}$, shown in Fig. 8.19, paints a slightly more complicated picture with two α lines
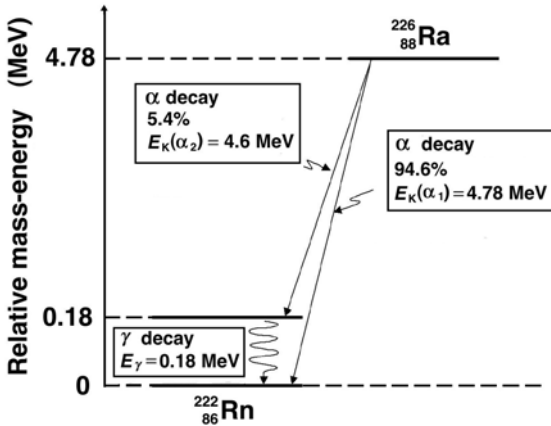
Fig. 8.19. Energy level diagram for the α decay of radium-226 into radon-222. The relative mass-energy levels for the ground states of the two nuclides are calculated from the respective atomic masses of the two radionuclides given in Table 8.6 on page 353

emitted; one with $(E_K)_{\alpha_1} = 4.78$ MeV emitted in 94.6% of decays and the other with $(E_K)_{\alpha_2} = 4.60$ MeV emitted in 5.4% of the decays. The 4.78 MeV transition ends at the ground state of $^{222}_{86}$Rn; the 4.60 MeV transition ends at the first excited state of $^{222}_{86}$Rn that instantaneously decays to the ground state through emission of a 0.18 MeV gamma ray (gamma decay; see Sect. 8.12).

The decay energy Q_α of 4.87 MeV is thus shared between the α particle (4.78 MeV) and the recoil daughter (0.09 MeV). The α particle, because of its relatively small mass in comparison with the daughter mass, picks up most of the decay energy; the magnitudes of the momenta for the two decay products are of course equal, but the momenta are opposite in direction to one another.

8.8 Beta Decay

8.8.1 General Aspects of Beta Decay

The term β decay encompasses modes of radioactive decay in which the atomic number Z of the parent nuclide changes by one unit (± 1), while the atomic mass number A remains constant. Thus, the number of nucleons and the total charge are both conserved in the β decay processes and the daughter (D) can be referred to as an isobar of the parent (P).

Three processes fall into the category of β decay:

1. β^- *decay* with the following characteristics: $Z \to Z + 1$; $A = \text{const}$

$$\text{n} \to \text{p} + \text{e}^- + \bar{\nu}_e \qquad {}^A_Z\text{P} \to {}^A_{Z+1}\text{D} + \text{e}^- + \bar{\nu}_e . \tag{8.154}$$

A neutron-rich radioactive nucleus transforms a neutron into proton and ejects an electron and an antineutrino. Free neutrons actually decay into protons through the β^- decay process with a life-time τ of 10.24 min. This decay is possible since the neutron rest mass exceeds that of the proton.

2. β^+ *decay* with the following characteristics: $Z \to Z - 1$; $A = \text{const}$:

$$p \to n + e^+ + \nu_e \qquad {}_Z^A P \to {}_{Z-1}^A D + e^+ + \nu_e \ . \tag{8.155}$$

A proton-rich radioactive nucleus transforms a proton into neutron and ejects a positron and a neutrino. Free protons cannot decay into neutrons through a β^+ decay process because the rest mass of the proton is smaller than that of the neutron.

3. *Electron capture* with the following characteristics: $Z \to Z - 1$; $A = \text{const}$:

$$p + e^- = n + \nu_e \qquad {}_Z^A P + e^- = {}_{Z+1}^A D + \nu_e \ . \tag{8.156}$$
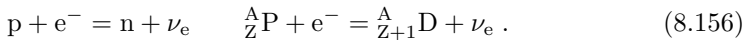
A proton-rich radioactive nucleus captures an inner shell orbital electron (usually K shell), transforms a proton into a neutron, and ejects a neutrino.

In many cases, β decay of a parent nucleus does not lead directly to the ground state of the daughter nucleus; rather it leads to an *unstable* or even *metastable excited state* of the daughter. The excited state de-excites through emission of gamma rays or through emission of internal conversion electrons (see Sect. 8.12). Of course, the orbital shell vacancies produced by the electron capture or internal conversion process will be followed by emission of discrete characteristic photons or Auger electrons, as is the case with all shell vacancies no matter how they are produced. A detailed discussion is given in Chap. 3. Beta decay can only take place when the binding energy of the daughter nucleus $E_b(D)$ exceeds the binding energy of the parent nucleus $E_B(P)$.

8.8.2 Beta Particle Spectrum

For a given β decay, similarly to the situation in α decay, the β-decay energy is uniquely defined by the difference in mass-energy between the parent and daughter nuclei. However, in contrast to the α decay where the energy of the emitted α particles is also uniquely defined, the β particles emitted in β decay are not mono-energetic, rather they exhibit a continuous spectral kinetic energy distribution with only the maximum kinetic energy $(E_{e^\pm})_{\max}$ corresponding to the β decay energy.

This apparent contravention of the energy conservation law was puzzling physicists for many years until in 1930 *Wolfgang Pauli* postulated the existence of the neutrino to explain the continuous spectrum of electrons emitted in β decay. In 1934 *Enrico Fermi* expanded on Pauli's neutrino idea and developed a theory of the β^- and β^+ decay. Only with the emission of a third
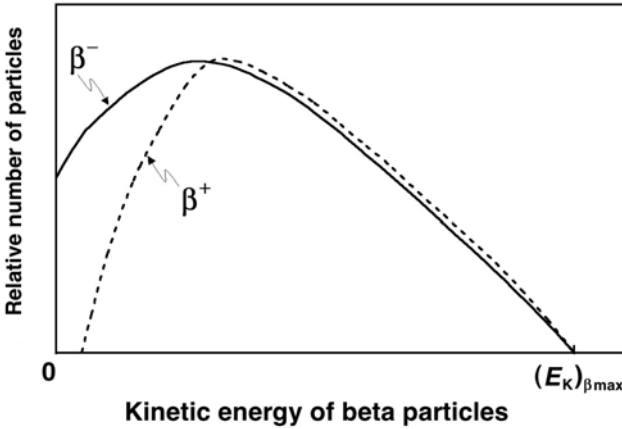
Fig. 8.20. Typical beta particle energy spectra for β^- and β^+ decay normalized to the maximum energy of the β particle

particle, the neutrino or antineutrino, could the momentum and energy be conserved in a β decay. The existence of the neutrino was finally proven experimentally in 1953.

The neutrino and antineutrino are assumed to have essentially zero rest mass and are moving with the speed of light c. They are also assumed to have only weak interactions with atoms of the absorber and are thus extremely difficult to detect. Their charge is equal to zero. It is obvious that detection of an essentially massless, momentless, uncharged relativistic particle that only experiences weak interactions with matter is extremely difficult. Nonetheless, several techniques were devised to detect the elusive particle experimentally and thus prove correct Fermi's contention about its existence in beta decay.

Typical shapes of β^- and β^+ spectra are shown in Fig. 8.20. In general, the spectra exhibit low values at small kinetic energies, reach a maximum at a certain kinetic energy and then decrease with kinetic energy until they reach zero at a maximum energy $(E_{e\pm})_{max}$ that corresponds to the β decay energy Q_β, if we neglect the small recoil energy acquired by the daughter nucleus.

The shapes of β^- and β^+ spectra differ at low kinetic energies owing to the charge of the β particles: electrons in β^- decay are attracted to the nucleus; positrons in β^+ decay are repelled by the nucleus. The charge effects cause an energy shift to lower energies for electrons and to higher energies for positrons, as is clearly shown in Fig. 8.20.

For use in internal dosimetry calculations of β sources the effective energy $(E_{e\pm})_{eff}$ of β decay spectra is usually estimated as

$$(E_\beta)_{eff} \approx \frac{1}{3}(E_\beta)_{max} \ . \tag{8.157}$$

8.8.3 Daughter Recoil in β^- and β^+ Decay

In a β^- and β^+ beta decay event the daughter nucleus recoils with a kinetic energy $(E_K)_D$ ranging from 0 to a maximum value.

1. The recoil kinetic energy of the daughter decay product is zero, i.e., $(E_K)_D = 0$ when the electron and antineutrino in β^- decay or positron and neutrino in β^+ decay are emitted with the same momentum but in opposite directions.
2. The maximum recoil kinetic energy $(E_K)_{Dmax} = $ max of the daughter occurs when either one of the two decay particles (electron or antineutrino in β^- decay; positron or neutrino in β^+ decay) is emitted with the maximum available kinetic energy $(E_\beta)_{max}$. The β decay energy Q_β is expressed as

$$Q_\beta = (E_K)_{Dmax} + (E_\beta)_{max} . \tag{8.158}$$

The maximum recoil kinetic energy of the daughter $(E_K)_D$ is determined using the laws of energy and momentum conservation and accounting for the relativistic mass changes of the β particle (electron or positron). A common name for electron or positron in beta decay is β particle.

1. The β particle momentum $p_{e\pm} = \gamma m_{e\pm} \upsilon_{e\pm}$ is equal to the daughter momentum $p_D = M(D)\upsilon_D$, where $m_{e\pm}$ and $M(D)$ are the rest masses of the β particle and daughter nucleus, respectively; $\upsilon_{e\pm}$ and υ_D are the velocities of the β particle and the daughter nucleus, respectively; and $\gamma = (1 - \beta^2)^{-1/2}$ with $\beta = \upsilon/c$.
2. The kinetic energy $(E_K)_D$ of the daughter nucleus is calculated classically as $(E_K)_D = M(D)\upsilon_D^2/2$; the maximum kinetic energy of the β particle is given relativistically as $(E_\beta)_{max} = (\gamma - 1)m_{e\pm}c^2$.

Since $p_{e\pm} = p_D$, we get

$$\upsilon_D = \gamma \frac{m_{e\pm}}{M(D)} \upsilon_{e\pm} . \tag{8.159}$$

Inserting (8.159) into the equation for the daughter kinetic energy $(E_K)_D = M(D)\upsilon_D^2/2$, we obtain

$$(E_K)_{Dmax} = \frac{M(D)\upsilon_D^2}{2} = \gamma^2 \frac{m_{e\pm}^2 \upsilon_{e\pm}^2}{2M(D)} = \gamma^2 \beta^2 \frac{(m_{e\pm}c^2)^2}{2M(D)c^2} =$$

$$= \frac{\beta^2}{1 - \beta^2} \frac{(m_{e\pm}c^2)^2}{2M(D)c^2} . \tag{8.160}$$

From the relationship $(E_\beta)_{max} = (\gamma - 1)m_{e\pm}c^2$ we calculate the expression for $\beta^2/(1 - \beta^2)$ to obtain

$$\frac{\beta^2}{1 - \beta^2} = \frac{2(E_\beta)_{max}}{m_{e\pm}c^2} + \left\{ \frac{(E_\beta)_{max}}{m_{e\pm}c^2} \right\}^2 . \tag{8.161}$$

Inserting (8.161) into (8.160) we obtain the following expression for the recoil kinetic energy $(E_K)_D$ of the daughter nucleus:

$$(E_K)_{Dmax} = \frac{\beta^2}{1 - \beta^2} \frac{(m_{e^\pm}c^2)^2}{2M(D)c^2} = \frac{m_{e^\pm}c^2}{M(D)c^2}(E_\beta)_{max} + \frac{(E_\beta)^2_{max}}{2M(D)c^2} \ . \ (8.162)$$

The daughter recoil kinetic energy $(E_K)_D$ is usually of the order of 10 eV to 100 eV; negligible in comparison to the kinetic energy of the β particle, yet sufficiently high to be able to cause atomic rearrangements in the neighboring molecules in biological materials.

The decay energy Q_β is now given as follows:

$$Q_\beta = (E_K)_D + (E_\beta)_{max} = (E_\beta)_{max} \left\{ 1 + \frac{m_{e^\pm}c^2 + \frac{1}{2}(E_\beta)_{max}}{M(D)c^2} \right\} \ ,$$
$$(8.163)$$

showing that in β^- and β^+ decay by far the larger energy component is the component shared between the β particle and neutrino, since these two particles in general share the energy $(E_\beta)_{max}$; the recoil kinetic energy given to the daughter is extremely small and may be neglected, unless, of course, we are interested in calculating it, so that we may determine the local damage produced by the daughter atom in biological materials.

8.9 Beta Minus Decay

8.9.1 General Aspects of Beta Minus (β^-) Decay

Several radionuclides decaying by β^- decay are used in medicine for external beam radiotherapy and brachytherapy. The parent nuclide decays by β^- decay into an excited daughter nuclide that instantaneously or through a metastable decay process decays into its ground state and emits the excitation energy in the form of gamma ray photons. These photons are then used for radiotherapy.

The most important characteristics of radionuclides used in external beam radiotherapy are:

1. *High gamma ray energy*
2. *High specific activity*
3. *Relatively long half-life*
4. *Large specific air-kerma rate constant*

Of the over 3000 natural or artificial radionuclides known, only a few are suitable for use in radiotherapy and of these practically only cobalt-60, with its high photon energy (1.17 MeV and 1.33 MeV), high practical specific activity, and a relatively long half-life (5.27 years), meets the source requirements for external beam radiotherapy.

8.9.2 Beta Minus (β^-) Decay Energy

The β^- decay can occur to a neutron-rich unstable parent nucleus when the mass $M(Z, A)$ of the parent nucleus exceeds the mass $M(Z + 1, A)$ of the daughter nucleus by more than one electron rest mass m_e. The decay energy Q_{β^-} for the β^- decay process is given as

$$Q_{\beta^-} = \{M(Z, A) - [M(Z + 1, A) + m_e]\}\, c^2 \,, \tag{8.164}$$

in terms of *nuclear mass* M.

Adding and subtracting $Z m_e c^2$ to the right-hand side of (8.164) and neglecting the electron binding energies to the nucleus we obtain

$$
\begin{aligned}
Q_{\beta^-} &= \{M(Z, A) + Z m_e - [M(Z + 1, A) + m_e + Z m_e]\}\, c^2 \\
&= \{\mathcal{M}(Z, A) - \mathcal{M}(Z + 1, A)\}\, c^2 \,,
\end{aligned}
\tag{8.165}
$$

where $\mathcal{M}(Z, A)$ and $\mathcal{M}(Z + 1, A)$ represent the *atomic masses* of the parent and daughter, respectively, noting that

$$\mathcal{M}(Z, A) = M(Z, A) + Z m_e \tag{8.166}$$

and

$$\mathcal{M}(Z + 1, A) = M(Z + 1, A) + (Z + 1) m_e \,. \tag{8.167}$$

For the β^- decay to occur the atomic mass of the parent $\mathcal{M}(Z, A)$ must exceed the atomic mass of the daughter $\mathcal{M}(Z + 1, A)$; i.e., $\mathcal{M}(Z, A) > \mathcal{M}(Z + 1, A)$.

The atomic rest energy difference between the parent and daughter provides the energy released in a β^- decay event, most generally consisting of:

1. Energy of the emitted electron
2. Energy of the antineutrino
3. Energy of the emitted γ ray photons or conversion electrons with characteristic x rays and Auger electrons.
4. Recoil kinetic energy of the daughter nucleus (small and usually neglected).

8.9.3 Beta Minus (β^-) Decay of Cobalt-60 into Nickel-60

For medical physics an important β^- decay example is the decay of unstable cobalt-60 radionuclide with a half life of 5.27 years into an excited nickel-60 nuclide that decays instantaneously into its ground state with emission of two γ ray photons of energies 1.173 MeV and 1.332 MeV, as shown schematically in Fig. 8.21:

$$^{60}_{27}\text{Co} \rightarrow\ ^{60}_{28}\text{Ni} + \text{e}^- + \bar{\nu}_e + Q_{\beta^-}(2.82\ \text{MeV}) \,. \tag{8.168}$$
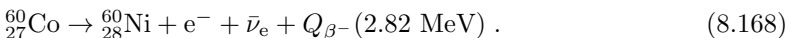
Cobalt-60 is used as a radiation source in teletherapy machines applied for external beam radiotherapy. Typical cobalt-60 source activities are of the order of 200 TBq to 400 TBq. There are several thousand cobalt units in
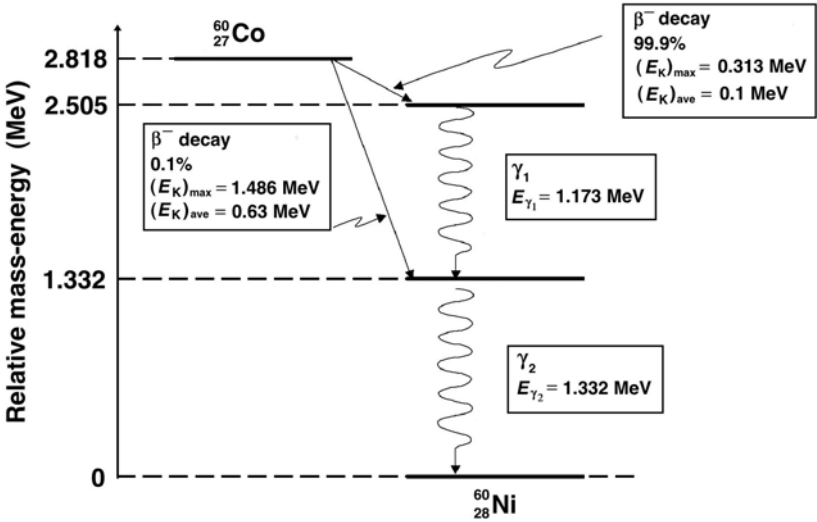
Fig. 8.21. Decay scheme for the β^- decay of cobalt-60 into nickel-60. The relative mass-energy levels for the ground states of the two nuclides are calculated from atomic masses given in Table 8.6 on page 353

operation around the world and Canada is a major producer of these units and cobalt-60 sources.

The decay energy Q_{β^-} for the Co-60 β^- decay into Ni-60 is calculated as follows:

$$
\begin{aligned}
Q_{\beta^-} &= \left\{ \mathcal{M}(^{60}_{22}\mathrm{Co}) - \mathcal{M}(^{60}_{28}\mathrm{Ni}) \right\} c^2 \\
&= \{59.933822u - 59.930791u\} \, 931.5 \text{ MeV}/u = 2.82 \text{ MeV} .
\end{aligned}
\tag{8.169}
$$

The calculated Q_{β^-} of 2.82 MeV is shown in Fig. 8.21 as the energy difference between the ground states of cobalt-60 and nickel-60. There are two β^- decay channels:

1. 99.9% of decays proceed from Co-60 to the second excited state of Ni-60 with maximum and effective electron energy of 0.313 MeV and 0.1 MeV, respectively.
2. Only 0.1% of decays proceed from Co-60 to the first excited state of Ni-60 with maximum and effective electron energy of 1.486 MeV and 0.63 MeV, respectively.

The excited nickel-60 nucleus attains its ground state through emission of γ ray photons, as discussed further in Sect. 8.12.

8.9.4 Beta Minus (β^-) Decay of Cesium-137 into Barium-137

Another example of β^- decay of interest in medical physics is the decay of cesium-137 into barium-137 with a half-life of 30.07 years:

$$^{137}_{55}\text{Cs} \rightarrow {}^{137}_{56}\text{Ba} + \text{e}^- + \bar{\nu}_\text{e} + Q_{\beta^-}\,(1.176 \text{ MeV}) \,. \tag{8.170}$$
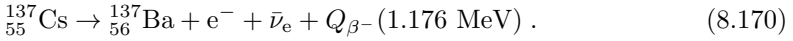
The decay energy Q_{β^-} for the decay of Cs-137 into Ba-137 by β^- decay is calculated as

$$
\begin{aligned}
Q_{\beta^-} &= \left\{ \mathcal{M}({}^{137}_{55}\text{Cs}) - \mathcal{M}({}^{137}_{56}\text{Ba}) \right\} c^2 \\
&= \{136.90708u - 136.90582u\}\, 931.5 \text{ MeV}/u = 1.176 \text{ MeV} \,.
\end{aligned}
\tag{8.171}
$$

The calculated Q_{β^-} of 1.176 MeV is shown in Fig. 8.22 as the energy difference between the ground states of cesium-137 and barium-137. There are two β^- decay channels:

1. 94.6% of β^- decays proceed from Cs-137 to the excited state of Ba-137m with maximum electron energy of 0.514 MeV. The Ba-137m is a metastable state that decays with a 2.552 min half-life to the ground state of Ba-137 with emission of a 0.662 MeV γ ray photon. The maximum electron energy of 0.514 MeV added to the γ ray energy of 0.662 MeV results in decay energy of 1.176 MeV, as calculated in (8.171).
2. 5.4% of β^- decays proceed directly from Cs-137 to the ground state of Ba-137 with maximum electron energy of 1.176 MeV.
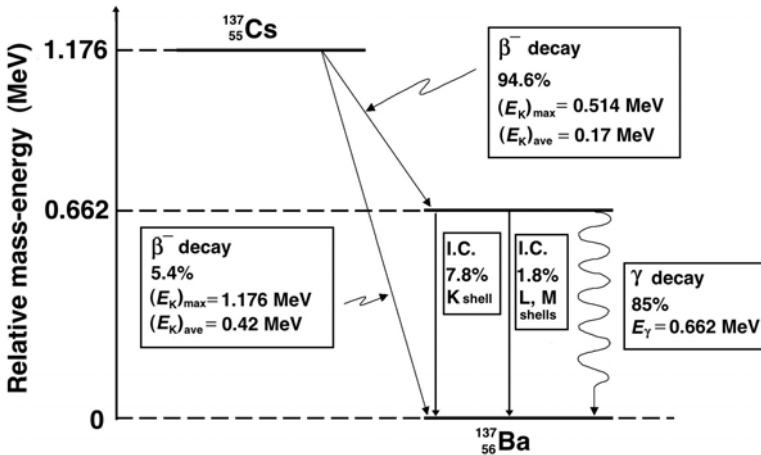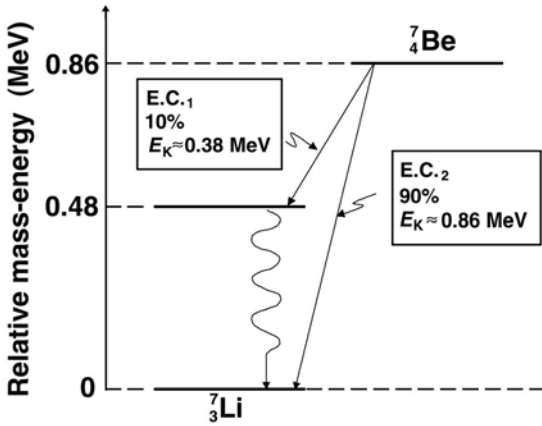

Fig. 8.22. The decay scheme for β^- decay of cesium-137 into barium-137. The relative mass-energy levels for the ground states of the two nuclides are calculated from atomic masses listed in Table 8.6 on page 353

8.10 Beta Plus Decay

8.10.1 General Aspects of the Beta Plus (β^+) Decay

The β^+ decay is characterized by the production of positrons that appear in a spectral distribution with maximum positron energy specific to the particular β^+ decay. As in the β^- decay, the daughter recoil kinetic energy in β^+ decay is essentially negligible. Radionuclides undergoing β^+ decay are often called positron emitters and are used for functional imaging with a special imaging technique called positron emission tomography (PET).

- PET provides information on metabolic function of organs or tissues by detecting how cells process certain compounds such as, for example, glucose. Cancer cells metabolize glucose at a much higher rate than normal tissues. By detecting increased radio-labelled glucose metabolism with a high degree of sensitivity, PET identifies cancerous cells, even at an early stage when other imaging modalities may miss them.
- In a PET study one administers a positron-emitting radionuclide by injection or inhalation. The radionuclide circulates through the bloodstream to reach a particular organ. The positrons emitted by the radionuclide have a very short range in tissue and undergo annihilation with an available electron. This process generally results in emission of two gamma photons, each with energy of 0.511 MeV, moving away from the point of production in nearly opposite directions.
- The radionuclides used in PET studies are produced by bombardment of an appropriate stable radionuclide with protons from a cyclotron (see Sect. 8.4.9) thereby producing positron-emitting radionuclides that are subsequently attached to clinically useful biological markers. The most commonly used positron emitting radionuclides are: carbon-11, nitrogen-13, oxygen-15, fluorine-18 and rubidium-82.
- Fluorine-18 radionuclide attached to the biological marker deoxyglucose forms the radiopharmaceutical fluorodeoxyglucose (FDG) that is the most commonly used tracer in studies involving glucose metabolism in cancer diagnosis.

8.10.2 Decay Energy in β^+ Decay

The β^+ decay can occur to a proton-rich unstable parent nucleus where the mass $M(Z, A)$ of the parent nucleus exceeds the mass $M(Z - 1, A)$ of the daughter nucleus by more than one positron mass m_e. The decay energy Q_{β^+} for the β^+ decay process is given as

$$Q_{\beta^+} = \{M(Z, A) - [M(Z - 1, A) + m_e]\} c^2 \tag{8.172}$$

in terms of *nuclear masses M*.

Adding and subtracting $Zm_e c^2$ to the right-hand side of (8.172) and neglecting the electron binding energies to the nucleus we obtain

$$Q_{\beta^+} = \{M(Z, A) + Zm_e - [M(Z-1, A) + m_e + Zm_e]\}\, c^2$$
$$= \{\mathcal{M}(Z, A) - [\mathcal{M}(Z-1, A) + 2m_e]\}\, c^2 \qquad (8.173)$$

where $\mathcal{M}(Z, A)$ and $\mathcal{M}(Z-1, A)$ represent the *atomic masses* of the parent and daughter, respectively.

We note that the relationships between *atomic* and *nuclear masses* of parent and daughter, ignoring the binding energies of orbital electrons, are

$$\mathcal{M}(Z, A) = M(Z, A) + Zm_e \qquad (8.174)$$

and

$$\mathcal{M}(Z-1, A) = M(Z-1, A) + (Z-1)m_e . \qquad (8.175)$$

For the β^+ decay to occur the atomic mass of the parent $\mathcal{M}(Z, A)$ must exceed the atomic mass of the daughter $\mathcal{M}(Z-1, A)$ by more than two electron rest masses, or in rest energies

$$\mathcal{M}(Z, A)c^2 > \mathcal{M}(Z-1, A)c^2 + 2m_e c^2 , \qquad (8.176)$$

where $m_e c^2$ is the electron rest energy of 0.5110 MeV.

8.10.3 Beta Plus (β^+) Decay of Nitrogen-13 into Carbon-13

An example for a simple β^+ decay is the decay of nitrogen-13 into carbon-13 with a half-life of 10 minutes. Nitrogen-13 is a proton-rich radionuclide produced in a cyclotron. The decay scheme is shown in Fig. 8.23 and the basic equation for the decay is as follows:

$$^{13}_{7}\text{N} \rightarrow {}^{13}_{6}\text{C} + \text{e}^+ + \nu_e + Q_{\beta^+}(1.2 \text{ MeV}) . \qquad (8.177)$$

The decay energy Q_{β^+} for the β^+ decay of nitrogen-13 into carbon-13 is calculated as follows, with the atomic masses for the two nuclides listed in Table 8.5:

$$Q_{\beta^+} = \left\{ \mathcal{M}(^{13}_{7}\text{N}) - [\mathcal{M}(^{13}_{6}\text{C}) + 2m_e] \right\} c^2$$
$$= (13.005739u - 13.003355u)c^2 - 2m_e c^2$$
$$= 0.002383u \times 931.5 \text{ MeV/}u = 2.220 \text{ MeV} - 1.022 \text{ MeV}$$
$$= 1.2 \text{ MeV}. \qquad (8.178)$$

The energy difference between the ground state of nitrogen-13 and carbon-13 is 2.22 MeV; however, only $2.22 \text{ MeV} - 2m_e c^2 = 1.2$ MeV is available for the maximum energy of the positron.

Ammonia is the substance that can be labeled with the nitrogen-13 radionuclide for use in functional imaging with positron emission tomography (PET) scanning. The nitrogen-13 labeled ammonia is injected intravenously and is mainly used for cardiac imaging for diagnosis of coronary artery disease and myocardial infarction. It is also occasionally used for liver and brain imaging.
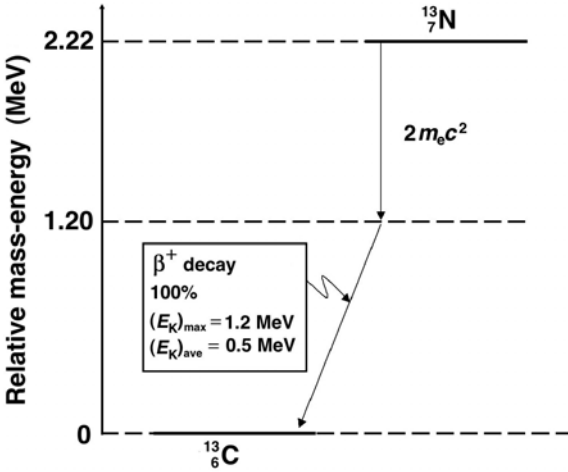
Fig. 8.23. The decay scheme for β^+ decay of nitrogen-13 into carbon-13. The relative mass-energy levels of the ground states of the two nuclides are calculated from atomic masses listed in Table 8.6 on page 353

8.10.4 Beta Plus (β^+) Decay of Fluorine-18 into Oxygen-18

The β^+ decay of fluorine-18 into oxygen-18 with a half-life of 110 min is an important practical example of the β^+ decay. Fluoro-deoxy-glucose (FDG) labeled with radionuclide fluorine-18 is a sugar compound that can be injected intravenously into a patient for use in positron emission tomography (PET) functional imaging. Based on demonstrated areas of increased glucose metabolism the FDG PET scan:

1. Can detect malignant disease.
2. Can distinguish benign from malignant disease.
3. Can be used for staging of malignant disease.
4. Can be used for monitoring response to therapy of malignant disease.

The decay energy $Q_{\beta+}$ for the β^+ decay of fluorine-18 into oxygen-13 is calculated as follows:

$$
\begin{aligned}
Q_{\beta+} &= \left\{ \mathcal{M}(^{18}_9\text{F}) - [\mathcal{M}(^{18}_8\text{O}) + 2m_e] \right\} c^2 \\
&= (18.000937u - 17.999160u)c^2 - 2m_ec^2 \\
&= 0.001777\text{u} \times 931.5 \text{ MeV}/u \\
&= 1.660 \text{ MeV} - 1.022 \text{ MeV} \\
&= 0.638 \text{ MeV}.
\end{aligned}
\tag{8.179}
$$

The energy difference between the ground states of fluorine-18 and oxygen-18 is 1.66 MeV; however, only 1.66 MeV $- 2m_ec^2 = 0.638$ MeV is available for
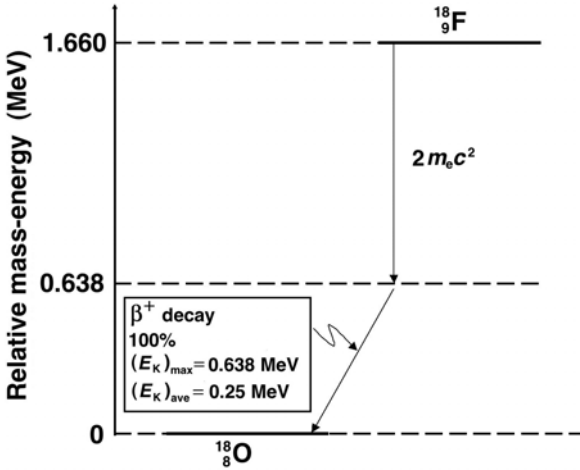
Fig. 8.24. The decay scheme for β^+ decay of fluorine-18 into oxygen-18. The relative mass-energy levels for the ground states of the two nuclides are calculated from atomic masses listed in Table 8.6 on page 353

the maximum energy of the positron, as shown schematically in Fig. 8.24 and in (8.180) below

$$_9^{18}\text{F} \rightarrow _8^{18}\text{O} + \text{e}^+ + \nu_\text{e} + Q_{\beta^+}(0.638 \text{ MeV}) \ . \qquad (8.180)$$

8.11 Electron Capture (EC)

8.11.1 Decay Energy in Electron Capture

Electron capture (EC) radioactive decay may occur when an atomic electron ventures inside the nuclear volume, is captured by a proton, and triggers a proton to neutron transformation. Of all atomic electrons, the K-shell electrons have the largest probability for venturing into the nuclear volume and thus contribute most often to the EC decay process. Typical ratios EC(K shell)/EC(L shell) are of the order of 10:1.

Electron capture can occur in proton-rich, unstable parent nuclei, when the mass $M(Z, A)$ of the parent nucleus combined with the mass of one electron m_e exceeds the mass of the daughter nucleus $M(Z - 1, A)$. The decay energy Q_EC for electron capture is given as

$$\begin{aligned} Q_\text{EC} &= \{[M(Z, A) + m_\text{e}] - M(Z - 1, A)\} \\ &= \{M(Z, A) - [M(Z - 1, A) - m_\text{e}\} c^2 \end{aligned} \qquad (8.181)$$

in terms of nuclear masses M. Adding and subtracting Zm_e to the right-hand side of (8.181) and neglecting the electron binding energies to the nucleus we

obtain the decay energy Q_{EC} in terms of atomic masses $\mathcal{M}$

$$Q_{\mathrm{EC}} = \{\mathcal{M}(Z, A) - \mathcal{M}(Z - 1, A)\}\, c^2 \ . \qquad (8.182)$$

For electron capture to occur, the atomic mass of the parent $\mathcal{M}(Z, A)$ must exceed the atomic mass of the daughter $\mathcal{M}(Z - 1, A)$; i.e., $\mathcal{M}(Z, A) > \mathcal{M}(Z - 1, A)$. The atomic rest energy difference between the parent and the daughter gives the energy released to the neutrino and the daughter atom in an EC radioactive decay event.

Electron capture is a competing process to β^+ decay; however, the conditions on electron capture as far as relative atomic masses of parent and daughter are concerned are less restrictive than those imposed on β^+ decay that results in positron emission and subsequent positron annihilation with emission of annihilation quanta. The condition on EC decay is that the parent atomic mass $\mathcal{M}(\mathrm{P})$ simply exceeds the daughter atomic mass $\mathcal{M}(\mathrm{D})$, while the condition on β^+ decay is that the parent atomic mass exceeds that of the daughter by a minimum of two electron masses.

- When the condition $Q_{\mathrm{EC}} > 0$ is satisfied but Q_{β^+} of (8.172) is negative, the β^+ decay will not happen because it is energetically forbidden and EC decay will happen alone.
- When $Q_{\beta^+} > 0$ then Q_{EC} is always positive and both decays (β^+ and EC) can happen. The branching ratios $\lambda_{\mathrm{EC}}/\lambda_{\beta^+}$ vary considerably from one nuclide to another; for example, from a low of 0.03 for fluorine-18 to several hundred for other proton-rich radionuclides.
- In contrast to the β^- and β^+ decay processes in which three decay products share the decay energy and produce a continuous spectral distribution, in the EC decay the two decay products do not have a continuous spectral distribution; rather they are given discrete (monoenergetic) energies. The monoenergetic neutrinos produce a line spectrum with energy E_ν, while the daughter has the recoil kinetic energy $(E_{\mathrm{K}})_{\mathrm{D}}$ discussed below.

8.11.2 Recoil Kinetic Energy of the Daughter Nucleus in Electron Capture Decay

The recoil kinetic energy $(E_{\mathrm{K}})_{\mathrm{D}}$ of the daughter nucleus in electron capture decay is determined in two steps:

1. First, we determine the momenta of the daughter $p_{\mathrm{D}} = M(\mathrm{D})\upsilon_{\mathrm{D}}$ and the neutrino $p_\nu = E_\nu/c$. The two momenta are identical in magnitude but opposite in direction, so we can write

$$p_{\mathrm{D}} = M(\mathrm{D})\upsilon_{\mathrm{D}} = p_\nu = \frac{E_\nu}{c} \ , \qquad (8.183)$$

where

E_ν is the neutrino energy

$M(D)$ is the mass of the daughter nucleus

υ_D is the velocity of the daughter nucleus

2. The recoil kinetic energy of the daughter (classically) is given as follows after inserting υ_D from (8.183):

$$(E_K)_D = \frac{M(D)\upsilon_D}{2} = \frac{E_\nu^2}{2M(D)c^2}\,. \tag{8.184}$$

The energy available for sharing between the daughter nucleus and neutrino is equal to the electron capture decay energy Q_{EC} decreased by the binding energy E_B of the captured electron, i.e.,

$$Q_{EC} - E_B = E_\nu + (E_K)_D = E_\nu + \frac{E_\nu^2}{2M(D)c^2} \tag{8.185}$$

or

$$\frac{E_\nu^2}{2M(D)c^2} + E_\nu - (Q_{EC} - E_B) = 0\,. \tag{8.186}$$

Equation (8.186) results in the following expression for the energy of the monoenergetic neutrino emitted in electron capture:

$$E_\nu = \left\{ -1 + \sqrt{1 + \frac{2(Q_{EC} - E_B)}{M(D)c^2}} \right\} M(D)c^2 \approx Q_{EC} - E_B\,. \tag{8.187}$$

In the first approximation the recoil kinetic energy $(E_K)_D$ of the daughter is neglected and so is the binding energy E_B of the captured electron. The energy of the monoenergetic neutrino in electron capture is then approximated by the electron capture decay energy, i.e., $E_\nu \approx Q_{EC}$.

8.11.3 Electron Capture Decay of Beryllium-7 into Lithium-7

An example for EC decay is given in Fig. 8.25 that shows a decay scheme for beryllium-7 decaying through EC into lithium-7. Beryllium-7 has too many protons for nuclear stability, so it achieves better stability by transforming a proton into a neutron. However, it can do so only through EC and not through β^+ decay, because the atomic rest energy of beryllium-7 exceeds that of lithium-7 by only 0.86 MeV and not by a minimum of 1.02 MeV required for β^+ decay to be energetically feasible.

The decay energy for the electron capture decay of berillium-7 into lithium-7 is calculated as follows:

$$\begin{aligned} Q_{EC} &= \left\{ \mathcal{M}(_4^7\text{Be}) - \mathcal{M}(_3^7\text{Li}) \right\} c^2 = (7.0169292u - 7.016004u)c^2 \\ &= 0.0009252u \times 931.5 \text{ MeV}/u = 0.862 \text{ MeV}. \end{aligned} \tag{8.188}$$

Fig. 8.25. The decay scheme for electron capture decay of berillium-7 into lithium-7. The relative mass-energy levels for the ground states of the two nuclides are calculated from the respective atomic masses listed in Table 8.6 on page 353

8.11.4 Decay of Iridium-192

Iridium-192 serves as an important radioactive source for use in brachytherapy with remote afterloading techniques. It decays with a half-life of 74 days into stable platinum-192 by β^- decay and into stable osmium-192 by electron capture decay. The source is produced through a neutron activation process on iridium-191 in a nuclear reactor (see Sect. 8.4.8). The natural abundance of stable iridium-191 is 37.3% in a mixture with 62.7% of stable iridium-193. The cross section σ for thermal neutron capture is 954 b.

As shown in Fig. 8.26, iridium-192 has a very complicated γ ray spectrum with 14 γ energies ranging from 0.2 MeV to ~0.9 MeV, providing effective photon energy of 0.38 MeV. Because of the relatively short half-life, the iridium-192 source requires a source change in remote afterloading machines every 3 to 4 months.

With $\mathcal{M}$ representing atomic masses, the β^- decay energy Q_{β^-} for iridium-192 decaying into platinum-192 is given as follows:

$$\begin{aligned}
Q_{\beta^-} &= \left\{ \mathcal{M}(^{192}_{77}\text{Ir}) - \mathcal{M}(^{192}_{78}\text{Pt}) \right\} c^2 \\
&= 191.96260u - 191.96104u)c^2 \\
&= 0.00156u \times 931.5 \text{ MeV}/u = 1.453 \text{ MeV}.
\end{aligned} \tag{8.189}$$

The electron capture decay energy Q_{EC} for iridium-192 decaying into osmium-192 is

$$\begin{aligned}
Q_{\text{EC}} &= \left\{ \mathcal{M}(^{192}_{77}\text{Ir}) - \mathcal{M}(^{192}_{76}\text{Os}) \right\} c^2 \\
&= (191.96260u - 191.96148u)c^2 \\
&= 0.00112u \times 931.5 \text{ MeV}/u = 1.043 \text{ MeV}
\end{aligned} \tag{8.190}$$
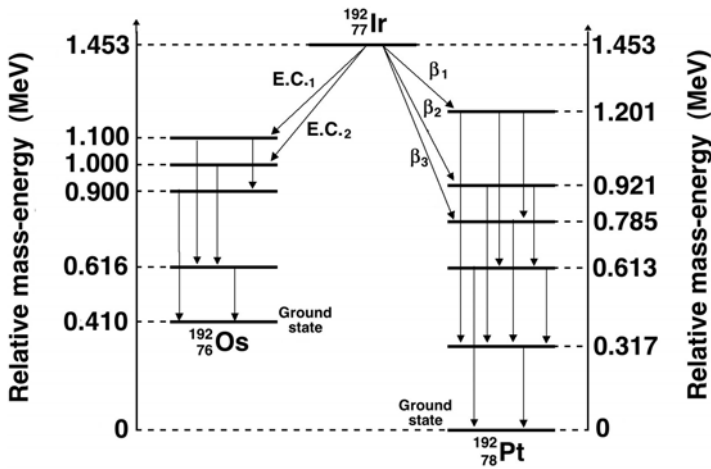
Fig. 8.26. The decay scheme for decay of iridium-192 into platinum-192 through
β^- decay and into osminum-192 through electron capture decay. The relative mass-
energy levels for the ground states of the three nuclides are calculated from the
respective atomic masses given in Table 8.6 on page 353

8.12 Gamma Decay

8.12.1 General Aspects of Gamma (γ) Decay

The α decay as well as the three beta decay modes may produce a daughter
nucleus in an excited state without expending the full amount of the decay
energy available.

The daughter nucleus will reach its ground state (i.e., it will de-excite)
through one of the following two processes:

1. Emit the excitation energy in the form of a γ photon (*pure γ decay*).
2. Transfer the excitation energy to one of its orbital electrons in a process
   called *internal conversion.*

In most radioactive α or β decays the daughter nucleus de-excitation occurs
instantaneously (i.e., within 10^{-12} s), so that we refer to the emitted γ rays as
if they were produced by the parent nucleus. For example, for the cobalt-60
β^- decay into nickel-60, the γ rays following the β^- decay actually originate
from nuclear de-excitations of nickel-60, yet for convenience, we refer to these
γ rays as the cobalt-60 γ rays. Similarly, we refer to γ photons following the
β^- decay of cesium-137 into barium-137m as cesium-137 γ rays even though
the γ photons actually originate from a transition in the barium-137 nucleus.

In certain α or β decays, the excited daughter nucleus does not immedi-
ately decay to its ground state; rather, it de-excites with a time delay:

• The excited state of the daughter is then referred to as a *metastable
  state* and the process of de-excitation is called an *isomeric transition.*

The metastable states are characterized by their own half-lives $t_{1/2}$ and mean (average) lives τ.

- The nucleus in a metastable state is identified with a letter m next to the atomic mass number designation (e.g, barium-137m or $^{137m}_{56}$Ba with a half-life of 2.552 min; technetium-99m or $^{99m}_{43}$Tc with a half-life of 6.01 hours).
- The term *isomer* is used for designation of nuclei that have the same atomic number Z and same atomic mass number A but differ in energy states.

In addition to α and β decay there are many other modes for producing nuclei in excited states that subsequently undergo γ decay. For example, excited states with energies up to 8 MeV may be produced with neutron capture (n, γ) reactions as well as with other nuclear reactions, such as (p, γ) and (α, γ), etc. Examples of γ rays following α and β decays are given in Fig. 8.19 for α decay and Figs. 8.21 and 8.22 for β^- decay.

8.12.2 Emission of Gamma Rays in Gamma Decay

In a general sense, γ decay stands for nuclear de-excitation either by emission of a γ ray photon or by internal conversion. In a more narrow sense, γ decay only implies emission of γ photons. The energy of γ rays emitted by a particular radionuclide is determined by the energy level structure of the radinuclides and can range from a relatively low value of 100 keV up to about 3 MeV.

The γ decay process may be represented as follows:

$$^A_Z X^* \to {}^A_Z X + \gamma + Q_\gamma \,, \tag{8.191}$$

where $^A_Z X^*$ strands for an excited state of the nucleus $^A_Z X$ and Q_γ is the gamma decay energy.

8.12.3 Gamma Decay Energy

The decay energy Q_γ in γ emission is the sum of the γ photon energy E_γ and the recoil kinetic energy of the daughter $(E_K)_D$, i.e.,

$$Q_\gamma = E_\gamma + (E_K)_D \,. \tag{8.192}$$

Since the magnitudes of the momenta of the daughter recoil nucleus $p_D = M(D)\upsilon_D$ and the γ photon $p_\gamma = E_\gamma/c$ are equal, i.e., $p_D = p_\gamma$, we can determine the partition of energy between $E_\gamma = p_\gamma c = M(D)\upsilon_D c$ and $(E_K)_D = M(D)\upsilon_D^2/2$ as

$$(E_K)_D = \frac{M(D)\upsilon_D^2}{2} = \frac{E_\gamma^2}{2M(D)c^2} \,, \tag{8.193}$$

where $M(D)$ and υ_D are the rest mass and recoil velocity, respectively, of the daughter nucleus.

The gamma decay energy Q_γ may now be written as

$$Q_\gamma = E_\gamma + (E_K)_D = E_\gamma \left(1 + \frac{E_\gamma}{2M(D)c^2} \right) \ . \tag{8.194}$$

Equation (8.194) shows that the recoil kinetic energy of the daughter $(E_K)_D$ represents less than 0.1% of the gamma photon energy E_γ. The recoil energy of the daughter nucleus is thus negligible for most practical purposes. The label for *daughter* in gamma decay is used in parallel with the same label used in other nuclear decays that are clearly defined with a parent decaying into a daughter. In gamma decay the parent and daughter represent the same nucleus, except that the parent nucleus is in an excited state and the daughter nucleus is in a lower excited state or the ground state.

8.12.4 Resonance Absorption and the Mössbauer Effect

The question of *resonance absorption* is of importance and deserves a brief discussion. The resonance absorption is a phenomenon in which a photon produced by a nuclear or atomic transition is re-absorbed by the same type of nucleus or atom, respectively. Since the photon shares the de-excitation energy with the atom or nucleus (recoil energy), it is quite possible that its energy will not suffice to allow triggering the reverse interaction and undergoing resonance absorption. However, if the recoil energy of the daughter atom or nucleus is not excessive, the resonance absorption is possible because of the natural width of the photon energy distribution and the finite lifetime of atomic and nuclear states, where the width and lifetime are governed by the uncertainty principle (see Sect. 1.23).

The photons' emission and absorption spectra differ because of the atomic or nuclear recoil energy that makes the emission energy slightly smaller than ΔE, the energy difference between the two states. However, if there is a region of overlap between the emission and absorption spectrum, resonance absorption is possible.

For atomic transitions that are of the order of eV to keV the resonance absorption is not hindered. On the other hand, for nuclear transitions that are of the order of 10 MeV, there is no overlap between the emission and the absorption photon spectrum and resonance absorption is not possible. However, there is a way around this problem. In 1957 *Rudolph Mössbauer* discovered that nuclear transitions occur with negligible nuclear recoil, if the decaying nucleus is embedded into a crystalline lattice. Here, the crystal as a whole rather than only the daughter nucleus absorbs the recoil momentum. This effect, called Mössbauer effect, minimizes the recoil energy and makes nuclear resonance absorption possible.

8.13 Internal Conversion

8.13.1 General Aspects of Internal Conversion

Nuclear de-excitation in which the de-excitation energy is transferred from the nucleus almost in full to an orbital electron of the same atom is called *internal conversion* (IC). The process is represented as follows:

$$\ce{_Z^A X^*} \to \ce{_Z^A X^+} + e^- + Q_{IC} \to \ce{_Z^A X} , \tag{8.195}$$
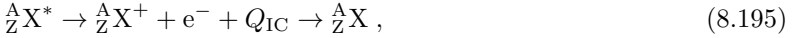
where

$\ce{_Z^A X^*}$ is the excited state of the nucleus most likely attained as a result of α or β decay;

$\ce{_Z^A X^+}$ is the singly ionized state of atom $\ce{_Z^A X}$ following internal conversion decay;

Q_{IC} is the decay energy for internal conversion.

A small portion of the nuclear de-excitation energy Q_γ is required to overcome the binding energy E_B of the electron in its atomic shell, the remaining part of the decay energy Q_γ is shared between the conversion electron and the recoil daughter nucleus, i.e,

$$Q_{IC} = Q_\gamma - E_B = (E_K)_{IC} + (E_K)_D . \tag{8.196}$$

In (8.196)

Q_γ is the energy difference between two excited nuclear states, equal to the energy of a γ photon in gamma decay

$(E_K)_{IC}$ is the kinetic energy of the internal conversion electron ejected from the atom

$(E_K)_D$ is the recoil kinetic energy of the daughter nucleus.

The recoil kinetic energy $(E_K)_D$ of the daughter is much smaller than the kinetic energy $(E_K)_{IC}$ of the conversion electron and is usually neglected. It can be calculated with exactly the same approach that was taken for the β^+ decay to get

$$(E_K)_D = \frac{m_e c^2}{M(D)c^2}(E_K)_{IC} + \frac{(E_K)_{IC}^2}{2M(D)c^2} \tag{8.197}$$

and

$$Q_{IC} = Q_\gamma - E_B = (E_K)_{IC}\left\{1 + \frac{m_e c^2}{M(D)c^2} + \frac{(E_K)_{IC}}{2M(D)c^2}\right\} , \tag{8.198}$$

where $M(D)$ stands for the rest mass of the daughter nucleus.

The kinetic energy of the conversion electrons is essentially monoenergetic except for small variations that result from variations in the binding energies of the shells from which the conversion electrons originate. Most of the conversion electrons come from the K shells, since K shell electrons have the highest probability for venturing into nuclear space.

8.13.2 Internal Conversion Factor

In any nuclear de-excitation both the γ ray emission and the internal conversion electron emission are possible. The two nuclear processes are competing with one another and are governed essentially by the same selection rules. Thus, similar to the situation in atomic competing processes represented by the emission of characteristic (fluorescent) photons and emission of Auger electrons that are governed by the fluorescent yield, the *internal conversion factor* governs the two nuclear processes: emission of gamma photons and ejection of conversion electrons. However, in contrast to the fluorescent yield ω (see Sect. 3.1.2) that is defined as the number of characteristic photons emitted per vacancy in a given atomic shell, the *total internal conversion factor* α_{IC} is defined as

$$\alpha_{\mathrm{IC}} = \frac{conversion\ probability}{\gamma - emission\ probability} = \frac{N_{IC}}{N_\gamma}\ , \tag{8.199}$$

where

N_{IC} is the number of conversion electrons ejected from all shells per unit time

N_γ is the number of γ photons emitted per unit time.

In addition to the total internal conversion factor α_{IC} one can define partial internal conversion factors according to the shell from which the electron was ejected, i.e.,

$$\frac{N_{\mathrm{IC}}}{N_\gamma} = \frac{N_{\mathrm{IC}}(\mathrm{K}) + N_{\mathrm{IC}}(\mathrm{L}) + N_{\mathrm{IC}}(\mathrm{M}) + ...}{N_\gamma}$$
$$= \alpha_{\mathrm{IC}}(\mathrm{K}) + \alpha_{\mathrm{IC}}(\mathrm{L}) + \alpha_{\mathrm{IC}}(\mathrm{M}) + ..., \tag{8.200}$$

where $\alpha_{\mathrm{IC}}(i)$ represents the partial internal conversion factors. Further distinction is possible when one accounts for subshell electrons.

The total internal conversion factors α_{IC} are defined with respect to N_γ so that α_{IC} can assume values greater or smaller than 1, in contrast to fluorescent yield ω that is always between 0 and 1.

Since the K-shell electrons of all atomic electrons are the closest to the nucleus, most often the conversion electrons originate from the K atomic shell. The vacancy in the K shell, of course, is filled by a higher shell electron and the associated emission of characteristic photon or Auger electron, as discussed in Sect. 3.1.

An example for both the emission of γ photons and emission of conversion electrons is given in Fig. 8.22 with the β^- decay scheme for cesium-137 decaying into barium-137. Two channels are available for β^- decay of cesium-137:

1. 94.6% of disintegrations land in a barium-137 isomeric state (barium-137m) that has a half-life of 2.552 min and de-excitation energy of 662 keV.
2. 5.4% of disintegrations land directly in the barium-137 ground state.

The de-excitation energy of 0.662 MeV is emitted either in the form of a 662 keV gamma photon or a conversion electron of kinetic energy ~ 662 keV.

As shown in Fig. 8.22, for 100 disintegrations of cesium-137, 94.6 transitions land in barium-137m; of these 85 result in γ photons; 7.8 in K conversion electrons and 1.8 in higher shell conversion electrons. The internal conversion factor α_{IC} is $(7.8 + 1.8)/85 = 0.113$.

8.14 Spontaneous Fission

In addition to disintegrating through α and β decay processes, nuclei with very large atomic mass numbers A may also disintegrate by splitting into two nearly equal fission fragments an concurrently emit 2 to 4 neutrons. This decay process is called *spontaneous fission* (SF) and is accompanied by liberation of a significant amount of energy. It was discovered in 1940 by Russian physicists *Georgij N. Flerov* and *Konstantin A. Petržak* who noticed that uranium-238, in addition to α decay, may undergo the process of spontaneous fission.

Spontaneous fission follows the same process as nuclear fission, except that it is not self-sustaining, since it does not generate the neutron fluence rate required to sustain a "chain reaction". In practice, SF is only energetically feasible for nuclides with atomic masses above $230\,u$ or with $Z^2/A \geq 235$ where Z is the atomic number and A the atomic mass number of the radionuclide. SF can thus occur in thorium, protactinium, uranium and transuranic elements.

Transuranic (or transuranium) elements are elements with atomic numbers Z greater than that of uranium ($Z = 92$). All transuranic elements have more protons than uranium and are radioactive, decaying through β decay, α decay, or spontaneous fission. Generally, the transuranic elements are man-made and synthesized in nuclear reactions in a process referred to as nucleosynthesis. The nucleosynthesis reactions are generally produced in particle accelerators or nuclear reactors; however, neptunium ($Z = 93$) and plutonium ($Z = 94$) are also produced naturally in minute quantities, following the spontaneous fission decay of uranium-238. The spontaneous fission neutrons emitted by U-238 can be captured by other U-238 nuclei thereby producing U-239 which is unstable and decays through β^- decay with a half-life of 23.5 m into neptunium-239 which in turn decays through β^- decay with a half-life 2.35 d into plutonium-239, as shown in (8.201):

$$^{238}_{92}\mathrm{U} + \mathrm{n} \xrightarrow[\text{capture}]{\text{neutron}} {}^{239}_{92}\mathrm{U} \xrightarrow{\beta^-} {}^{239}_{93}\mathrm{Np} + \mathrm{e}^- + \bar{\nu}_{\mathrm{e}}$$

$$^{239}_{93}\mathrm{Np} \xrightarrow{\beta^-} {}^{239}_{94}\mathrm{Pu} + \mathrm{e}^- + \bar{\nu}_{\mathrm{e}} \tag{8.201}$$
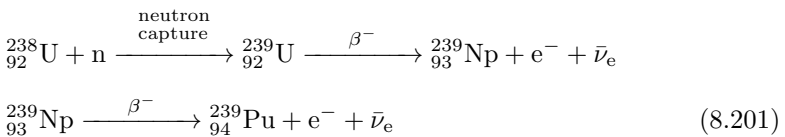
SF is a competing process to α decay; the higher is A above uranium-238, the more prominent is the spontaneous fission in comparison with the α decay

and the shorter is the half-life for spontaneous fission. For the heaviest nuclei, SF becomes the predominant mode of radioactive decay suggesting that SF is a limiting factor in how high in atomic number Z and atomic mass number A one can go in producing new elements.

- In uranium-238 the half-life for SF is $\sim 10^{16}$ y, while the half-life for α decay is 4.5×10^9 y. The probability for SF in uranium-238 is thus about 2×10^6 times lower than the probability for α decay.
- Fermium-256 has a half-life for SF of about 3 hours making the SF in fermium-256 about 10 times more probable than α decay.
- Another interesting example is californium-256 which decays essentially 100% of the time with SF and has a half-life of 12.3 m.
- For practical purposes, the most important radionuclide undergoing the SF decay is the transuranic californium-252 (Cf-252), used in industry and medicine as a very efficient source of fast neutrons (see Sect. 6.6.4). Californium-252 decays through α decay into curium-248 with a half-life of 2.65 y; however, about 3% of Cf-252 decays occur through SF producing on the average 3.8 neutrons per fission decay. The neutron production rate of Cf-252 is thus equal to 2.35×10^6 $(\mu g \cdot s)^{-1}$.

8.15 Proton Emission Decay

Proton-rich nuclides normally approach stability through β^+ decay or α decay. However, in the extreme case of a very large proton excess a nucleus may also move toward stability through emission of one or even two protons. Proton emission is thus a competing process to β^+ and α decay and is, similarly to α decay, an example of particle tunneling through the nuclear barrier potential.

Proton emission decay is much less common than are the β^+ and α decay and is not observed in naturally occurring radionuclides. In this type of decay the atomic number Z decreases by 1 and so does the atomic mass number A:

$$\begin{array}{r}{}_{Z}^{A}\mathrm{P} \rightarrow {}_{Z-1}^{A-1}\mathrm{D} + \mathrm{p}\end{array} \qquad (8.202)$$

- When a proton is ejected from a radionuclide P, the parent nucleus P sheds an orbital electron from its outermost shell to become a neutral daughter atom ${}_{Z-1}^{A-1}\mathrm{D}$.
- The energetic proton slows down in moving through the absorber medium and captures an electron from its surroundings to become a neutral hydrogen atom ${}_{1}^{1}\mathrm{H}$.
- Since N, the number of neutrons does not change in proton emission decay, the parent P and daughter D are isotones.
- For lighter, very proton-rich nuclides with an odd number of protons Z, proton emission decay is likely (see example in Sect. 8.16.2).

- For lighter, very proton-rich nuclides ($A \approx 50$) with an even number of protons Z, a simultaneous two-proton emission may occur in situations where a sequential emission of two independent protons is energetically not possible (see example in Sect. 8.16.3).

8.15.1 Decay Energy in Proton Emission Decay

The decay energy Q_p released in proton emission decay appears as kinetic energy shared between the emitted proton and the daughter nucleus and is expressed as follows:

$$Q_\mathrm{p} = \{\mathcal{M}(\mathrm{P}) - [\mathcal{M}(\mathrm{D}) + \mathcal{M}(\mathrm{H})]\}c^2 = \{M(\mathrm{P}) - [M(\mathrm{D}) + m_\mathrm{p}]\}c^2 \; ,$$
(8.203)

where $\mathcal{M}(\mathrm{P})$, $\mathcal{M}(\mathrm{D})$, and $\mathcal{M}(^1_1\mathrm{H})$ are the atomic rest masses of the parent, daughter and hydrogen atom, respectively, and $M(\mathrm{P})$, $M(\mathrm{D})$ and m_p are nuclear rest masses of the parent, daughter and hydrogen nucleus (proton), respectively.

The total number of protons as well as the total number of neutrons does not change in the proton emission decay. Therefore, Q_p may also be expressed in terms of binding energies of the parent and daughter nucleus as follows:

$$Q_\mathrm{p} = E_\mathrm{B}(\mathrm{D}) - E_\mathrm{B}(\mathrm{P}) \; ,$$
(8.204)

where

$E_\mathrm{B}(\mathrm{D})$ is the total binding energy of the daughter D nucleus
$E_\mathrm{B}(\mathrm{P})$ is the total binding energy of the parent P nucleus.

The nuclear binding energy is defined in Eq. (1.13). For proton emission decay to be feasible, Q_p must be positive and this implies that the total binding energy of the daughter nucleus $E_\mathrm{B}(\mathrm{D})$ must exceed the total binding energy of the parent nucleus $E_\mathrm{B}(\mathrm{P})$; that is, $E_\mathrm{B}(\mathrm{D}) > E_\mathrm{B}(\mathrm{P})$, or else that the rest mass of the parent nucleus must exceed the combined rest masses of the daughter nucleus and the proton, that is, $M(\mathrm{P}) > M(\mathrm{D}) + m_\mathrm{p}$.

Two products are released in proton emission decay: a proton and the daughter product. For a decay of the parent nucleus at rest this implies that the proton and the daughter will acquire momenta p equal in magnitude but opposite in direction. The kinetic energy of the proton is $(E_\mathrm{K})_\mathrm{P} = p^2/2m_\mathrm{p}$ and of the daughter nucleus it is $(E_\mathrm{K})_\mathrm{D} = p^2/2M(\mathrm{D})$.

The total decay energy Q_p must be positive for the proton emission decay and can be written as the sum of the kinetic energies of the two decay products:

$$Q_\mathrm{p} = (E_\mathrm{K})_\mathrm{p} + (E_\mathrm{K})_\mathrm{D} = \frac{p^2}{2m_\mathrm{p}} + \frac{p^2}{2M(\mathrm{D})} = \frac{p^2}{2m_\mathrm{p}}\left\{1 + \frac{m_\mathrm{p}}{M(\mathrm{D})}\right\}$$

$$= (E_\mathrm{K})_\mathrm{p}\left\{1 + \frac{m_\mathrm{p}}{M(\mathrm{D})}\right\} \; .$$
(8.205)

From (8.205) we determine the emitted proton kinetic energy $(E_K)_p$ as

$$(E_K)_p = Q_p \frac{1}{1 + \frac{m_p}{M(D)}}. \tag{8.206}$$

The kinetic energy of the recoil daughter $(E_K)_D$, on the other hand, is given as follows

$$(E_K)_D = Q_p - (E_K)_p = Q_p \frac{1}{1 + \frac{M(D)}{m_p}}. \tag{8.207}$$

The decay energy Q_{2p} released in two-proton emission decay appears as kinetic energy shared among the three emitted particles (two protons and the daughter nucleus) and may be calculated simply from the difference in binding energies E_B between the daughter D and the parent P nucleus

$$Q_{2p} = E_B(D) - E_B(P) \tag{8.208}$$

or from the following expression

$$\begin{aligned} Q_{2p} &= \{\mathcal{M}(P) - [\mathcal{M}(D) + 2\mathcal{M}(_1^1H)]\}c^2 \\ &= \{M(P) - [M(D) + 2m_p]\}c^2, \end{aligned} \tag{8.209}$$

where $\mathcal{M}$ stands for the atomic rest masses, M for nuclear rest masses and m_p for the proton rest mass.

8.15.2 Example of Proton Emission Decay

An example of proton emission decay is the decay of lithium-5 into helium-4 with a half-life of 10^{-21} s. The decay is schematically written as follows

$$_3^5\text{Li} \rightarrow {}_2^4\text{He} + p \tag{8.210}$$

and the decay energy may be calculated from (8.203) or (8.204). The required atomic and nuclear data are given as follows

$$\mathcal{M}(_3^5\text{Li})c^2 = 5.012541u \times 931.5 \text{ MeV}/u = 4669.18 \text{ MeV}$$

$$\mathcal{M}(_2^4\text{He})c^2 = 4.002603u \times 931.5 \text{ MeV}/u = 3728.43 \text{ MeV}$$

$$\mathcal{M}(_1^1\text{H})c^2 = 1.007825u \times 931.5 \text{ MeV}/u = 938.79 \text{ MeV}$$

$$E_B(_3^5\text{Li}) = 26.330674 \text{ MeV}$$

$$E_B(_2^4\text{He}) = 28.295673 \text{ MeV}$$

We first notice that $\mathcal{M}(_3^5\text{Li}) > \mathcal{M}(_2^4\text{He}) + \mathcal{M}(_1^2\text{H})$ and that $E_B(_2^4\text{He}) > E_B(_3^5\text{Li})$. This leads to the conclusion that the proton emission decay is possible. Next we use (8.203) and (8.204) to calculate the decay energy Q_p and get 1.96 MeV from both equations. Equations (8.206) and (8.207) give 1.57 MeV and 0.39 MeV for the kinetic energies of the ejected proton and the recoil helium-4 atom, respectively.

8.15.3 Example of Two-Proton Emission Decay

An example of two-proton emission decay is the decay of iron-45 (a highly proton rich radionuclide with $Z = 26$ and $N = 19$) which decays with a simultaneous emission of two protons at a half-life of 0.35 μs into chromium-43 (a proton-rich radionuclide with $Z = 24$ and $N = 19$). The decay is schematically written as follows:

$$^{45}_{26}\text{Fe} \rightarrow {}^{43}_{24}\text{Cr} + 2\text{p} \tag{8.211}$$

and the decay energy $Q_{2\text{p}}$ may be calculated from (8.208) or (8.209).

At first glance one could expect the iron-45 radionuclide to decay by a single proton emission into manganese-44; however, a closer inspection shows that the one-proton decay would produce negative decay energy Q_p from (8.203) and (8.204) and thus is not energetically feasible.

The atomic and nuclear data for radionuclides $^{45}_{26}\text{Fe}$, $^{44}_{25}\text{Mn}$, and $^{43}_{24}\text{Cr}$ are given as follows:

$$\mathcal{M}(^{45}_{26}\text{Fe})c^2 = 45.014564u \times 931.5 \text{ MeV}/u = 41931.07 \text{ MeV}$$

$$\mathcal{M}(^{44}_{25}\text{Mn})c^2 = 44.006870u \times 931.5 \text{ MeV}/u = 40992.40 \text{ MeV}$$

$$\mathcal{M}(^{43}_{24}\text{Cr})c^2 = 42.997711u \times 931.5 \text{ MeV}/u = 40052.37 \text{ MeV}$$

$$\mathcal{M}(^{1}_{1}\text{H})c^2 = 1.007825u \times 931.5 \text{ MeV}/u = 938.79 \text{ MeV}$$

$$E_\text{B}(^{45}_{26}\text{Fe}) = 329.306 \text{ MeV}$$

$$E_\text{B}(^{44}_{25}\text{Mn}) = 329.180 \text{ MeV}$$

$$E_\text{B}(^{43}_{24}\text{Cr}) = 330.426 \text{ MeV} .$$

Inspection of (8.204) shows that one-proton emission decay of $^{45}_{26}\text{Fe}$ into $^{44}_{25}\text{Mn}$ is not possible, since it results in a negative Q_p. On the other hand, (8.208) results in positive decay energy $Q_{2\text{p}}$ for a two-proton decay of $^{45}_{26}\text{Fe}$ into its isotone $^{43}_{24}\text{Cr}$. The decay energy $Q_{2\text{p}}$ calculated from (8.208) and (8.209) then amounts to 1.12 MeV for the two-proton decay of $^{45}_{26}\text{Fe}$ into $^{43}_{24}\text{Cr}$.

8.16 Neutron Emission Decay

Neutron emission from a neutron-rich nucleus is a competing process to β^- decay but is much less common then the β^- decay and is not observed in naturally occurring radionuclides. In contrast to spontaneous fission which also produces neutrons, in neutron emission decay the atomic number Z remains the same but the atomic mass number A decreases by 1. Both the parent nucleus P and the daughter nucleus D are thus isotopes of the same nuclear species. The neutron emission decay relationship is written as follows:

$$^{A}_{Z}\text{X} \rightarrow {}^{A-1}_{Z}\text{X} + \text{n} \tag{8.212}$$

8.16.1 Decay Energy in Neutron Emission Decay

The decay energy Q_n released in neutron emission decay appears as kinetic energy shared between the emitted neutron and the daughter nucleus and is expressed as follows:

$$Q_n = \{\mathcal{M}(P) - [\mathcal{M}(D) + m_n]\}c^2 = \{M(P) - [M(D) + m_n]\}c^2 \ , \tag{8.213}$$

where $\mathcal{M}(P)$ and $\mathcal{M}(D)$ are atomic masses of the parent and daughter atom, respectively; $M(P)$ and $M(D)$ are the nuclear masses of the parent and daughter respectively, and m_n is the neutron rest mass.

The total number of protons Z as well as the total number of neutrons N does not change in the neutron emission decay. Therefore, Q_n may also be expressed in terms of binding energies of the parent and daughter nucleus as follows

$$Q_n = E_B(D) - E_B(P) \ , \tag{8.214}$$

where

$E_B(D)$ is the total binding energy of the daughter D nucleus
$E_B(P)$ is the total binding energy of the parent P nucleus.

For the neutron emission decay to be feasible, Q_n must be positive and this implies that the total binding energy of the daughter nucleus $E_B(D)$ must exceed the total binding energy of the parent nucleus $E_B(P)$; that is, $E_B(D) > E_B(P)$, or else that the rest mass of the parent nucleus $M(P)$ must exceed the combined rest masses of the daughter nucleus and the neutron; that is, $M(P) > M(D) + m_n$.

Two products are released in neutron emission decay: a neutron and the daughter product. For a decay of the parent nucleus at rest this implies that the neutron and the daughter will acquire momenta p equal in magnitude but opposite in direction. The kinetic energy of the neutron is $(E_K)_n = p^2/2m_n$ and of the daughter nucleus the kinetic energy is $(E_K)_D = p^2/2M(D)$.

The total decay energy Q_n must be positive for the neutron emission decay and is expressed as follows:

$$Q_n = (E_K)_n + (E_K)_D = \frac{p^2}{2m_n} + \frac{p^2}{2M(D)} = \frac{p^2}{2m_n}\left\{1 + \frac{m_n}{M(D)}\right\}$$

$$= (E_K)_n\left\{1 + \frac{m_n}{M(D)}\right\} \ . \tag{8.215}$$

From (8.212) we determine the emitted neutron kinetic energy $(E_K)_n$ as

$$(E_K)_n = Q_\alpha \frac{1}{1 + \frac{m_n}{M(D)}} \ . \tag{8.216}$$

The kinetic energy of the recoil daughter $(E_K)_D$, on the other hand, is given as follows:

$$(E_K)_D = Q_n - (E_K)_n = Q_n \frac{1}{1 + \frac{M(D)}{m_n}} \ . \tag{8.217}$$

8.16.2 Example of Neutron Emission Decay

An example of neutron emission decay is the decay of helium-5 into helium-4 with a half-life of 8×10^{-22} s. The decay is schematically written as follows:

$$^5_2\text{He} \to {}^4_2\text{He} + \text{n} \tag{8.218}$$

and the decay energy may be calculated from (8.210) or (8.211). The required atomic and nuclear data are as follows:

$$\mathcal{M}(^5_2\text{He})c^2 = 5.012221u \times 931.5 \text{ MeV}/u = 4668.88 \text{ MeV}$$

$$\mathcal{M}(^4_2\text{He})c^2 = 4.002603u \times 931.5 \text{ MeV}/u = 3728.43 \text{ MeV}$$

$$m_n c^2 = 1.008665u \times 931.5 \text{ MeV}/u$$

$$E_B(^5_2\text{He}) = 27.405673 \text{ MeV}$$

$$E_B(^4_2\text{He}) = 28.295673 \text{ MeV} \ .$$

We first notice that $\mathcal{M}(P) > \mathcal{M}(D) + m_n$ and $E_B(^4_2\text{He}) > E_B(^5_2\text{He})$ and conclude that neutron emission decay is possible. Next we use (8.210) and (8.211) to calculate the decay energy Q_n and get 0.89 MeV from both equations. Equations (8.212) and (8.213) give 0.71 MeV and 0.18 MeV for the kinetic energies of the ejected neutron and recoil helium-4 atom, respectively.

8.17 Chart of the Nuclides

All known nuclides are uniquely characterized by their number of protons Z (atomic number) and their number of neutrons $N = A - Z$ where A is the number of nucleons (atomic mass number). The most pertinent information on the 275 known stable nuclides and over 3000 known radioactive nuclides (radionuclides) is commonly summarized in the *Chart of the Nuclides* in such a way that it is relatively easy to follow the atomic transitions resulting from the various radioactive decay modes used by radionuclides to attain more stable configurations. Usually the ordinate of the chart represents Z and the abscissa represents N with each nuclide represented by a unique square (pixel) that is placed onto the chart according to the N and Z value of the nuclide.

The chart of the nuclides is also referred to as the *Segrè chart* in honor of *Emilio Segrè* who was first to suggest the arrangement in the 1930s. Similarly
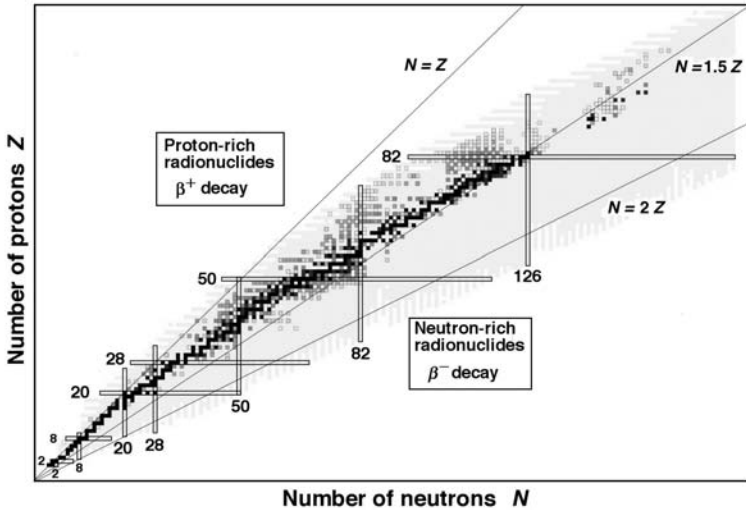
Fig. 8.27. *Chart of the Nuclides* also known as the *Segrè Chart*. Each known stable and radioactive nuclide is characterized by its unique combination of the number of protons Z and number of neutrons N, and assigned a pixel in a chart displaying Z on the ordinate axis and N on the abscissa axis. The stable nuclides are shown by dark pixel squares, radioactive nuclides by light pixel squares. The plot of stable nuclides forms a "*curve of stability*", neutron-rich radionuclides are below the curve of stability and proton-rich radionuclides are above the curve of stability. The magic numbers for neutrons and protons are also indicated

to the *Periodic Table of Elements* introduced by *Mendeleyev* in the 1870s to represent conveniently the periodicity in chemical behavior of elements with increasing atomic number Z, Segrè's chart of the nuclides presents an orderly formulation of all nuclear species (stable and radioactive) against both Z and N and, in addition, indicates the possible decay paths for radionuclides.

In addition to Z and N for a given nuclide the Segrè Chart usually provides other data, such as:

- *For stable nuclides* the atomic mass number A; the nuclear mass in u; and the natural abundance.
- *For radionuclides* the atomic mass number A, nuclear mass in u, radioactive half-life, and mode of decay.

A schematic representation of the Segrè Chart is given in Fig. 8.27 for the currently known stable and radioactive nuclides ranging in number of protons Z from 1 to 118 and in number of neutrons N from 0 to 292. The magic numbers (see Sect. 1.15.2) for protons and neutrons are shown on the chart; the stable nuclides are shown with black squares, the radionuclides with light squares. For each element the rows in the Segrè Chart give a list of isotopes (Z = const), the vertical columns give a list of isotones (N = const).

The stable nuclides contain a balanced configuration of protons and neutrons and follow a *curve of stability* on the graph. The curve of stability follows $Z \approx N$ for low Z nuclides and then slowly transforms into $N \approx 1.5Z$ with increasing Z.

- Below the curve of stability are neutron-rich radionuclides. Most of neutron-rich radionuclides undergo a nuclear transmutation by β^- decay but a few do so by direct neutron emission.
- Above the curve of stability are proton-rich radionuclides. Most of proton-rich radionuclides undergo a nuclear transmutation by β^+ decay or electron capture but a few do so by direct emission of one proton or even two protons.
- All nuclides with $Z > 82$ undergo α decay or spontaneous fission and some may also undergo β decay.

A small part of a simplified complete Segrè Chart is shown in Fig. 8.28 for $1 \leq Z \leq 13$ and $0 \leq N \leq 18$ (from hydrogen to aluminum). The stable nuclides are shown in light grey squares indicating the curve of stability that is given by $Z \approx N$ for low atomic number elements; neutron-rich and proton-rich radionuclides are shown in dark grey squares below and above the region of stability, respectively. For stable nuclides their relative abundance is given; for radionuclides the half-life is given. The black framed squares above the region of the proton-rich radionuclides present the first 13 elements of the *Periodic Table of Elements* along with their nuclear mass in u given as the average for all stable isotopes of a given nuclear species.

As suggested by the individual rows in Fig. 8.28 ($Z = $ const), a given atomic species in general consists of one or more stable isotopes and several radioactive isotopes; neutron-rich isotopes to the right of the stable ones and proton-rich to the left. For example, aluminum has only one stable isotope ($^{27}_{13}$Al); hydrogen has two ($^{1}_{1}$H and $^{2}_{1}$H) and oxygen has three ($^{16}_{8}$O, $^{17}_{8}$O $^{18}_{8}$O). On the other hand, hydrogen has one radioactive isotope, the neutron-rich ($^{3}_{1}$H), while aluminum has 4 neutron-rich isotopes and 4 proton-rich isotopes.

8.18 General Aspects of Radioactive Decay

Nuclear physics has come a long way since Ernest Rutherford's momentous discovery that most of the atomic mass is concentrated in the atomic nucleus which has a size of the order of 1 fm = 10^{-15} m in comparison to the atomic size of the order of 1 Å = 10^{-10} m. The atomic nucleus consists of nucleons – positively charged protons and neutral neutrons, and each nuclear species is characterized with a unique combination of the number of protons (atomic number) Z and number of neutrons N, the sum of which gives the number of nucleous $A = Z + N$ (atomic mass number).

Nucleons are bound together into the nucleus by the strong nuclear force which, in comparison to the proton-proton Coulomb repulsive force, is at

Stable nuclides

Number of protons Z

Proton-rich radionuclides
β⁺ decay

Neutron-rich radionuclides
β⁻ decay

Z	element										
13	Al 26.9814				Al 23 0.47s	Al 24 2.07s	Al 25 7.23s	Al 26 7.3E5y	Al 27 100%	Al 28 2.24m	Al 29 6.5m	Al 30 3.6s	Al 31 0.64s
12	Mg 24.305	Mg 20 0.6s	Mg 21 122ms	Mg 22 3.86s	Mg 23 11.3s	Mg 24 78.99%	Mg 25 10.00%	Mg 26 11.01%	Mg 27 9.45m	Mg 28 21.0h	Mg 29 1.4s	Mg 30 ~1.2s
11	Na 22.98977	Na 19 30ms?	Na 20 446ms	Na 21 22.5s	Na 22 2.601y	Na 23 100%	Na 24 15.02h	Na 25 60s	Na 26 1.07s	Na 27 0.29s	Na 28 30.5ms	Na 29 43ms
10	Ne 20.179	Ne 17 109ms	Ne 18 1.67s	Ne 19 17.2s	Ne 20 90.51%	Ne 21 0.27%	Ne 22 9.22%	Ne 23 37.5s	Ne 24 3.38m	Ne 25 0.61s
9	F 18.99840	F 16 ~1E-20s proton	F 17 64.5s	F 18 109.8m	F 19 100%	F 20 11.0s	F 21 4.33s	F 22 4.23s	F 23 2.3s
8	O 15.9994	O 13 8.9ms	O 14 70.5s	O 15 122ms	O 16 99.758%	O 17 0.038%	O 18 0.204%	O 19 26.8s	O 20 13.5s
7	N 14.0067	N 12 11.0ms	N 13 9.97m	N 14 99.63%	N 15 0.37%	N 16 7.10s	N 17 4.17s	N 18 0.63s	N 19 0.42s
6	C 12.011	C 9 127ms	C 10 19.3s	C 11 20.3m	C 12 98.89%	C 13 1.11%	C 14 5730y	C 15 2.45s	C 16 0.75s
5	B 10.81	B 8 770ms	B 9 ~8E-19s proton	B 10 20%	B 11 80%	B 12 20.4ms	B 13 17.3ms	B 14 16ms
4	Be 9.01218	Be 6 ~5E-21s proton	Be 7 53.28d	Be 8 ~1E-16s alpha	Be 9 100%	Be 10 1.6E6y	Be 11 13.8s	Be 12 ~11.4ms
3	Li 6.941	Li 5 ~1E-21s proton	Li 6 7.5%	Li 7 92.5%	Li 8 844ms	Li 9 177ms
2	He 4.00260	He 3 0.00014%	He 4 99.99986%	He 5 ~8E-22s neutron	He 6 805ms	He 8 122ms
1	H 1.0079	H 1 99.985%	H 2 0.015%	H 3 12.33y
	n 1 10.4m

Number of neutrons N

Fig. 8.28. A portion of the Chart of the Nuclides (Segrè Chart) for nuclides with proton numbers Z from 1 through 13, neutron numbers N from 0 through 18, and atomic mass numbers A from 1 through 31. Stable nuclides are shown with light pixel squares, radionuclides with darker pixel squares. Relative natural abundance is shown for the stable nuclides; half-lives and modes of decay are shown for radionuclides. The black-framed squares give the mean atomic mass in u for nuclides from hydrogen to aluminum. Each horizontal row (Z = const) represents one element including all stable and radioactive isotopes. Each vertical column (N = const) represents nuclides with the same neutron numbers (isotones)

least two orders of magnitude larger but of extremely short range of a few femtometers. To bind the nucleons into a stable nucleus a delicate equilibrium between the number of protons and the number of neutrons must exist. As evident from Figs. 8.27 and 8.28, for light (low A) nuclear species, a stable nucleus is formed from an equal number of protons and neutrons ($Z = N$). Above the nucleon number $A \approx 40$, more neutrons than protons must constitute the nucleus to form a stable configuration in order to overcome the Coulomb repulsion of the charged protons.

If the optimal equilibrium between protons and neutrons does not exist, the nucleus is unstable (radioactive) and decays with a specific decay constant into a more stable configuration that may also be unstable and decays further, forming a decay chain that eventually ends with a stable nuclide.

As discussed in detail in this chapter, nine main processes are available to unstable nuclei (radionuclides) to advance toward a more stable nuclear configuration; for a given radionuclide generally only one type or at most two types of decay process will occur.

Nuclides with an excess number of neutrons are referred to as neutron-rich; nuclides with an excess of protons are referred to as proton-rich.

- For a slight imbalance, radionuclides will decay by beta decay characterized by transformation of a proton into a neutron in β^+ decay and a transformation of a neutron into a proton in β^- decay.
- For a large imbalance, the radionuclides will decay by emission of nucleons: α particles in alpha decay, protons in proton emission decay, and neutrons in neutron emission decay. For very large atomic mass number nuclides ($A > 230$) spontaneous fission which competes with α decay is also possible.

Figure 8.29 shows schematically the decay paths (except for the spontaneous fission) possibly open to a radionuclide (N, Z) in its transition toward a more stable configuration. The following general features of radioactive decay processes are noted:

1. When radionuclide (Z, N) is below the curve of stability (i.e., is neutron-rich), the β^- decay and neutron emission are possible means to attain a more stable configuration. The resulting nucleus will be characterized by $(Z + 1, N - 1)$ for β^- decay and by $(Z, N - 1)$ for neutron emission decay.
2. When radionuclide (Z, N) is above the curve of stability (i.e., is proton-rich), the β^+ decay, electron capture or proton emission may be possible means to attain a more stable configuration. The resulting nucleus will be characterized by $(Z - 1, N + 1)$ for β^+ decay and electron capture, and by $(Z - 1, N)$ for proton emission decay.
3. Proton and neutron emission decays are much less common than α and β decays and occur only in artificially produced radionuclides. The main characteristics of radionuclides which decay by proton or neutron emission are an extreme imbalance between the number of protons and the number of neutrons in their nuclei as well as very short half-lives.
4. In addition to β decay the radionuclides (Z, N) with $Z < 83$ may decay by α decay or spontaneous fission. In α decay the resulting nucleus is characterized by $(Z - 2, N - 2)$, in contrast to spontaneous fission where the resulting nuclei are much lighter than the parent nucleus.
5. In gamma decay and internal conversion decay the parent nucleus is excited and undergoes a de-excitation process by emitting a γ photon or a conversion electron, respectively. Both the parent and the daughter nuclei are characterized by (Z, N), since the number of protons as well as the number of neutrons does not change in the decay process.
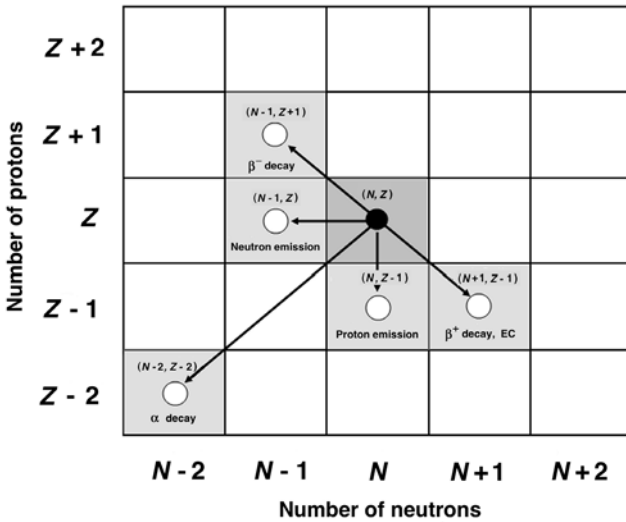
Fig. 8.29. Decay paths possibly available in the Chart of the Nuclides (Segrè Chart) to a parent radionuclide (N, Z) in its quest to attain a more stable configuration. The parent radionuclide is shown by the solid black circle, the daughter nuclides are shown by open circles

Table 8.6 lists the main attributes of nuclides presented in this chapter. The atomic masses $\mathcal{M}(u)$ were obtained from the tabulated data provided by the NIST. For a given nuclide, its nuclear rest energy Mc^2 is calculated from (8.219), its total binding energy E_B from (8.220) and its binding energy per nucleon E_B/A from (8.221). These data can be used to determine the decay energies for the radioactive decay examples presented in this chapter.

A summary of the main characteristics of the eight most common radioactive decay modes is given in Table 8.7 which for each mode provides expressions for the basic relationship, the decay energy as well as the energy of the decay products (daughter nucleus and emitted particles). In radioactive decay the daughter recoil kinetic energy $(E_K)_D$ is generally ignored when determining the energy of the other, lighter decay products. However, we must keep in mind that in α decay as well as in proton and neutron emission decay $(E_K)_D$ is of the order of 100 keV, while in other radioactive decay modes, except for the spontaneous fission, it is of the order of 10 eV to 100 eV. Thus the daughter recoil kinetic energy in α decay and in proton and neutron emission decay is not negligible and should be accounted for, while for the other common radioactive decays it may be ignored.

Table 8.8 presents a summary of the main attributes of the nine most common radioactive decay modes showing the changes in Z and N as well as the expressions for the decay energy Q calculated using either the nuclear masses M or the atomic masses $\mathcal{M}$.

Table 8.6. Main attributes of nuclides presented in this chapter

Element	Symbol	Z	A	ATOMIC MASS u	NUCLEAR Rest Energy Mc^2 (MeV)	BINDING ENERGY E_B (MeV)	E_B (MeV) nucleon	Decay mode	Half-life
Hydrogen	H	1	1	1.00782503	938.2720149	-	-	-	Stable
Deuterium	D	1	2	2.01410178	1875.612809	2.224579715	1.1123	-	Stable
Tritium	T	1	3	3.01604927	2808.920927	8.481821847	2.8273	β^-	12.3 y
Helium	He	2	4	4.00260325	3727.379086	28.29569225	7.0739	-	Stable
Helium	He	2	5	5.01222	4667.831074	27.40906363	5.4818	n	8×10^{-22} s
Lithium	Li	3	5	5.01254	4667.618154	26.32865345	5.2657	α, p	10^{-21} s
Lithium	Li	3	7	7.016004	6533.832935	39.24459209	5.6064	-	Stable
Beryllium	Be	4	7	7.0169292	6534.183754	37.60044172	5.3715	EC	53 d
Beryllium	Be	4	9	9.0121821	8392.749945	58.16497109	6.4628	-	Stable
Boron	Be	5	10	10.012937	9324.436174	64.75077116	6.4751	-	Stable
Carbon	C	6	13	13.0033548	12109.48158	97.10811708	7.4699	-	Stable
Nitrogen	N	7	13	13.0057386	12111.19102	94.10534334	7.2389	β^+	10 min
Oxygen	O	8	18	17.9991604	16762.0227	139.8071317	7.7671	-	Stable
Fluorine	F	9	18	18.0009377	16763.16725	137.3692553	7.6316	β^+	1.83 h
Chromium	Cr	24	43	42.99771	40039.84675	330.4237824	7.6843	EC, p	21 ms
Manganese	Mn	25	44	44.00687	40979.36228	329.1802819	7.4814	p	0.1 μs
Iron	Fe	26	45	45.01456	41917.50852	329.3060776	7.3179	2p	0.35 μs
Cobalt	Co	27	59	58.9332002	54882.12795	517.3083526	8.7679	-	Stable
Cobalt	Co	27	60	59.9338222	55814.20138	524.8002803	8.7467	β^-	5.27 y
Nickel	Ni	28	60	59.9307906	55810.86647	526.8418655	8.7807	-	Stable
Molybdenum	Mo	42	98	97.9054078	91176.84219	846.2431894	8.6351	-	Stable
Technetium	Tc	43	99	98.9062546	92108.61402	852.7433851	8.6136	γ	6 h
Cesium	Cs	55	137	136.907084	127500.0283	1149.292865	8.3890	β^-	30.2 y
Barium	Ba	56	137	136.905821	127498.3408	1149.68701	8.3919	-	Stable
Osmium	Os	76	192	191.961479	178772.1383	1526.117708	7.9485	-	Stable
Iridium	Ir	77	191	190.960591	177839.306	1518.091225	7.9481	-	Stable
Iridium	Ir	77	192	191.962602	178772.6733	1524.289308	7.9390	β^-	74 d
Iridium	Ir	77	193	192.962924	179704.4673	1532.060684	7.9381	-	Stable
Platinum	Pt	78	192	191.961035	178770.7027	1524.966627	7.9425	-	Stable
Radon	Rn	86	222	222.017571	206764.0985	1708.184999	7.6945	α	3.8 d
Radium	Ra	88	226	226.025403	210496.3482	1731.610048	7.6620	α	1602 y
Thorium	Th	90	232	232.03805	216096.0718	1766.691936	7.6151	α, SF	1.4×10^{10} y
Uranium	U	92	235	235.043923	218895.0023	1783.870837	7.5909	α	0.7×10^9 y
Uranium	U	92	238	238.050783	221695.874	1801.695205	7.5701	α, SF	4.5×10^9 y
Uranium	U	92	239	239.054288	222630.6331	1806.501449	7.5586	β^-	23.5 min
Neptunium	Np	93	239	239.052931	222628.8587	1806.982596	7.5606	β^-	2.35 d
Plutonium	Pu	94	239	239.052157	222627.6258	1806.922078	7.5603	β^-	24×10^3 y
Californium	Cf	98	252	252.08162	234762.4495	1881.274796	7.4654	α, SF	2.65 y
Californium	Cf	98	256	256.09344	238499.4359	1902.549805	7.4318	SF	12.3 m
Fermium	Fm	100	256	256.091767	238496.8555	1902.54353	7.4318	α, SF	158 m

Data for atomic masses were obtained from the NIST. M stands for the nuclear rest mass; $\mathcal{M}$ for the atomic rest mass. The nuclear mass-energy is calculated as follows:

$$Mc^2 = \mathcal{M}c^2 - Zm_ec^2 = (\mathcal{M} \times 931.494043 \text{ MeV}/u) - (Z \times 0.510999 \text{ MeV}) \quad (8.219)$$

and the nuclear binding energies are calculated as:

$$E_B = Zm_pc^2 + (A - Z)m_nc^2 - Mc^2 \quad (8.220)$$

and

$$E_B/\text{nucleon} = E_B/A . \quad (8.221)$$

The rest energies of the proton, neutron and electron are given as follows:

$$m_Pc^2 = 938.2703 \text{ MeV}, \quad m_nc^2 = 939.56536 \text{ MeV}, \quad m_ec^2 = 0.5109998918 \text{ MeV}.$$

Table 8.7. Basic characteristics of α decay, electron capture, β^- decay, β^+ decay, γ decay, internal conversion, proton emission and neutron emission. The table gives the basic relationships, the decay energy Q, and the kinetic energy E_K of the decay products. P stands for the parent nucleus or atom; D for the daughter nucleus or atom. M represents the nuclear mass, $\mathcal{M}$ the atomic mass, m_e the electron rest mass, m_p the proton rest mass, and m_n the neutron rest mass

---

Alpha (α) Decay

Basic relationship: [see (8.142)]

$$\ ^A_Z P \rightarrow\ ^{A-4}_{Z-2} D + \alpha + Q_\alpha \tag{8.222}$$

Decay energy: [see (8.143) and (8.144)]

$$Q_\alpha = \{M(P) - [M(D) + m_\alpha]\}\, c^2 = \{\mathcal{M}(P) - [\mathcal{M}(D) + \mathcal{M}(^4_2 He)]\}\, c^2$$
$$= E_B(D) + E_B(\alpha) - E_B(P) = (E_K)_\alpha + (E_K)_D \tag{8.223}$$

Kinetic energy of α particle:

$$(E_K)_\alpha = \frac{Q_\alpha}{1 + \dfrac{m_\alpha}{M(D)}} = \frac{A_P - 4}{A_P} Q_\alpha \tag{8.224}$$

Daughter recoil kinetic energy: [see (8.148)]

$$(E_K)_D = \frac{Q_\alpha}{1 + \dfrac{M(D)}{m_\alpha}} = \frac{4}{A_P} Q_\alpha \tag{8.225}$$

Electron Capture (EC)

Basic relationship: [see (8.156)]

$$\ ^A_Z P + e^- =\ ^A_{Z-1} D + \nu_e + Q_{EC} \tag{8.226}$$

Decay energy: [see 8.181) and (8.182)]

$$Q_{EC} = \{[M(P) + m_e] - M(D)\}\, c^2 =$$
$$= \{M(P) - [M(D) - m_e]\}\, c^2 = \{\mathcal{M}(P) - \mathcal{M}(D)\}\, c^2 = (E_K)_D + E_{\nu_e} \tag{8.227}$$

Daughter recoil kinetic energy: [see (8.185)]

$$(E_K)_D = \frac{E_\nu^2}{2M(D)c^2} \approx \frac{Q_{EC}}{2M(D)c^2} \tag{8.228}$$

Energy given to neutrino: [see (8.187)]

$$E_\nu = \left\{ -1 + \sqrt{1 + \frac{2(Q_{EC} - E_B)}{M(D)c^2}} \right\} M(D)c^2 \approx Q_{EC} - E_B \tag{8.229}$$

Table 8.7. (continued)

Beta Minus (β^-) Decay

Basic relationship: [see (8.154)]

$$^A_Z P \to \, _{Z+1}^{A}D + e^- + \bar{\nu}_e + Q_{\beta-} \tag{8.230}$$

Decay energy: [see (8.163), (8.164), and (8.165)]

$$Q_{\beta-} = \{M(P) - [M(D) + m_e]\}\, c^2 = \{\mathcal{M}(P) - \mathcal{M}(D)\}\, c^2$$

$$= (E_{\beta-})_{\max} + (E_K)_{D\max} = (E_\beta)_{\max} \left\{ 1 + \frac{m_e c^2 + \frac{1}{2}(E_\beta)_{\max}}{M(D)c^2} \right\} \tag{8.231}$$

Daughter maximum recoil kinetic energy: [see (8.162)]

$$(E_K)_{D\max} = \frac{m_e}{M_D}(E_{\beta-})_{\max} \left\{ 1 + \frac{(E_{\beta-})_{\max}}{2m_e c^2} \right\} \tag{8.232}$$

Combined energy given to electron/antineutrino:

$$(E_{\beta-})_{\max} = Q_{\beta-} - (E_K)_{D\max} \approx Q_{\beta-} \tag{8.233}$$

Beta Plus (β^+) Decay

Basic relationship: [see (8.155)]

$$^A_Z P \to \, _{Z+1}^{A}D + e^- + \nu_e + Q_{\beta-} \tag{8.234}$$

Decay energy: [see (8.163), (8.172), and (8.173)]

$$Q_{\beta+} = \{M(P) - [M(D) + m_e]\}\, c^2 = \{\mathcal{M}(P) - \mathcal{M}(D) + 2m_e\}\, c^2$$

$$= (E_{\beta+})_{\max} + (E_K)_{D\max} = (E_\beta)_{\max} \left\{ 1 + \frac{m_e c^2 + \frac{1}{2}(E_\beta)_{\max}}{M(D)c^2} \right\} \tag{8.235}$$

Daughter maximum recoil kinetic energy: [see (8.162)]

$$(E_K)_{D\max} = \frac{m_e}{M(D)}(E_{\beta+})_{\max} \left\{ 1 + \frac{(E_{\beta+})_{\max}}{2m_e c^2} \right\} \tag{8.236}$$

Combined energy given to positron/neutrino

$$(E_{\beta+})_{\max} = Q_{\beta+} - (E_K)_{D\max} \approx Q_{\beta+} \tag{8.237}$$

Table 8.7. (continued)

Gamma (γ) Decay

Basic relationship: [see (8.191)]

$$\,_{Z}^{A}\mathrm{P}^* \to \,_{Z}^{A}\mathrm{P} + \gamma + Q_\gamma \tag{8.238}$$

Decay energy: [see (8.194)]

$$\begin{aligned} Q_\gamma &= E^* - E = E_\gamma + (E_\mathrm{K})_\mathrm{D} \\ &= E_\gamma \left\{ 1 + \frac{E_\gamma}{2M(\mathrm{D})c^2} \right\} \end{aligned} \tag{8.239}$$

Daughter recoil kinetic energy: [see (8.193)]

$$(E_\mathrm{K})_\mathrm{D} = \frac{E_\gamma^2}{2M(\mathrm{D})c^2} \tag{8.240}$$

Energy of gamma photon:

$$E_\gamma = Q_\gamma - (E_\mathrm{K})_\mathrm{D} = Q_\gamma \left\{ 1 + \frac{E_\gamma}{2M(\mathrm{D})c^2}) \right\} \approx Q_\gamma \tag{8.241}$$

Internal Conversion

Basic relationship: [see (8.195)]

$$\,_{Z}^{A}\mathrm{P}^* \to \,_{Z}^{A}\mathrm{P}^+ + e^- + Q_\mathrm{IC} \tag{8.242}$$

Decay energy: [see (8.196)]

$$Q_\mathrm{IC} = (E^* - E) - E_\mathrm{B} = (E_\mathrm{K})_\mathrm{IC} + (E_\mathrm{K})_\mathrm{D} \tag{8.243}$$

Daughter recoil kinetic energy: [see (8.197)]

$$(E_\mathrm{K})_\mathrm{D} = \frac{m_\mathrm{e}}{M(\mathrm{D})}(E_\mathrm{K})_\mathrm{IC} + \frac{(E_\mathrm{K})_\mathrm{IC}^2}{2M(\mathrm{D})c^2} = \frac{(E_\mathrm{K})_\mathrm{IC}}{M(\mathrm{D})c^2} \left\{ m_\mathrm{e}c^2 + \frac{1}{2}(E_\mathrm{K})_\mathrm{IC} \right\} \tag{8.244}$$

Kinetic energy of internal conversion electron:

$$(E_\mathrm{K})_\mathrm{IC} = Q_\mathrm{IC} - (E_\mathrm{K})_\mathrm{D} \approx Q_\mathrm{IC} \tag{8.245}$$

Table 8.7. (continued)

Proton Emission Decay

Basic relationship: [see (8.202)]

$$^A_Z P \rightarrow ^{A-1}_{Z-1} D + p + Q_P \tag{8.246}$$

Decay energy: [see (8.203) and (8.204)]

$$Q_P = \{M(P) - [M(D) + m_p]\}c^2 = \{\mathcal{M}(P) - [\mathcal{M}(D) + \mathcal{M}(^1_1 H)]\}c^2$$
$$= E_B(D) = E_B(P)) = (E_K)_P + (E_K)_D \tag{8.247}$$

Kinetic energy of the emitted proton: [see (8.206)]

$$(E_K)_P = \frac{Q_P}{1 + \dfrac{m_p}{M(D)}} \tag{8.248}$$

Daughter recoil kinetic energy: [see (8.207)]

$$(E_K)_D = \frac{Q_P}{1 + \dfrac{M(D)}{m_p}} \tag{8.249}$$

Neutron Emission Decay

Basic relationship: [see (8.212)]

$$^A_Z P \rightarrow ^{A-1}_{Z} D + n + Q_n \tag{8.250}$$

Decay energy: [see (8.213) and (8.214)]

$$Q_n = \{M(P) - [M(D) + m_n]\}c^2 = \{\mathcal{M}(P) - [\mathcal{M}(D) + m_n]\}c^2$$
$$= E_B(D) - E_B(P) = (E_K)_n + (E_K)_D \tag{8.251}$$

Kinetic energy of the emitted neutron: [see (8.216)]

$$(E_K)_n = \frac{Q_n}{1 + \dfrac{m_n}{M(D)}} \tag{8.252}$$

Daughter recoil kinetic energy: [see (.217)]

$$(E_K)_D = \frac{Q_n}{1 + \dfrac{M(D)}{m_n}} \tag{8.253}$$

Table 8.8. Main attributes of the seven decay modes available to an unstable nucleus for reaching a more stable

Decay	Before decay	After decay	$\Delta Z = Z_a - Z_b$	$\Delta N = N_a - N_b$	$\Delta A = A_a - A_b$	Decay energy Q
α	P	D, α	-2	-2	-4	$\{M(P) - [M(D) + M(\alpha)]\}\,c^2$ $\{\mathcal{M}(P) - [\mathcal{M}(D) + \mathcal{M}(^4_2\text{He})]\}\,c^2$
β^-	P	D, e^-, $\bar{\nu}_e$	$+1$	-1	0	$\{M(P) - [M(D) + m_e]\}\,c^2$ $\{\mathcal{M}(P) - \mathcal{M}(D)\}\,c^2$
β^+	P	D, e^+, ν_e	-1	$+1$	0	$\{M(P) - [M(D) + m_e]\}\,c^2$ $\{\mathcal{M}(P) - [\mathcal{M}(D) + 2m_e]\}\,c^2$
Electron capture	P, e^-	D, ν_e	-1	$+1$	0	$\{[M(P) + m_e] - M(D)\}\,c^2$ $\{\mathcal{M}(P) - \mathcal{M}(D)\}\,c^2$
γ	P*	P, γ	0	0	0	
Internal conversion	P*	P, e_{orb}	0	0	0	
Spontaneous fission	P	D_1, D_2	$\sim Z/2$		$\sim A/2$	
Proton emission	P	D, p	-1	0	-1	$\{M(P) - [M(D) + m_p]\}\,c^2$ $\{\mathcal{M}(P) - [\mathcal{M}(D) + \mathcal{M}(H)]\}\,c^2$
Neutron emission	P	D, n	0	-1	-1	$\{M(P) - [M(D) + m_n]\}\,c^2$ $\{\mathcal{M}(P) - [\mathcal{M}(D) + m_n]\}\,c^2$

Legend: P = *parent nucleus*; D = *daughter nucleus*; e_{orb} = *orbital electron*
M = *nuclear mass*; $\mathcal{M}$ = *atomic mass*; $\mathcal{M}(H)$ = *mass of hydrogen atom*
m_e = *electron mass*; m_p = *proton mass*; m_n = *neutron mass*;
b = *before decay*; a = *after decay*

Bibliography

F.H. Attix: Introduction to Radiological Physics and Radiation Dosimetry (John Wiley & Sons, New York 1986)

V. Balashov: Interaction of Particles and Radiation with Matter (Springer, Berlin, Heidelberg, New York 1997)

British Journal of Radiology, Suppl. 25, "Central Axis Depth Dose Data for Use in Radiotherapy: 1996", British Institute of Radiology, London, U.K. (1996)

J.R. Cameron, J.G. Skofronick, R.M. Grant: The Physics of the Body, 2nd edn. (Medical Physics Publishing, Madison, WI 1999)

S.R. Cherry, J.A. Sorenson, M.E. Phelps: Physics in Nuclear Medicine, 3rd edn. (Saunders, Philadelphia, PA, USA 2003)

W.H. Cropper: Great Physicists: The Life and Times of Leading Physicists from Galileo to Hawking (Oxford University Press, Oxford, UK 2001)

R. Eisberg, R. Resnick: Quantum Physics of Atoms, Molecules, Solids, Nuclei and Particles (John Wiley & Sons, New York 1985)

R.D. Evans: The Atomic Nucleus (Krieger, Malabar, FL, USA 1955)

H. Goldstein, C.P. Poole, J.L. Safco: Classical Mechanics, 3rd edn. (Addison Wesley, Boston, MA, USA 2001)

J. Hale: The Fundamentals of Radiological Science (Thomas, Springfield, IL USA 1974)

W. Heitler: The Quantum Theory of Radiation, 3rd edn. (Dover Publications, New York 1984)

W.R. Hendee, G.S. Ibbott: Radiation Therapy Physics (Mosby, St. Louis, MO, USA 1996)

W.R. Hendee, E.R. Ritenour: Medical Imaging Physics, 4th edn. (John Wiley & Sons Inc, New York, USA 2002)

International Commission on Radiation Units and Measurements (ICRU), "Stopping Powers for Electrons and Positrons", ICRU Report 37 (ICRU, Bethesda, MD, USA 1984)

J.D. Jackson: Classical Electrodynamics, 3rd edn. (John Wiley & Sons, New York 1999)

H.E. Johns, J.R. Cunningham: The Physics of Radiology, 4th edn. (Thomas, Springfield, IL, USA 1984)

F. Khan: The Physics of Radiation Therapy, 3rd edn. (Williams & Wilkins, Baltimore, MD, USA 2003)

S.C. Klevenhagen: Physics and Dosimetry of Therapy Electron Beams (Medical Physics Publishing, Madison, WI 1993)

K. Krane: Modern Physics (John Wiley & Sons, New York, USA 1996)

D.R. Lide: CRC Handbook of Chemistry and Physics, 86th edn. (CRC Press, Boca Raton, FL, USA 2005)

P. Marmier, E. Sheldon: Physics of Nuclei and Particles (Academic Press, New York 1986)

P. Metcalfe, T. Kron, P. Hoban: The Physics of Radiotherapy X-Rays from Linear Accelerators (Medical Physics Publishing, Madison, WI USA 1997)

J.W. Rohlf: Modern Physics from A to Z (John Wiley & Sons, New York 1994)

R.A. Seaway, C.J. Moses, C.A. Moyer: Modern Physics (Saunders College Publishing, Philadelphia, PA, USA 1989)

P. Sprawls: Physical Principles of Medical Imaging (Medical Physics Publishing, Madison, WI USA 1995)

J. Van Dyk (Ed.): The Modern Technology of Radiation Oncology (Medical Physics Publishing, Madison, WI, USA 1999)

Appendix 1. Short Biographies of Scientists Whose Work Is Discussed in This Book

The biographical data were obtained mainly from two sources:

1. Book by William H. Cropper: "*Great Physicists: The Life and Times of Leading Physicists from Galileo to Hawking*" published by Oxford University Press in 2001.
2. The website `www.Nobelprize.org` that contains biographies and Nobel lectures of all Nobel Prize winners in Physics, Chemistry, Physiology or Medicine, Literature, Peace, and Economic Sciences from 1901 to date.

ANDERSON, Carl David (1905–1991)

American physicist, educated at the California Institute of Technology (Caltech) in Pasadena (B.Sc. in Engineering Physics in 1927; Ph.D. in Engineering Physics in 1930). He spent his entire professional career at Caltech, becoming Professor of Physics in 1939, Chairman of the Physics, Mathematics & Astronomy division (1962–1970), and Professor Emeritus in 1976.

Early in his career Anderson concentrated on studies of x rays, later on on studies of cosmic rays with cloud chambers that lead to the discovery of the positron in 1932. Positron was the first known particle in the category of antimatter. *Paul A.M. Dirac* enunciated its existence in 1928 with his relativistic quantum theory for the motion of electrons in electric and magnetic fields. Dirac's theory incorporated Albert Einstein's special theory of relativity and predicted the existence of an antiparticle to the electron (same mass, opposite charge). In 1933 Anderson succeeded in producing positrons by gamma radiation through the effect of pair production. In 1936 Anderson, in collaboration with his graduate student Seth Neddermeyer, discovered, again while studying cosmic radiation, the muon (μ meson), the first known elementary particle that is not a basic building block of matter.

In 1936 Anderson shared the Nobel Prize in Physics with Victor Franz Hess, an Austrian physicist. Anderson received the Prize *"for his discovery of the positron"* and Hess *"for his discovery of cosmic radiation"*.

AUGER, Pierre Victor (1899–1993)

French physicist who was active as a basic scientist in atomic, nuclear and cosmic ray physics but also made important contributions to French and

international scientific organizations. The world's largest cosmic ray detector, the Pierre Auger observatory, is named after him. Auger is also credited with the discovery in 1925 of radiation-less electronic transitions in atoms that are followed by emission of orbital electrons. The process is named after him as the Auger effect and the emitted electrons are called Auger electrons. *Lise Meitner* actually discovered the radiation-less atomic transition process in 1923, two years before Auger; nonetheless, the process is referred to as the Auger effect.

AVOGADRO, Amedeo (1776–1856)

Italian lawyer, chemist, physicist, best known for the "Avogadro's principle" and "Avogadro's number". The Avogadro's principle states that "equal volumes of all gases at the same temperature and pressure contain the same number of molecules." The concepts of gram-atom and gram-mole were introduced long after Avogadro's time; however, Avogadro is credited with introducing the distinction between the molecule and the atom. The number of atoms per gram-atom and number of molecules per gram-mole is constant for all atomic and molecular entities and referred to as Avogadro's number ($N_A = 6.022 \times 10^{23}$ atom/g-atom) in honor of Avogadro's contributions to chemistry and physics.

BALMER, Johann Jakob (1825–1898)

Swiss mathematician who studied in Germany at the University of Karlsruhe and the University of Berlin before receiving a doctorate at the University of Basel. He then spent his professional life teaching mathematics at the University of Basel.

Balmer is best known for his work on spectral lines emitted by the hydrogen gas. In 1885 he published a formula that predicted the wavelengths of the lines in the visible part of the hydrogen spectrum. The formula predicted the lines very accurately but was empirical rather than based on any physical principles. Several other scientists subsequently proposed similar empirical formulas for hydrogen lines emitted in other portions of the photon spectrum (Lymann in the ultraviolet and Paschen, Brackett and Pfund in the infrared). In 1913 *Niels Bohr* derived from first principles the general relationship for spectral lines of hydrogen. The relationship is governed by n, the principal quantum number, and contains a constant that is now referred to as the Rydberg constant ($R_\infty = 109\,737$ cm^{-1}). The spectral line series for $n = 1$ is called the Lymann series; for $n = 2$ the Balmer series; for $n = 3$ the Paschen series; for $n = 1$ the Brackett series; and for $n = 5$ the Pfund series.

BARKLA, Charles Glover (1877–1944)

British physicist, educated in mathematics and physics at the University College in Liverpool from where he graduated in 1898. He worked as research assistant with *Joseph J. Thomson* in the Cavendish Laboratory in Cambridge

and as academic physicist at the University of London. In 1913 he was appointed Chair of Natural Philosophy at the University of Edinburgh and held the position until his death in 1944.

Barklas's most important research involved studies of the production of x rays and of their interactions with matter. He is credited with the discovery of characteristic (fluorescent) radiation and the polarization of x rays between 1904 and 1907.

In 1917 he was awarded the Nobel Prize in Physics *"for his discovery of the characteristic Röntgen radiation of the elements"*.

BECQUEREL, Henri Antoine (1852–1908)

French physicist, educated at the École Polytechnique in basic science and at the École des Ponts et Chaussées becoming an *ingénieur* in 1877. In 1888 he acquired the degree of *docteur-ès-sciences*. In 1895 he became Professor of Physics at the École Polytechnique.

Becquerel was active in many areas of physics investigating polarization of visible light, naturally occurring phosphorescence in uranium salts, and terrestrial magnetism. In 1896, shortly after *Wilhelm Röntgen*'s discovery of x rays, Becquerel accidentally discovered natural radioactivity while investigating phosphorescence in uranium salts upon exposure to light. He observed that when the salts were placed near a photographic plate covered with opaque paper, the developed plate was nonetheless fogged. Becquerel concluded that the uranium salts were emitting penetrating rays that were emanating from uranium atoms. He subsequently showed that the rays were causing ionization of gases and that, in contrast to Röntgen's x rays, they were deflected by electric and magnetic fields.

In 1903 Becquerel shared the Nobel Prize in Physics with *Pierre* and *Marie Curie*. He was awarded the prize *"in recognition of the extraordinary services he has rendered by his discovery of spontaneous radioactivity"* and the Curies received their prize *"in recognition of the extraordinary services they have rendered by their joint researches on the radiation phenomena discovered by Professor Henri Becquerel"*.

Becquerel and his work are honored by the SI unit of radioactivity named Becquerel (Bq). In addition, there are Becquerel craters on the moon and Mars.

BERGER, Martin (1922–2004)

Austrian-born American physicist, educated at the University of Chicago where he received his degrees in Physics: B.Sc. in 1943, M.Sc. in 1948, and doctorate in 1951. In 1952 Berger joined the Radiation Theory Section at the National Bureau of Standards (NBS), now National Institute of Science and Technology (NIST) in Washington D.C. In 1964 he became the Section Chief and later, as well, Director of the Photon and Charged-Particle Data Center at the NBS/NIST, a position he held until his retirement in 1988.

Berger is best known for his early work on the transport of gamma rays and applications of Monte Carlo calculations in complex media involving boundaries and inhomogeneities. He also worked on charged-particle transport with emphasis on electrons and protons, and developed algorithms for use in charged particle Monte Carlo codes. His ETRAN code, first published in the 1960s, became the industry standard for coupled electron-photon transport. Berger, in collaboration with *Stephen Seltzer*, also developed cross-section data for electron and heavy charged particle interactions as well as for electron bremsstrahlung production. He was also involved in applications of Monte Carlo calculations to important problems in radiological physics and radiation dosimetry.

BETHE, Hans Albrecht (1906–2005)

German-born American physicist, educated at the Universities of Frankfurt and Munich. He received his doctorate in Theoretical Physics under Arnold Sommerfeld in 1928. For four years he worked as Assistant Professor at the University of Munich, then spent a year in Cambridge and a year in Rome with *Enrico Fermi*. He returned to Germany as Assistant Professor at the University of Tübingen but lost the position during the rise of Nazism. He first emigrated to England and then in 1935 moved to Cornell University in Ithaca, New York as Professor of Physics. He stayed at Cornell essentially all his professional life, but also served as Director of Theoretical Physics on the Manhattan project at Los Alamos (1943–1946).

Bethe made important theoretical contributions to radiation physics, nuclear physics, quantum mechanics, and quantum electrodynamics. He was also a strong advocate for peaceful use of atomic energy, despite having been involved with the Manhattan project as well as with the development of the hydrogen bomb. In collision theory Bethe derived the stopping power relationships that govern inelastic collisions of fast particles with atoms. With Heitler, he developed the collision theory for relativistic electrons interacting with atomic nuclei and producing bremsstrahlung radiation in the process. Bethe's work in nuclear physics lead to the discovery of the reactions that govern the energy production in stars.

In 1967 Bethe was awarded the Nobel Prize in Physics "*for his theory of nuclear reactions, especially his discoveries concerning the energy production in stars*".

BLOCH, Felix (1905–1983)

Swiss-born American physicist, educated at the Eidgenössische Technische Hochschule in Zürich (ETHZ) and at the University of Leipzig where he received his doctorate in physics in 1928. During the next few years he held various assistantships and fellowships that gave him the opportunity to work with the giants of modern physics (Pauli, Heisenberg, Bohr, and Fermi) and to further his understanding of solid state physics in general and stopping

powers of charged particles in particular. In 1933 Bloch left Germany and in 1934 accepted a position at Stanford University where he got involved with experimental physics of neutron momenta and polarized neutron beams. During the war years he worked on the Manhattan project at Los Alamos and on radar technology at Harvard where he became familiar with modern techniques of electronics. This helped him upon return to Stanford in 1945 with development of new techniques for measuring nuclear moments that culminated in 1946 with the invention of the nuclear magnetic resonance (NMR) technique, a purely electromagnetic procedure for the study of nuclear moments in solids, liquids, and gases. At Harvard *Edward M. Purcell* with students Robert Pound and Henry C. Torrey invented the NMR technique independently and at about the same time as Bloch.

In 1952 Bloch and Purcell received the Nobel Prize in Physics "*for their development of new methods for nuclear magnetic precision measurements and discoveries in connection therewith*". Since the late 1970s NMR provided the basis for magnetic resonance imaging (MRI), which is widely used as a non-invasive diagnostic imaging technique.

BOHR, Niels Henrik David (1885-1962)

Danish physicist, educated at the University of Copenhagen where he obtained his M.Sc. degree in Physics in 1909 and doctorate in Physics in 1911. Between 1911 and 1916 Bohr held various academic appointments in the U.K. and Copenhagen. In 1911 he worked in Cambridge with *Joseph J. Thomson* and in 1912 he worked in Manchester with *Ernest Rutherford*. He was a Lecturer in physics at the University of Copenhagen in 1913 and at the University of Manchester between 1914 and 1916. In 1916 he was appointed Professor of Theoretical Physics and in 1920 he also became the first Director of the Institute of Theoretical Physics (now Niels Bohr Institute) at the University of Copenhagen. He remained in both positions until his death in 1962.

Bohr was an exceptionally gifted theoretical physicist who made important contributions to atomic, nuclear, and quantum physics. He is best known for his expansion in 1913 of the Rutherford's atomic model into the realm of Planck's quantum physics to arrive at a model that is now called the Rutherford-Bohr atomic model. With four postulates that merged simple classical physics concepts with the idea of quantization of angular momenta for electrons revolving in allowed orbits about the nucleus, he succeeded in explaining the dynamics of one-electron structures and in predicting the wavelengths of the emitted radiation.

Bohr is also known as the author of the principle of complementarity which states that a complete description of an atomic scale phenomenon requires an evaluation from both the wave and particle perspective. In 1938 he proposed the so-called liquid drop nuclear model and in 1939 he succeeded in explaining the neutron fission of natural uranium in terms of fissionable

uranium-235 (an isotope with an abundance of only 0.7% in natural uranium) and the much more abundant non-fissionable uranium-238.

During World War II Bohr worked on the Manhattan project in Los Alamos but his contribution to the development of atomic weapons was only minor. After the war he used his considerable credibility and influence to promote peaceful use of the atomic energy and in 1954 helped found the CERN (Centre Européen de Recherche Nucléaire) in Geneva, touted as the world's largest particle physics laboratory and the birthplace of the *worldwide web*. In addition to producing his theoretical masterworks, Bohr was also keenly interested in politics and advised Presidents Roosevelt and Truman as well as Prime Minister Churchill on nuclear matters. Only Albert Einstein and Marie Curie among scientists of the 20th century have attained such esteem from physics colleagues, world leaders, and the general public.

In tribute to Bohr's contributions to modern physics the element with atomic number 107 is named bohrium (Bh). Bohr received the 1922 Nobel Prize in Physics *"for his services in the investigation of the structure of atoms and of the radiation emanating from them"*.

BORN, Max (1882–1970)

German mathematician and physicist, educated at universities of Breslau (1901), Heidelberg (1902), Zürich (1903), and Göttingen where he received his doctorate in 1907. In 1909 he was appointed Lecturer at the University of Göttingen and in 1912 he moved to the University of Chicago. In 1919 he became Professor of Physics at the University of Frankfurt and then in 1921 Professor of Physics at the University of Göttingen. From 1933 until 1936 he lectured at the University of Cambridge and from 1936 until 1953 at the University of Edinburgh.

Born is best known for his work on relativity in general and the relativistic electron in particular. He was also working on crystal lattices and on quantum theory, in particular on the statistical interpretation of quantum mechanics. He is best known for his formulation of the now-standard interpretation of the probability density for $\psi^*\psi$ in the Schrödinger equation of wave mechanics.

In 1954 Born shared the Nobel Prize in Physics with Walther Bothe. Born received his half of the prize *"for his fundamental research in quantum mechanics, especially for his statistical interpretation of the wavefunction"* and Bothe *"for the coincidence method and his discoveries made herewith"*.

BRAGG, William Henry (1862–1942)

British physicist, educated at King William College on Isle of Man and at the Trinity College at Cambridge where he graduated in 1884. His first academic appointment was at the University of Adelaide in Australia from 1885 until 1909. In 1909 he returned to England and worked as Professor of Physics at the University of Leeds from 1909 until 1915 and at the University College

in London from 1915 until 1923. From 1923 until 1942 he was Director of the Royal Institution in London.

Henry Bragg is best known for the work he carried out in collaboration with his son Lawrence on the diffraction of x rays on crystalline structures. *von Laue* discovered the diffraction of x rays on crystals; however, it was the father-son Bragg team that developed the discipline of x-ray crystallography based on the Bragg crystal spectrometer, a very important practical tool in solid state physics and analytical chemistry.

The 1915 Nobel Prize in Physics was awarded to William Henry Bragg and his son William Lawrence Bragg "*for their services in the analysis of crystal structure by means of x rays*".

BRAGG, William Lawrence (1890–1971)

Australian-born British physicist, educated at Adelaide University where he graduated at age 18 with an honors B.A. degree in Mathematics. He then entered Trinity College in Cambridge, continued his studies in mathematics but switched to physics the second year and graduated in physics in 1912. He first worked as Lecturer at the Cavendish Laboratory in Cambridge but from 1915 spent three years in the army. He became Langworthy Professor of Physics at the University of Manchester in 1919. During 1938 he was Director of the National Physical Laboratory in Teddington and then worked in Cambridge as the Cavendish Professor of Experimental Physics from 1939 until 1954 and as Director of the Royal Institution from 1954 until 1966.

In 1912 William L. Bragg became interested in the great debate on the nature of x rays: were they waves or particles? Following the experiments of *von Laue* and colleagues he developed an ingenious way of treating the phenomenon of x-ray diffraction on crystalline structures. He pointed out that the regular arrangement of atoms in a crystal defines a large variety of planes on which the atoms effectively lie. This means that the atoms in a regular lattice simply behave as if they form reflecting planes. The well-known Bragg equation is then expressed as $2d\sin\phi = m\lambda$, with d the separation between two atomic planes, ϕ the angle of incidence of the x-ray beam, λ the x-ray wavelength, and m an integer. The basis of a Bragg spectrometer is then as follows: For a known d, an x-ray spectrum can be analyzed by varying ϕ and observing the intensity of the reflected x rays that are scattered through and angle $\theta = 2\phi$ from the direction of the incident collimated beam. On the other hand, if mono-energetic x rays with a known λ are used, it is possible to determine various effective values of d in a given crystal and hence the basic atomic spacing a. With the knowledge of a one may determine the *Avogadro*'s number N_A with great accuracy.

The 1915 Nobel Prize in Physics was awarded to William Lawrence Bragg and his father William Henry Bragg "*for their services in the analysis of crystal structure by means of x rays*".

ČERENKOV, Pavel Alekseyevič (1904–1990)

Russian physicist, educated at the Voronezh State University in Voronezh in Central Russia, where he graduated with a degree in mathematics and physics in 1928. In 1930 he accepted a post as senior scientific officer in the Peter N. Lebedev Institute of Physics in the Soviet Academy of Sciences (now the Russian Academy of Sciences in Moscow) under the directorship of Sergei I. Vavilov. In 1940 Čerenkov was awarded a doctorate in physics and in 1953 he became Professor of Experimental Physics. In 1970 he became an Academician of the USSR Academy of Sciences.

Čerenkov is best known for his studies of the visible light emitted by energetic charged particles which move through a transparent medium with a velocity that exceeds c/n, the speed of light in the medium, where c is the speed of light in vacuum and n is the index of refraction. In 1934 Čerenkov and Sergei I. Vavilov observed that gamma rays from a radium source, besides causing luminescence in solutions, also produce a faint light from solvents. Their subsequent research lead to two important conclusions: firstly, the emitted light was not a luminescence phenomenon and secondly, the light they observed was not emitted by photons, rather, it was emitted by high energy electrons released in the medium by photon interactions with orbital electrons of the medium. The effect is now referred to as the Čerenkov effect (or sometimes as the Čerenkov-Vavilov effect) and the blue light emitted by energetic charged particles is called Čerenkov radiation. Ilja Frank and Igor Tamm, also from the Lebedov Institute, explained the Čerenkov effect theoretically in 1937 showing that Čerenkov radiation originates from charged particles that move through the medium faster then the speed of light in the medium. The Čerenkov effect is used in Čerenkov counters in nuclear and particle physics for determination of particle energy and velocity.

The 1958 Nobel Prize in Physics was awarded to Čerenkov, Frank, and Tamm *"for the discovery and the interpretation of the Čerenkov effect"*.

CHADWICK, James (1891–1974)

British physicist, educated at Manchester University (B.Sc. in 1911 and M.Sc. in 1913) before continuing his studies in the Physikalisch-Technische Reichsanstalt at Charlottenburg. In 1919 he moved to Cambridge to work with *Ernest Rutherford* on nuclear physics research. He remained in Cambridge until 1935 when he became the Chairman of Physics at the University of Liverpool. From 1943 to 1946 he was the Head of the British Mission attached to the Manhattan project.

Chadwick is best known for his discovery of the neutron, a constituent of the atomic nucleus that in contrast to the proton is devoid of any electrical charge. In recognition of this fundamental discovery that paved the way toward the discovery of nuclear fission, Chadwick was awarded the 1935 Nobel Prize in Physics *"for the discovery of the neutron"*.

COMPTON, Arthur Holy (1892–1962)

American physicist, educated at College of Wooster (B.Sc. in 1913) and Princeton University (M.A. in 1914 and Ph.D. in 1916). He worked as physics instructor at the University of Minnesota, research engineer at Westinghouse in Pittsburgh, and research fellow at Cambridge University. Upon return to the U.S. in 1920 he worked as Chairman of the Physics department at the Washington University in St. Louis and in 1923 he moved to the University of Chicago as Professor of Physics.

Compton is best known for his experimental and theoretical studies of x-ray scattering on atoms that lead to his discovery, in 1922, of the increase in wavelength of x rays scattered on essentially free atomic electrons. This effect illustrates the corpuscular nature of photons and is now known as the Compton effect. As Chairman of the "National Academy of Sciences Committee to Evaluate Use of Atomic Energy in War", Compton was instrumental in developing the first controlled uranium fission reactors and plutonium-producing reactors.

In 1927 Compton was awarded the Nobel Prize in Physics *"for the discovery of the effect that bears his name".* The co-recipient of the 1927 Nobel Prize was C.T.R. Wilson for his discovery of the cloud chamber.

COOLIDGE, William David (1873–1975)

American physicist and inventor, educated at the Massachusetts Institute of Technology (MIT) in Boston (B.Sc. in Electrical Engineering in 1896) and the University of Leipzig (doctorate in Physics in 1899). In 1899 he returned for five years to Boston as a research assistant in the Chemistry department of the MIT. In 1905 Coolidge joined the General Electric (GE) Company in Schenectady, New York, and remained with the company until his retirement in 1945. He served as director of the GE Research Laboratory (1932–1940) and as vice president and director of research (1940–1944).

During his 40-year career at General Electric, Coolidge became known as a prolific inventor and was awarded 83 patents. He is best known for his invention of ductile tungsten in the early years of his career. He introduced ductile tungsten for use as filament in incadescent lamps in 1911 producing a significant improvement over Edison's design for incadescent lamps. In 1913 he introduced ductile tungsten into x-ray tubes and revolutionized x-ray tube design that at the time was based on three major components: cold cathode, low pressure gas, and anode (target). The role of the low pressure gas was to produce ions which produced electrons upon bombardment of the cold aluminum cathode. This x-ray tube design was based on the Crookes device for studying cathode rays, and is now referred to as the Crookes tube. The performance of the Crookes x-ray tube was quite erratic and Coolidge introduced a significant improvement when he replaced the cold aluminum cathode with a hot tungsten filament and replaced the low pressure gas with high vacuum. Coolidge's x-ray tube design is now referred to as the Coolidge

tube and is still used today for production of superficial and orthovoltage x rays. In the Coolidge x-ray tube the electrons are produced by thermionic emission from the heated filament cathode and accelerated in the applied electric field toward the anode (target).

In honor of Coolidge's contribution to radiology and medical physics through his hot filament innovation, the highest award bestowed annually by the American Association of Physicists in Medicine is named the William D. Coolidge Award.

CORMACK, Allen MacLeod (1924–1998)

South African-born American physicist, educated in x-ray crystallography at the University of Cape Town where he obtained his B.Sc. in 1944 and M.Sc. in 1945. For a year he continued his studies in nuclear physics at the Cavendish Laboratory in Cambridge, and then returned to a lectureship in the Physics department at the University of Cape Town. On a part time basis he assumed responsibilities for supervising the use of radioactive nuclides in the Groote Shuur hospital, thus learning about medical physics in a radiotherapy department. In 1956 Cormack took a sabbatical at Harvard and developed there a crude theory for the x-ray absorption problem to be used in future CT algorithms. From Harvard he returned to Cape Town for a few months and carried out actual experiments on a crude cylindrical CT phantom. In 1957 Cormack moved to Tufts University in Boston and continued intermittent work on his tomography idea.

During 1963 and 1964 Cormack published two seminal CT papers in the "Journal of Applied Physics". The two papers were largely ignored, but earned him the 1979 Nobel Prize in Physiology or Medicine which he shared with *Godfrey N. Hounsfiled* "*for the development of computer assisted tomography*".

CURIE, Pierre (1859–1906)

French physicist and chemist, educated in Paris where, after obtaining his "Licence ès Sciences" (equivalent to M.Sc.) at the age of 18, he was appointed a laboratory assistant at the Sorbonne. In 1882 he was appointed supervisor at the École de Physique et Chimie Industrielle in Paris and in 1895 obtained his doctorate. In 1900 he was appointed lecturer and in 1904 Professor of Physics at the Sorbonne.

Pierre Curie's contributions to physics have two distinct components clearly separated by the date of his wedding to *Maria Sklodowska-Curie* in 1895. Before that date, he was involved in crystallography and magnetism discovering the piezoelectric effect as well as showing that magnetic properties of a given substance change at a certain temperature that is now referred to as the Curie point. To carry out his experiments he constructed delicate devices that proved very useful in his collaborative studies of radioactivity with his wife Marie Curie. After their discovery of polonium and radium,

Pierre Curie concentrated on investigating the physical properties of radium while Marie concentrated on preparing pure compounds.

Pierre Curie and one of his students are credited with making the first observation of nuclear power through measuring the continuous production of heat in a sample of radium. He was also the first to report the decay of radioactive materials and the deleterious biological effects of radium after producing a radium burn and wound on his own skin.

In his honor the 1910 Radiology Congress accepted the definition of the curie (Ci), a unit of activity, as the activity of 1 g of radium-226 corresponding to 3.7×10^{10} s^{-1}. The curie is still defined as 3.7×10^{10} s^{-1}; however, subsequent measurements have shown that the specific activity of radium-226 is 0.988 Ci/g. In tribute to the work of Pierre and Marie Curie the element with atomic number 96 was given the name curium (Cm).

Pierre and Marie Curie shared the 1903 Nobel Prize in Physics with *Henri Becquerel* "*in recognition of the extraordinary services they have rendered by their joint researches on the radiation phenomena discovered by Professor Henri Becquerel*". Becquerel was awarded his share of the Nobel Prize "*in recognition of the extraordinary services he has rendered by his discovery of spontaneous radioactivity*".

CURIE-SKLODOWSKA, Marie (1867–1934)

Polish-born French physicist, educated at the Sorbonne in Paris where she obtained a "Licence ès Sciences" (equivalent to M.Sc.) in Physical Sciences (1893) and Mathematics (1894) and her doctorate in Physics in 1903. Curie spent her professional life at various institutions in Paris. In 1906 she was appointed Lecturer in Physics at the Sorbonne and was promoted to Professor of Physics in 1908.

In 1914 Marie Curie helped found the "Radium Institute" in Paris dedicated to scientific disciplines of physics, chemistry and biology applied to prevention, diagnosis and treatment of cancer. The institute had two divisions: the Curie Laboratory dedicated to research in physics and chemistry of radioactivity and the Pasteur Laboratory devoted to studies of biological and medical effects of radioactivity. The Curie Laboratory was headed by Marie Curie; the Pasteur Laboratory by Claudius Regaud who is regarded as the founding father of both radiotherapy and radiobiology. In 1920, the Curie Foundation was inaugurated to raise funds to support the activities of the Radium Institute. In 1970 the Radium Institute and the Curie Foundation were merged into the Curie Institute mandated to carry out cancer research, teaching and treatment.

After obtaining her "licence" at the Sorbonne, Curie, looking for a doctoral degree subject, decided to investigate the phenomenon of radiation emission from uranium discovered by *Henri Becquerel* in 1896. She coined the name "radioactivity" for the spontaneous emission of radiation by uranium and established that radioactivity was an atomic rather than chemical

phenomenon process. She then investigated if the peculiar property of uranium could be found in any other then-known element and discovered that thorium is also an element which exhibits radioactivity. Noticing that some minerals (for example, pitchblende uranium ore) exhibited a much larger rate of radioactivity than warranted by their uranium or thorium content, she surmised that the minerals must contain other highly radioactive unknown elements. In collaboration with her husband *Pierre Curie*, Marie Curie discovered miniscule amounts of new elements radium and polonium after sifting through several tons of pitchblende uranium ore. In tribute to the work of Pierre and Marie Curie the element with atomic number 96 was given the name curium (Cm).

The discovery of the new radioactive elements in 1898 earned Marie Curie a doctorate in Physics and, in addition, both Marie and Pierre Curie shared, with *Henry Becquerel*, the 1903 Nobel Prize in Physics "*in recognition of the extraordinary services they have rendered by their joint researches on the radiation phenomena discovered by Professor Henri Becquerel*".

In 1911 Marie Curie was awarded another Nobel Prize, this time in Chemistry, "*in recognition of her services to the advancement of chemistry by the discovery of the elements of radium and polonium, by the isolation of radium and the study of the nature and compounds of this remarkable element*".

Marie Curie's contribution to science has been enormous not only in her own work but also in the work of subsequent generations of physicists whose lives she touched and influenced. She was the first woman to teach at the Sorbonne, the first woman to receive a Nobel Prize, and the first scientist to have received two Nobel Prizes.

DAVISSON, Clinton Joseph (1881–1958)

American physicist, educated at the University of Chicago (B.Sc. in 1908) and Princeton University where he received his doctorate in Physics in 1911. He spent most of his professional career at the Bell Telephone Laboratories. Upon retirement from Bell Labs he became Visiting Professor of Physics at the University of Virginia in Charlottesville.

Davisson is best known for his work on electron diffraction from metallic crystals. In 1927 he was studying elastic electron scattering on a nickel single crystal in collaboration with *Lester H. Germer*. When they analyzed the angular distribution of scattered electrons they discovered that electrons produced diffraction patterns similar to those produced by x rays. The diffraction patterns were governed by the Bragg formula with a wavelength λ given by the de Broglie equation: $\lambda = h/p$ with h the Planck's constant and p the momentum of the electron. The experiment, now known as the Davisson-Germer experiment, confirmed the hypothesis formulated in 1924 by *Louis de Broglie* that electrons exhibit dual nature, behaving both as waves and as particles. *George P. Thomson*, a physicist at the University of Aberdeen in Scotland, confirmed the de Broglie's hypothesis with a different experiment. He stud-

ied the behavior of electrons as they traversed very thin films of metals and also observed that electrons under certain conditions behave as waves despite being particles. Thomson's apparatus is referred to as an electron diffraction camera and produces a series of rings when a narrow electron beam is made to traverse a thin metallic foil.

In 1937 Davisson and Thomson shared the Nobel Prize in Physics "*for their experimental discovery of the diffraction of electrons by crystals.*"

DE BROGLIE, Louis (1892–1987)

French theoretical physicist, educated at the Sorbonne in Paris, first graduating with an arts degree in 1909 and then with "Licence ès Sciences" (equivalent to M.Sc.) in 1913. De Broglie spent the war years 1914–1918 in the army and in 1920 resumed his studies in Theoretical Physics at the Sorbonne. He obtained his doctorate in theoretical physics in 1924, taught physics at the Sorbonne for two years and became Professor of Theoretical Physics at the Henri Poincaré Institute. From 1932 to his retirement in 1962 he was Professor of Theoretical Physics at the Sorbonne.

De Broglie is best known for his theory of electron waves based on the work of *Max Planck* and *Albert Einstein*. The theory, presented in his doctorate work, proposed the wave-particle duality of matter. De Broglie reasoned that if x rays behave as both waves and particles, then particles in general and electrons in particular should also exhibit this duality. De Broglie's theory was confirmed experimentally by *Clinton J. Davisson* and *Lester H. Germer* in the United States and by *George P. Thomson* in the U.K. The theory was subsequently used by *Ervin Schrödinger* to develop wave mechanics.

The 1929 Nobel Prize in Physics was awarded to de Broglie "*for his discovery of the wave nature of electrons*".

DIRAC, Paul Adrien Maurice (1902–1984)

British physicist, educated at the University of Bristol where he obtained his Bachelor's degree in Electrical Engineering in 1921 and at the St. John's College in Cambridge where he received his doctorate in Mathematics in 1926. In 1927 he became a Fellow of the St. John's College and from 1932 until 1969 he was Lucasian Professor of Mathematics in Cambridge. In 1969 Dirac moved to Florida to become Professor of Physics at the Florida State University.

Dirac was an extremely productive and intelligent theoretical physicist, mainly involved with mathematical and theoretical aspects of quantum mechanics. Quantum mechanics, dealing with dimensions of the order of the atomic size, introduced the second revolution in physics, the first one being *Albert Einstein*'s special theory of relativity that deals with velocities of the order of the speed of light in vacuum.

In 1926 Dirac developed his version of quantum mechanics that merged the "matrix mechanics" of *Werner Heisenberg* with the "wave mechanics"

of *Erwin Schrödinger* into a single mathematical formalism. In 1928 he derived a relativistic equation for the electron that merged quantum mechanics with relativity and is now referred to as the Dirac equation. The equation predicts the existence of an anti-particle (same mass, opposite charge) to the electron and infers the electron quantum spin. Dirac also predicted that in an electron/anti-electron encounter the charges cancel, and the two particles annihilate with the combined mass transforming into radiation according to Albert Einstein's equation $E = mc^2$. Four years later, in 1932 *Carl D. Anderson* discovered the anti-electron, a new particle which is now called the positron. In 1931 Dirac showed theoretically that the existence of a magnetic monopole would explain the observed quantization of the electrical charge (all charges found in nature are multiples of the electron charge). No monopoles have been found in nature so far.

The 1933 Nobel Prize in Physics was awarded to Paul M. Dirac and *Erwin Schrödinger* "*for their discovery of new productive forms of atomic theory*".

EINSTEIN, Albert (1879–1955)

German-born theoretical physicist, educated at the Eidgenössische Technische Hochschule in Zürich (ETHZ) from which he graduated in 1900 as a teacher of mathematics and physics. He did not succeed in obtaining an academic post after graduating and spend two years teaching mathematics and physics in secondary schools. From 1902 until 1909 he worked as a technical expert in the Swiss Patent Office in Bern. In 1905 he earned a doctorate in Physics from the University of Zürich.

Following publication of three seminal theoretical papers in 1905 and submission of his "Habilitation" thesis in 1908, Einstein's credibility in physics circles rose dramatically; he started to receive academic job offers and entered a period of frequent moves and changes in academic positions. In 1908 he became lecturer at the University of Bern and in 1909 Professor of Physics at the University of Zürich. During 1911 he was Professor of Physics at the Karl-Ferdinand University in Prague and in 1912 he moved back to Zürich to take a chair in theoretical physics at the ETHZ. Finally, in 1914 he moved to Berlin to a research position without teaching responsibilities at the then world-class center of physics at the University of Berlin.

During the Berlin period (1914–1933) Einstein produced some of his most important work, became an international "star" physicist and scientist, got involved in political issues, and traveled a great deal to visit physics colleagues and present invited lectures on his work. In 1932 he moved to the United States to become Professor of Theoretical Physics at the Institute for Advanced Study in Princeton, one of the world's leading centers for theoretical research and intellectual inquiry.

Einstein was an extremely gifted physicist and his contribution to modern physics is truly remarkable. His three papers published in Volume 17 of the

"Annalen der Physik" each dealt with a different subject and each is now considered a masterpiece.

The first of the three papers dealt with the photoelectric effect and contributed to quantum theory by assuming that light under certain conditions behaves like a stream of particles (quanta) with discrete energies. The second paper dealt with statistical mechanics and lead to an explanation of Brownian motion of molecules. The third paper addressed the connection between the electromagnetic theory and ordinary motion and presented Einstein's solution as the "special theory of relativity". In 1916, after a decade of futile attempts, Einstein completed his "general theory of relativity" based on the "equivalence principle" stating that uniform acceleration of an object is equivalent to a gravitational field. The gravitational field causes curvature of space-time as observed experimentally by measuring the precession of the mercury perihelion and the bending by the sun of light from the stars.

At the end of the Berlin period and during his American period from 1933 until his death in 1955 Einstein concentrated on developing a unified field theory, unsuccessfully attempting to unify gravitation, electromagnetism and quantum physics. Throughout his life Einstein was a pacifist detesting both militarism as well as nationalism. In tribute to Einstein's contributions to modern physics the element with atomic number 109 is named einsteinium (Es).

In 1921 the Nobel Prize in Physics was awarded to Einstein "*for his services to Theoretical Physics and especially for his discovery of the law of the photoelectric effect*".

In recognition of Einstein's tremendous contribution to modern physics the year 2005, the centenary of Einstein's "annus mirabilis", was proclaimed the world year of physics, a worldwide celebration of physics and its impact on humanity.

EVANS, Robley (1907–1995)

American nuclear and medical physicist, educated at the California Institute of Technology (Caltech) where he studied physics and received his B.Sc. in 1928, M.Sc. in 1929, and Ph.D. under Robert A. Millikan in 1932. After receiving his doctorate he studied biological effects of radiation as post-doctoral fellow at the University of California at Berkeley before accepting a faculty position at the Massachusetts Institute of Technology (MIT) in Boston. He remained an active member of the MIT faculty for 38 years and retired in 1972 to become a special project associate at the Mayo Clinic in Rochester, Minnesota.

At the MIT Evans was instrumental in building the first cyclotron in the world for biological and medical use. He established the Radioactivity Center in the Physics department at the MIT for research in nuclear physics related to biology, introduced the first iodine radionuclide for diagnosis and treatment of thyroid disease, and built the first total body counter to measure

the uptake and body burden of radium in the human body. In 1941 he established one ten-millionth of a gram of radium (0.1 μCi) as the maximum permissible body burden. The standard is still internationally used and has been adapted for other radioactive substances including plutonium-239 and strontium-90. Evans's book "The Atomic Nucleus" was first published in 1955 and remained the definitive nuclear physics textbook for several decades and is still considered an important nuclear physics book.

In 1985 Evans received the William D. Coolidge Award from the American Association of Physicists in Medicine in recognition to his contribution to medical physics and in 1990 he received the Enrico Fermi Award in recognition of his contributions to nuclear and medical physics.

FERMI, Enrico (1901–1954)

Italian-born physicist who graduated from the University of Pisa in 1921. He was a Lecturer at the University of Florence for two years and then Professor of Theoretical Physics at the University of Rome from 1923 to 1938. In 1938 he moved to the United States and worked first for four years at Columbia University in New York and from 1942 till his death in 1954 at the University of Chicago.

Fermi is recognized as one of the great scientists of the 20th Century. He is best known for his contributions to nuclear physics and quantum theory. In 1934 he developed the theory of the beta nuclear decay that introduced the neutrino and the weak force as one of the basic forces in nature. The existence of the neutrino was actually enunciated by *Wolfgang Pauli* in 1930 and experimentally confirmed only in 1956.

In 1934, while at the University of Rome, Fermi began experiments bombarding various heavy elements with thermal neutrons. He discovered that the thermal neutrons bombarding uranium were very effective in producing radioactive atoms, but did not realize at the time that he succeeded in splitting the uranium atom. *Otto Hahn* and *Fritz Strassmann* in 1938 repeated Fermi's experiments and discovered that uranium bombarded with thermal neutrons splits into two lighter atoms. *Lise Meitner* and *Otto Frisch* explained the process theoretically and named it nuclear fission.

Upon his move to the United States Fermi continued his fission experiments at Columbia University and showed experimentally that uranium fission results in two lighter by-products, releasing several neutrons and large amounts of energy. In 1942 he was appointed Director of the Manhattan project at the University of Chicago with a mandate to develop an "atomic bomb". With his team of scientists Fermi produced the first nuclear chain reaction and developed the atomic bombs that were dropped on Hiroshima and Nagasaki by the United States at the end of the World War II.

In 1938 Fermi was awarded the Nobel Prize in Physics *"for his demonstrations of the existence of new radioactive elements produced by neutron*

irradiation, and for his related discovery of nuclear reactions brought about by slow neutrons".

Fermi's name is honored by the unit of length that is of the order of the size of the atomic nucleus (1 fermi = 1 femtometer = 1 fm = 10^{-15} m). One of the American national laboratories is named Fermi National Laboratory (Fermilab), and the oldest and most prestigious science and technology prize awarded in the United States is the Enrico Fermi Award. A common name for particles with half-integer spin, such as electron, neutron, proton and quark, is fermion; the artificially produced element with atomic number Z of 100 is fermium (Fm); and the quantum statistics followed by fermions is known as the Fermi-Dirac statistics, after its inventors.

FLEROV, Georgi Nikolaevič (1913–1990)

Russian nuclear physicist, educated in physics at the Polytechnical Institute of Leningrad (now St. Petersburg) from where he graduated in 1938. He started his scientific career at the Leningrad Institute of Physics and Technology and was involved in basic research in a number of fundamental and applied areas of nuclear physics. From 1941 to 1952 Flerov, together with Igor V. Kurčatov, participated in investigations linked with the use of atomic energy for military purposes and nuclear power industry. From 1960 to 1988 he was the director of the Nuclear Reactions Laboratory of the Joint Institute for Nuclear Research in Dubna.

Flerov is best known for his discovery in 1940 (in collaboration with Konstantin A. Petržak) of the spontaneous fission of uranium-238. With colleagues in Dubna, Flerov carried out research that resulted in the synthesis of new heavy elements (nobelium No-102, rutherfordium Rf-104, dubnium Db-105), the production of a large number of new nuclei on the border of stability, and the discovery of new types of radioactivity (proton radioactivity) and new mechanisms of nuclear interactions.

FRANCK, James (1882–1964)

German-born American physicist, educated at the Univeristy of Heidelberg and the University of Berlin where he received his doctorate in Physics in 1906. He worked at the University of Berlin from 1911 to 1918 and at the University of Göttingen until 1933 when he moved to the United States to become Professor at Johns Hopkins University in Baltimore. From 1938 to 1947 he was Professor of Physical Chemistry at the University of Chicago.

Franck is best known for the experiment he carried out in 1914 at the University of Berlin in collaboration with *Gustav Hertz*. The experiment is now known as the Franck-Hertz experiment and it demonstrated the existence of quantized excited states in mercury atoms. This provided the first experimental substantiation of the Bohr atomic theory which predicted that atomic electrons occupied discrete and quantized energy states.

In 1925 James Franck and Gustav Hertz were awarded the Nobel Prize in Physics *"for their discovery of the laws governing the impact of electron upon an atom"*. In addition to the Nobel Prize, Franck was also honored by the 1951 Max Planck medal of the German Physical Society and was named honorary citizen of the university town of Göttingen.

GAMOW, George (1904–1968)

Ukranian-born American physicist and cosmologist, educated at the Novorossia University in Odessa (1922–1923) and at the Leningrad University (1923-1928) where he received his doctorate in Physics in 1928. After a fellowship with Niels Bohr at the Institute for Theoretical Physics in Copenhagen and a short visit to Ernest Rutherford at the Cavendish Laboratory in Cambridge, he returned to SSSR in 1931 to become a Professor of Physics at the University of Leningrad. From 1934 until 1956 he was Chair of Physics at the George Washington University in Washington D.C. and from 1956 until his death in 1968 he was Professor of Physics at the University of Colorado in Boulder. During World War II he was involved with the Manhattan nuclear weapon project in Los Alamos.

Gamow is best known for his (1928) theory of the alpha decay based on tunneling of the alpha particle through the nuclear potential barrier. He was also a proponent of the Big-Bang theory of the Universe and worked on the theory of thermonuclear reactions inside the stars that is still today relevant to research in controlled nuclear fusion. His name is also associated with the beta decay in the so-called Gamow-Teller selection rule for beta emission. Gamow was also well known as an author of popular science books and received the UNESCO Kalinga Prize for popularization of science.

GEIGER, Hans (1882–1945)

German physicist, educated in physics and mathematics at the University of Erlangen where he obtained his doctorate in 1906. From 1907 to 1912 he worked with *Ernest Rutherford* at the University of Manchester where, with *Ernest Marsden*, he carried out the α-particle scattering experiments that lead to the Rutherford–Bohr atomic model. He also discovered, in collaboration with John M. Nuttall, an empirical linear relationship between log λ and log R_α for naturally occurring α emitters with the decay constant λ and range in air R_α (Geiger–Nuttall law). In collaboration with Walther Müller he developed a radiation detector now referred to as the Geiger-Müller counter.

GERLACH, Walther (1889–1979)

German physicist, educated at the University of Tübingen where he received his doctorate in physics in 1912 for a study of blackbody radiation and the photoelectric effect. He worked at the University of Göttingen and the University of Frankfurt before returning in 1925 to Tübingen as Professor of

Physics. From 1929 to 1952 he was Professor of Physics at the University of Munich.

Gerlach made contributions to radiation physics, spectroscopy and quantum physics. He is best known for his collaboration with *Otto Stern* in 1922 at the University of Frankfurt on an experiment that demonstrated space quantization using a beam of neutral silver atoms that, as a result of passage through an inhomogeneous magnetic field, split into two district components, each component characterized by a specific spin (angular momentum) of the silver atoms.

GERMER, Lester Halbert (1896–1971)

American physicist, educated at Columbia University in New York. In 1927 he worked as graduate student at Bell Laboratories under the supervision of *Clinton T. Davisson* on experiments that demonstrated the wave properties of electrons and substantiated the Louis de Broglie's hypothesis that moving particles exhibit particle-wave duality. The electron diffraction experiments on metallic crystals are now referred to as the Davisson-Germer experiment.

HAHN, Otto (1879–1968)

German chemist, educated at the University of Munich and University of Marburg. In 1901 he obtained his doctorate in Organic Chemistry at the University of Marburg. He spent two years as chemistry assistant at the University of Marburg, and then studied radioactivity for one year under William Ramsay at the University College in London and for one year under *Ernest Rutherford* at McGill University in Montreal. In 1905 he moved to the Kaiser Wilhelm Institute (now Max Planck Institute) for Chemistry in Berlin and remained there for most of his professional life. From 1928-1944 he served as the Director of the Institute.

Early in his career in Berlin he started a life-long professional association with Austrian-born physicist *Lise Meitner*; a collaboration that produced many important discoveries in radiochemistry and nuclear physics. Hahn's most important contribution to science is his involvement with the discovery of nuclear fission. In 1934 the Italian physicist *Enrico Fermi* discovered that uranium bombarded with neutrons yields several radioactive products. Hahn and Meitner, in collaboration with *Fritz Strassmann*, repeated Fermi's experiments and found inconclusive results. In 1938, being Jewish, Meitner left Germany for Stockholm to escape persecution by the Nazis; Hahn and Strassmann continued with the neutron experiments and eventually concluded that several products resulting from the uranium bombardment with neutrons were much lighter than uranium suggesting that the neutron bombardment caused uranium to split into two lighter components of more or less equal size. Hahn communicated the findings to Meitner in Stockholm, who, in cooperation with Otto Frisch, explained the theoretical aspects of

the uranium splitting process and called it nuclear fission. The discovery of nuclear fission led to the atomic bomb and to modern nuclear power industry.

In 1944 Hahn alone was awarded the Nobel Prize in Chemistry *"for his discovery of the fission of heavy nuclei"*. In 1966 Hahn, Strassmann and Meitner shared the Enrico Fermi Prize for their work in nuclear fission. It is now universally accepted that four scientists are to be credited with the discovery of the nuclear fission process: Hahn, Strassmann, Meitner and Frisch.

HARTREE, Douglas (1897–1958)

British mathematician and physicist, educated in Cambridge where he obtained a degree in Natural Sciences in 1921 and a doctorate in 1926. In 1929 he was appointed Professor of Applied Mathematics at the University of Manchester and in 1937 he moved to a Chair of Theoretical Physics. In 1946 he was appointed Professor of Mathematical Physics at Cambridge University and held the post until his death in 1958.

Hartree was both a mathematician and physicist and he is best known for applying numerical analysis to complex physics problems such as calculations of wave functions for multi-electron atoms. Hartree approached the problem by using the method of successive approximations, treating the most important interactions in the first approximation and then improving the result with each succeeding approximation. Hartree's work extended the concepts of the Bohr theory for one-electron atoms or ions to multi-electron atoms providing reasonable, albeit not perfect, approximations to inter-electronic interactions in multi-electron atoms.

HEISENBERG, Werner (1901–1976)

German theoretical physicist, educated in physics at the University of Munich and the University of Göttingen. He received his doctorate in Physics at the University of Munich in 1923 and successfully presented his habilitation lecture in 1924. During 1924-1926 he worked with *Niels Bohr* at the University of Copenhagen. From 1927 until 1941 Heisenberg held an appointment as Professor of Theoretical Physics at the University of Leipzig and in 1941 he was appointed Professor of Physics at the University of Berlin and Director of the Kaiser Wilhelm Institute for Physics in Berlin. From 1946 until his retirement in 1970 he was Director of the Max Planck Institute for Physics and Astrophysics in Göttingen. The institute moved from Göttingen to Munich in 1958.

In 1925 Heisenberg invented matrix mechanics which is considered the first version of quantum mechanics. The theory is based on radiation emitted by the atom and mechanical quantities, such as position and velocity of electrons, are represented by matrices. Heisenberg is best known for his uncertainty principle stating that a determination of particle position and momentum necessarily contains errors the product of which is of the order of the Planck's

quantum constant h. The principle is of no consequence in the macroscopic world; however, it is critical for studies on the atomic scale.

In 1932 Heisenberg was awarded the Nobel Prize in Physics "*for creation of quantum mechanics, the application of which has, inter alia, led to the discovery of allotropic forms of hydrogen*".

HEITLER, Walter (1904–1981)

German physicist who studied physics at Universities of Münich, Berlin, Zürich, and Göttingen with many important contemporary theoretical physicists. He completed his studies in Physics at the University of Münich in 1926 and from 1933 till 1941 worked at the University of Bristol. He then moved to the Dublin Institute for Advanced Study. In 1950 he moved to Zürich as Professor of Theoretical Physics and remained in Zürich for the rest of his life.

Heitler is considered one of the pioneers of the quantum field theory, but he also applied and developed quantum mechanics in much of his theoretical work in many other areas of physics. In addition to the quantum field theory, his other notable contributions are in the theory of the chemical bond in molecules, theory of photon interactions with absorbing media, theory of photon production by energetic electrons and positrons, and in the cosmic ray theory. His book *"The Quantum Theory of Radiation"* was first published in 1934 and is still considered a seminal textbook on the subject of ionizing radiation interaction with matter. In 1968 Heitler was awarded the Max Planck medal. The medal is awarded annually by the Deutsche Physikalische Gesellschaft (German Physical Society) for extraordinary achievements in theoretical physics.

HERTZ, Gustav (1887–1975)

German physicist, educated at the Universities of Göttingen, Munich and Berlin, and graduating with a doctorate in Physics in 1911. During 1913-1914 he worked as research assistant at the University of Berlin. Hertz alternated work in industry (Philips in Eindhoven; Siemens in Erlangen) with academic positions at the Universities of Berlin, Halle and Leipzig.

Hertz made many contributions to atomic physics but is best known for the experiment in which he studied, in collaboration with *James Franck*, the impact of electrons on mercury vapor atoms. The experiment is now referred to as the Franck-Hertz experiment and demonstrated the existence of quantized excited states in mercury atoms, thereby substantiating the basic tenets of the Bohr atomic theory.

In 1925 James Franck and Gustav Hertz were awarded the Nobel Prize in Physics *"for their discovery of the laws governing the impact of an electron upon an atom"*. Hertz was also the recipient of the Max Planck Medal of the German Physical Society.

HOUNSFIELD, Godfrey Newbold (1919–2004)

British electrical engineer and scientist, educated at the Electrical Engineering College in London from which he graduated in 1951. The same year he joined the research staff of the EMI in Middlesex. He remained associated with the EMI throughout his professional career.

Hounsfield made a significant contribution to early developments in the computer field and was responsible for the development of the first transistor-based solid-state computer in the U.K. He is best known, however, for the invention of computed tomography (CT), an x-ray-based diagnostic technique that non-invasively forms two-dimensional cross sections through the human body. Originally, the technique was referred to as computer assisted tomography (CAT), now the term computed tomography (CT) is more commonly used.

Following his original theoretical calculations, he first built a laboratory CT model to establish the feasibility of the approach, and then in 1972 built a clinical prototype CT-scanner for brain imaging. From the original single slice brain CT-scanner the technology evolved through four generations to the current 64 slice body and brain CT-scanners. Roentgen's discovery of x rays in 1895 triggered the birth of diagnostic radiology as an important medical specialty; Hounsfield's invention of the CT-scanner placed diagnostic radiology onto a much higher level and transformed it into an invaluable tool in diagnosis of brain disease in particular and human malignant disease in general. In 1979 Hounsfield shared the Nobel Prize in Physiology or Medicine with *Allan M. Cormack* "*for the development of computer assisted tomography*". Cormack derived and published the mathematical basis of the CT scanning method in 1964.

Hounsfield's name is honored with the Hounsfield scale which provides a quantitative measure of x-ray attenuation of various tissues relative to that of water. The scale is defined in hounsfield units (HF) running from air at -1000 HF, fat at -100 HF, through water at 0 HF, white matter at ~ 25 HF, grey matter at ~ 40 HF, to bone at $+400$ HF or larger, and metallic implants at $+1000$ HF.

HUBBELL, John (born 1925)

American radiation physicist, educated at the University of Michigan in Ann Arbor in Engineering Physics (B.Sc. in 1949, MSc. in 1950). In 1950 he joined the staff of the National Bureau of Standards (NBS) now known as the National Institute of Science and Technology (NIST) in Washington D.C. and spent his professional career there, directing the NBS/NIST X-Ray and Ionizing Radiation Data Center from 1963 to 1981. He retired in 1988.

Hubbell's collection and critical evaluation of experimental and theoretical photon cross section data resulted in the development of tables of attenuation coefficients and energy absorption coefficients, as well as related quantities such as atomic form factors, incoherent scattering functions, and atomic

cross sections for photoelectric effect, pair production and triplet production. Hubbell's most widely known and important work is the "National Standard Reference Data Series Report 29: Photon Cross Sections, Attenuation Coefficients and Energy Absorption Coefficients from 10 keV to 100 GeV".

JOHNS, Harold Elford (1915–1998)

Born in Chengtu, China to Canadian parents who were doing missionary work in China, Johns obtained his Ph.D. in Physics from the University of Toronto and then worked as physicist in Edmonton, Saskatoon, and Toronto. His main interest was diagnosis and therapy of cancer with radiation and his contributions to the field of medical physics are truly remarkable. While working at the University of Saskatchewan in Saskatoon in the early 1950s, he invented and developed the cobalt-60 machine which revolutionized cancer radiation therapy and had an immediate impact on the survival rate of cancer patients undergoing radiotherapy.

In 1956 Johns became the first director of the Department of Medical Biophysics at the University of Toronto and Head of the Physics division of the Ontario Cancer Institute in Toronto. He remained in these positions until his retirement in 1980 and built the academic and clinical departments into world-renowned centers for medical physics. With his former student John R. Cunningham, Johns wrote the classic book "The Physics of Radiology" that has undergone several re-printings and is still considered the most important textbook on medical and radiological physics.

In 1976 Johns received the William D. Coolidge Award from the American Association of Physicists in Medicine.

JOLIOT-CURIE, Irène (1897–1956)

French physicist, educated at the Sorbonne in Paris where she received her doctorate on the alpha rays of polonium in 1925 while already working as her mother's (Marie Curie) assistant at the Radium Institute. In 1927 Irène Curie married Frédéric Joliot who was her laboratory partner and Marie Curie's assistant since 1924. In 1932 Joliot-Curie was appointed Lecturer and in 1937 Professor at the Sorbonne. In 1946 she became the Director of the Radium Institute.

Joliot-Curie is best known for her work, in collaboration with her husband Frédéric Joliot, on the production of artificial radioactivity through nuclear reactions in 1934. They bombarded stable nuclides such as boron-10, aluminum-27, and magnesium-24 with naturally occurring α particles and obtained radionuclides nitrogen-13, phosphorus-30, and silicon-27, respectively, accompanied by release of a neutron. The discovery of artificially produced radionuclides completely changed the periodic table of elements and added several thousand artificial radionuclides to the list. In 1938 Joliot-Curie's research of neutron bombardment of the uranium represented an important

step in eventual discovery of uranium fission by *Otto Hahn*, *Fritz Strassmann*, *Lise Meitner*, and *Otto Frisch*.

The 1935 Nobel Prize in Chemistry was awarded to Frédéric Joliot and Irène Joliot-Curie "*in recognition of their synthesis of new radioactive elements*".

JOLIOT, Jean Frédéric (1900–1958)

French physicist, educated at the École de Physique et Chimie Industriele in Paris where he received an Engineering Physics degree in 1924. Upon graduation he became Marie Curie's assistant at the Radium Institute. He married Irène Curie, Marie Curie's daughter, in 1927 and worked on many nuclear physics projects in collaboration with his wife. In 1930 he obtained his doctorate in Physics and in 1937 he became Professor of Physics at the Collège de France in Paris. In 1939 he confirmed the fission experiment announced by *Otto Hahn* and *Fritz Strassmann* and recognized the importance of the experiment in view of a possible chain reaction and its use for the development of nuclear weapons.

In 1935 Joliot and *Irène Joliot-Curie* shared the Nobel Prize in Chemistry "*in recognition of their synthesis of new radioactive elements*".

KERST, Donald William (1911–1993)

American physicist, educated at the University of Wisconsin in Madison where he received his doctorate in Physics in 1937. From 1938 to 1957 he worked through academic ranks to become Professor of Physics at the University of Illinois. He then worked in industry from 1957 to 1962 and from 1962 to 1980 he was Professor of Physics at the University of Wisconsin. Kerst made important contributions to the general design of particle accelerators, nuclear physics, medical physics, and plasma physics. He will be remembered best for this development of the betatron in 1940, a cyclic electron accelerator that accelerates electrons by magnetic induction. The machine found important use in industry, nuclear physics and medicine during the 1950s and 1960s before it was eclipsed by more practical linear accelerators.

KLEIN, Oskar (1894–1977)

Swedish-born theoretical physicist. Klein completed his doctoral dissertation at the University of Stockholm (Högskola) in 1921 and worked as physicist in Stockholm, Copenhagen, Lund and Ann Arbor. He is best known for introducing the relativistic wave equation (Klein-Gordon equation); for his collaboration with *Niels Bohr* on the principles of correspondence and complementarity; and for his derivation, with *Yoshio Nishina*, in 1929 of the equation for Compton scattering (Klein-Nishina equation). Klein's attempts to unify general relativity and electromagnetism by introducing a five-dimensional space-time resulted in a theory now known as the Kaluza-Klein theory.

LARMOR, Joseph (1857–1942)

Irish physicist, educated at Queen's University in Belfast where he received his B.A. and M.A. In 1877 he continued his studies in mathematics at the St. Johns College in Cambridge. In 1880 he returned to Ireland as Professor of Natural Philosophy at Queens College Galway. In 1885 he moved back to Cambridge as lecturer and in 1903 he became the Lucasian Chair of Mathematics succeeding George Stokes. He remained in Cambridge until retirement in 1932 upon which he returned to Ireland.

Larmor worked in several areas of physics such as electricity, dynamics, thermodynamics, and, most notably, in ether, the material postulated at the end of the 19th century as a medium pervading space and transmitting the electromagnetic radiation. He is best known for calculating the rate at which energy is radiated from a charged particle (Larmor law); for explaining the splitting of spectral lines by a magnetic field; and for the Larmor equation $\omega = \gamma \mathscr{B}$, where ω is the angular frequency of a precessing proton, γ the gyromagnetic constant, and $\mathscr{B}$ the magnetic field.

LAUE, Max von (1879–1960)

German physicist, educated at the University of Strassbourg where he studied mathematics, physics and chemistry, University of Göttingen and University of Berlin where he received his doctorate in Physics in 1903. He then worked for two years at the University of Göttingen, four years at the Institute for Theoretical Physics in Berlin, and three years at the University of Munich, before starting his series of Professorships in Physics in 1912 at the University of Zürich, 1914 at the University of Frankfurt, 1916 at the University of Würzburg and 1919 at the University of Berlin from which he retired in 1943.

Von Laue is best known for his discovery in 1912 of the diffraction of x rays on crystals. Since the wavelength of x rays was assumed to be of the order of inter-atomic separation in crystals, he surmised that crystalline structures behave like diffraction gratings for x rays. Von Laue's hypothesis was proven correct experimentally and established the wave nature of x rays and the regular internal structure of crystals. The crystalline structure essentially forms a three-dimensional grating, presenting a formidable problem to analyze. *William L. Bragg* proposed a simple solution to this problem now referred to as the Bragg equation. Von Laue also made notable contributions to the field of superconductivity where he collaborated with Hans Meissner who with Robert Ochsenfeld established that, when a superconductor in the presence of a magnetic field is cooled below a critical temperature, all of the magnetic flux is expelled from the interior of the sample.

The 1914 Nobel Prize in Physics was awarded to von Laue *"for his discovery of the diffraction of x rays by crystals"*.

LAUTERBUR, Paul Christian (born 1929)

American chemist, educated at the Case Institute of Technology in Cleveland (B.Sc. in chemistry in 1951) and University of Pittsburgh (Ph.D. in chemistry in 1962). His first academic position was at Stony Brook University as Associate Professor and from 1969 until 1985 as Professor of Chemistry. From 1985 until 1990 he was Professor of Chemistry at the University of Illinois at Chicago and since 1985 he is Professor and Director of the Biomedical MR Laboratory at the University of Illinois at Urbana-Champaign.

Being trained in nuclear magnetic resonance (NMR), Lauterbur started his academic career in this area. However, in the early 1970s when investigating proton NMR relaxation times of various tissues obtained from tumor-bearing rats, he observed large and consistent differences in relaxation times from various parts of the sacrificed animals. Some researchers were speculating that relaxation time measurements might supplement or replace the observations of cell structure in tissues by pathologists but Lauterbur objected to the invasive nature of the procedure. He surmised that there may be a way to locate the precise origin of the NMR signals in complex objects, and thus non-invasively form an image of their distribution in two or even three dimensions. He developed the method of creating a two dimensional image by introducing gradients into the NMR magnetic field, analyzing the characteristics of the emitted radio waves, and determining the location of their source. To allay fears by the general public of everything nuclear, the NMR imaging became known as magnetic resonance imaging or MRI.

Lauterbur shared the 2003 Nobel Prize in Physiology or Medicine with *Peter Mansfield "for their discoveries concerning magnetic resonance imaging"*.

LAWRENCE, Ernest Orlando (1900–1958)

American physicist, educated at the University of South Dakota (B.A. in Chemistry in 1922), University of Minnesota (M.A. in Chemistry in 1923) and Yale University (Ph.D. in Physics in 1925). He first worked at Yale as research fellow and Assistant Professor of Physics and was appointed Associate Professor at the University of California at Berkeley in 1928 and Professor of Physics in 1930. In 1936 he was appointed Director of the University's Radiation Laboratory and remained in these posts until his death in 1958.

The reputation of the Berkeley Physics department as an eminent world-class center of physics is largely based on Lawrence's efforts. He was not only an excellent physicist, he was also an excellent research leader, director of large-scale physics projects, and government advisor. Lawrence is best known for his invention of the cyclotron (in 1930), a cyclic accelerator that accelerates heavy charged particles to high kinetic energies for use in producing nuclear reactions in targets or for use in cancer therapy. During World War II Lawrence worked on the Manhattan project developing the atomic fis-

sion bomb. His research interests were also in the use of radiation in biology and medicine.

In 1939 Lawrence was awarded the Nobel Prize in Physics "*for the invention and development of the cyclotron and for results obtained with it, especially with regard to artificial radioactive elements*". Lawrence's name is honored by Lawrence Berkeley Laboratory in Berkeley, Lawrence Livermore National Laboratory in Livermore, California, and lawrencium, an artificial element with an atomic number 103.

LICHTENBERG, Georg Christoph (1742–1799)

German physicist and philosopher, educated at the University of Göttingen, where he also spent his whole professional life, from 1769 until 1785 as Assistant Professor of Physics and from 1785 until his death in 1799 as Professor of Physics.

In addition to physics, Lichtenberg taught many related subjects and was also an active researcher in many areas, most notably astronomy, chemistry, and mathematics. His most prominent research was in electricity and in 1777 he found that discharge of static electricity may form intriguing patters in a layer of dust, thereby discovering the basic principles of modern photocopying machines and xeroradiography. High voltage electrical discharges on the surface or inside of insulating materials often result in distinctive patterns that are referred to as Lichtenberg figures or "trees" in honor of their discoverer.

Lichtenberg is credited with suggesting that Euclid's axioms may not be the only basis for a valid geometry and his speculation was proven correct in the 1970s when *Benoit B. Mandelbrot*, a Polish-American mathematician, introduced the techniques of fractal geometry. Coincidentally, these techniques also produce patterns that are now referred to as Lichtenberg patterns.

Lichtenberg was also known as a philosopher who critically examined a range of philosophical questions and arrived at intriguing, interesting and often humorous conclusions. Many consider him the greatest German aphorist and his "Waste Books" contain many aphorisms and witticisms that are still relevant to modern societies.

LORENTZ, Hendrik Antoon (1853–1928)

Dutch physicist, educated at the University of Leiden where he obtained a B.Sc. degree in Mathematics and Physics in 1871 and a doctorate in Physics in 1875. In 1878 he was appointed to the Chair of Theoretical Physics at the University of Leiden and he stayed in Leiden his whole professional life.

Lorentz made numerous contributions to various areas of physics but is best known for his efforts to develop a single theory to unify electricity, magnetism and light. He postulated that atoms were composed of charged particles and that atoms emitted light following oscillations of these charged particles inside the atom. Lorentz further postulated that a strong magnetic field would affect these oscillations and thus the wavelength of the emitted

light. In 1896 Pieter Zeeman, a student of Lorentz, demonstrated the effect now known as the Zeeman effect. In 1904 Lorentz proposed a set of equations that relate the spatial and temporal coordinates for two systems moving at a large constant velocity with respect to each other. The equations are now called the Lorentz transformations and their prediction of increase in mass, shortening of length, and time dilation formed the basis of *Albert Einstein*'s special theory of relativity.

In 1902 Lorentz and Zeeman shared the Nobel Prize in Physics *"in recognition of the extraordinary service they rendered by their researches into the influence of magnetism upon radiation phenomena"*.

MANDELBROT, Benoit (born in 1924)

Polish-born American mathematician, educated in France at the École Polytechnique in Paris and the California Institute of Technology (Caltech) in Pasadena. Mandelbrot received his doctorate in Mathematics from the University of Paris in 1952. From 1949 until 1957 he was on staff at the Centre National de la Recherche Scientifique. In 1958 he joined the research staff at the IBM T.J. Watson Research Center in Yorktown Heights, New York and he remained with the IBM until his retirement in 1987 when he became Professor of Mathematical Sciences at Yale University.

Mandelbrot is best known as the founder of fractal geometry, a modern invention in contrast to the 2000 years old Euclidean geometry. He is also credited with coining the term "fractal". Man-made objects usually follow Euclidean geometry shapes, while objects in nature generally follow more complex rules defined by iterative or recursive algorithms. The most striking feature of fractal geometry is the self-similarity of objects or phenomena, implying that the fractal contains smaller components that replicate the whole fractal when magnified. In theory the fractal is composed of an infinite number of ever diminishing components, all of the same shape.

Mandelbrot discovered that self-similarity is a universal property that underlies the complex fractal shapes, illustrated its behavior mathematically and founded a completely new methodology for analyzing these complex systems. His name is now identified with a particular set of complex numbers which generate a type of fractal with very attractive properties (Mandelbrot Set).

MANSFIELD, Peter (born in 1933)

British physicist, educated at the Queen Mary College in London where he obtained his B.Sc. in Physics in 1959 and doctorate in Physics in 1962. He spent 1962-1964 as research associate at the University of Illinois in Urbana and 1964-1978 as lecturer and reader at the University of Nottingham. In 1979 he was appointed Professor of Physics at the University of Nottingham and since 1994 he is Emeritus Professor of Physics at the University of Nottingham.

Mansfield's doctoral thesis was on the physics of nuclear magnetic resonance (NMR), at the time used for studies of chemical structure, and he spent the 1960s perfecting his understanding of NMR techniques. In the early 1970s Mansfield began studies in the use of NMR for imaging and developed magnetic field gradient techniques for producing two-dimensional images in arbitrary planes through a human body. The term "nuclear" was dropped from NMR imaging and the technique is now referred to as magnetic resonance imaging or MRI. Mansfield is also credited with developing the MRI protocol called the "echo planar imaging" which in comparison to standard techniques allows a much faster acquisition of images and makes functional MRI (fMRI) possible.

Mansfield shared the 2003 Nobel Prize in Physiology or Medicine with *Paul C. Lauterbur* "*for their discoveries concerning magnetic resonance imaging*".

MARSDEN, Ernest (1889–1970)

New Zealand-born physicist who made a remarkable contribution to science in New Zealand and England. He studied physics at the University of Manchester and as a student of Ernest Rutherford, in collaboration with Hans Geiger, carried out the α-particle scattering experiments that inspired Rutherford to propose the atomic model, currently known as the Rutherford-Bohr model of the atom. In 1914 he returned to New Zealand to become Professor of Physics at Victoria University in Wellington. In addition to scientific work, he became involved with public service and helped in setting up the New Zealand Department of Scientific and Industrial Research. During World War II, he became involved with radar technology in defense work and in 1947 he was elected president of the Royal Society of New Zealand. He then returned to London as New Zealand's scientific liaison officer and "ambassador" for New Zealand science. In 1954 he retired to New Zealand and remained active on various advisory committees as well as in radiation research until his death in 1970.

MEITNER, Lise (1878–1968)

Austrian-born physicist who studied physics at the University of Vienna and was strongly influenced in her vision of physics by Ludwig Boltzmann, a leading theoretical physicist of the time. In 1907 Meitner moved to Berlin to work with *Max Planck* and at the University of Berlin she started a life-long friendship and professional association with radiochemist *Otto Hahn*. At the Berlin University both Meitner and Hahn were appointed as scientific associates and progressed through academic ranks to attain positions of professor.

During her early days in Berlin, Meitner discovered the element protactinium with atomic number $Z = 91$ and also discovered, two years before Auger, the non-radiative atomic transitions that are now referred to as the Auger effect. Meitner became the first female physics professor in Germany

but, despite her reputation as an excellent physicist, she, like many other Jewish scientists, had to leave Germany during the 1930s. She moved to Stockholm and left behind in Berlin her long-term collaborator and friend *Otto Hahn*, who at that time was working with *Fritz Strassmann*, an analytical chemist, on studies of uranium bombardment with neutrons. Their experiments, similarly to those reported by Irene Joliot-Curie and Pavle Savić were yielding surprising results suggesting that in neutron bombardment uranium was splitting into smaller atoms with atomic masses approximately half of that of uranium. In a letter Hahn described the uranium disintegration by neutron bombardment to Meitner in Stockholm and she, in collaboration with Otto Frisch, succeeded in providing a theoretical explanation for the uranium splitting and coined the term nuclear fission to name the process.

The 1944 Nobel Prize in Chemistry was awarded to Hahn "*for the discovery of the nuclear fission*". The Nobel Committee unfortunately ignored the contributions by Strassmann, Meitner and Frisch to the theoretical understanding of the nuclear fission process. Most texts dealing with the history of nuclear fission now recognize the four scientists: Hahn, Strassmann, Meitner, and Frisch as the discoverers of the fission process.

Despite several problems that occurred with recognizing Meitner's contributions to modern physics, her scientific work certainly was appreciated and is given the same ranking in importance as that of Marie Curie. In 1966 Meitner together with Hahn and Strassmann shared the prestigious Enrico Fermi Award. In honor of Meitner's contributions to modern physics the element with atomic number 109 was named meitnerium (Mt).

MENDELEYEV, Dmitri Ivanovič (1834–1907)

Russian physical chemist, educated at the University of St. Petersburg where he obtained his M.A. in Chemistry in 1856 and doctorate in Chemistry in 1865. The years between 1859 and 1861 Mendeleyev spent studying in Paris and Heidelberg. He worked as Professor of Chemistry at the Technical Institute of St. Petersburg and the University of St. Petersburg from 1862 until 1890 when he retired from his academic posts for political reasons. From 1893 until his death in 1907 he was Director of the Bureau of Weights and Measures in St. Petersburg.

While Mendeleyev made contributions in many areas of general chemistry as well as physical chemistry and was an excellent teacher, he is best known for his 1869 discovery of the Periodic Law and the development of the Periodic Table of Elements. Until his time elements were distinguished from one another by only one basic characteristic, the atomic mass, as proposed by John Dalton in 1805. By arranging the 63 then-known elements by atomic mass as well as similarities in their chemical properties, Mendeleyev obtained a table consisting of horizontal rows or periods and vertical columns or groups. He noticed several gaps in his Table of Elements and predicted that they represented elements not yet discovered. Shortly afterwards ele-

ments gallium, germanium and scandium were discovered filling three gaps in the table, thereby confirming the validity of Mendeleyev's Periodic Table of Elements. Mendeleyev's table of more than a century ago is very similar to the modern 21st century Periodic Table, except that the 111 elements of the modern periodic table are arranged according to their atomic number Z in contrast to Mendeleyev's table in which the 63 known elements were organized according to atomic mass. To honor Mendeleyev's work the element with atomic number Z of 101 is called mendelevium.

MILLIKAN, Robert Andrews (1868–1952)

American physicist, educated at Oberlin College (Ohio) and Columbia University in New York where he received a doctorate in Physics in 1895. He then spent a year at the Universities of Berlin and Götingen, before accepting a position at the University of Chicago in 1896. By 1910 he was Professor of Physics and remained in Chicago until 1921 when he was appointed Director of the Norman Bridge Laboratory of Physics at the California Institute of Technology (Caltech) in Pasadena. He retired in 1946.

Millikan was a gifted teacher and experimental physicist. During his early years at Chicago he authored and coauthored many physics textbooks to help and simplify the teaching of physics. As a scientist he made many important discoveries in electricity, optics and molecular physics. His earliest and best known success was the accurate determination, in 1910, of the electron charge with the "falling-drop method" now commonly referred to as the Millikan experiment. He also verified experimentally the Einstein's photoelectric effect equation and made the first direct photoelectric determination of Planck's quantum constant h.

The 1923 Nobel Prize in Physics was awarded to Millikan "*for his work on the elementary charge of electricity and on the photoelectric effect*".

MÖSSBAUER, Rudolf Ludwig (born in 1929)

German physicist, educated at the Technische Hochschule (Technical University) in Munich, where he received his doctorate in Physics in 1958, after carrying out the experimental portion of his thesis work in Heidelberg at the Institute for Physics of the Max Planck Institute for Medical Research. During 1959 Mössbauer worked as scientific assistant at the Technical University in Munich and from 1960 until 1962 as Professor of Physics at the California Institute of Technology (Caltech) in Pasadena. In 1962 he returned to the Technical Institute in Munich as Professor of Experimental Physics and stayed there his whole professional career except for the period 1972-1977 which he spent in Grenoble as the Director of the Max von Laue Institute.

Mössbauer is best known for his 1957 discovery of recoil-free gamma ray resonance absorption; a nuclear effect that is named after him and was used to verify *Albert Einstein*'s theory of relativity and to measure the magnetic field of atomic nuclei. The Mössbauer effect involves the emission and absorp-

tion of gamma rays by atomic nuclei. When a free excited nucleus emits a gamma photon, the nucleus recoils in order to conserve momentum. The nuclear recoil uses up a minute portion of the decay energy, so that the shift in the emitted photon energy prevents the absorption of the photon by another target nucleus of the same species. While working on his doctorate thesis in Heidelberg, Mössbauer discovered that, by fixing emitting and absorbing nuclei into a crystal lattice, the whole lattice gets involved in the recoil process, minimizing the recoil energy loss and creating an overlap between emission and absorption lines thereby enabling the resonant photon absorption process and creating an extremely sensitive detector of photon energy shifts.

Mössbauer received many awards and honorable degrees for his discovery; most notably, he shared with Robert Hofstadter the 1961 Nobel Prize in Physics *"for his researches concerning the resonance absorption of gamma radiation and his discovery in this connection of the effect which bears his name."* Hofstadter received his share of the 1961 Nobel Prize for his pioneering studies of electron scattering in atomic nuclei.

MOSELEY, Henry Gwen Jeffreys (1887–1915)

British physicist, educated at the University of Oxford where he graduated in 1910. He began his professional career at the University of Manchester as Lecturer in physics and research assistant under *Ernest Rutherford*.

Based on work by *Charles Barkla* who discovered characteristic x rays and on work of the team of *William Bragg* and *Lawrence Bragg* who studied x ray diffraction, Moseley undertook in 1913 a study of the K and L characteristic x rays emitted by then-known elements from aluminum to gold. He found that the square root of the frequencies of the emitted characteristic x-ray lines plotted against a suitably chosen integer Z yielded straight lines. Z was subsequently identified as the number of positive charges (protons) and the number of electrons in an atom and is now referred to as the atomic number Z. Moseley noticed gaps in his plots that corresponded to atomic numbers Z of 43, 61, and 75. The elements with $Z = 43$ (technetium) and $Z = 61$ (promethium) do not occur naturally but were produced artificially years later. The $Z = 75$ element (rhenium) is rare and was discovered only in 1925. Moseley thus found that the atomic number of an element can be deduced from the element's characteristic spectrum (non-destructive testing). He also established that the periodic table of elements should be arranged according to the atomic number Z rather than according to the atomic mass number A as was common at his time.

There is no question that Moseley during a short time of two years produced scientific results that were very important for the development of atomic and quantum physics and were clearly on the level worthy of Nobel Prize. Unfortunately, he perished during World War I shortly after starting his professional career in physics.

NISHINA, Yoshio (1890–1951)

Japanese physicist, educated at the University of Tokyo where he graduated in 1918. He worked three years as an assistant at the University of Tokyo and then spent several years in Europe: 1921-1923 at the University of Cambridge with *Ernest Rutherford* and 1923–1928 at the University of Copenhagen with *Niels Bohr*. From 1928 to 1948 he worked at the University of Tokyo.

Nishina is best known internationally for his collaboration with *Oskar Klein* on the cross section for Compton scattering in 1928 (Klein-Nishina formula). Upon return to Japan from Europe, Nishina introduced the study of nuclear and high energy physics in Japan and trained many young Japanese physicists in the nuclear field. During World War II Nishina was the central figure in the Japanese atomic weapons program that was competing with the American Manhattan project and using the same thermal uranium enrichment technique as the Americans. The race was tight; however, the compartmentalization of the Japanese nuclear weapons program over competing ambitions of the army, air force and the navy gave the Americans a definite advantage and eventual win in the nuclear weapons competition that resulted in the atomic bombs over Hiroshima and Nagasaki and Japanese immediate surrender in 1945.

PAULI, Wolfgang (1900–1958)

Austrian-born physicist, educated at the University of Munich where he obtained his doctorate in Physics in 1921. He spent one year at the University of Göttingen and one year at the University of Copenhagen before accepting a Lecturer position at the University of Hamburg (1923-1928). From 1928 to 1958 he held an appointment of Professor of Theoretical Physics at the Eidgenössische Technische Hochschule in Zürich. From 1940 to 1946 Pauli was a visiting professor at the Institute for Advanced Study in Princeton.

Pauli is known as an extremely gifted physicist of his time. He is best remembered for enunciating the existence of the neutrino in 1930 and for introducing the exclusion principle to govern the states of atomic electrons in general. The exclusion principle is now known as the Pauli Principle and contains three components. The first component states that no two electrons can be at the same place at the same time. The second component states that atomic electrons are characterized by four quantum numbers: principal, orbital, magnetic and spin. The third component states that no two electrons in an atom can occupy a state that is described by exactly the same set of the four quantum numbers. The exclusion principle was subsequently expanded to other electronic and fermionic systems, such as molecules and solids.

The 1945 Nobel Prize in Physics was awarded to Pauli *"for his discovery of the Exclusion Principle, also called the Pauli Principle"*.

PLANCK, Max Karl Ernst (1858–1947)

German physicist, educated at the University of Berlin and University of Munich where he received his doctorate in Physics in 1879. He worked as Assistant Professor at the University of Munich from 1880 until 1885, then Associate Professor at the University of Kiel until 1889 and Professor of Physics at the University of Berlin until his retirement in 1926.

Most of Planck's work was on the subject of thermodynamics in general and studies of entropy and second law of thermodynamics in particular. He was keenly interested in the blackbody problem and the inability of classical mechanics to predict the blackbody spectral distribution. Planck studied the blackbody spectrum in depth and concluded that it must be electromagnetic in nature. In contrast to classical equations that were formulated for blackbody radiation by Wien and Rayleigh, with Wien's equation working only at high frequencies and Rayleigh's working only at low frequencies, Planck formulated an equation that predicted accurately the whole range of applicable frequencies and is now known as Planck's equation for blackbody radiation. The derivation was based on the revolutionary idea that the energy emitted by a resonator can only take on discrete values or quanta, with the quantum energy ε equal to $h\nu$, where ν is the frequency and h a universal constant now referred to as the Planck's constant. Planck's idea of quantization has been successfully applied to the photoelectric effect by *Albert Einstein* and to the atomic model by *Niels Bohr*.

In 1918 Planck was awarded the Nobel Prize in Physics *"in recognition of the services he rendered to the advancement of Physics by his discovery of energy quanta"*. In addition to Planck's constant and Planck's formula, Planck's name and work are honored with the Max Planck Medal that is awarded annually as the highest distinction by the German Physical Society (Deutsche Physikalische Gesellschaft) and the Max Planck Society for the Advancement of Science that supports basic research at 80 research institutes focusing on research in biology, medicine, chemistry, physics, technology and humanities.

PURCELL, Edward Mills (1912–1997)

American physicist, educated at Purdue University in Indiana where he received his Bachelor's degree in Electrical Engineering in 1933 and Harvard where he received his doctorate in Physics in 1938. After serving for two years as Lecturer of physics at Harvard, he worked at the Massachusetts Institute of Technology on development of new microwave techniques. In 1945 Purcell returned to Harvard as Associate Professor of Physics and became Professor of Physics in 1949.

Purcell is best known for his 1946 discovery of nuclear magnetic resonance (NMR) with his students Robert Pound and Henry C. Torrey. NMR offers an elegant and precise way of determining chemical structure and properties of materials and is widely used not only in physics and chemistry but also in

medicine where, through the method of magnetic resonance imaging (MRI), it provides non-invasive means to image internal organs and tissues of patients.

In 1952 Purcell shared the Nobel Prize in Physics with *Felix Bloch* "*for their development of new methods for nuclear magnetic precision measurements and discoveries in connection therewith*".

RAYLEIGH, John William Strutt (1842–1919)

English mathematician and physicist who studied mathematics at the Trinity College in Cambridge. Being from an affluent family he set up his physics laboratory at home and made many contributions to applied mathematics and physics from his home laboratory. From 1879 to 1884 Rayleigh was Professor of Experimental Physics and Head of the Cavendish Laboratory at Cambridge, succeeding James Clark Maxwell. From 1887 to 1905 he was Professor of Natural Philosophy at the Royal Institution in London.

Rayleigh was a gifted researcher and made important contributions to all branches of physics known at his time, having worked in optics, acoustics, mechanics, thermodynamics, and electromagnetism. He is best known for explaining that the blue color of the sky arises from the scattering of light by dust particles in air and for relating the degree of light scattering to the wavelength of light (Rayleigh scattering). He also accurately defined the resolving power of a diffraction grating; established standards of electrical resistance, current, and electromotive force; discovered argon; and derived an equation describing the distribution of wavelengths in blackbody radiation (the equation applied only in the limit of large wavelengths).

In 1904 Rayleigh was awarded the Nobel Prize in Physics "*for his investigations of the densities of the most important gases and for his discovery of the noble gas argon in connection with these studies*". He discovered argon together with William Ramsey who obtained the 1904 Nobel Prize in Chemistry for his contribution to the discovery.

RICHARDSON, Owen Willans (1879–1959)

British physicist, educated at Trinity College in Cambridge from where he graduated in 1990 as a student of *Joseph J. Thomson* at the Cavendish Laboratory. He was appointed Professor of Physics at Princeton University in the United States in 1906 but in 1914 returned to England to become Professor of Physics at King's College of the University of London.

Richardson is best known for his work on thermionic emission of electrons from hot metallic objects that enabled the development of radio and television tubes as well as modern x-ray (Coolidge) tubes. He discovered the equation that relates the rate of electron emission to the absolute temperature of the metal. The equation is now referred to as the Richardson's law or the Richardson-Dushman equation.

In 1928 Richardson was awarded the Nobel Prize in Physics *"for his work on the thermionic phenomenon and especially for the law that is named after him"*.

RÖNTGEN, Wilhelm Conrad (1845–1923)

German physicist, educated at the University of Utrecht in Holland and University of Zürich where he obtained his doctorate in Physics in 1869. He worked as academic physicist at several German universities before accepting a position of Chair of Physics at the University of Giessen in 1979. From 1888 until 1900 he was Chair of Physics at the University of Würzburg and from 1900 until 1920 he was Chair of Physics at the University of Munich.

Röntgen was active in many areas of thermodynamics, mechanics and electricity but his notable research in these areas was eclipsed by his accidental discovery in 1895 of "a new kind of ray". The discovery occurred when Röntgen was studying cathode rays (now known as electrons, following the work of *Joseph J. Thomson*) in a Crookes tube, a fairly mundane and common experiment in physics departments at the end of the 19th century. He noticed that, when his energized Crookes tube was enclosed in a sealed black and light-tight envelope, a paper plate covered with barium platinocianide, a known fluorescent material, became fluorescent despite being far removed from the discharge tube. Röntgen concluded that he discovered an unknown type of radiation, much more penetrating than visible light and produced when cathode rays strike a material object inside the Crookes tube. He named the new radiation x rays and the term is generaly used around the World. However, in certain countries x rays are often called Röntgen rays. In 1912 *Max von Laue* showed with his crystal diffraction experiments that x rays are electromagnetic radiation similar to visible light but of much smaller wavelength. In tribute to Röntgen's contributions to modern physics the element with the atomic number 111 was named röntgenium (Rg).

In 1901 the first Nobel Prize in Physics was awarded to Röntgen *"in recognition of the extraordinary services he has rendered by the discovery of the remarkable rays subsequently named after him"*.

RUTHERFORD, Ernest (1871–1937)

New Zealand-born nuclear physicist, educated at the Canterbury College in Christchurch, New Zealand (B.Sc. in Mathematics and Physical Science in 1894) and at the Cavendish Laboratory of the Trinity College in Cambridge. He received his science doctorate from the University of New Zealand in 1901. Rutherford was one of the most illustrious physicists of all time and his professional career consists of three distinct periods: as MacDonald Professor of Physics at McGill University in Montreal (1898–1907); as Langworthy Professor of Physics at the University of Manchester (1908–1919); and as Cavendish Professor of Physics at the Cavendish Laboratory of Trinity College in Cambridge (1919–1937).

With the exception of his early work on magnetic properties of iron exposed to high frequency oscillations, Rutherford's career was intimately involved with the advent and growth of nuclear physics. Nature provided Rutherford with α particles, an important tool for probing the atom, and he used the tool in most of his exciting discoveries that revolutionized physics in particular and science in general.

Before moving to McGill in 1898, Rutherford worked with *Joseph J. Thomson* at the Cavendish Laboratory on detection of the just-discovered x rays (*Wilhelm Röntgen* in 1895) through studies of electrical conduction of gases caused by x-ray ionization of air. He then turned his attention to the just-discovered radiation emanating from uranium (*Henri Becquerel* in 1896) and radium (*Pierre Curie* and *Marie Curie* in 1898) and established that uranium radiation consists of at least two components, each of particulate nature but with different penetrating powers. He coined the names α and β particles for the two components.

During his 10 years at McGill, Rutherford published 80 research papers, many of them in collaboration with *Frederick Soddy*, a chemist who came to McGill from Oxford in 1900. Rutherford discovered the radon gas as well as gamma rays and speculated that the gamma rays were similar in nature to x rays. In collaboration with Soddy he described the transmutation of radioactive elements as a spontaneous disintegration of atoms and defined the half-life of a radioactive substance as the time it takes for its activity to drop to half of its original value. He noted that all atomic disintegrations were characterized by emissions of one or more of three kinds of rays: α, β, and γ.

During the Manchester period Rutherford determined that α particles were helium ions. He guided Hans Geiger and Ernest Marsden through the now-famous α particle scattering experiment and, based on the experimental results, in 1911 proposed a revolutionary model of the atom which was known to have a size of the order of 10^{-10} m. He proposed that most of the atomic mass is concentrated in a miniscule nucleus with a size of the order of 10^{-15} m and that the atomic electrons are distributed in a cloud around the nucleus. In 1913 *Niels Bohr* expanded Rutherford's nuclear atomic model by introducing the idea of the quantization of electrons' angular momenta and the resulting model is now called the Rutherford-Bohr atomic model. During his last year at Manchester, Rutherford discovered that nuclei of nitrogen, when bombarded with α particles, artificially disintegrate and produce protons in the process. Rutherford was thus first in achieving artificial transmutation of an element through a nuclear reaction.

During the Cambridge period Rutherford collaborated with many world-renowned physicists such as John Cocroft and Ernest Walton in designing a proton accelerator now called the Cocroft-Walton machine, and with *James Chadwick* in discovering the neutron in 1932. Rutherford's contributions to modern physics are honored with the element of atomic number 104 which was named rutherfordium (Rf).

In 1908 Rutherford was awarded the Nobel Prize in Chemistry *"for his investigations into the disintegration of the elements and the chemistry of radioactive substances"*.

RYDBERG, Johannes (1854–1919)

Swedish physicist, educated at Lund University. He obtained his Ph.D. in Mathematics in 1879 but worked all his professional life as a physicist at Lund University where he became Professor of Physics and Chairman of the Physics department.

Rydberg is best known for his discovery of a mathematical expression that gives the wavenumbers of spectral lines for various elements and includes a constant that is now referred to as the Rydberg constant ($R_\infty = 109\ 737\ \text{cm}^{-1}$). In honor of Rydberg's work in physics the absolute value of the ground state energy of the hydrogen atom is referred to as the Rydberg energy ($E_\text{R} = 13.61$ eV).

SCHRÖDINGER, Erwin (1887–1961)

Austrian physicist, educated at the University of Vienna where he received his doctorate in Physics in 1910. He served in the military during World War I and after the war moved through several short-term academic positions until in 1921 he accepted a Chair in Theoretical Physics at the University of Zürich. In 1927 he moved to the University of Berlin as Planck's successor. The rise of Hitler in 1933 convinced Schrödinger to leave Germany. After spending a year at Princeton University, he accepted a post at the University of Graz in his native Austria. The German annexation of Austria in 1938 forced him to move again, this time to the Institute for Advanced Studies in Dublin where he stayed until his retirement in 1955.

Schrödinger made many contributions to several areas of theoretical physics; however, he is best known for introducing wave mechanics into quantum mechanics. Quantum mechanics deals with motion and interactions of particles on an atomic scale and its main attribute is that it accounts for the discreteness (quantization) of physical quantities in contrast to classical mechanics in which physical quantities are assumed continuous. Examples of quantization were introduced by *Max Planck* who in 1900 postulated that oscillators in his blackbody emission theory can possess only certain quantized energies; *Albert Einstein* who in 1905 postulated that electromagnetic radiation exists only in discrete packets called photons; and *Niels Bohr* who in 1913 introduced the quantization of angular momenta of atomic orbital electrons. In addition, *Louis de Broglie* in 1924 introduced the concept of wave-particle duality.

Schrödinger's wave mechanics is based on the so-called Schrödinger's wave equation, a partial differential equation that describes the evolution over time of the wave function of a physical system. Schrödinger and other physicists have shown that many quantum mechanical problems can be solved by means

of the Schrödinger equation. The best known examples are: finite square well potential; infinite square well potential; potential step; simple harmonic oscillator; and hydrogen atom.

In 1933 Schrödinger shared the Nobel Prize in Physics with *Paul A.M. Dirac "for the discovery of new productive forms of atomic theory"*.

SEGRÈ, Emilio Gino (1905–1989)

Italian-born American nuclear physicist, educated at the University of Rome, where he received his doctorate in Physics as Enrico Fermi's first graduate student in 1928. In 1929 he worked as assistant at the University of Rome and spent the years 1930–1931 with Otto Stern in Hamburg and Pieter Heman in Amsterdam. In 1932 he became Assistant Professor of Physics at the University of Rome and in 1936 he was appointed Director of the Physics Laboratory at the University of Palermo. In 1938 Segrè came to Berkeley University, first as research associate then as physics lecturer. From 1943 until 1946 he was a group leader in the Los Alamos Laboratory of the Manhattan Project and from 1946 until 1972 he held an appointment of Professor of Physics at Berkeley. In 1974 he was appointed Professor of Physics at the University of Rome.

Segrè is best known for his participation with Enrico Fermi in neutron experiments bombarding uranium-238 with neutrons thereby creating several elements heavier than uranium. They also discovered thermal neutrons and must have unwittingly triggered uranium-235 fission during their experimentation. It was Otto Hahn and colleagues, however, who at about the same time discovered and explained nuclear fission. In 1937 Segrè discovered technetium, the first man-made element not found in nature and, as it subsequently turned out, of great importance to medical physics in general and nuclear medicine in particular. At Berkeley Segrè discovered plutonium-239 and established that it was fissionable just like uranium-235. Segrè made many other important contributions to nuclear physics and high-energy physics and, most notably, in collaboration with Owen Chamberlain discovered the antiproton. Segrè and Chamberlain shared the 1959 Nobel Prize in Physics *"for their discovery of the antiproton"*.

SELTZER, Stephen (born in 1940)

American physicist, educated at the Virginia Polytechnic Institute where he received his B.S. in Physics in 1962 and at the University of Maryland, College Park where he received his M.Sc. in Physics in 1973. In 1962 he joined the Radiation Theory Section at the National Bureau of Standards (NBS), now the National Institute of Standards and Technology (NIST), and has spent his professional career there, becoming the Director of the Photon and Charged-Particle Data Center at NIST in 1988 and the Leader of the Radiation Interactions and Dosimetry Group in 1994. He joined the International Commission on Radiation Units and Measurements (ICRU) in 1997.

Seltzer worked with *Martin Berger* on the development of Monte Carlo codes for coupled electron-photon transport in bulk media, including the transport-theoretical methods and algorithms used, and the interaction cross-section information for these radiations. Their ETRAN codes, underlying algorithms and cross-section data have been incorporated in most of the current radiation-transport Monte Carlo codes. Seltzer was instrumental in the development of extensive data for the production of bremsstrahlung by electrons (and positrons), electron and positron stopping powers, and a recent database of photon energy-transfer and energy-absorption coefficients. His earlier work included applications of Monte Carlo calculations to problems in space science, detector response, and space shielding, which led to the development of the SHIELDOSE code used for routine assessments of absorbed dose within spacecraft.

SODDY, Frederick (1877–1956)

British chemist, educated at Merton College in Oxford where he received his degree in Chemistry in 1898. After graduation he spent two years as research assistant in Oxford, then went to McGill University in Montreal where he worked with *Ernest Rutherford* on radioactivity. In 1902 Soddy returned to England to work with William Ramsay at the University College in London. He then served as Lecturer in Physical Chemistry at the University of Glasgow (1910–1914) and Professor of Chemistry at the University of Aberdeen (1914–1919). His last appointment was from 1919 until 1936 as Lees Professor of Chemistry at Oxford University.

Soddy is best known for his work in the physical and chemical aspects of radioactivity. He learned the basics of radioactivity with *Ernest Rutherford* at McGill University and then collaborated with William Ramsay at the University College. With Rutherford he confirmed the hypothesis of *Marie Curie* that radioactive decay was an atomic rather than chemical process, postulated that helium is a decay product of uranium, and formulated the radioactive disintegration law. With Ramsay he confirmed that the alpha particle was doubly ionized helium atom. Soddy's Glasgow period was his most productive period during which he enunciated the so-called displacement law and introduced the concept of isotopes. The displacement law states that emission of an alpha particle from a radioactive element causes the element to transmutate into a new element that moves back two places in the Periodic Table of Elements. The concept of isotopes states that certain elements exist in two or more forms that differ in atomic mass but are chemically indistinguishable.

Soddy was awarded the 1921 Nobel Prize in Chemistry "*for his contributions to our knowledge of the chemistry of radioactive substances, and his investigations into the origin and nature of isotopes*".

STERN, Otto (1888–1969)

German-born physicist educated in physical chemistry at the University of Breslau where he received his doctorate in 1912. He worked with *Albert Einstein* at the University of Prague and at the University of Zürich before becoming an Assistant Professor at the University of Frankfurt in 1914. During 1921–1922 he was an Associate Professor of Theoretical Physics at the University of Rostock and in 1923 he was appointed Professor of Physical Chemistry at the University of Hamburg. He remained in Hamburg until 1933 when he moved to the United States to become a Professor of Physics at the Carnegie Institute of Technology in Pittsburgh.

Stern is best known for the development of the molecular beam epitaxy, a technique that deposits one or more pure materials onto a single crystal wafer forming a perfect crystal; discovery of spin quantization in 1922 with *Walther Gerlach*; measurement of atomic magnetic moments; demonstration of the wave nature of atoms and molecules; and discovery of proton's magnetic moment.

Stern was awarded the 1943 Nobel Prize in Physics *"for his contribution to the development of the molecular ray method and his discovery of the magnetic moment of the proton"*.

STRASSMANN, Fritz (1902–1980)

German physical chemist, educated at the Technical University in Hannover where he received his doctorate in 1929. He worked as an analytical chemist at the Kaiser Wilhelm Institute for Chemistry in Berlin from 1934 until 1945. In 1946 Strassmann became Professor of Inorganic Chemistry at the University of Mainz. From 1945 to 1953 he was Director of the Chemistry department at the Max Planck Institute.

Strassmann is best known for his collaboration with *Otto Hahn* and *Lise Meitner* on experiments that in 1938 lead to the discovery of neutron induced fission of uranium atom. Strassmann's expertise in analytical chemistry helped with discovery of the light elements produced in the fission of uranium atoms. In 1966 the nuclear fission work by Hahn, Strassmann and Meitner was recognized with the Enrico Fermi Award.

THOMSON, George Paget (1892–1975)

British physicist, educated in mathematics and physics at the Trinity College of the University of Cambridge. He spent the first world war years in the British army and after the war spent three years as lecturer at the Corpus Christi College in Cambridge. In 1922 he was appointed Professor of Natural Philosophy at the University of Aberdeen in Scotland and from 1930 until 1952 he held an appointment of Professor of Physics at the Imperial College of the University of London. From 1952 until 1962 he was Master of the Corpus Christi College in Cambridge.

In Aberdeen Thomson carried out his most notable work studying the passage of electrons through thin metallic foils and observing diffraction phenomena which suggested that electrons could behave as waves despite being particles. This observation confirmed *Louis de Broglie*'s hypothesis of particle-wave duality surmising that particles should display properties of waves and that the product of the wavelength of the wave and momentum of the particle should equal to the Planck's quantum constant *h*. *Clinton J. Davisson* of Bell Labs in the United States noticed electron diffraction phenomena with a different kind of experiment.

In 1937 Thomson shared the Nobel Prize in Physics with Clinton J. Davisson "*for their experimental discovery of the diffraction of electrons by crystals*".

THOMSON, Joseph John (1856–1940)

British physicist, educated in mathematical physics at the Owens College in Manchester and the Trinity College in Cambridge. In 1884 he was named Cavendish Professor of Experimental Physics at Cambridge and he remained associated with the Trinity College for the rest of his life.

In 1987 Thomson discovered the electron while studying the electric discharge in a high vacuum cathode ray tube. In 1904 he proposed a model of the atom as a sphere of positively charged matter in which negatively charged electrons are dispersed randomly ("plum-pudding model of the atom").

In 1906 Thomson received the Nobel Prize in Physics *"in recognition of the great merits of his theoretical and experimental investigations on the conduction of electricity by gases."* Thomson was also an excellent teacher and seven of his former students also won Nobel Prizes in Physics during their professional careers.

Appendix 2. Roman Letter Symbols

A

a	acceleration; radius of atom; apex-vertex distance for a hyperbola; specific activity
$a_{\max}$	maximum specific activity
a_{o}	Bohr radius (0.5292 Å)
a_{TF}	Thomas-Fermi atomic radius
a_{theor}	theoretical specific activity
A	ampère (SI unit of current)
A	atomic mass number
Å	angstrom (unit of length or distance: 10^{-10} m)
$A_2(z)$	spatial spread of electron beam
$\mathscr{A}$	activity
$\mathscr{A}_{\mathrm{D}}$	daughter activity
$\mathscr{A}_{\mathrm{P}}$	parent activity
$\mathscr{A}_{\mathrm{sat}}$	saturation activity

B

b	barn (unit of area: 10^{-24} cm^2)
b	impact parameter
$b_{\max}$	maximum impact parameter
$b_{\min}$	minimum impact parameter
$\mathscr{B}$	magnetic field
B	build-up factor in broad beam attenuation
B_{col}	atomic stopping number in collision stopping power
B_{rad}	parameter in radiation stopping power
$B(E_{\mathrm{Ko}})$	bremsstrahlung yield for particle with initial kinetic energy E_{Ko}
Bq	becquerel (SI unit of activity)

C

c	speed of light in vacuum (3×10^8 m/s)
c_n	speed of light in medium
C	coulomb (unit of electric charge)
C	constant
Ci	curie (old unit of activity: 3.7×10^{10} s^{-1})
C_K	K-shell correction for stopping power

D

d	deuteron
d	distance; spacing
D	dose
$D_{\alpha-\mathrm{N}}$	distance of closest approach (between α particle and nucleus)
D_eff	effective characteristic distance
$D_\mathrm{eff}(\alpha - N)$	effective characteristic distance of closest approach between α particle and nucleus
$D_\mathrm{eff}(e - a)$	effective characteristic distance between electron and atom
$D_\mathrm{eff}(e - e)$	effective characteristic distance between the electron and orbital electron
$D_\mathrm{eff}(e - N)$	effective characteristic distance between electron and nucleus
D_s	surface dose

E

e	electron charge (1.6×10^{-19} C)
e$^-$	electron
e$^+$	positron
eV	electron volt (unit of energy: 1.6×10^{-19} J)
$e\phi$	work function
$\mathscr{E}$	electric field
E	energy
E_ab	energy absorbed
$\bar{E}_\mathrm{ab}$	average energy absorbed
E_B	binding energy
E_col	energy lost through collisions
E_i	initial total energy of charged particle
E_in	electric field for incident radiation
E_K	kinetic energy
E_{K_o}	initial kinetic energy of charged particle
$(E_\mathrm{K})_\mathrm{crit}$	critical kinetic energy
$(E_\mathrm{K})_\mathrm{D}$	recoil kinetic energy of the daughter
$(E_\mathrm{K})_\mathrm{f}$	final kinetic energy

$(E_K)_i$	initial kinetic energy
$(E_K)_{IC}$	kinetic energy of conversion electron
$(E_K)_{max}$	maximum kinetic energy
$(E_K)_n$	kinetic energy of incident neutron
$(E_K)_{thr}$	threshold kinetic energy
E_n	allowed energy state (eigenvalue)
E_o	rest energy
E_{out}	electric field for scattered radiation
E_p	barrier potential
E_R	Rydberg energy
E_{rad}	energy radiated by charged particle
E_{thr}	threshold energy
E_{tr}	energy transferred
$\bar{E}_{tr}$	average energy transferred
E_v	energy of neutrino
$\bar{E}_{tr}^{\kappa}$	average energy transferred from photons to charged particles in pair production
$\bar{E}_{tr}^{\sigma}$	average energy transferred from photons to electrons in Compton effect
$\bar{E}_{tr}^{\tau}$	average energy transferred from photons to electrons in photoeffect
E_{β}	energy of beta particle
$(E_{\beta})_{max}$	maximum kinetic energy of electron or positron in β decay
E_{γ}	energy of gamma photon
$(E_{\gamma})_{thr}$	threshold energy for pair production

F

f	function; theoretical activity fraction
f^{κ}	mean fraction of energy transferred from photons to charged particles in pair production
f^{σ}	mean fraction of energy transferred from photons to electrons in Compton effect
f^{τ}	mean fraction of energy transferred from photons to electrons in photoelectric effect
fm	femtometer (10^{-15} m); fermi
F	force
F_{coul}	Coulomb force
F_{KN}	Klein-Nishina form factor
F_L	Lorentz force
F_n	neutron kerma factor
$F(x, Z)$	atomic form factor
F^+	stopping power function for positrons
F^-	stopping power function for electrons

G

g	gram (unit of mass: 10^{-3} kg)
$\bar{g}$	radiative fraction
G	Newtonian gravitational constant
Gy	gray (SI unit of kerma and dose: 1 J/kg)

H

h	hour (unit of time)
h	Planck's constant (6.626×10^{-34} J·s)
H	hydrogen
H	equivalent dose [H] hamiltonian operator
Hz	unit of frequency (s^{-1})
$\hbar$	reduced Planck's constant ($h/2\pi$)

I

$\mathscr{I}$	magnitude of Poynting vector; intensity of emitted radiation
I	electric current; mean ionization/excitation potential; beam intensity; radiation intensity

J

j	current density; quantum number in spin-orbit interaction
J	joule (SI unit of energy)

K

k	wave number
keV	kiloelectronvolt (unit of energy: 10^3 eV)
kg	kilogram (SI unit of mass)
$k(\mathrm{K}_\alpha)$	wave number for K_α transition
kVp	kilovolt peak (in x-ray tubes)
k^*	ratio $\sigma_\mathrm{P}/\sigma_\mathrm{D}$ in neutron activation
K	$n = 1$ allowed shell (orbit) in an atom; Kelvin temperature
K	kerma
K_col	collision kerma
K_rad	radiative kerma
K_α	characteristic transition from L shell to K shell

L

l	length

L	$n = 2$ allowed shell (orbit) in an atom
L	angular momentum
L_Δ	restricted collision mass stopping power
ℓ	orbital quantum number; distance; path length

M

m	meter (SI unit of length or distance)
m	mass; magnetic quantum number; decay factor in parent-daughter-granddaughter decay; activation factor in nuclear activation; integer in Bragg relationship
m_e	electron rest mass (0.5110 MeV/c^2)
m_ℓ	magnetic quantum number
m_n	neutron rest mass (939.6 MeV/c^2)
m_o	rest mass of particle
m_p	proton rest mass (938.3 MeV/c^2)
m_α	rest mass of α particle
$m(\upsilon)$	relativistic mass m at velocity υ
m^*	modified activation factor
$\mathcal{M}$	mass of atom (atomic mass)
M	$n = 3$ allowed shell (orbit) in an atom
M	rest mass of nucleus (nuclear mass)
MeV	megaeletronvolt (unit of energy: 10^6 eV)
MHz	megahertz (unit of frequency: 10^6 Hz)
MV	megavoltage (in linacs)
$M(Z, A)$	nuclear mass in atomic mass units
$\mathcal{M}(Z, A)$	atomic mass in atomic mass units

N

n	neutron
nm	nanometer (unit of length or distance: 10^{-9} m)
n	principal quantum number; index of refraction
n_i	initial principal quantum number
n_f	final principal quantum number
$n^\square$	number of atoms per volume
N	$n = 4$ allowed shell (orbit) in an atom
N	number of radioactive nuclei; number of experiments in central limit theorem; number or monoenergetic electrons in medium
N_a	number of atoms
N_A	Avogadro's number (6.022×10^{23} atom/gram-atom)
N_e	number of electrons
N_t/m	number of specific nuclei per unit mass of tissue

P

p	proton
p	momentum
p_e	electron momentum
p_ν	photon momentum
P	power; probability
$P(\varepsilon, Z)$	pair production function
Ps	positronium
P_K	fraction of photoelectric interactions that occur in the K shell
P_n	fraction of photoelectric interactions that occur in the M shell

Q

q	charge
Q	charge; nuclear reaction energy; Q value
$\bar{Q}$	expectation (mean) value of physical quantity Q
$[Q]$	operator associated with the physical quantity Q
Q_{EC}	decay energy (Q value) for electron capture
Q_{IC}	decay energy (Q value) for internal conversion
Q_α	decay energy (Q value) for α decay
Q_β	decay energy (Q value) for beta decay
Q_P	decay energy (Q value) for gamma decay

R

r	radius vector; separation between two interacting particles
rad	unit of absorbed dose (100 erg/g); radian
r_e	classical electron radius (2.818 fm)
r_n	radius of the n-th allowed Bohr orbit
$\bar{r}$	average electron radius
R	roentgen (unit of exposure: 2.58×10^{-4} C/kg$_{air}$)
R	radial wave function; radius (of nucleus); reaction rate
$\bar{R}$	average range
R_{CSDA}	continuous slowing down approximation range
R_H	Rydberg constant for hydrogen (109 678 cm^{-1})
R_o	nuclear radius constant (1.2 or 1.4 fm)
$R_{\alpha-N}$	distance between the α particle and nucleus in a non-direct hit collision
R_∞	Rydberg constant assuming an infinite nuclear mass (109 737 cm^{-1})

S

s	second (unit of time)
s	spin quantum number
S	mass stopping power: Poynting vector
$\bar{S}$	average total mass stopping power
S_{col}	mass collision stopping power (unrestricted)
$\bar{S}_{\text{col}}$	average mass collision stopping power
S_{in}	Poynting vector of incident radiation
$\bar{S}_{\text{in}}$	average Poynting vector of incident radiation
S_{out}	Poynting vector of scattered radiation
$\bar{S}_{\text{out}}$	average Poynting vector of scattered radiation
S_{rad}	mass radiative stopping power
S_{tot}	total mass stopping power
Sv	sievert (unit of equivalent dose)
$S(x, Z)$	incoherent scattering function

T

t	triton
t	time; thickness of absorber in mass angular scattering power
$t_{\max}$	characteristic time in nuclear decay series or nuclear activation
$t_{1/2}$	half life
T	temperature; angular scattering power; temporal function
T/ρ	mass angular scattering power

U

u	atomic mass unit (931.5 MeV/c^2); particle velocity after collision

V

υ	velocity
υ_{thr}	threshold velocity in Cerenkov effect
V	volt (unit of potential difference)
V	applied potential; volume; potential energy
$V_{\text{TF}}(r)$	Thomas-Fermi potential

W

w_{R}	radiation weighting factor
W	transmitted particle in weak interaction

X

x	momentum transfer variable $(x = \sin(\theta/2)/\lambda)$; normalized time $x = t/t_{1/2}$; horizontal axis in cartesian coordinate system; coordinate in cartesian coordinate system
x	photon originating in an atomic transition
x_{f}	final particle position
x_{i}	initial particle position
x_{o}	target thickness
$\bar{x}$	mean free path
$(x_{\max})_{\mathrm{D}}$	maximum normalized characteristic time of the daughter
$x_{1/10}$	tenth value layer
$x_{1/2}$	half-value layer
$_{Z}^{A}\mathrm{X}$	nucleus with symbol X, atomic mass number A and atomic number Z
X	exposure
X_{o}	target thickness; radiative length

Y

y	vertical axis in cartesian coordinate system; coordinate in cartesian coordinate system
y	year (unit of time)
y_{P}	normalized activity
$(y_{\max})_{\mathrm{D}}$	maximum normalized daughter activity
Y_{D}	radioactivation yield of the daughter
y_{P}	normalized parent activity

Z

z	atomic number of the projectile; depth in phantom; coordinate in cartesian coordinate system
$z_{\max}$	depth of dose maximum
Z	atomic number
Z_{eff}	effective atomic number
Z^{o}	transmitted particle in weak interaction

Appendix 3. Greek Letter Symbols

α

α	fine structure constant (1/137); ratio σ_P/σ_D; nucleus of helium atom (alpha particle)
α_{IC}	internal conversion factor

β

β	normalized particle velocity (υ/c)
β^+	beta plus particle (positron)
β^-	beta minus particle (electron)

γ

γ	photon originating in a nuclear transition; ratio of total to rest energy of a particle; ratio of total to rest mass of a particle

δ

δ	polarization (density effect) correction for stopping power; delta particle (electron)
Δ	cut-off energy in restricted stopping power

ε

ε	eccentricity of hyperbola; normalized photon energy: $\varepsilon = h\nu/(m_e c^2)$
ε^*	ratio λ_D^*/λ_D
ε_o	electric permittivity of vacuum

θ

θ	scattering angle for a single scattering event; scattering angle of projectile in projectile/target collision; scattering angle of photon

θ_{cer} Čerenkov characteristic angle

$\theta_{\max}$ characteristic angle in bremsstrahlung production; maximum scattering angle

$\theta_{\min}$ minimum scattering angle

θ_{R} characteristic angle for Rayleigh scattering

Θ scattering angle for multiple scattering

η

η pair production parameter

κ

κ linear attenuation coefficient for pair production

$_{\mathrm{a}}\kappa$ atomic attenuation coefficient for pair production

κ/ρ mass attenuation coefficient for pair production

λ

λ wavelength; separation constant; decay constant

λ_{c} Compton wavelength

λ_{D} decay constant of daughter

λ_{D}^{*} modified decay constant of daughter

λ_{p} decay constant of parent

Λ separation constant

μ

μ linear attenuation coefficient; reduced mass

μ_{ab} linear energy absorption coefficient

μ_{m} mass attenuation coefficient

μ_{o} magnetic permeability of vacuum

μ_{tr} linear energy transfer coefficient

μ/ρ mass attenuation coefficient

$(\mu/\rho)_{\mathrm{ab}}$ mass energy absorption coefficient

$(\mu/\rho)_{\mathrm{tr}}$ mass energy transfer coefficient

$_{\mathrm{a}}\mu$ atomic attenuation coefficient

$_{\mathrm{e}}\mu$ electronic attenuation coefficient

$\mu\mathrm{m}$ unit of length or distance (10^{-6} m)

ν

ν frequency

ν_{eq} photon frequency at which the atomic cross sections for Rayleigh and Compton scattering are equal

| ν_{orb} | orbital frequency |
| ν_{trans} | transition frequency |

$$\xi$$

| ξ | ratio between daughter and parent activities at time t |

$$\pi$$

| π | pi meson (pion) |

$$\rho$$

| ρ | density; energy density |

$$\sigma$$

σ	cross section; linear attenuation coefficient
σ_{c}	Compton cross section (attenuation coefficient)
$\sigma_{\mathrm{c}}^{\mathrm{KN}}$	Klein-Nishina cross section for Compton effect
$_{\mathrm{a}}\sigma_{\mathrm{c}}$	atomic attenuation coefficient for Compton effect
$_{\mathrm{e}}\sigma_{\mathrm{c}}$	electronic attenuation coefficient for Compton effect
σ_{D}	daughter cross section in particle radioactivation
σ_{P}	parent cross section in particle radioactivation
σ_{pn}	cross section for photo-nuclear interaction
σ_{R}	Rayleigh cross section (linear attenuation coefficient)
σ_{Ruth}	cross section for Rutherford scattering
σ_{Th}	Thomson cross section (linear attenuation coefficient for Thomson scattering)
$_{\mathrm{a}}\sigma$	atomic cross section (in $\mathrm{cm}^2/\mathrm{atom}$)
$_{\mathrm{e}}\sigma$	electronic cross section (in $\mathrm{cm}^2/\mathrm{electron}$)

$$\tau$$

τ	linear attenuation coefficient for photoeffect; normalized electron kinetic energy; average (mean) life
$_{\mathrm{a}}\tau$	atomic attenuation coefficient for photoelectric effect
τ/ρ	mass attenuation coefficient for photoelectric effect

$$\phi$$

| ϕ | angle between radius vector and axis of symmetry on a hyperbola; recoil angle of the target in projectile/target collision; neutron recoil angle in elastic scattering on nucleus |

φ particle fluence
$\dot{\varphi}$ particle fluence rate

χ

χ homogeneity factor

ψ

ψ wavefunction (eigenfunction) depending on spatial coordinates; energy fluence
Ψ wavefunction depending on spatial and temporal coordinates

ω

ω fluorescent yield; angular frequency
ω_K fluorescent yield for K-shell transition
Ω solid angle

Appendix 4. Acronyms

BNCT	Boron Neutron Capture Therapy
BNL	Brookhaven National Laboratory
CODATA	Committee on Data for Science and Technology
CPA	Charged Particle Activation
CPE	Charged Particle Equilibrium
CSDA	Continuous Slowing Down Approximation
CT	Computerized Tomography
DT	Deuterium-Tritium
EC	Electron Capture
EM	Electromagnetic
FDG	Fluoro-deoxy-glucose
FWHM	Full Width at Half Maximum
HVL	Half Value Layer
IAEA	International Atomic Energy Agency
IC	Internal Conversion
ICRP	International Commission on Radiation Protection
ICRU	International Commission on Radiation Units and Measurements
IP	Ionization Potential
KN	Klein-Nishina
LINAC	Linear Accelerator
MFP	Mean Free Path
MLC	Multi Leaf Collimator
MRI	Magnetic Resonance Imaging
MV	Megavoltage
NDS	Nuclear Data Section
NIST	National Institute of Standards and Technology
NNDC	National Nuclear Data Center
OER	Oxygen Enhancement Ratio
PET	Positron Emission Tomography
RF	Radiofrequency
SF	Spontaneous Fission
SI	Système International
STP	Standard Temperature and Pressure
TVL	Tenth Value Layer

Appendix 5. Electronic Databases of Interest in Nuclear and Medical Physics

Bibliography of Photon Attenuation Measurements
J. H. Hubbell

This bibliography contains papers (1907–1995) reporting absolute measurements of photon (XUV, x-ray, gamma-ray, bremsstrahlung) total interaction cross sections or attenuation coefficients for the elements and some compounds used in a variety of medical, industrial, defense, and scientific applications. The energy range covered is from 10 eV to 13.5 GeV.

`www.physics.nist.gov/PhysRefData/photoncs/html/attencoef.html`

Elemental Data Index
M.A. Zucker, A.R. Kishore, and R.A. Dragoset

The Elemental Data Index provides access to the holdings of *National Institute for Science and Technology* (NIST) Physics Laboratory online data organized by element. It is intended to simplify the process of retrieving online scientific data for a specific element.

`www.physics.nist.gov/PhysRefData/Elements/cover.html`

Fundamental Physical Constants
CODATA

CODATA, the *Committee on Data for Science and Technology*, is an interdisciplinary scientific committee of the *International Council for Science* (ICSU), which works to improve the quality, reliability, management and accessibility of data of importance to all fields of science and technology. The CODATA committee was established in 1966 with its secretariat housed at 51, Boulevard de Montmorency, 75016 Paris, France. It provides scientists and engineers with access to international data activities for increased awareness, direct cooperation and new knowledge. The committee was established to promote and encourage, on a world wide basis, the compilation, evaluation and dissemination of reliable numerical data of importance to science and technology. Today 23 countries are members, and 14 International Scientific Unions have assigned liaison delegates.

`www.codata.org`

Fundamental Physical Constants
The NIST Reference on Constants, Units, and Uncertainty.

`www.physics.nist.gov/cuu/constants/`

Ground Levels and Ionization Energies for the Neutral Atoms
W.C. Martin, A. Musgrove, S. Kotochigova, and J.E. Sansonetti

This table gives the principal ionization energies (in eV) for the neutral atoms from hydrogen ($Z = 1$) through rutherfordium ($Z = 104$). The spectroscopy notations for the electron configurations and term names for the ground levels are also included.

`www.physics.nist.gov/PhysRefData/IonEnergy/ionEnergy.html`

International System of Units (SI)
The NIST Reference on Constants, Units, and Uncertainty

The SI system of units is founded on seven SI base units for seven base quantities that are assumed to be mutually independent. The SI base units as well as many examples of derived units are given.

`www.physics.nist.gov/cuu/Units/units.html`

Nuclear Data

The National Nuclear Data Center (NNDC) of the *Brookhaven National Laboratory* (BNL) in the USA developed a software product (NuDat 2) that allows users to search and plot nuclear structure and nuclear decay data interactively. The program provides an interface between web users and several databases containing nuclear structure, nuclear decay and some neutron-induced nuclear reaction information. Using NuDat 2, it is possible to search for nuclear level properties (energy, half-life, spin-parity), gamma-ray information (energy, intensity, multipolarity, coincidences), radiation information following nuclear decay (energy, intensity, dose), and neutron-induced reaction data from the BNL-325 book (thermal cross section and resonance integral). The information provided by NuDat 2 can be seen in tables, level schemes and an interactive chart of nuclei. The software provides three different search forms: one for levels and gammas, a second one for decay-related information, and a third one for searching the Nuclear Wallet Cards file.

`www.nndc.bnl.gov/NuDat2/`

Nuclear Data Services

The Nuclear Data Section (NDS) of the *International Atomic Energy Agency* (IAEA) of Vienna, Austria maintains several major databases as well as nuclear databases and files, such as: ENDF – evaluated nuclear reaction cross section libraries; ENSDF – evaluated nuclear structure and decay data; EXFOR – experimental nuclear reaction data; CINDA – neutron reaction data

bibliography; NSR – nuclear science references; NuDat 2.0 – selected evaluated nuclear data; Wallet cards – ground and metastable state properties; Masses 2003 – atomic mass evaluation data file; Thermal neutron capture gamma rays; Q-values and Thresholds.

`www-nds.iaea.or.at`

Nuclear Energy Agency Data Bank

The nuclear energy agency data bank of the Organization for Economic Co-operation and Development (OECD) maintains a nuclear database containing general information, evaluated nuclear reaction data, format manuals, pre-processed reaction data, atomic masses, and computer codes.

`www.nea.fr/html/databank/`

Photon Cross Sections Database: XCOM
M.J. Berger, J.H. Hubbell, S.M. Seltzer, J.S. Coursey, and D.S. Zucker

A web database is provided which can be used to calculate photon cross sections for scattering, photoelectric absorption and pair production, as well as total attenuation coefficients, for any element, compound or mixture ($Z \leq 100$) at energies from 1 keV to 100 GeV.

`www.physics.nist.gov/PhysRefData/Xcom/Text/XCOM.html`

Stopping-Power and Range Tables for Electrons, Protons, and Helium Ions
M.J. Berger, J.S. Coursey, and M.A. Zucker

The databases ESTAR, PSTAR, and ASTAR calculate stopping-power and range tables for electrons, protons, or helium ions, according to methods described in ICRU Reports 37 and 49. Stopping-power and range tables can be calculated for electrons in any user-specified material and for protons and helium ions in 74 materials.

`www.physics.nist.gov/PhysRefData/Star/Text/contents.html`

X-Ray Form Factor, Attenuation, and Scattering Tables
C.T. Chantler, K. Olsen, R.A. Dragoset, A.R. Kishore, S.A. Kotochigova, and D.S. Zucker

Detailed Tabulation of Atomic Form Factors, Photoelectric Absorption and Scattering Cross Section, and Mass Attenuation Coefficients for Z from 1 to 92. The primary interactions of x-rays with isolated atoms from $Z = 1$ (hydrogen) to $Z = 92$ (uranium) are described and computed within a self-consistent Dirac-Hartree-Fock framework. The results are provided over the energy range from either 1 eV or 10 eV to 433 keV, depending on the atom. Self-consistent values of the $f1$ and $f2$ components of the atomic scattering factors are tabulated, together with the photoelectric attenuation coefficient τ/ρ and the K-shell component τ_{K}/ρ, the scattering attenuation coefficient

σ/ρ (coh + inc), the mass attenuation coefficient μ/ρ, and the linear attenuation coefficient μ, as functions of energy and wavelength.

www.physics.nist.gov/PhysRefData/FFast/Text/cover.html

X-Ray Mass Attenuation Coefficients
and Mass Energy-Absorption Coefficients
J.H. Hubbell and S.M. Seltzer

Tables and graphs of the photon mass attenuation coefficient μ/ρ and the mass energy-absorption coefficient μ_{en}/ρ are presented for all elements from $Z = 1$ to $Z = 92$, and for 48 compounds and mixtures of radiological interest. The tables cover energies of the photon (x-ray, gamma ray, bremsstrahlung) from 1 keV to 20 MeV.

www.physics.nist.gov/PhysRefData/XrayMassCoef/cover.html

X-ray Transition Energies
R.D. Deslattes, E.G. Kessler Jr., P. Indelicato, L. de Billy, E. Lindroth, J. Anton, J.S. Coursey, D.J. Schwab, K. Olsen, and R.A. Dragoset

This X-ray transition table provides the energies and wavelengths for the K and L transitions connecting energy levels having principal quantum numbers $n = 1, 2, 3$, and 4. The elements covered include $Z = 10$, neon to $Z = 100$, fermium. There are two unique features of this database: (1) all experimental values are on a scale consistent with the International System of measurement (the SI) and the numerical values are determined using constants from the Recommended Values of the Fundamental Physical Constants: 1998 and (2) accurate theoretical estimates are included for all transitions.

www.physics.nist.gov/PhysRefData/XrayTrans/index.html

Appendix 6. International Organizations

whose mission statements fully or partially address radiation protection and the use of ionizing radiation in medicine:

European Federation of Organisations in Medical Physics (EFOMP)
Dijon, France   www.efomp.org

European Society for Therapeutic Radiology and Oncology (ESTRO)
Brussels, Belgium   www.estro.be

International Atomic Energy Agency (IAEA)
Vienna, Austria   www.iaea.org

International Commission on Radiological Protection (ICRP)
Stockholm, Sweden   www.icrp.org

International Commission on Radiation Units and Measurements (ICRU)
Bethesda, Maryland, USA   www.icru.org

International Electrotechnical Commission (IEC)
Geneva, Switzerland   www.iec.ch

International Organisation for Standardization (ISO)
Geneva, Switzerland   www.iso.org

International Organisation of Medical Physics (IOMP)
                                       www.iomp.org

International Radiation Protection Association (IRPA)
Fortenay-aux-Roses, France   www.irpa.net

International Society of Radiology (ISR)
Bethesda, Maryland, USA   www.isradiology.org

Pan American Health Organization (PAHO)
Washington, D.C., USA   www.paho.org

Radiological Society of North America (RSNA)
Oak Brook, Illinois, USA   www.rsna.org

World Health Organisation (WHO)
Geneva, Switzerland   www.who.int

Index